Numerical Simulation of Unsteady Separated Flows

Andrea Petrocchi

Submitted in fulfilment of the requirements for the
Degree of Doctor of Philosophy

James Watt School of Engineering
College of Science and Engineering
University of Glasgow

November 2023

Abstract

Transonic buffet is a phenomenon occurring at particular flight conditions and has an adverse effect on structural integrity, controllability, and passenger safety. The research carried out so far evidenced a lack of accuracy in the prediction of this phenomenon and high costs associated with numerical simulations. Moreover, a variety of flow control strategies were proposed in recent years, all presenting disadvantages in terms of aerodynamic performance, ease of implementation, and reduction of engine efficiency. This thesis studies transonic buffet by means of computational fluid dynamics and aims at expanding the current state of the art by filling gaps in the literature. In particular, this work focuses on buffet prediction by means of time marching simulations and, in a second part, engineeristic criteria are investigated. In the last part, the problem of flow control is addressed.

A detailed survey of past works was carried out with the aim of determining the optimal computational strategy and a detailed test case for this study, and understanding the current research status on transonic buffet and its control. The conclusion of the survey motivated the development of the rest of the thesis.

A Partially-Averaged Navier-Stokes approach was then used, as a good compromise between computational costs and accuracy. The method is first validated on a circular cylinder in the subcritical regime by comparison against available experiments. Several approaches targeting an adequate reduction of eddy viscosity around the body were proposed in the literature, and the most promising were validated here. The use of the method was then extended to transonic buffet. A comparison between two-dimensional and three-dimensional buffet on unswept wings confirms the substantial differences between 2D and 3D buffet, and detailed descriptions of the buffet dynamics, spectral content, and flow topology are given.

To avoid the costs associated with time marching simulations, engineeristic criteria, based on steady simulations, were used for 2D aerofoil sections. Their accuracy was validated against available datasets for buffet onset. An algorithm combining the aforementioned criteria with an adjoint method was formulated and validated on the same test cases, to obtain a reduction of the computer costs without loss of accuracy.

A second algorithm was then proposed. It uses the harmonic balance method to estimate the load oscillations at several flow conditions and detect buffet. The harmonic balance gives additional information on dynamic quantities and allows for the description of buffet in its phases over a period of oscillations. The advantages and limitations of this method over the engineeristic criteria are pointed out.

Finally, two flow control devices, i.e. spoilers and upper trailing edge flaps, were modelled on 2D and 3D configurations. Their ability to alleviate buffet was investigated and differences between infinite and finite-extent devices were described. The role of piloting in coupling with automatic flow control was briefly investigated.

Declaration

I certify that the thesis presented here for examination for a PhD degree of the University of Glasgow is solely my own work other than where I have clearly indicated that it is the work of others (in which case the extent of any work carried out jointly by me and any other person is clearly identified in it) and that the thesis has not been edited by a third party beyond what is permitted by the University's PGR Code of Practice.

I declare that the thesis does not include work forming part of a thesis presented successfully for another degree.

I declare that this thesis has been produced in accordance with the University of Glasgow's Code of Good Practice in Research.

I acknowledge that if any issues are raised regarding good research practice based on review of the thesis, the examination may be postponed pending the outcome of any investigation of the issues.

November 2023

.....

Andrea Petrocchi

Acknowledgements

The financial support of TEAMAero European project No. 860909 - Towards Effective Flow Control and Mitigation of Shock Effects In Aeronautical Applications is gratefully acknowledged, as well as the use of the Cirrus system of EPCC.

I want to express my gratitude to my Ph.D. supervisor George Barakos, who smartly selected me for this position, for his committment and technical support over the past three years, and for being a person to learn a lot from.

Taking on a three-year-long PhD and moving abroad meant taking a risk. My family supported me unconditionally. They did and they will, no matter the decision, no matter whether right or wrong. *Thank you for that*.

It also meant testing the boundaries of relationships and leaving people behind. I guess it is natural selection. Anyway, I met very interesting people. With some of them, I shared the fate - at times ingrateful - of doing a PhD. TEAMAero meant a lot of fun, making friends in unexpected situations, and having a break from the daily routine. *It was a pleasure to meet you all. Ciao Puto*.

If the PhD thesis was a paper, the other authors would be my colleagues from the CFD Lab. They have not actively contributed to my work and probably do not even know what I have been working on. Still, they have been precious people who have become good friends over time. *Thank you for the moments of daily lightness. Your presence made my journey much easier. Total shamble.*

Thanks to my lifelong friends from Italy, who have almost never disappointed. They bridged the physical distance between us by being on my side when I most needed it, asking for nothing in return. *Your effort and kindness are not to be forgotten.*

Publications

Journal Papers

- A. Petrocchi, G. N. Barakos, "Buffet boundary prediction using RANS-based criteria and adjoint methods", Aerospace Science and Technology, Vol. 126, 2022, 107664, http://doi.org/10.1016/j.ast.2022.107664.
- A. Petrocchi, G. N. Barakos, "Buffet boundary estimation using a harmonic balance method", Aerospace Science and Technology, Vol. 132, 2023, 108086, https://doi.org/10.1016/j.ast.2022.108086.
- A. Petrocchi, M. Mauriello, G. N. Barakos, " Transonic Buffet Alleviation via Virtual Surfaces", Aerospace Science and Technology, Vol. 140, 2023, 108478, https://doi.org/10.1016/j.ast.2023.108478.
- A. Petrocchi, G. N. Barakos, "Transonic Buffet Simulation using a Partially-Averaged Navier-Stokes Approach", Aerospace Science and Technology (under review).

Papers in Conference Proceedings

- A. Petrocchi, G. N. Barakos, "Transonic Buffet Simulation Using A Partially-Averaged Navier-Stokes Approach". In: 8th European Congress on Computational Methods in Applied Sciences and Engineering (ECCOMAS 2022), Oslo, Norway, 5-9 June 2022. https://doi.org/10.23967/eccomas.2022.278.
- A. Petrocchi, G. N. Barakos, "Transonic Buffet Simulation using Harmonic Balance Method". In: AIAA SCITECH 2023 Forum, 23-27 January 2023, National Harbor, MD, US & Online. https://doi.org/10.2514/6.2023-2276.
- A. Petrocchi, G. N. Barakos, "Modelling of Transonic Buffet Alleviation via Spoilers". In: AIAA AVIATION 2023 Forum, 12-16 June 2023, San Diego, CA, US & Online. https://doi.org/10.2514/6.2023-3527.
- A. Petrocchi, G. N. Barakos, "Dynamic f_k Estimates for Partially-Averaged Navier-Stokes Around a Circular Cylinder". In: AIAA SCITECH 2024 Forum, 8-12 January 2024, Orlando, FL, US. (To be presented).

Book Chapters

- A. Petrocchi, G. N. Barakos, "Transonic Buffet Simulation Using A Partially-Averaged Navier-Stokes Approach". In: T. Touvinen, J. Periaux, D. Knoerzer, G. Bugeda and J. Pons-Prats. *Advanced Computational Methods and Design for Greener Aviation*, Computational Methods in Applied Sciences, Springer, 2023.
- A. Petrocchi, R. Steijl, G. N. Barakos, "Numerical Study of Unsteady Shock/Boundary Layer Interaction". (Book title to be decided) Springer, 2024.

Technical Reports

- C. Jimenez Navarro, A. Petrocchi, M. Braza and G.N. Barakos, "Shock Wave Boundary Layer Interaction in external flow cases without flow control", TEAMAero-860909, 2022.
- A. Petrocchi, C. Jimenez Navarro, "Numerical prediction of flow control effectiveness in esternal flow cases", TEAMAero-860909, 2023.
- A. Ceci, A. Joseph, S. Kahraman, P. Nel, M. Mauriello, A. Petrocchi, N. Goffart, C. Jimenez Navarro, "Analysis of numerical methods in the context of applicability for SBLI" TEAMAero-860909, 2023.
- A. Petrocchi, "Harmonic Balance with Variable Frequency", CFD Laboratory, James Watt School of Engineering, University of Glasgow, 2023.
- A. Petrocchi, "Fast Methods for Transonic Buffet Prediction with Applications", CFD Laboratory, James Watt School of Engineering, University of Glasgow, 2023.
- A. Petrocchi, "PANS Method in HMB3", CFD Laboratory, James Watt School of Engineering, University of Glasgow, 2023.

Contents

List of Tables

List of Figures

Nomenclature

Subscripts, superscripts and operators

hb	=	harmonic balance
imp	=	implicit
max	=	maximum
min	=	minimum
ref	=	reference value
rms	=	root-mean-square
u	=	unresolved quantity
∞	=	freestream value
$\langle\cdot\rangle$	=	mean value

Latin Symbols

arg_1, arg_2	=	arguments of F_1, F_2 in the SST model blending functions
a_1	=	SST model closure coefficients
a_p	=	sound speed in the downstream shock motion phase [ms^{-1}]
a_u	=	sound speed in the upstream shock motion phase [ms^{-1}]
AR	=	wing aspect ratio b^2/S
b	=	wing span [m]
B	=	threshold for unsteady buffet boundary criterion
c	=	chord [m]
C_p	=	pressure coefficient $(p-p_\infty)/(0.5\rho U_\infty^2)$
C_B	=	generic buffet coefficient
C_D	=	drag coefficient $D/(0.5\rho U_\infty^2 c)$
C_{DES}	=	DES model coefficient
CD	=	cross diffusion term in the ω-equation of the SST model
C_L	=	lift coefficient $L/(0.5\rho U_\infty^2 c)$
C_M	=	pitching moment coefficient $M/(0.5\rho U_\infty^2 c^2)$
C_{PANS}	=	PANS model constant
C_μ	=	turbulent viscosity coefficient
D	=	pseudospectral operator
	=	diameter [m]
	=	drag [N]

D_2	=	temporal spectral viscosity operator
E	=	energy per unit mass $[m^2/s^2]$
	=	Fourier transformation matrix in the HB formulation
E^{-1}	=	inverse Fourier transformation matrix
E_{cutoff}	=	cutoff Fourier transformation matrix
f	=	frequency $[1/s]$
f_B	=	buffet frequency of oscillation
f_k	=	unresolved-to-total ratio of turbulent kinetic energy
f_ε	=	unresolved-to-total ratio of turbulent dissipation
f_ω	=	unresolved-to-total ratio of turbulent frequency
F_1, F_2	=	SST model blending functions
$\mathbf{F}$	=	inviscid flux vector in the x direction
$\mathbf{F}^v$	=	viscous flux vector in the x direction
$\mathbf{G}$	=	inviscid flux vector in the y direction
$\mathbf{G}^v$	=	viscous flux vector in the y direction
H	=	total enthalpy per unit mass $E + p/\rho$, $[m^2/s^2]$
$\mathbf{H}$	=	inviscid flux vector in the z direction
$\mathbf{H}^v$	=	viscous flux vector in the z direction
J_{imp}	=	Jacobian matrix
k	=	turbulent kinetic energy per unit mass $[m^2/s^2]$
	=	reduced frequency $2\pi f_B c/U_\infty$ in Chapter 8
I	=	cost function in eq. (3.72)
L	=	length [m]
L_G	=	Gurney length [m]
L_{UTEF}	=	UTEF length [m]
L_{vK}	=	Von Karman length scale
m	=	cutoff harmonic
M_∞	=	Mach number
N_{act}	=	Number of steps required for the actuation
N_H	=	number of harmonics
N_T	=	number of sub-intervals in a period of oscillation
p	=	pressure $[kg/(ms^2)]$
p_0	=	stagnation pressure $[\text{W}\,\text{m}^{-2}\,\text{s}^{-2}]$
P_k	=	turbulent kinetic energy production term $\tau_{ij}\partial u_i/\partial x_j$ $[\text{kg}\,\text{m}^{-1}\,\text{s}^{-3}]$
$\mathbf{q}$	=	heat flux vector $[\text{W}\,\text{m}^{-2}]$
Re_c	=	Reynolds number $\rho U_\infty c/\mu$
Re_θ	=	momentum thickness Reynolds number
S_{ij}	=	mean strain rate tensor $[\text{s}^{-1}]$
St	=	Strouhal number fL_{ref}/U_∞
t	=	time [s]
T	=	temperature [K]
	=	period of oscillation [s]
T_B	=	buffet period [s]
T_{off}	=	device retraction time [s]
T_t	=	turbulent time scale [s]
T_0	=	total temperature $[K]$

u_η	=	Kolmogorov velocity [ms^{-1}]
u_i	=	flow velocity [ms^{-1}]
U_i	=	mean flow velocity [ms^{-1}]
$V_{i,j,k}$	=	cell volume
$\mathbf{W}$	=	flow variable vector in eq. (3.13)
x_i	=	spatial coordinates in cartesian system [m]
$\mathbf{X}$	=	grid position [m]
$\dot{\mathbf{X}}$	=	grid velocity [$\mathrm{m\,s}^{-1}$]
$\ddot{\mathbf{X}}$	=	grid acceleration [$\mathrm{m\,s}^{-2}$]

Greek Symbols

α	=	angle of attack [deg]
	=	design variables vector in Section 3.5
α_B	=	onset angle of attack [deg]
δ	=	boundary layer thickness [m]
$\delta_{i,j}$	=	Kronecker delta
$\dot{\delta}_s$	=	spoiler deflection rate [deg/s]
Δ	=	characteristic grid size [m]
Δx, Δy, Δz	=	grid size in the x, y, z directions [m]
$\Delta \mathrm{M}_\infty$	=	Mach number increment
δ_s	=	spoiler deflection angle [deg]
Δt	=	timestep [s]
Δt_{act}	=	device time of deployment [s]
ε	=	turbulent energy dissipation rate [$\mathrm{m}^2\mathrm{s}^{-3}$]
ε_α	=	angle of attack tolerance [deg]
ε_N	=	spectral viscosity coefficient
η	=	Kolmogorov scale [m]
θ	=	momentum thickness [m] or deflection angle [deg]
Λ	=	turbulent length scale [m]
	=	wing sweep angle [deg]
μ	=	dynamic Viscosity [$\mathrm{kgm}^{-1}\mathrm{s}^{-1}$]
μ_t	=	eddy viscosity [$\mathrm{kgm}^{-1}\mathrm{s}^{-1}$]
ν_t	=	kinematic eddy viscosity [$\mathrm{m}^2\mathrm{s}^{-1}$]
ω	=	specific turbulent dissipation rate [s^{-1}]
Ω	=	fundamental frequency of oscillation [s^{-1}]
Ω_{ij}	=	mean rotational part of the velocity gradient [s^{-1}]
ρ	=	density [$\mathrm{kg\,m}^{-3}$]
τ	=	viscous stress tensor [$\mathrm{kgm}^{-1}\mathrm{s}^{-2}$]
	=	pseudo time
τ^R	=	Reynolds stress tensor $-\langle u_i' u_j' \rangle$ [$\mathrm{kgm}^{-1}\mathrm{s}^{-2}$]
τ_η	=	Kolmogorov timescale [s]
β^*, β, γ, σ_k, σ_ω	=	SST model closure coefficients

Acronyms

AJVG Air Jet Vortex Generator

ALE Arbitrary Lagrangian-Eulerian

AZDES Automatic Zonal Detached Eddy Simluation

BILU Block Incomplete Lower-Upper

BOS Background-Oriented Schlieren

BSCB Backward Shock-Control Bump

CFD Computational Fluid Dynamics

CPU Central Processing Unit

CSD Cross-Spectral Density

CRM Common Research Model

DDES Delayed Detached Eddy Simulation

DES Detached Eddy Simulation

DMD Dynamic Mode Decomposition

DNS Direct Numerical Simulation

DPSP Dynamic Pressure-Sensitive Painting

FFT Fast Fourier Transorm

FSCB Forward Shock-Control Bump

GCG Generalised Conjugate Gradient

GMRES Generalised Minimum Residual

GBVTP Gradient-Based Variable Time Period

HB Harmonic Balance

IDDES Improved Detached Eddy Simulation

ILES Implicit Large Eddy Simulation

JAXA Japan Aerospace Exploration Agency

LDV Laser Doppler Velocimetry

LES Large Eddy Simulation

MUSCL Monotone Upstream-centered Scheme for Conservation Laws

MVG Micro-Vortex Generator

NASA National Aeronautical and Space Administration

OES Organised Eddy Simulation

PANS Partially Averaged Navier-Stokes

PDE Partial Differential Equation

PIV Particle Image Velocimetry

POD Proper Otrhogonal Decomposition
PSD Power Spectral Density
PSP Pressure-Sensitive Painting
RANS Reynolds-Average Navier-Stokes
RMS Root Mean Square
ROM Reduced-Order Model
RSM Reynolds-Stress Model
SA Spalart Allmaras
SALSA Strain-Adaptive Spalart Allmaras
SAS Scale Adaptive Simulation
SBLI Shock wave Boundary Layer Interaction
SCB Shock-Control Bump
SGS Sub-Grid Scale
SIO Shock-Induced Oscillation
SPL Sound Pressure Level
SRS Scale-Resolving Simulation
SST Shear Stress Tensor
TMS Time-Marching Simulation
TE Trailing-Edge
TED Trailing-Edge Deflector
TSV Temporal Spectral Viscosity
URANS Unsteady Reynolds-Averaged Navier-Stokes
UTEF Upper Trailing-Edge Flap
UTW Upstream Travelling Wave
VG Vortex Generator
WMLES Wall-Modelled Large Eddy Simluation
ZDES Zonal Detached Eddy Simluation

Chapter 1

Motivation and Objectives

1.1 Motivation

Over the last decades, research has focused on Shock wave Boundary Layer Interaction (SBLI) because of its impact on several transonic, supersonic, and hypersonic applications for external and internal flows. Aircraft wings, helicopter blades, rockets, missiles, and launch and re-entry vehicles fall into the first category. Among the internal flow cases we find high-speed inlets, nozzles at off-design conditions, compressor and turbine stages operating at transonic conditions, and scramjet isolators. SBLI may lead to pressure losses and distortion, boundary layer deformation (thickening), transition and separation, turbulence generation, vortex formation, and enhanced convective heat transfer. Ultimately, these flow phenomena introduce drag penalties, large, low-frequency flow unsteadiness, adverse structural response, undesired thermomechanical loads, and deterioration of aero-propulsive performance and efficiency.

To sustain the ever-growing air mobility demand in a sustainable manner, airfract manufacturers and airlines are pushing towards a greener aviation. In this view, the improvement of transonic wing aerodynamics is vital. The goals are to reduce drag and obtain higher aerodynamic efficiency. Flying at transonic speed is beneficial in terms of efficiency over long range flights. Therefore, the vast majority of commercial airplanes have a cruise point falling in this regime. At these conditions, both subsonic and supersonic regions are present, with a shock separating them. The interaction with the incoming boundary layer gives rise to a normal SBLI, which introduces complications associated with the aforementioned effects.

In general, a safe flight is sustained within a certain range of load factor (n) and speed (V). Figure 1.1 represents a typical flight envelope which sets the boundary of safe flight operating conditions. The regular envelope ensures to have flight conditions not undermining the structural integrity of the aircraft, and to avoid stall. Nevertheless, even within the regular envelope, some combinations of Mach number and angle of attack are still not completely safe. At these conditions,

the unsteady SBLI and the induced flow separation give rise to a large-amplitude, low-frequency, self-sustained, Shock-Induced Oscillation (SIO) on the wing. This phenomenon takes the name of *transonic buffet*. Buffet has consequences on the structural aircraft response as it can lead to structural fatigue. Moreover, it deteriorates the aircraft handling qualities and can also cause passenger discomfort in flight. Therefore, an airplane must be free from oscillations at any operating conditions and a buffet boundary (dotted, black line in Figure 1.1) limits the flight envelope.

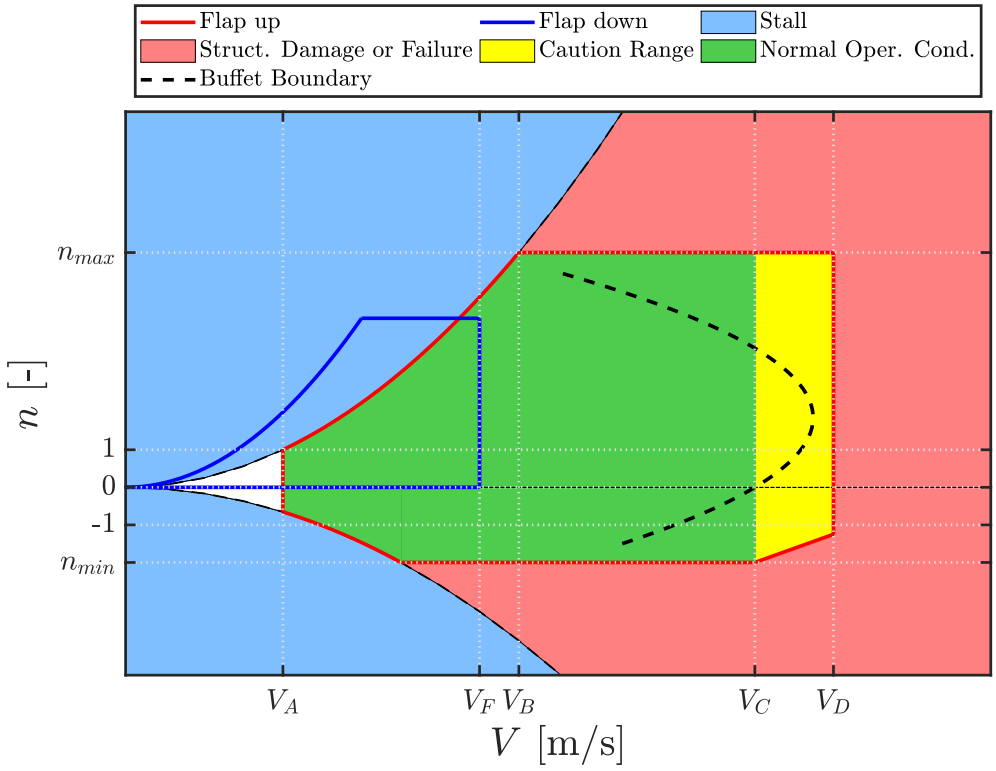

Figure 1.1: Sketch of a typical flight envelope. V_A: normal stall speed; V_B: manoeuvring speed; V_C: maximum structural cruise speed; V_D: never exceed speed; V_F: limit airspeed with flap down.

A full comprehension of the phenomena driving SBLI and buffet is far from being reached, and experiments of full configurations are sometimes prohibitively difficult due to the extreme flow conditions. Therefore, over the past decade, Computational Fluid Dynamics (CFD) has been extensively used to investigate transonic buffet flows. Predictions of this phenomenon by means of Time-Marching Simulation (TMS) proved to be challenging, and not consistently accurate. In principle, an Unsteady Reynolds-Averaged Navier-Stokes (URANS) approach seemed optimal because of the large time scales associated with the shock oscillations (especially in case of turbulent transonic buffet). Because of the sensitivity to the turbulence modelling, numerical schemes, and spatio-temporal discretisation adopted, no consensus was found on the ability of Reynolds-Average Navier-Stokes (RANS) to cope with this kind of flows at different flow conditions. However, with the recent rise in computer power, increasingly detailed yet expensive computations, spanning from

hybrid RANS-LES to Large Eddy Simulation (LES) and Direct Numerical Simulation (DNS), have been used to analyse this class of flows. The main drawback of these methods is the considerably higher Central Processing Unit (CPU) costs stemming from the fine spatio-temporal discretisation required. This makes the application of scale-resolving methods to complex geometries, at high Reynolds numbers, highly expensive. Here, it arises the need for a computational approach which is accurate for the prediction of the buffet without introducing the CPU costs of the aforementioned approaches.

Transonic buffet must be accounted for in the aerodynamic design process. Therefore it arises the need for an accurate method for the buffet boundary determination across a wide range of operating conditions. In this regard, engineering criteria have been proposed for the buffet boundary estimation, based on the results of experimental investigations. They use buffet indicators, either local or global flow quantities, which allows to estimate the onset of the instability. The application of fast criteria over a large range of flight conditions allows to determine the buffet boundary for the desired configuration.

An aircraft should never exceed the threshold set by the buffet boundary. Nonetheless, variations of the flight conditions due to gusts or emergency manoeuvres may cause the plane to cross the buffet boundary and undergo buffet. Therefore, in recent years, increasing attention has been paid to control methods to eliminate or alleviate SIOs. A plethora of flow control devices and strategies were proposed in this context and an overview will be given in the next sections. Most methods proved able to eliminate the SIO at design conditions. So far, the main issues of mechanical devices are installation drag and off-design penalties, which introduce the need for expensive, and sometimes unsuccessful, works of optimisation involving shape, number, and position of the devices. Alternatively, feedback control based on flow measurements can be implemented to obtain a dynamic actuation.

This work aims at giving a complete computational framework for the understanding, prediction and control of transonic buffet. In particular, the objectives are:

- To determine the optimal computational strategies for carrying out extensive CFD simulation campaigns. The optimal trade-off between accuracy and cost is pursued. At this stage, the selected method must be able to adequately capture the relevant flow physics. If unavailable, the targeted method must be implemented in the in-house CFD code adopted in this work.

- To formulate criteria for the prediction of the buffet onset. For these to be applied in an actual industrial context, they must not overestimate the onset (they must be conservative). Any additional information coming from the criteria will be considered as a factor of merit.

- To determine a flow control strategy which limits the impact of buffet on the aerodynamic efficiency with respect to those available in the literature.

1.2 Thesis Objectives and Organisation

In the view of the available literature, the objective of this work is to build a computational apparatus able to accurately predict and describe transonic buffet. Buffet prediction via numerical simulations showed significant scatter in the results depending on the adopted turbulence model and simulation strategy. Furthermore, a total understanding of the mechanism itself is far from being reached. In particular, the differences between two- and three-dimensional cases were not fully explained, despite the large number of works carried out.

For practical buffet computations, the use of TMSs can result in excessive CPU costs. The problem becomes more evident if a range of flow conditions must be computed to ensure wings are free from SIOs during different flight phases. In this view, there is a need for an efficient and precise tool for buffet onset prediction.

Finally, the aspect of flow control was addressed. An airplane can undergo buffet because of unexpected gusts or emergency manoeuvres, and the SIO must be suppressed. A great effort was devoted to the control of SBLI and the related unsteadiness. From the pool of numerical and experimental works in the literature, it is clear that no optimum control device was found yet. A compromise between several parameters must be sought: ability to suppress buffet, impact on the aerodynamic performance, off-design and installation penalties, ease of implementation, and impact on the other components.

To address all aforementioned matters, this work is put forward. The thesis is organised as follows.

Chapter 2 is devoted to the literature survey carried out. The topics mentioned in this section will be addressed to provide a detailed description of the physics involved in this work, the available flow control strategies, and the CFD methodologies commonly used to compute flows with SBLI and buffet. The literature was critically scrutinised, and the conclusions motivated the author in his research.

Chapter 3 describes the HMB3 solver and methods adopted in this work. The chapter contains the CFD solver formulation, turbulence model, and numerical methods used in the results chapters. In particular, attention will be paid to the Partially Averaged Navier-Stokes (PANS) model adopted for TMSs, the adjoint method, the harmonic balance method, and the modelling of virtual surfaces for buffet control.

Chapter 4 sees the validation of the PANS method on a case with self-induced instabilities. The chapter aims at studying the effect of different PANS approaches, and on building best practices for the use of PANS.

Chapter 5 presents an application of the PANS method to the buffet flow around the OAT15A test case, considered the most detailed one in terms of experimental data. The results will assess **(i)** the ability of PANS to predict buffet on moderate grid sizes, and **(ii)** accurately describe the flow

physics. Attention will be paid to the role of the wind-tunnel facility in the context of 3D buffet.

Chapter 6 introduces a novel algorithm for a quick prediction of buffet. It combines results from some of the criteria used in industry with the adjoint method implemented in HMB3. The combination with the adjoint method allows for a reduction of CPU costs associated with buffet prediction without impacting significantly on the accuracy.

In Chapter 7, the prediction of buffet is carried out by means of the harmonic balance method. The implementation of a frequency-adaptive method in HMB3 allowed for the use of harmonic balance for buffet flows. A simple algorithm was developed to quickly trace the buffet boundary. The obtained results are compared with those of Chapter 6.

Chapter 8 covers the flow control aspect. The ability of Upper Trailing-Edge Flap (UTEF)s and spoilers is assessed by using TMSs of 2D and 3D configurations. The control surfaces are modelled by using *ad hoc* boundary conditions. A strategy for automatic surface deployment based on local flow quantities was formulated, implemented, and tested.

Chapter 9 is devoted to conclusions and future work.

Chapter 2

Background and Literature Survey

An extensive literature survey was carried out early in the thesis. In a first instance, the documents were selected by looking for keywords (e.g. SBLI, RANS, Vortex Generators) in established databases (Scopus, Web Of Science, Aerospace Research Centre, etc.). The outcome was collected in text files and the significance of each relevant work was categorised in order of priority, based on the abstract content. After removing duplicates from different keywords, the documents (consisting of journal papers, conference papers, technical reports, books, and Ph.D. theses) were studied and summarised. References in the aforementioned works that were also of interest were collected and studied. The process was repeated periodically over the entire duration of this work.

The literature survey first covers the basic SBLI in Section 2.1, through the study of simplified 2D cases, which are often used to explain more complex 3D interactions. There, an initial description of the unsteadiness present in canonical SBLI is provided. That section serves as an introduction to the main topic of the thesis. In Section 2.2, the transonic buffet mechanism is described. The topic is covered in detail, by listing and commenting on all studies in the available literature. Experimental and numerical works are investigated, and reported in chronological order. Two- and three-dimensional cases are distinguished, as the buffet mechanism seems related to different causes, affected by wing aspect ratio and sweep angle. The experimental works are also looked at, with interest to find a complete dataset to validate the CFD computations in this work. In parallel, the literature on buffet prediction via CFD is investigated to select an adequate strategy among the available ones. Section 2.3 is devoted to buffet control. After a brief introduction to flow control for SBLI, the survey summarises the main strategies for buffet control, underlining the advantages and disadvantages of each category.

The outcome of each section motivated the strategies adopted in this work and developed in the next chapters.

2.1 Governing Physics

2.1.1 Shock-Wave/Boundary-Layer Interaction

Shock wave boundary layer interaction takes place when a shock-wave, consisting of a discontinuity in fluid dynamic quantities across the wave front, encounters the flow field in the vicinity of a solid wall, i.e. a boundary layer. Typical interactions are oblique shock reflections (Figure 2.1, (c) with separation; (d) without separation), ramp induced shock waves (Figure 2.1 (b)), normal shocks (Figure 2.1 (a)), and adaptation shocks at nozzle exit. The 2D interactions illustrated in this figure can be used to explain more complicated 3D configurations (conical interactions, single- and double-fin interactions, shock trains, etc).

The boundary layer is stratified such that an inner, viscous sub-layer confines with an intermediate one, where the flow is inviscid but rotational, and a potential, upper layer. Some differences, mainly of quantitative nature, arise if the boundary layer is turbulent. Nevertheless, the mechanism of SBLI can be explained regardless the nature of the boundary layer. The streamwise momentum equation for a boundary layer to a flat wall reads:

$$\rho u \frac{\partial u}{\partial x} + \rho v \frac{\partial u}{\partial y} = -\frac{\partial p}{\partial x} + \frac{\partial \tau}{\partial y}, \tag{2.1}$$

and suggests that the shock-boundary layer interaction can be analysed as a competition between the flow momentum, the shear stress (boundary layer properties, in principle) and the adverse pressure gradient given by the discontinuity. In the lower part of the boundary layer, there is a region, below the sonic line, where pressure disturbances are sensed from the boundary layer. The equilibrium between viscous forces and pressure affects the growth of the boundary layer and the formation of a compression fan in the supersonic region of the boundary layer due to the thickening of the boundary layer. This mechanism is the basis of all aforementioned interactions. The structure of different types of interaction strongly depends on the shock type (see Figure 2.1).

For an impinging shock, like those in Figure 2.1 (c-d), an oblique shock wave is generated far from the wall and approaches the boundary layer. For weak interactions, like that in Figure 2.1 (d), the boundary layer is deflected and compression waves are generates from the sonic line. These interact with the impinging shock and coalesce into the reflected shock. The shock impinges on the sonic line and reflects as an expansion fan that, in turn, interacts again with the reflected shock. Overall, this kind of interaction can be thought as inviscid, where an oblique shock hitting a wall is reflected. The downstream boundary layer recovers slowly and, after some length ($\simeq 100\delta$), comes to undisturbed conditions. In inviscid conditions the pressure rise is quick. For viscous flows, the pressure distribution is smeared: the pressure rise starts before the ideal shock impingement position, due to the presence of the compression waves, and is more gradual.

When the shock is strong enough, boundary layer separation is induced. The abrupt pressure

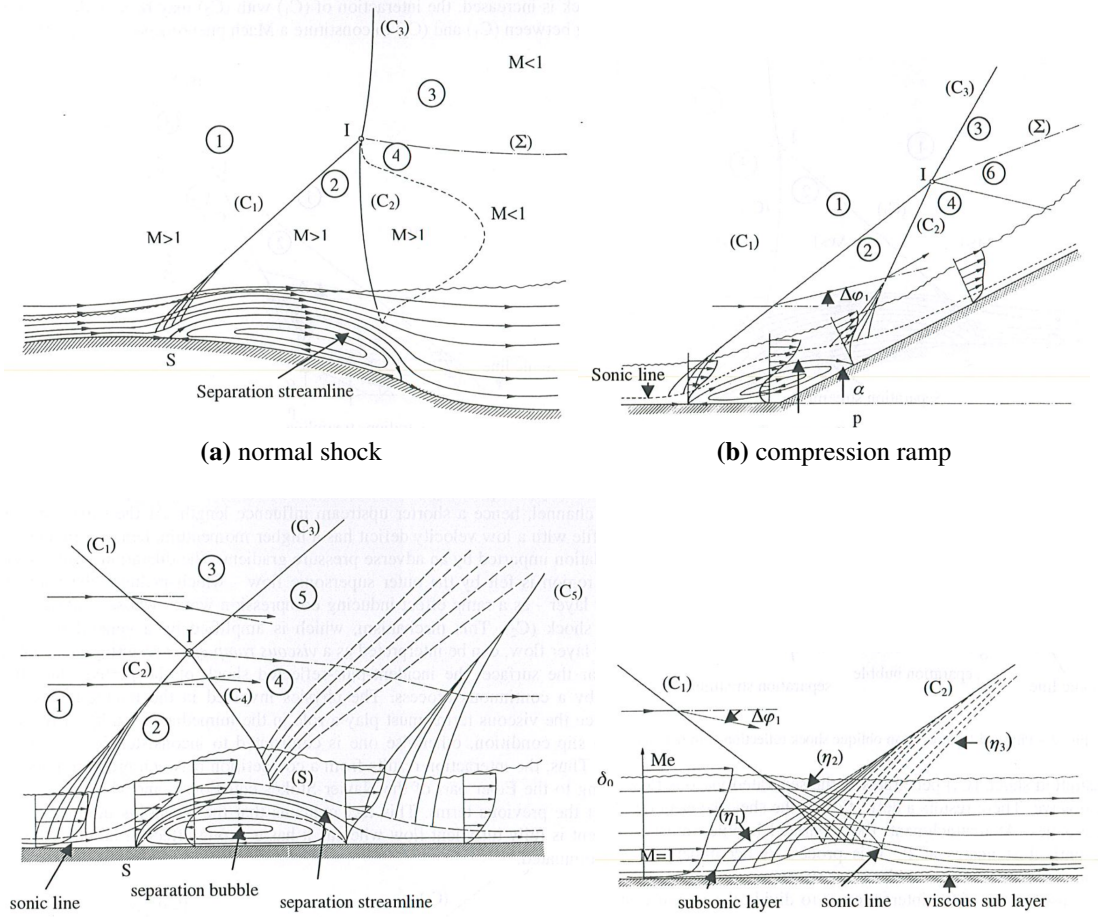

(a) normal shock **(b)** compression ramp

(c) oblique impinging shock with separation **(d)** oblique impinging shock without separation

Figure 2.1: Flow structure in presence of shock-wave boundary layer-interaction for several configurations [61].

rise and the adverse gradient can easily induce separation of the boundary layer, characterised by a negative $\partial u/\partial y$ at the wall, hence by a region of local flow reversal. In this case, the strong deflection of the streamlines due to the presence of the separation bubble (see Figure 2.1 (b-d)), lead the compression waves to rapidly merge into a shock that interacts with the incoming shock, whether normal or oblique. In the former case, the oblique shock generated is not enough to achieve the overall pressure rise, and a secondary shock - the rear leg - is formed. The shocks meet in the triple point, where a slip line forms, separating two flow domains, sharing the same pressure. This configuration is named λ-shock.

The scenario is similar for impinging shocks, maintaining the same structure of the attached case with the addition of the triple point where the impinging and reflected shocks meet. Also in this case, a slip line can form. There is also the extreme case where a Mach stem is formed with a curved shock linking the two oblique ones. An example can be seen in the LES computation of Matheis and Hickel [174]. After the separation point, the concave shape of the sonic line allows for the formation of a second compression fan merging in the re-attachment shock. The same

happens for SBLIs formed on compression ramps, for weak and strong interactions. In this case, the impinging shock is missing and the shock is formed from the compression fan generated by the boundary layer thickening in correspondence of the separation. The presence of the shock allows for the flow to deviate according to the wall slope.

In the past 70 years, SBLI was investigated by means of increasingly accurate and sophisticated experimental and numerical techniques. Several review papers summarise the milestones in the understanding of this phenomenon [43,62,63,65,83,118,160]. Nevertheless, several questions have not been answered yet. Among them, we see **(i)** uncertainty around the origin of the low-frequency unsteadiness developing for canonical SBLI configurations, **(ii)** inaccuracy in the prediction of heat transfer rates, especially for turbulent SBLI, and **(iii)** flow control to reduce the effects associated with SBLI. In this thesis, the first and third topics will be partially covered. In the following, a brief introduction to unsteadiness associated with SBLI is presented.

2.1.2 Shock Unsteadiness

Cases of SBLI with shock-induced separation seem to be inherently unsteady. The frequencies associated with the dynamic change in size of the separated bubble (the so called *breathing*) are order of magnitudes smaller than those of turbulence in the attached boundary layer, and in the shear layer. These are the main sources of concern for practical applications, as they can harm the structural integrity or induce an undesired structural response. The causes for the unsteadiness have been extensively researched, but so far, no definitive answer has been given. Dolling [65] investigated whether the low-frequency unsteadiness was merely due to unwanted effects of the wind tunnels used for the experimental studies of SBLI. With the increase in computer power, Scale-Resolving Simulations (SRSs) such as LES and DNS ruled out this hypothesis. The presence of low-frequency unsteadiness was observed regardless of the presence of sidewalls. The review of Dussauge *et al.* [66] was an attempt to characterise the dominant frequency of the shock motion has been done by collecting experimental results obtained at supersonic conditions. To quantify the shock unsteadiness, the Strouhal number was used:

$$St = \frac{fL}{U}. \tag{2.2}$$

Here, f is the shock oscillation frequency and L and U are the characteristic lenghtscale and velocity, respectively. The interaction length and the outer velocity were considered for impinging shocks. Although the nature of the oscillation was not established, it could be related to the recirculation bubble or to the acoustic feedback of the reflected shock that propagates in the subsonic layer. The Strouhal number associated with the motion was found to be in the range of $0.02-0.05$.

According to Délery and Dussauge [62], causes for instabilities are the distortion of the turbulence structures across the shock and the downstream separated flow influencing the shock dynam-

ics. In the first case, the turbulence is distorted across the shock and influences the downstream boundary layer that can couple with the shock; in the second case, in case of separated flow, an almost common pattern has been found in experiments, where the dominant non-dimensional frequency is around $0.03 - 0.04$. In situations where most of the flow is subsonic, the downstream boundary layer may affect the shock motion with an acoustic feedback mechanism, for which the acoustic feedback coming from the downstream boundary layer couples with the shock. Alternatively, always in presence of wide region of separated flow, the shock motion is mainly attributed to the bubble breathing or mixing layer flapping. High-frequency, unsteady flows are associated with the interaction with the incoming turbulence, while low-frequency/large scale unsteadiness is due to instabilities in the separation bubble, and mainly associated with transonic SBLI.

Low-frequency unsteadiness has been extensively studied, and several works have been summarised in the review of Clemens and Narayanaswamy [43]. In their work, the main sources of unsteadiness have been identified as the upstream influence, i.e. turbulence in the incoming boundary layer, and the downstream mechanism. Both mechanisms seem to play a role in cases where shock-induced separation is present. The downstream influence seems the main cause of unsteadiness for strongly separated flows. If the separation is weaker, the upstream turbulence could influence the shape of the separated flow bubble, or add disturbances in the free shear layer that grow and lead to large scale flapping.

Transonic buffet is a particular type of low-frequency, large-amplitude unsteadiness. While a moderate agreement in terms of fundamental frequency (St$= 0.05 - 0.07$) was found with the aforementioned studies, transonic buffet differs from canonical SBLI instabilities. The next section presents a detailed description of this phenomenon, which is the main topic of this work of thesis.

2.2 Transonic Buffet

A phenomenon limiting the performance of aerofoils and wings is buffet. This phenomenon was widely investigated in the works of Lee [157] and Giannelis *et al.* [100], among others. It is defined as a self-sustained shock oscillation on transonic lifting structures, associated with dynamic structural response. This oscillation can be detrimental in terms of structural integrity or flight controllability. Indeed, EASA certification standards require that "an aeroplane must be demonstrated in flight to be free from any vibration and buffeting that would prevent continued safe flight in any likely operating condition". For these reasons, buffet has been widely investigated but the cause of the mechanism remains obscure. It is known that buffet occurs as the angle of attack, or flight Mach number increase. This allows drawing the buffet boundary. Sometimes, as in case of gusts or emergency manoeuvres, an aircraft can cross the boundary, undergoes buffet, and its flight safety can be significantly affected. An example can be found in the work of Mabey [167], who sketched a common scenario for transonic civil and military aircraft in terms of aircraft lift coefficient and flight Mach number (Figure 2.2).

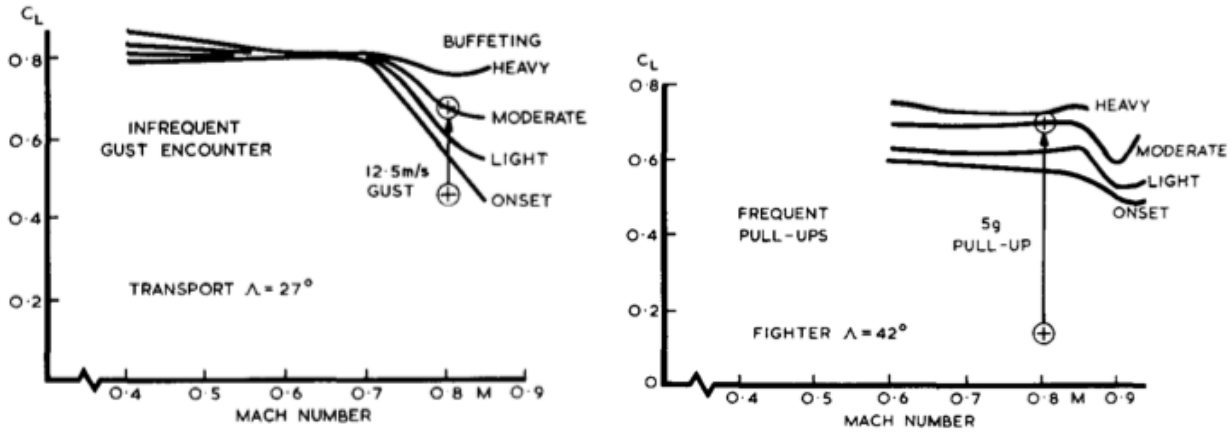

Figure 2.2: Buffet criteria for civil and fighter aircraft. Figure from Mabey [167].

A number of researchers tried to shed light on the buffet mechanism generating and driving the oscillations over aerofoils and wings [44, 126, 159, 203, 262]. The first explanation of buffet onset was given more than fifty years ago by Pearcey [203] who related the oscillation to bubble bursting due to an increase of Mach number or angle of attack. When the shock was strong enough to cause separation extending from the shock foot to the trailing edge (type 3 separation in the characterisation of Mundell and Mabey [193]), low frequency, high amplitude fluctuations were measured in the separated region, together with a periodic and self-sustained shock motion. In recent years, that hypothesis was almost completely surpassed (see [120]). Nevertheless, the relationship between buffet and the aforementioned parameters is not clear, and was studied in many recent works (see [98]). Tijdeman [262] proposed a characterisation of the shock motion for flap-equipped aero-

foils and generalised to plunging or pitching aerofoils. The type A buffet consists of a sinusoidal shock oscillation over the aerofoil, with a varying strength and position of the shock throughout the buffet cycle. Type B follows the same pattern of type A, with the shock disappearing during the downstream excursion. Type C sees a strengthening and weakening of the shock as it moves upstream and the propagation into the incoming flow as a free shock-wave. A sketch from [262] is given in Figure 2.3.

One of the most plausible explanation behind buffet is the acoustic feedback mechanism proposed by Lee [159] for the shock motion of type A. The shock oscillation on the upper side of the aerofoil generates pressure waves propagating through the separated flow region extending from the shock to the leading edge. Once the leading edge is reached, another disturbance propagates backwards at the local speed of sound. These waves interact with the shock and transfer the energy required to sustain the oscillation. The buffet period is the time necessary for a pressure wave to depart from the shock and reach the trailing edge plus the time needed for the disturbance to move backwards and hit the shock. The work of Xiao *et al.* [283] strengthened this theory, where URANS simulations around the BGK aerofoil were performed, and cross-correlations allowed computations of the perturbations travel times. The more recent experimental work of Feldhusen-Hoffmann *et al.* [75] pointed out, once again, the crucial role of the acoustic waves emanated from the aerofoil trailing edge and confirmed that the shock motion is driven by acoustic perturbations. This was achieved by introducing artificial disturbances in the wind tunnel. The same upstream travelling waves were also observed and studied by D'Aguanno *et al.* [50]. In the experimental work of Jacquin *et al.* [126] on the supercritical aerofoil OAT15A, the authors also observed the presence of upstream travelling perturbations on the pressure side that are diffracted at the leading edge, and play a role in the self-sustained motion. The LES computations of Garnier and Deck [91] seem to confirm this latest findings. The sketches of Lee's acoustic feedback mechanism and the one proposed by Jacquin *et al.* [126] are shown in Figure 2.4.

Starting from Crouch *et al.* [44], buffet has been associated with a global instability mechanism, and studied by means of stability analyses and the URANS equations. Buffet is seen as a Hopf bifurcation, for which the least stable eigenvalue of the associated linear system crosses the imaginary axis of the complex plane and becomes unstable. The eigenmode associated with the unstable eigenvalue is qualitatively different from the mechanism of Lee [159] and similar to that from Jacquin *et al.* [126]. A pressure disturbance is generated at the shock foot and moves along the shock up to the end of the supersonic region. As the perturbation moves upward, the shock approaches the trailing edge and intensifies. A pressure wave generates, goes around the trailing edge, propagates forward along the pressure side and, once at the leading edge, is ingested into the sonic zone. From the same authors, the same approach has been tested on the OAT15A [45] and the NACA0012 [44] aerofoils, for which the comparison was done with respect to the early experiments of McDevitt and Okuno [178]. The same approach was followed by Sartor *et al.* [226]. In

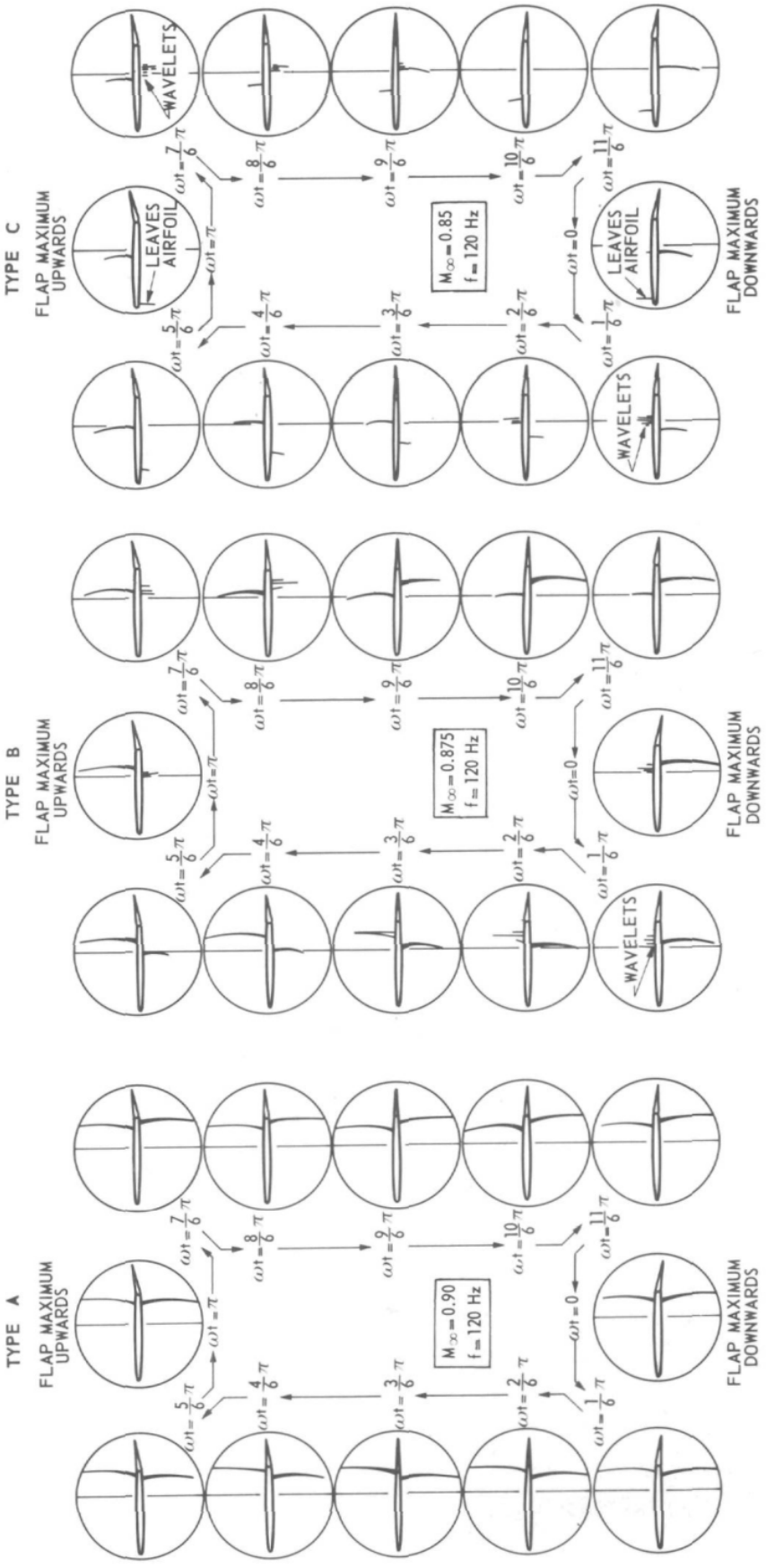

Figure 2.3: Time history of the three types of periodical shock motions. Figure from [262].

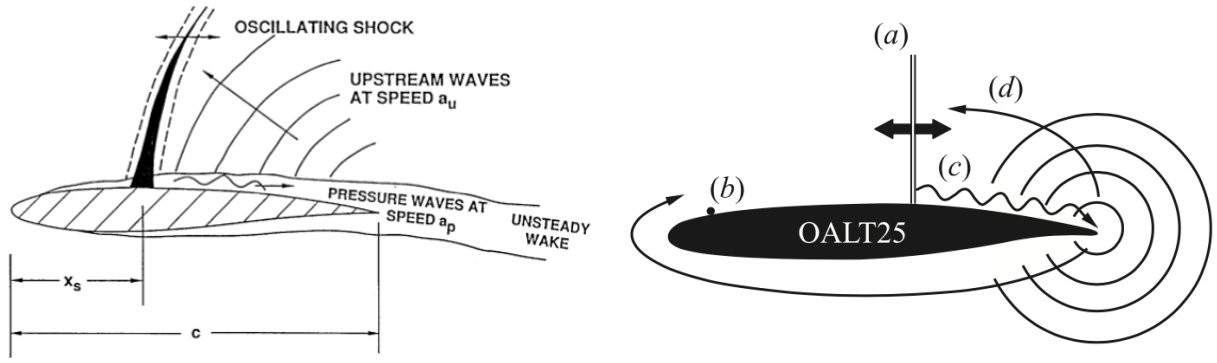

Figure 2.4: sketch of the acoustic feedback mechanism proposed by Lee [159] (left) and Jacquin *et al.* [126] (fig. from [31]).

their study of the flow around the NACA0012 aerofoil, by means of RANS simulations, a strong link between the buffet onset and the appearance of an unstable global mode was found.

Buffet is caused by an increase in the angle of attack or the Mach number. These two parameters are used to define the buffet boundaries, upper and lower (buffet *onset* and *offset* [120], respectively), within which buffet takes place. For a two-dimensional case, Giannelis *et al.* [98] investigated the effect of both parameters by means of 2D URANS, while a similar study was carried out by Masini *et al.* [173] for an aircraft wing.

In three-dimensional configurations, the shock dynamics is affected by several factors. Experimental investigations [53, 137, 138, 153, 190] have been carried out on transonic wings, although the degree of completeness of the results is not as high as for aerofoils. The experimental findings were confirmed and used for numerical simulations. The work of Ionovich and Raveh [122] reported differences between straight and swept wings, and studied the influence of the sweep angle on the shock dynamics. In general, the 3D buffet is characterised by a broadband spectrum of frequencies rather than a single frequency driving the oscillation. Moreover, the spanwise organisation of the flow in "buffet cells" was shown, characterised by regions of alternated pressure propagating in the spanwise direction, and usually outboard. The approach of Crouch *et al.* [45, 46] and Timme [263] covered models of infinite and finite swept wings. The onset of buffet on the National Aeronautical and Space Administration (NASA) Common Research Model (CRM) was studied by means of global stability. The eigenvalues and eigenmodes were analysed to enforce the theory that 3D buffet can be connected to a global instability mechanism. As the angle of attack increases, the eigenvalues cross the imaginary axis and give rise to the buffet.

The remainder of this section presents experimental (Section 2.2.1) and numerical (Section 2.2.2) works which shedded light on the causes of buffet. A distinction between two- and three-dimensional cases was made, as the development of buffet in the two cases, follows different patterns. An effort to bridge them was recently made (see Sugioka *et al.* [252], e.g.). Similarities and differences will

also be explored before briefly commenting on the role of fluid-structure interaction (Section 2.2.3) and laminar buffet (Section 2.2.4). These latter topics are not of interest in this thesis, but are presented for completeness. Moreover, these showed some connections with the results presented in the next chapters.

2.2.1 Buffet Experiments

This section presents a collection of experimental works in the context of transonic buffet. Some of them laid the foundations for the study of transonic buffet by documenting the phenomenon. More recent works helped formulate hypotheses to understand and predict it. In this section, the experiments observing and analysing transonic buffet are presented to:

- guide the reader towards the understanding of buffet and present the state of the art;
- determine the limitations of the experimental facilities and the lack of tools, which introduce the need for integrated research with CFD;
- determine a test case that is suitable for the numerical investigations in this work.

The list of works analysed here is provided in Table 2.1.

Table 2.1: Summary of experiments on transonic buffet. UP: unsteady pressure measurement; LM: load measurements; LDV: laser doppler velocimetry; Sch: schlieren visualisation; OF: oil flow visualisation; (D)PSP: (dynamic) pressure-sensitive painting; PIV: particle image velocimetry; SF: skin-friction; BOS: background-oriented schlieren; Sh: shadowgraph visualisation.

Author	Geometry	M_∞	$Re \times 10^6$	α [deg]	Measured Data
Circular Arc Aerofoil					
McDevitt *et al.* [179]	Cyrc. Arc	0.7 ÷ 0.8	1÷14	0.0 ÷ 4.0	UP
Levy Jr [132]	Cyrc. Arc	0.7 ÷ 0.8	1÷14	0.0 ÷ 4.0	UP, SF
2D Configurations					
Roos [220]	NACA0012	0.7 ÷ 0.8	1÷14	0.0 ÷ 4.0	UP, LM
	Withcomb aerofoil	0.7 ÷ 0.8	1÷14	0.0 ÷ 4.0	
McDevitt & Okuno [178]	NACA0012	0.7 ÷ 0.8	1÷14	0.0 ÷ 4.0	SP, UP
Benoit & Legrain [21]	RA16SC1	0.73	4.0	0.0 ÷ 6.0	UP
Lee [159]	BGK1	0.69 ÷ 0.75	20.0	4.52 ÷ 8.02	UP, LM
Jacquin *et al.* [126]	OAT15A	0.7 ÷ 0.75	3.0	2.5 ÷ 3.9	OF, UP, LDV, Sch
Hartmann *et al.* [111, 112]	DRA 2303	0.73	1.9	3.5	UP, Sch, PIV
Koike *et al.* [137]	NASA CRM	0.736	5.0	0.0 - 0.8	OF, UP
Brion *et al.* [31, 32]	OALT25	1.69	0.05(Re_θ)	6	UP, Sch
Feldhusen-Hoffmann *et al.* [74, 75]	DRA 2303	0.73	1.9	3.5	UP, PIV
D'Aguanno *et al.* [47, 49]	OAT15A	0.7	2.6	3.5	BOS, PIV
Accorinti *et al.* [6–8]	OAT15A	0.71÷0.78	3.0	2.5÷6.5	BOS,
Kokmanian *et al.* [142]	OAT15A	0.65÷0.77	2.8÷3.1	3.8÷6.3	PIV
Korthauer *et al.* [143]	OAT15A	0.71÷0.78	3.0	2.5÷6.5	$x_s(t)$, $w(x,y)$, k,
Scharnowski *et al.* [231]	OAT15A	0.74	3.1	5.8	PIV
Sugioka *et al.* [252]	CRM	0.85	2.27		Sh, OF, PSP

Continued on next page

Table 2.1 – *Continued from previous page*

Author	Geometry	M_∞	$Re \times 10^6$	α [deg]	Meas. Techniques
3D Configurations					
Roos [220]	NACA0012	0.7 ÷ 0.8	1÷14	0.0 ÷ 4.0	UP, Def
Molton *et al.* [190]	OAT15A	0.8	2.5	2 ÷ 4	OF, UP, LDV
Koike *et al.* [137]	NASA CRM	0.848	2.27	−2 - 8	OF, UP
Koike *et al.* [138]	NASA CRM	0.85	0.947, 1.515	−3 - 6	OF, UP
Lawson *et al.* [153]	RBC12	0.7 ÷ 0.84	3	0 ÷ 8	LM, UP, DPSP
Dandois [53]	OAT15A	0.78 ÷ 0.86	2.83 ÷ 8.49	3.5	UP, LM , OF
Masini *et al.* [169]	RBC12	0.7 ÷ 0.84	3	0 ÷ 8	LM, UP, DPSP
Sugioka *et al.* [251, 253, 254]	NASA CRM	0.85	1.54	2.82÷6.52	PSP
Uchida *et al.* [270]	M4 Wing	0.85	2.27		PSP
D'Aguanno *et al.* [50]	OAT15A	0.7	2.6	3.5	BOS, PIV, OF

2.2.1.1 2D Configurations

The first experimental studies were conducted on a thick symmetric aerofoil by McDevitt *et al.* [179] and Levy Jr [132]. Through unsteady pressure measurements they detected shock oscillations on both sides of the aerofoil, with alternating movement of the shocks on the two sides. The study revealed a periodic motion at a precise frequency (St = 0.16) occurring together with a significant shock-induced separation region extended from the shock foot to the trailing edge. McDevitt *et al.* [179] provided the first experimental map to indicate where the conditions leading to transonic buffet are met in the undertaken experiments, shown in Figure 2.5.

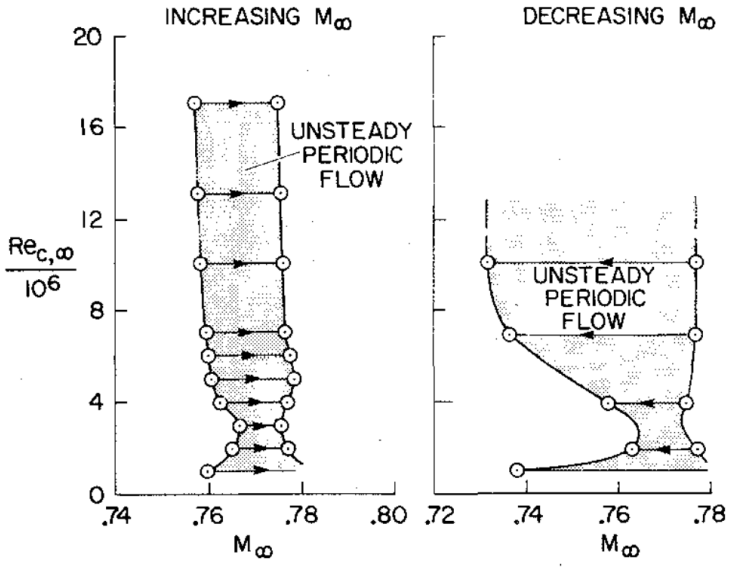

Figure 2.5: Cartography of the buffet instability amplification map. Figure from [179].

Studies on conventional and supercritical aerofoils were carried out afterwards. Roos [220] per-

formed experiments using the NACA0012 and Whitcomb aerofoils, at various Mach numbers and angles of attack. Pressure measurements over the suction side of the aerofoils allowed the detection of SIOs, with the amplitude of the lift oscillations correlating with the trailing edge pressure divergence. In his work, cross correlation between the signals was employed to observe a downstream disturbance propagation for fully separated flow. The influence of the test section was also pointed out, as the separation seemed to develop at the shock foot for the NACA0012, while it first appeared at the trailing edge for the Whitcomb aerofoil. Buffet over the NACA0012 was extensively investigated in the work of McDevitt and Okuno [178]. It was studied at the Ames High Reynolds Number Facility by McDevitt and Okuno [178]. Mach numbers were in the range of 0.71-0.8 and Reynolds number spanning between 1 million and 10 million. The buffet onset was detected by means of steady and unsteady pressure measurements. The tunnel walls were adapted to follow the free air streamlines, while the sidewall interference was reduced by thinning the sidewall boundary layer by means of suction applied on porous panels. Further details are given in the corresponding experimental reference [178]. Although these experiments are more than 30 years old, they still represent the broadest database for buffet onset, covering a wide range of conditions. Moreover, the treatment of the wind tunnel wall allowed for the flow to be as close as possible to 2D, making this test case particularly suitable for modelling using 2D cases. Lee and Ohman [158] and Lee [154] performed experiments on the BGK1 aerofoil, and confirmed many of the results of Roos [220]. The comparison with the WHEA II aerofoil, which is thicker than the BGK1, put into evidence a more drastic lift drop in the first case, and hence a more significant impact of buffet on thick aerofoils. Following the experimental campaigns, Lee [159] proposed the aforementioned acoustic feedback mechanism. The buffet period can be estimated as the summation of the time needed from a pressure disturbance to reach the trailing edge from the shock foot, and of the time needed to the sound waves to propagate back and hit the shock. The period T_b can be approximated as:

$$T_b = \int_{x_s}^{c} \frac{1}{a_p} \mathrm{d}x - \int_{c}^{x_s} \frac{1}{a_u} \mathrm{d}x \,, \tag{2.3}$$

where x_s is the shock position, a_p and a_u are the propagation velocities in the downstream and upstream phases, respectively.

One of the most successful experiments on buffet was carried out by Jacquin *et al.* [126] on the supercritical OAT15A aerofoil in the ONERA wind tunnel SCh3. The aerofoil was equipped with Kulite pressure transducers and pressure sensors on both sides. Schlieren and oil flow visualisation methods were used at different Mach number and at several angles of attack to detect buffet. Because of the employed experimental apparatus, a large amount of data was provided for comparison with CFD results. Schlieren and oil flow visualisation allowed the study of the shock position and of the separation location. Spectral analysis was performed by means of short-time Fourier transform. A two component Laser Doppler Velocimetry (LDV) allowed measurements

of velocity components at selected flow conditions. The experiment revealed a 2D behaviour on the wing, and different frequencies were detected in the shock and at the separation regions. A main frequency of around 70 Hz was computed (in scarce agreement with the theory of Lee [157]). The buffet frequencies and the associated peak in the power spectral densities also varied with the Mach number. By computing the correlation between pressure signals on both sides of the aerofoil, the presence of upstream travelling waves on the pressure side, was also observed. The spectral analysis carried out on the wing showed the independence of the fundamental buffet frequency on the spanwise and streamwise coordinates, and the buffet evolution was deemed to be of purely 2D nature. Nevertheless, the oil flow visualisation detected the presence of mushroom-shaped vortical regions of the separated boundary layer, shown in Figure 2.6, left figure. Their presence resulted in a non-uniform shock front without affecting the spectral content, as shown in Figure 2.6, right.

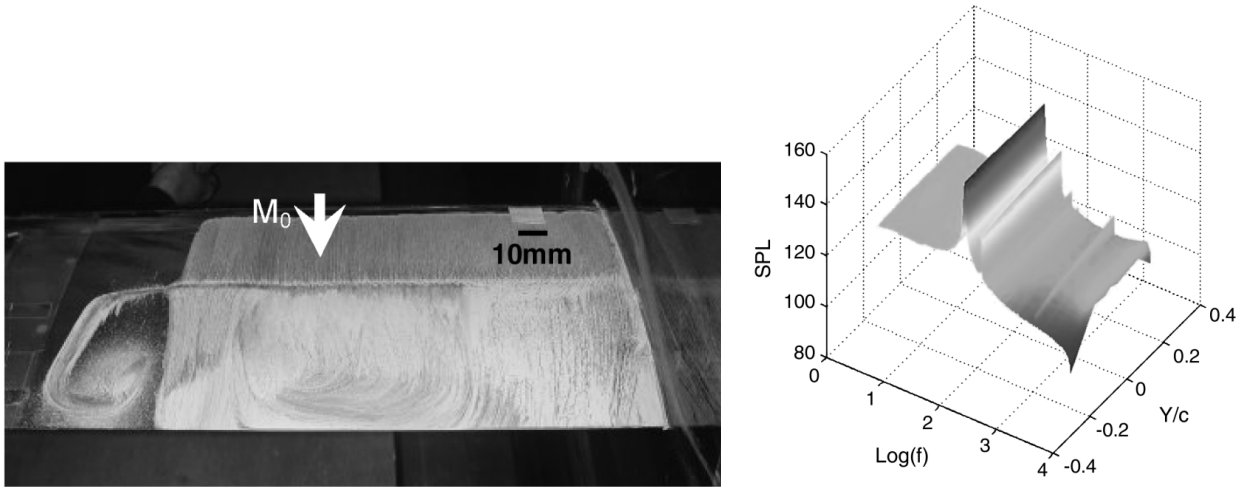

Figure 2.6: Right: oil flow visualisation of the flow around the OAT15A aerofoil at $\alpha = 3.5$ deg; left: PSD of the pressure signal at $x/c = 0.6$ and different spanwise locations (Y/c). Figure from [126].

Given the amount of data provided, and the availability of the geometry, the OAT15A could be considered as a good test case for assessing the ability of turbulence models in the context of unsteady simulations for external aerodynamics flows with SBLI. Therefore, this test case has been the subject of several computational works, as mentioned in Section 2.2.2.

The experimental campaigns of Hartmann *et al.* [111, 112] and Feldhusen-Hoffmann *et al.* [74, 75] studied the flow around the DRA2303 aerofoil at conditions of well established buffet. They employed Particle Image Velocimetry (PIV) together with pressure measurements to study the buffet dynamics. At the condition of natural buffet, the upstream shock motion was associated with the upstream-propagating pressure disturbance generated at the trailing edge, corroborating the theory of Lee [159]. The authors stated that the mechanism holds until the sound pressure level is too low, the extent of separation is too large, and the shock is no longer influenced by the disturbances. They also introduced artificial disturbances to reproduce the disturbances at the trailing

edge emanated during the shock buffet period. A horn placed behind the aerofoil emitted a sound wave with frequency close to the natural buffet frequency, and another frequency almost bigger by an order of magnitude. The frequency spectra, computed after the application of PIV on the plane of symmetry of the wind tunnel, evidenced a shift of the fundamental frequency according to that of the loudspeaker and a new peak corresponding to the higher frequency. The work underlined again the fundamental role of pressure feedback mechanism in two-dimensional buffet flows. The results from the experimental PIV were used to perform sparsity-promoting Dynamic Mode

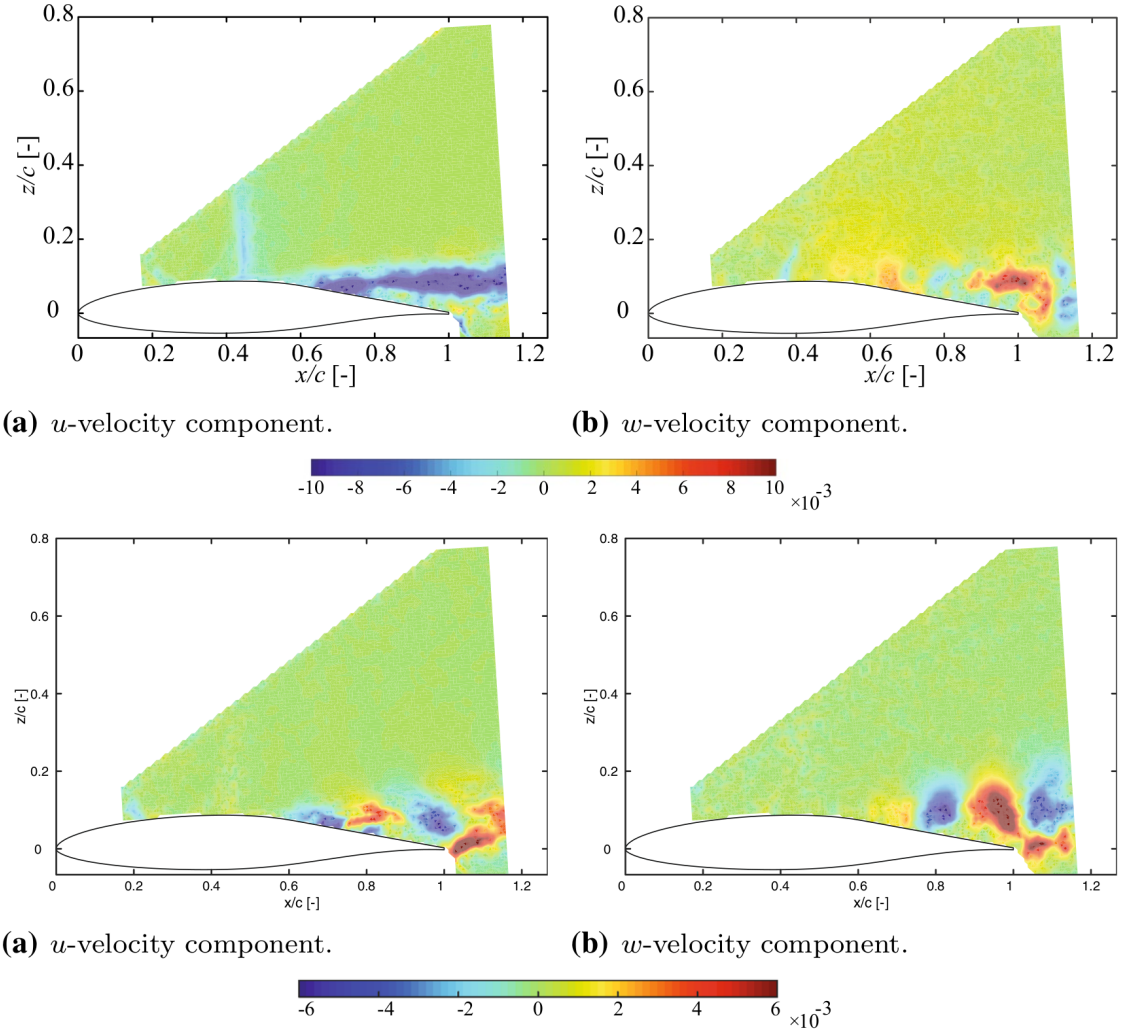

(a) u-velocity component. **(b)** w-velocity component.

(a) u-velocity component. **(b)** w-velocity component.

Figure 2.7: Horizontal (left) and vertical (right) velocity components of DMD modes. Top: buffet mode; bottom: vortex mode.

Decomposition (DMD). Two main modes, associated with the most energetic frequencies, were observed. These are shown in Figure 2.7. The low-frequency buffet mode (Figure 2.7, top) sees the coupling of the shock wave oscillation, and the changes in size of the separated flow region. The changes in the velocity downstream of the shock propagate from the shock foot. The sound waves generated at the trailing edge are weakened in different ways depending on the extent of the

separation region. On the other hand, the high-frequency vortex mode (Figure 2.7, bottom) sees the downstream propagation of vortices in the separated region. Once they pass over the trailing edge, the interaction with this latter results in sound generation. The strengths of the downstream propagating vortices vary according to the shock strength, i.e. it is modulated with a frequency equal to the buffet frequency. This reinforced the idea of Lee [159] for which buffet is sustained by sound waves of different Sound Pressure Level (SPL).

The OAT15A aerofoil was later investigated by D'Aguanno *et al.* [47,49] in the TST-27 transonic-supersonic wind tunnel of Delft University of Technology. Due to the slightly different flow conditions (Reynolds and Mach number), the predicted buffet frequency and onset were different from the previous investigation of Jacquin *et al.* [126]. The adoption of a reduced wing aspect ratio (2.8 against 3.4 in [126]) resulted in the absence of 3D mushroom-shaped structures. In [47], the main shock buffet features were investigated by means of Proper Otrhogonal Decomposition (POD) modes of the PIV snapshots obtained from the experiments. The three most energetic modes consisted of **(i)** a mode with the shock motion caused by breathing of the separated flow region; **(ii)** a mode associated with the shear layer thickening and thinning; **(iii)** and a mode associated with a second expansion of the first breathing mode. Figure 2.8 shows the first and second modes summed and subtracted to the average flow field. Phase averaging allowed for the analysis of the

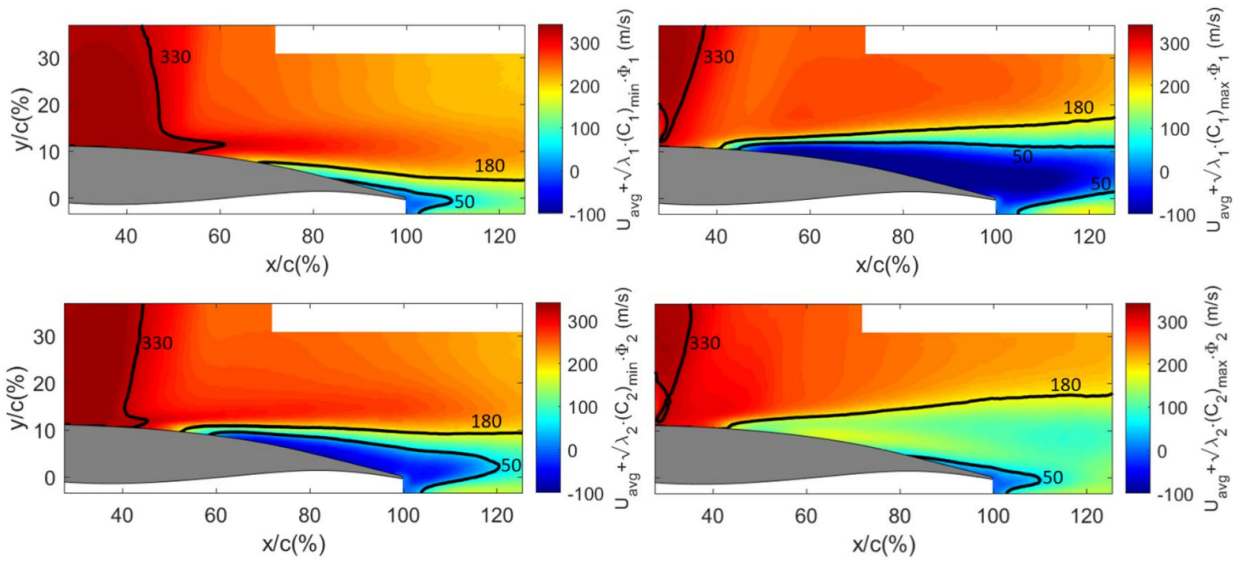

Figure 2.8: First (top) and second (bottom) modes summed (right) and subtracted (left) to/from the average longitudinal velocity field. Figure from [47].

shock dynamics according to the phase over the buffet period. Because of the relative velocity between the shock and incoming flow, the shock was stronger in its upstream motion, and assumed an oblique shape, while it was weaker in the downstream motion. This reflected in different separation sizes. Moreover, by subtracting a reconstructed field based on the first 11 modes from the instantaneous flow field, the presence of Upstream Travelling Waves (UTWs) was detected. This is

shown in Figure 2.9. The differences in the shock velocity in the upstream and downstream motion can be justified by the relative propagation direction with respect to the shock motion. In [49],

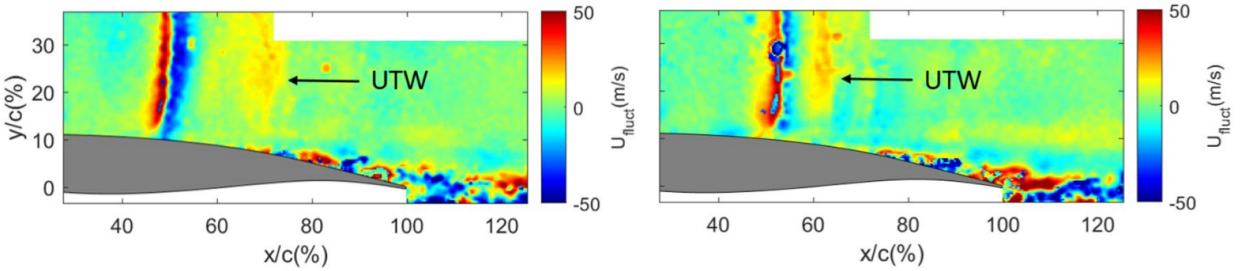

Figure 2.9: Horizontal velocity fluctuation at two different time steps on the OAT15A aerofoil in [47].

the spanwise organisation of the UTWs was studied on the same experimental model by means of Background-Oriented Schlieren (BOS). Their formation coincided with the three-dimensional turbulent structures reaching the trailing edge. It was speculated by the authors, that the 3D nature of such structures resulted in an inclination of the UTWs with no dependence on the buffet phase. Their strength and velocity, on the other hand, varied with the shock phase, confirming previous studies suggesting that these waves travel at the local sound speed (as found in [47]). Moreover, the strength of the UTWs was higher when the shock was at its most downstream position. In this view, the structures causing the propagation of UTWs may be formed in the separated Trailing-Edge (TE) area rather that at the shock foot.

The same test case was later analysed by Accorinti *et al.* [6] in the Trisonic Windtunnel Munich by means of BOS, and deformation and force measurements, on a flexible wing model. Although the general buffet features, i.e. mean value and standard deviation of the shock position, reduced buffet frequency, and onsets angle of attack, had similar trends as the ones reported in the literature, there was no quantitative agreement with previous published investigations [47, 126]. Indeed, several factors were deemed to contribute to this discrepancy (the onset AoA is delayed by about 2 deg) and were mainly linked to differences in experimental setups. Their work *et al.* [6] focused on the role of the shock motion inversion in the development of buffet. It was found that the shock inversion is a necessary but not sufficient condition for the buffet onset. Nevertheless, the delay between the shock motion inversion and the buffet onset (see Figure 2.10) was not explained in their work. In a later work [8], the same group attempted to justify the shock motion inversion with the need to satisfy the compatibility condition at the trailing edge, i.e. that the pressure must be identical on both sides of the aerofoil. Nevertheless, the continuous change in the effective aerofoil shape driven by the unsteady SBLI led the authors to discard that hypothesis. The investigation was complemented with the adoption of PIV measurements by Kokmanian *et al.* [142]. In a following work [7], the role of the wind tunnel walls was investigated by means of BOS. Approaching the sidewalls, the shock was weakened by the corner separation, and shifts upstream. From the corners, compression waves were emanated toward the centreplane. As the Mach number or the

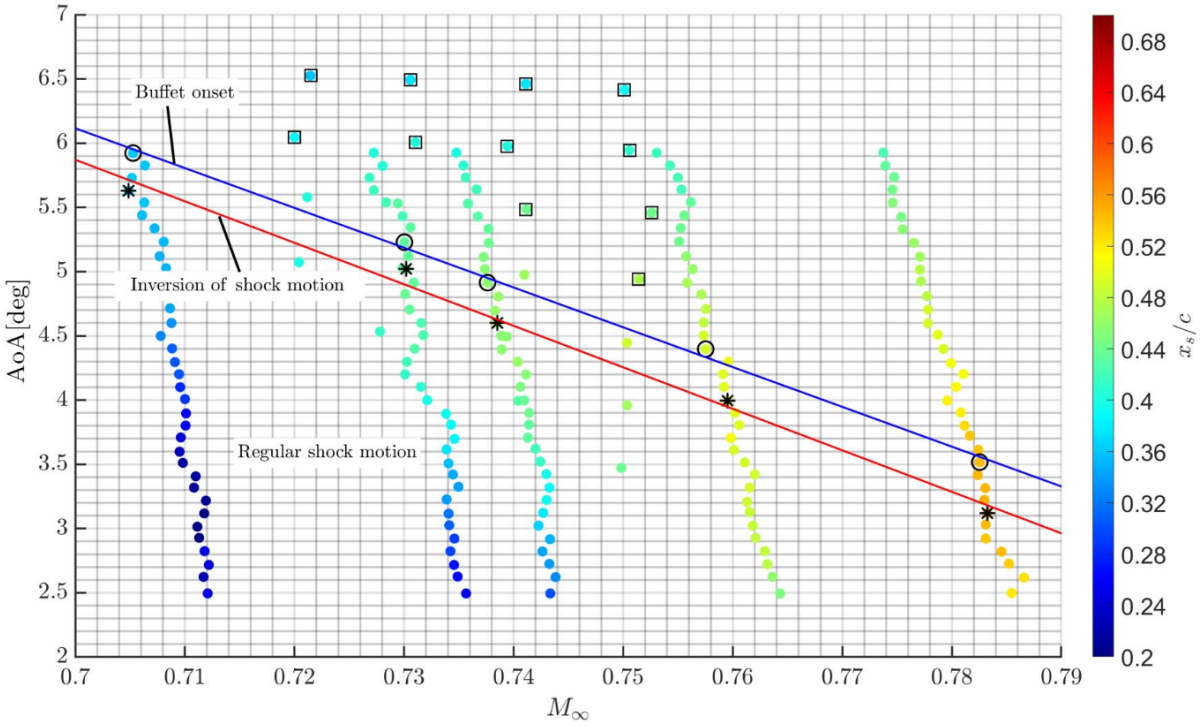

Figure 2.10: Time averaged shock location (colour legend) at different Mach numbers and angles of attack. Black stars: shock invertion points; Black circles: buffet onset; black squares: measured periodic buffet cases. Figure from [6].

angle of attack increased, the side-wall influence decreased. Coherently with the results of Jacquin *et al.* [126] and Sugioka *et al.* [252], the shock was weaker only in a small spanwise portion and the amplitude of the shock oscillation became uniform for great part of the span. Corresponding to the corner separation, a low-frequency content was detected in both pre- and post-buffet. An even lower frequency was observed in the separated flow region around the centreplane at buffet conditions. This was attributed by the authors to the interaction between the separated boundary layer and the shock, i.e. the one forming mushroom-like structures in [126, 252]. Nevertheless, such structures were not present in that campaign, mainly because of the reduced wing aspect ratio with respect to the other cases (2 compared to 3.4 [126] and 4.5 [252]).

2.2.1.2 3D Configurations

Experimental investigations of buffet were extended on a 30-degree swept configuration by Molton *et al.* [190]. The model, called BUFET'N Co, was studied in the S3Ch wind tunnel of ONERA to characterise uncontrolled buffet phenomena, help CFD validation, and study flow control. Accurate measurements on pressure (static pressure taps, Kulite pressure transducers, and accelerometers) and flow velocity (LDV and PIV) allowed for the characterisation of the uncontrolled flow around the wing. Measurements were performed at different angles of attack, with special attention at

$\alpha = 3.5$ deg, that presented a well-established buffet. In that work, only the pressure coefficient and a snapshot of the mean longitudinal velocity provided by PIV were proposed. For a large portion of the wing the results were not available due to restrictions in the experiments. Oil flow visualisation was also employed for the cases at pre-onset, onset, and post-onset (see Figure 2.11). A large separated flow region was observed for the cases at buffet conditions. Moreover, the flow revealed to be strongly three-dimensional, with the streamlines deflecting outboard. At the highest angle of attack, the separated flow region spanned from the shock foot to the trailing edge. For this configuration, this region was not significantly extended in the spanwise coordinates.

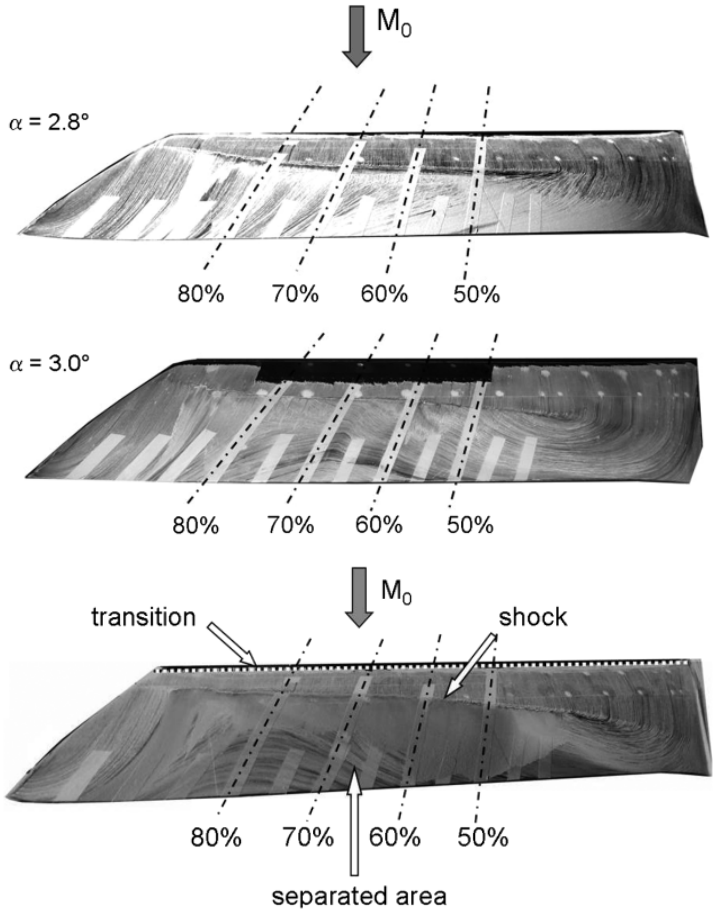

Figure 2.11: Oil flow visualisation around the BUFET'N Co model at $M_\infty = 0.82$. Top: $\alpha = 2.8$ deg; centre: $\alpha = 3.0$ deg; bottom: $\alpha = 3.5$ deg. Figure adapted from [190].

In a following work, Dandois *et al.* [53] investigated the flow around the AVERT model in the S2MA wind tunnel of ONERA. They determined a dual frequency content associated with the large amplitude motion at low frequency, and high frequency Kelvin-Helmoltz instabilities. Unlike 2D buffet cases, where a distinct peak was present in the spectrum, the swept wing spectrum exhibited an extended region of frequency content, centred around the main buffet frequency. The convection velocities were also computed, and different values were found for the buffet instability and the

Kelvin-Helmoltz one. The simple configuration exhibited a convection velocity associated with buffet directed outboard and towards the trailing edge (see Figure 2.12). This is consistent with the formation of buffet cells on 3D configurations [122].

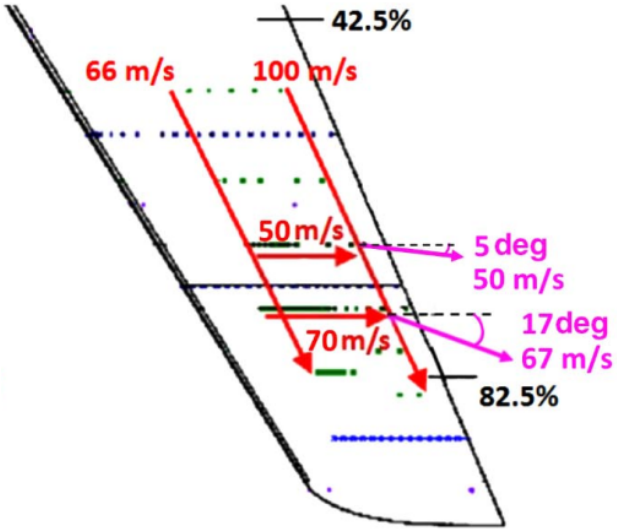

Figure 2.12: Convection velocities on the AVERT model. Figure from [53].

Investigations on the NASA Common Research Model (CRM) were carried out by Koike *et al.* [137, 138] and Sugioka *et al.* [251]. Koike *et al.* [137, 138] investigated the buffeting flow around this wing-body configuration in the Japan Aerospace Exploration Agency (JAXA) 2m $\times$ 2m transonic tunnel at $M_\infty = 0.85$, and $\mathrm{Re}_c = 5 \times 10^6$. The 80% scaled model was equipped with pressure ports, unsteady pressure sensors at two sections of the wing, and markers for wing deformation measurements. The flow was tripped ahead of the shock to enhance turbulence. The aforementioned tools allowed for measurements of the aerodynamic coefficients at several angles of attack ($\alpha = -1$ to 6 deg) and the buffet onset ($\alpha_B \simeq 3$ deg). At that condition, breaks in the lift and pitching moment curves were detected. Moreover, trailing edge pressure divergence was observed together with an upstream shock motion. Compared to the 2D configuration the extent of the fluctuations was reduced. The Root Mean Square (RMS) of the pressure coefficient exhibited a kink, moving upstream and growing with higher angles of attack. At higher angles of attack the oscillations became stronger. Three regions were then distinguished: **(i)** the pre-buffet one at $\alpha < 3^\circ$ with small and uniform pressure fluctuations, **(ii)** one with small chordwise shock oscillations at $3^\circ < \alpha < 5.5^\circ$, and **(iii)** the one presenting larger oscillations at higher angles of attack. Looking at the Power Spectral Density (PSD) of the pressure coefficient C_p in Figure 2.13, it is possible to notice the same subdivision: in the second region the PSD shows a bump around $St = 0.3$ while in the third, the spectrum is broadband at low frequencies. Finally, cross-correlation and coherence calculations detected an outboard motion of the pressure disturbances between the two sections equipped with unsteady sensors, to evaluate the convection velocity. The spanwise

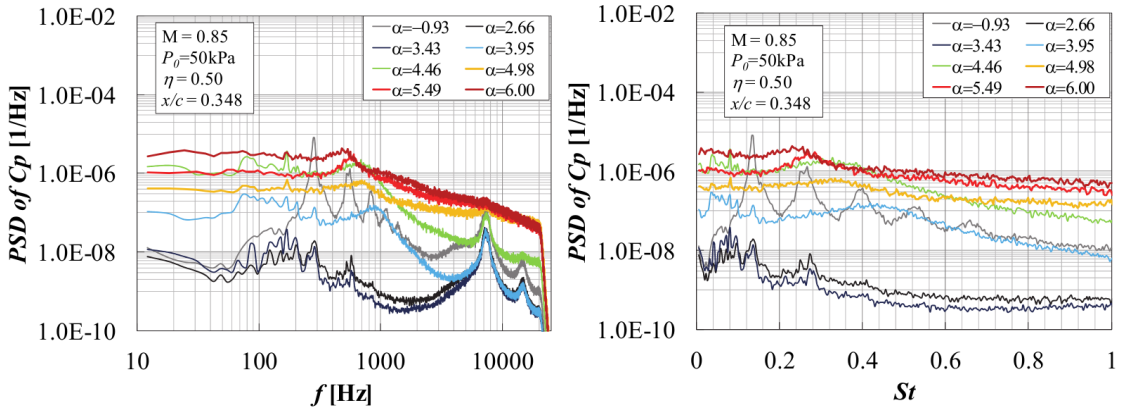

Figure 2.13: Power spectral density of the pressure coefficient at mid-span and $x/c = 0.38$ and $\mathrm{Re}_\infty = 0.947 \times 10^6$ on the NASA CRM. Figure from [138].

shock oscillations are sketched in Figure 2.14.

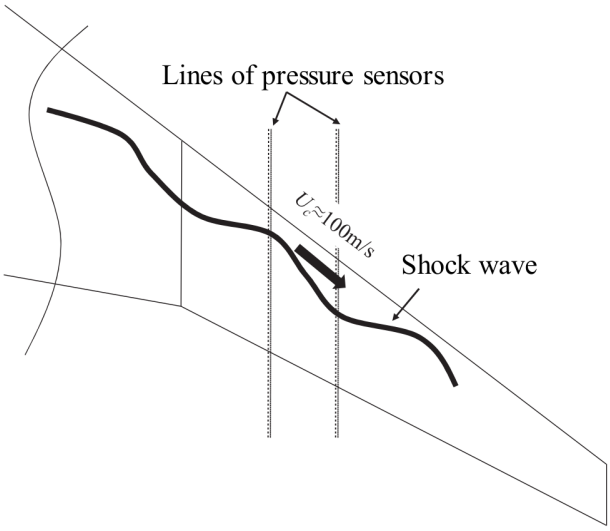

Figure 2.14: Sketch of the shock wave oscillations around the NASA CRM. Figure from [138].

This work was complemented with measurements based on Pressure-Sensitive Painting (PSP) from Sugioka *et al.* [251]. PSP allowed for the acquisition of pressure snapshots over the wing and provided a clear visualisation of the evolving pressure field. With these measurements, a new low frequency at higher angles of attack stemming from the interaction with the trailing edge separation was detected. This finding was confirmed by the work of Sugioka *et al.* [253], who employed fast-response PSP to acquire pressure data at different angles of attack. When the angle exceeded the buffet onset ($\alpha_B = 3.34$ at $\mathrm{M}_\infty = 0.85$ and $\mathrm{Re}_c = 2.27 \times 10^6$), buffet cells with an outboard propagation velocity of about $0.5U_\infty$ and a wavelength of $1.3c$ were observed. The frequencies associated with the buffet fluctuations were $0.2 \leq \mathrm{St} \leq 0.5$. An illustration of the coherence and phase-shift at pre- and post-buffet conditions is shown in Figure 2.15.

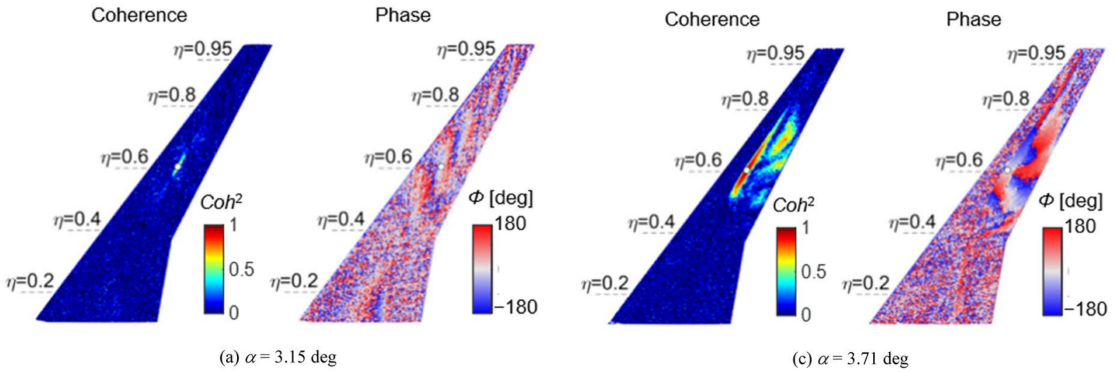

Figure 2.15: Coherence and phase-shift around the NASA CRM at pre- (left) and post- (right) buffet onset. Figure from [253].

The work of Lawson *et al.* [153] focused on three-dimensional buffet around the 3D swept wing RBC12 of ARA. The experiment conditions are reported in Table 2.1 and the experimental apparatus is described in reference [153]. The static pressure was measured by static pressure taps and the aerodynamic forces with a five-component strain gauge, accelerometers and a root strain gauge. The rich experimental setup allowed for the comparison of several buffet indicators. A Dynamic Pressure-Sensitive Painting (DPSP) technique was employed to capture the 3D flow development through unsteady surface pressure measurements. In the work of Masini *et al.* [173], Cross-Spectral Density (CSD), PSD, and phase angles between signals were calculated to estimate the energy content and the convective velocity of the shock. As the main focus of the work, modal decomposition through POD and DMD was used to capture the most influent modes on pressure fluctuation, reconstruct the pressure field, and identify the shock position from the extracted modes. Using the DPSP obtained from camera acquisition they could collect snapshots of the entire pressure fields over the wing, unlike point-wise measurements using Kulite sensors. The obtained POD modes are shown in Figure 2.16. In their work, two phenomena were underlined at the basis of shock motion: **(i)** low-frequency shock-unsteadiness, characterised by inboard-propagating pressure disturbances, and **(ii)** intermediate-frequency perturbations that propagated outboard. The first phenomenon was also present before at pre-buffet conditions. Many other results were given about the unsteady shock motion, the determination of the main modes related to elasticity and the shock, and the very detailed 3D pressure field along the wing. These measurements determined the shock position and motion over all the wing suction side, putting into evidence the "deformation" of the shock depending on the spanwise position, and the disturbance propagation over the buffet period. Therefore, the RBC12 has been extensively investigated by means of CFD [169–171, 228, 230].

The features of 3D buffet were synthesised in the comparative work of Paladini *et al.* [201]. In their study, the results from four experimental campaigns on half-wing body configuration were scritunised and compared. The models were: the BUFET'N Co model [190], the AVERT model [53], the DPT Tremblement, and the FLIRET model. Power spectral densities, cross-spectra and

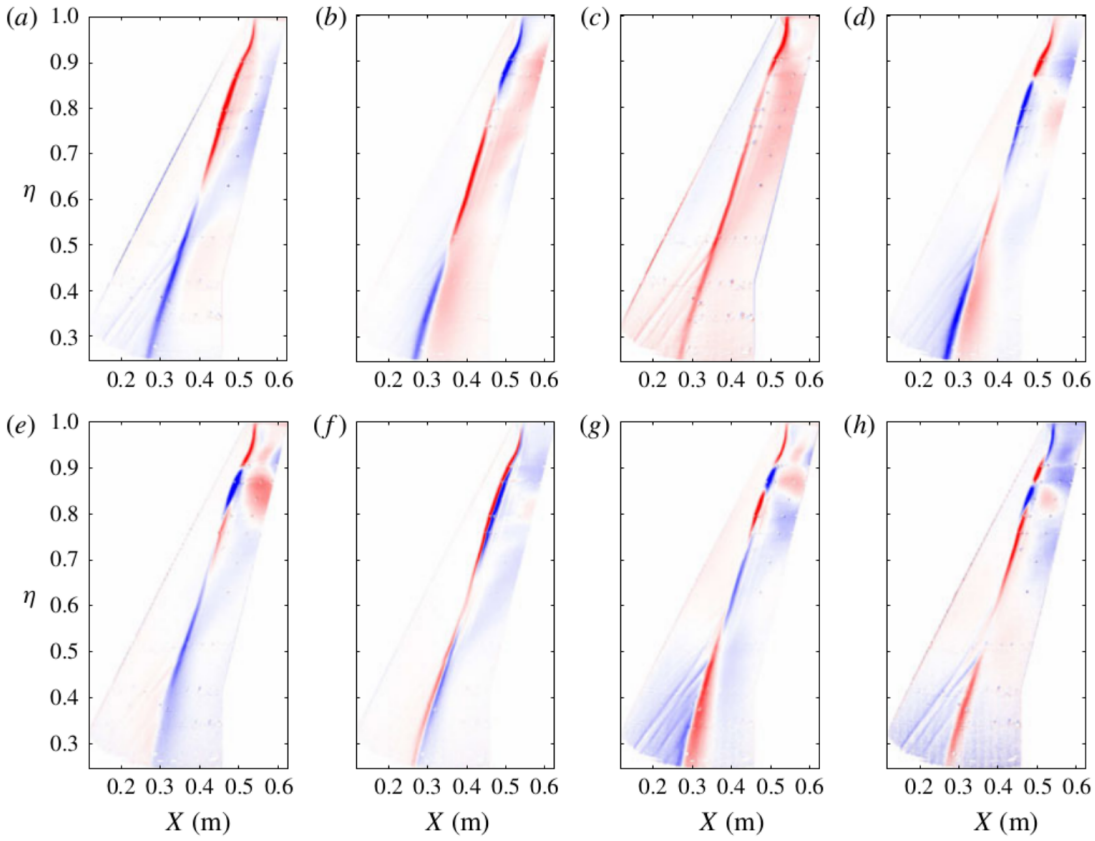

Figure 2.16: Dominant POD modes around the RBC12 wing in buffet flow. Figure from [173].

frequency-wave number spectra of the measured pressure were computed. The main outcomes were:

- No definite peaks were detected in the PSDs. Frequency content centred around St $= 0.2 -$ 0.3 was found for every configuration;
- At the buffet Strouhal number, the convection velocities were in the range of $U/U_0 = 0.245 \pm$ 0.015 in the spanwise direction;
- Buffet cells were observed (except for the DTP model, most probably because of the reduced aspect ratio);
- The buffet cells wavelength was geometry dependent. When non-dimensionalised with the mean aerodynamic chord, it assumed values bound between 0.6 and 1.3.

Although the majority of the experimental (and numerical, Section 2.2.2) works showed the presence of 3D buffet in the form of buffet cells, the unsteady PSP on the ONERA-M4 wing from Uchida *et al.* [270] showed a different pattern. The significant differences in the geometry led to a different buffet development with respect to the one observed in previous analysed works. The

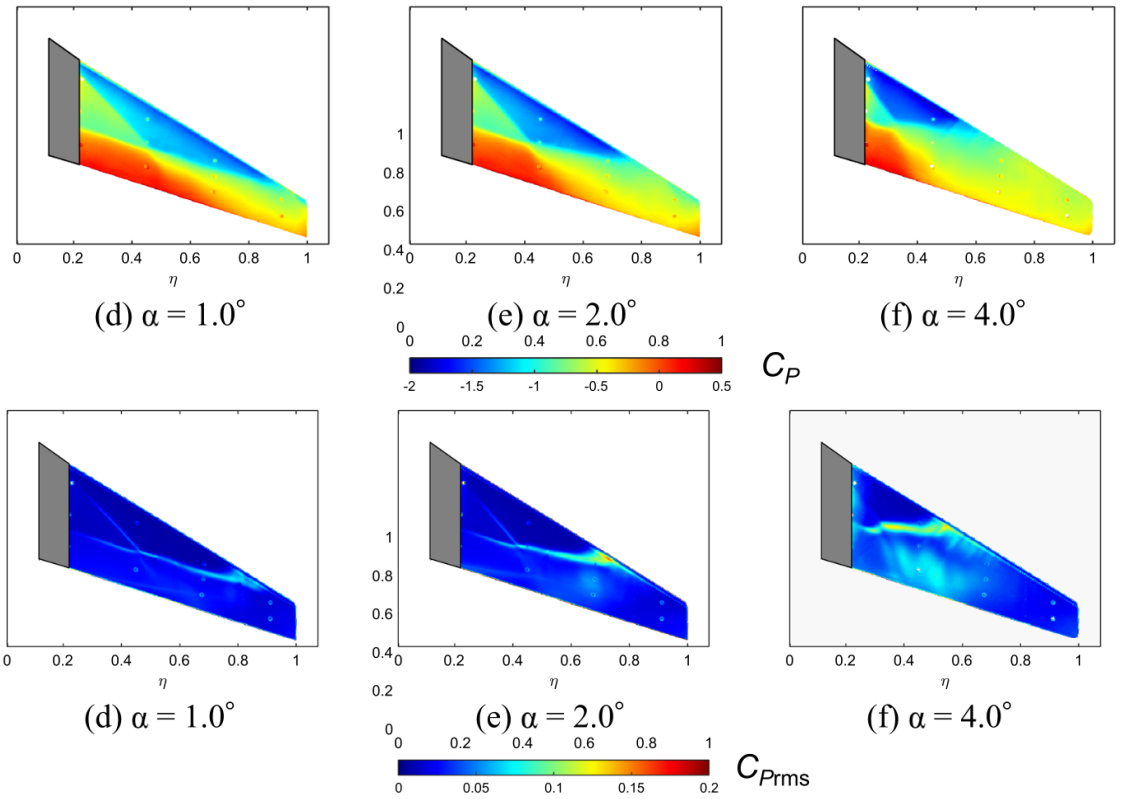

Figure 2.17: Mean pressure coefficient and RMS on the M4 wing at different angles of attack. Figure from [270].

analysed wing displayed a dual shock topology and boundary layer separation starting from the wingtip at high angles of attack, as shown in Figure 2.17. Still, some oscillations were detected. At low angles, with the separation reaching the leading edge, the shock oscillated with large amplitude and frequency St < 0.05. At higher angles, the shock oscillated with a frequency of St $\simeq 0.11$ and the fluctuations propagated outboard. This distinction is sketched in Figure 2.18. One can speculate that this case, for geometric reasons, displayed intermediate features between 2D and "common" 3D buffet. The buffet mechanism shifted from a 2D-like scenario to a different one, displaying spanwise convection velocities.

In this view, Sugioka *et al.* [252] tried to shed light on the differences in shock oscillations on swept and unswept wings. They carried out experiments on unswept and low-sweep wings extruded from a CRM profile. Shadowgraph, oil flow and unsteady pressure measurements were carried out in the JAXA Second Transonic Wind Tunnel, JTWT2. The large wing aspect ratio $AR = 4.5$ allowed for the development of three dimensional structures even on the unswept configuration (see Figure 2.19, left). This was in common with the results of Jacquin *et al.* [126]. In the swept case (see Figure 2.19, right), the oil flow showed a strong flow three-dimensionality, culminating in spanwise-directed flow at high angles of attack. By means of DMD corresponding to the most energetic frequencies (extracted by Fast Fourier Transorm (FFT) of the pressure signals), two

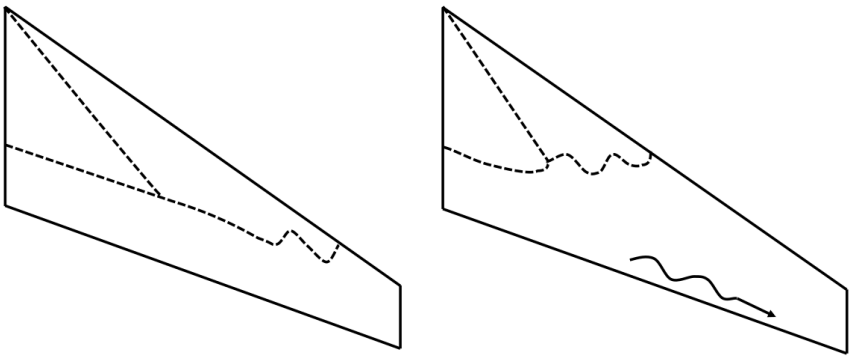

(a) $St = 0.011$ (b) St = 0.11

Figure 2.18: Sketches of the shock oscillation for the ONERA-M4 wing at different frequencies. Figure from [270].

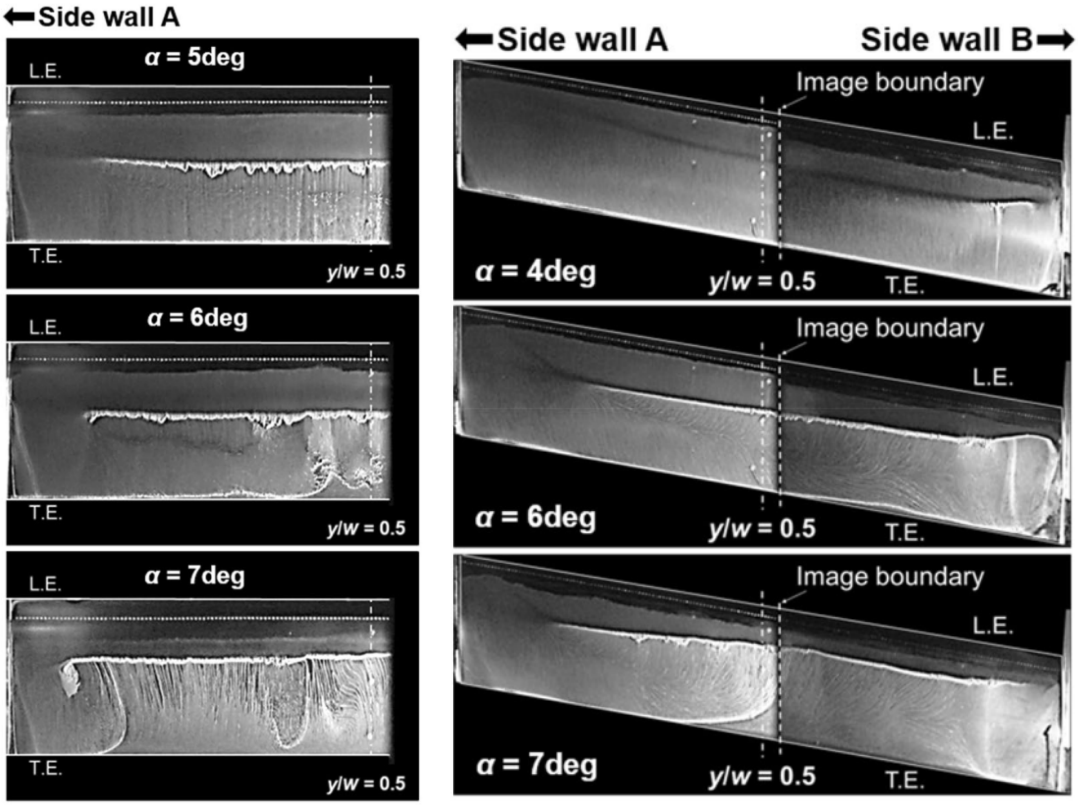

Figure 2.19: Oil flow visualisation of the 0 deg (left), and 10 deg (right) swep-wing model. Figures from [252].

fundamental mechanisms were found to be concurrent in the development of buffet of the swept configuration. At low frequency, the reconstructed mode showed large-amplitude shock oscillations in the longitudinal direction and pressure disturbances propagating inboard. At higher frequencies, the location of the oscillation was shifted in the second half-span with outboard-travelling disturbances. In this work, buffet cells were not observed in the swept configuration, but the propagation

direction was the same as for previous studies presenting buffet cells. The comparison of the local Strouhal number with the sweep angle for different works (the aforementioned experimental ones and some numerical ones in the next section) showed a clear correlation between the two quantities (see Figure 2.20). The only exception was the work of Uchida *et al.* [270], which presented significant differences in the geometry investigated, and therefore in the buffet development.

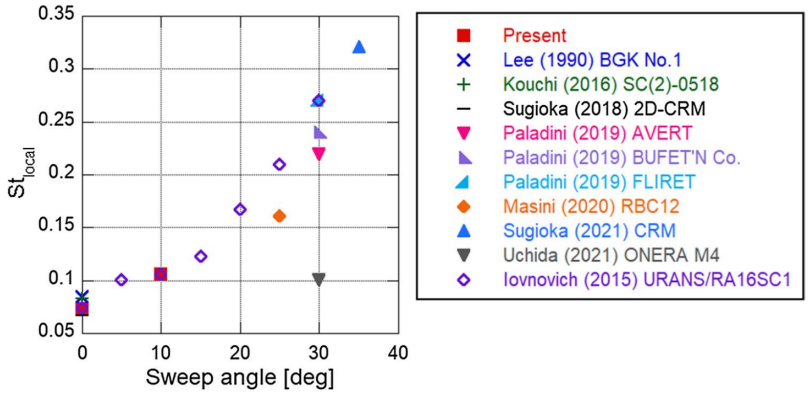

Figure 2.20: Collection of Strouhal numbers associated with several studies against sweep angle. Figure from [252].

A similar study was carried out by D'Aguanno *et al.* [50], who compared the buffet development around an OAT15A aerofoil, an unswept finite wing (untapered), and two swept finite wings (also untapered). The incoming Mach number was selected to have a common normal Mach number equal to 0.7. Oil flow visualisation, BOS, and PIV were used in the experimental campaign. The comparison between the aerofoil and the unswept wing revealed substantial differences, as shown in Figure 2.21. The shock excursion on the aerofoil was much wider, and the mean position far downstream (42.8% against 28.3%). Moreover, the trailing edge flow was - on average - only separated in the first case. In the unswept wing, the shock front was curved, while it remained straight on the aerofoil. The tip effect on the finite wing resulted in an inboard deviation of the streamlines, while corner separation was observed at both ends of the model. As the sweep angle increased, two differences were observed. The first, was the occurrence of an intermittent secondary pocket for the highest sweep case, observed in the streamwise and spanwise velocity components. Moreover, at the highest angle, the frequency content associated with the 2D buffet decreased while in all cases, a region of strong frequency content was observed around frequencies 3 to 5 times higher. This hinted at a transition from 2D to 3D buffet. Nevertheless, the limited wing aspect ratio did not allow for the development of buffet cells.

2.2.2 Transonic Buffet CFD

The prediction of buffet by means of CFD is still challenging. The difficulties stems from the presence of shock waves and boundary layer separation, culminating in a self-induced instability.

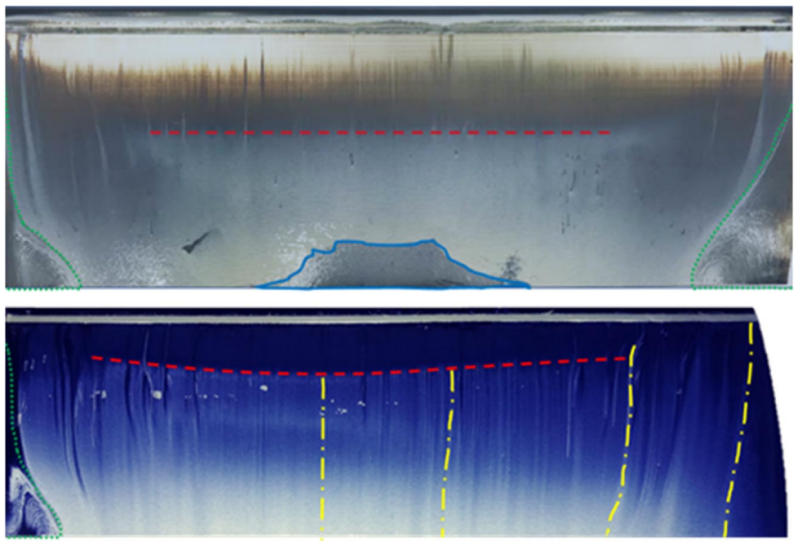

Figure 2.21: Oil flow visualisation for the OAT15A aerofoil (top) and unswept finite wing (bottom). Figure from [50].

This has introduced questions about the performance of different turbulence models in the URANS context, and led to the use of hybrid modelling approaches. For an extensive covering of the topic the reader is referred to the review paper of Lee [157] and, for more recent developments, to the work of Giannelis *et al.* [100]. This section sees a collection of past numerical works, summarised in Table 2.2. This survey aims at

- pointing out strength and flaws of turbulence models across a variety of configurations and flight conditions;
- underlining, if any, advantages and disadvantages of scale resolving simulations over URANS;
- mentioning alternatives to time-marching simulations and assessing their reliability and utility;
- corroborating experimental results, and building a better understanding of 2D transonic buffet;
- further pointing out and investigating differences between 2D and 3D buffet.

Table 2.2: Reviewed numerical works for transonic buffet without flow control. SRS: scale-resolving simulations; GSA: global stability analysis; TSM: time-spectral method.

Author	Geometry	M_∞	Re $\times 10^6$	α	Turb. Modelling
RANS					
Barakos & Drikakis [15]	NACA0012	0.72-0.8		1-5	URANS
Goncalves & Houdeville [105]	RA16SC1	0.723	4.2	0-3.5	KL, SST, KE, KW, SA

Continued on next page

Table 2.2 – *Continued from previous page*

Author	Geometry	M_∞	Re $\times 10^6$	α	Turb. Modelling
Xiao *et al.* [283]	BGK1	0.71	20	6.97	URANS
Thiery & Coustols [257, 258]	OAT15A 2D	0.73	3	3.5	SST, SA, BSL, KKL
	OAT15A 2D conf.	0.73	3	3.5	SST, SA, BSL, KKL
	OAT15A 3D conf.	0.73	3	3.5	SST, SA, BSL, KKL
Illi *et al.* [119]	OAT15A (3D)	0.73	3	3.5	URANS
Iovnovich & Raveh [120]	NACA0012	0.72	10	>9	SA
	RA16SC1	0.732	4.2	>9	SA
	NACA64A204	0.75	10	>9	SA
Iovnovich & Raveh [122]	OAT15A Wing	0.82	2.5-10	3-3.5	EC-SA
	RA16SC1 Wing	0.732	4-20	5	EC-SA
Sartor *et al.* [228]	RBC12 Wing	0.8	3.75	0-4.2	SST-SA
Zimmermann *et al.* [293]	OAT15A (2D)	0.73	3	3.5	SALSA
	RAE2822(2D)	0.73	6.5	3.19	SALSA
	NACA0012(2D)	0.72-0.77	10.0	3-4.2	SALSA
Giannelis *et al.* [98]	OAT15A (2D)	0.56-0.74	3	3-9.5	SST *
Poplingher *et al.* [216]	RA16SC1	0.732	4.2	0-4.5	URANS
Giannelis *et al.* [99]	OAT15A (2D)	0.61-0.74	3	3-9.0	SST †
Zhao *et al.* [290]	OAT15A (2D)	0.73	3	3.5	SA-SST-EARS
Plante *et al.* [210]	OALT25 Wing	0.7352	3	4.0	SA-EDW
	NACA4412 Wing	0.2	0.35	0.0-10.0	SA-EDW
Poplingher & Raveh [215]	OAT15A	0.7-0.75	3.0	2.9-3.5	SA-EDW
	AVERT Wing	0.82	3.6	2-4	SA-EDW
	BSCW	0.8	2.8	1-7	SA-EDW
SRS					
Deck [59]	OAT15A (3D)	0.73	3	3.5	ZDES
Brunet & Deck [35]	CAT3D (3D)	0.82	2.8	2.2-4.2	ZDES
Garnier & Deck [91]	OAT15A (3D)	0.73	3	3.5	LES
Huang *et al.* [117]	OAT15A (3D)	0.73	3	3.5	IDDES
Grossi *et al.* [107, 108]	OAT15A (3D)	0.73	3	3.5	DDES
Szubert *et al.* [255]	OAT15A (3D)	0.73	3	3.5	OES
Ishida *et al.* [124]	OAT15A (3D)	0.73	3.0	3.57	ZDES, IDDES
Ishida *et al.* [123]	CRM	0.85	1.5	4.87	ZDES
Bonnifet *et al.* [28]	OAT15A (3D)	0.73	3	3.5	PANS-RSM
Sartor & Timme [230]	RBC12 Wing	0.8	3.75	3.8	DDES
Dandois *et al.* [56]	OALT25 (3D)	0.735	2.8	4.0	ILES
Memmolo & Pirozzoli [181]	V2C (3D)	0.7	3.0	4.0-7.0	IDDES,ILES
Masini *et al.* [170]	RBC12 Wing	0.8	3.75	3.1	DDES
Ohmichi *et al.* [198, 199]	CRM	0.85	1.516	4.87	ZDES
Fukushima & Kawai [80]	OAT15A (3D)	0.73	3	3.5	WMLES
Masini *et al.* [171]	RBC12 Wing	0.8	3.75	3.1	DDES
Masini *et al.* [172]	RBC12 Wing	0.8	3.75	3.1,3.8	DDES
Ehrle *et al.* [70]	CRM	0.85	30	5.0	URANS, DDES, AZDES
Kojima & Hashimoto [139, 140]	OAT15A (3D)	0.73	3	3.5	ELES
GSA					
Crouch *et al.* [44, 45]	NACA0012	0.76	10.0	3-3.2	RANS(GSA)
Crouch *et al.* [46]	OAT15A Wing	0.76	10.0	3-3.2	RANS(GSA)
Timme [264]	CRM	0.72-0.73	3.0	2.5-5.5	RANS(GSA)
He & Timme [114]	OAT15A Wing	0.73	3.2	3.2-3.5	RANS(GSA)
Sansica *et al.* [223]	CRM-2D	0.72	2.5	4,7	RANS(GSA)
Other					

Continued on next page

*The a_1 coefficient was reduced here to promote flow unsteadiness

†The a_1 coefficient was reduced here to promote flow unsteadiness

Table 2.2 – *Continued from previous page*

Author	Geometry	M_∞	Re $\times 10^6$	α	Turb. Modelling
Chung *et al.* [41,42]	NACA0012 (2D)	0.7-0.8	6	0-5	Steady Criteria
Plante & Laurendeau [211]	OAT15A (2D)	0.73	3	3.5	TSM

2.2.2.1 2D Configurations

Statistical turbulence modelling

Because of the low frequency of the shock oscillation driving buffet, the URANS approach may seem the most appropriate to describe the phenomenon. Therefore, a number of authors investigated the ability of this approach to capture buffet around two- and three-dimensional configurations. Still, there is no consensus on the ability of URANS to predict buffet, being this influenced by a number of factors: turbulence modelling, numerical schemes, spatio-temporal discretisation and influence of the wind tunnel geometry.

Barakos and Drikasis [15] compared the performance of several two-equation turbulence model on a NACA0012 buffet case. Together with the Baldwin-Lomax and the Spalart Allmaras (SA) model, other k-ε and k-ω based models were tested, with the addition of non-linear terms in the Reynolds stress tensor expansion and even with a functional C_μ. The used of variable C_μ was beneficial in the prediction of buffet when coupled with non-linear models, and the SA model was equally good. On the other hand, the use of Menter's Shear Stress Tensor (SST) model [184] was recommended by Goncalves and Houdeville [105], who assessed its validity against other one- and two- equation models for the RA16SC1 aerofoil buffet case. Moreover, they deemed as secondary the effect of the numerical schemes over that of turbulence models. Thiery and Coustols [257] pointed out the influence of the aerofoil shape by comparing results, obtained using the SA and SST models, for the RA16SC1 and OAT15A aerofoils. The SA models predicted the SIOs on the first configuration, while the addition of upper and lower walls of the wind tunnel geometry were needed to unlock the flow unsteadiness in the second case. The SST model was sensitive to the near-wall strategy adopted. In a later work [258], the same authors investigated the influence of the wind tunnel presence. On the OAT15A aerofoil, the SST model was the only one able to predict the SIO in every case. The SA model, on the other hand, failed when the sidewalls were also accounted for. Illi *et al.* [119] performed simulations around the OAT15A aerofoil using unstructured and hybrid grids using a Reynolds stress model, that was shown to be more accurate with respect to the SST model, the Strain-Adaptive Spalart Allmaras (SALSA) version of the SA model, and the Linear Explicit Algebraic k-ω. Grossi *et al.* [108], compared the performance of several one- and two-equation models, for the same configuration. Although the SA or SST models performed well at pre-buffet condition, the Edwards-Chandra [69] model

with compressibility correction proved to be the best in that study, due a reduced eddy viscosity in the boundary layer that enables an early separation. The same turbulence closure was used in the work of Iovnovich and Raveh [120] and the SIO was well predicted around three different geometries. For the flow around the NACA0012, the SA model failed at predicting the correct onset angle at high Mach numbers leading to a difference of almost 2 degrees. In a recent study, Giannelis *et al.* [98] stated that the SA and the SST models were not able to predict the SIO on the OAT15A aerofoil. Therefore, a reduction in the a_1 coefficient of the SST model was applied to obtain a fair comparison with the experiments. In addition, a Stress-Omega Reynolds Stress Model was employed. This latter slightly over-predicted the amplitude of oscillation and the RMS, but was able to detect the SIO without the need for further corrections. Recently, the SALSA model, which was previously used with contradictory results [108, 119], was successfully modified by Zimmermann [293] to improve the prediction for buffet flows. The applications of URANS on the OAT15A aerofoil, the most investigated configuration for buffet studies, were collected in Appendix A to put into perspective the impact of several factor on the prediction of buffet with a rigorous and more quantitative review of the literature.

When successful, it was possible to explore the global features of transonic buffet by means of URANS. CFD computations were used to corroborate existing experimental results. This was the case of the work of Xiao *et al.* [283] who investigated the flow around the BGK1 aerofoil. By probing the aerofoil suction side and computing cross-correlation, the presence of downstream-propagatin pressure waves was observed (see Figure 2.22, left). The same tool allowed for the detection of upstream travelling waves outside of the boundary layer (Figure 2.22, right), confirming the findings of Lee [159]. The buffet period was then evaluated as the time needed from a wave to reach the trailing edge from the shock foot, plus the one needed to hit the shock when a disturbance propagates back out side of the boundary layer. Following the experiments of Jacquin *et al.* [126] and the work of Crouch *et al.* [45], pressure disturbances propagating towards the leading edge on the pressure side were observed. To exclude the impact of such disturbances, Memmolo and Pirozzoli [181] introduced a sponge region before the trailing edge on the pressure side of a V2C aerofoil. In their study, this effect was found to have limited impact on the overall buffet prediction.

Iovnovich and Raveh [120] focused on the behaviour at the buffet onset and offset, for different aerofoils. The authors excluded buffet to be caused by separation bubble bursting. Instead, the onset of buffet was reconnected to the unsteady interaction between the shock and the separation bubble. At the onset (see Figure 2.23, left images), the shock was located after the point of maximum curvature on the upper surface. That specific location helped promote flow separation, as it coincided with the beginning of an adverse pressure gradient region. Once the shock foot separation and the trailing edge separation merged, buffet took place. After the offset (see Figure 2.23, right images), the flow was stalled and the shock assumed a forward position.

When successful, URANS simulations were also used to study buffet at different flight con-

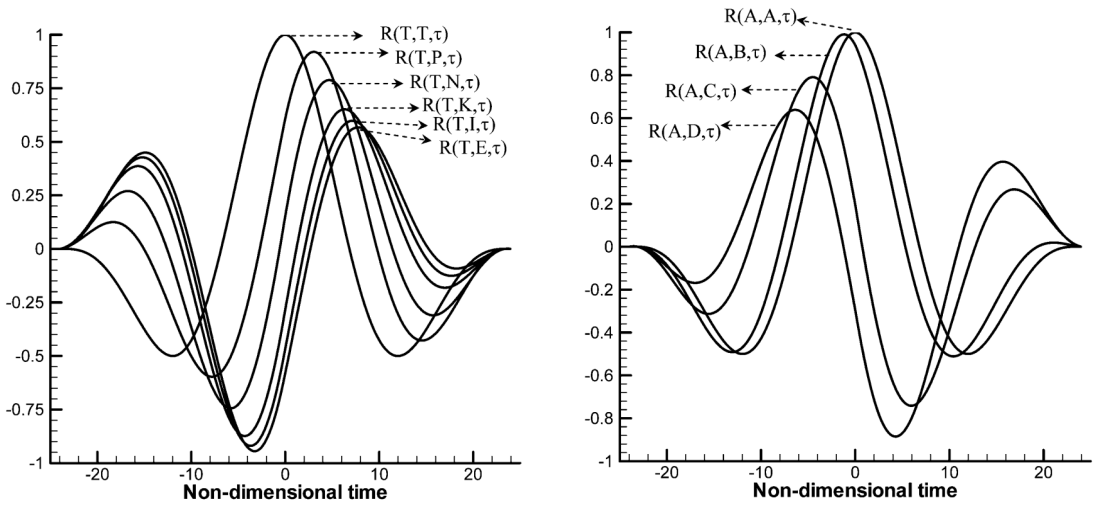

Figure 2.22: Cross correlation for probes in the suction side boundary layer (left) and outside of the boundary layer (right). Probes E to T have increasing x/c, while probes A to D have decreasing x/c. Figures from [283].

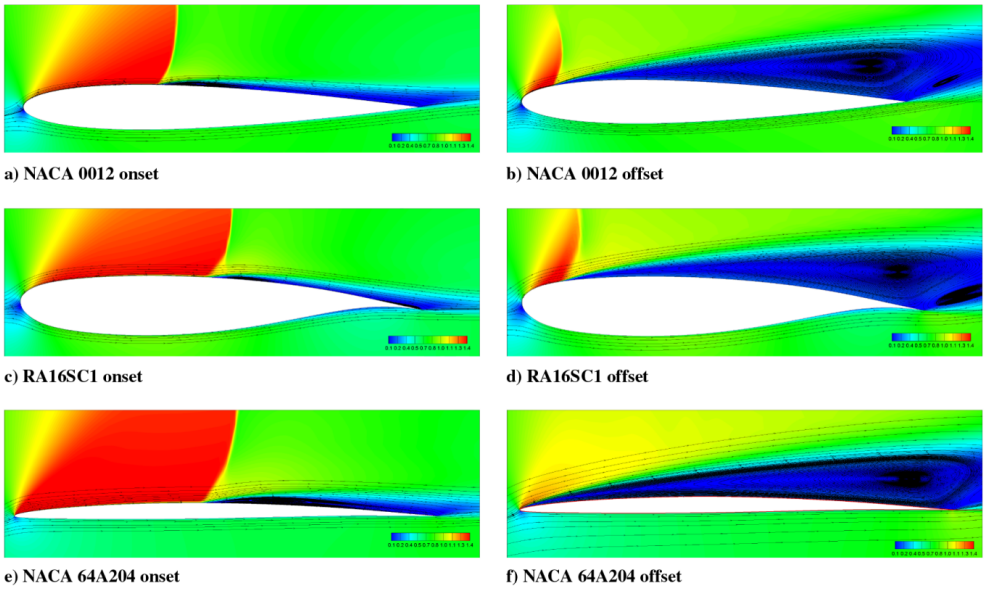

Figure 2.23: Mach contours for different aerofoils at onset and offset conditions. Figures from [120].

ditions. Giannelis *et al.* [98] studied the influence of the flight parameters, i.e. angle of attack and Mach number, on the dynamic features of buffet for the OAT15A aerofoil. The main findings of their work are summarised in Figure 2.24. The figure shows the buffet frequency and the lift oscillation amplitude according to Mach and angle of attack variations. The study confirmed the presence of buffet onset and offset for the OAT15A aerofoil. The severity of the oscillations increased with both Mach number, and angle of attack, reached a maximum, and decreased approaching the offset. Same considerations held for the natural buffet frequency. In the majority of the cases, the shock oscillation was of type A, while at high angles of attack, a combination of type

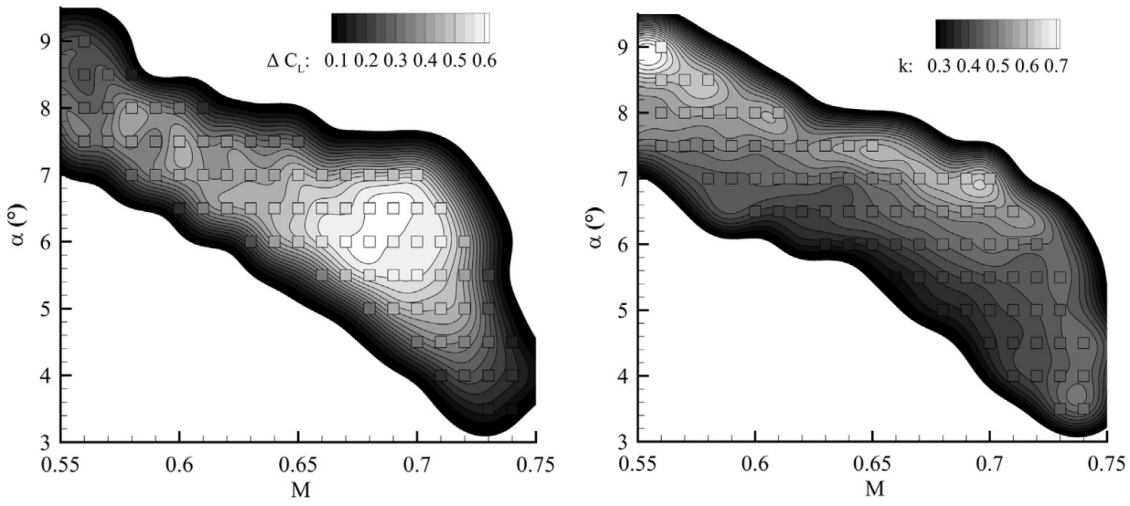

Figure 2.24: Contours of lift amplitude and buffet frequency with flight conditions for the OAT15A aerofoil at $\mathrm{RE}_c = 3 \times 10^6$. Figures from [98].

A and C took place, with the shock propagating in the upstream flow. The nature of this atypical case was studied by the same authors in a later paper [99]. The development of the phenomenon is shown in Figure 2.25. The lift coefficient history sees a strongly irregular behaviour, caused by the ingestion of the shock in the free stream and the propagation of recirculation pockets towards the leading edge, causing eddy roll-up, and vortex shedding in the wake. Type A/C shock dynamics were found in conjunction with the emergence of sub-harmonics having same the energy content of the fundamental buffet mode. The analysis of the pressure surface modes revealed an inversion of the pressure propagation direction, coinciding with disturbances propagating upstream in the free stream.

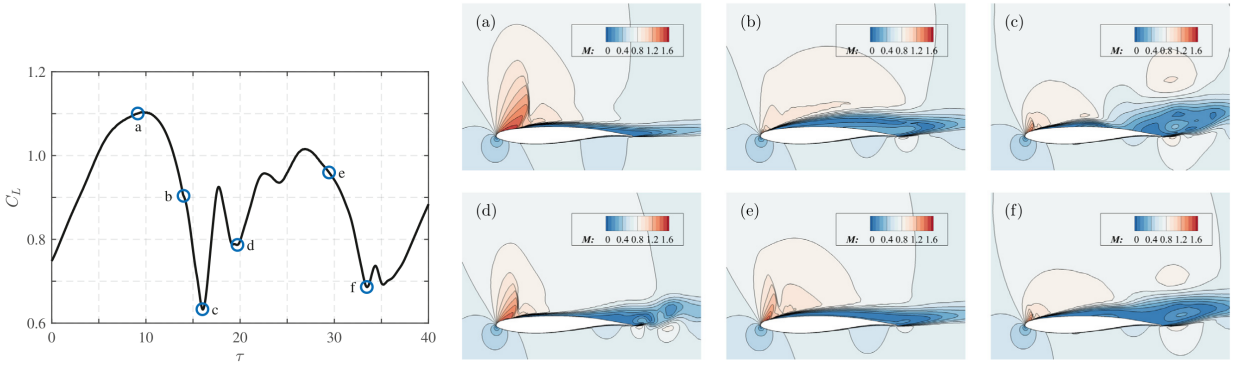

Figure 2.25: Mach number contour (right) at different phases (left) over a buffet period for the OAT15A aerofoil at $\mathrm{RE}_c = 3 \times 10^6$, $\alpha = 7$ deg, and $\mathrm{M} = 0.65$. Figures from [99].

Scale-Resolving simulations

Because of the uncertainty around the use of unsteady RANS, an increasing number of authors started adopting hybrid RANS/LES approaches to analyse the flow around two-dimensional and three-dimensional configurations. They showed an improvement in the prediction of buffet, with the scale-resolving simulations (SRSs) employed able to represent more accurately the flow physics of transonic buffet. The main drawback of these methods is the considerably higher CPU cost stemming from the fine spatio-temporal discretisation required. Nevertheless, it is believed that an increase in accuracy is beneficial when looking for the exact buffet onset, and required, since RANS may not be able to accurately predict this. Several 3D computations over 2D configurations were performed to assess the ability of hybrid methods in this context. The test case of Jacquin *et al.* [126] was looked with particular interest for this purpose, because of the large variety of results obtained in the experimental campaign carried out at ONERA. The numerical works up to the year 2009 provided as a reference a previous non peer-reviewed work from 2005 [125]. The buffet mechanism was addressed as mostly two-dimensional, although some 3D structures were still present. In the aforementioned work of Thiery and Coustols [258], URANS simulations were used to study the effect of the wind tunnel, and it was stated that the addition of the lateral and upper and lower walls did not affect the ability of turbulence modelling to predict the buffet. Moreover, the results obtained in the full 3D case were in close agreement with the 2D, unconfined, case. Following this study, the majority of the works adopted a 2D free-stream approach, extending the domain in the third dimension, in order to enable three-dimensional flow developing, and imposing periodic boundary conditions on the lateral walls.

Deck [59] was the first to opt for a SRS on the OAT15A aerofoil. The author claimed the need for Zonal Detached Eddy Simluation (ZDES) to overcome the issues encountered from standard Detached Eddy Simulation (DES) in the framework of thin layer separation, since this latter was not able to predict the self-sustained shock motion even well beyond the experimental onset. Computationally cheaper than the non-zonal version, it was used in conjunction with a 2D URANS. The predictions did not lead to a satisfactory agreement with the experiment, mainly because of the over-prediction of the pressure fluctuations, especially at the trailing edge. Moreover, the use of a zonal approach relies on *a priori* knowledge of the boundary layer thickness and the shock position, and it is not appropriate for buffet flows where these quantities vary significantly over a period of oscillation.

A similar study was carried out by Grossi *et al.* [108] by means of Delayed Detached Eddy Simulation (DDES). Despite a slight improvement in the prediction with respect to ZDES, a too high level of unsteadiness was still predicted at the aerofoil trailing edge. The DDES was formulated from the Edwards-Chandra turbulence model with compressibility correction and the results were compared with the URANS computation. The high-resolution simulation emphasised the for-

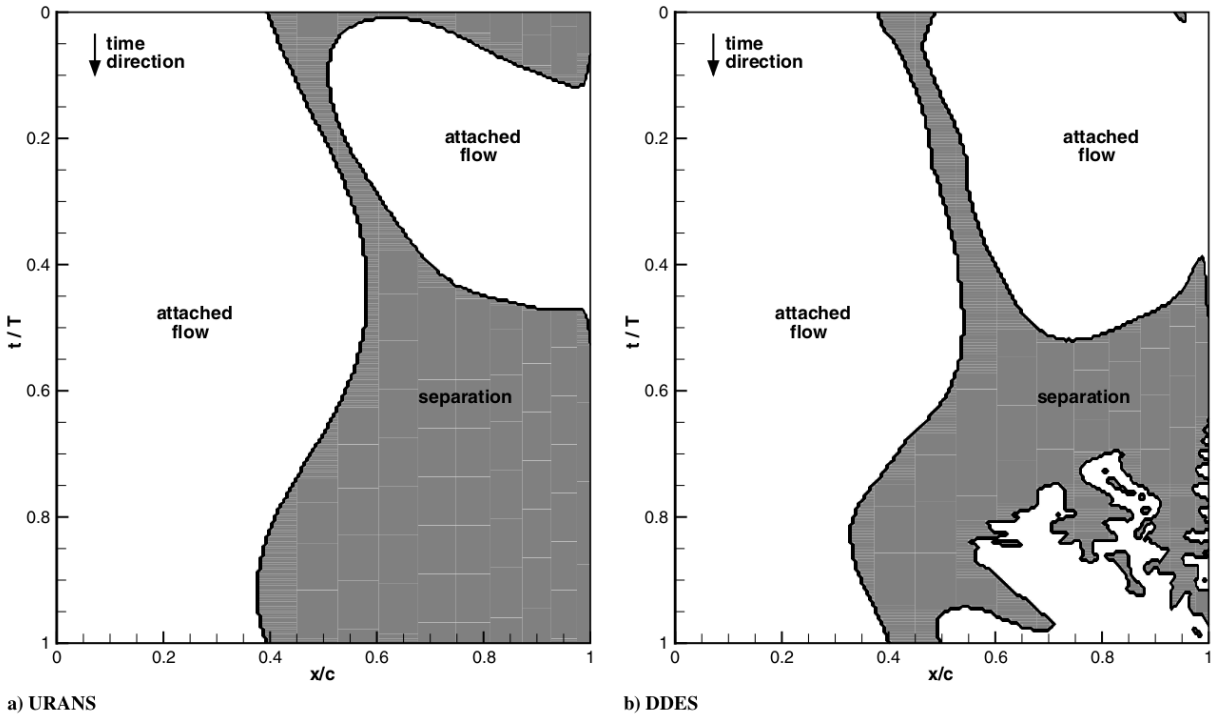

Figure 2.26: Temporal evolution of the separated region over the OAT15A in the work of Grossi *et al.* [108].

mation of three-dimensional structures at the trailing edge and an irregular separation region. Figure 2.26 shows the time evolution of the separated region over a period of buffet. In the URANS computation, flow separation clearly evolved from the foot of the shock towards the trailing edge as the shock approached its most downstream position. In the case of the DDES, the separation bubble and the rear separation grew simultaneously, and joined each other to create a single large separated flow region. Moreover, the DDES suffered from a deficit in the mean velocity and a small gap in the pressure coefficient plateaux. The same holds for the work of Huang *et al.* [117] where Improved Detached Eddy Simulation (IDDES) was employed. The timestep used was more than an order of magnitude higher than the other cases. This resulted in an overall wrong prediction of the shock position. The large, employed timestep possibly prevented the resolution of smaller structures, and the reduced eddy viscosity promoted a too-upstream shock position. The failure when comparing the experimental results enforces the need for a temporal discretisation that follows the spatial one. An improvement was obtained by Szubert *et al.* [255], who used Organised Eddy Simulation (OES), a technique which resolves coherent structures developing in the separated region and modelling turbulence at different frequencies. Spectral analysis underlined the presence of three distinct contributions: **(i)** a low-frequency contribution representing the shock motion, **(ii)** the Von Karmann shedding at the trailing edge, and **(iii)** the Kelvin-Helmholts instability in the shear layer.

Bonnifet *et al.* [28] tried to simulate buffet on the OAT15A aerofoil using a PANS-Reynolds-

Stress Model (RSM) approach. The 7-equation model saw the presence of six equations for the Reynolds stress transport and one equation for the turbulent kinetic energy dissipation rate. PANS, unlike RANS, was able to model the self-sustaining buffet but failed to compare well with experiments. Their work suggests the use of a variable f_k to improve the prediction of buffet.

All aforementioned works share the need for an overly fine grid in the separated region. Whether a computation of this type can be affordable for a simplified geometry, the expenses become prohibitive for complex 3D structures. The issue of CPU cost becomes even worse when LES are performed. The early work of Garnier and Deck [91] employed LES to study the flow around the OAT15A. The results confirmed the theory that pressure disturbances also propagate on the pressure side of the aerofoil and their frequency as evaluated using the formula of Lee [159], differs from the actual one. Fukushima *et al.* [80] employed Wall-Modelled Large Eddy Simluations (WMLESs) to reduce the CPU cost for resolving the boundary layer. They showed that their method worked well for the case under analysis, and the accuracy was higher than previous computations using hybrid RANS-LES methods. The main drawback was that the grid employed was more than an order of magnitude bigger, leading to computational times that did not justify the slight improvement in the buffet characterisation.

Another attempt to reduce the computational costs associated with WMLES was carried out by Kojima and Hashimoto [139, 140], who employed embedded LES to simulate the same test case. The interface between the RANS and LES region was imposed at $x_{tr}/c = 0.25$, where turbulence was artificially generated in the boundary layer. The results were comparable with the WMLES of Fukushima *et al.* [80]. A narrower shock excursion was observed, in closer agreement with the experiments. On the other hand, the shock position was slightly over-predicted. In general, embedded LES delivered a reduction in the required CPU. However, the location of the RANS-LES interface could play an important role and impact on the overall prediction.

Global stability analysis

To investigate the origin of buffet on aerofoils, some researchers performed a global stability analysis using RANS simulations as base-flow for their analysis. Crouch *et al.* [44, 45] linearised the RANS equations around the equilibrium position and solved the associated eigenproblem. The buffet was seen as an Hopf bifurcation associated with a couple of eigenvalues crossing the imaginary axis and leading to instability. The pressure propagation mechanism was qualitatively different from Lee's mechanism and more in agreement with the findings of Jacquin *et al.* [126]. The pressure disturbances were generated at the shock foot and propagated in two different ways. A first disturbance moved upward along the shock and was than ingested into the sonic region. As the shock moved downstream, a second pressure wave propagated downstream, travelled around the trailing edge, and propagated again towards the leading edge on the pressure side. This is shown in Figure 2.27. Poplingher *et al.* [216] obtained similar results by using DMD reconstruction from

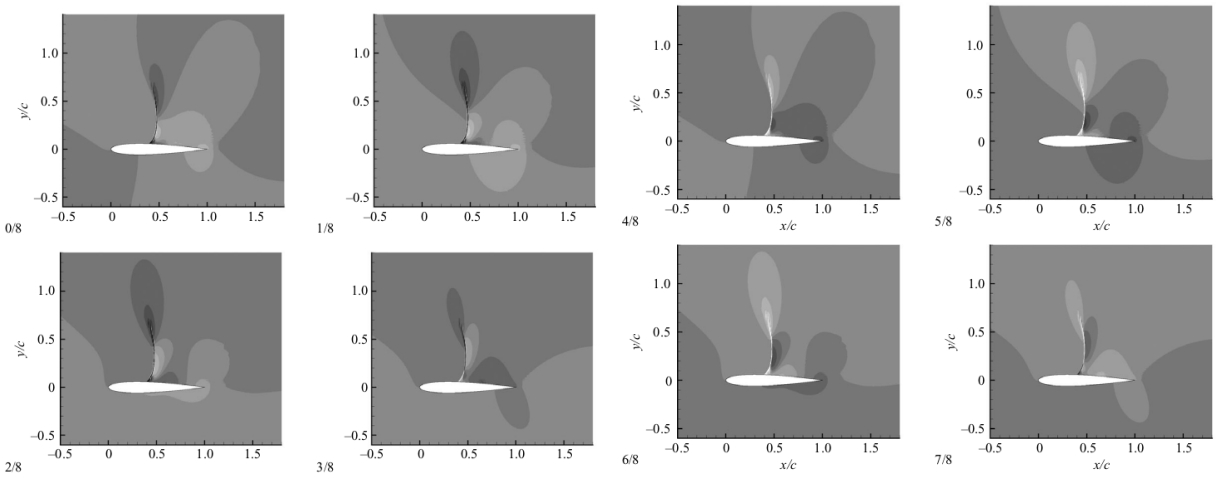

Figure 2.27: Evolution of pressure distribution of the global unstable mode associated with buffet in [45].

TMSs. Sartor *et al.* [228] adopted the same approach for the flow around the OAT15A aerofoil, and also solved the adjoint equation to study the receptivity of the buffeting flow to the location of flow control. The distinction between global modes and adjoint modes allowed them to determine where the unstable mode was more energetic and where it was more receptive to flow control, respectively. They [228] stated that the buffet flow is mostly sensitive in the leading edge region and downstream of the shock (see Figure 2.28). This means that the influence of incoming turbulence is not negligible and that the disturbances propagating downstream of the shock can affect the global flow structure because of the waves scattering from the trailing edge and propagating in the subsonic free stream.

Alternative Methods

Because of the expensive nature of SRSs and the uncertainty around URANS, several researchers started proposing alternatives to the use of the aforementioned methods. Szubert *et al.* [255] applied POD while Poplingher *et al.* [216] used DMD to analyse the flow field snapshots acquired from the CFD computations. Using these techniques, they were able to reconstruct the flow evolution of a variable over a period of oscillation, with a level of accuracy limited by the accuracy of the TMS. Poplingher *et al.* [216] suggested the possibility to use one of these techniques to build a surrogate model for buffet.

An alternative was proposed by Plante and Laurendeau [211], who employed a spectral method to reproduce a buffet period, assuming buffet periodic. The method was previously applied on other configurations, e.g. helicopter blades and turbomachinery, allowing to solve an unsteady flow like a steady-state problem. The main drawbacks of the method was the required knowledge of the buffet frequency. This requirement was the reason as to why the method was mainly used for the aforementioned flow cases [71, 106, 109, 180, 192, 281], where the frequency was dictated by design

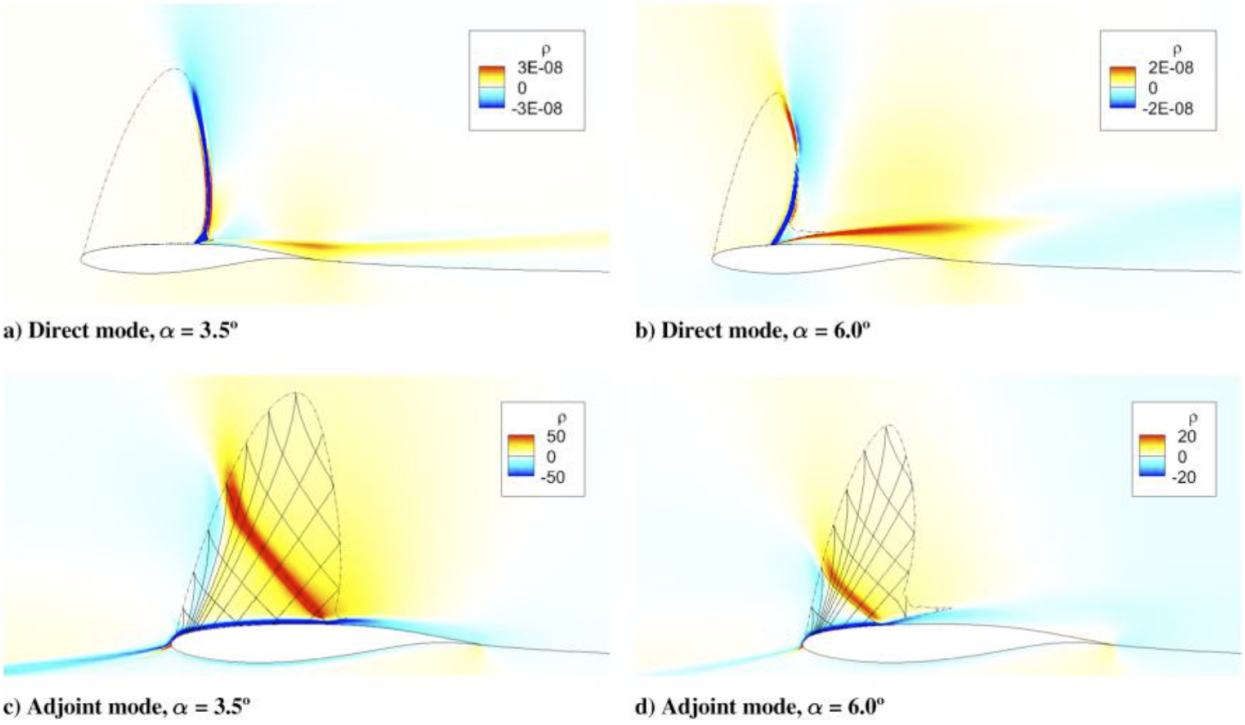

Figure 2.28: Distinction between global and adjoint modes proposed in [228].

constraints.

2.2.2.2 3D Configurations

Numerical simulations over three-dimensional cases have been carried out only in the recent past, because the computational resources to resolve flows with low-frequency oscillations on fine grids were not affordable before. They complemented the experiments cited in the previous section and provided some new insight on the topic.

Some applications of URANS were found in literature, like the works of Sartor and Timme [228], Iovnovich and Raveh [122], and Apetrei *et al.* [10]. The early computations of Brunet and Deck [35] on the CAT3D wing body model put forward difficulties of the SA model to capture buffet, and the authors expressed the need for SRSs to describe transonic buffet on wings. They employed ZDES using the same approach of Deck [59] on 2D buffet case, limiting the LES region to the wing wake, and on the upper boundary layer, in the region where buffet was expected. In the wall-normal direction, the switch between RANS and LES was fixed to the boundary layer thickness found at the shock foot in the steady, preliminary RANS simulation. In this early work, the results of ZDES correlated well with the experiments of Caruana *et al.* [39], and some backward propagating waves were detected, as in 2D buffet. In addition, a spanwise component was found, hinting at differences between the 2D and 3D cases.

Sartor and Timme [228] successfully performed URANS simulations on the RBC12 model,

showing that the SST and SA models, as implemented in the DLR TAU solver, were able to predict buffet since its onset. With a limited separation size, steady RANS provided accurate results, whereas unsteady simulations were needed for bigger separation sizes. On this configuration, buffet started from a region close to the wing tip, and the amplitude of the aerodynamic coefficients increased with the angle of attack. Although it showed some periodicity, the dynamics could not be identified as perfectly periodic, like in the case of 2D buffet, mainly because of 3D effects. From the spectral analysis it was shown that the frequency content was no longer limited to a single frequency, but the PSD showed an extended frequency region, where the mean frequency was higher than the common values for 2D buffet (100-300 Hz against the $\simeq$70 Hz). In a later work [229], the same authors investigated the influence of the Mach number using the same technique and configuration. In their work, higher Mach numbers reflected in reduced levels of pressure fluctuations, although the standard deviation of the lift coefficient reached a plateaux after the onset. The onset angle of attack decreased with the Mach number, in agreement with the 2D case.

Iovnovich and Raveh [122] studied the effect of the sweep angle and the aspect ratio on a RA16SC1-based wing using URANS simulations. On infinite wings, buffet presented a 3D component even at zero angle of attack, and the mechanism could still be described as mainly two-dimensional. At higher sweep angles, alternated positive-negative pressure fluctuations propagated outboard from the λ-shock structure at the wing root and gave rise to the so called *buffet cells*, that were confirmed in many subsequent works ([53, 172, 199, 252, 264], among the others). These structures are shown in Figure 2.29 for a wing with an aspect ratio of 6. Regarding the effect of

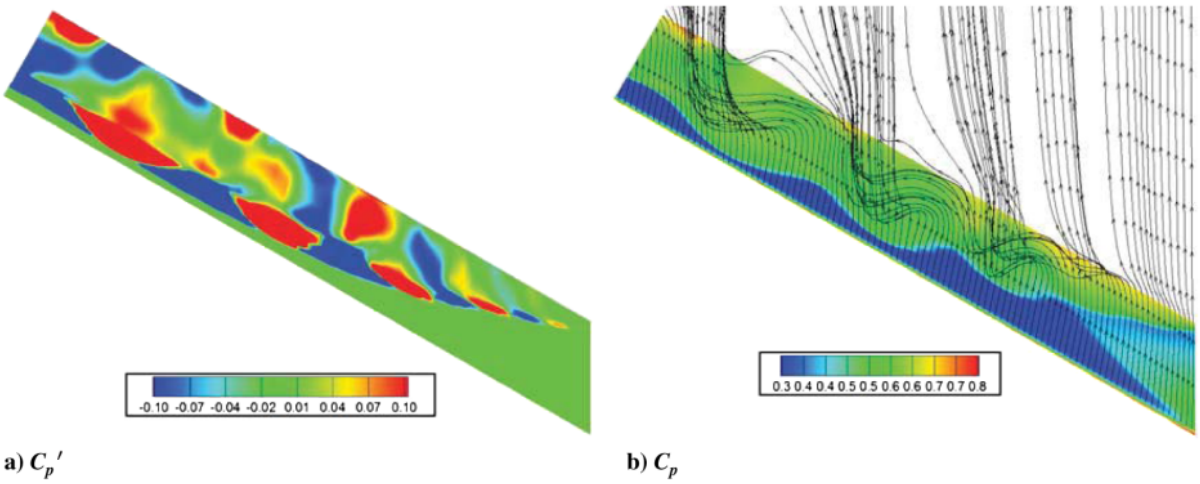

Figure 2.29: Buffet cells visualisation provided in [122].

finite span, a low aspect ratio confined the shock oscillation to the wing root. The buffet region was extended with increasing aspect ratio (see. Figure 2.30). This also justifies the absence of buffet cells in some experimental works [270].

The mechanism occurring at transonic buffet conditions was compared with the cellular pattern

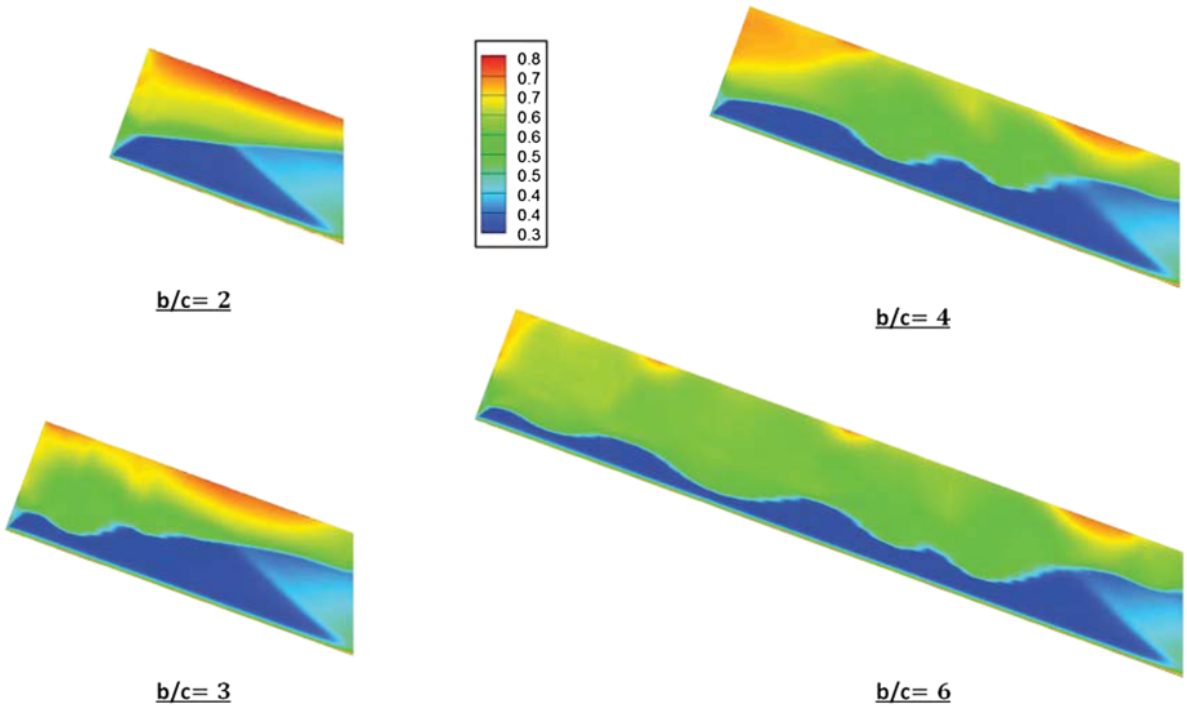

Figure 2.30: Effect of the wing aspect-ratio on the wing surface pressure shown in [122].

present in situation of subsonic stall by Plante *et al.* [210]. In their 2.5D computations on infinite wings with variable aspect ratio, it was confirmed that buffet cells occur regardless of root and tip effects. Moreover, the frequency content was independent of the sweep angle, unlike for finite wings. This led to the conclusion that the Strouhal-sweep dependency observed in other works [201, 252] is only valid for finite wings, and is due to the full 3D effects. Nevertheless, with increasing sweep angles, the convection velocity of the buffet cells increased. The relation between this latter and the sweep angle was formulated: $V_C/V_\infty \simeq 0.7\tan(\Lambda)$. The Fourier modes extracted for $\Lambda = 20$ deg revealed the superposition of a 2D mode and a high-frequency mode associated with buffet cells. This latter only manifested with $\Lambda \neq 0$, with the associated frequency strongly depending on the sweep angle. At low sweep angles, its frequency was lower than that of the 2D buffet-mode. Similarities with subsonic stall cells were also found. Figure 2.31 shows the comparison between the pressure coefficient distributions in the two cases. The model describing the convection velocity with respect to the sweep angle was similar to the transonic one, but varied by a factor between 0.7 and 0.8.

Making use of DDES, Sartor and Timme [230] partly confirmed the conclusion of Brunet and Deck [35] about the need for SRSs for a better characterisation of buffet. Despite the closer agreement of DDES with the experiments, the URANS simulations were able to predict the SIOs. The DDES solution put into light the non-periodic behaviour of the aerodynamic coefficients, and the broadband peak in the spectral visualisation. The higher resolution of DDES allowed for the de-

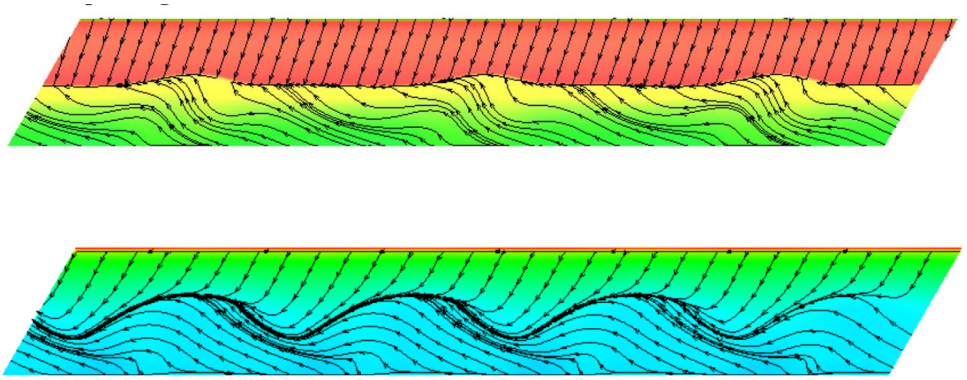

Figure 2.31: Pressure coefficient distribution with friction lines for the flow in buffet (top) and subsonic stall (bottom) conditions. Figure from [210].

tection of small scales pressure propagations, that are crucial in the understanding of 3D buffet. Masini *et al.* [171] investigated the effect of the Reynolds number through a combined study through experimental DPSP and CFD (DDES). They compared full-scale and rescaled models, with the former having a Reynolds number about 7 times higher (27 million agains 3.75 million). It was observed that buffet was slightly delayed at higher Re, and presented shorter excursion in both the spanwise and chordwise directions. POD and DMD were used for 3D configurations to reconstruct the buffet motion and give further insight. Masini *et al.* [170–172] found the development of two different phenomena around this configuration. At angles of attack in proximity of the onset, inboard propagating pressure perturbations running along the shock from tip to root were observed. These spanwise perturbations were, however, dependent on the incidence. At developed buffet conditions, an additional outboard propagating perturbation also appeared, associated with the higher-frequency bumps in the pressure spectra and buffet cells. In the work of Masini *et al.* [172], the adoption of a sub-grid lenghtscale based on the vorticity content helped the prediction in the shallow shear layer, leading to a less regular oscillation and to a better agreement with the experiments.

A similar computational campaign was carried out at JAXA on the CRM wing-body model. The ZDES approach of Deck [59] was implemented in the Unsteady-FaSTAR code of JAXA [123, 124] and the results were analysed with POD and DMD [198, 199]. The zonal approach used proved to be extremely sensitive to the height of the transition from RANS to LES in the work of Ishida *et al.* [123]. The outcomes of the modal analysis were the same as the aforementioned works on the RBC12 configuration [171, 172]. In the works of Ohmichi *et al.* [198, 199], both POD and DMD were adopted to decompose buffet into dominant modes. Both techniques were able to put into light two main mechanisms. A first, broadband, mode centred around $\mathrm{St} \simeq 0.42$ showed the usual development of buffet cells with outboard propagation of pressure fluctuations, as indicated in Figure 2.32 (top). The second, at $\mathrm{St} \simeq 0.055$, was associated with large shock oscillation near the root, and its frequency was comparable to two-dimensional buffet (see Figure 2.32, bottom

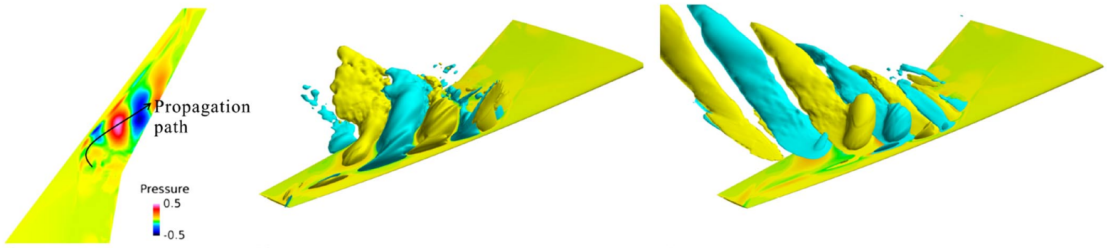

(a) Mode no. 1 (St = 0.42)

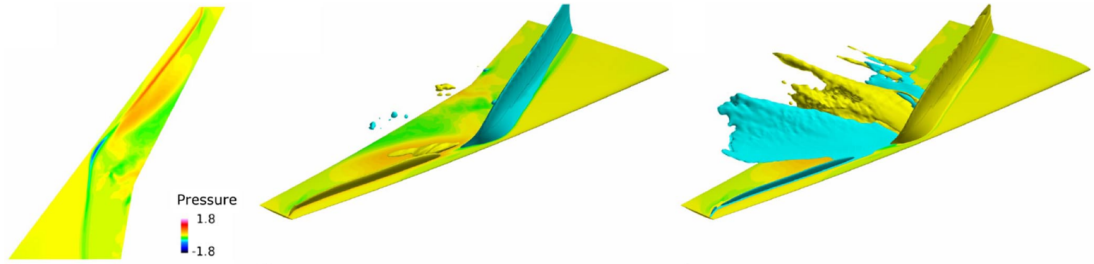

(b) Mode no. 3 (St = 0.055)

Figure 2.32: Surface pressure components (left), pressure isosurfaces (centre), and longitudinal velocity isosurfaces (right) for the two dominant DMD modes in [199].

image). The results corroborated the experimental outcomes mentioned in the previous section. In addition, the phase distribution of the low-frequency modes allowed the detection of inboard travelling disturbances near the root. In terms of prediction, the comparison with the experiments of Koike *et al.* [138] showed large discrepancies in the mean shock position. As observed in other works adopting hybrid RANS-LES approaches [59, 108, 117], an upstream shock position and an excessive pressure RMS peak was predicted. A modification of ZDES, called Automatic Zonal Detached Eddy Simluation (AZDES), was proposed by Ehrle *et al.* [70]. The method was tested on the CRM configuration and showed intermediate results between URANS and DDES, leading to better agreement with the experiments. AZDES further delayed the transition to SRS in the separated flow region. The excessive separation predicted by DDES led to a misprediction of frequency and convection velocity associated with the buffet cells.

The approach of Crouch *et al.* [45] was extended by Crouch *et al.* [46] and Timme [263, 264] on model of infinite and finite swept wings. This latter studied the onset of buffet on a NASA Common Research Model (CRM) by means of global stability. In their work, the base flow was evaluated with a RANS approach, and the Jacobian was evaluated only once on the base flow. After the linearisation of the system, the eigenvalues and eigenmodes were analysed to enforce the theory that 3D buffet is also the result of a global instability mechanism. As the angle of attack increased, one eigenvalue crossed the imaginary axis and gave rise to the flow instability. Moreover, a number of other eigenvalues having similar frequencies moved towards the positive semi-plane shortly after the onset. This suggests that in conditions of well-established buffet the bump in the

pressure spectra, observed in many previous investigationsi (see Figure 2.13), is actually connected to such modes becoming unstable. The eigenvalues on the complex plane, and the first unstable

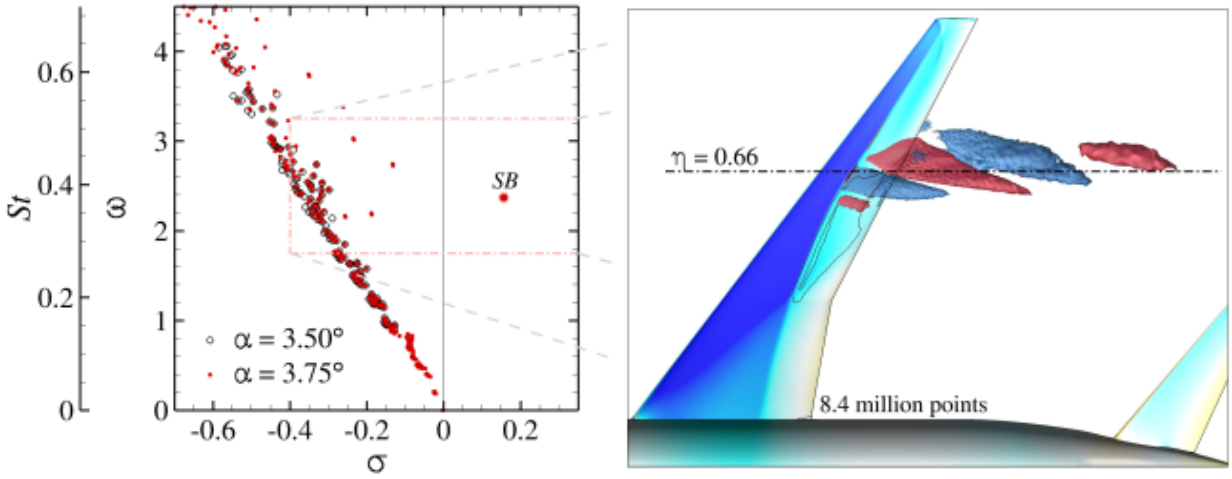

Figure 2.33: Eigenvalues and first unstable eigenmode in the study of Timme [263] around the NASA CRM.

mode over the CRM are shown in Figure 2.33. The results found agreement in the previous work of Timme and Thormann [266] on the RBC12 wing model.

In Crouch *et al.* [46], the solution of linear system was performed after the following decomposition of the perturbation vector $\mathbf{q}'$:

$$\mathbf{q}'(x,y,z,t) = \mathbf{q}(x,y) \cdot \exp(i\beta z) \cdot \exp(-i\omega t) , \tag{2.4}$$

where $\mathbf{q}(x,y)$ is the mode shape, β is the wavenumber of the spanwise oscillation and ω is the frequency associated with the mode. For the unswept case, two classes of modes were found: **(i)** oscillating modes ($\beta \simeq 0$, $\omega > 0$) and **(ii)** stationary modes ($\beta > 0$, $\omega \simeq 0$). The oscillating modes were responsible for the instability while the others added the spanwise component. The study was performed on an unswept configuration and repeated for a swept wing. The addition of the sweep angle broke the flow symmetry, and the stationary modes became outboard-travelling. Three different modes were found on the swept case: **(i)** a low-frequency mode associated with 2D buffet, **(ii)** an intermediate-frequency mode responsible for the three dimensionality, and **(iii)** a high-frequency, short-wavelength mode related to turbulence in the shear layer. This corroborated the results of the TMS of Plante *et al.* [210]. Similar results were observed in the triglobal stability analysis of He and Timme [114].

A global stability analysis was performed by Sansica *et al.* [223], on the same configuration investigated by Sugioka *et al.* [253]. Several considerations could be drawn by observing the development of the unstable modes. The presence of the wind tunnel sidewalls triggered the convection of three-dimensional structures towards the centreplane even in the unswept configuration,

as shown in Figure 2.34. The presence of large mushroom-shaped structures was found on experi-

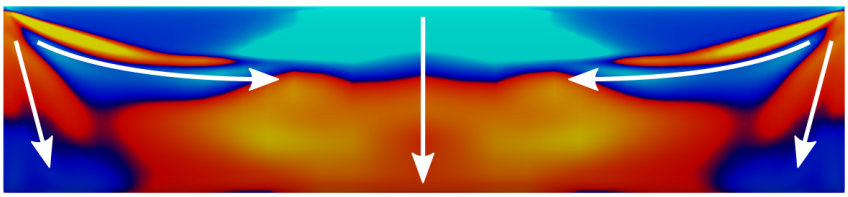

Figure 2.34: Pressure contour propagation for the unstable mode in [223] for the unswept configuration at $\alpha = 7$ deg.

mental models with a sufficient aspect-ratio [126,253]. On the swept configuration, the much larger separated flow region on the outboard wall caused the perturbation propagation direction to reverse and counteract the main cross-flow introduced by the sweep angle (see Figure 2.35). This might

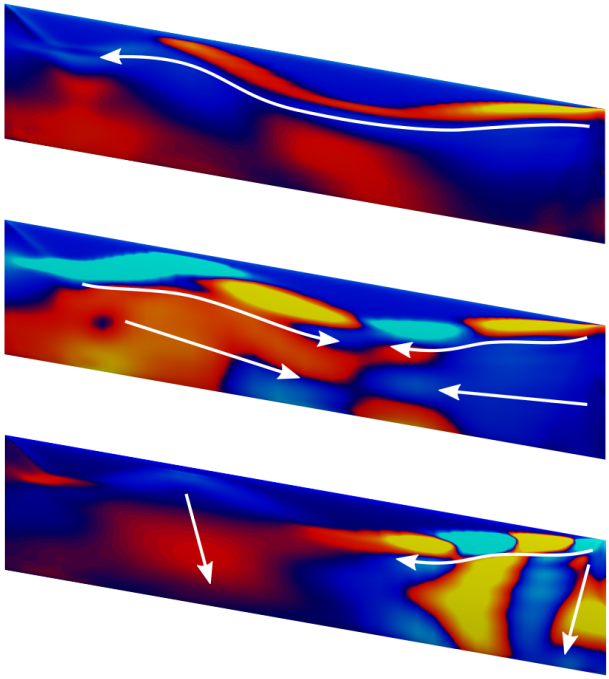

Figure 2.35: Pressure contour propagation for the unstable modes in [223] for the swept configuration at $\alpha = 7$ deg. Top: low frequency mode; centre: middle-frequency mode; bottom: high-frequency mode.

explain the presence of inboard traveling disturbances at the root of swept wings as a consequence of flow separation, confirming the findings of several past works [172, 173, 199].

To further investigate differences between 2D and 3D configurations, Poplingher and Raveh [215] performed a comparative analysis by using URANS and DMD for the OAT15A aerofoil and the AVERT wing. The AVERT wing was designed using the OAT15A profile, making the comparison as rigorous as possible. The obtained results were similar to the aforementioned works, nevertheless, some points are worth to be underlined. The 3D phase shifted from the dominant

DMD mode revealed a modulation of the spanwise convection velocity around the shock. Moreover, it was stated that while 2D buffet was the result of the unsteady SBLI, 3D buffet was mainly due to outboard propagation of disturbances, generated at inboard stations. This station was the intersection of the two branches of the lambda shock. No inboard convection velocity was observed in the inboard sections of the wing. A qualitative comparison allowed for summarising the differences between the main quantities associated with 2D and 3D buffet:

- the 3D buffet frequency is almost an order of magnitude higher than 2D;
- the shock excursion is limited in the 3D case, while a large streamwise shock motion characterises 2D buffet;
- the lift coefficient oscillation amplitude is much smaller in the 3D case;
- the chordwise convection velocities are comparable.

2.2.3 Buffet and Fluid-Structure Interaction

In the previous sections, buffet was solely analysed as an aerodynamic phenomenon under certain flow conditions. By definition, transonic buffet is indeed a self sustained SIO. In this view, the majority of the past numerical and experimental investigations considered a rigid response, i.e. aeroelasticity was not accounted for. That means that the experimental models used were not free to move under the action of the SIO, and the configurations adopted in CFD were kept fixed.

Nevertheless, this approach ignored the feedback effect of the structural response on the buffet dynamics, and simplified the problem. Therefore, attention was paid to the fluid-structure interaction under buffet conditions. The numerical investigations carried out by Raveh [217] and Iovnovich and Raveh [121] revealed strong coupling between imposed heave and pitch oscillations, and the buffet phenomenon. It was observed that under certain conditions, buffet locks into the frequency of the structural excitation. When the frequency of excitation was far from the fundamental buffet frequency, or its amplitude was too low, two distinct frequencies would appear, associated with structural excitation and transonic buffet, and did not vary with the flow conditions. As shown in Figure 2.36, Iovnovich and Raveh [121] observed that the effect of a sufficiently strong flap motion was able to avoid resonance, and positively affected the SIO.

When the aerofoil was elastically suspended, as in the experimental work of Hartmann *et al.* [113], a self-sustained heave-pitch motion emerged at the same frequency as that of the SIO. The shock oscillation was slightly reduced in this case. The application of a forced heave-pitch oscillation at frequencies close to the buffet frequency resulted in the lock-in of the shock motion into the excitation frequency, and a slightly increased SIO amplitude.

Gao *et al.* [84] studied the interaction between structural and fluid modes on an one degree-of-freedom NACA0012 aerofoil by means of a Reduced-Order Model (ROM) accounting for both

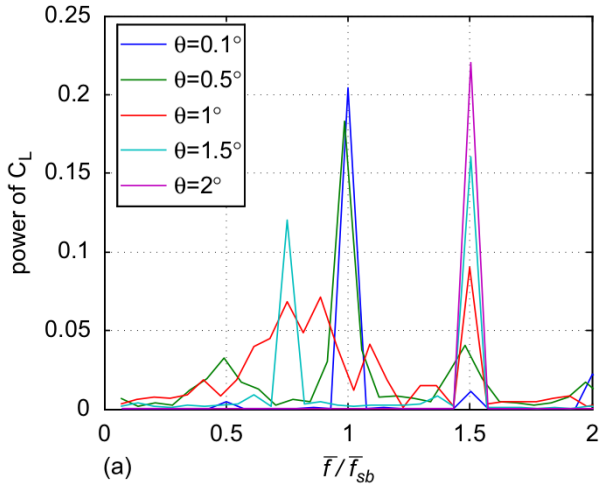

Figure 2.36: Lift coefficient PSD for variable pitch oscillation amplitudes θ at $f/f_{sb} = 1.5$ on the NACA0012 at $\alpha = 6$ deg and M $= 0.72$. Figure from [121].

the aerodynamic and the structural parts. URANS simulations were used to construct an associated ROM for the aerodynamic part, while the structural motion equation was rewritten in state-space form. The combination of the aerodynamic and structural state-space equations led to a unified system, whose eigenvalues were used for stability analyses. Structural damping was not accounted for. The main findings can be summarised by Figure 2.37. Plot (a) shows the veering of the two branches associated with fluid and structural modes. The branches did not intersect each other, but the behaviour of the response associated with each changed. The real eigenvalue parts (b) showed the dominance of the fluid (F) mode over the structural (S) mode for small and high structural rigidities, i.e. buffet dominates the aerodynamic system. In between, the aeroelastic frequency locked into the structural one, as shown in (c). In this intermediate region, a single degree-of-freedom flutter took place, with the aerodynamic loads exciting the structural mode of the aerofoil, as shown in (d). The structural parameters, i.e. mass ratio, structural damping and rigidity, play an important role, and were studied in [222]. It was shown that high damping results in no coupling. Moreover, the higher the mass ratio the narrower the veering region, and a critical mass ratio could be determined after which the veering was replaced by crossing. Coupling happened for structural frequencies equal or higher to the buffet frequency (see Figure 2.38, left). The combined influence of mass ratio and structural frequencies are shown in Figure 2.38, right. The experimental work of Korthauer on the OAT15A aerofoil [143] further confirmed the numerical findings of [86, 88].

In the work of Scharnowski *et al.* [231], the buffet flow around the same configuration and test facility of [6] was studied with the addition of a pitching degree of freedom. With respect to the "rigid" case, the dominant frequency increased, becoming slightly higher than the rigid buffet and torsional structural frequencies. The motion locked into the buffet frequency at the new value. Moreover, the shock excursion increased with respect to the one measured at the same flow con-

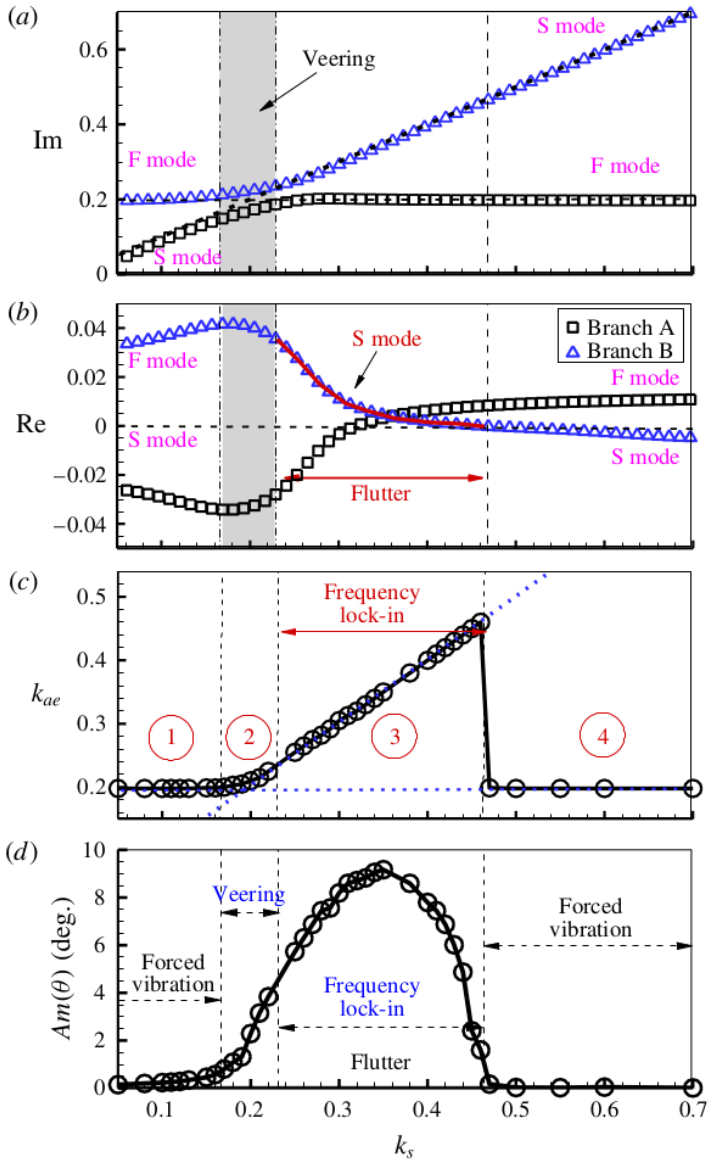

Figure 2.37: (a) and (b): imaginary and real parts of the eigenvalue loci; (c); coupled frequency of the system; (d): oscillation amplitude of the coupled system. k_s is the structural frequency. Figure from [86].

ditions. The shock position and the angle of attack had a non zero phase, with the angle of attack slightly preceding the shock position. Therefore, the relationship between the angle of attack and the aerodynamic coefficients is non-linear, and this prevents the dynamic system from diverging.

2.2.4 Laminar Buffet

In the previous sections, attention was mainly paid to buffet with incoming turbulent boundary layers. In recent times, flow laminarity has been studied with the aim to improve the aerodynamic performance of transonic wings. Therefore, an increasing number of studies were carried out.

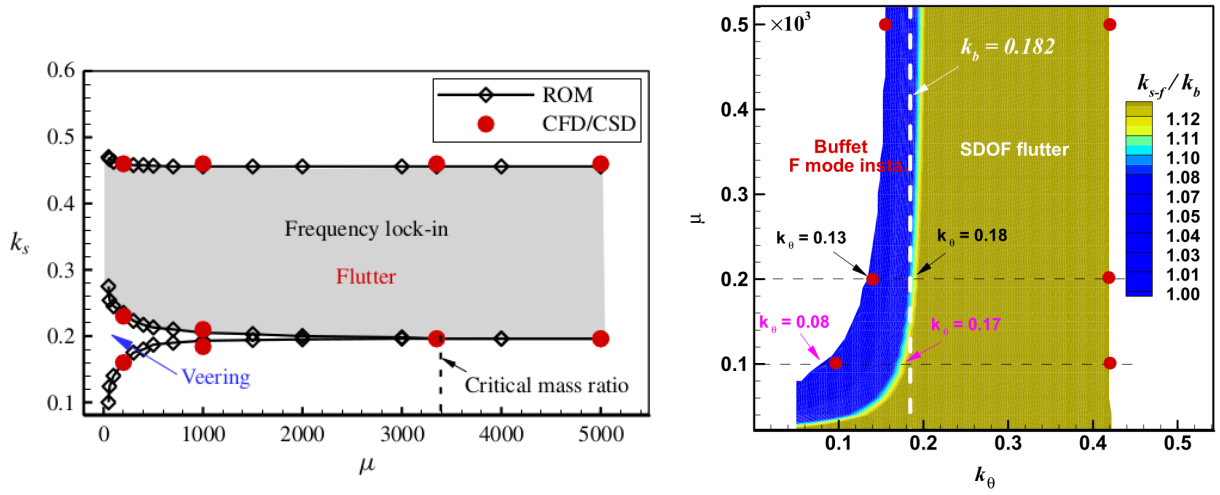

Figure 2.38: Left: influence of the mass ratio on the lock-in frequency range from [86]; right: combined effect mass ratio and structural frequency on the type of instability [88].

Although laminar buffet is not investigated in the present thesis, the topic is briefly introduced and documents showing the main differences with turbulent buffet are presented.

A comparison between the two cases was performed in the S3Ch wind tunnel of ONERA by Brion *et al.* [31] on the OALT25 aerofoil. The configuration resembles the OAT15A used in the work of Jacquin *et al.* [126], and the flow conditions were the same. Three cases were analysed: **(i)** suction side tripped at 7% **(ii)** and 40% of the chord, **(iii)** natural developing boundary layer. The pressure side was always tripped at 7% of the chord like in [126]. The laminar case presented different frequency and shock oscillation amplitude. Moreover, the acoustic feedback mechanism used for explaining turbulent buffet, failed for the laminar case, leading to a frequency much lower than the one observed ($f_B = 1130$ Hz against 75 Hz for the turbulent case). The convective velocity was found to change depending on the streamwise location (see Dandois *et al.* [56]). For this reason, bubble breathing and Kelvin-Helmoltz instabilities seemed to be more reasonable causes of laminar buffet. Finally, the boundary layer tripping at 40% of the chord induced an attenuated dynamics around the fully turbulent frequency of buffet, while the high-frequency oscillations disappeared. As pointed out by Brion *et al.* in a following work [32], the rear shock position with respect to the turbulent case introduces pressure losses and therefore, the wave drag might significantly increase, counteracting the positive effects on the skin friction.

Recent works of Moise *et al.* [188, 189] seem to overrule the findings of earlier works [31, 56]. In their works, wall-resolved LES simulations were carried out on a larger time window. In the laminar case, the normal shock was replaced by a large lambda structure. The laminar boundary layer separated earlier and thickened after the first shock, inducing a re-expansion. This resulted in the presence of multiple shock waves. Nevertheless, the comparison between the forced and natural transition case did not show large differences in terms of buffet frequency and oscillation

amplitude. Both cases could still be decomposed in a low-frequency mode associated with buffet and a high-frequency contribution associated with smaller scales.

2.2.5 Section Overview

In this section, the state of the art regarding transonic buffet studies was presented. The question about the origin of the two-dimensional transonic buffet has not been answered yet. Nonetheless, two hypotheses are now recognised by the research community as plausible explanations of 2D buffet. The first is the acoustic feedback mechanism proposed by Lee [159] and revised by Hartmann *et al.* [111]. The mechanism found agreement in numerical and experimental works [59, 75, 283] and the presence of acoustic waves emanated from the aerofoil trailing edge was documented in several works [50, 75]. On the other hand, buffet was described as the result of a global flow instability [45, 223, 228].

Three dimensional buffet showed strong differences with respect to the two-dimensional case in frequency content, flow topology, and amplitude of oscillation [201, 215]. Buffet cells on large aspect ratio wings [120] were deemed as the first cause of the aforementioned differences. When present, they were associated with the outboard propagation of pressure disturbances having a more broadband frequency content. Low-frequency oscillations were often associated with 2D-like behaviour at the wing root, and inboards convection velocities were present.

An effort has recently been made to compare/bridge 2D and 3D cases [50, 223, 252]. An example is the work of Sugioka *et al.* [252] who compared swept and unswept configurations to underline differences and similarities between the two cases. A trend in terms of frequencies associated with buffet was clearly found, but without physical evidences from tests. One could speculate that 2D buffet is a special type of 3D buffet cells. In this view, several works [114, 120, 126, 210, 223, 252] documented the presence of large mushroom-like structures on unswept wings. On the other hand, 3D buffet can be thought as a 2D buffet with a superimposed, more energetic, high frequency mode [46].

The experiments carried out provided increasingly precise and detailed results, following an improvement in the experimental facilities. The employment of dynamic techniques like DPSP and PIV allowed for more detailed studies of the 2D buffet mechanism. 3D cases were limited by the strong influence of the spanwise location, and the inability to sample large volumes. In these cases, surface measurements were mostly used. The collection of snapshots enabled the use of techniques like POD and DMD which helped shed light on the origin of buffet, and on key features associated with this mechanism through the fundamental modes.

With regard to CFD, the prediction through statistical turbulence models revealed to be influenced by several factors. Flow conditions, wing shape, turbulence model, and spatio-temporal discretisation are causes of uncertainties in the flow prediction. Therefore, the use of scale-resolving

simulations has become increasingly popular. On the other hand, LES and DNS simulations are still limited to low Reynolds numbers (with respect to the ones for aeronautical cases). Moreover, the need for incoming turbulent boundary layers introduced the issue of turbulence generation and boundary layer tripping, that must be carefully modelled and can strongly affect the prediction outcome [139, 140]. Because of the high CPU costs associated with LES, hybrid RANS-LES methods were mostly used for 3D investigations. The simulations carried out for 2D and 3D cases mostly adopted methods falling in the DES family (ZDES, DDES, IDDES, AZDES). They showed an improved ability to resolve structures associated with turbulence in the separated boundary layer region and the wake, while treating the attached boundary layer as a RANS region. Nevertheless, significant differences between the adopted methods (see e.g. [70]) underlined the need for further studies, and the exploration of different methods.

In recent years, there has been an increasing interest on fluid-structure interaction under buffet conditions. In early studies, the structure was considered rigid and no deformation was accounted for. Following the work of Raveh [217] and Iovnovich and Raveh [121], computational works were carried out to investigate the relationship between aerodynamic and structural parameters. Recently, these works [84, 121, 217, 222] were corroborated by experimental tests [231]. Another branch of study is related to laminar buffet, associated with to laminar wings, which are thought to have better aerodynamic performance. These last two topics are beyond the scope of this work and will not be examined further.

2.3 Flow Control for Buffet

SBLI has a detrimental effect in several applications. On aerofoils and wings, the shock induces total pressure losses, reflecting in increased wave drag, together with the boundary layer thickening; in supersonic inlets, the shock system induces changes in the wall friction and temperature, introduces distortion and total pressure losses in flows in compressors or combustors, degrading the engine performance; in turbo-machines the shock induced separation may modify the flow structure leading to undesired phenomena. The shock unsteadiness is also a problem in terms of structural fatigue or, thinking of a transonic wing of a civil aircraft undergoing buffet, controllability.

These and several other reasons - hypersonic or high supersonic applications are not within the scope of this work - pushed engineers to find the most effective flow control strategy. Babinsky and Ogawa [13] considered flow control applied to SBLI. In their work, a distinction between *boundary layer control* and *shock control* was introduced. Boundary layer control devices aim at reducing or eliminating boundary layer separation and improving boundary layer health; they are usually placed ahead of the shock. The second category of devices act to change the shock structure to reduce the stagnation pressure losses. Usually, this effect is obtained by smearing the shock to achieve higher pressure recovery in the region underneath the shock triple point. Boundary layer control devices are mostly used in supersonic inlets, while the shock control devices are preferred for transonic aerofoils and wings.

Among boundary layer control methods, we find blowing, suction, and Vortex Generators (VGs) [268]. These latter are used on transonic aircraft because of the proven ability to delay or prevent the shock-induced separation. The main aim of such devices is that of energising the boundary layer by promoting turbulence through the vortices detaching from vanes or ramps, and inducing momentum transfer from the flow outside the viscous region. Usually, they are slightly higher than the boundary layer thickness. They proved their ability to delay shock-induced separation since more energetic boundary layers are more resilient to separation. On the other hand, an amount of installation drag is due to the presence of the devices, and the modified structure of the boundary layer ahead of the shock reduces the length of the shock-smearing. This leads to a reduction of the pressure recovery downstream, due to the benefit of the lambda structure. Some studies of VGs on normal shocks have been carried on by the group at the University of Cambridge [33, 267], among others.

To reduce the excessive installation drag of VGs, Micro-Vortex Generators (MVGs) were tested in both vane and ramp configurations. Usually, they are of the order of half or less of the boundary layer height, and because of the minor wetted surface the parasite drag is significantly reduced. Moreover, the mechanism of flow control through MVGs is different from that of the traditional VGs: while these letter entrain momentum from outside the boundary layer, MVGs tend to redistribute momentum inside the boundary layer through streamwise vortices embedded in the vis-

cous region of the flow. The main drawback of such devices is that the vortex strength is less than that of conventional VGs so MVGs. Therefore, they must be placed closer to the shock position with respect to their traditional counterpart. Micro-vanes are preferred on wings to micro-ramps that find employment on inlets due to their structural rigidity.

An alternative is Air Jet Vortex Generators (AJVGs), working with the same mechanism as conventional VGs. They offer advantages in terms of structural rigidity and device drag, and can be shut off to avoid off-design penalties. On the other hand, they require a line for air mass flow injection and this makes the application on aircraft complicated. The effect of AJVGs was studied, e.g., by Souverein *et al.* [239].

Other forms of shock control are blowing and suction. These strategies are sketched in [61], and reported in Figure 2.39. By playing with mass injection/suction the streamline shape is modified, and separation can be partially controlled. In case of suction, the separation bubble size is reduced since flow is sucked out of the boundary layer. Unfortunately, the high flow velocity at large distances from the wall, like in Figure 2.39 (left), can result in a second region of separation downstream of the suction vane. The opposite situation is also depicted in Figure 2.39, right: the air blowing has the effect of increasing the bubble length but also adds momentum, i.e. decreases drag. Distributed suction, or bleeding, is commonly used in supersonic inlets and is preferred to VGs for the higher structural rigidity. It has the additional benefit of sucking out the downstream boundary layer, to prevent its thickening.

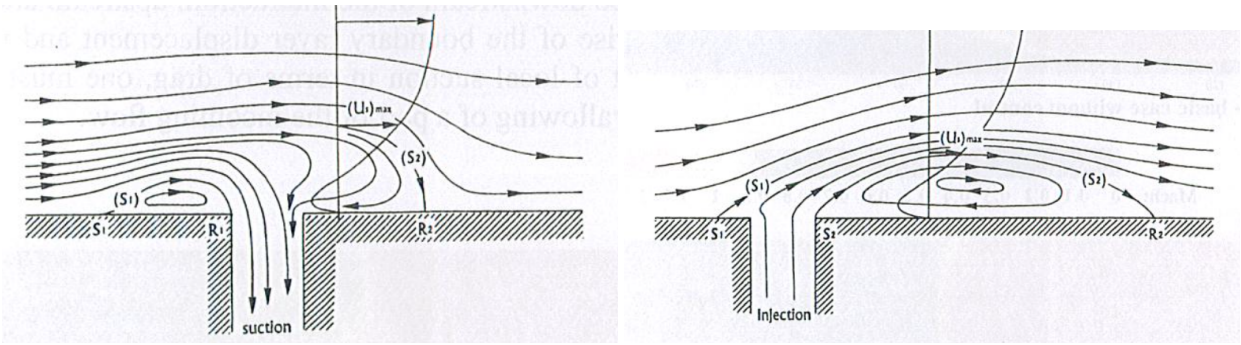

Figure 2.39: Sketch of boundary layer suction (left) and blowing (right) techniques. Figures from [61].

Shock control devices tend to modify the structure of the normal shock and split it into two oblique shocks (λ-structure) to reduce the pressure loss across two less strong shocks. Two dimensional devices, like all-span bumps and passive control [256], compete with three-dimensional ones, like 3D bumps [12,197] or slots [12,236], that are seen to be more successfully because of the addition of the third-dimension component. They aim at maintaining the pressure in the interaction region as uniform as possible. This is difficult to obtain, especially at off-design conditions.

The mechanism involved in shock control is depicted in Figure 2.40, and is similar to what happens in presence of the separation bubble. As a consequence, drawbacks in terms of viscous drag

are expected. Shock control devices aim at recreating a lambda structure without flow separation, and benefit from the larger pressure recovery stemming from the modified shock structure. This is the case for two dimensional bumps, that also show some disadvantages: on wings, they have to be perfectly located following the shock footprint; moreover, their off-design performance is poor, if not detrimental, because of the unfavourable re-expansion either inside or outside the supersonic region. The effect of three-dimensional bumps will be analysed in the review of some specific experimental works. A detailed review on the use of Shock-Control Bumps (SCBs) was provided by Bruce and Collins [34].

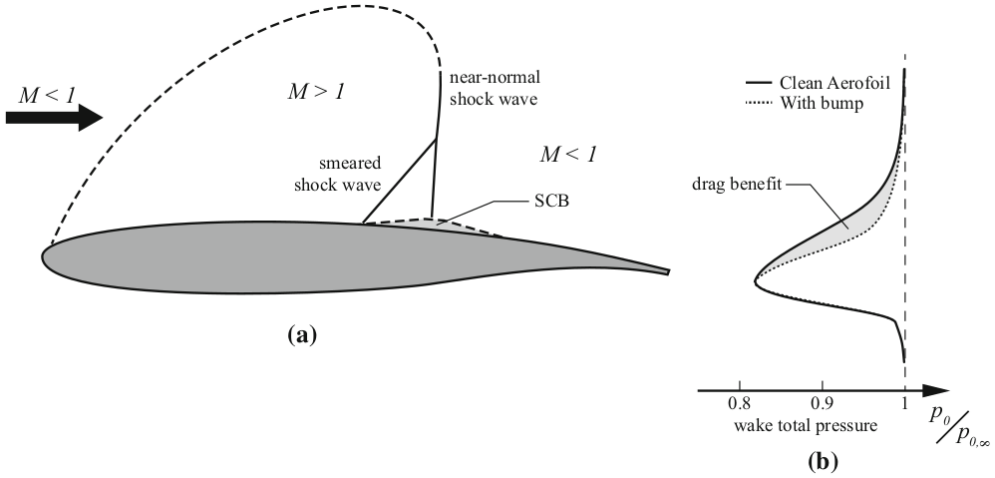

Figure 2.40: Sketch of flow control by means of SCB on a transonic aerofoil (a) and the associated total pressure recovery with respect to the uncontrolled case (b). Figure from [34].

The same effect can be obtained using passive control, e.g. transpiration. The sketch of the mechanism is provided in Figure 2.41, right. If correctly placed, the pressure in the vane under the wall is between the values on the two sides of the shock, and generates a coupled effect of blowing and suction, respectively, before and after the shock, reproducing the same flow deflection as a bump. Passive control is hence able to self-adjust to the shock position, and stabilises the shock creating a *shock trap*. The main drawback is that of an increased viscous drag, because the rear suction is often not strong enough to prevent boundary layer thickening: the addition of viscous drag counteracts the decrease in wave drag.

This section is a collection of experimental and computational works investigating flow control at transonic buffet flows. Previous works [157, 228] underlined the influence of the incoming boundary layer properties and the trailing edge on the buffet dynamics. In this view, VGs, and Trailing-Edge Deflectors (TEDs) are the most used techniques. Some authors recently employed SCBs to smear the shock and reduce its intensity. SCBs are suitable for optimisation since their shape and number can be modified to obtain the desired performance. The works reviewed in this section are collected in Table 2.3

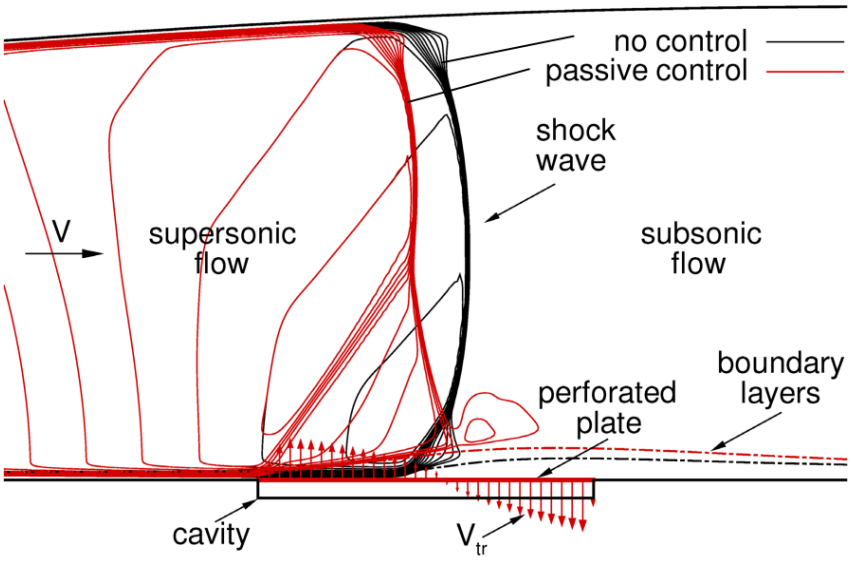

Figure 2.41: Flow control by means of wall transpiration. Figure from [64].

Table 2.3: Reviewed works for transonic buffet control. VGS: vortex generators; SCB: shock control bumps; TEC: trailing edge control.

First Author	Geometry	M_∞	Re $\times 10^6$	α [deg]
VGS				
Caruana *et al.* [38, 39]	OAT15A (2D)	0.72 - 0.78	4.5	1.0 - 4.0
	OALT25(2D)	0.72 - 0.78	4.5	2.5 - 3.75
	AVERT(3D)	0.80 - 0.84	8.3	0 - 5.5
Dandois *et al.* [54, 55]	BUFET'N Co(3D)	0.82	2.5	3.5
	AVERT	0.82	2.83	-1 ÷ 6.0
Huang *et al.* [117]	OAT15A(2D)	0.73	3.0	3.5
Molton *et al.* [190]	BUFET'N Co(3D)	0.82	2.5	2.0 - 4.0
Timme & Sartor [265]	RBC-12 (3D)	0.8	3.75	0-4.2
Kouchi *et al.* [144, 145]	NASA SC(2)-0518 (2D)	0.7	5.0	4.0 - 7.0
Masini *et al.* [169]	RBC-12 (3D)	0.8	2.8 - 3.9	0.0 - 8.0
Vishnyakov *et al.* [234, 276]	P-184-SR (2D)	0.73-0.78	2.64-2.8	5.0
Kuya *et al.* [150]	NASA SC(2)-0518 (2D)	0.7	5.0	2.52 - 7.0
Brion *et al.* [32]	OALT25	0.74	3.0	4.0
SCB				
Birkenmeyer *et al.* [25]	-	0.84-0.85	5-6.7	0.0
Eastwood & Jarret [68]	DFVLR-R4(3D)	0.705	3.0	0.0
Bogdanski *et al.* [26, 27]	Pathfinder laminar wing (2D)	0.74 - 0.76	20.0	0.0 - 4.0
Tian *et al.* [260]	RAE2822(2D)	0.69-0.76	3.0	0-7
Geoghegan *et al.* [92]	OAT15A(2D)	0.73	3.0	3.5
Jiang *et al.* [130]	RAE2822 (2D)	0.69-0.76	10.0	4.5

Continued on next page

Table 2.3 – *Continued from previous page*

First Author	Geometry	M_∞	Re $\times 10^6$	α [deg]
	Wing 1 (3D)	0.74-0.78	10.0	2.0-4.5
Mayer *et al.* [175, 176]	OAT15A(3D)	0.73	3.0	3.5
Mayer *et al.* [177]	AVERT (3D)	0.826	2.84	3.5
Yang & Ogawa [284]	OAT15A (2D)	0.73	3.0	3.5
Geoghegan *et al.* [93, 94]	OAT15A(2D)	0.73	3.0	3.5
Brion *et al.* [32]	OALT25	0.74	3.0	4.0
D'Aguanno *et al.* [47, 52]	OAT15A(Exp)	0.7	2.6	3.5
TEC				
Lee [154, 156]	BGK	0.61-0.79	20	$-2 \div 8$
Caruana *et al.* [38, 39]	OAT15A (2D)	0.72 - 0.78	4.5	1.0 - 4.0
	OALT25(2D)	0.72 - 0.78	4.5	2.5 - 3.75
	AVERT(3D)	0.80 - 0.84	8.3	0 - 5.5
Gao *et al.* [84, 87]	NACA0012 (2D)	0.7	3.0	5.5
Tian *et al.* [259]	OAT15A(2D)	0.73	3.0	3.5
	SC(2)-0710	0.72 - 0.78	-	-0.5 $\div$ 4.0
Tian *et al.* [261]	RAE2822(2D)	0.72 - 0.76	6.5	$0 \div 6.0$
Giannelis *et al.* [97]	NACA64A204(2D)	0.75	10.0	0-8
Ren *et al.* [218, 219]	NACA0012(2D)	0.7	3.0	5.5
Sartor *et al.* [227]	OAT15A (2D)	0.73-0.74	2.6	2.02-3.71
	AVERT (3D)	0.7	2.6	2,3.55
Zhang *et al.* [289]	OAT15A (2D)	0.73	3.0	2.5, 3.5
D'Aguanno *et al.* [51]	OAT15A(Exp)	$0.7 \div 0.74$	2.6	$2.5 \div 3.5$
Other				
Zhou *et al.* [291, 292]	ARC-18	0.76	11.0	0.0
Abramova *et al.* [2–5]	P-184-15SR(2D)	0.73	2.6	5.0
Liu & Yang [162]	NASA SC(2)-0714	0.725	15.0	3.5
Stalewski & Sznajder [246]	V2C (2D)	0.7	2.67	-
Gao *et al.* [85, 88, 222]	RAE2822(2D)	0.73	3.0	4.5-6.5
	DPW-1(3D)	0.74-0.78	3.0	2.0-5.0
	NACA0012(2D)	0.7	3.0	5.5
Firsov *et al.* [76]	P-184-15SR(2D)	0.74	2.6	4.0-6.0
Polivanov *et al.* [213]	NLF (2D)	0.68-0.72	-	-
Dang *et al.* [57]	NACA0012(2D)	0.751	10.0	$0 \div 6$
Bruytan *et al.* [36]	P-184-15(3D)	0.6-0.8	2.3-2.8	4.0
Runpei *et al.* [221]	RAE2822 (2D)	0.73	6.5	5.0
Degregori & Kim [60]	V2C (3D)	0.7	0.5	7.0
Gaifullin & Khairullin [82]	P-184 15SR (2D)	0.72-0.745	-	0-6
Polivanov & Sidorenko [212]	-	0.55-0.72	-	5.5
Voevodin *et al.* [277]	P-184-15 (2D)	0.73 - 0.78	3.0	5.0, 6.0
Zhang *et al.* [288]	OAT15A (2D)	0.73	3.0	3.5

2.3.1 Vortex Generations

Vortex generators are already in use on civil aircraft wings, because of their ability to delay separation without eccessively penalising the lift-to-drag ratio at off-design conditions. In the previous sections, the general operational mechanism was presented. Here, attention is devoted to the effect that vortex generators, of any type, have on the buffet mechanism.

Among the first works on transonic buffet control, Caruana *et al.* [39] carried out experiments on the OAT15A and OALT25 aerofoils equipped with rectangular VGs. The devices were placed well ahead of the shock, to energise the boundary layer and delay its separation. As a result, increased lift and drag were obtained, and the effect was extremely beneficial for buffet flow, since the shock oscillation was practically quenched. Therefore, the lift coefficient was increased at angles of attacks higher than the onset angle. In this configuration, the spacing between the co-rotating VGs was tenfold their height. Reducing the spacing between VGs could lead to a reduction of the installed drag. Similar works were carried out on OAT15A-based 3D wings by Dandois *et al.* [54, 55] and Molton *et al.* [190]. In [54], a computational study on geometric parameters of mechanical and fluidic vortex generators was performed. In the optimal configuration, the VGs were able to suppress the oscillation and reduce the wake drag at the cost of a drag increase at low angles of attack. The fluidic and mechanical VGs were tested experimentally and proved to be effective in suppressing the large-scale separation on the wing. Molton *et al.* [190] performed experiments using mechanical, fluidic and pulsating VGs. Although the fluidic and pulsating VGs did not introduce penalties due to the devices installation, their effect was quite sensitive to the momentum coefficient:

$$C_\mu = \frac{\dot{m} U_{jet}}{\frac{1}{2}\rho_0 S U_0^2}, \tag{2.5}$$

and to the frequency of blowing. In the equation, $\dot{m}$ is the mass flow rate, U_{jet} is the jet velocity, S is the orifice area, and U_0 is the reference velocity magnitude. It is thus reasonable to embody their action in a closed loop control as done by Dandois *et al.* [55].

Huang *et al.* [117] performed IDDES of the flow around the OAT15A aerofoil at uncontrolled and controlled conditions. The initial prediction using IDDES was able to show the self-sustained oscillation of the shock. The mean shock location was upstream with respect to the experimental one of about $0.1c$, while the peak of pressure RMS was close to the experiments. The comparison is shown in Figure 2.42. In view of the numerical results, two rectangular (aspect ratio of 8), co-rotating VGs were introduced to suppress the buffet. They were placed at $0.3c$ from the leading edge, with an inclination of 30 deg, and far $36h$ from each other, being h their height. Figure 2.42 shows the effect of flow control on the time-averaged distribution of pressure. The shock moved

downstream, and the pressure on the suction side of the aerofoil decreased. The shock motion was kept almost fixed over the buffet cycle, leading to the conclusion that VGs are able to alleviate shock buffet. Nevertheless, the boundary layer beyond the shock became thicker, and led to an increase in drag that is more severe than the obtained lift benefit. This is shown in Figure 2.43.

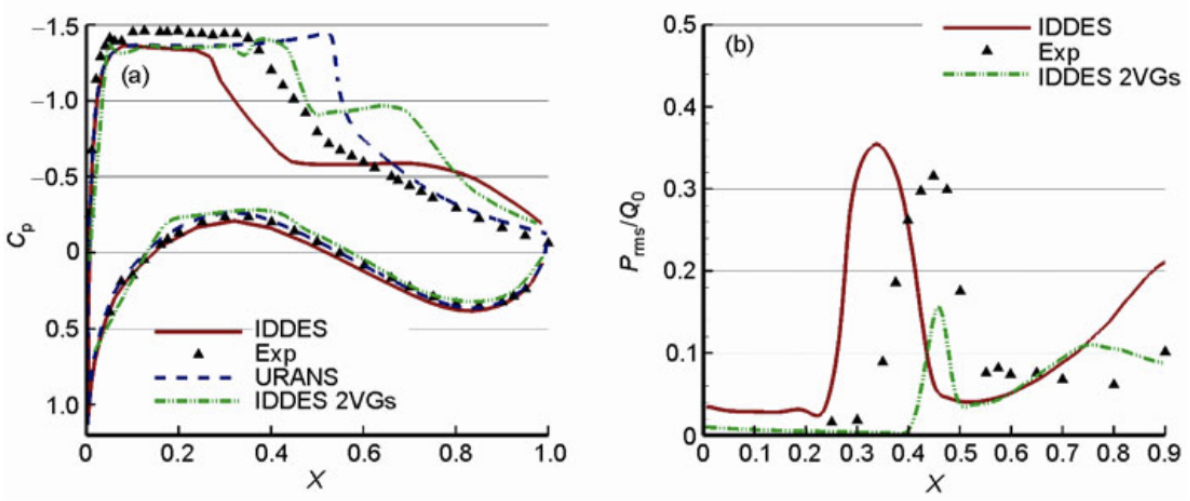

Figure 2.42: C_p and RMS pressure over the OAT15 aerofoil in [117].

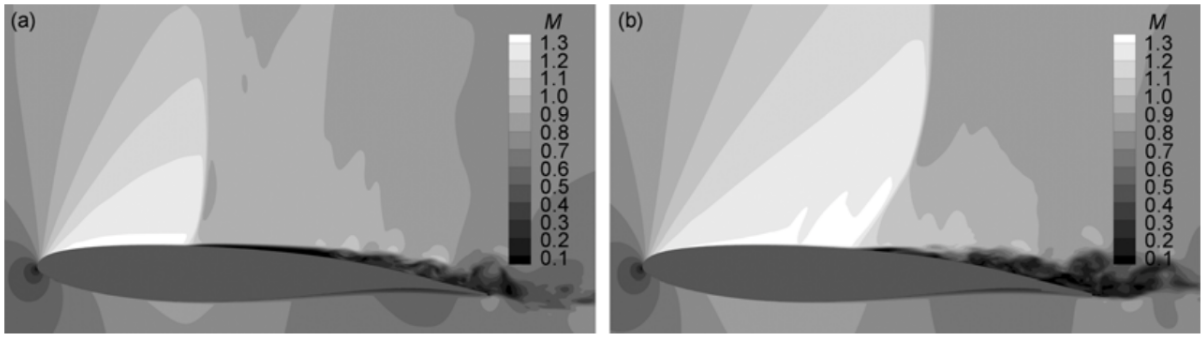

Figure 2.43: Effect of vortex generators on Mach number around the OAT15 aerofoil in [117]. Left: uncontrolled case; right: controlled case.

The experiments of Kouchi *et al.* [145] on a NASA SC(2)-0518 aerofoil put into light the effect of VGs in the flow frequency content. Wavelet analysis showed that buffet was not completely eliminated, although the frequency content associated with the fundamental frequency was decreased. The Fourier spectrum at buffet conditions was smeared into a bump around the fundamental frequency. Due to the three-dimensionality introduced by the VGs, the shock-motion was no longer periodic. Before the buffet onset, the frequency content was the same with and without the applications of VGs. The experiments were complemented by the URANS computations of Kuya *et al.* [150], and were enriched with a counter-rotating VG configuration. To model co-rotating

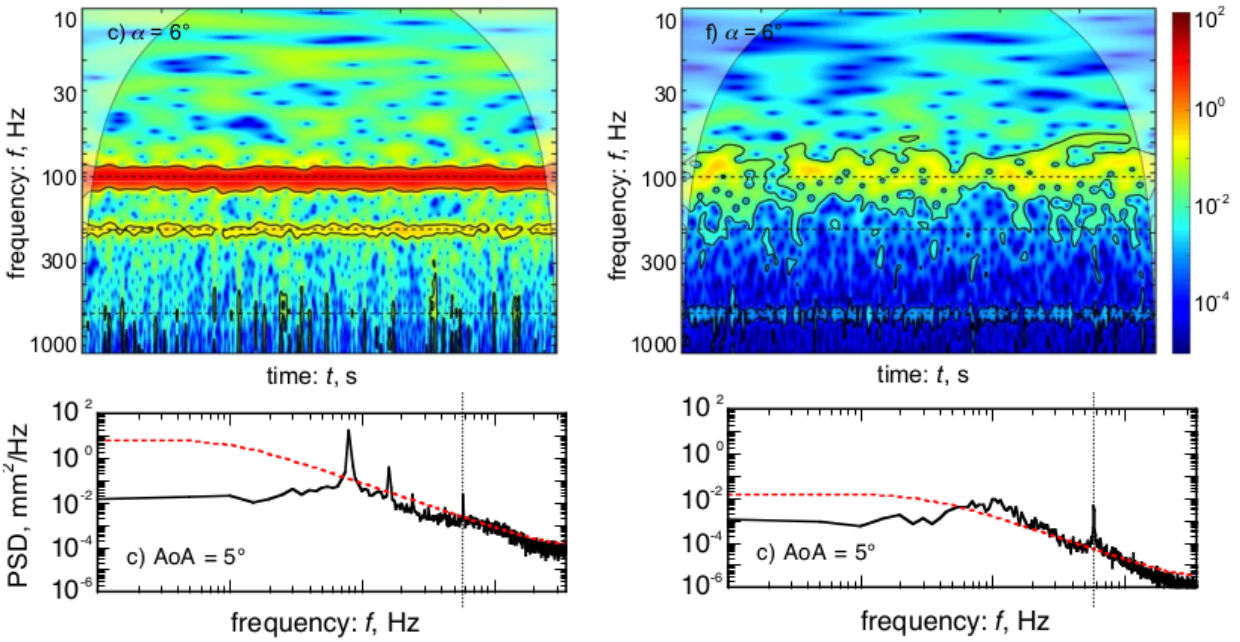

Figure 2.44: Wavelet spectrogram and shock motion PSD with (left) and without (right) VGs [145].

and counter-rotating VGs, periodic and symmetric boundary conditions were applied at the sides of the computational domain, respectively. The counter-rotating configuration proved to be more efficient in suppressing the oscillations, although a larger separated region was present downstream of the shock. Unfortunately, data on the drag penalty and the mean lift coefficient are not available for any of the configurations.

Koike *et al.* [137] performed an experimental analysis on 2D and 3D NASA CRM cases. In the experimental work, they pointed out some difference between 2D and 3D configurations. The introduction of VGs was proven to be more beneficial on 3D configurations because of the interaction with the cross flow due to the sweep angle of the wing. Therefore, in the 2D configuration, the lift increase was strongly related to the number of VGs introduced, while this was less prominent for 3D cases. The drag penalty was computed for the 3D case and similar conclusions to those of Caruana et al [38, 39] were drawn: at small angle of attack, the VGs configuration was detrimental, while the suppression of the separation brought benefit in terms of C_D. Timme and Sartor [265] performed RANS simulations around the RBC12 wing-body configuration. An array of 30 VGs having a span-wise spacing-to-height ratio of 7.7, taper ratio of 0.6, an aspect ratio of 1.3, and 60 deg sweep were used to simulate the flow at angles below and above the buffet onset. Steady computations underlined differences in the shock position between the clean and controlled configurations. The presence of VGs pushed the shock more downstream. In doing so, the buffet onset was delayed by almost half degree for the analysed flow conditions. Unsteady simulations were carried out for angles beyond the onset. The PSD of the lift coefficient showed the shift towards higher frequencies for the controlled case (from $\simeq$ 200 Hz to $\simeq$ 300 Hz), as shown in Figure 2.45.

Moreover, the broadband nature of buffet was partially preserved when installing VGs. A new high frequency content at higher frequency was visible, possibly associated with the devices promoting turbulence. For the controlled case, the shock aligned with the VG's array, promoting flow unsteadiness (see Figure 2.46). The experiments from Masini *et al.* [169] studied the RBC12 wing-body

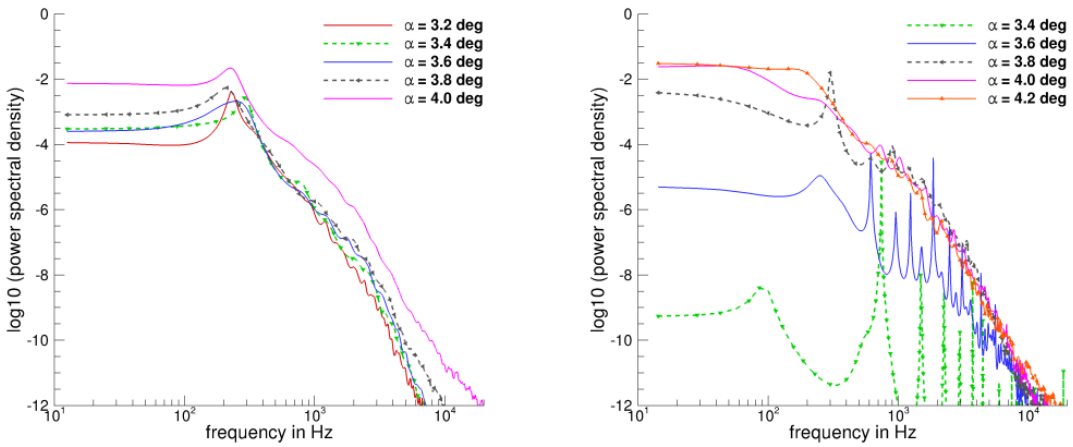

(a) clean configuration (b) with vortex generators

Figure 2.45: Lift power spectral density without (left) and with (right) VGs for the RBC12 wing in [265].

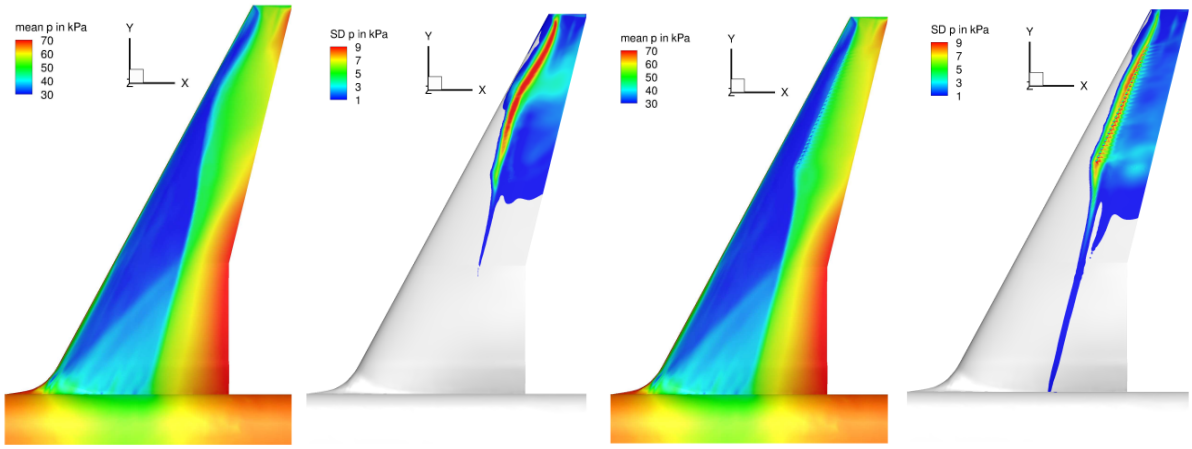

(a) $\langle p \rangle$, no VGs **(b)** $\langle p'^2 \rangle$, no VGs **(c)** $\langle p \rangle$, with VGs **(d)** $\langle p'^2 \rangle$, with VGs

Figure 2.46: Mean pressure and RMS distribution around the RBC12 wing in [265].

configuration. A clear delay (0.2-0.4 deg) and a reduction of the amplitude of buffet was found with the introduction of VGs. Two configurations with different numbers of VGs were analysed. The one with more VGs was more effective in delaying the buffet and reducing the chordwise extent of the oscillations, although an higher parasitic drag was expected. Moreover, the presence of VGs helped eliminate the higher frequency instabilities developing further after the buffet onset.

Recently, Sidorenko *et al.* [234] applied plasma vortex generators to mitigate buffet around a P-184-SR aerofoil wing in the T-112 transonic wind tunnel of TsAGI. The control was exerted by means of an array of 5 actuators over the wingspan aligned with the free stream. At pre-buffet conditions, CFD was performed to assess the effect of the actuator on the flow field. For the reference case, the actuators had little effect on the flow field and did not prevent SIO from forming at M$\geq$ 0.74. In the active case, the state of the boundary layer was altered, and formation of vortices on one side of the actuator was detected, as shown in Figure 2.47. At conditions of $M_\infty = 0.76$

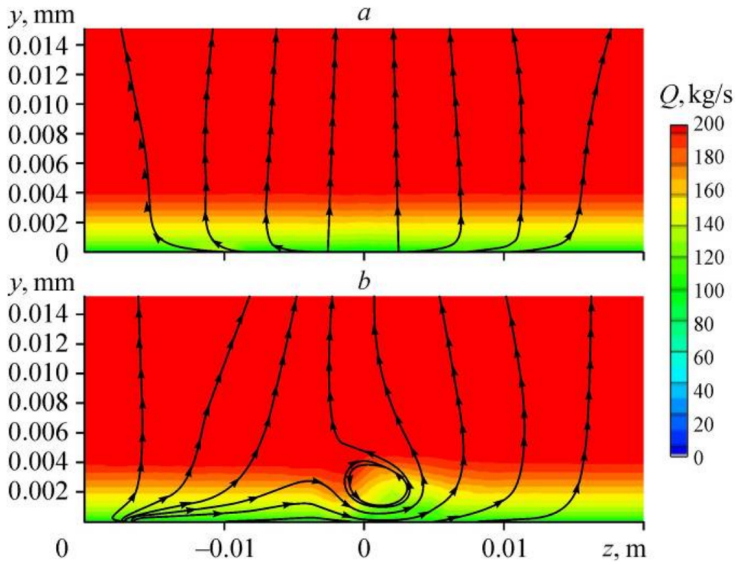

Figure 2.47: The field of mass-flow rate and the flow streamlines in the wake of an actuator for the reference case (a) and for the case with the supply of energy in the vicinity of the plasma vortex generator (b) at $x = 100$ mm [234]. Flow directions orthogonal to the plane.

and $\alpha = 5$ deg, continuous and modulated discharge were tested. For the continuous case, when using a discharge frequency around the buffet frequency, the oscillations were amplified, while a reduction was noticed in all other cases. At a discharge frequency one order of magnitude above the buffet frequency, several modulation frequencies were used. In all cases, the control strategy was effective. A Mach number sensitivity later revealed the dependency on the Mach number of the device ability to suppress buffet. The excitation in packet-mode (discountinuous) failed at reducing the SIO at almost all investigated Mach numbers; at the same time, an increase in mean drag was noted. The discharge in continuous mode, and at high frequency, led to better results. In general, the amplitude of the shock motion was reduced, while a small drag penalty was introduced (see Figure 2.48). At certain flow conditions, both quantities of interested were improved.

As an alternative, passive air-jet VGs can be adopted. Bruytan *et al.* [36] connected regions at different pressures to promote vortex generations. The adopted model is shown Figure 2.49, where the air flows through a plenum from high to low pressure region, and promotes the generation of turbulence. The experimental investigation on the P-184-15 aerofoil revealed that inclined jets (45

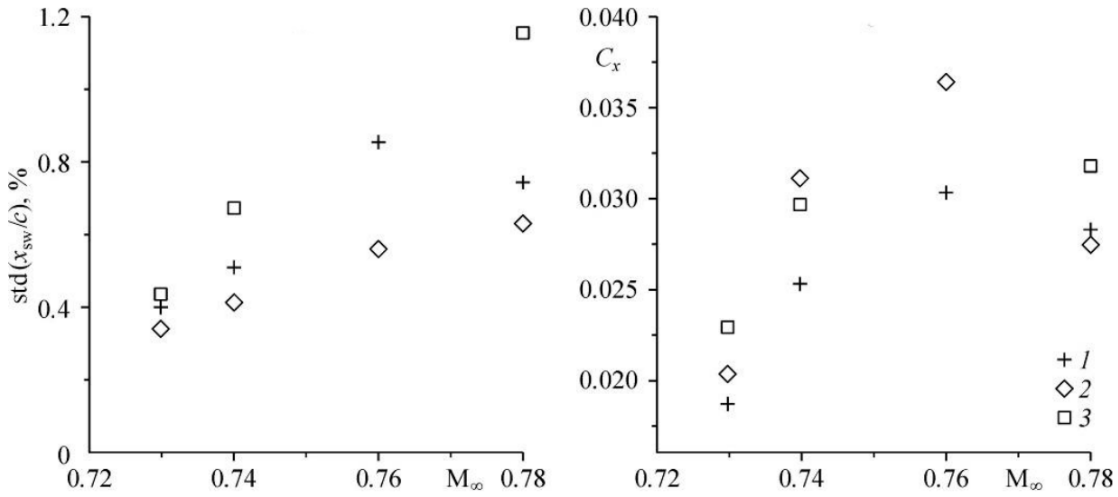

Figure 2.48: Dependencies of the RMS values of shock-wave pulsations (left) and the drag coefficient (right) on the Mach number of the oncoming flow at $\alpha = 5$ deg. In the legend: 1) no discharge; 2) discharge in continuous mode at $f = 1500$ Hz; 3) discharge in packet mode at $f = 1500$ Hz and rate of pulse packet $F = 100$ Hz.

deg with respect to the flow direction) were more effective than transversal jets, at the investigated conditions. Under buffet conditions, the presence of AJVGs **(i)** introduced an oblique shock which weakened the main shock strength, and **(ii)** promoted turbulence in the boundary layer which helped counteract boundary layer separation. This resulted in buffet onset delay and lift increase at various Mach numbers. The aerodynamic performance in terms of drag and lift-to-drag ratio were not provided.

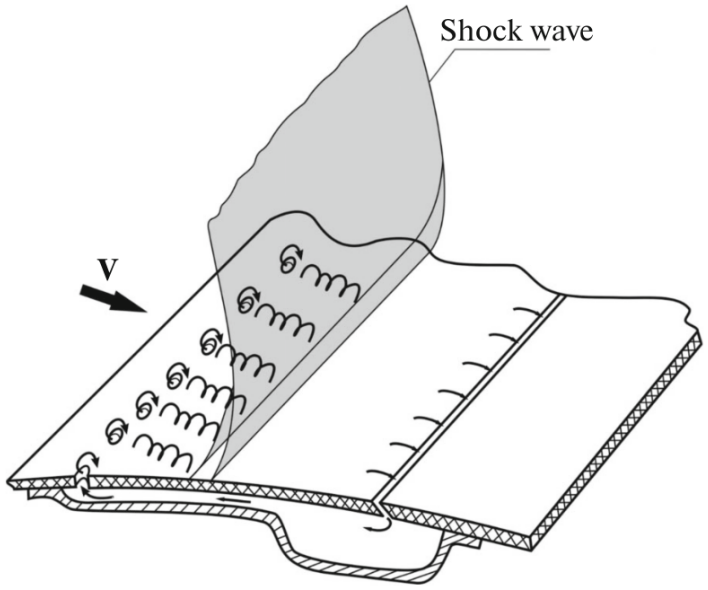

Figure 2.49: Sketch of the control strategy adopted in [36]: the air flows from high to low pressure regions through the plenum and generates turbulence in the boundary layer.

Promoting turbulence on laminar wings helps alleviate buffet by enhancing the momentum exchange in the boundary layer, which becomes less prone to separation. On modern laminar wings, such an emergency activation may bring a temporary benefit. In this view, Stalewski and Sznajder [246] used smart micro vanes for turbulence generation to alleviate the wing load on the Natural Laminar Flow (NLF) wing. In their work, a four-equation SST model was adopted to compute the response to a gust. An angle of attack increase by means of mesh rotation was applied to simulate the gust. As shown in Figure 2.50, the wing load can be alleviated, and the buffet onset

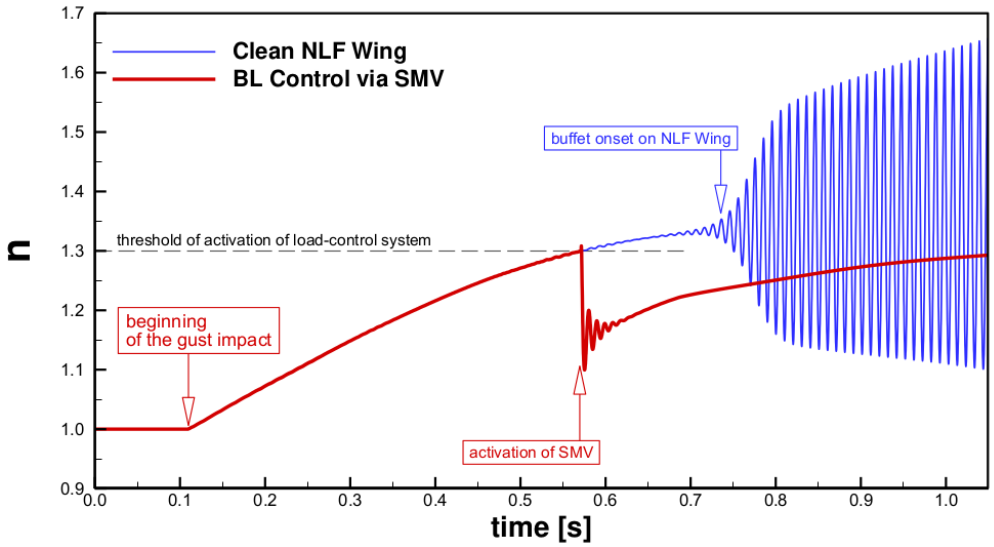

Figure 2.50: Load factor response to gust for uncontrolled and controlled cases [246]. SMV: smart micro vane.

delayed. The presence of vanes enhanced turbulence in the boundary layer, and the strong buffet on the clean wing was interrupted. With the wing load, the lift coefficient was also reduced. In this view, turbulence generation for laminar wings can only be used as a temporary remedy. On the other hand, this strategy revealed effective in case of gusts. In a similar way to the work of Molton *et al.* [190], Brion *et al.* [32] tested steady jets for both laminar and turbulent buffet around the OALT25 aerofoil. In their experimental investigation, a varying jet momentum coefficient was adopted, and the jet were oriented with at pitch and toe angles of 30 deg and 90 deg, respectively. The case with fixed transition exhibited a peak in the PSD, for St $= 0.07$, and large oscillations, while the laminar case had a fundamental frequency of St $\simeq 1.0$, seeing much more limited shock oscillations. Laminar buffet was suppressed when using $C_\mu \geq 0.03$, while $C_\mu \geq 0.06$ was required for turbulent buffet. In both cases, tangential jets promoted the formation of longitudinal vortices, and turbulence, in the boundary layer, that helped delay the separation and stabilised the shock.

Vortex generation can alternatively be induced by means of plasma devices. Plasma actuators were used in the work of Firsov *et al.* [76]. Their work consisted of experimental and numerical investigation over the P-184-15SR aerofoil. In the experimental campaign, the plasma actuators

played a minor role in the pre-buffet flow, and helped alleviate (but not suppress) buffet. URANS simulations complemented the experiments. The spark discharge was modelled by introducing a volumetric energy source in a CFD domain. As a result, a heat cavity and a shock waves were formed. The shock wave propagated, and the heat pocket stretched. From the interaction between the root of the heat pocket, and the front of the lambda shock, a pair of counter rotating vortices were generated. This is showed in Figure 2.51 and was beneficial to buffet reduction. Polivanov

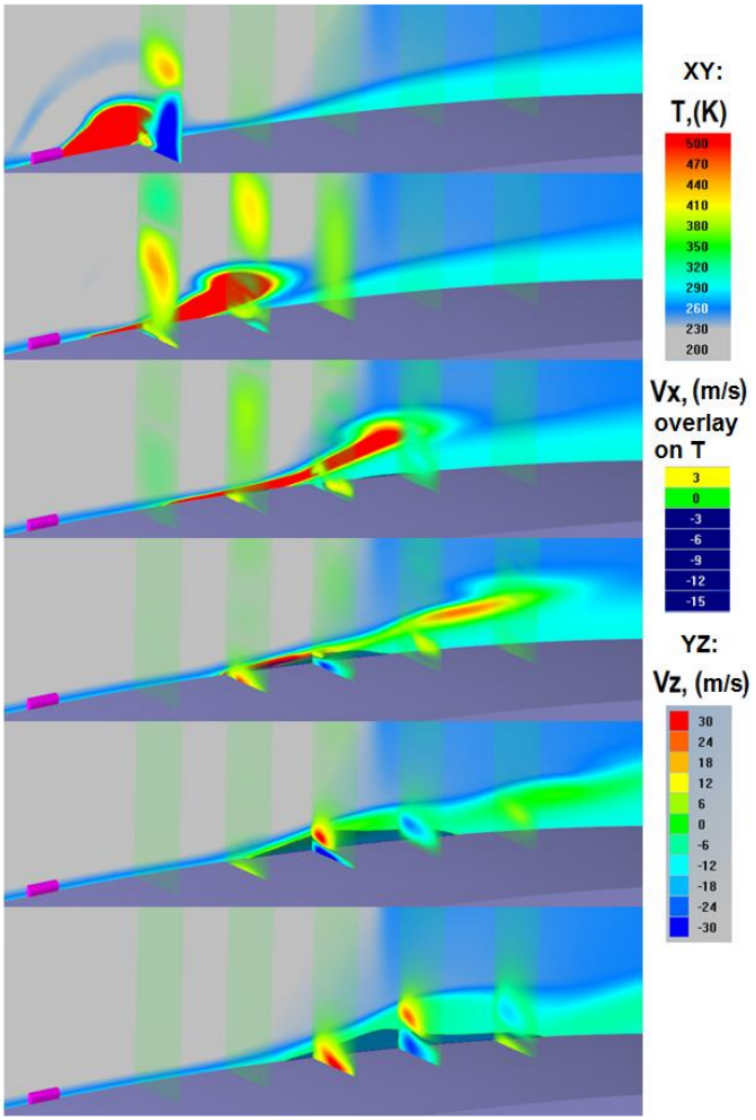

Figure 2.51: Temperature, vertical velocity component (in the background), and horizontal velocity component (in the transversal planes) contours at different times (in order from top to bottom) after the discharge on the P-184-15SR aerofoil, at $M_\infty = 0.74$ and $\alpha = 5$ deg. Figure from [76].

et al. [213] used plasma turbulators to control laminar buffet on the NLF aerofoil. The turbulators were placed in such a way to reproduce quasi 2D flow in the T-325 wind tunnel. Laminar buffet conditions were obtained by varying the position of an elliptic shaft near the wind tunnel end, and

were confirmed by computing the RMS of Schlieren images. Plasma turbulators promoted turbulence by creating vortices and reduced the separated flow region under the shock. Nevertheless, a conspicuous reduction of the separation region due to high turbulence led the shock too upstream at certain conditions. In that case, excessive turbulence in the boundary layer may break the multiple shock configuration on the wing. It was found that beyond a frequency equal to 3-4 times the fundamental buffet frequency, there was no benefit. Before that value, an increase in frequency led to reduced flow separation without significant effect on the shock position. The authors claimed that the advantage of plasma turbulators over other mechanical devices is the possibility to vary the intensity of the intermittence by changing the discharge parameters. Simulating conditions close to laminar-to-turbulent transition would be beneficial for buffet alleviation and drag reduction at the same time. In a later paper [212], the same authors confirmed the same findings by for a different configuration. The significant reduction in the extent of the separated flow region allowed for a downstream shift of the shock, and for a reduction of the unsteadiness. The positive effect of plasma discharge was validated across several Mach numbers.

2.3.2 Shock Control Bumps

Shock control bumps are relatively new devices with respect to VGs and TEDs. The review paper of Bruce and Colliss [34] details the challenges regarding this type of devices, and distinguishes between 2D and 3D configurations. With regards to control for buffet, a summary is found in the literature review of Giannelis et al. [100].

Birkenmeyer et al. [25] were the first to adopt SCBs for buffet flow control. They carried out experimental and numerical works to show the effect of 2D-SCB on the buffet boundary. The introduction of the device in the shock region did not bring any benefit in terms of onset delay. On the other hand, SCBs placed downstream of the main wing shock wave had a positive effect by introducing a region of attached flow between the shock wave and the trailing edge. This postponed the complete flow breakdown without offering any drag benefit. Eastwood and Jarret [68] focused on the design of 3D-SCB to provide both better L/D, and buffet alleviation. They estimated the buffet onset by extrapolating the conditions where the two separated flow regions at the shock foot, and at the trailing edge would merge. Using this approach they were able to test several geometries and come to the conclusion that the delay of the onset can be obtained even by placing the SCB at the shock foot. Nonetheless, the delay in the buffet onset was accompanied by a penalty in the peak aerodynamic performance.

Bogdanski *et al.* [26, 27] investigated the performance of different bump shapes by means of steady and unsteady RANS simulations for the Pathfinder laminar wing. The adopted shapes are shown in figure Figure 2.52, and consist of a hill-shaped bump, a wedge bump, and one with extended flanks. The bumps were designed to minimise drag at two Mach numbers corresponding

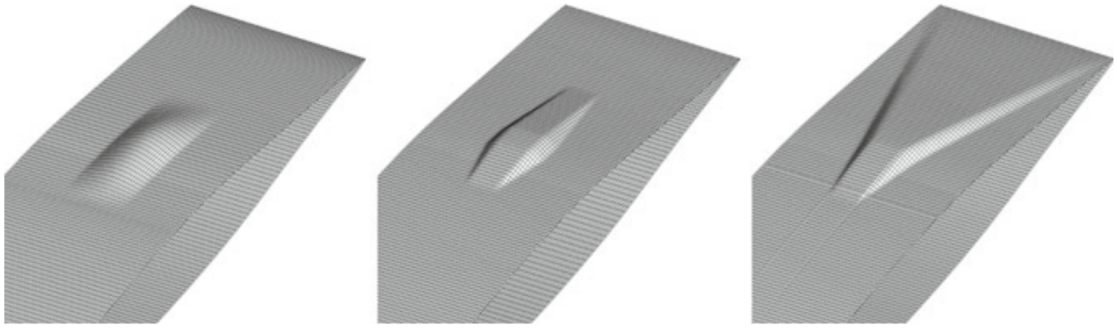

Figure 2.52: Shape of the bumps tested in [27].

to the design value and a lower one. Although a drag decrease was obtained by a reduction in the separated flow region over the aerofoil, they ended up anticipating the buffet onset by almost half degree. Spanwise finite devices generated downstream vortices, estimated to have roughly half the strength of those generated by vortex generators. The work investigated the effect of fork

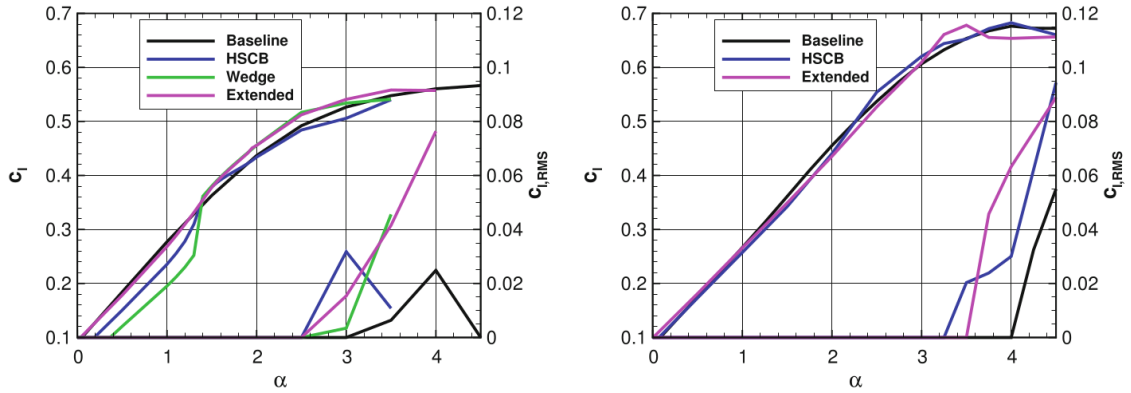

Figure 2.53: Lift polar and lift RMS for different configurations at $M_\infty = 0.76$ (left) and $M_\infty = 0.74$ (right). Figure from [26].

configurations, exhibiting teeth on one or both flanks. The buffet performance was only improved with respect to the previous designs, but the baseline configuration still exhibited the best behaviour among the tested ones.

The two dimensional URANS computations of Tian *et al.* [260] studied the ability of Forward Shock-Control Bump (FSCB) and Backward Shock-Control Bump (BSCB) on a RAE2822 aerofoil to alleviate buffet at several flight conditions. In general terms, FSCB and BSCB are located upstream and downstream of the mean shock locations, respectively. At times, some authors used this nomenclature to distinguish between more upstream or downstream configurations. TMSs highlighted a beneficial effect of the bumps according to the relative position with the shock. In particular, when the shock was upstream, the FSCBs allowed for the smearing of the shock, while BSCBs prevented the boundary layer separation. If the shock was rearward, the FSCB configuration could also be detrimental, as the shock was now located in a region of adverse gradient (the

second part of the bump). The BSCB had the same effect of the other configuration in the previous case. At pre-buffet, the forward configuration resulted in a double shock system. Overall, the FSCB worsened the aerodynamic performance at low angles of attack but delayed the $C_L - \alpha$ break in the aerodynamic polar. On the other hand, the BSCB had benefit at high angles, but showed a behaviour similar to the clean configuration. The forward configuration anticipated the onset, if not at low Mach numbers. The BSCB configuration had a beneficial effect at any Mach number. The reason is that the rear position helped prevent the separation of the boundary layer due to the presence of a new favourable pressure gradient region. The buffet frequency was also modified according to the buffet mechanism. For the Forward configuration, especially at high Mach numbers, the boundary layer was mostly separated during the buffet period while for the Backward and uncontrolled configurations, separation and re-attachment of the boundary layer were present. By computing the cross correlation between several sensors on the aerofoil upper surface, it was observed that pressure waves in the boundary layer moved at different speeds according to the presence of one unified or two distinct separated flow regions. When two regions were present on the aerofoil, the speed was reduced. Therefore, the buffet frequency increased significantly in the FSCB case, with respect to the clean and BSCB configuration. In the latter, boundary layer separation was inhibited, and the buffet frequency was further reduced.

The work was extended by Jiang *et al.* [130] who performed simulations around the Wing 1 wing with BSCB having variable locations over the span ($x_b/c = 0.58$ at the wing root, $x_b/c = 0.43$ approaching the tip). The presence of the device did not reduce the shock intensity but delayed the buffet onset by reducing the separation behind the shock. The merging of the separation bubble and the trailing edge separation was prevented, as shown in Figure 2.54. Even if not fully cancelled, the buffet intensity was significantly reduced at many flight conditions. At low angles, the SCB induced trailing edge separation, and a dual-shock configuration was observed. This resulted in the worsening of the aerodynamic performance. At high angles of attack, the aerodynamic performance was similar to that of the clean wing. Overall, the devices introduced off-design penalties but were successful at alleviating buffet at several flight conditions.

Geoghegan *et al.* [92] carried out a similar study by using oscillating SCBs mounted on a OAT15A aerofoil. The SCB was able to vibrate inducing a positive-negative surface displacement ($0.005 \div 0.01c$) with frequencies ranging from 50 Hz to 90 Hz, being the natural buffet frequency 72.55 Hz. The activation caused the shock to lock into the selected frequency, over the entire range of tested values. Two mean bump locations were investigated: $x_s/c = 0.45, 0.55$. In both cases, when the bump was deployed, the shock moved downstream in response to the flattening of the aerofoil upper surface. The opposite happened when the SCB was retracted. This caused the buffet frequency to lock into the excitation frequency. To assess the ability of the device to alleviate buffet, the mean lift coefficient variation, and the peak to peak lift coefficient, were compared to the clean configuration for different amplitudes and frequencies of vibration. For the oscillating device, the

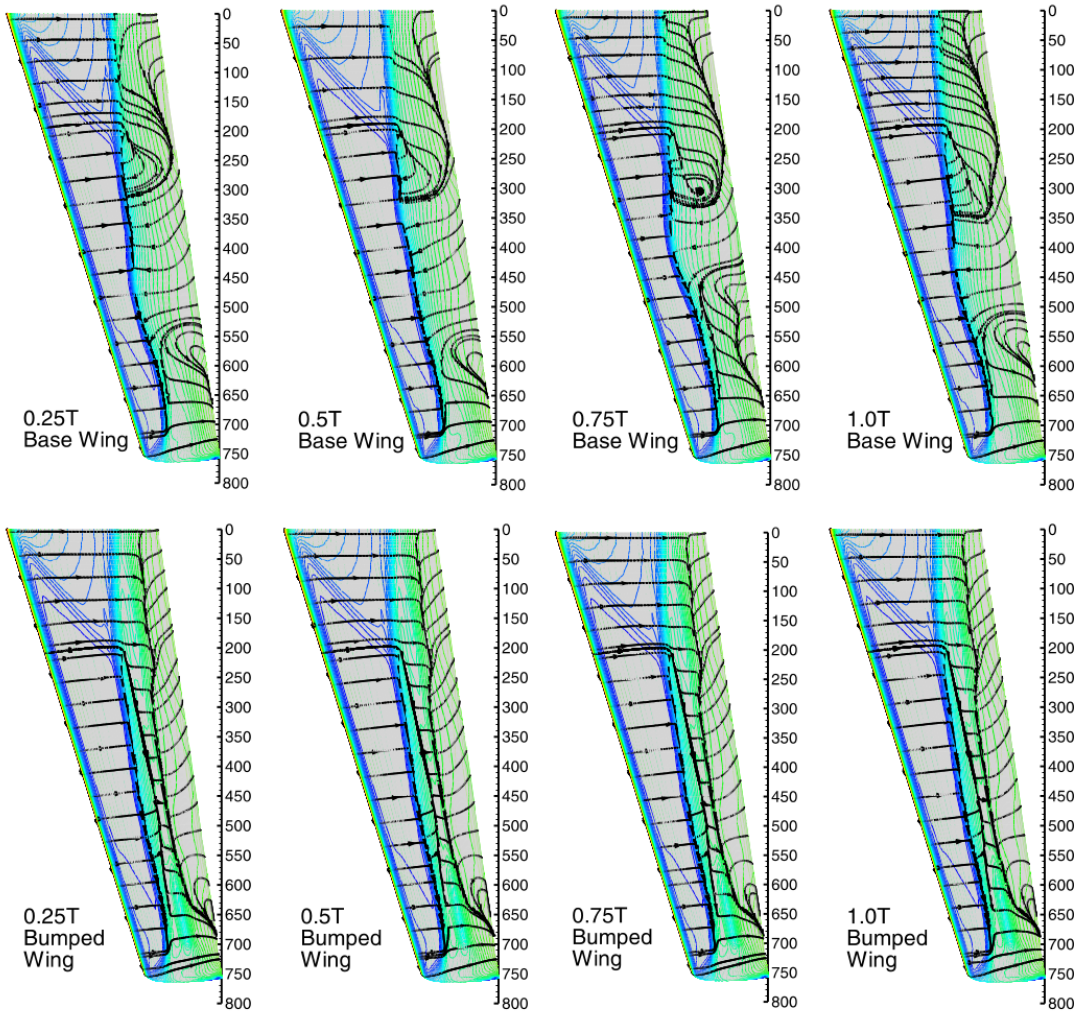

Figure 2.54: Pressure coefficient and CFD friction lines on the upper surface of the Wing1 without (top) and with (bottom) shock control bumps. $M_\infty = 0.78$, $\alpha = 2.5$ deg. Image from [130].

effectiveness depended on the mean shock position, and no common trend was determined. For the forward configuration, higher frequencies led to a reduction of the peak to peak lift coefficient, while for the backward configuration, small amplitude and frequencies led to better results. Two optimal configurations were selected, one for each geometry. Case A had $x_m/c = 0.45$, amplitude $A = 0.005c$, and $f_d = 90$Hz ($f_B \simeq 72$ Hz), and provided 66% reduction in buffet loading, at the cost of 1.8% decrease in the design lift coefficient; Case B, at $x_m = 0.55c$, a shock control bump with amplitude $A = 0.005c$ with driving frequency $f_d = 50$Hz, only provided 6% reduction in buffet loading. Both cases showed the ability to alleviate buffet without impacting on the mean lift coefficient. Because of the oscillating nature of the control, buffet was not completely suppressed.

In a following work [93], the same authors further explored the effect of the geometric parameters of 2D, non-vibrating bumps by using the same numerical approach. The SCBs were deployed following a sinusoidal law to reach the maximum amplitude and the motion was halted afterwards.

Four main parameters were investigated. The results by studying their isolated effects were:

- *deployment frequency*: higher frequencies corresponded to more drastic changes in the aerodynamic coefficient at the actuation, but also to shorter transients;
- *bump crest position*: the time-to-steady state reduced when the bump was at a forward position, and at the design conditions. A bump having a crest position between $-0.1c$ and $0.1c$ from the main shock position was able to alleviate buffet. After the threshold, SIO took place again. The mean lift coefficient increased almost linearly as the bump moved backward. In particular, the position of the SCB on the aerofoil was responsible for the distance between the separated flow regions on the suction side, that decreased with more downstream crest positions;
- *bump height*: above a threshold, the bump was able to suppress buffet. For very high bumps, the main shock was pushed too upstream, and the flow re-accelerated over the bump giving rise to a second shock (see Figure 2.55). The dual shock configuration was found to be steady but introduced heavy aerodynamic penalties. In between, the lift coefficient decreased linearly and mildly;

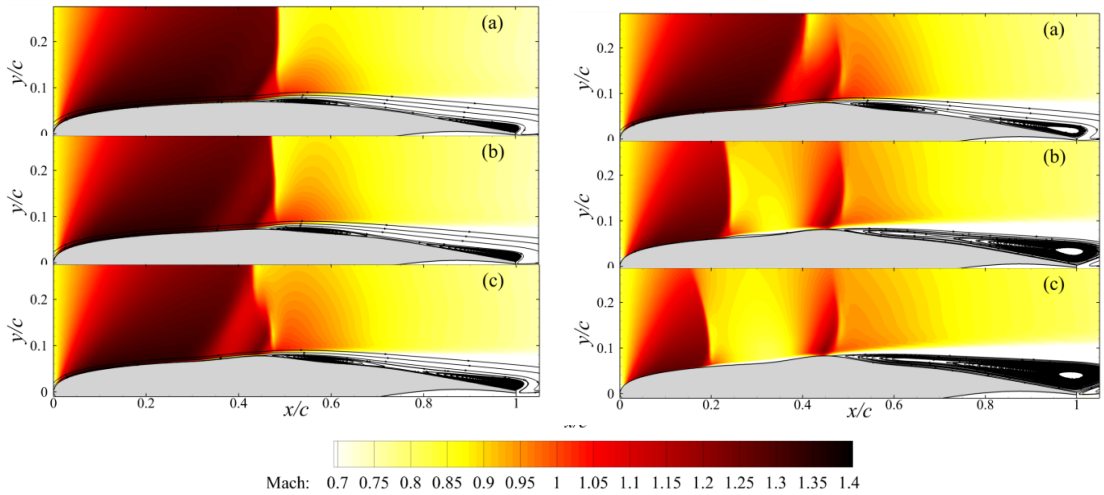

Figure 2.55: Mach contours and streamlines of the flow around the bump for varying bump heights. Left: $h/c = 0.002$(a), 0.005(b), 0.01(c); right: $h/c = 0.012$(a), 0.013(b), 0.015(c). Image from [93].

- *bump length*: the bump length was found to have a negligible impact as long as the height-to-length ratio was high enough to suppress buffet. A longer bump resulted in a larger shock smearing, and a less intense recirculation.

Keeping fixed the first and last parameters, the joint effect of bump height and position on the aerofoil was studied. To be considered a good combination of the two parameters, buffet had to be

suppressed. Lift, drag, and lift-to-drag ratio were studied and the trends are shown in Figure 2.56. Overall, an aft bump position must be accompanied by an increase in height to be able to suppress

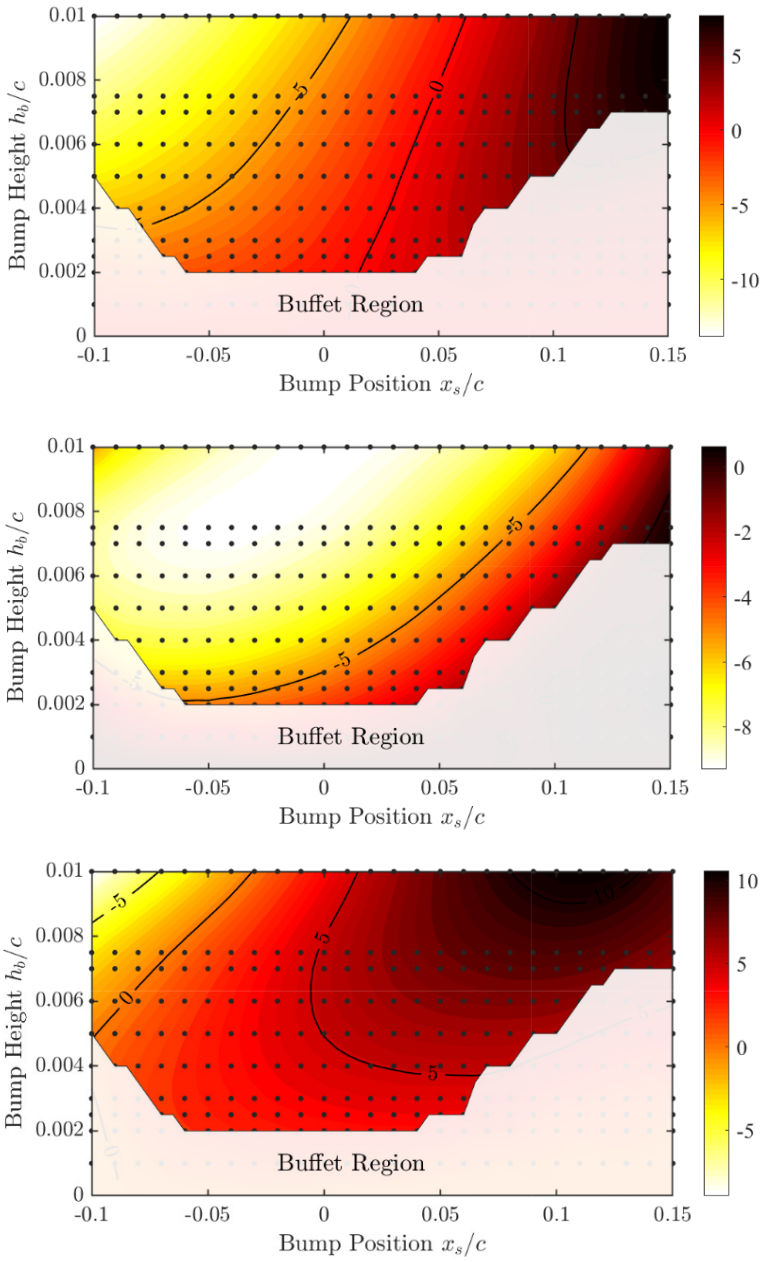

Figure 2.56: Percentage difference in mean lift (top), drag (centre) and lift-to-drag ratio (bottom) with varying bump position and height on the OAT15A at $M_\infty = 0.73$, $\alpha = 3.5$ deg. Image from [93].

buffet without deteriorating the aerodynamic properties of the aerofoil. Two configurations were tested at off-design, both with heights of $0.01c$ and at position of $0.51c$ and $0.56c$. The forward configuration was able to suppress buffet between onset and offset, introducing a mild penalty in lift at the onset and an increase elsewhere. The backward configuration gave an increase in the main lift, at all angles of attack, but SIO occurred again close to the offset. Therefore, a too aft position

is not safe at high angles of attack, as the dual recirculation system can be broken. A work from the same authors [94] pointed out differences between positively and negatively deployed bumps. Their ability to reduce buffet is related to the relative position on the aerofoil. For the positive bump, the considerations on the *bump crest position* made by previous works hold. For the negative deployment the trend is different. The device was now able to suppress buffet when placed far from the shock, while it enhanced the shock oscillation amplitude at design conditions. The curvature on the aerofoil promoted separation, as the effect was the opposite of the one expected for a positive deflection. When placed forward, the second part of the bump smeared the shock, like the positive bump at design point. In this case, the mean lift was higher than for the positively deployed bump. When placed further aft, the upper surface depression caused by the bump generated a stable re-circulation bubble which served to increase the effective thickness of the aerofoil at that location. The bubble was localised in the depression, and the shock was pushed upstream where lost strength. At the same time, the mean lift was reduced.

An asymmetric bump with flat crest, and different ramp angles, was adopted by Yang and Ogawa [284]. The position was selected to be under the mean shock and allowed for smearing of the normal shock occurring on the OAT15A aerofoil at $M_\infty = 0.73$, $\mathrm{Re}_c = 3 \times 10^6$ and $\alpha = 3.5$ deg. On that configuration, the controlled case exhibited the alternated presence of flow re-expansion on the bump, until the SIO was cancelled. Other data were not made available, and the mean lift coefficient was slightly reduced.

The work of Brion *et al.* [32] looked at laminar buffet control. In this case, 11 three-dimensional bumps having $l_b = 0.338c$, $h_b = 0.0028c$, with a crest having $\Delta y_c = 0.1c$ and $l_c = 0.03c$ were mounted on the OALT25 aerofoil-based wing and studied in S3Ch transonic wind tunnel of ONERA. Laminar buffet developed at much higher frequencies that turbulent buffet. The bump array was not able to fully suppress the SIO as the intensity of the vortex generated by the bumps was not strong enough. The reason may lay in the high frequency associated with laminar buffet, that might be similar to that of the vortices detaching from the SCB.

A more quantitative overview of the aerodynamic performance using 2D bumps was provided by Zhang *et al.* [289], who carried out LES simulations around the OAT15A aerofoil at angles of attack of 2.5 deg and 3.5 deg, i.e. pre- and post- buffet onset. Four configurations were tested, as shown in Figure 2.57. The predicted flow physics was coherent with the previous works. In particular, the higher the bump the more effective it was in alleviating buffet. The highest rear bump resulted in an upstream motion of the shock, and a double shock configuration. The fore bump was located under the shock, and caused the development of a well defined lambda structure. In Table 2.4, the main effects on the aerodynamic performance are listed. Bump 1 was not high enough to suppress buffet. From the table, some key considerations can be drawn:

- Bump 1 was not able to suppress buffet due to the reduced height;

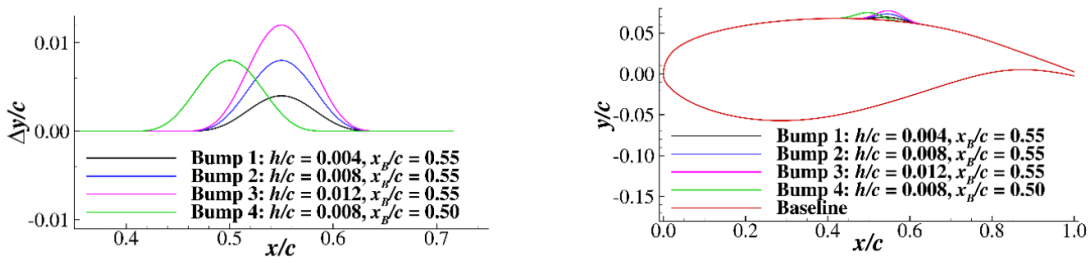

Figure 2.57: Shock control bump geometries around the OAT15A aerofoil in [289]. Left: bump profile on a flat surface; right: bumps mounted on the aerofoil.

Table 2.4: Aerodynamic performance in [289] for different bump shapes and conditions.

Configuration	α	$\langle C_L \rangle$	$C_{L,\mathrm{RMS}}$	$\langle C_D \rangle$	$C_{D,\mathrm{RMS}}$	L/D	$C_{M,\mathrm{RMS}}$
Baseline	2.5	0.919	0.006884	0.03009	0.000724	30.54	-0.1335
	3.5	0.968	0.037572	0.04823	0.003737	20.07	-0.1262
Bump 1	3.5	0.965 (-0.3%)	0.027828 (-25.9%)	0.04634 (-3.9%)	0.003107 (-16.8%)	20.82 (+3.7%)	-0.1252 (+0.8%)
Bump 2	2.5	0.866 (-5.8%)	0.004527 (-34.2%)	0.03174 (+5.5%)	0.000662 (-8.6 %)	27.28 (-10.6%)	-0.1260 (+5.6%)
	3.5	0.953 (-1.5%)	0.012188 (-67.6%)	0.04484 (-7.0%)	0.001569 (-58.0%)	21.25 (+5.9%)	-0.1229 (+2.6%)
Bump 3	3.5	0.917 (-5.3%)	0.008297 (-77.9%)	0.04642 (-3.8%)	0.001343 (-64.1%)	19.75 (-1.6%)	-0.1184 (+6.2%)
Bump 4	2.5	0.870 (-5.3%)	0.003852 (-44.0%)	0.03395 (+12.8%)	0.000549 (-24.2%)	25.63 (-16.1%)	-0.1271 (+4.8%)
	3.5	0.925 (-4.4%)	0.016171 (-56.9%)	0.04559 (-5.5%)	0.002168 (-42.0%)	20.29 (+1.1%)	-0.1193 (+5.5%)

- The other devices guaranteed a net reduction of the oscillations, quantified by the RMS of the aerodynamic coefficients;
- At buffet conditions, the lift-to-drag ratio increased for Bumps 2 and 4; Bump 3, the highest one, deteriorated the aerodynamic efficiency. Both lift and drag decreased with respect to the clean configuration;
- The moment coefficient increased, i.e. the bump had a nose-down effect;
- The aerodynamic performances were deteriorated at pre-buffet conditions.

This suggests that a controlled actuation might be desirable for practical application to avoid off-design penalties.

Numerical simulations on a spanwise periodic configuration performed by Mayer et al. [176] revealed some differences between 2D and 3D configurations of shock bumps. It is crucial for the design to balance the vortex generation in 3D configurations, without excessively deteriorating the downstream boundary layer. Indeed, 3D configurations see higher crests and longer tails to mitigate the effect of the higher pressure gradient generated. As result, they showed a worse ability to alleviate buffet at typical off-design, and at $C_{L,max}$ conditions. The flow turning effect decays in the streamwise direction, and causes a deterioration of the performance with respect to the 2D configurations. The bump horizontal position and crest height are also important in buffet delay. If

not correctly set, a wrong combination of the two can lead to an increase in the shock oscillations. The application of different SCB configurations was shown by Mayer et al. [177] on the AVERT model. Two types of 2D configurations were tested, aiming at drag reduction at design point and buffet delay, together with a 3D configuration consisting of an array of bumps. The study was carried out by means of RANS simulations for the steady case and URANS simulations for selected flight conditions. The 2D configuration showed a better ability to reduce drag, at design conditions, while it introduced a penalty at low C_L. The 2D configuration targeting buffet alleviation was located at a more downstream position to promote flow re-attachment after the main shock wave. Nonetheless, because of the relative position with respect to the main shock wave, it introduced a drag penalty from low C_L conditions to the design point. At high C_L, i.e. in excess of Mach number or angle of attack, the main shock moved downstream, and the shock bump position introduced significant benefits even for drag reduction. The 3D configuration was thought to meet a trade-off between the two design objectives but ended up being less effective than the 2D configuration in both cases, leading to the conclusion that the 3D configuration was not successful for that case. The reason of the failure was related to the larger crest-flow separation and the milder impact of the vortical wakes with respect to the 2D case (see Figure 2.58). The role of the sweep angle on the 3D

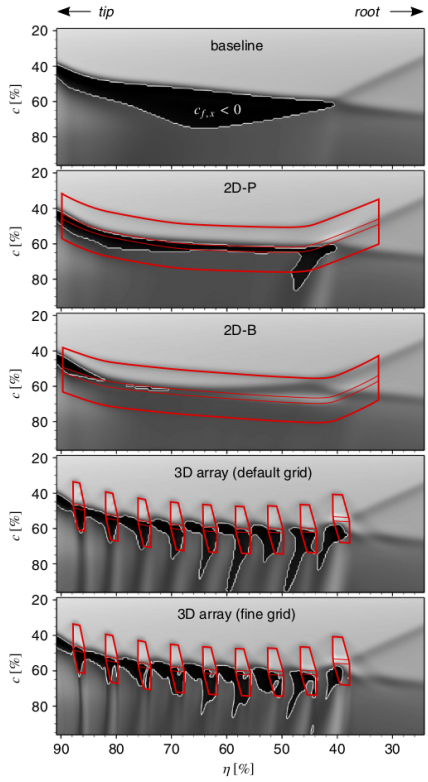

Figure 2.58: Friction coefficient around 2D and 3D array of SCB's from [177].

SCB array was investigated. When the sweep angle exceeded 5 deg, the flow topology was strongly influenced by the cross-flow which modified the system of counter-rotating vortices generated at

the sides of the device (see Figure 2.59).

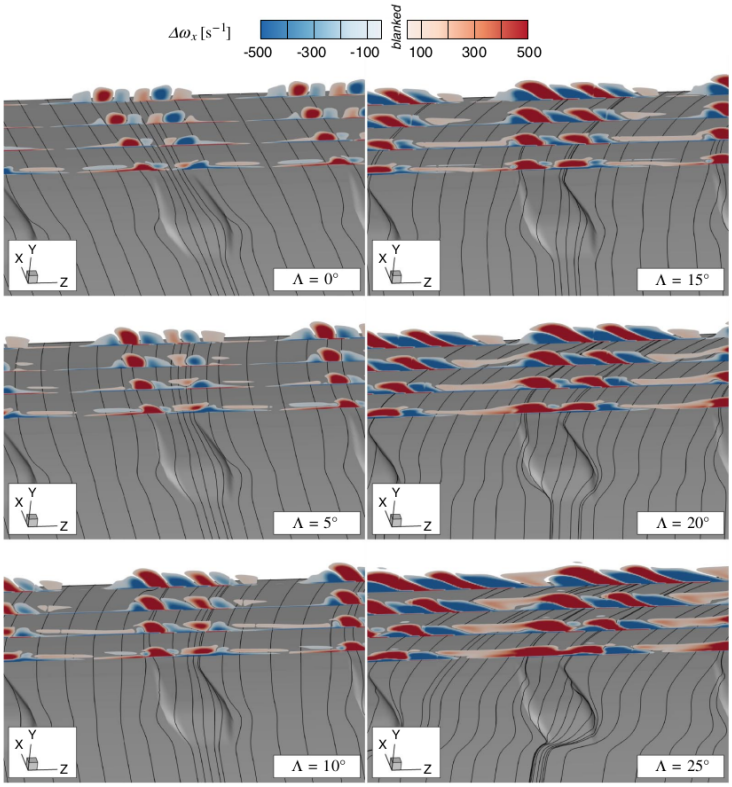

Figure 2.59: Effect of wing sweep on vortical wake of a 3D SCB around the OAT15A aerofoil from from [177].

Ren *et al.* [219] applied control by using local smart skin, modelled by a varying height bump, to alleviate buffet around the RAE2822 aerofoil at different conditions. They used model-free adaptive control, a data driven method based on two constraints: **(i)** the prediction of the lift coefficient based on the past values of the coefficient itself and the bump height, and **(ii)** the minimisation of a cost function to reach a desired lift coefficient without abrupt changes in the bump height. The 20%c bump was initially placed downstream of the main shock position. The bump was negatively displaced during the upstream motion of the shock to prevent the shock bubble separation from moving downstream, while it was positively displaced for an opposite shock motion to prevent the upstream growth of the trailing edge bubble (see Figure 2.60). Placing the bump around the mean shock position allowed for a reduction of the maximum bump height. Even applying a constraint on the maximum bump height, the control method revealed successful, although delayed. Moreover, the application at different flow conditions demonstrated the robustness of the control strategy.

Greater physical characterisation was given in the experiments of D'Aguanno *et al.* [47,52] on the unswept OAT15A wing section carried out in the TST-27 transonic-supersonic wind tunnel of Delft University of Technology. The main design parameter was the spacing between the bumps of the array. The use of schlieren and PIV on two different planes allowed for a detailed flow

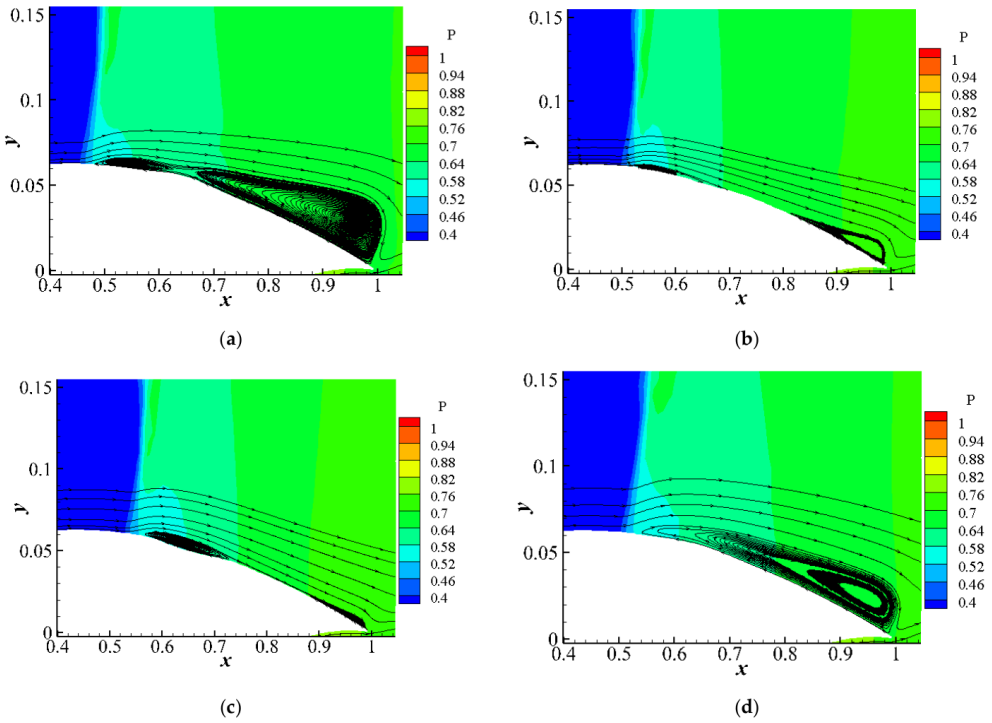

Figure 2.60: Pressure contours and streamlines around the RAE2822 at different buffet phases: (a) most upstream position; (b) downstream shock motion; (c) most downstream position; (d) upstream shock motion. Figure from [219].

investigation. One plane of view was on the central bump symmetry plane, and the other provided a top view of the wing. Overall, the presence of bumps allowed for a decrease in the shock excursion, confining it to a more downstream average position. Among the other configurations, spacings between 25-30% of the model chord were optimal. The flow topology was influenced by the presence of the bump array. The bumps had the merit to smear the shock, replacing it with a lambda system, as documented in other control works. Nevertheless, at the bump leading edge an oblique shock was generated in the spanwise direction and interacted with the other shocks coming from the close bumps. They interact twice, once at half the distance between consecutive bumps, and once on the bump symmetry plane (see Figure 2.61). The separated region downstream the shock displayed a uniform behaviour. In-plane PIV measurements allowed for the characterisation in terms of average and standard deviation of the velocity components. They underlined a net decrease in size of the shear layer for the best configuration (spacing of $c/4$ between bumps), in spite of a smaller increase in the separated region. This must be related to the fact that the bump is placed underneath the shock, and not at an aft position. Finally, the influence of the bump spacing was found to play an important role on the influence of the BL downstream of the shock, showing that a smaller spacing gave better results for the configuration under analysis.

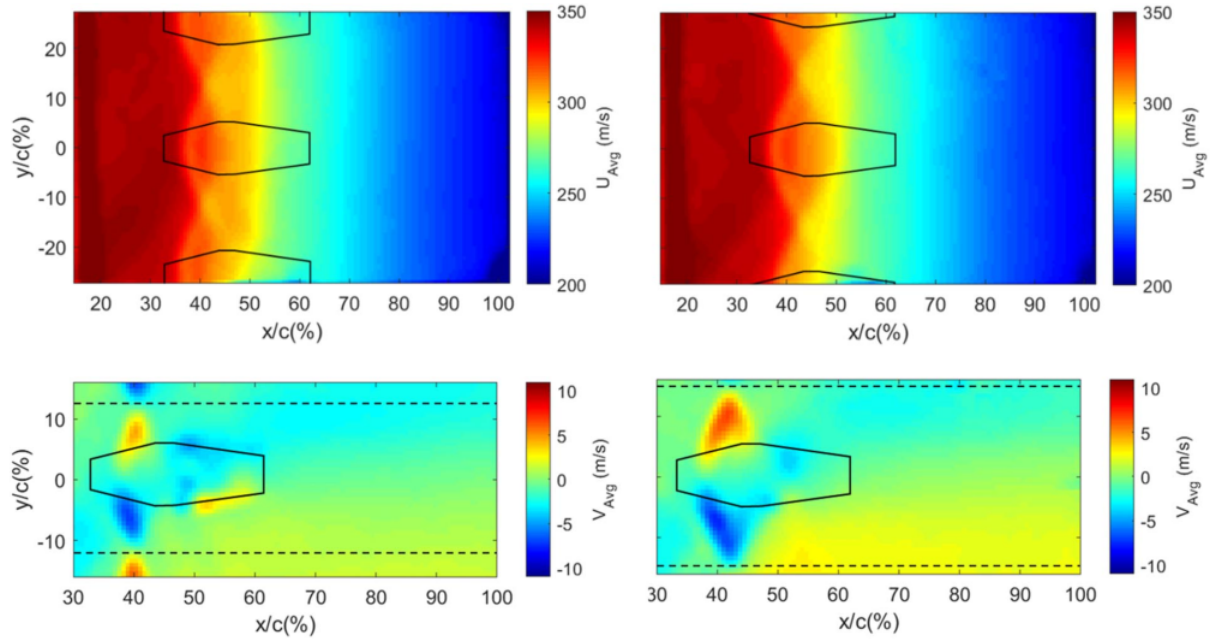

Figure 2.61: Mean longitudinal and spanwise velocity around a 3D SCB array installed on the OAT15A aerofoil for the 25% (left) and 30% (right) soacing configurations. Flow from left to right. Figure from [52].

2.3.3 Trailing Edge Deflection

Due to the importance of the trailing edge region in the shock buffet dynamics, several attempts were made to introduce trailing edge control devices to mitigate the buffet effect. Lee and Tang [155] and Lee [156] analysed the characteristics of the BGK1 aerofoil equipped with flaps at different flap angles. The impact on the buffet boundary was quantified based on the normal coefficient divergence. A positive (downward) flap angle produced an increase in lift, and a positive shift of the aerodynamic polar. The C_L-M buffet boundary was therefore shifted upward, as shown in Figure 2.62. The same positive outcome was not obtained when looking at the $\alpha-$M buffet boundary. Usually, lift and angle of attack are tightly linked, and therefore the two buffet boundary can be confused, or equivalently adopted. In this case, the presence of the flap introduced a lift variation that was, al least in the linear regime, independent of the angle of attack. Indeed, the measured mean pressure distributions were smeared for positive flap angles, indicating the presence of SIO, while the shock was kept fixed for negative flap angles, as shown in Figure 2.63. Therefore, a positive deflection anticipates the buffet onset angle, as shown in Figure 2.64, where the normal coefficient fluctuation is plotted against the angle of attack. On the other hand, a negative flap deflection results in a decrease in lift, as the shock position is shifted upstream, and therefore its employment should be limited to the proximity to the buffet onset.

Caruana *et al.* [38, 39] employed TED with fixed angle deflection, in closed- and open-loop. Applied on the OAT15A aerofoil, the first option was proved useful to delay the buffet onset, but it introduced a decrease in the aerodynamic performance at small angles of attack. Using a

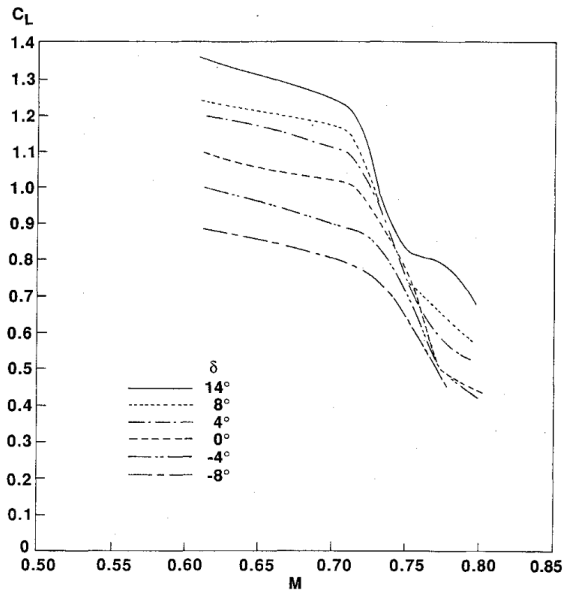

Figure 2.62: C_L-M buffet boundary in [155].

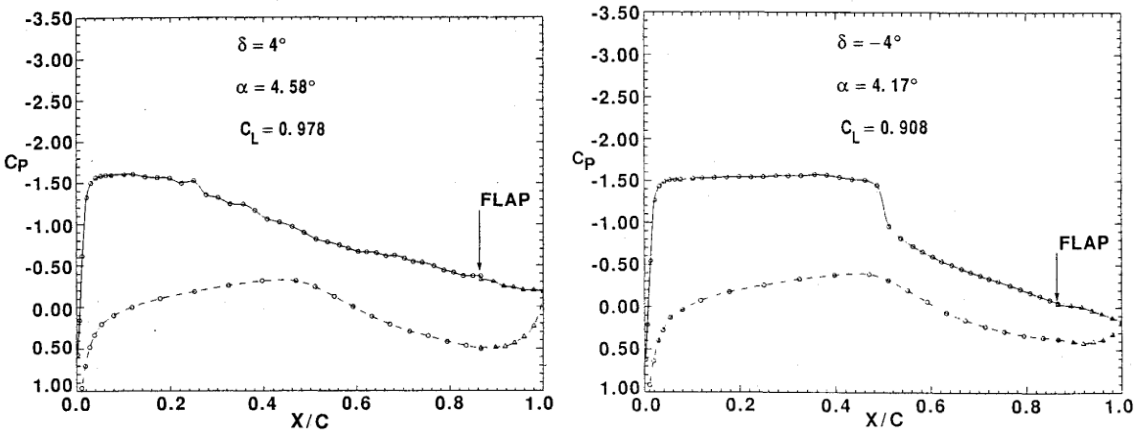

Figure 2.63: Pressure coefficient distributions around the BGK1 aerofoil at different flap angles. Figure from [155].

prescribed shock deflection, e.g. a sinusoidal function, the shock oscillation became dependent on the frequency of excitation, while in a closed loop TEDs were able to reduce the amplitude of the oscillation. In particular, the TED acted to contrast the shock motion based on the pressure unsteady measurements. On a 3D configuration, static TEDs led to a delay of the buffet onset, and an increase of drag at low angles of attack. The authors also suggested that the introduction of several trailing edge deflectors along the wing span may be useful in redistributing the wing-load to obtain a dependency on the local lift coefficient. Also in this case, open loop-control was not effective in terms of buffet mitigation, and increased the level of structural vibrations. In a closed loop, the energy needed is more than in the 2D case, because of the higher buffet frequency and the broadband nature of buffet in 3D. By low-pass filtering the pressure signal, it was still possible

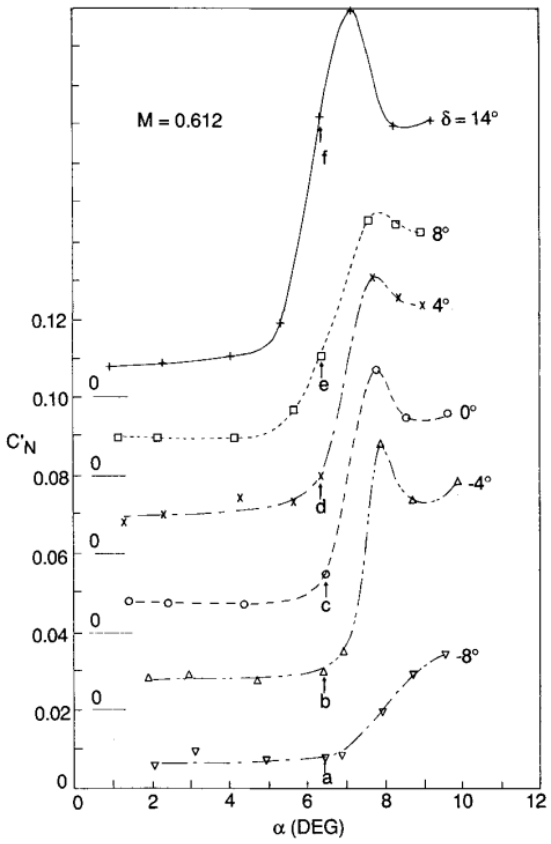

Figure 2.64: Normal force coefficient divergence vs angle of attack at fixed Mach number. Figure from [156].

to alleviate the oscillations. Moreover, because of the three-dimensionality of buffet, the effect of TED was observed to be mostly in the direction perpendicular to the trailing edge.

Tian *et al.* [259] investigated the effect of an upward spoiler deflection, spanning from the 80 to the 100% of the chord, on the OAT15A aerofoil, and the Wing1 case, through steady and unsteady RANS simulations. The spoiler presence was modelled by increasing the trailing edge thickness corresponding to a 5 deg upward deflection. Before the buffet onset, the shock was pushed upstream because of the different pressure distribution at the trailing edge. This resulted in a slight lift drop. Around the buffet onset, the spoiler deflection prevented trailing edge separation and weakened the shock foot separation (see Figure 2.65), causing an overall delay in the buffet onset of around one degree in the range of Mach number analysed. The same beneficial effect was found in the 3D configuration, where the unified separated region was avoided. In a similar way, the influence of UTEFs was studied by Tian *et al.* [261] on the RAE2822 aerofoil. The presence of the UTEF induced an increase in the trailing edge pressure (see Figure 2.66), that caused an upstream motion of the shock and, in turn, decreased the shock strength. Therefore, the shock foot separation was avoided and the buffet significantly delayed. The use of UTEFs caused a lift drop at low angles of attack, but delayed the onset of the SIO. Therefore, the onset lift coefficient was increased

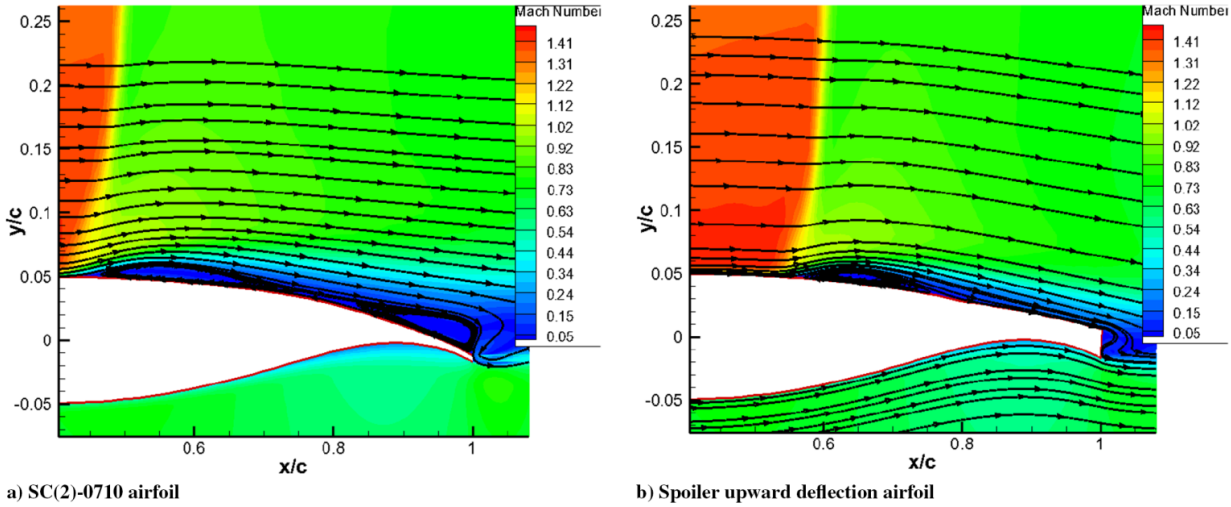

Figure 2.65: Mach number contour and streamlines around the OAT15A aerofoil with and without the upward spoiler deflection [259].

throughout the range of Mach numbers simulated. In these works [259, 261], no information on the drag penalty at buffet conditions was given.

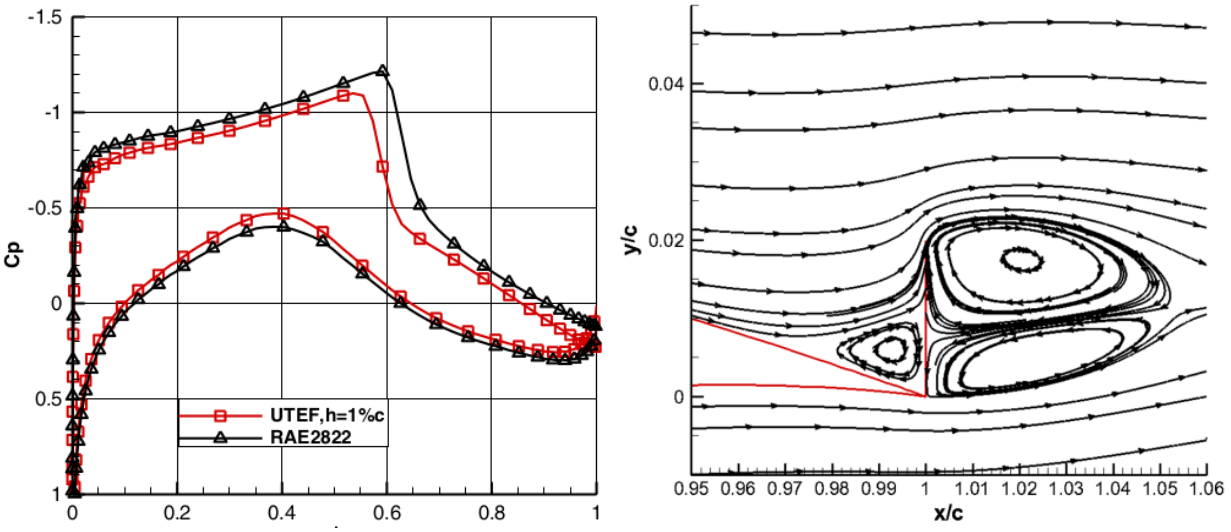

Figure 2.66: Mach number contour and streamlines around the OAT15A aerofoil with and without the upward spoiler deflection [261].

The findings of Tian *et al.* [261] were confirmed by the experimental work of D'Aguanno *et al.* [51] on an OAT15A aerofoil equipped with straight and serrated UTEF's. When using a straight configuration, the device revealed effective in alleviating the oscillation (detected by means of schlieren images) only when their height was at least equal to that of the trailing edge boundary layer. In their work, it amounted to 1.5% of the chord. In that case, the amount of unsteadiness in the separated region, as well as its extent (see Figure 2.67), were reduced. The authors claimed

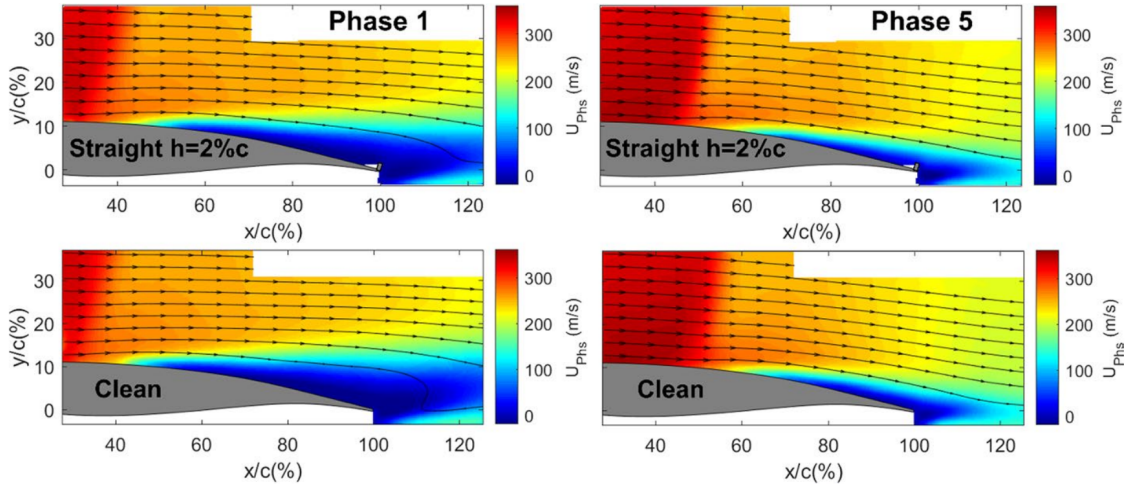

Figure 2.67: Mean longitudinal velocity contours around the OAT15A aerofoil at two phases of the buffet period. Phase 1: most upstream shock position; phase 5: most downstream shock position. Figure from [51].

that the positive effect on buffet stems from the interruption of the communication between the separated region and the trailing edge. In particular, upstream and downstream travelling waves were no longer communicating. PIV measurements showed only a mild circulation modification, leading to the conclusion that the actual aerofoil shape modification only had little effect on the alleviation.

An attempt to use a delayed, closed-loop control by means of flap deflection was made by Gao *et al.* [87]. In their numerical study around the NACA0012, the feedback mechanism shown in Figure 2.68 was employed to alleviate buffet. The temporal law for the flap angle targeted the unstable steady state, following the law:

$$\beta(\tau) = \lambda \left[C_l(\tau - \Delta\tau) - C_{l0} \right], \tag{2.6}$$

where λ is a gain, i.e. it determines the magnitude of the flap deflection, $\Delta\tau$ is a fixed delay, and C_{l0} is the balanced lift coefficient, in this case the unstable steady-state lift coefficient. The closed-loop mechanism was successful when using certain combinations of gain and delay. Moreover, the optimal phase lead, i.e. time delay, was found to be such that the summation of the phase lead and the lift response lag was π. The adoption of the optimal phase allowed for a significant reduction of the gain, and was helpful across different flight conditions. The findings were the same as the work of Gao *et al.* [84], where a ROM to predict flow instability was developed. An open loop control was also tested and revealed effective when the flap oscillation frequency was approximately 1.6 times the buffet frequency. The results on the optimal delay were confirmed, as shown in Figure 2.69. Based on the ROM, two closed-loop controllers based on the pole assignment, and linear quadratic methods, were developed. While the first consists of finding a control law which shifts the system

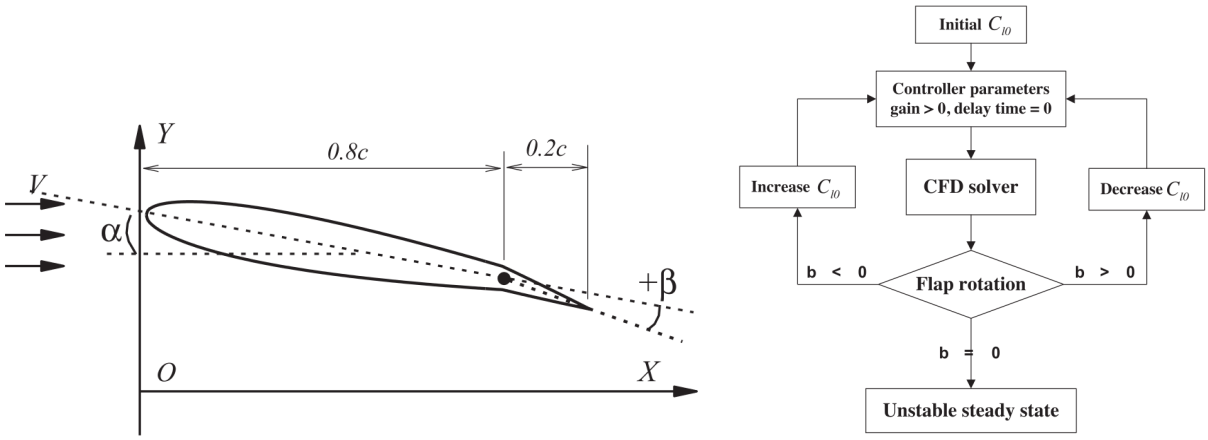

Figure 2.68: Left: sketch of the aerofoil with the flap rotation; right: schematic of the closed-loop control. Figures from [87].

poles in the left semi-plane of the complex plane, the second acts by minimising a cost function. In both cases, the optimal law based on the ROM was similar, and a rough agreement with the finding of Gao *et al.* [87] was found. The best control was when operating close to the anti-resonance, i.e. phase opposition control was obtained. The idea was further explored by Ren *et al.* [218] who

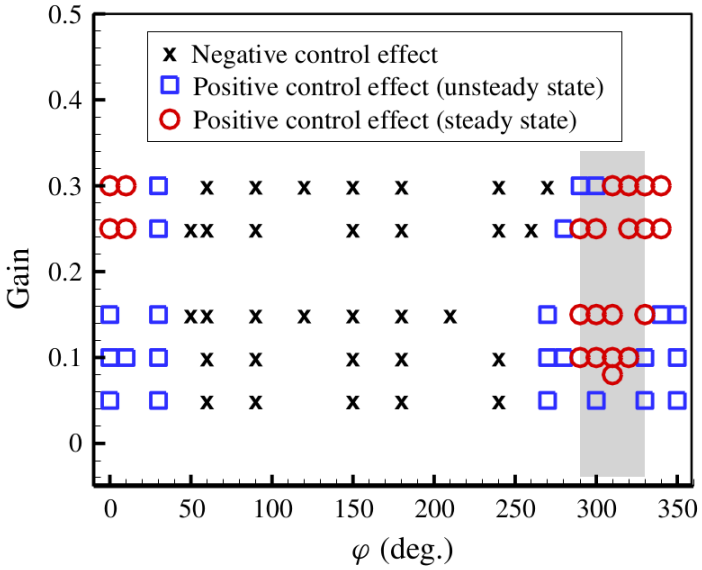

Figure 2.69: Effective control regions for different gains and time delay in [84]. Figure adapted from [87].

proposed an adaptive control mechanism through radial-basis function neural networks. Even in that case, the control used the lift coefficient as feedback quantity. The adoption of neural network allowed the control to work optimally across a wide range of operating conditions, revealing its superiority with respect to fixed control law mechanism. Moreover, the independence of the physics guarantees a higher robustness and make such a strategy usable for different applications.

Giannelis *et al.* [97] compared the effect of flap and slat deflections on the NACA 64A204 by

means of unsteady CFD simulations. While tests on a positive flap deflection confirmed the results previously obtained by Lee [156], a leading edge deflection resulted less impacting on the buffet onset angle. A mild deflection of the slat did not reflect in a reduction of the onset angle of attack. An abrupt slat deflection, on the other hand, led to a premature buffet onset and a significant lift decrease. The dominant mode of the DMD procedure applied revealed that the sonic region was shifted aft due to an abrupt slat deflection, causing the drop in lift, as shown in Figure 2.70. Further

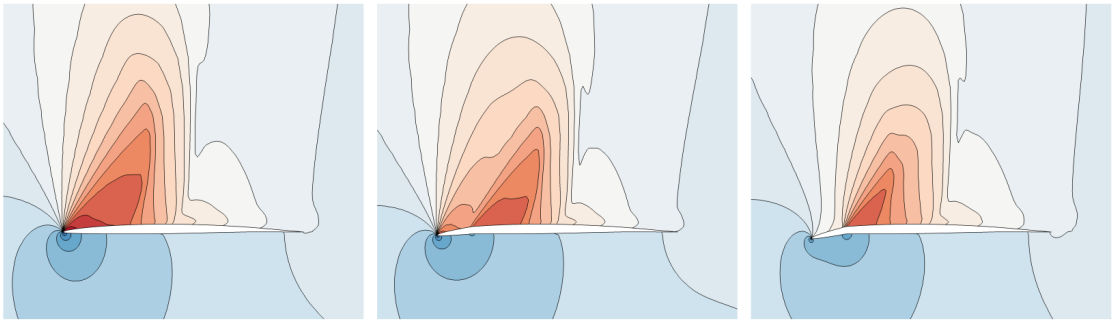

(a) $\delta_s = 0°$ (b) $\delta_s = 5°$ (c) $\delta_s = 10°$

Figure 2.70: Dominant DMD pressure mode for different leading edge deflections around the NACA64204 aerofoil. Figure from [97].

tests using harmonic oscillations of the control surfaces were carried out. In both cases, a lock-in between the aerodynamic response and the structural excitation was obtained for an increasing number of frequencies, as the amplitude of the flap/slat motion increased. Among them, the region of coupling was narrower for the slat case (see Figure 2.71). The lift variation was also studied

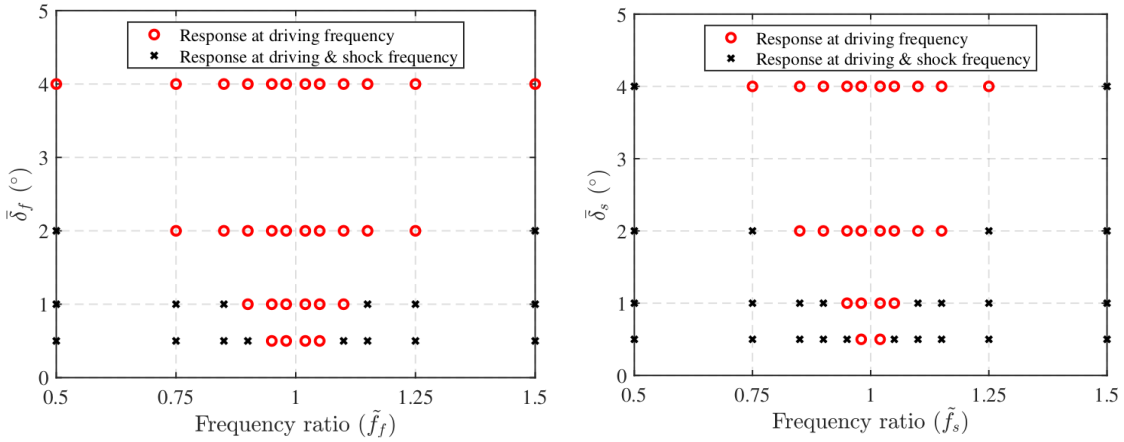

Figure 2.71: Map of lock-in region for TE (left) and LE (right) excitations, for different flap angles (δ_f) and control frequencies (rescaled with the buffet frequency, $\tilde{f}_f = f_f/f_B$), around the NACA64204 aerofoil. Figure from [97].

across several frequencies. In both cases, a excitation frequency slightly above the buffet frequency revealed at times beneficial in reducing the lift oscillation amplitude, confirming the findings of

Gao *et al.* [84] for open loop control. Therefore, a closed-loop system might introduce significant benefits to buffet reduction.

The potential of fluidic TED to be adopted for lift increase and buffet alleviation, and to be in a closed-loop approach, was the main reason for a long investigation in the AFLoNext project, whose results are summarised in the paper of Sartor *et al.* [227]. The paper aimed at providing benchmark cases for CFD investigations with flow control. The adopted geometries were the OAT15A aerofoil and the AVERT wing-body model. Both uncontrolled and controlled configurations were investigated using URANS. Fluidic TEDs were modelled using *ad hoc* boundary conditions to simulate the injection, with an idealised geometry, or a more realistic geometry. For the 2D case, the use of TEDs on the pressure side resulted in an aft shock motion. At buffet conditions, fluidic Gurney flaps induced an increase in the shock excursion, i.e. a worsening of buffet, as shown in Figure 2.72. On the other hand, a lift increase was obtained. Similar considerations held for the 3D

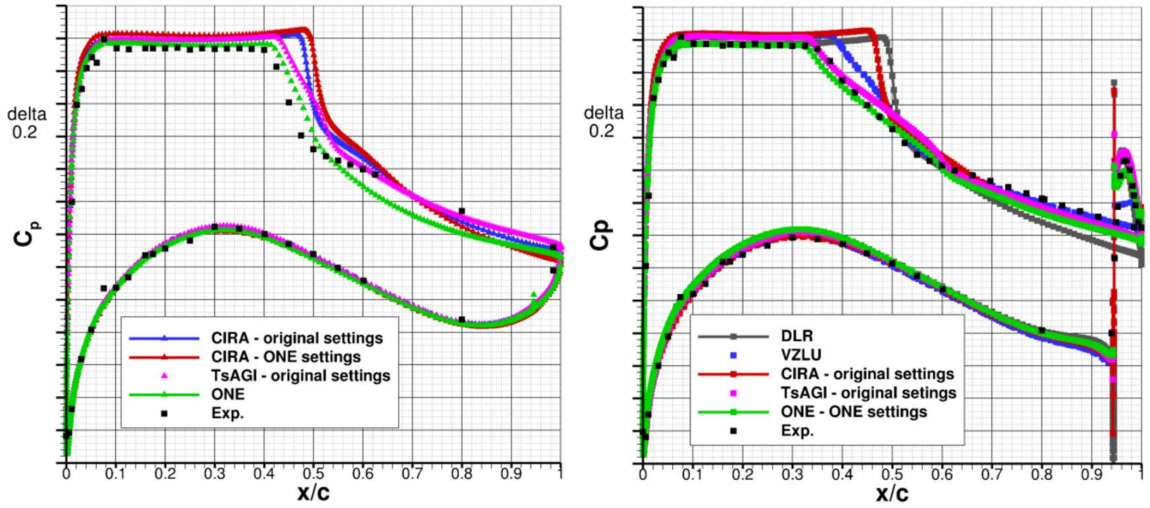

Figure 2.72: Pressure coefficient distribution around the OAT15A aerofoil at buffet conditions ($\alpha = 3.71$ deg and $M_\infty = 0.7366$) without (left) and with (right) fluidic Gurney flaps. Figure from [227].

configuration. In this case, the structural deformation played an important role in the prediction of the shock position and pressure distribution. Moreover, the jet momentum coefficient was found to be the most impacting parameter on the aerodynamic performance. Overall, the controlled configuration showed an increased lift-to-drag ratio, without drastic increases in the drag coefficient. As the pressure distribution near the trailing edge on the pressure side drops under the action of the Gurney flap, a nose-down can be expected, and therefore, it would be worth investigating the pitching moment changes. On the other hand, a downstream shift of the shock may counteract the aforementioned effect.

2.3.4 Alternative Methods

Other devices for buffet alleviation have been used, and do not fall into any of the categories introduced in the previous paragraphs. Here, some works on combination of the aforementioned devices or different ones are analysed.

Jets upstream of the trailing edge were used to mitigate buffet around an 18% thick biconvex circular-arc aerofoil in the work of Zhou *et al.* [291]. URANS simulations predicted the alternated shock motion typical of bi-convex aerofoils. The main parameter under investigation was the jet velocity. In general, a tangential jet can reduce the extent of the separated flow region. Therefore, the shock excursion can also be reduced. This effect was more evident with increasing jet velocities. At the same time, the amplitude of the lift and drag coefficients oscillations were reduced. While the lift coefficient oscillated around zero, the drag mean value was reduced for higher jet velocities, in response to a reduced extent of the separated region. Together with the shock amplitude, the shock oscillation frequency was also reduced. Even higher jet velocities were tested in a following work, by the same authors [292], and it was found that not only an alleviation, but suppression of buffet was achieved. The authors stated that the success of this control strategy is due to the ability to hamper the communication between suction and pressure side of the aerofoil. Nevertheless, the presence of jets act as a modification of the aerofoil shape, by forcing the flow to be attached near the trailing edge and by adding a region of essentially steady flow (see Figure 2.73). In the same

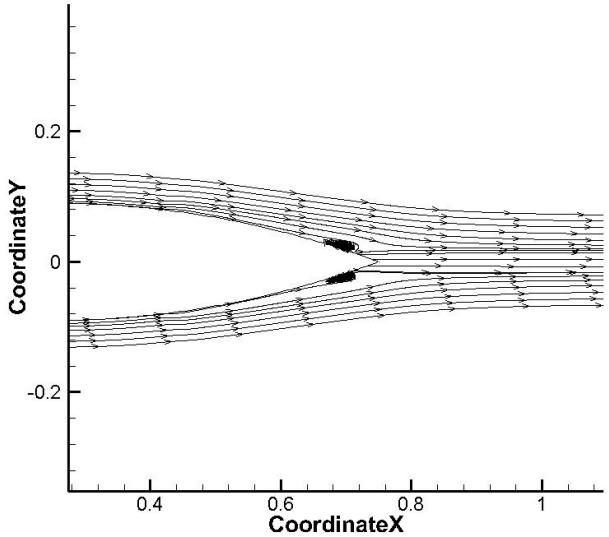

Figure 2.73: Velocity streamlines around a biconvex circular-arc aerofoil with TE tangential jets. Figure from [292].

work, a cavity on the suction side was also used. The cavity acted as a passive control device applying blowing and suction according to the pressure difference between the inner and outer flow (and the instantaneous shock position). The main effect observed was a reduction of the oscillation amplitude with respect to the uncontrolled case. While the effectiveness was dependent on the

cavity depth, it revealed almost uncorrelated with the number of slots.

Runpei *et al.* [221] used buffet breathers around a RAE2822 aerofoil, and the Wing1 case. The device consisted of a hole connecting the two sides of the aerofoil/wing to generate a jet due to the pressure gradient between the pressure and suction sides (see. Figure 2.74, left). The idea was to avoid the separated flow regions at the shock foot, and at the trailing edge to merge into a unique one by means of a normal/vertical flow (see. Figure 2.74, right). The separated flow region was broken, and the flow was made more stable, thus diminishing or avoiding SIO. In their work they conducted a sensitivity analysis to some design parameters, i.e. chord-wise position of exit, diameter of entrance, angle of exit and, exit-to-entrance ratio. Among these parameters, only the exit position and the flow direction played a significant role. In spite of the good results for buffet control, the aerodynamic performance was deteriorated by the buffet breather. Reducing the exit diameter and locating it further downstream helped reducing the gap with the base configuration. Similar results were found after the application of buffet breathers to the 3D configuration.

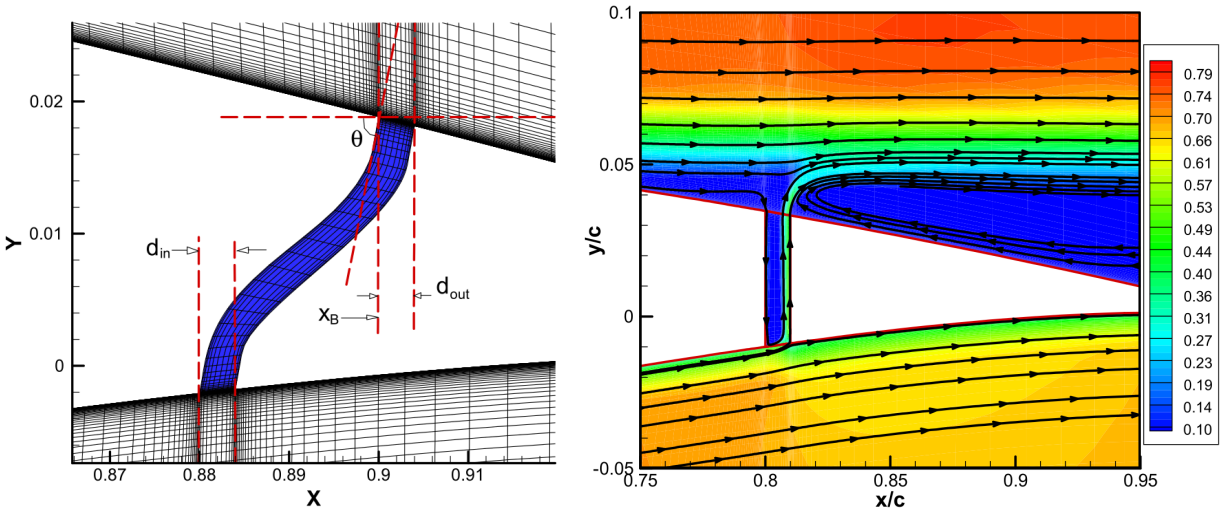

Figure 2.74: Left: CFD grid around the buffet breather and design parameters; right: time-averaged Mach number contour with streamlines. Figure from [221].

In a similar way, Abramova *et al.* [2–5], carried out a long computational and experimental campaign using tangential jets to alleviate buffet on the transonic aerofoil P-184-15SR. By using RANS and URANS simulations (SA model performed better in predicting buffet), they showed that the injection of momentum in the boundary layer delayed the onset of the instability according to the momentum coefficient C_μ. The location of the injection hole slightly downstream of the nominal shock location allowed for the prevention of the boundary layer separation, necessary for buffet to happen. Figure 2.75 shows the dependence on the momentum coefficient. A high momentum coefficient led to a net lift coefficient increase for all the angles of attack, an extension of the linear regime, and a delay of buffet. A smaller C_μ did not impact on the mean lift coefficient, but it delayed the onset of buffet by 0.4-0.6 deg. An experimental investigation by means of schlieren

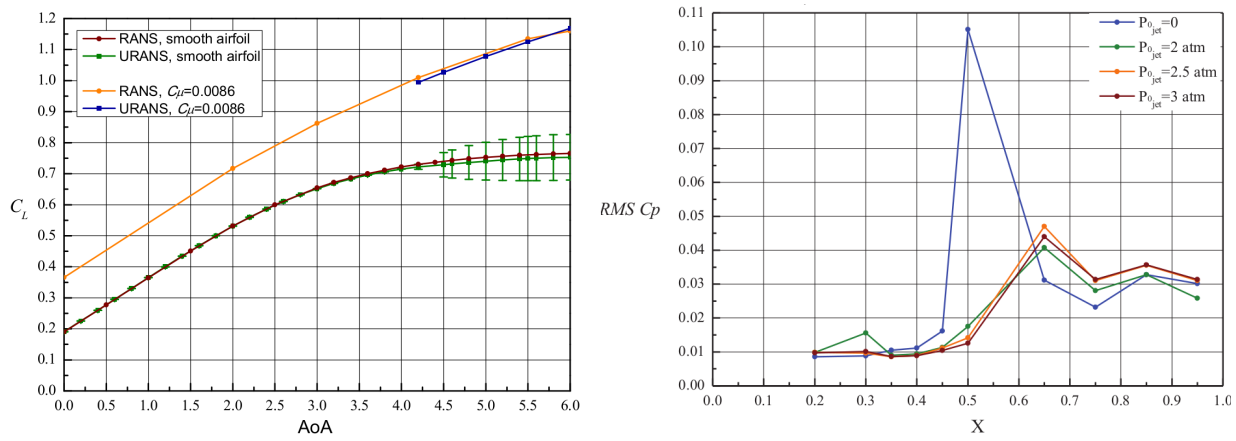

Figure 2.75: Mean lift coefficient predicted by URANS computations for different momentum coefficients. Where available, the standard deviation was also plotted. Figure from [2].

images and pressure measurements complemented the CFD investigation [3]. The main result was a downstream shift of the shock (see Figure 2.76) and the increase of the pressure RMS downstream of the holes. Such an unsteadiness was not detected by the URANS simulations. When the total pressure of the blown jet was high enough, trailing edge separation was prevented.

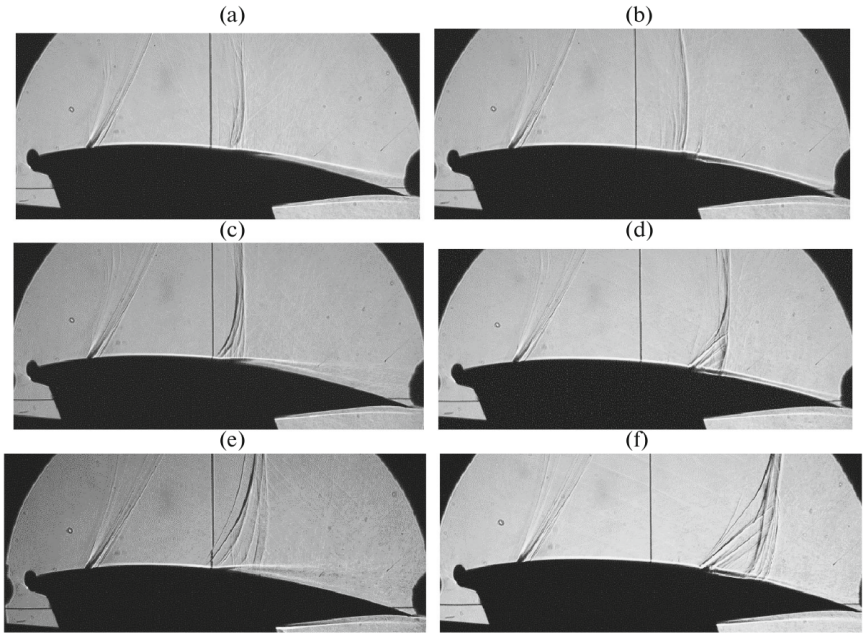

Figure 2.76: Shadow pattern of the flow past the P-184-15SR aerofoil without (a,c,e) and with (b,d,e, C_μ = 0.009) jet blowing. From top to bottom $M_\infty = 0.73, 0.76, 0.81$. Figure from [4].

Dang *et al.* [57] investigated the ability of steady and periodic tangential jets to reduce buffet around the NACA0012 aerofoil using RANS simulations. The jets were modelled as Venturi nozzles on the upper surface with adjustable total pressure ratio. Because of the aft maximum thickness position with respect to other geometries, the shock oscillations were usually closer to the leading

edge. Therefore, among the possible choices, the more upstream jet position gave the best results. The injection of momentum in the boundary layer reduced the separation region extent and counteracted the backward propagation of Kutta waves, therefore stabilising the shock. The frequency content and lift variation were not strongly affected by the jet total pressure ratio. In general, steady jets revealed more successful than periodic jets with frequency close to the fundamental buffet one, guaranteeing higher lift. As pointed out in several other studies [84,87,97], there is a strong impact of delay and frequency of the excitation. Therefore, the results are not conclusive.

Liu and Yang [162] adopted micro-tabs of different heights to alleviate buffet around the NASA SC(2)-0714 supercritical aerofoil. The numerical investigation was carried out using SST-Scale Adaptive Simulation (SAS) on a 2D configuration. The tested micro-tab positions were $x/c = 0.6, 0.7, 0.8, 0.9$. In the first three cases, the presence of the micro-tab introduced a low-frequency content, called *micro-tab mode* by the authors. The position within the separated flow region (roughly extending on the second half of the aerofoil) was crucial to suppress buffet. In that case, the intermediate positions revealed the most successful. The positive outcome of the control was deemed to a geometric effect introduced from the micro-tab. Even the application of the micro-tab at $x/c = 0.6$ resulted in a significant reduction of the oscillation. Figure 2.77 shows the velocity streamlines of the four configurations. In the view of the results obtained, the ability to suppress

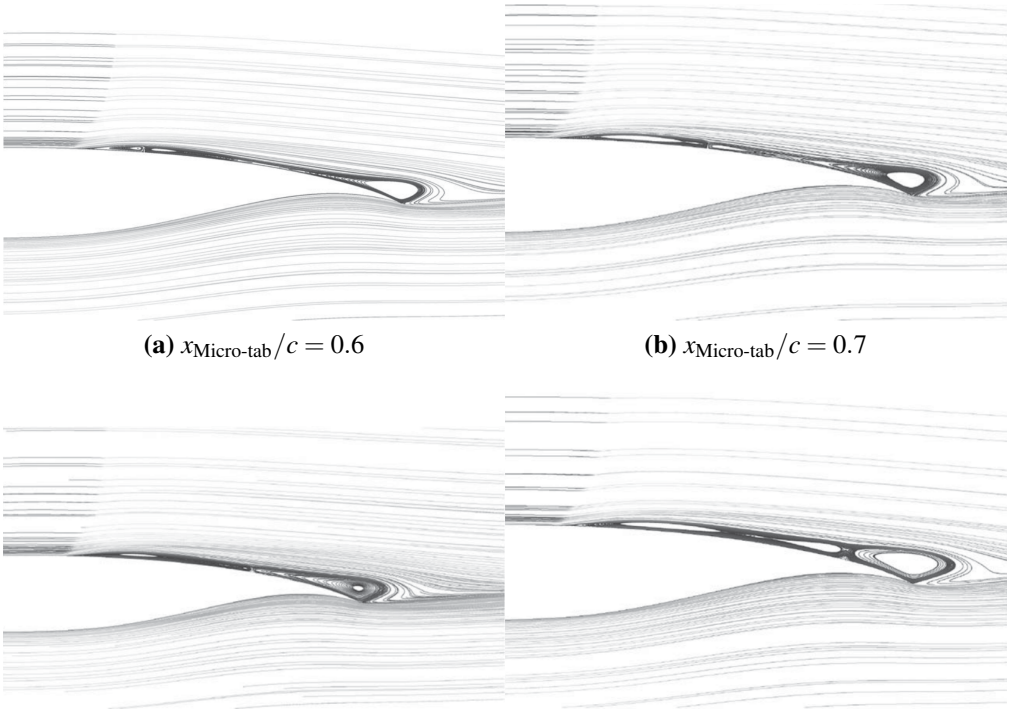

(a) $x_{\text{Micro-tab}}/c = 0.6$ **(b)** $x_{\text{Micro-tab}}/c = 0.7$

(c) $x_{\text{Micro-tab}}/c = 0.8$ **(d)** $x_{\text{Micro-tab}}/c = 0.9$

Figure 2.77: Streamlines around the SC(2)-0714 aerofoil at the same phase over a buffet period with micro-tabs installed at different positions. Figure from [162].

buffet seems to be linked to the ability to interrupt the communication within the separated flow

region. In cases (b) and (c), the micro-tab was located in the region of minimum height of the separated flow region, and had higher chances to hamper the passage of disturbances in the boundary layer. In the first and, especially, in the last case, the device was completely immersed in the boundary layer. The adoption of a higher device, which reached the upper limit of the separated region, allowed for further reduction of the load oscillations.

Gao *et al.* [222] combined UTEF and BSCBs for 2D and 3D configurations. The paper confirms the findings of some of the aforementioned works which studied the devices singularly. The flap-only configuration caused an upstream shock motion, while the shock bump broke the separated flow region. As a result, the onset was further delayed on both 2D and 3D configurations. As shown in Figure 2.78, the main drawback stemmed from the decrease in lift caused by the upward deflected TE. Also, the pitching moment varied significantly from the uncontrolled case. In this view, the authors suggested the need for an active TE deflection while using a passive SCB. The

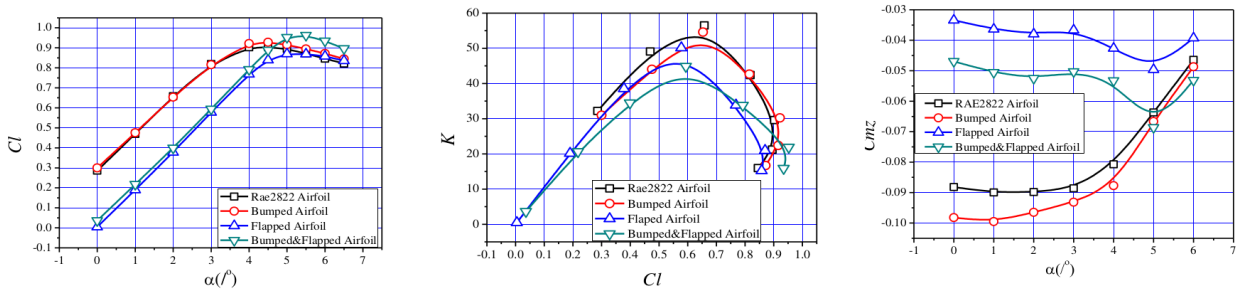

(a) Lift coefficient **(b) Drag coefficient** **(c) Pitching moment coefficient**

Figure 2.78: Aerodynamic performance of different modification of the RAE2822 aerofoil. Figure (b) shows the lift-to-drag ratio. Figure from [222].

effect of the devices was similar for 3D configurations. The application of a trailing edge active flap in conjunction with shock bumps was proposed by Zhang *et al.* [288]. In their CFD study on a 2D OAT15A aerofoil, they proposed a closed-loop application targeting lift increase and drag reduction by means of the combined action of the devices, following the guidelines of Gao *et al.* [87]. First, the two strategies were singularly simulated. Active control via flap motion revealed to be sensitive to gain and delay, as mentioned in reference [97]. On the other hand, two bump configurations helped alleviate buffet, delay the onset, and improving the lift-to-drag ratio at buffet conditions. The combination with a fixed bump allowed for a reduction of the flap displacement, because of the stabilising action of the bump itself. This is shown in Figure 2.79. The maximum flap deflection angle was reduced, and the steady lift coefficient was increased in presence of bumps. Bump 2 in figure was located downstream with respect to bump 1 and led to a higher lift increase. The trailing edge flap acted to counteract the shock motion by displacing downward during the upstream shock motion phase, and vice versa. The minor shock excursion induced by the bump reduced the required time-to-steady state in the active configuration. The presence of the bump enhanced the

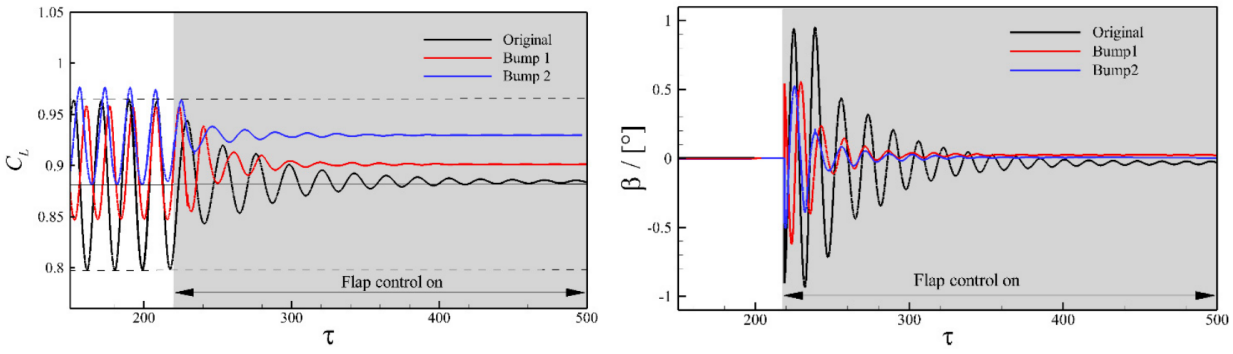

Figure 2.79: Lift coefficient (left) and flap deflection angle (right) response to active control on the OAT15A aerofoil. Figure from [288].

control robustness by enlarging the range of effective gain-delay combinations. Overall, the lift-to-drag ratio at the investigated flow conditions was raised together with a negligible increase in drag. The mean lift and drag coefficients were almost unaffected by the active control. Nevertheless, for the investigated configurations and flight conditions, only the use of active control allowed for buffet suppression.

Gaifullin and Khairullin [82] simulated a moving surface on the suction side of the TsAGI P-184 15SR aerofoil. The control can be thought as a belt moving at constant speed covering a portion of the upper surface. RANS and URANS simulations were used for the investigation, and the control was simulated by assigning a tangential velocity to a portion of the surface. Several configuration were tested, and the results showed that locating the surface underneath the shock was beneficial with respect to upstream or downstream positions. Moreover, the longer the control strip and higher the velocity (oriented with the free stream), the more efficient the control. Unsteady simulations confirmed that the method did not lead to penalties in terms of lift at pre-onset conditions and almost suppressed the SIO at buffet conditions. A full overview on the aerodynamic performance (in terms of drag and pitching moment, e.g.) was not provided.

Voevodin *et al.* [277] adopted a combination of boundary layer suction and trailing edge jets for buffet reduction. They carried out computational and experimental work to assess the flow features with respect to the wind tunnel presence on an $AR = 3$, unswept wing, based on the P-184-15 section. A sketch of the control model is shown in Figure 2.80. The CFD computations took into account the wind tunnel geometry by using a Darcy's condition in correspondence of the perforated walls used in the experiments. A comparison with the results on an unconfined configuration showed the presence of sidewall separation. Also mushroom-shaped structures were observed during buffet, similarly to past works [126, 223, 253]. The activation of flow control brought benefits in terms of lift increase and shock stabilisation. In that case, the 3D structures arising around the centreplane were stabilised.

The impact of wavy leading edge was investigated for laminar buffet by Degregori and Kim [60]

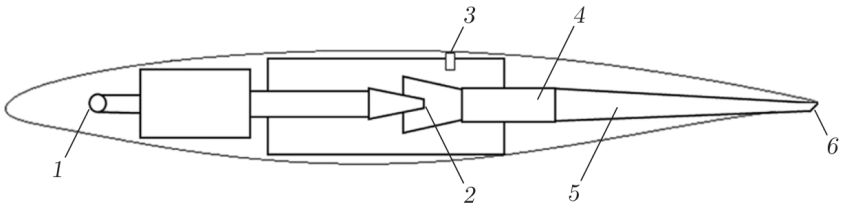

Figure 2.80: Sketch of the wing model. 1: high-pressure inlet chamber; 2: ejector nozzle; 3: suction slot; 4: mixing chamber; 5: outlet diffuser; 6: diffuser nozzle. Figure from [277].

by using Implicit Large Eddy Simulation (ILES) around the V2C aerofoil. The modified design helped improve the aerodynamic efficiency and alleviated, if not suppress, transonic buffet. In particular, the flow distortion at the aerofoil trailing edge resulted in vortices which **(i)** enhanced boundary layer transition, **(ii)** making the boundary layer more resistant to separation. The appearance of a breathing laminar separation bubble at the leading edge trough was responsible for the vortex generation, which introduced a high frequency contribution, in addition to the low frequency associated with large shock oscillations. This latter was also attenuated. Figure 2.81 shows

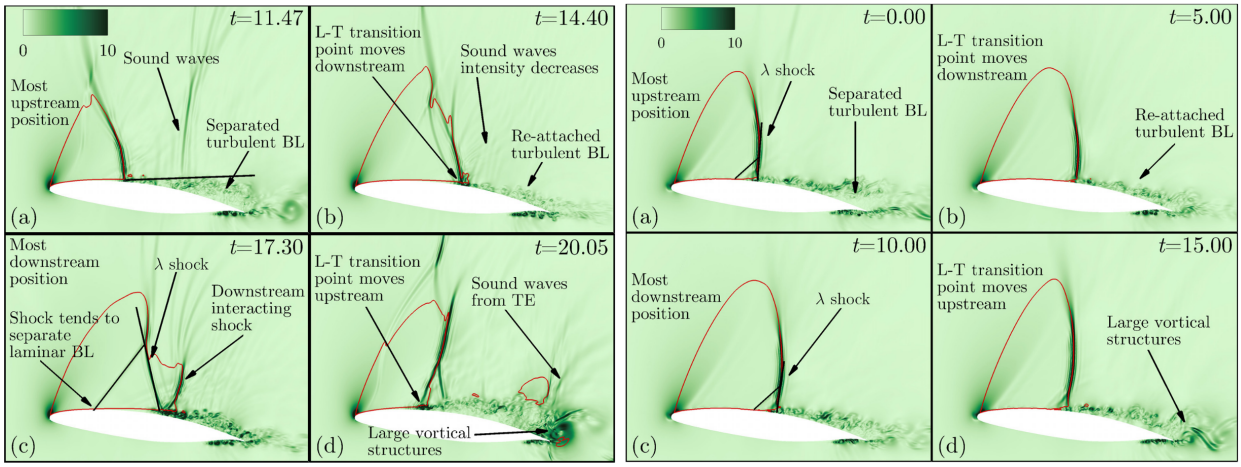

Figure 2.81: Density gradient magnitude over for different buffet period phases for the controlled (left) and uncontrolled (right) case for the flow around the V2C aerofoil. Figure from [60].

the evolution of buffet for the original (left) and modified (right) configurations. In the former, the shock exhibited large oscillations, and the lambda structure strongly varied in size over a period. The modified configuration showed similarities with turbulent transonic buffet cases. The influence of the wave amplitude, by comparing three values, was also investigated. In general, a smaller amplitude gave better results, targeting both an increase in the aerodynamic efficiency, and a drop in the loads variation. A mid-value allowed for a complete suppression of buffet. Whether this design can help control turbulent buffet is still unclear. By adopting this design, some benefits of having flow laminarity would be lost. Therefore, it could be optimal to apply such a shape modification in an active way.

Recently Gao *et al.* [85] investigated the structural parameters, with the aim to alleviate buffet on a NACA0012 aerofoil with activated elasticity. They built a ROM, verified with CFD/CSD calculations, to study the stability of the system by looking at the loci of the system eigenvalues. It was demonstrated by Gao *et al.* [88] that in absence of damping, the activation of the structural degree of freedom lowered the onset angle with respect to purely aerodynamic cases. By using a good combination of damping ratio, mass ratio, and structural frequency, it was possible to force the coupling of the structural and fluid modes to be on the stable semi-plane of the complex plane. It was found that, for the analysed configuration, the stiffness must be between 0.1 and 0.5, while the mass ratio should not exceed 600. By adopting a mass-damping parameter of 20-60, it was possible to stabilise the system. Figure 2.82 shows the stable areas as functions of the structural parameters.

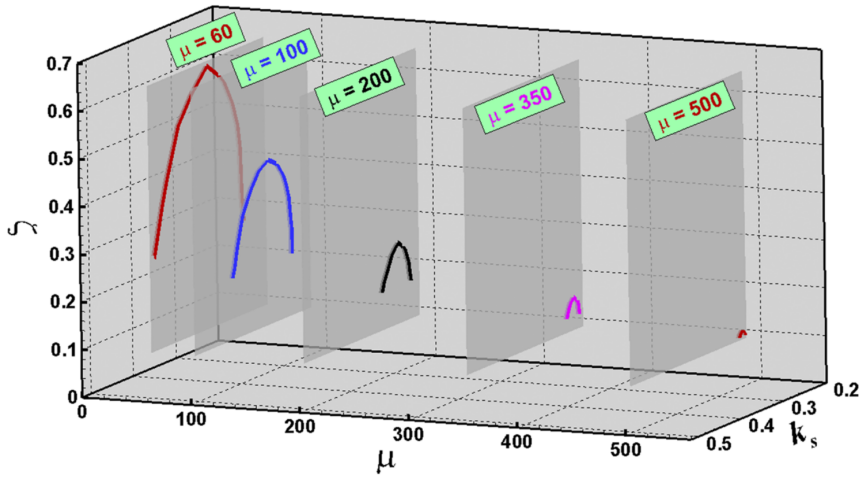

Figure 2.82: Stable areas as functions of the structural parameters. Each plane represents a fixed value of the mass ratio. On any plane, a line separates stable and unstable regions, depending on the combination of structural frequency and damping. Figure from [85].

2.3.5 Summary and Conclusions

In this section, the literature on transonic buffet flow control was reviewed. As hinted in the review paper of Jana and Kaushik [128], all of the conventional strategies present benefits and drawbacks. In this section, VGs, SCBs, and TEDs were distinguished, as they are the most discussed in the literature. Along with them, some alternatives were also proposed.

VGs were effective in suppressing buffet by promoting turbulence in the boundary layer. Enhanced levels of turbulence made the boundary layer more resistant to separation, and therefore delayed the occurrence of buffet. On the other hand, the well known drawbacks of VGs is their installation drag. To overcome this side effect, both AJVGs and plasma jets can be used. Their ability to suppress buffet is strongly related to their design and operating parameters, i.e. inflow mass rate

and frequency, respectively. Moreover, AJVGs consume extra energy and need pressurised air from the engine, reducing the engine efficiency. Plasma actuators present the problem of implementation of high frequency pulsed jets, which are energy demanding.

SCBs act differently from VGs. Their presence under the shock aims at a smearing it by forming a lambda structure, and thereby reducing the pressure losses across the SBLI. The application of SCBs revealed beneficial for buffet cases. The presence of SCBs in the separated boundary layer can hamper the merging of the separated flow regions at the shock foot, and the TE. Their performance was strongly related to the position of the devices on the wing, their size, and shape. Therefore, several studies investigated the best configuration for buffet alleviation and lift-to-drag improvement. The main drawback of SCBs is the strong off-design penalties obtained. The work of optmisation should therefore account for different design conditions, i.e. cruise and buffet at least, quite different between each other. Even there, the SCBs might still deteriorate the aircraft performance in flight phases like take-off and landing. Therefore, the popularity of active control by means of SCBs has increased over the last years. Always more complicated and, apparently effective, control laws were developed to guarantee a beneficial effect of SCBs at several flight conditions. The complexity of implementation of active SCBs would be the main issue with their presence on civil airplanes in the next future.

TEDs act on the aerofoil/wing TE to modify the effective sectional shape by inducing local flow separation. Gurney flaps reduce the buffet onset angle of attack. UTEFs give the completely opposite effect. Therefore, the adoption of active devices was proposed by some of the authors. Because of the orientation with respect to the flow direction, UTEFs might result in structural failure when undergoing high loads. Serrated configurations, on the other hand, did not give the same performance of the plain ones (see, e.g., [52]).

Flaps and slats were also adopted in some works. These devices might be used dynamically to stabilise the shock. Nevertheless, the adoption of slotted configurations on commercial airplanes is in contrast with the studies available in the literature, which account for dynamic changes in the flap deflection angle.

Other collected works fall into the categories of tangential jets, micro-tabs, and combination of the aforementioned devices. These present similar pros and cons as other methods. An interesting concept is that of wavy leading edges to enhance turbulence. Nevertheless, the application in conjunction with laminar aerofoils seems to cancel out the benefits of having a laminar configuration. In this view, such a drastic aerofoil modification should be applied under the form of active control.

Several authors underlined the possibility of frequency lock-in between the shock and the control frequency, thus suggesting that sinusoidal, fixed-amplitude, control might not always be beneficial for buffet alleviation. The combination of control amplitude and delay between the control and the targeted load history, strongly impact the control performance. Therefore, more accurate and robust control laws must be sought before application on actual airplanes.

Chapter 3

Governing Equations and CFD Methods

For this work, numerical simulations were conducted using the Helicopter Multi-Block (HMB3) CFD Solver [248, 249] of the University of Glasgow. The methods used for this work are detailed and discussed here. In particular, after introducing the governing flow equations and the adopted discretisation in HMB3, the PANS equations are presented. The implementation in the CFD solver is then detailed. Other CFD methods used in this thesis, i.e. the harmonic balance method, the adjoint method, and the virtual surface method, are also presented in this chapter. Details are especially provided for the contribution of the thesis to the HMB3 solver in Section 3.4, Section 3.6, and Section 3.7.

3.1 CFD Solver

Helicopter Multi-Block (HMB3) [248,249] is a three-dimensional, fully implicit, structured, multi-block solver for the Navier-Stokes equations. The Navier-Stokes equations were discretised using a cell-centered finite volume approach. The computational domain was divided into a finite number of non-overlapping control volumes, and the governing equations were applied to each cell in turn. Also, the flow equations were re-written in a curvilinear co-ordinate system which simplified the formulation of the discretised terms since body-conforming grids were adopted here. The solver is mainly used to run URANS computations with a several one-, two-, three-, and four equation models. The LES, DES, DDES, IDDES, SAS, and PANS methods are also available.

3.1.1 Navier-Stokes Equations

The Navier-Stokes equation, consisting of conservation of mass, momentum and energy, in their compressible formulation are solved using CFD. They are expression of continuity, of Newton's

2nd Law, and of the 1st principle of thermodynamics. In tensor form, they read:

$$\begin{aligned}
&\frac{\partial \rho}{\partial t} + \frac{\partial}{\partial x_i}(\rho u_i) = 0\,, \\
&\frac{\partial \rho u_i}{\partial t} + \frac{\partial}{\partial x_j}\left(\rho u_i u_j\right) = \rho f_i - \frac{\partial p}{\partial x_i} + \frac{\partial \tau_{ij}}{\partial x_j}\,, \\
&\frac{\partial \rho E}{\partial t} + \frac{\partial}{\partial x_j}\left[u_j(\rho E + p)\right] = \frac{\partial}{\partial x_j}\left(u_i \tau_{ij} - q_j\right)\,.
\end{aligned} \tag{3.1}$$

In the continuity equation, ρ is the density, u_i is the velocity field, and t is time. The momentum equations introduces the pressure p, body forces f_i, and the viscous stress tensor τ_{ij}. In the energy equation, E is the total energy per unit mass, and q_j is the heat flux vector. The total energy per mass unit $E = e + u_i u_j/2$ is the summation of internal energy per unit mass e and kinetic energy per unit mass. For Newtonian fluids, under the assumption of Stokes' hypothesis, the viscous stress tensor is written as:

$$\tau_{ij} = \mu\left[\left(\frac{\partial u_i}{\partial x_j} + \frac{\partial u_j}{\partial x_i}\right) - \frac{2}{3}\delta_{ij}\frac{\partial u_k}{\partial x_k}\right]\,, \tag{3.2}$$

where μ is the molecular dynamic viscosity and δ_{ij} is the Kronecker delta. The molecular viscosity is evaluated trough the Sutherland Law:

$$\mu = \mu_0\left(\frac{T}{T_0}\right)^{3/2}\frac{T_0 + T_S}{T + T_S} \tag{3.3}$$

where μ_0 is a reference viscosity at the reference value T_0, while T_S is the Sutherland's temperature. Throughout the following investigation, the adopted values are $\mu_0 = 1.7894 \times 10^{-5}\mathrm{kg}/(\mathrm{m\ s})$, $T_0 = 288.16\mathrm{K}$ and $T_S = 110.4\mathrm{K}$. In the energy equation, the heat flux vector is computed using Fourier's Law for thermal conduction:

$$q_j = -k_h\frac{\partial T}{\partial x_j}\,, \tag{3.4}$$

where k_h is the heat transfer coefficient. Alternatively, the laminar Prandtl number Pr can be used to recast the equation, that now reads:

$$q_j = -\frac{c_p \mu}{\mathrm{Pr}}\frac{\partial T}{\partial x_j}\,. \tag{3.5}$$

c_p is the heat capacity at constant pressure. Under the assumption of ideal gas, the state equation links pressure and density and is used to close the system of equations:

$$p = \rho R_{air} T\,, \tag{3.6}$$

where the ideal gas constant for air is $R_{air} = 287.058\ \mathrm{J}/(\mathrm{kg\ K})$.

In HMB3, the equation are recast in non-dimensional form by means of a rescaling procedure based on reference values for length L_{ref}, density ρ_{ref}, velocity U_{ref}, and temperature T_{ref}. The dimensional-to-nondimensional rescaling is performed by means of the following relations:

$$x = \frac{x^*}{L_{ref}} \quad \rho = \frac{\rho^*}{\rho_{ref}} \quad u = \frac{u^*}{U_{ref}} \quad T = \frac{T}{T_{ref}}$$
$$t = \frac{t^*}{L_{ref}/U_{ref}} \quad p = \frac{p^*}{\rho_{ref}U_{ref}^2} \quad \mu = \frac{\mu^*}{\mu_{ref}} \quad E = \frac{E}{U_{ref}} \tag{3.7}$$

3.1.2 Vector Form of Governing Equations

In the conservative form of the governing equations, the continuity, energy, and momentum equations are presented by the same generic equation. This helps simplify the implementation in a computer program. The vector of conserved variables **W** reads:

$$\mathbf{W} = \begin{pmatrix} \rho \\ \rho u \\ \rho v \\ \rho w \\ \rho E \end{pmatrix}, \tag{3.8}$$

and gathers the conserved variables of the Navier-Stokes equations written in the previous section. The vector form of the conservation laws in Cartesian coordinates reads:

$$\frac{\partial \mathbf{W}}{\partial t} + \frac{\partial (\mathbf{F}^i - \mathbf{F}^v)}{\partial x} + \frac{\partial (\mathbf{G}^i - \mathbf{G}^v)}{\partial y} + \frac{\partial (\mathbf{H}^i - \mathbf{H}^v)}{\partial z} = \mathbf{S}. \tag{3.9}$$

There, i and v superscripts denote the inviscid and viscous component, respectively, of the flux vector **F**, **G**, and **H** in the three directions x, y, and z. **S** is the source term, that for the reminder of this work will be assumed equal to zero. The convective (inviscid) fluxes are written as:

$$\mathbf{F}^i = \begin{pmatrix} \rho u \\ \rho u^2 + p \\ \rho uv \\ \rho uw \\ \rho uH \end{pmatrix} \quad \mathbf{G}^i = \begin{pmatrix} \rho v \\ \rho vu \\ \rho v^2 + p \\ \rho vw \\ \rho vH \end{pmatrix} \quad \mathbf{H}^i = \begin{pmatrix} \rho w \\ \rho wu \\ \rho wv \\ \rho w^2 + p \\ \rho wH \end{pmatrix}, \tag{3.10}$$

where $H = E + p/\rho$ is the total enthalpy. The viscous fluxes are:

$$\mathbf{F}^v = \frac{1}{\mathrm{Re}} \begin{pmatrix} 0 \\ \tau_{xx} \\ \tau_{xy} \\ \tau_{xz} \\ u\tau_{xx} + v\tau_{xy} + w\tau_{xz} + q_x \end{pmatrix}$$

$$\mathbf{G}^v = \frac{1}{\mathrm{Re}} \begin{pmatrix} 0 \\ \tau_{xy} \\ \tau_{yy} \\ \tau_{yz} \\ u\tau_{xy} + v\tau_{yy} + w\tau_{yz} + q_y \end{pmatrix}$$

$$\mathbf{H}^v = \frac{1}{\mathrm{Re}} \begin{pmatrix} 0 \\ \tau_{xz} \\ \tau_{yz} \\ \tau_{zz} \\ u\tau_{xz} + v\tau_{yz} + w\tau_{zz} + q_z \end{pmatrix}, \tag{3.11}$$

where $\mathrm{Re} = \rho_{ref} U_{ref} L_{ref} / \mu_{ref}$ is the Reynolds number.

3.1.3 Spatial Discretisation

The governing equations in Section 3.1.2 are discretised using the Arbitrary Lagrangian-Eulerian (ALE) formulation for time-dependent domains with moving boundaries. The equations read:

$$\frac{d}{dt}\int_{V(t)} \mathbf{W} dV + \int_{\partial V(t)} \left(\mathbf{F}^i - \mathbf{F}^v, \mathbf{G}^i - \mathbf{G}^v, \mathbf{H}^i - \mathbf{H}^v\right) \cdot \mathbf{n} dS = \int_{V(t)} \mathbf{S} dV\,, \tag{3.12}$$

where $V(t)$ and $\partial V(t)$ are the time-dependent control volume and its boundary, respectively, while $\mathbf{n}$ is the outer normal to the volume boundary. The fluxes include the effect of a time-dependent domain, i.e. a mesh velocity is included in the velocity components. The Navier-Stokes equations are discretised using a cell-centred finite volume approach. The spatial discretisation of the equations leads to a set of ordinary differential equations in time,

$$\frac{d}{dt}(\mathbf{W}_{ijk} V_{ijk}) = -\mathbf{R}_{ijk}(\mathbf{W}_{ijk}), \tag{3.13}$$

where $\mathbf{W}$ and $\mathbf{R}$ are the vectors of cell conserved variables and residuals, respectively. The convective terms are discretised using the Osher's upwind scheme [200]. Monotone Upstream-centered Scheme for Conservation Laws (MUSCL) variable extrapolation [273] is used to provide second-

order accuracy with the Van Albada limiter [272] to prevent spurious oscillations around shock waves. Viscous terms are discretised using central differences. In each block, boundary conditions are imposed by means of ghost cells.

3.1.4 Steady State Solution Method

For steady-state problems, the time derivative in Equation (3.13) is identically zero. Nevertheless, the popular pseudo-time integration method is used in HMB3. Therefore, the integration in time of Equation (3.13) to a steady-state solution is performed using an implicit time-marching scheme by:

$$\frac{\mathbf{W}_{ijk}^{n+1} - \mathbf{W}_{ijk}^{n}}{\Delta t} = -\frac{1}{V_{i,j,k}} \mathbf{R}_{ijk}\left(\mathbf{W}_{ijk}^{n+1}\right), \tag{3.14}$$

where $n+1$ denotes the time $(n+1) * \Delta t$. Equation (3.14) represents a set of non-linear algebraic equations and to simplify the solution procedure, the flux residual $\mathbf{R}_{ijk}\left(\mathbf{Wi}_{ijk}^{n+1}\right)$ is linearised in time as follows:

$$\begin{aligned}
\mathbf{R}_{ijk}\left(\mathbf{W}^{n+1}\right) &= \mathbf{R}_{ijk}^{n}\left(\mathbf{W}^{n}\right) + \frac{\partial \mathbf{R}_{ijk}}{\partial t}\Delta t + O(\Delta t^2) \\
&\simeq \mathbf{R}_{ijk}^{n}\left(\mathbf{W}^{n}\right) + \frac{\partial \mathbf{R}_{ijk}}{\partial \mathbf{W}_{ijk}}\frac{\partial \mathbf{W}_{ijk}}{\partial t}\Delta t \\
&\simeq \mathbf{R}_{ijk}^{n}\left(\mathbf{W}^{n}\right) + \frac{\partial \mathbf{R}_{ijk}}{\partial \mathbf{W}_{ijk}}\Delta \mathbf{W}_{ijk},
\end{aligned} \tag{3.15}$$

where $\Delta \mathbf{W}_{ijk} = \mathbf{W}_{ijk}^{n+1} - \mathbf{W}_{ijk}^{n}$. Equation (3.14) now becomes the following linear system

$$\left[\frac{V_{ijk}}{\Delta t}\mathbf{I} + \frac{\partial \mathbf{R}_{ijk}}{\partial \mathbf{W}_{ijk}}\right]\Delta \mathbf{W}_{ijk} = -\mathbf{R}_{ijk}^{n}\left(\mathbf{W}^{\mathbf{n}}\right). \tag{3.16}$$

The linearised system of equations is solved using the Generalised Conjugate Gradient (GCG) method with a Block Incomplete Lower-Upper (BILU) factorisation as a pre-conditioner [11]. The Jacobian is approximated by evaluating the derivatives of the residuals with a first-order scheme for the inviscid fluxes. The first-order Jacobian requires less storage and ensures a better convergence rate to the GCG iterations. The steady-state solver for turbulent flows is formulated and solved in an identical manner to that of the mean flow. The eddy viscosity is calculated from the latest values of the turbulent variables, e.g. k and ω, and is used to advance the mean and the turbulent flow solutions. An approximate Jacobian is used for the source term of the models by only taking into account the contribution of their dissipation terms, i.e. no account of the production terms is taken on the left-hand side of the system.

3.1.5 Unsteady Solution Method

The implicit dual-time stepping method of Jameson [127] is used for time-accurate calculations. The method is implicit and allows for solving the implicit equations at each real time step using inner iterations in the pseudo time, as described in the previous section. To allow for the same steady solver to be re-used, the residual is redefined to obtain a steady-state equation which can be solved using acceleration techniques. The residual is first modified following a three-level discretisation $(n-1, n, n+1)$ of the conserved variables time derivative:

$$\mathbf{R}^* = V\frac{3\mathbf{W}^{n+1} - 4\mathbf{W}^n + \mathbf{W}^{n-1}}{2\Delta t} + \mathbf{R}(\mathbf{W}^{n+1}). \tag{3.17}$$

The equations are then recast after the introduction of the pseudo-time τ, as for the steady-state solver:

$$\frac{\mathbf{W}^{n+1,m+1} - \mathbf{W}^{n-1,m}}{\Delta\tau} = -\frac{1}{V}\mathbf{R}^*(\mathbf{W}^{n+1,m+1}), \tag{3.18}$$

where m refers to the m-th inner iteration of the implicit integration in pseudo time. The solution of the non-linear system follows is obtained in the same way as for the steady-state problem.

3.2 Turbulence modelling and Simulation Strategies

The main issue with flow simulations at high Reynolds number is the modelling and characterisation of turbulence. Generally speaking, turbulence can be defined as a fluid regime where viscous effects are not strong enough to compensate the inertial effects. This induces a chaotic motion in which streamlines are strongly deflected, and flow scales mix. More rigorously, turbulence is a condition under which different realisations of the same random process, with slight differences on the initial conditions, result in big differences after a certain time. Turbulent flows are strongly unsteady, three-dimensional, and show large gradients in all of the quantities. Energy exchange between scales takes place and involves a great variety of length scales, up to the Kolmogorov scale, where the energy dissipation occurs. A flow is turbulent when the Reynolds number:

$$\mathrm{Re} = \frac{\text{inertial effects}}{\text{viscous effects}} = \frac{\rho U L}{\mu}, \tag{3.19}$$

exceeds some case-dependent value. In Equation (3.19), ρ is the density, U is the flow velocity, L is a reference length, and μ is the dynamic viscosity.

This section gives an overview of the available CFD simulation strategies. As already mentioned, dealing with turbulence brings additional challenges in computational and numerical modelling. The equations to be solved, the Navier-Stokes equations (Equation (3.1)), are a set of Partial Differential Equation (PDE) describing the motion of viscous flows through the conservation of

mass, momentum, and energy, and must be solved for the flow quantities, to obtain their temporal evolution.

Direct numerical simulations (DNS) consists of resolving all scales of motion up to the Kolmogorov scale:

$$\eta = \left(\nu^3/\varepsilon\right)^{1/4}, \tag{3.20}$$

where turbulent kinetic energy is dissipated into thermal energy. In Equation (3.20), ε is the turbulent kinetic energy dissipation, and ν is the kinematic viscosity. Alongside the Kolmogorov length scale, a time scale and a velocity scale are defined, respectively, as:

$$\tau_\eta = \left(\nu/\varepsilon\right)^{1/2}, \quad u_\eta = \left(\nu\varepsilon\right)^{1/4}. \tag{3.21}$$

The ratios between the integral (spatial L, and temporal T) and Kolmogorov micro-scales can be related to the large scale Reynolds number and read:

$$\frac{L}{\eta} \simeq \left(\frac{UL}{\nu}\right)^{3/4} = \mathrm{Re}^{3/4}, \quad \frac{T}{\tau_\eta} \simeq \left(\frac{UL}{\nu}\right)^{1/2} = \mathrm{Re}^{1/2}. \tag{3.22}$$

Therefore, the size of the spatio-temporal grid can be written as a function of the Reynolds number through $N \simeq Re^{11/4}$. At high Reynolds numbers, DNS computations become prohibitive even for the most powerful machines. In absence of the technology to solve DNS (if not for canonical flows at low Reynolds), a great effort was devoted to the development of models to reduce the CPU costs associated with CFD of turbulence flows. The sketch in Figure 3.1 is an overview of the available simulation strategies based on the portion of the resolved turbulent spectrum. All of them will be introduced and described in the following sections.

3.2.1 Reynolds-Average Navier-Stokes Equations

To overcome the CPU drawback, Osborne Reynolds in 1897 proposed a decomposition of every instantaneous function $\phi(\mathbf{x},t)$ into its ensemble average part $\langle\phi(\mathbf{x})\rangle$, defined as:

$$\langle\phi(\mathbf{x})\rangle = \lim_{N\to\infty} \frac{1}{N} \sum_{j=1}^{N} \phi_j(\mathbf{x},t), \tag{3.23}$$

and a fluctuation part $\phi'(\mathbf{x},t) = \phi(\mathbf{x},t) - \langle\phi(\mathbf{x})\rangle$. For steady flows, under the ergodicity assumption, the ensemble average, i.e. the average over the sample space, can be replaced by time average [40], reading:

$$\overline{\phi}(\mathbf{x}) = \lim_{T\to\infty} \frac{1}{T} \int_t^{t+T} \phi(\mathbf{x},t)\, dt. \tag{3.24}$$

Taking the average of the Navier-Stokes equation, the RANS equations are found. Tackling

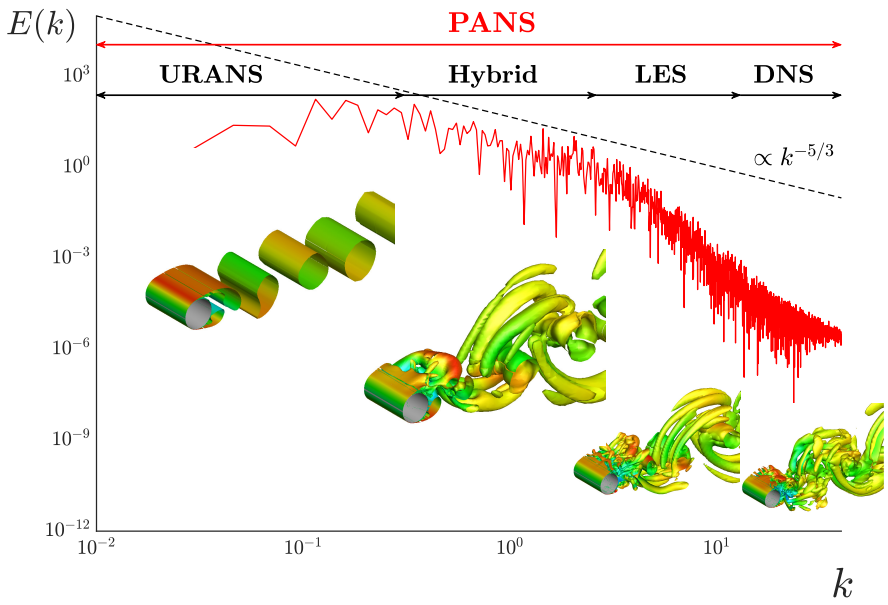

Figure 3.1: Example of turbulence spectrum. At the top, the portion of the spectrum solved by each approach is indicated.

turbulence solving the RANS equation has been the most used approach, since they only account for the average quantities, and the cost for solving this set of equation is reduced. Clearly, the advantage in terms of cost is balanced by the lack of information on the smaller scales of turbulence. On the other hand, from the averaging operation, several terms involving the averages of fluctuations arise, cannot be neglected, and must be modelled. Among them, the Reynolds stress tensor $\tau_{ij}^{R} = -\rho\overline{u_i' u_j'}$ is of critical importance. It represents the effect of the turbulence fluctuations on the main field and appears in both momentum and energy equations. It is around the modelling of the Reynolds stress tensor that the attention of CFD scientists focused in the last decades of the past century. Among the proposed models, we list algebraic models (e.g. Baldwin-Lomax [14] and Cebeci-Smith [237]), eddy viscosity models (the $k-\varepsilon$ [131], the $k-\omega$ [279], the Menter SST [182], and the SA [241], among others), and Reynolds stress models, that solve transport equations for the six components of the Reynolds stress tensor.

By accounting for the temporal derivatives in the RANS equations, URANS simulations can be carried out. Due to their dissipative nature, only large instabilities occurring at relatively low frequencies can be resolved by URANS. This is beneficial for highly unsteady problems on complex configurations. Nevertheless, the prediction of some classes of flows with RANS simulations is not always accurate. Examples of this are flows involving separation, where the extent of the separated region is almost always mispredicted and strongly dependent on the adopted turbulence model. Flows with SBLI are also renowned for being difficult to predict using RANS.

3.2.2 Large Eddy Simulations (LES)

As the computational resources have grown, an intermediate approach in terms of resolution and costs, called LES, has become popular in the context of numerical simulation of turbulence. LES are performed on grids fine enough to resolve the majority of the scales, containing the 80% or more of the flow field energy content [214], and model the smaller scales. The filtering operation of an instantaneous quantity $\phi(\mathbf{x},t)$, reading:

$$\overline{\phi}(\mathbf{x},t) = \int_{\mathbb{R}^3} G(\mathbf{x}-\xi,\Delta(\mathbf{x}))\,\phi(\xi,t)\,d\xi\,, \tag{3.25}$$

leads to a decomposition similar to the Reynolds one, where the filtered quantity is now time dependent, and the fluctuating part is called Sub-Grid Scale (SGS) part. It has to be pointed out that the G is a filter function of the grid spacing Δ, i.e. the physical accuracy of the flow field is governed by the numerical resolution. In the spectral space, the cut-off wavenumber can be related to the grid spacing through $\kappa_c \simeq \pi/\Delta$, meaning that the spatial filtering results in a spectral truncation. LES models the small scales of the energy spectrum and resolves explicitly the larger ones. Also in this case, the filtering operation applied to the equation leads to the birth of the SGS tensor, that is the equivalent of the Reynolds stress tensor for LES. Like in the RANS context, the SGS tensor can be modelled through the eddy viscosity assumption - the Smagorinsky model [235] is iconic - or other methods (see [214]).

Boris *et al.* [29] were the first to see the potential of the finite volume discretisation as a built-in filter of the finite volume method to replace the SGS terms. In the work of Fureby and Grinstein [81] it is pointed out that while LES are obtained from successive filtering and cell averaging, ILES are obtained from cell averaging only, that acts as a built-in filter with top-hat kernel:

$$\Phi_{P,LES} = \frac{1}{\delta V_P}\int_{\Omega_P}(\Phi * G)\,dV\,, \quad \Phi_{P,ILES} = \frac{1}{\delta V_P}\int_{\Omega_P}\Phi\,dV\,, \tag{3.26}$$

where Φ is an arbitrary quantity, G is the filter and P is the index associated with the cell. However, in practical LES implementations, the pre-filtering has no explicit effect on the variables that are solved for. Indeed, the filtering operation is only performed when deriving the LES equations, which are then to be discretised. For ILES, the discretisation of the convective terms leads to SGS-like terms, which replace the SGS tensor that is derived when formulating the LES equations. By selecting appropriate numerical schemes, it is possible to neglect the SGS terms. It follows that ILES are extremely sensitive to the choice of the numerical schemes and the adopted grid (see, e.g., [141]). Usually, high-order schemes are used in smooth-flow regions, while low-order, dissipative schemes are adopted in regions with steep gradients (shock, discontinuities) [168], ensuring sufficient energy dissipation.

Although significant CPU cost reduction can be achieved with respect to standard LES [90,275],

the costs are still prohibitive for large industrial applications. If several flow conditions are targeted, LES are still too expensive even for simple cases. The reader is referred to the works of Uzun and Malik [271], Dandois *et al.* [56], Zauner *et al.* [285,286], and Moise *et al.* [188,189], which give an order of magnitude of the computer power required for cases at similar flow conditions of those of interest in this work.

3.2.3 Hybrid RANS-LES Methods

In the following, some hybrid RANS/LES models will be presented. The aim of the strategies proposed is that of combining the advantages of the two approaches, alternating the calculation in RANS-mode and LES-mode to obtain a compromise in terms of flow characterisation and CPU costs.

3.2.3.1 Detached Eddy Simulations (DES)

The detached eddy simulation (DES) approach was introduced to take advantage of the strengths of RANS and LES approaches in different flow regions. Modelling the boundary layer using LES can be easily turned into expensive computations, especially at high Reynolds number. The use of RANS allows to circumvent the grid issue in the boundary layer. On the other hand, RANS are not able to correctly predict separated flow and resolve turbulent structures, where LES perform well. In 1997, Spalart *et al.* [243] introduced the first version of DES (DES97), that is a three-dimensional unsteady numerical solution using a turbulence model which functions as an SGS model in the region where the grid is fine enough for LES, and as a RANS model in regions where the grid is coarse. In the original formulation, the model was proposed in conjunction an SA model [241]. In the one-equation model, the distance to the nearest wall d_w in the destruction term was replaced by the DES length scale, defined as:

$$\tilde{l} = \min\{d_w, C_{DES}\Delta\}\,, \tag{3.27}$$

where C_{DES} is the model constant and $\Delta = \max\{\Delta_x, \Delta_y, \Delta_z\}$. In this way, the model behaves like RANS near the wall, while, in the far field, it becomes grid-dependent and acts as LES. Assuming $\Delta_x, \Delta_y, \Delta_z$ the grid spacing in the streamwise, wall-normal, and spanwise directions, a distinction can be done: near the wall, $\Delta_x \sim \Delta_z >> \Delta_y$ and $\tilde{l} = d_w$, and the model reduces to the RANS-SA; far from the wall, where $d_w >> \Delta$, $\tilde{l} = C_{DES}\Delta$ and the model acts as an SGS model.

Strelets [250] extended this approach to the SST turbulent model, widely used and accepted when dealing with wall flows, by using a length scale $l_{k-\omega} = k^{1/2}/(\beta^*\omega)$ based on the turbulent variables. The quantity $l_{k-\omega}$ will influence the destruction of turbulent kinetic energy leading to a reduction of the overall eddy viscosity.

Spalart *et al.* [242] addressed some problems of the original DES and proposed a revised method called delayed DES (DDES). The use of high aspect ratio cells in the boundary layer can lead to grid-induced separation when the DES limiter activates early in the boundary layer. In DDES, the length scale was modified as follows:

$$\tilde{d} = d - f_d \max\{0, d - C_{DES}\Delta\}, \tag{3.28}$$

where f_d is a function going to 0 for RANS mode and 1 to LES mode. This new formulation makes the DES length scale time-dependent on the turbulent viscosity, and local velocity, and allows for a delay in the switch from RANS to LES.

Later on, Shur *et al.* [232] proposed a new modification, called IDDES. It consists of a blending between the DDES and the WMLES. WMLES are intended to be used only if some incoming turbulent content is present and the grid is fine enough to solve the boundary-layer dominant eddies.

3.2.3.2 Scale Adaptive Simulation (SAS)

The SAS method presented by Menter and Egorov [183] avoids the dependency of the switch on the grid size, unlike in DES. It consists of the addition of another destruction term in the specific dissipation rate equation of the SST model. The SAS method allows to evaluate the turbulent length scale independently of the thickness of the shear layer and adapts to the resolved scales. Despite being based on a URANS paradigm, SAS allows for the formation of clear and more complex turbulent structures. The name SAS comes indeed from the ability of the method of adapting to the resolved scales. To do this the Von Karman length:

$$L_{vK} = \kappa \sqrt{\frac{2S_{ij}S_{ij}}{\frac{\partial^2 U_i}{\partial x_k^2}\frac{\partial^2 U_i}{\partial x_j^2}}}, \quad \kappa = 0.41 \tag{3.29}$$

is used, as it is a first approximation of the characteristic length of the local vortices. The method reverts to URANS in the steady parts of the domain, allowing to gain in efficiency (also with respect to DES for which the switching is governed by the grid resolution). Nevertheless, the ability to produce a realistic energy spectrum is limited to low wave numbers. To allow for the energy dumping at high wave numbers, the Von Karman length must be limited by the local grid size.

3.2.3.3 Partially-Average Navier-Stokes (PANS)

The PANS method was presented by Girimaji *et al.* [101, 102]. It is a bridging model between RANS and DNS based on an underling turbulence model. In the PANS equations, the filtering is

no longer on a numerical basis, like in LES where high wave numbers were cut off, but on a physical basis. In particular, the ratios of modelled-to-total turbulent quantities are imposed according to the parent RANS model. They read:

$$f_k = \frac{k_u}{k}, \quad f_\varepsilon = \frac{\varepsilon_u}{\varepsilon}, \quad f_\omega = \frac{\omega_u}{\omega}, \tag{3.30}$$

being k the turbulent kinetic energy, ε the turbulent kinetic energy dissipation, and ω the specific turbulent dissipation. Deriving an expression for one of the three parameters as a function of the others is trivial. Therefore, they can be used without distinction. The method was mostly used in conjunction with two-equation eddy viscosity models, namely k-ε , k-ω , and SST. The physical constraint $0 < f_k < f_\varepsilon < 1$ is imposed because k is mostly contained at the larger scales while the dissipation acts at smaller ones. For the aforementioned eddy viscosity models, an unresolved eddy viscosity is employed in line with the adopted model:

$$\mu_{t,u} = C_{\mu,u}\frac{k_u^2}{\varepsilon_u} = C_\mu \frac{f_k^2 k^2}{f_\varepsilon \varepsilon} = \frac{f_k^2}{f_\varepsilon}\mu_t\,, \tag{3.31}$$

$$\mu_{t,u} = C_{\mu,u}\frac{k_u}{\omega_u} = C_\mu \frac{f_k k}{f_\omega \omega} = \frac{f_k}{f_\omega}\mu_t\,. \tag{3.32}$$

The parameters are the energetic-based parameters regulating the filtering, since the PANS to RANS ratios of velocity, length, and time scale can be expressed as functions of f_k, f_ε, and f_ω. The closure equations are written as in the standard RANS model, as a summation of convection, dissipation, production, and transport terms, where the constraint on the unresolved-to-total ratios of k, ε, and ω has been imposed. This mainly results in changes in the model coefficients. The application to the k-ω SST model will be commented in the next chapter along with the numerical method. The original formulation was derived for the $k-\varepsilon$ [103], and the method was then extended to the $k-\omega$ model [152] and SST model [164].

In [103] some features of PANS have been underlined. The f_k parameter prescribes the flow resolution: it is the main character of the bridging model, able to smoothly switch from RANS ($f_k = 1$), to DNS ($f_k = 0$). Unitary f_k corresponds to model all the scales of turbulence and $\mu_{t,u} = \mu_t$; if the parameter is equal to zero, the unresolved eddy viscosity $\mu_{t,u}$ is equal to zero and the modelled terms disappear from the equations. The role of f_ε is strongly related to the Reynolds number. Klapwijk *et al.* [135] analysed the effect of the parameter distinguishing three approaches:

- high Reynolds approach: $f_\varepsilon = 1$. Dissipative scales are small and separated from the large energy-containing scales;
- low Reynolds approach: $f_\varepsilon \simeq f_k$. Dissipative and energy-containing scales are overlapping;
- intermediate Reynolds approach: $f_\varepsilon = a f_k$. The effect is quantitatively the same of that in

the low Reynolds approach but in a reduced measure.

They investigated the accuracy of the different approaches over a rectangular domain at low and moderate Reynolds number. Figure 3.2 shows the effect of both parameters. As f_ε decreases, the turbulent dissipation is no longer confined to small scales, hence smaller scales are suppressed. An excess of diffusion is present using the low Reynolds approach. The moderate-Reynolds approach does not present many differences with the high Reynolds one, but introduces the complication of tuning appropriately the a coefficient. The approximation $f_\varepsilon = 1$ is commonly accepted, and there is no presence of variable f_ε in the literature.

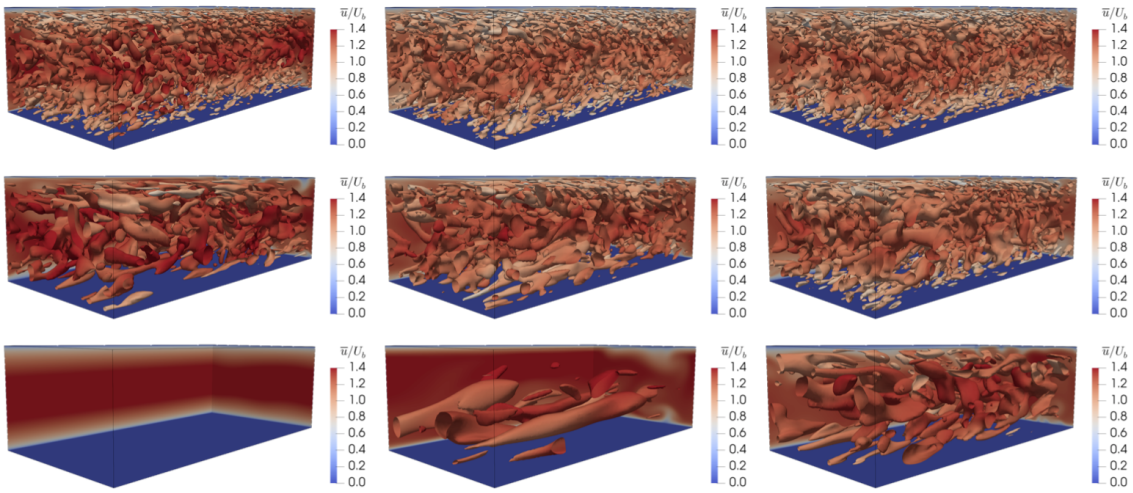

Figure 3.2: Top: high Reynolds approach; centre: moderate Reynolds approach; bottom: Low Reynolds approach. From left to right: $f_k = 0.15, 0.1$ and 0.05 [135].

The parameter f_k determines the degree of resolution of the simulation. Nevertheless, very low values of this parameter must be supported by corresponding fine grid, allowing to resolve the scales according to the potential of the simulation dictated by f_k. Alternatively, once the grid is given, the optimum value of f_k must be found to exploit the grid at its best. The role of f_k is crucial to obtain a good flow prediction and the estimates proposed will be discussed alongside the numerical method in Section 3.4.

3.2.3.4 Organised Eddy Simulation (OES)

In the work of Bourguet *et al.* [30], a different concept, based on previous experimental findings, has been expressed. By knowing that some structures are highly energetic and are located at specific frequencies, it is possible to apply a spectral decomposition that aims at resolving such coherent structures and modelling the remaining spectral contents. A sketch is provided in Figure 3.3. The splitting of the spectrum in time leads to phase-averaged Navier-Stokes equations. The flow quantities decomposition consists of a steady component, a periodic fluctuation, and a

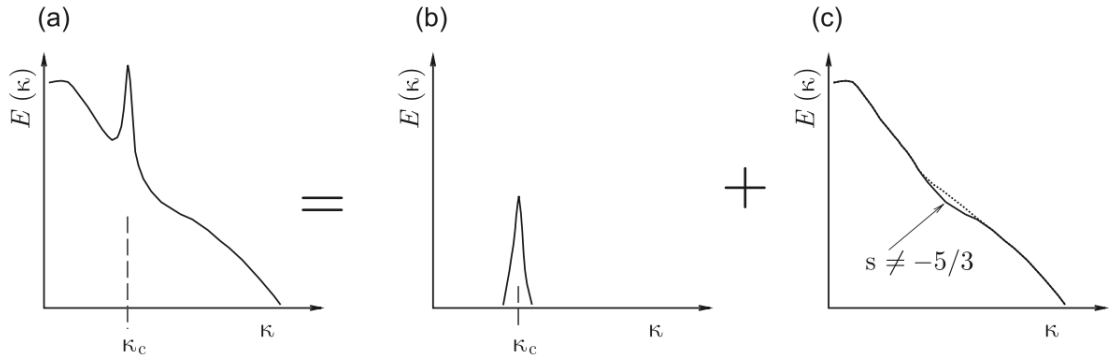

Figure 3.3: OES energy spectrum decomposition proposed in [30].

random component. Nevertheless, not many details are provided about the averaging and the implementation of the method. The method has a good intuition at the basis and could be linked to the experimental findings to isolate the frequencies of the shock motion and the vortex shedding (as an example), and solve the corresponding structures. Still, it seems that an *a priori* knowledge of the phenomenon is required or that some inceptive study must be carried out before.

3.3 RANS Formulation

As anticipated in Section 3.2, the direct solution of Equation (3.1) is computationally unaffordable for modern computers at Reynolds numbers typical for aeronautical applications ($\geq 10^6$). The most common approach is to solve the RANS equations. Turbulence is filtered by means of time averaging (see. Equation (3.24)), and each quantity is represented as the sum of a mean $\overline{(\cdot)}$ and a fluctuating component $(\cdot)'$, in the so-called Reynolds decomposition:

$$\phi = \overline{\phi} + \phi' . \tag{3.33}$$

For compressible flows, where the density shows large variations, a density-weighted averages (Favre average) is introduced to avoid fluctuations between density and other variables. The Favre average reads:

$$\widetilde{\phi} = \overline{\rho\phi}/\overline{\rho} , \tag{3.34}$$

where $\widetilde{(\cdot)}$ denotes the averaged quantity and $(\cdot)''$ indicates the corresponding fluctuating part.

By applying Favre averaging to Equation (3.1), the RANS equations are obtained:

$$
\begin{aligned}
\frac{\partial \overline{\rho}}{\partial t} + \frac{\partial \left(\overline{\rho}\widetilde{u}_i\right)}{\partial x_i} &= 0\,, \\
\frac{\partial \overline{\rho}\widetilde{u}_i}{\partial t} + \frac{\partial \left(\overline{\rho}\widetilde{u}_i\widetilde{u}_j\right)}{\partial x_j} &= -\frac{\partial \overline{p}}{\partial x_i} - \frac{\partial \left(\boxed{\overline{\rho u_i'' u_j''}} + \overline{\tau_{ij}}\right)}{\partial x_j}\,, \\
\frac{\partial \overline{\rho}\widetilde{E}}{\partial t} + \frac{\partial \left[u_j\left(\overline{\rho}\widetilde{E} + \overline{p}\right)\right]}{\partial x_j} &= -\frac{\partial \left(\boxed{c_p\overline{\rho u_j'' T''}} - \widetilde{u}_i\boxed{\overline{\rho u_i'' u_j''}} + \boxed{\frac{1}{2}\overline{\rho u_i'' u_i'' u_j''}} + \overline{q}_j\right)}{\partial x_j} \\
&\quad + \frac{\partial \left(\boxed{\overline{u_i'' \tau_{ij}}} + \widetilde{u}_i\overline{\tau_{ij}''}\right)}{\partial x_j}\,,
\end{aligned}
\tag{3.35}
$$

The four extra terms arising from the averaging process (boxed in Equation (3.35)), are:

- the Reynolds stress tensor $\tau_{ij}^R = -\overline{\rho u_i'' u_j''}$ represents the contribution of the velocity fluctuations to the mean flow equations. The modelling of the Reynolds stresses is the crucial problem of turbulence modelling. Several approaches were proposed in the last decades, consisting of algebraic models, one-, two- equation models and Reynolds stress models. The next section is devoted to the turbulence model adopted in this work;

- the turbulent heat flux $c_p\overline{\rho u_j'' T''}$. This term is modelled by means of a Reynolds analogy by writing it like the heat flux vector in Equation (3.5), where a turbulent Prandtl number: $\mathrm{Pr}_t = c_p\mu_t/k_h$ is now adopted:

$$
c_p\overline{\rho u_j'' T''} \simeq -\frac{c_p\widetilde{\mu}_t}{\mathrm{Pr}_t}\frac{\partial \widetilde{T}}{\partial x_j}\,. \tag{3.36}
$$

  The turbulent Prandtl number is often taken to be constant, and the common value of 0.9 was adopted in this work;

- the molecular diffusion $\overline{u_i'' \tau_{ij}}$ and the turbulent transport $\frac{1}{2}\overline{\rho u_i'' u_i'' u_j''}$ must also be modelled.

3.3.1 The k-ω SST Turbulence Model

As introduced in Section 3.2, the biggest challenge in turbulence modelling is to find an adequate formulation for estimating the Reynolds stress tensor. Several formulations are available in the literature. In this work, the Menter SST model [182] is used for its good performance for adverse pressure gradient flows. Most of the proposed models relied on the Boussinesq assumption, stating

the similarity between the Reynolds stress tensor τ^R and the viscous one τ:

$$\begin{aligned} \tau_{ij} &= 2\mu S_{ij} - \frac{2}{3}\mu \frac{\partial u_k}{\partial x_k}\delta_{ij} \\ \tau^R_{ij} &= 2\mu_t S_{ij} - \frac{2}{3}k\delta_{ij}\,, \end{aligned} \tag{3.37}$$

where S_{ij} is the traceless mean strain rate, k is the turbulent kinetic energy, and μ_t is the turbulent viscosity (or *eddy viscosity*), representing the additional contribution of turbulence to dissipation. In the SST model, the eddy viscosity can be computed by following:

$$\mu_t = \rho \frac{k}{\omega}\,, \tag{3.38}$$

where ω is the turbulent specific dissipation. In the SST model, two transport equations for k and ω are solved. They read:

$$\begin{aligned} \frac{\partial \rho k}{\partial t} + \frac{\partial \rho U_j k}{\partial x_j} &= \overbrace{\tau_{ij}\frac{\partial U_i}{\partial x_j}}^{\text{production}} \overbrace{-\beta^* \rho \omega k}^{\text{destruction}} + \overbrace{\frac{\partial}{\partial x_j}\left[(\mu + \mu_t \sigma_k)\frac{\partial k}{\partial x_j}\right]}^{\text{diffusion}}, \\ \frac{\partial \rho \omega}{\partial t} + \frac{\partial \rho U_j \omega}{\partial x_j} &= \underbrace{\frac{\gamma}{\nu_t}\tau_{ij}\frac{\partial U_i}{\partial x_j}}_{\text{production}} \underbrace{-\beta \rho \omega^2}_{\text{destruction}} + \underbrace{\frac{\partial}{\partial x_j}\left[(\mu + \mu_t \sigma_\omega)\frac{\partial \omega}{\partial x_j}\right]}_{\text{diffusion}} \underbrace{+2(1-F_1)\frac{\rho \sigma_{\omega 2}}{\omega}\frac{\partial k}{\partial x_j}\frac{\partial \omega}{\partial x_j}}_{\text{cross-diffusion}}. \end{aligned} \tag{3.39}$$

In the above equations, F_1 is a blending function used to determine the model closure coefficients γ, σ_k, σ_ω, and β. This method is a combination between the two most popular two-equation turbulence closures, the k-ε and k-ω, and exploits the advantages of each model in different flow regions. The k-ω is adopted in the near-wall region, while the k-ε in the wake and free shear layer. The result is a model that behaves like the k-ω without the undesired dependency on the free-stream value of the turbulent specific dissipation found in the original version [182]. The main character of the two equations is the function F_1, that seamlessly switches between the two model. Indeed, every closure coefficient is evaluated as a blending between the values for the two models through F_1 as follows:

$$\phi = F_1 \phi_1 + (1 - F_1)\phi_2\,. \tag{3.40}$$

In the above, ϕ_1 and ϕ_2 stand for the k-ω and k-ε coefficients, respectively. In the derivation of the model, the ε-equation was first written in terms of ω exploiting the relation between the turbulent variables $\omega = \varepsilon/(C_\mu k)$. The coefficients adopted in the Wilcox k-ω model [279] are:

$$\sigma_{k1} = 0.5\,, \quad \sigma_{\omega 1} = 0.5\,, \quad \beta_1 = 0.075\,, \quad \gamma_1 = \beta_1/\beta^* - \sigma_{\omega 1}\kappa^2/\sqrt{\beta^*}\,, \tag{3.41}$$

while the coefficients for the k-ε model are:

$$\sigma_{k2} = 1.0\,, \quad \sigma_{\omega 2} = 0.856\,, \quad \beta_2 = 0.0828\,, \quad \gamma_2 = \beta_2/\beta^* - \sigma_{\omega 2}\kappa^2/\sqrt{\beta^*}\,. \tag{3.42}$$

In both cases, $\beta^* = 0.09$ and $\kappa = 0.41$. The F_1 blending function is defined as:

$$F_1 = \tanh(arg_1^4), \tag{3.43}$$

$$arg_1 = \min\left[\max\left(\frac{\sqrt{k}}{0.09 d_w \omega}, \frac{500\nu}{d_w^2 \omega}\right), \frac{4\rho\sigma_{\omega 2} k}{CD_{k\omega} d_w^2}\right], \tag{3.44}$$

$$CD_{k\omega} = \max\left(2\rho\sigma_{\omega 2}\frac{1}{\omega}\frac{\partial k}{\partial x_j}\frac{\partial \omega}{\partial x_j}, 10^{-20}\right). \tag{3.45}$$

The model in Equation (3.39), is called baseline k-ω (BSL).

Significant improvements were obtained by modifying the eddy viscosity according to the Bradshaw assumption, stating that the turbulent shear stress in the boundary layer is proportional to the turbulent kinetic energy such that $-\rho\overline{u'v'} = \rho a_1 k$. Through the introduction of the function F_2, the eddy viscosity is defined to satisfy the Bradshaw relationship in the boundary layer, while using the original formulation elsewhere. Indeed, the function F_2 drops to zero in the free shear layers. The modified eddy viscosity reads:

$$\mu_t = \frac{a_1 k}{\max(a_1\omega; \Omega F_2)}\,, \tag{3.46}$$

$$\Omega = \sqrt{2\Omega_{ij}\Omega_{ij}}\,, \tag{3.47}$$

$$\Omega_{ij} = \frac{1}{2}\left(\frac{\partial U_i}{\partial x_j} - \frac{\partial U_j}{\partial x_i}\right). \tag{3.48}$$

where Ω is the absolute value of the mean vorticity vector. This modification avoids the over-prediction of the turbulent shear stress in the boundary layer, where $\Omega > a_1\omega$. The function F_2 reads:

$$F_2 = \tanh(arg_2^4), \tag{3.49}$$

$$arg_2 = \max\left(\frac{\sqrt{k}}{0.09 d_w \omega}, \frac{500\nu}{d_w^2 \omega}\right). \tag{3.50}$$

After the eddy viscosity correction, the model is called SST.

Turbulent Sustainability Term

When approaching a solid body, the turbulent quantities k, ε, ω undergo free decay (or controlled decay if close to some floor value). The turbulent kinetic energy and dissipation (or specific fre-

quency) equations are reduced to only advection and destruction terms. This leads to a non-physical exponential decay of turbulent quantities, all with different exponents. Although in most cases, the turbulent kinetic energy, dissipation, or frequency do not play a crucial role themselves, they govern the value of the eddy viscosity, which is a combination of two of the three quantities mentioned. The problem was addressed in the work Spalart & Rumsey [244], which discussed upper and lower boundary for typical ambient boundary conditions on turbulent kinetic energy and dissipation, or turbulent frequency. To prevent the non-physical decay, a *sustainability* term can be added in each of the equations of the turbulent closure. These terms are the opposite of the destruction terms at free-stream conditions. In a k-ω framework, the equation are modified by adding to their right-hand side:

$$k-\text{equation} \quad +\beta\omega_{FS}k_{FS}\,, \tag{3.51}$$

$$\omega-\text{equation} \quad +\beta\omega_{FS}^2\,, \tag{3.52}$$

where the subscripts FS refer to the free-stream values. This correction prevents the depletion of k, ω, ε, and allows them to arrive almost unaltered from the free stream to the body. At the same time, the impact of the additional terms in the boundary layer is insignificant; indeed, k_{fs} and ω_{fs} are negligible with respect to the values of the corresponding variables in the boundary layer and do not inhibit the destruction terms.

Laminar-to-turbulent Transition

When a laminar-to-turbulent solution is expected transition must be modelled. The adoption of a 3- or 4- equation model is more suitable for natural transition problems. On the other hand, if a tripping device is adopted (an example will be given in Chapter 5), the transition to turbulence can be forced. By taking advantage of the multi-block nature of HMB3, it is possible to impose $\mu_t = 0$ on certain blocks. This approach is suitable when the tripping device is able to promote an immediate transition to turbulence in the boundary layer and the experimental (or expected) location of the transition to turbulence is known.

3.4 PANS Formulation

The partially-averaged Navier-Stokes (PANS) formulation was introduced for the first time by Girimaji *et al.* [103] as a bridging model between RANS and DNS. This method is based on a RANS paradigm, where the blending is obtained by means of the user-prescribed unresolved-to-total ratios of turbulent kinetic energy f_k and dissipation f_ε, bounded between 0 and 1, acting on the turbulence

closure equations. They read:

$$f_k = \frac{k_u}{k}, \quad f_\varepsilon = \frac{\varepsilon_u}{\varepsilon}, \tag{3.53}$$

where the u subscripts stand for unresolved, and the quantities at the denominator are the total ones (modelled and resolved). The PANS method was initially derived for a k-ε closures and then extended to the Wilcox k-ω model [279] by Lakshmipathy *et al.* [152] and to the Menter SST model [182] by Luo *et al.* [164]. In k-ω based formulations the parameter f_ε is replaced by the unresolved-to-total turbulence frequency f_ω through the following relation:

$$f_\omega = \frac{\omega_u}{\omega} = \frac{f_\varepsilon}{f_k}. \tag{3.54}$$

These formulations inherit from the parent RANS models an eddy viscosity based on the Boussinesq approximation, that is reduced with respect to the RANS value via the f_k parameter: since only a fraction of the turbulent kinetic energy is modelled, the corresponding value of the eddy viscosity is reduced. This gives the possibility for the turbulent structures to be resolved. Alternative formulations like those in ref. [17, 146], based on a k-ε-ζ-f model, and the PANS-RSM approach of Bonnifet *et al.* [28].

In this work the SST-PANS formulation is adopted:

$$\begin{aligned}
\frac{\partial(\rho k)}{\partial t} + \frac{\partial(\rho U_j k)}{\partial x_j} &= \overbrace{\tau_{ij}\frac{\partial U_i}{\partial x_j}}^{\text{production}} \overbrace{-\beta^*\rho\omega k}^{\text{destruction}} + \overbrace{\frac{\partial}{\partial x_j}\left[\left(\mu + \mu_t\sigma_k\boxed{\frac{f_\omega}{f_k}}\right)\frac{\partial k}{\partial x_j}\right]}^{\text{diffusion}}, \\
\frac{\partial(\rho\omega)}{\partial t} + \frac{\partial(\rho U_j \omega)}{\partial x_j} &= \underbrace{\frac{\gamma}{\nu_t}\tau_{ij}\frac{\partial U_i}{\partial x_j}}_{\text{production}} \underbrace{-\boxed{\beta'}\rho\omega^2}_{\text{destruction}} + \underbrace{\frac{\partial}{\partial x_j}\left[\left(\mu + \mu_t\sigma_\omega\boxed{\frac{f_\omega}{f_k}}\right)\frac{\partial\omega}{\partial x_j}\right]}_{\text{diffusion}} + \underbrace{2\boxed{\frac{f_\omega}{f_k}}(1-F_1)\frac{\rho\sigma_{\omega 2}}{\omega}\frac{\partial k}{\partial x_j}\frac{\partial\omega}{\partial x_j}}_{\text{cross-diffusion}},
\end{aligned} \tag{3.55}$$

where the differences with Equation (3.39) are shown using boxes. In Equation (3.55), the turbulent kinetic energy k and frequency ω are the modelled, or unresolved, fractions where the subscripts were dropped for simplicity. In the ω-equation, $\beta' = \left(\gamma\beta^* - \frac{\gamma\beta^*}{f_\omega} + \frac{\beta}{f_\omega}\right)$. F_1, the model coefficients, and μ_t are evaluated as explained in Section 3.3.

Estimate of the f_k Function

A topic of current research is how to prescribe the value of f_k [135]. Three main approaches are distinguished here:

- *Constant* f_k, where the parameter is not dependent on space and time;

- *Static* f_k, where an optimal spatial distribution is found after a preliminary steady RANS simulation and is kept constant in time;
- *Dynamic* f_k, where the parameter is a function of space and updated over time.

There is no consensus on which of these three approaches should be used; the *Constant* approach is preferred by its advocates because adopting a spatially and temporally constant filter, modelling and discretisation errors can be quantified. On the other hand, since the value of the parameter is not known *a priori*, a sensitivity study is required. Moreover, in flows where confined regions of high turbulent content and anisotropies in the grid are present, e.g. boundary layers, this approach does not seem reasonable. Conversely, a variable filter allows for an optimal usage of resources, since it usually adapts to both the turbulent content and the local grid size. Many estimates were proposed over time, and again no consensus was found. Moreover, comparing *Static* and *Dynamic* approaches, it is clear how the latter introduced some additional CPU costs due to the dynamic evaluation of f_k over the former, as well as, the *Constant* approach. The implementation ease is also reduced. This is the reason why a *Static* approach is more suitable for problems with localized statistically steady turbulence, whereas the *Dynamic* approach is required when coming to intrinsically unsteady flows like for the case of buffet flows, and hence is adopted in this work. The features associated with the three approaches are listed in Table 3.1.

Table 3.1: Comparison between different PANS approaches.

Approach	Constant f_k	Static f_k	Dynamic f_k
Algorithm	• steady RANS • compute $f_{k,min/max}$ (optional) • calibrate f_k • PANS	• steady RANS • compute $f_k(\mathbf{x})$ • PANS with $f_k(\mathbf{x})$	• steady RANS • unsteady RANS/constant-PANS time step • compute $f_k(\mathbf{x},\mathbf{t})$ • re-run PANS with $f_k(\mathbf{x},\mathbf{t})$
Pros	• easy implementation • no commutation error	• optimal use of grid • SRS enabled • one estimate of $f_k(\mathbf{x})$ required	• optimal use of grid • SRS enabled • optimal for unsteady flows
Cons	• fine grid in the entire domain • near wall problems • f_k must be calibrated (flow and grid dependency)	• commutation error ($\mathbf{x}$-variation of f_k) [104] • no consensus on estimates [134] • far-field and boundary layer are critical [134] • RANS-based f_k not optimal for unsteady flows	• commutation error ($\mathbf{x},t$-variation of f_k) [104] • no consensus on estimates [134] • far-field and boundary layer are critical [134] • harder implementation • $f_k(\mathbf{x},t,\mathbf{W}(\mathbf{x},t),\mathbf{Q}(\mathbf{x},t))$ may lead to instability • higher computational times
Solutions	• $f_k = 1$ in the BL (zonal PANS)	• $\min(f_{k,est},1)$ useful for BL and FF • $f_\varepsilon \neq 1$ in the BL (Low/Moderate Reynolds) • $f_k < 1$ with synthetic turbulence	• same as Static f_k • periodic flows: f_k can be reused or $f_k(t)$ can be modelled

The f_ε parameter is usually set to one, under the assumption that no dissipative scales are resolved in the computation. This approach is suitable for high Reynolds numbers for which there is a net separation between energy-containing and dissipative scales [103]. The estimates adopted in this work are:

$$f_k = C_{\mathrm{PANS}} \left(\frac{\Delta}{\Lambda_u} \right)^{2/3}, \tag{3.56}$$

$$f_k = \frac{1+\tanh(2\pi(\Lambda-0.5))}{2}, \Lambda = \frac{1}{1+\left(\frac{\Lambda_u}{\Delta}\right)^{4/3}}, \tag{3.57}$$

where $\Lambda_u = \sqrt{k}/(C_\mu \omega)$ is the local turbulent length scale, and Δ is the local grid size. The constant C_{PANS} is reduced with respect to the value of $1/\sqrt{C_\mu}$ prescribed for static estimates. Since the turbulent length scale is not based on total quantities, like in the case of estimates based on preliminary RANS calculations, it is reduced and, in turn, f_k is overly increased.

The choice is motivated by the work of Klapwijk *et al.* [134]. The two estimates presented gave the desired behaviour of f_k for simulations around a circular cylinder.

Estimate of Δt

While many estimates were given for the f_k parameter, not many sensitivity studies to determine the timestep are present in the literature. For the specific case, the timestep can be chosen as a suitable fraction of the main unsteadiness period to describe adequately the time evolution of the flow. At the same time, the turbulence Strouhal number, or frequency, is much higher than the dominant one and this also helps in the choice of Δt. An estimate of this flow feature can be given a posteriori from the spectral energy content in sensitive regions of the flow field. Here, nevertheless, a relation similar to that between f_k and Δ is given to determine the right timestep. An unresolved Kolmogorov time scale can be determined only considering modelled quantities, and related to the RANS time scale $1/(c_\mu \omega)$ by means of f_k through the following:

$$\tau_{\eta,u} = \left(\frac{\nu_u}{\varepsilon_u} \right)^{1/2} = \left(C_\mu \frac{k_u^2}{\varepsilon_u^2} \right)^{1/2} = C_\mu^{1/2} \frac{k_u}{\varepsilon_u} = C_\mu^{1/2} \frac{f_k k}{f_\varepsilon \varepsilon} = C_\mu^{1/2} \frac{f_k}{f_\varepsilon} T_\Lambda . \tag{3.58}$$

Again, the local optimal timestep is influenced by the local turbulence and the grid size by means of f_k. The above estimate can also be used to evaluate which scales can be solved with the current resolution. The idea is to choose the minimum value of $\tau_{\eta,u}$ over the computational domain and set it as Δt. In practice, the boundary layer must be neglected in this process, because the estimate goes to zero in the vicinity of the walls, where the turbulent specific dissipation reaches high values.

3.4.1 Evaluation of total turbulent scales: runtime statistics

The estimate in Equation (3.56) is a modification of the formulation by Girimaji *et al.* [103]. Here the ratio behind the formulation is summarised, and a modification is proposed. The basic idea is to define a Kolmogorov length scale associated with the unresolved turbulent quantities, i.e. k_u and ε_u, or $\omega_u = \varepsilon_u/(C_\mu k_u)$, reading:

$$\eta_u = \frac{\nu_u^{3/4}}{\varepsilon_u^{1/4}}. \tag{3.59}$$

As in a two-equation eddy viscosity model, the kinematic eddy viscosity can be written as:

$$\nu_u = C_\mu \frac{k_u^{3/2}}{\varepsilon_u} = C_\mu \Lambda_u = C_\mu \frac{k^{3/2} f_k^{3/2}}{\varepsilon f_\varepsilon} = C_\mu \frac{f_k^{3/2}}{f_\varepsilon} \Lambda. \tag{3.60}$$

The group $k^{3/2}/\varepsilon$ is the turbulent length scale Λ, and its unresolved counterpart is indicated as Λ_u.

In a direct numerical simulation, the grid spacing should be of the order of the Kolmogorov length scale. For an under resolved simulation, the idea is to set the spacing equal to the smaller resolved length scale ν_u. Under the assumption of $f_\varepsilon = 1$, a relation between the parameter f_k and the grid spacing Δ and the local turbulence content, by means of Λ_u, can be worked out:

$$f_k = C_\mu^{-1/2} \left(\frac{\Delta}{\Lambda_u} \right)^{2/3}. \tag{3.61}$$

Luo [164], stated that the estimate in Equation (3.61) did not lead to a sufficient reduction of eddy viscosity, as the quantities used to compute Λ_u are the unresolved ones, and not the totals. Always assuming $f_\varepsilon = 1$, this means that the replacing the total turbulent kinetic energy with the unresolved part leads to high values of f_k. In this view, the constant $C_\mu^{-1/2}$ in Equation (3.61) was replaced by an arbitrary constant C_{PANS}. This way, f_k still shows a dependency on grid size, and on local turbulent content. On the other hand, the introduction of an arbitrary constant introduced the need for an *a-priori* calibration.

Here, a simple modification is proposed. The need for calibration is highly impractical, and it is seen as a big disadvantage of this estimate. Therefore, the main goal is to remove C_{PANS} starting from the original formulation in Equation (3.61). To do so, the turbulent length scale Λ is reintroduced in the formulation:

$$f_k = C_\mu^{-1/2} \left(\frac{\Delta}{\Lambda} \right)^{2/3}. \tag{3.62}$$

To compute the integral turbulent scales, the flow statistics must be updated. In this way, the resolved part of the turbulent kinetic energy can be evaluated at each iteration as:

$$k_i = \frac{1}{2} \left(\overline{u'^2} + \overline{v'^2} + \overline{w'^2} \right)_i \tag{3.63}$$

where $\overline{u_i'^2}$ is the variance of the three velocity components. When dealing with flows with strong periodicity, it might not be the best option to compute statistics based on the total number of iterations. For flows with self induced instabilities, i.e. vortex shedding or buffet flows, the risk is to overestimate the resolved turbulent kinetic energy. Therefore, the statistics can be evaluated based on a selected number of samples N_s. If the flow is statistically steady, N_s is not expected to influence the statistics significantly. If the flow is strongly periodic, and N_s is smaller than the number of timesteps required to compute a period, this method helps neglect the mean flow variation from the statistics and focuses on the contributions from the smaller scales. We define $\mu(x,N_s)_i$ and $\sigma^2(x,N_s)_i$ the mean and variance of x at the timestep i using the last N_s samples, respectively:

$$\mu(x,N_s)_i = \frac{1}{N_S}\sum_{k=i-N_S+1}^{i} x_k\,, \tag{3.64}$$

$$\sigma^2(x,N_s)_i = \frac{1}{N_S}\sum_{k=i-N_S+1}^{i} [x_k-\mu(x,N_s)_i]^2\,. \tag{3.65}$$

They can be updated by using:

$$\mu(x,N_s)_{i+1} \simeq \frac{\mu(x,N_s)_i(N_s-1)+x_i}{N_s}\,, \tag{3.66}$$

$$\sigma^2(x,N_s)_{i+1} \simeq \frac{\sigma^2(x,N_s)_i(N_s-1)+(x_i-\mu(x,N_s)_{i+1})^2}{N_s}\,. \tag{3.67}$$

This method is exact when all timesteps are considered, while it becomes an approximation when $N_s \neq i$.

When adopting estimates based on total quantities, a distinction between k-ε and k-ω closures leads to different equations for the turbulent length scale Λ. To put this into evidence, the contribution of the resolved part of the turbulent kinetic energy, k_{res}, to the length scale can be written as:

$$\Lambda = \frac{[k_u\,(1+k_{res}/k_u)]^{3/2}}{\varepsilon}\,, \tag{3.68}$$

$$\Lambda = \frac{[k_u\,(1+k_{res}/k_u)]^{1/2}}{C_\mu\,\omega}\,, \tag{3.69}$$

for k-ε and k-ω models, respectively. While it is possible to assume that f_ε is 1 for high Reynolds number, f_ω is the inverse of f_k. As we cannot estimate the total value of the turbulent specific dissipation, ε_u is first evaluated based on the modelled turbulent quantities, and the equation for k-ε models is adopted (Equation (3.68)).

3.4.2 Constraint due to timestep

The model of Luo can be further constrained on the basis of Equation (3.58), by imposing $\tau_{\eta,u} = \Delta t$, giving:

$$f_k = C_\mu^{-1/2} \frac{\Delta t}{T_\Lambda}. \tag{3.70}$$

When used with Luo's formulation, the group $C_\mu^{-1/2}$ can be replaced with the same coefficient C_{PANS} used in the old formulation. This way, the estimate based on Δ, denoted $f_{k,x}$, and the current proposal based on Δt, called $f_{k,t}$, will adopt the same coefficient.

3.4.3 Characteristic grid size

As mentioned in the previous chapter, the grid size adopted for the estimate of f_k varied between different works. Several approaches are possible, including:

- $\Delta_{\max} = \max(\Delta x, \Delta y, \Delta z)$. This formula is the one of the original DES formulation [243] and used in many PANS works (see [1, 20, 72, 164], among the others). The idea behind this formula is that the eddy resolution is limited by the maximum cell size and, therefore, it should also limit the local reduction of eddy viscosity. This will result in a conservative estimate of f_k.

- $\Delta_{\min} = \min(\Delta x, \Delta y, \Delta z)$. This formulation was used in [78, 103] since it was found that, for the cases under analysis, the previous grid size, $\Delta_{\max}$, resulted in too high f_k. Nonetheless, the small normal spacing required to satisfy the constraint on $\Delta y^+ < 1$ results in too low value of the grid size. Therefore, this estimate will not be used in this work.

- $\Delta_{\mathrm{vol}} = \sqrt[3]{\Delta x \Delta y \Delta z}$. This is the formula used in the majority of LES works, where anisotropies in the grid are avoided. It also found use in several PANS works (see [18, 77, 110], among the others). In this case, the three spacings give the same contribution to the determination of the grid size. Therefore, the estimate accounts for the presence of a small size in the boundary layer, but its effect is mitigated by accounting for the two larger sizes. The f_k distribution obtained with this formulation is seen as satisfactory for our purposes and will represent the benchmark for the investigation on 3D configurations.

- $\Delta_{\mathrm{L2}} = \sqrt{\Delta x^2 + \Delta y^2 + \Delta z^2}$. Here, the cell diagonal is taken as characteristic grid size. This formula gives a length scale that is even greater than $\Delta_{\max}$ and, therefore, will not be used in the remainder.

- Δ_{PBR}. Here, a distinction between isotropic, pencil, book, and ribbon cells [233] is done a priori. For pencil grid elements, the longest size is discarded, while for ribbon elements the

shortest one is discarded. This estimate introduced discontinuities in the Δ distribution and, therefore, was not used.

The three grid sizes $\Delta x, \Delta y, \Delta z$ correspond to the distances between opposite face centres of the hexahedral cells.

3.4.4 Implementation in HMB3

Since PANS is based on a RANS paradigm, the main modification consists of the addition of f_k in the diffusion terms, the destruction term in the ω-equation and the cross-diffusion term. The turbulent length sale is computed through the local values of the turbulent kinetic energy and frequency. Different characteristic grid sizes can be considered (see Section 3.4.3).

The minimum allowed value of the turbulent length scale is set to 10^{-10} to avoid division by zero in the boundary layer. A feature to force f_k to be between a minimum and maximum value has also been added to the code. The maximum value is always 1, since not all estimates adopted prevent the parameter to exceed unity, while the minimum value can be tuned by the user. It should be pointed out that too low values of f_k correspond to a significant reduction of the eddy viscosity that must be followed by a reduction of the spatial and temporal discretisations. Moreover, excessively low values of this parameter can compromise the stability of the computation and increase the CPU cost. The role of the minimum f_k will be investigated in the next sections. As an alternative, the constant approach can be used, and a fixed value can be stored in the memory, avoiding the need to recompute the two length scales.

Exploiting the capability of the solver to work with multi-block grids, it was possible to enable the zonal approach setting $f_k = 1$ a priori in selected blocks. This allows the solver to skip the PANS routine in blocks where a RANS behaviour is expected.

3.5 Adjoint Formulation

To compute the derivatives of the buffet coefficient with respect to flight conditions, the sensitivity equation casted in adjoint form is solved. The underlying idea is to write explicitly the cost functional I, as a function of the flow variables $(\mathbf{W})$ and of the design variables α, that is, $I = I(\mathbf{W}(\alpha), \alpha)$. The flow variables are subject to satisfy the fluid dynamics governing equations written in compact form as:

$$\mathbf{R}(\mathbf{W}(\alpha), \alpha) = 0\,. \tag{3.71}$$

Formally, taking the derivative of I with respect to α we obtain:

$$\frac{\mathrm{d}I}{\mathrm{d}\alpha} = \frac{\partial I}{\partial \alpha} + \frac{\partial I}{\partial \mathbf{W}} \frac{\partial \mathbf{W}}{\partial \alpha}. \tag{3.72}$$

By introducing the adjoint variable λ as the solution of the following linear system:

$$\left(\frac{\partial \mathbf{R}}{\partial \mathbf{W}}\right)^{\mathrm{T}} \lambda = -\left(\frac{\partial I}{\partial \mathbf{W}}\right)^{\mathrm{T}}, \tag{3.73}$$

Equation (3.72) can be rewritten as:

$$\frac{\mathrm{d}I}{\mathrm{d}\alpha} = \frac{\partial I}{\partial \alpha} + \lambda^{\mathrm{T}} \frac{\partial \mathbf{R}}{\partial \alpha}, \tag{3.74}$$

The CPU cost of the dual sensitivity problem Equations (3.73) and (3.74) scales with the number of outputs, since the right-hand side of Equation (3.73) depends on I, but it is independent of the input parameters. The adjoint form of the sensitivity equation is particularly efficient for cases where the number of (output) cost functionals is small, while the number of (input) design variables is large. Options for the solution of the linear system in Equation (3.73) are a fixed-point iteration scheme or a nested Krylov-subspace method based on the Generalised Minimum Residual (GMRES) method. For further details the reader is referred to the work of Biava & Barakos [23] and Biava et al. [22].

3.6 Harmonic Balance Formulation

Here, the harmonic balance formulation is described together with the implementation in HMB3 following the work of Woodgate and Barakos [281]. The harmonic balance method approximates the flow solution and residual vectors in Equation (3.13) with a Fourier expansion truncated to a specific number of harmonics N_H, after assuming the flow periodicity in time with frequency Ω. The two vectors are, therefore, written as:

$$W(t) = \sum_{k=-N_H}^{N_H} \hat{W}_k e^{ik\Omega t}, R(t) = \sum_{k=-N_H}^{N_H} \hat{R}_k e^{ik\Omega t}. \tag{3.75}$$

Once the discrete Fourier transforms are substituted into Equation (3.13) and the orthogonality of the Fourier terms is used, an equation for each wave number k is obtained:

$$\Omega k V \hat{W}_k + \hat{R}_k = \Omega A \hat{W}_k + \hat{R}_k = 0, \tag{3.76}$$

where A is an $N_T \times N_T$ matrix and $N_T = 2N_H + 1$. Equation (3.76) is solved following the pseudo-spectral approach of Hall et al. [109], where the equation is transformed back into the time domain. The solution and the residual are split into N_T discrete, equally-spaced sub-intervals over the period

$T = 2\pi/\Omega$:

$$W_{hb} = \begin{pmatrix} W(t_0+\Delta t) \\ W(t_0+2\Delta t) \\ \vdots \\ W(t_0+T) \end{pmatrix}, R_{hb} = \begin{pmatrix} R(t_0+\Delta t) \\ R(t_0+2\Delta t) \\ \vdots \\ R(t_0+T) \end{pmatrix}. \tag{3.77}$$

By introducing a transformation matrix E, such that $\hat{W} = EW_{hb}$ and $\hat{R} = ER_{hb}$, Equation (3.76) can be recast as:

$$\Omega AEW_{hb} + ER_{hb} = 0 = \Omega E^{-1}AEW_{hb} + E^{-1}ER_{hb} = \Omega DW_{hb} + R_{hb}\,, \tag{3.78}$$

where $D = E^{-1}AE$ is defined as:

$$D_{ij} = \frac{2}{N_T}\sum_{k=1}^{N_T} k\sin\left(2\pi k(j-i)/N_T\right). \tag{3.79}$$

The two matrices E and E^{-1} are defined as:

$$E = \frac{2}{2N+1}\begin{bmatrix} 0.5 & 0.5 & 0.5 & 0.5 & 0.5 \\ \cos(\Omega t_1) & \cos(\Omega t_2) & \cos(\Omega t_3) & \dots & \cos(\Omega t_{2N+1}) \\ \vdots & \vdots & \vdots & \ddots & \vdots \\ \cos(N\Omega t_1) & \cos(N\Omega t_2) & \cos(N\Omega t_3) & \dots & \cos(N\Omega t_{2N+1}) \\ \sin(\Omega t_1) & \sin(\Omega t_2) & \sin(\Omega t_3) & \dots & \sin(\Omega t_{2N+1}) \\ \vdots & \vdots & \vdots & \ddots & \vdots \\ \sin(N\Omega t_1) & \sin(N\Omega t_2) & \sin(N\Omega t_3) & \dots & \sin(N\Omega t_{2N+1}) \end{bmatrix}, \tag{3.80}$$

$$E^{-1} = \frac{2}{2N+1}\begin{bmatrix} 1 & \cos(\Omega t_1) & \dots & \cos(N\Omega t_1) & \sin(\Omega t_1) & \dots & \sin(N\Omega t_1) \\ 1 & \cos(\Omega t_2) & \dots & \cos(N\Omega t_2) & \sin(\Omega t_2) & \dots & \sin(N\Omega t_2) \\ 1 & \cos(\Omega t_3) & \dots & \cos(N\Omega t_3) & \sin(\Omega t_3) & \dots & \sin(N\Omega t_3) \\ \vdots & \vdots & \ddots & \vdots & \vdots & \ddots & \vdots \\ 1 & \cos(\Omega t_{2N+1}) & \dots & \cos(N\Omega t_{2N+1}) & \sin(\Omega t_{2N+1}) & \dots & \sin(N\Omega t_{2N+1}) \end{bmatrix}, \tag{3.81}$$

The harmonic balance equation is solved by pseudo-time marching, leading to:

$$\frac{\mathrm{d}W_{hb}}{\mathrm{d}\tau} + \Omega DW_{hb} + R_{hb} = 0\,. \tag{3.82}$$

An implicit method is then used in conjunction with an implicit treatment of the source term, as follows:

$$\Omega DW_{hb}^{n+1} = \Omega DW_{hb}^{n} + \Omega D(\Delta W_{hb})\,, \tag{3.83}$$

and the harmonic balance equation is recast in the form:

$$\frac{W_{hb}^{n+1} - W_{hb}^{n}}{\Delta\tau} = -\left[\Omega D W_{hb}^{n+1} + R_{hb}(W_{hb}^{n+1})\right] . \tag{3.84}$$

The Jacobian matrix J_{Imp} reads

$$J_{\text{Imp}} = \begin{bmatrix} \left.\frac{\partial R}{\partial W}\right|_{t_0+\Delta t} & \Omega D_{12} & \dots & \Omega D_{1N_T} \\ \Omega D_{21} & \left.\frac{\partial R}{\partial W}\right|_{t_0+2\Delta t} & & \\ \vdots & & \ddots & \\ \Omega D_{N_T 1} & \Omega D_{N_T 2} & & \left.\frac{\partial R}{\partial W}\right|_{t_0+T} \end{bmatrix} , \tag{3.85}$$

and the linear system to be solved becomes:

$$\left[\frac{V}{\Delta\tau} + J_{\text{Imp}}\right](W_{hb}^{n+1} - W_{hb}^{n}) = -\Omega D W_{hb}^{n} - R_{hb}(W_{hb}^{n}) . \tag{3.86}$$

The system is solved using a Krylov subspace method with BILU factorisation [11].

Temporal spectral viscosity

With respect to the implementation of Woodgate and Barakos [281], the second-order Temporal Spectral Viscosity (TSV) term of Huang and Ekici [116] is added in Equation (3.82). This term damps the contribution associated with high frequencies and maintains the accuracy of the time-spectral solution. The equation now reads:

$$\frac{\mathrm{d}W_{hb}}{\mathrm{d}\tau} = -R_{hb} - \Omega D W_{hb} + \Omega^2 D_2 W_{hb} = -R_{hb}^{*} , \tag{3.87}$$

where

$$\Omega^2 D_2 = \varepsilon_N \frac{\mathrm{d}^2 E^{-1}}{\mathrm{d}t^2} E_{\text{cutoff}} . \tag{3.88}$$

The ε_N is a viscosity coefficient that is usually equal to $1/N_H$. The matrix E_{cutoff} is defined as:

$$E_{\text{cutoff}} = \frac{2}{2N+1}\begin{bmatrix} 0.5\rho_0 & 0.5\rho_0 & 0.5\rho_0 & 0.5\rho_0 & 0.5\rho_0 \\ \rho_1\cos(\Omega t_1) & \rho_1\cos(\Omega t_2) & \rho_1\cos(\Omega t_3) & \dots & \rho_1\cos(\Omega t_{2N+1}) \\ \vdots & \vdots & \vdots & \ddots & \vdots \\ \rho_N\cos(N\Omega t_1) & \rho_N\cos(N\Omega t_2) & \rho_N\cos(N\Omega t_3) & \dots & \rho_N\cos(N\Omega t_{2N+1}) \\ \rho_1\sin(\Omega t_1) & \rho_1\sin(\Omega t_2) & \rho_1\sin(\Omega t_3) & \dots & \rho_1\sin(\Omega t_{2N+1}) \\ \vdots & \vdots & \vdots & \ddots & \vdots \\ \rho_N\sin(N\Omega t_1) & \rho_N\sin(N\Omega t_2) & \rho_N\sin(N\Omega t_3) & \dots & \rho_N\sin(N\Omega t_{2N+1}) \end{bmatrix}, \tag{3.89}$$

where

$$\rho_i = \begin{cases} 0, \, i \leq m \\ 1, \, i \geq m \end{cases}, \tag{3.90}$$

and m is the cut-off harmonic that determines where the additional viscosity is applied. The D_2 matrix can be easily computed through matrix multiplication, and a compact formula, similar to that of D, is obtained:

$$D_{2,ij} = -\frac{2\varepsilon_N}{N_T}\sum_{k=1}^{N_T} k^2 \cos\left(2\pi k(j-i)/N_T\right). \tag{3.91}$$

The introduction of the TSV leads to a modification of the implicit Jacobian in Equation (3.85), now reading:

$$J_{\text{Imp}} = \begin{bmatrix} \left.\frac{\partial R}{\partial W}\right|_{t_0+\Delta t} & \Omega D_{12} - \Omega^2 D_{2,12} & \dots & \Omega D_{1N_T} - \Omega^2 D_{2,1N_T} \\ \Omega D_{21} - \Omega^2 D_{2,21} & \left.\frac{\partial R}{\partial W}\right|_{t_0+2\Delta t} & & \\ \vdots & & \ddots & \\ \Omega D_{N_T1} - \Omega^2 D_{2,N_T1} & \Omega D_{N_T2} - \Omega^2 D_{2,N_T2} & & \left.\frac{\partial R}{\partial W}\right|_{t_0+T} \end{bmatrix}, \tag{3.92}$$

where out-of-diagonal terms are introduced after applying the same implicit treatment of Equation (3.83) to the term $\Omega^2 D_2 W_{hb}$.

Time Period Estimation

The main limitation of the harmonic balance is the need for prior knowledge of the frequency associated with the time periodicity of the flow. While this parameter is known for some cases, like flows in turbomachinery and helicopter rotors, for some other problems, like transonic buffet, the main frequency of oscillation is not known a priori and varies with the flight conditions. To overcome this drawback, the adaptive-frequency method called Gradient-Based Variable Time Pe-

riod (GBVTP) [106, 180] is used in this work. It is assumed that the solution can only converge when the exact frequency is used, while for a wrong guess value, the flow residual tends to stall around some value. Therefore, the derivative of the right-hand-side in Equation (3.87), called R^*, with respect to the time period must be zero at such condition. The derivative is taken on the square of R^* in agreement with the original formulation [180]:

$$\begin{aligned} R_n^{*^2} &= \Omega^2 (DW)_n (DW)_n + 2\Omega (DW)_n R(W)_n - 2\Omega (DW)_n (D_2W)_n \\ &+ R(W)_n R(W)_n - 2\Omega^2 (D_2W)_n R(W)_n + \Omega^4 (D_2W)_n (D_2W)_n \\ &= 4\frac{\pi^2}{T^2}(DW)_n (DW)_n + 4\frac{\pi}{T}(DW)_n R(W)_n - 16\frac{\pi^3}{T^3}(DW)_n (D_2W)_n \\ &+ R(W)_n R(W)_n - 8\frac{\pi^2}{T^2}(D_2W)_n R(W)_n + 16\frac{\pi^4}{T^4}(D_2W)_n (D_2W)_n, \end{aligned} \tag{3.93}$$

$$\begin{aligned} \frac{\partial R_n^{*^2}}{\partial T} &= -8\frac{\pi^2}{T^3}(DW)_n (DW)_n - 4\frac{\pi}{T^2}(DW)_n R(W)_n + 48\frac{\pi^3}{T^4}(DW)_n (D_2W)_n \\ &+ 16\frac{\pi^2}{T^2}(D_2W)_n R(W)_n - 64\frac{\pi^4}{T^5}(D_2W)_n (D_2W)_n. \end{aligned} \tag{3.94}$$

Here, the subscript n refers to the n-th time instant and the *hb* subscripts were dropped for simplicity. After averaging the gradient over the number of time instants and the cells of the computational domain, the time period is updated following:

$$T^{n+1} = T^n - \Delta T \frac{\partial R_n^2}{\partial T}, \tag{3.95}$$

where ΔT is a constant gain and the time period correction is limited to a constant value to limit the instability of the algorithm due to drastic changes in the associated frequency Ω, updated together with the time period. Doing this, the solution and time period are simultaneously updated. To make the computation even more stable, the time period correction can be applied once every a user-prescribed number of iterations of the CFD solver.

3.7 Virtual Control Surface Modelling

In HMB3, Gurney flaps and UTEFs can be modelled either by an *ad-hoc* multi-block grid or virtually. As the first strategy makes difficult to simulate an actuation, the second method is preferred. The method adopted in this work was formulated in [282] and it is briefly discussed, here. The flap is located along a block face (see Figure 3.4) of the multi-block grid by defining a planar surface with three points. At each iteration, the length of the flap is updated according to a temporal, user-

prescribed law, and only part of the plane is accounted for. In each block, cells faces coinciding with block faces are flagged if their distance from the flap plane and their orientation with respect to the plane falls within a user-prescribed tolerance. If the projection of a cell face does not fall entirely in the defined plane, the cell is only flagged if its centroid projection falls onto the plane. Cells which do not satisfy those requirements are discarded, while no-slip boundary conditions are imposed on the flagged cells. The algorithm to identify Gurney/UTEF cell faces is repeated in Algorithm 1. Figure 3.4, right images, shows the location of an UTEF at the initial (top) and final

Algorithm 1 Pseudo-code for Gurney flaps/UTEF definition. From [282]

```
Data: Define the Gurney as a set of points
for all the blocks in the mesh do
    for all the internal boundaries of each block do
        for all the faces on each internal boundary do
            if the centroid of the face is close to the Gurney/UTEF then
                if the normal to the Gurney/UTEF is nearly parallel to the normal of the face then
                    if the centroid of the face is inside the polygon of the Gurney/UTEF then
                        Flag this face as in the Gurney/UTEF
                    end if
                end if
            end if
        end for
    end for
end for
All the cell faces up to that node will be flagged as boundary cells
```

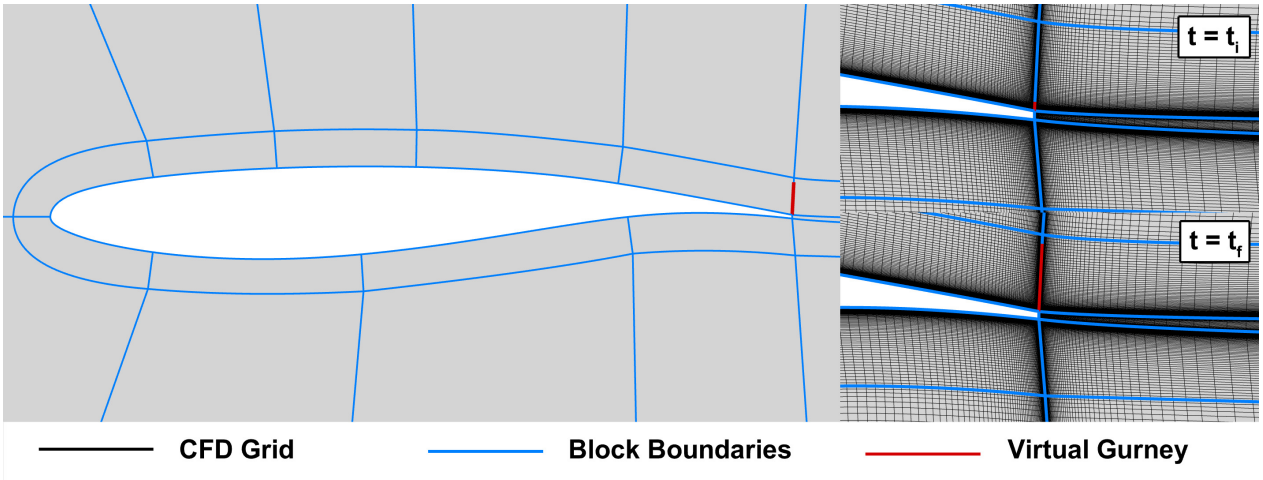

Figure 3.4: Left: multi-block grid topology around the OAT15A aerofoil; right: grid around the trailing edge at the initial and final instants of the UTEF deployment.

(bottom) instants of the actuation. The number of flagged cells is modified at each timestep according to the specified temporal law of actuation. In Figure 3.4, the portion of the block boundary

occupied by the control surface is indicated by the change in colour. Using this method, it is only important to place a block boundary at a convenient position to represent the control surface.

3.7.1 Spoilers

Virtual spoilers are modelled following the implementation in HMB3 of Pastrikakis and Barakos [202] for swinging Gurney flaps. In Figure 3.5, left image, the mesh adopted around the OAT15A aerofoil with virtual spoilers is shown. To build such a grid around the spoiler location, a hinge (see. Figure 3.5, right image) must be introduced. Using this grid topology, the virtual spoiler

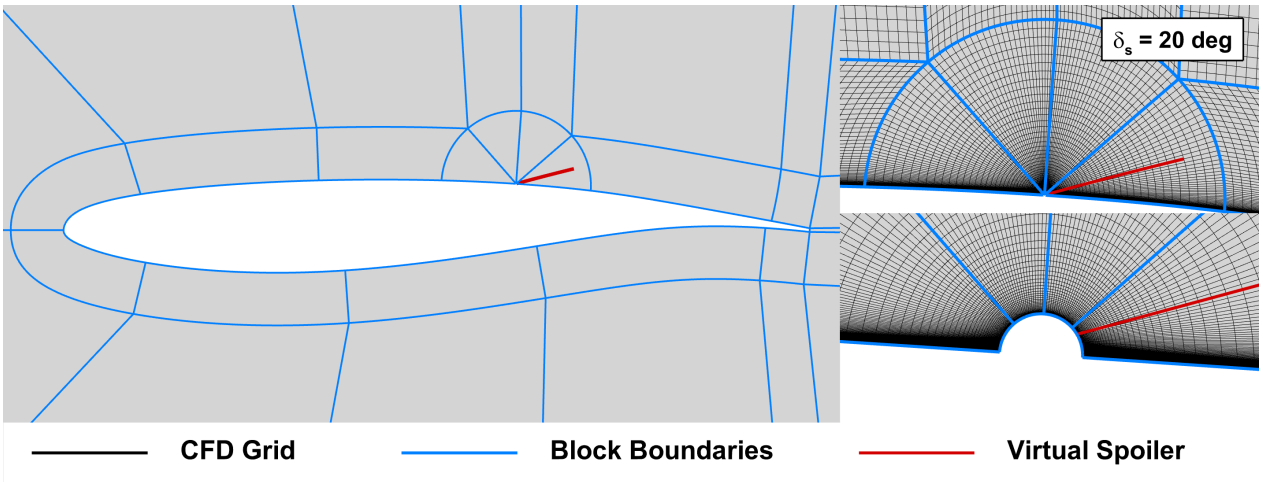

Figure 3.5: Left: multi-block grid topology around the OAT15A aerofoil with virtual spoiler; right: grid around the spoiler hinge for a spoiler angle deflection of 20 deg.

can be simulated by flagging the nearest cell faces at their instantaneous positions as boundary faces, and imposing no-slip boundary conditions. Adopting this method, once the grid is properly built, no additional effort is required in terms of mesh generation, and the moving surface can be modelled without the need for over-set or overly fine grids. Figure 3.5, right, shows a close view of the hinge location with the deployed spoiler. No-slip boundary conditions are imposed on the red cell faces. Given the multi-block nature of the solver, the user can specify within which blocks the spoiler is contained. In Figure 3.5, the two rightmost blocks around the hinge are flagged as *spoiler blocks*, and the spoiler cannot be deployed more than, roughly, 90 degrees from its initial position. As for the UTEF/Gurney flaps, the spoiler position is given in input by specifying three points corresponding to the beginning and end of the hinge and a third point to define the spoiler plane. Once the initial spoiler position is calculated, it can be deployed following a linear law, or a temporal law based on a summation of harmonics.

To determine the instantaneous spoiler position and the corresponding boundary flags, we use the algorithm of [282], repeated here in Algorithm 2.

Algorithm 2 Pseudo-code for spoiler definition.

```
Find the spoiler size
Find the spoiler angle
for all spoiler blocks in the mesh do
    if the point is inside the radius then
        Flag the cells behind and in front of the spoiler with -1 and 1
    else
        Flag the cells behind and in front of the spoiler with -2 and 2
    end if
end for
Sweep along the lines
if the sign changes between two cells then
    if the sum of the four neighbor cells of a node is 6 then
        This node is the end of the spoiler
    end if
end if
All the cell faces up to that node will be flagged as boundary cells
```

3.7.1.1 Automatic Control for Buffet

Buffet control by means of control surfaces could be made automatic using probes in the boundary layer to detect separation. At design conditions, flow separation (if any) takes place at the shock foot, while in buffet regimes the separated flow region extends, during a fraction of the buffet period, from the shock foot to the trailing edge. In this view, the idea is to place a sensor in the boundary layer at an appropriate location, i.e. where separation is not expected in cruise (design) conditions, and exploit the information at that point to activate flow control when required.

The sketch in Figure 3.6, left, illustrates the control point for buffet detection. The probe located on the aerofoil surface at a specified location ($x/c = 0.7$ in figure) samples the conserved flow variables at each timestep. The printed values are the ones at a distance $\Delta y/2$ from the wall, being Δy the normal spacing of the first cell. When flow reversal is detected the spoiler is deployed following a linear law:

$$\delta_s = \delta_{s,0} + \min(\dot{\delta}_s(t - t_{B,0}), \delta_{s,\max}), \tag{3.96}$$

where $\delta_{s,0}$ is the position of the undeployed spoiler, $\dot{\delta}_s$ is the user-described angular velocity, assumed constant over the spoiler excursion, and $\delta_{s,\max}$ is the maximum displacement. The instance when buffet is first detected is indicated by $t_{B,0}$. In the solver, this is implemented by applying a discrete increment for each timestep:

$$\delta_s^i = \delta_{s,0} + \min(\dot{\delta}_s(i\Delta t - t_{B,0}), \delta_{s,\max}), \quad \dot{\delta}_s = \delta_{s,\max}\Delta t_{act}, \quad \Delta t_{act} = 1/N_{act}, \tag{3.97}$$

where the velocity is specified by means of the parameter Δt_{act}, equal to the inverse of the number

of unsteady steps required to deploy the device N_{act}. A demonstration will be given in Chapter 8.

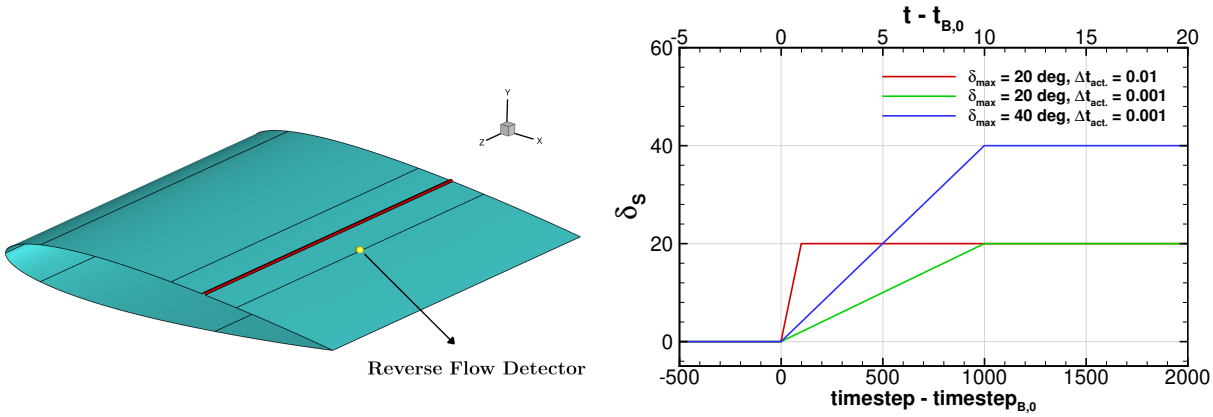

Figure 3.6: Left: sketch of the buffet sensor employed around a NACA0012 aerofoil. Black lines represent surface block boundary while the red surface indicates the hinge; right: spoiler angle versus time for different value of the parameters Δt_{act} and $\delta_{s,\text{max}}$.

Figure 3.6, right, shows the temporal laws corresponding to different values of $\delta_{s,\text{max}}$ and Δt_{act}. The device retraction follows the same linear behaviour shown in Equation (3.97). As the deployment of a control surface generates separation on the aerofoil, the presence of reversed flow is no longer a valuable buffet indicator. Therefore, the spoiler retraction, when necessary, is applied at an arbitrary time. It must be pointed out that dynamic control, based on observables, is beyond the scope of this work. Nevertheless, a smooth deployment and retraction of the control devices allows for a more plausible description of the control dynamics and avoids abrupt changes in the flow field due to the appearance/disappearance of the control surfaces.

3.7.1.2 Changing flow conditions with grid motion

Regardless of their ability to suppress buffet, slotted flow control surfaces are likely to introduce drag penalties or non-equilibrium in lift and pitching moment (for 2D and quasi-2D configurations). Therefore, the devices must be retracted to avoid such penalties for a long period of time. If the flow conditions do not vary after the application of flow control, SIO will take place again. To prevent this, the pilot (or the automatic control system) should return to flight conditions below the buffet boundary by reducing the flight speed, the angle of attack, or both. Hence, while the control surface temporarily suppresses buffet, a change in flight conditions will prevent the appearance of new oscillations. To account for such an action, in this work, we simulated a reduction of the Mach number by moving the entire CFD grid. A positive, or negative, grid velocity U_{grid} aligned with the free-stream velocity will result in a reduced, or increased, respectively, local flow velocity, i.e. Mach number. Figure 3.7, left plot, shows the control strategy adopted. The spoiler (blue lines in figure) is first deployed following Equation (3.97), and, after the SIO is stopped, it is retracted within an equal time window. At the same time, the grid is put in motion with constant acceleration

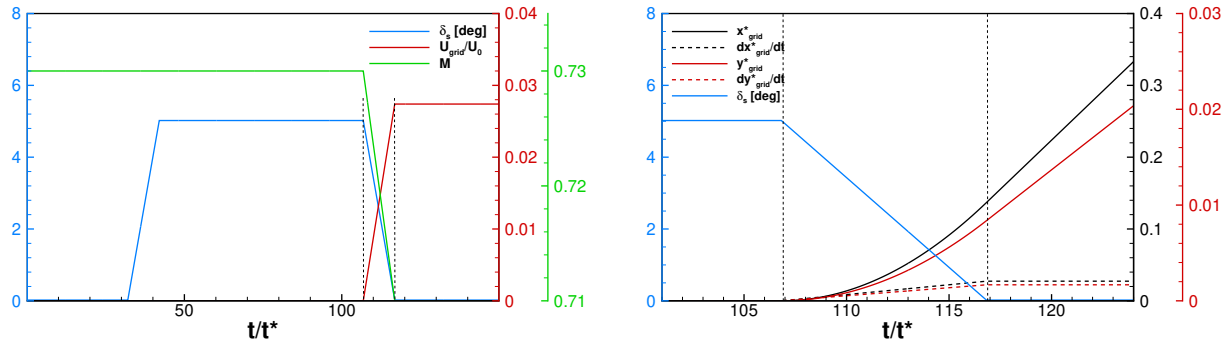

Figure 3.7: Left: time history of the Mach number in response to the grid velocity. Right: instantaneous x and y components of position and velocity vectors within the spoiler retraction time window.

until the spoiler is retracted. At this point, the local Mach number (green line) is such to avoid the occurrence of buffet. Given the initial and final Mach numbers $M_{\infty,0}$ and $M_{\infty,F}$, respectively, the grid acceleration, velocity and displacement can be written as:

$$\ddot{\mathbf{X}} = \frac{\mathbf{U}_\infty \left(\frac{M_{\infty,F}}{M_{\infty,0}} - 1 \right)}{T_{\text{off}}}, \quad \dot{\mathbf{X}} = \max(\ddot{\mathbf{X}} t', \dot{\mathbf{X}}_{\max}), \quad \mathbf{X} = \dot{\mathbf{X}} t' + \frac{1}{2} \ddot{\mathbf{X}} t'^2, \tag{3.98}$$

where $t' = t - t_{\text{off},i}$ is the time from the beginning of the spoiler retraction. The time windows of the spoiler retraction (T_{off}) and the aerofoil deceleration might be selected to have different lengths and locations in time. Nevertheless, in this work, the two actions will be simultaneous. The right plot in Figure 3.7 shows the $x-$ and $y-$ components of the grid velocity and position within the spoiler retraction time window. The $x-$ and $y-$components are obtained by projecting the $\ddot{\mathbf{X}}, \dot{\mathbf{X}}, \mathbf{X}$ onto the parallel and perpendicular direction of the free-stream velocity, i.e. by multiplying by $\cos(\alpha)$ and $\sin(\alpha)$, respectively. In this work, an application will be shown in conjunction with spoilers, but might be used with any deployable flow control surface.

Chapter 4

PANS Validation on a Laminar Circular Cylinder

RANS simulations have become the most popular tool in industrial CFD because of their reduced CPU costs and wide range of applicability. Nevertheless, the prediction of some classes of flows with RANS simulations is not always accurate. Examples of this are flows involving large, shallow separation, where the extent of the separated region is almost always mispredicted, and strongly dependent on the employed turbulence model. Following the increase in the availability of computational resources, DNS and LES are no longer out of reach for canonical flows at moderate Reynolds numbers. Nevertheless, cases of aeronautical interest, cannot yet be studied with such high-resolution methods. Therefore, in recent years, hybrid RANS/LES approaches have been introduced to reduce the cost associated with the fine spatio-temporal discretisation required from the aforementioned approaches. In this context, the PANS [103] method, detailed in Section 3.4, was introduced. With respect to URANS, the resolution of smaller scales is enabled, leading to a more accurate characterisation of turbulent, unsteady flows. On the other hand, if f_k and f_ε assume reasonable values, PANS offer better results on coarse grids [163]. This is an advantage over LES and hybrid RANS-LES methods, which are constrained by the requirements on the spatio-temporal discretisation in the LES domain [240] and result in high CPU costs.

So far, PANS simulations have been mainly tested on canonical flows in the incompressible formulation. Flows around circular [1, 72, 152, 206] and square [19, 129, 238] cylinders, backward-facing steps [78], turbulent channels [18], or humps and hills [58, 79, 165, 166] were mostly investigated. Rare exceptions are found in the works of Basu *et al.* [20] on transonic cavity flows, Luo *et al.* [164] on flows around a circular cylinder and ramped cavity at supersonic conditions, and Bonnifet *et al.* [28] on transonic buffet. Early works are mostly based on the k-ε model as a RANS parent, while some others employed a k-ω closure. More recently, the formulation has been adapted to the Shear-Stress Transport model of Menter [182] and used by a number of authors [135, 163, 164, 206]. Bonnifet *et al.* [28] adopted an RSM model while the group of Basara,

Krajnovic *et al.* [17–19,146,147] proposed a four-equation model for a more accurate near-wall prediction. Only recently, PANS have been used for flows of industrial relevance [161, 186, 278, 287].

The main parameter of the PANS approach is f_k and imposing a correct distribution over the CFD domain is crucial if good accuracy is required. As explained in Section 3.4, f_ε can be set to 1. A debated point is how to prescribe the value of f_k [135]. All of the approaches discussed in Section 3.4 present pros and cons, and none can be selected *a priori*. Flows with self-induced instabilities seem suited for a dynamic approach, where f_k varies in space and time, and therefore adapts to the flow unsteadiness.

In this chapter, we assess the ability of some dynamic estimates in the prediction of the flow around a circular cylinder at Reynolds number $\mathrm{Re}_D = 50000$. The case was previously investigated using several simulations of various resolutions, spanning from URANS to LES. The constant approach is also adopted to show the strong link between spatio-temporal discretisation and the adopted value of f_k. Moreover, some new estimates of f_k are proposed based on modifications of the most common estimates of the literature. These were introduced in Section 3.4.1 and Section 3.4.2

Section 4.1 presents the investigated test case and an overview of the CFD computations; Section 4.2 contains the CFD results, and Section 4.3 is a summary of the conducted research.

4.1 Test Case Description and Numerical Setup

The case used for this work is a circular cylinder at $\mathrm{Re}_D = \rho U_\infty D/\mu = 5 \times 10^4$. This flow was experimentally studied by Norberg [195, 196] who investigated the flow around circular cylinders of different aspect ratios, and at several Reynolds numbers, spanning from laminar to supercritical conditions. The same case was studied at $\mathrm{Re}_D = 1.4 \times 10^5$ in the work of Cantwell and Coles [37], from which velocity statistics were collected and used for comparison purposes. Numerous numerical simulations were also carried out, like that of Travin *et al.* [269], Vatsa and Singer [274], and Elmiligui *et al.* [73], among others.

The Reynolds number adopted in this work falls in the subcritical regime, i.e. the cylinder presents a laminar boundary layer separation and a completely turbulent wake. Both numerical and experimental works revealed an oscillatory behaviour of the aerodynamic loads associated with vortex shedding behind the cylinder. A modulation of the shedding phenomenon was observed with a temporal scale an order of magnitude larger than the vortex shedding period. High-amplitude and low-lift amplitude cycles alternated, corresponding to higher and lower drag, respectively. Nevertheless, the spectrum only presentsed a dominant frequency associated with Von Karman shedding. The Strouhal number ranges from 0.18 to 0.22 in the previous studies.

Time marching simulations were carried out on a CFD domain extending $20D$ in the radial direction and $2D$ in the spanwise direction. Adiabatic boundary conditions were imposed on the wall, free-stream conditions were imposed at the far field, and periodic boundary conditions were

Table 4.1: Main features of the different grids used for computations.

Grid #	N_θ	N_y	N_z	N_{tot}
Coarse	136	99	32	3.8×10^5
Medium	208	135	40	1.1×10^6
Fine	304	201	60	3.7×10^6

applied in the spanwise direction. Three grids were tested (see Figure 4.1 and Table 4.1), for the configuration under analysis. In each direction, the number of cells was increased by 1.5 at each refinement. The refinement was also applied in the boundary layer. The Mach number used was 0.3 according to Elmiligui *et al.* [73], to lower the effect of compressibility. A reference non-dimensional timestep of $\Delta t U_\infty / D = 0.01$ was adopted, if not otherwise specified, and corresponds to about 500 unsteady steps per period of oscillation.

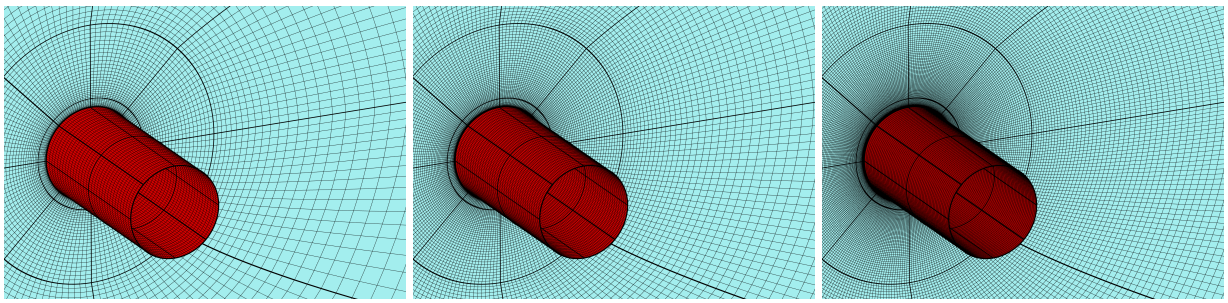

(a) Coarse **(b)** Medium **(c)** Fine

Figure 4.1: Grids used for the computations around the circular cylinder at Re= 50000. Grid specifications are listed in Table 4.1.

Table 4.2 presents an overview of the simulations carried out for this work. Both the dynamic estimates of f_k introduced in the previous section, and fixed values of 0.2, 0.4, 0.6, and 1 (URANS) were employed on all grids. For the estimate in Equation (3.57), the lower value of f_k was fixed to 0.2, 0.4, 0.6, in agreement with the fixed value-cases, to compare the performance between corresponding simulations. For the estimate in Equation (3.56), values of $C_{\text{PANS}} = 0.1, 0.3, 0.5$ were tested in the same as Luo [163].

The quantities of interest used as a comparison with the experiments are the Strouhal number $\text{St} = fD/U_\infty$ associated with the vortex shedding, the base pressure coefficient C_{pb}, and the mean drag coefficient C_D. Moreover, the mean pressure coefficient on the cylinder was compared with the available experimental data. Different timesteps were used according to the adopted grid.

Table 4.2: List of computations performed for the flow around a circular cylinder at Re$= 5 \times 10^4$. The first line indicates experimental values of the Strouhal number St, the mean drag coefficient $\overline{C_D}$ and the base pressure coefficient C_{pb}. C: coarse; M: medium; F: fine; E: f_k estimate in Equation (3.57); L: Equation (3.56). The error on the Strouhal number corresponds to the sampling frequency adopted to evaluate the spectrum.

Run #	**Mesh**	f_k	$f_{k,\text{inf}}$	C_{PANS}	N_S	Δt	St	$\overline{C_D}$	$-C_{pb}$
Exp.							**0.18-0.21**	**1.15-1.25**	**1.2**
C1	Coarse	1.0	-	-	-	0.01	0.235 ± 0.007	1.004	1.847
C2	Coarse	0.6	-	-	-	0.01	0.200 ± 0.005	1.632	1.654
C3	Coarse	0.4	-	-	-	0.01	0.193 ± 0.006	1.549	1.566
C4	Coarse	0.2	-	-	-	0.01	0.191 ± 0.004	1.549	1.570
M1	Medium	1.0	-	-	-	0.01	0.244 ± 0.010	1.049	1.757
M2	Medium	0.6	-	-	-	0.01	0.181 ± 0.015	1.554	1.493
M3	Medium	0.4	-	-	-	0.025	0.229 ± 0.008	1.508	1.446
M4	Medium	0.4	-	-	-	0.01	0.182 ± 0.005	1.404	1.342
M5	Medium	0.4	-	-	-	0.005	0.186 ± 0.010	1.437	1.414
M6	Medium	0.2	-	-	-	0.01	0.178 ± 0.005	1.460	1.369
F1	Fine	0.4	-	-	-	0.01	0.180 ± 0.015	1.498	1.427
F2	Fine	0.2	-	-	-	0.1	0.178 ± 0.007	1.151	1.206
F3	Fine	0.2	-	-	-	0.01	0.180 ± 0.009	1.369	1.210
F4	Fine	0.2	-	-	-	0.005	0.176 ± 0.010	1.212	1.239
EM1	Medium	Eq. 3.57	0.6	-	-	0.01	0.198 ± 0.013	1.437	1.683
EM2	Medium	Eq. 3.57	0.4	-	-	0.01	0.187 ± 0.006	1.421	1.565
EF1	Fine	Eq. 3.57	0.4	-	-	0.01	0.187 ± 0.012	1.220	1.334
EM3	Medium	Eq. 3.57	0.2	-	-	0.01	0.186 ± 0.015	1.357	1.547
EF2	Fine	Eq. 3.57	0.2	-	-	0.01	0.203 ± 0.011	1.201	1.316
EF3	Fine	Eq. 3.57	0.2	-	-	0.0025	0.205 ± 0.014	1.184	1.285
EF100	Fine	Eq. 3.57	0.2	-	100	0.005	0.198 ± 0.013	1.437	1.683
LM1	Medium	Eq. 3.56	0.2	0.5	-	0.01	0.211 ± 0.009	1.124	1.508
LM2	Medium	Eq. 3.56	0.2	0.3	-	0.01	0.192 ± 0.007	1.309	1.553
LM3	Medium	Eq. 3.56	0.2	0.1	-	0.01	0.174 ± 0.007	1.425	1.410
LF100	Fine	Eq. 3.62	0.2	3.33	100	0.005	0.195 ± 0.010	1.379	1.525
LF200	Fine	Eq. 3.62	0.2	3.33	200	0.005	0.175 ± 0.010	1.323	1.459
LF400	Fine	Eq. 3.62	0.2	3.33	400	0.005	0.195 ± 0.010	1.320	1.379
LF800	Fine	Eq. 3.62	0.2	3.33	800	0.005	0.185 ± 0.010	1.416	1.334
LF100T1	Fine	Eq. 3.62 $+f_{k,T}$	0.2	3.33	100	0.01	0.180 ± 0.006	1.270	1.416
LF100T2	Fine	Eq. 3.62 $+f_{k,T}$	0.2	3.33	100	0.05	0.191 ± 0.003	1.246	1.323

4.2 Results

In this section, the results for the constant f_k approach are first presented. Then, the two dynamic estimates of Section 3.4.1 and Section 3.4.2 are tested for the configuration under analysis. Finally, the new proposed estimates are adopted, and the basic working principle is described.

4.2.1 Constant f_k

Here, the constant approach is adopted, and the results for different values of f_k are presented. As explained in Section 3.4, the f_k parameter governs the reduction of eddy viscosity, and the flow resolution increases with smaller values of f_k. An example is given in Figure 4.2, displaying the Q-Criterion isosurfaces ($Q = 0.1$) for the runs on the medium grid and $\Delta t = 0.01$. The size of the resolved structures diminishes with smaller f_k values. In the URANS case ($f_k = 1$), the spanwise velocity remains zero and no three-dimensionality was found. As expected, modelling the entire spectrum resulted in a dissipative behaviour, with no triggered crossflow. Nevertheless, because of the strong unsteady nature of the flow, URANS still predicted 2D vortex shedding. In the other cases, crossflow was increasingly promoted with decreasing f_k. The boundary layer was more prone to separation for lower values of the eddy viscosity. This resulted in earlier separation and lower values of the base pressure coefficient C_{pb}. Averages of the wall pressure on half of the solid surface were computed and compared to the experiments in Figure 4.3. The results depend on both grid size and f_k values. Nevertheless, some conclusions can be drawn from this preliminary analysis. The URANS simulations are mesh converged. Changes between the coarse and medium grids are negligible. On the other hand, PANS simulations are strongly depending on both grid size and f_k. The figure suggests that the smaller f_k the earlier the separation and the better the prediction. On the other hand, a reduction of f_k, must be accompanied by a mesh refinement to improve the agreement with the experiments. This is expected, as a reduction of f_k coincides with the shift from a RANS solution to an LES-like solution. Indeed, for the case with $f_k = 0.2$, the fine grid performed better than the others, and the comparison with the experiment was improved. The smaller the grid size, the higher the resolution, as shown in Figure 4.4, where the iso-Q-Criterion surfaces are shown for the three grids with $f_k = 0.2$. The development of turbulence on the second part of the cylinder ($\theta > 90$ deg) allowed for the desired pressure recovery. Alongside the grid sensitivity, a timestep sensitivity was carried out for the medium and fine grids using f_k equal to 0.4 and 0.2, respectively. Figure 4.5 shows that values of $\Delta t * U_\infty / D$ of 0.01 and 0.005 can be selected for the medium and fine grids, respectively.

This preliminary study suggests that PANS can be used for the prediction of the turbulent flow for this test case. Nevertheless, care must be taken in the simulation setup. To correctly predict the separation point, the eddy viscosity must be adequately reduced according to the mesh size. In parallel, a mesh refinement introduced the need for timestep reduction. For this test case, the

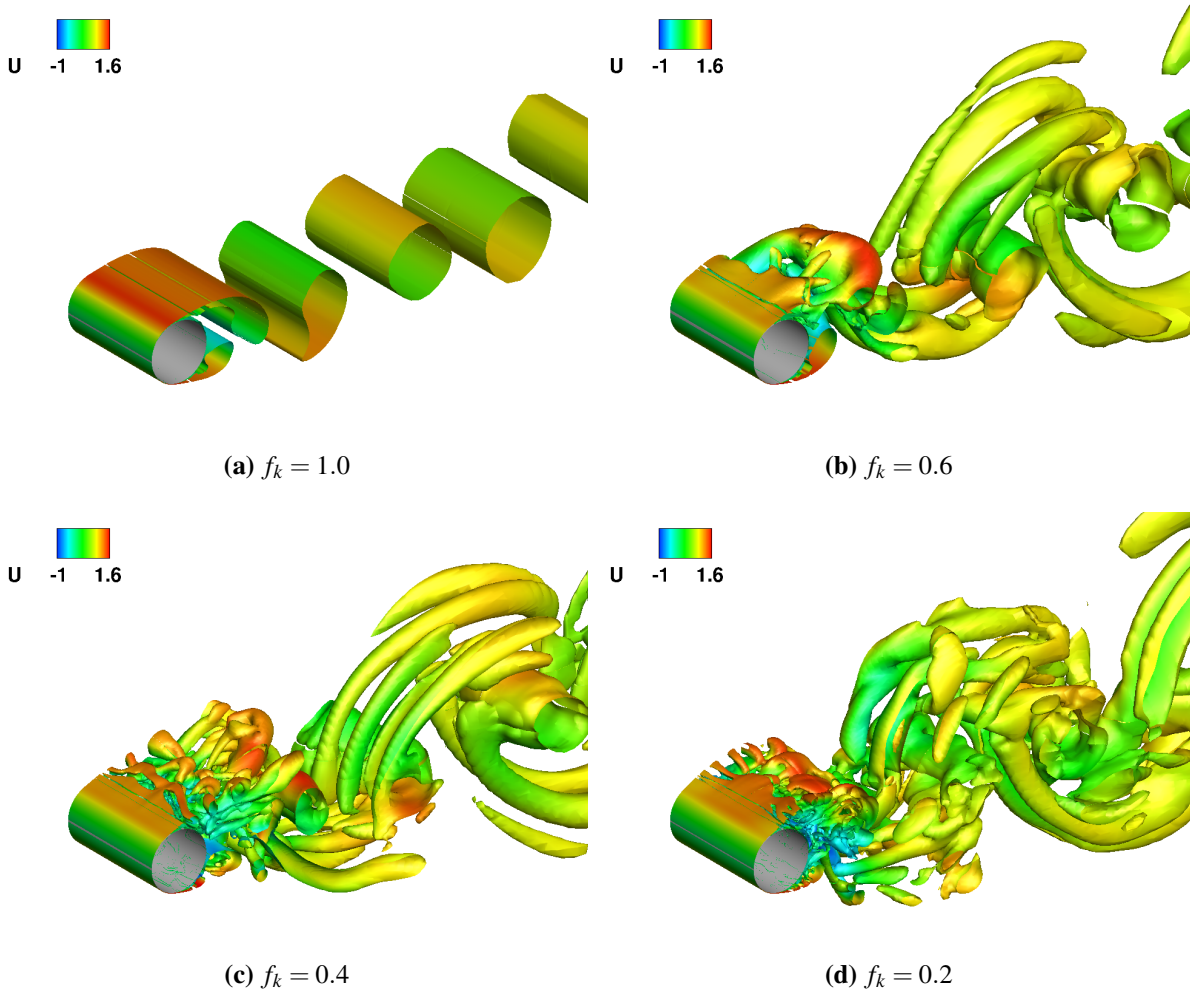

(a) $f_k = 1.0$ **(b)** $f_k = 0.6$

(c) $f_k = 0.4$ **(d)** $f_k = 0.2$

Figure 4.2: Q-Criterion isosurfaces ($Q = 0.1$) for the runs on the medium grid and $\Delta t = 0.01$ and several f_k.

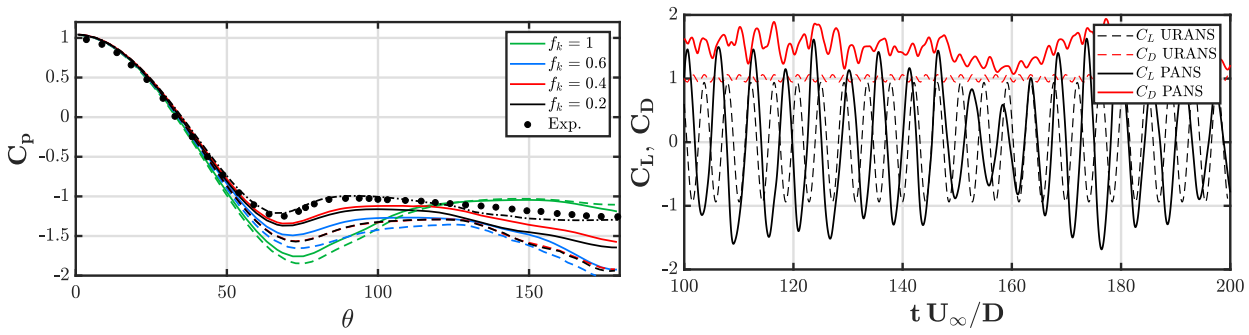

Figure 4.3: Mean pressure coefficient on the upper half of the cylinder for the runs on different grids, $\Delta t = 0.01$ and several f_k. Dotted lines: coarse grid; solid lines: medium grid; dash-dotted lines: fine grid; dots: experiments.

simulation on a fine mesh with $f_k = 0.2$ and $\Delta t * U_\infty / D = 0.005$ provided the best agreement with the experiments. Adopting intermediate values of f_k, coarser grids, or smaller time steps led to improved results with respect to URANS using the same spatio-temporal grids (see Figure 4.6.

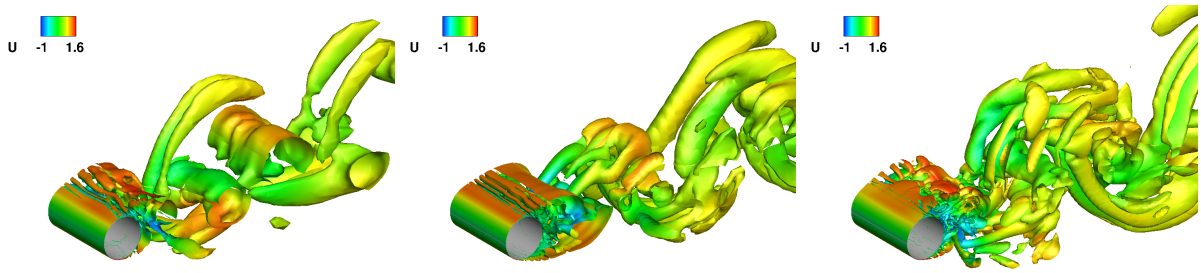

(a) Coarse **(b)** Medium **(c)** Fine

Figure 4.4: Q-Criterion isosurfaces ($Q = 0.1$) for the runs on different grids, $\Delta t = 0.01$ and $f_k = 0.2$.

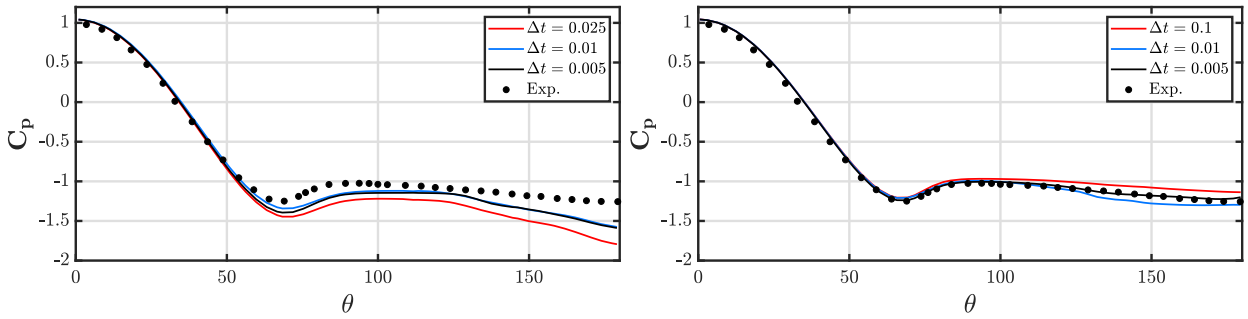

Figure 4.5: Mean pressure coefficient on the upper half of the cylinder for different timesteps. Left: medium grid, $f_k = 0.4$; right: fine grid, $f_k = 0.2$.

The scatter in the results suggests that a constant approach needs a preliminary calibration of the f_k parameter. Therefore, a different estimate of f_k is required for the flow under analysis.

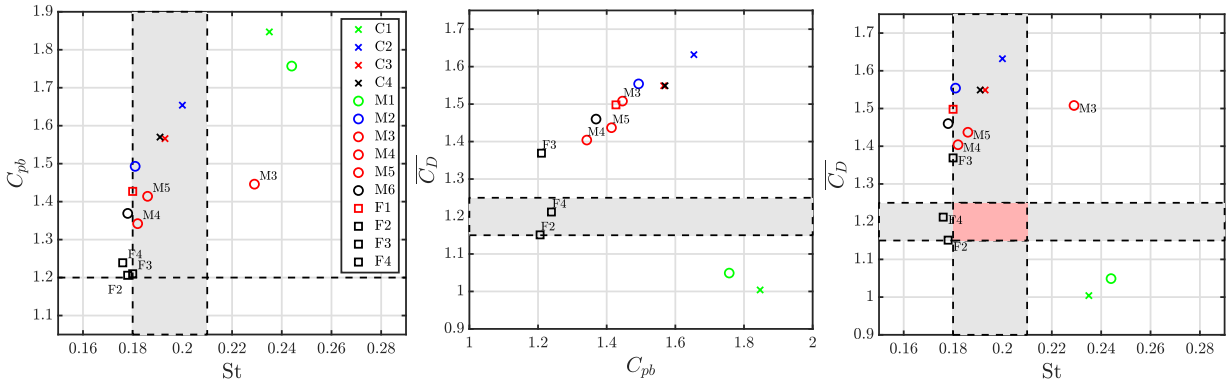

Figure 4.6: Comparison of mean drag coefficient, Strouhal number and base pressure coefficient with the experimental values for different simulations at constant f_k.

4.2.2 Dynamic f_k estimates

The estimate of Luo [164] is first investigated. In this case, a constant C_{PANS} was chosen to replace the original multiplication factor of $1/\sqrt{C_\mu}$ to compensate for the high values of f_k obtained.

Keeping fixed grid and timestep, the assumed C_{PANS} values were 0.5, 0.3, and 0.1, as in [163, 164]. Figure 4.7 shows the mean f_k distributions around the cylinder for the three cases. Qualitatively,

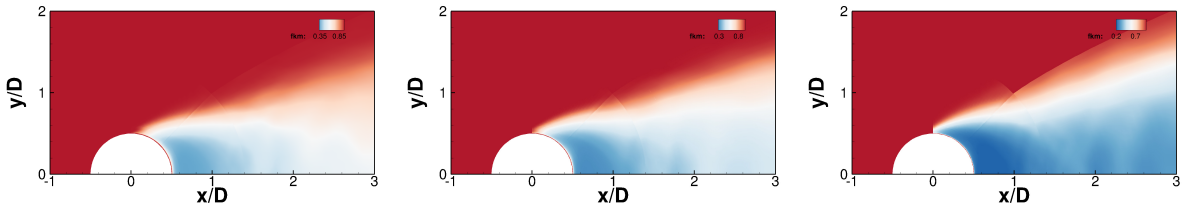

(a) $C_{\text{PANS}} = 0.5$ **(b)** $C_{\text{PANS}} = 0.3$ **(c)** $C_{\text{PANS}} = 0.1$

Figure 4.7: Mean f_k distribution for the medium grid, $\Delta t = 0.01$ and f_k in Equation (3.56) with different C_{PANS} .

the distributions are similar to each other. As expected, $f_k = 1$ in the far-field and on the wall, where $k \to 0$, $\Lambda_u \to 0$. The effect is analogous to that of the popular approaches of the DES family [232, 242, 243], where the transition from RANS ($f_k = 1$) to LES ($f_k < 1$) occurs somewhere near the upper boundary layer end. Behind the cylinder, the turbulent content is high and f_k drastically reduces until it hits the lower value prescribed (0.2 in this study). The results in Figure 4.8 show strong dependence on the coefficient C_{PANS} coefficient. A lower C_{PANS} resulted in lower values of f_k at the highest and lowest points of the cylinder, and therefore earlier separation. Once again, the model requires an *a priori* calibration of the PANS coefficient. Even on the fine grid, the estimate preserving the original constant $1/\sqrt{C_\mu}$ led to high values of f_k, confirming that the original estimate is too conservative.

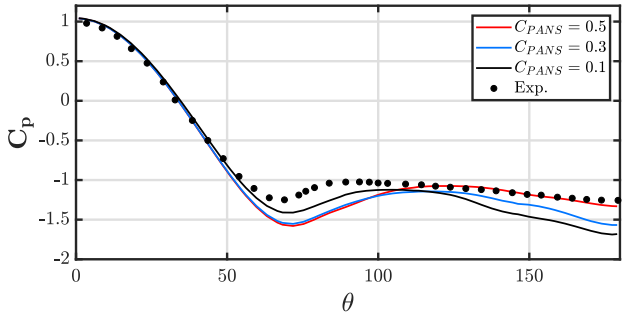

Figure 4.8: Mean C_p (left) and longitudinal velocity in the wake (right) for the medium grid, $\Delta t = 0.01$ and f_k of Equation (3.56) with different C_{PANS} .

The estimate of Equation (3.57) is based on the same ratio between the turbulence length scale and the grid size. Conversely, no constants are needed. Here, attention is paid to the effect of the lower clip value of f_k, called $f_{k,\text{min}}$. Ideally, f_k must be bounded between 0 and 1, and in the estimate in Equation (3.57), it falls within the desired range. Nevertheless, f_k can be clipped to prevent numerical instabilities where its value approaches zero. Figure 4.9, shows the parameter distribution around the cylinder for three different values of $f_{k,\text{min}}$. The mean distribution in the

low-pressure regions is unaffected by $f_{k,\min}$. Conversely, behind the cylinder, f_k reaches different values according to the clip. As a consequence, the investigated parameter does not affect the base pressure coefficient nor the separation point, but it helps improve the prediction of the pressure coefficient and the velocity in the wake (see. Figure 4.9). As it decreases with the grid size, f_k

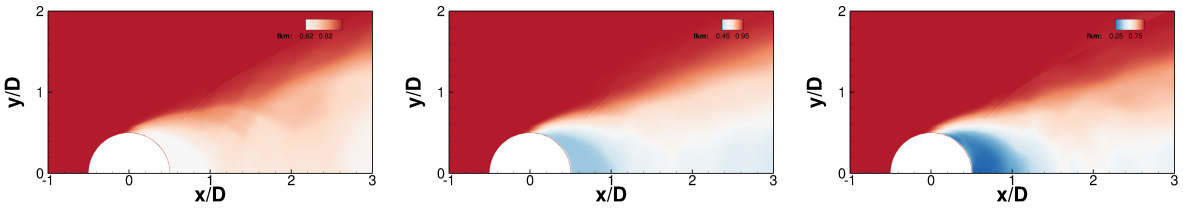

(a) $f_{k,\min} = 0.6$ **(b)** $f_{k,\min} = 0.4$ **(c)** $f_{k,\min} = 0.2$

Figure 4.9: Mean f_k distribution for the medium grid, $\Delta t = 0.01$ and f_k in Equation (3.57) for different $f_{k,\min}$.

was overall lowered when adopting a finer grid. The overall reduction of the modelled turbulent kinetic energy results in a better agreement with the experiments. For this case, a low clip value is therefore recommended and the best results were obtained for $f_{k,\min}$ equal to 0.2. The comparison

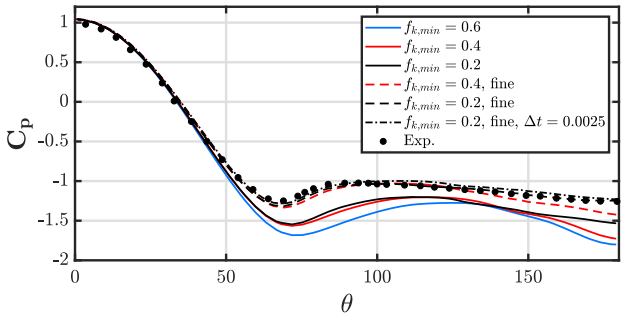

Figure 4.10: Mean C_p and longitudinal velocity in the wake for the medium grid, $\Delta t = 0.01$ and f_k in Equation (3.57) for different $f_{k,\min}$.

with the experiments in Figure 4.11 shows the improved vortex shedding frequency prediction by adopting a fine grid with respect to the constant f_k case. For constant f_k, it was not possible to obtain good agreement in terms of both drag coefficient and Strouhal number. Now, by adopting a fine grid, both quantities fall within the ranges indicated by the experiments. In the previous case, the Strouhal number was influenced by f_k. The lower f_k, the lower the Strouhal number associated with vortex shedding. Now, as the f_k distribution on the first half of the cylinder is independent of $f_{k,\min}$, the Sthroual number does not vary with $f_{k,\min}$.

4.2.3 Results using runtime statistics

In this section, the accuracy of runtime statistics evaluation through the method of Section 3.4.1 is assessed. This is used for the runtime computations of total turbulent kinetic energy. Figure 4.12,

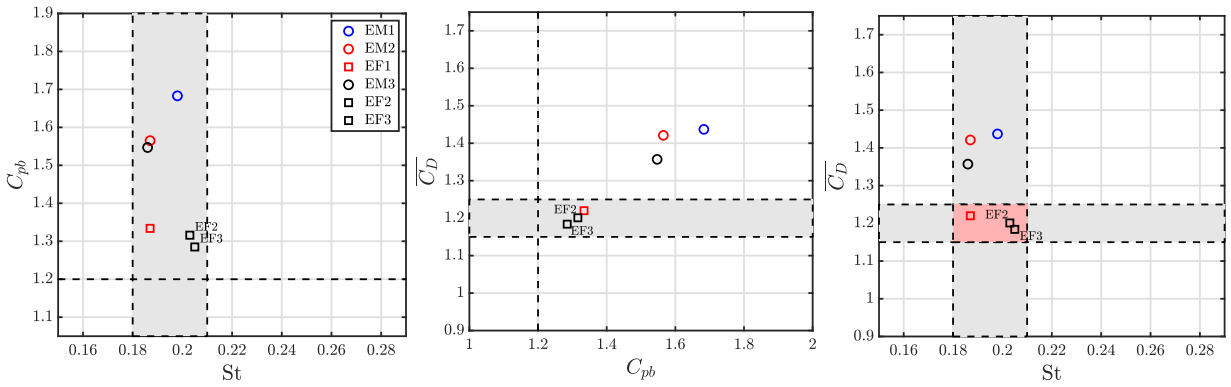

Figure 4.11: Comparison of mean drag coefficient, Strouhal number and base pressure coefficient with the experimental values for different simulations using the f_k estimate of Equation (3.57).

left, shows the computed mean value of the horizontal velocity component u (dashed, black line) over a number of samples N_S. The red lines represent the mean value computed by means of Equation (3.67), while the blue ones are the values computed *a posteriori*. Four different N_S were adopted, ranging from 100 to 800. The signal was extracted from a probe located in the wake of the cylinder for the EF3 computation. For this case, the vortex shedding period corresponds to about 2000 computational timesteps. In Figure 4.12, it is not possible to identify a dominant frequency or a strong periodicity. The PSD of the signal, shown in Figure 4.13 (red line, right plot), does not show any peak associated with vortex shedding. For comparison purposes, the PSD from another probe displaying a well-defined peak in the spectrum is shown in blue. Both signals are shown in Figure 4.13 (a), over a shorter time window. In the same figure, the labelled black lines indicate the duration of the sampling window with respect to the entire time trace. In the right plot, the range of frequencies resolved from the adopted time window is indicated. The need to evaluate runtime turbulent kinetic energy on a restricted time window stems from the fact that the second moments are strongly influenced by the prominent flow periodicity. Figure 4.12 (b), shows the $\langle u'u' \rangle$ component for different values of N_S. The green lines show the same quantity computed across the whole simulation. Overall, the "total" statistics are above the ones computed over a restricted number of timesteps. The reason is that the self-induced instability leads to large changes in the velocity field, mostly associated with large scales, which results in a higher deviation from the mean values. As a result, the turbulent kinetic energy is overestimated. Therefore, the idea is to neglect the contribution given by the fundamental frequency associated with large scales, and focus on the effect of smaller scales. The selected time windows are, indeed, smaller than the ones associated with the fundamental frequency ($\simeq 2000$). The statistics in Figure 4.12, left, suggest that the smaller N_S the more the mean values adhere to the time signal. At the same time, the computed second-order moments in the right plots are lower. In all cases, the approximated $\langle u'u' \rangle$ overestimates the real one, by a factor that decreases with increasing N_S. From the PSD, values of $N_S = 400$ and 800 seem appropriate, as the range of resolved frequencies contains the part of the

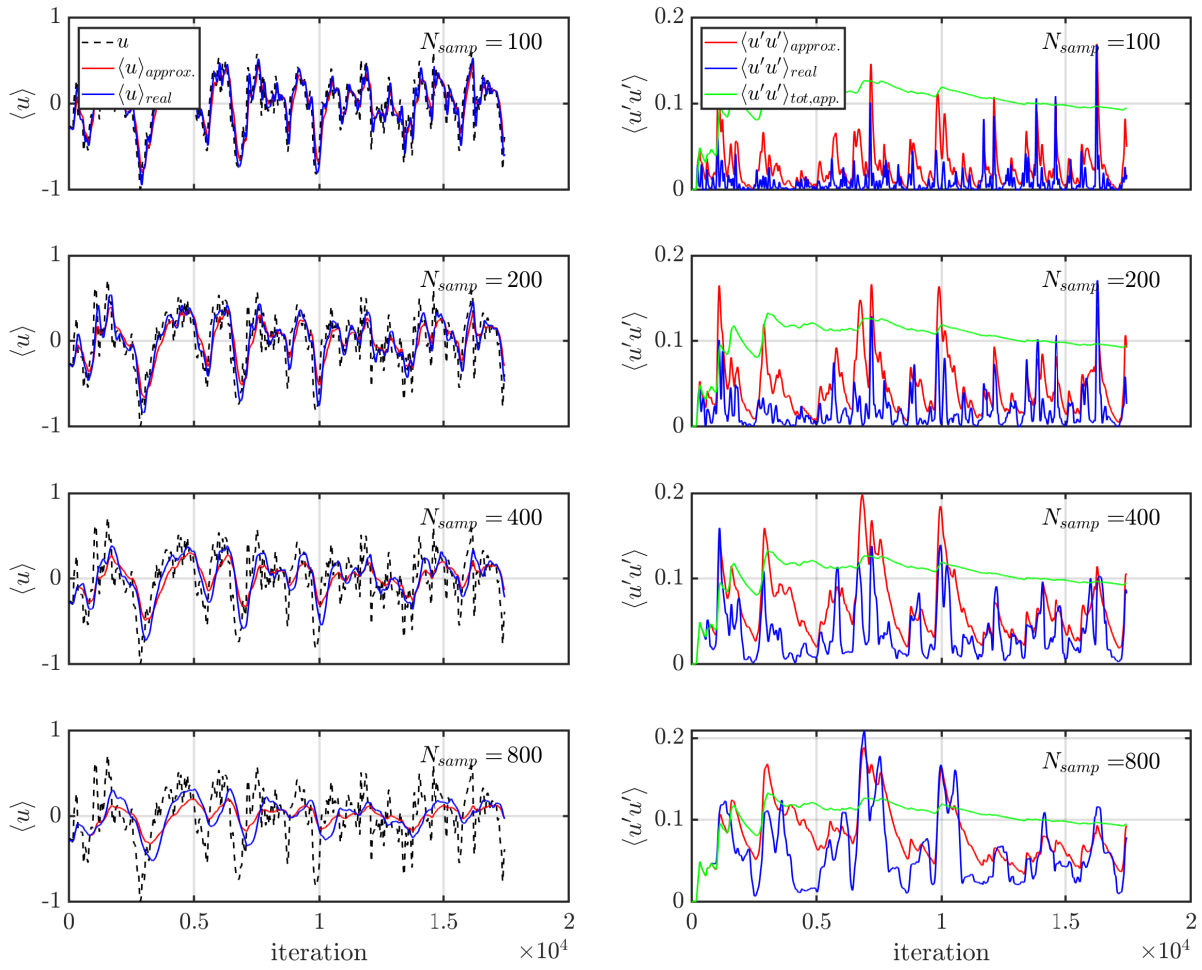

(a) $\langle u \rangle$ **(b)** $\langle u'u' \rangle$

Figure 4.12: Computed mean value and variance of the horizontal velocity component on a probe around a laminar cylinder at $\mathrm{Re}_D = 5 \times 10^4$ using Equation (3.67) for different N_S. The comparison with the exact statistics is shown.

spectrum obeying the $-5/3$ power law. The lower values of N_S mostly correspond to frequencies in the decaying part of the spectrum.

Figure 4.14 shows the mean value and RMS of f_k for different N_S values evaluated on around 20 vortex shedding periods. The mean distribution differs significantly from the previous dynamic estimates. f_k assumes small values in the far field and on the first part of the cylinder, and the reason can be explained by looking at Equation (3.73). In those regions, both k_u and ω_u approach zero, while at the numerator, the presence of small fluctuations results in $k_{res} >> k_u$. Therefore, the turbulent length scale grows, leading to a reduction of f_k. On the other hand, in the boundary layer and in the mixing layer, Λ assumes smaller values, leading to $f_k \to 1$, as expected. With an increase in N_S, the resolved part of turbulent kinetic energy grows, leading to an overall reduction of f_k (see, Figure 4.14 (d), top half). The bottom halves of Figure 4.14 show the variance of

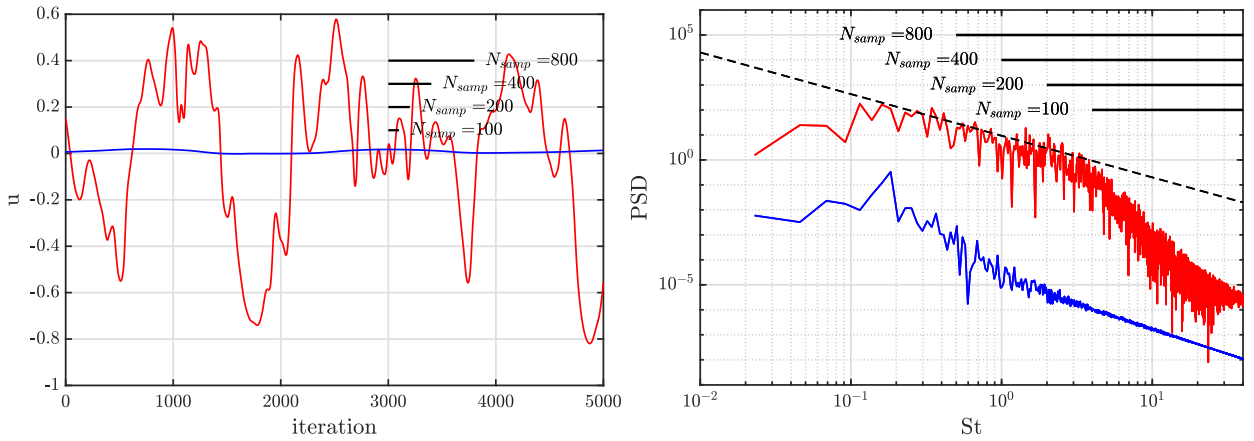

Figure 4.13: Left: horizontal velocity component over a restricted time window (5000 time steps). In black: duration of the selected time window. Right: power spectral density of the signals on the left. In black: range of frequencies solved using the selected N_S. Red: probe placed in the cylinder wake; blue: probe placed on the cylinder surface, ahead of the separation point.

f_k over a time window of the same length. Higher values are observed for small N_S, when the statistics are computed over a shorter time window and follow the detachment of vortices on the second half of the cylinder. As N_S increases, the second-order statistics of the velocity become time-independent. For the higher value, f_k is almost uniformly equal to its floor value. Around the region of vortex formation, the RMS is little, showing the inability to filter the contribution to k of vortex shedding. Smaller N_S lead to more reasonable results. This can be explained in

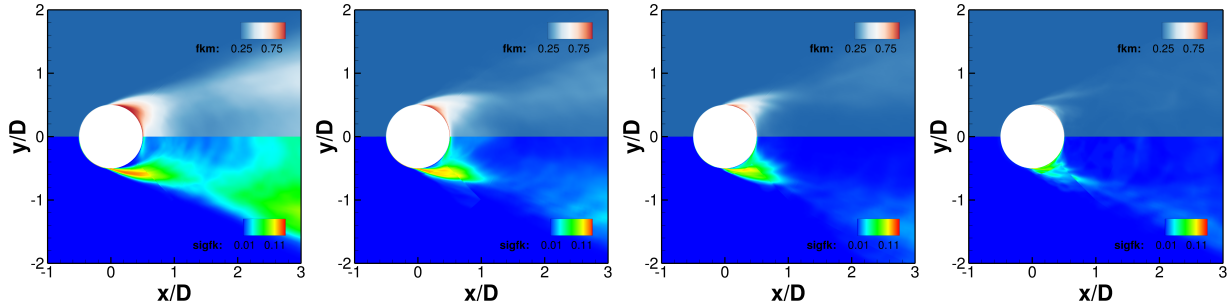

(a) $N_S = 100$ **(b)** $N_S = 200$ **(c)** $N_S = 400$ **(d)** $N_S = 800$

Figure 4.14: Mean (top half) f_k and RMS (bottom half) using the estimate in Section 3.4.1 for different values of N_S. The statistics were computed using 201 equispaced samples over the simulation window.

Figure 4.15, showing the instantaneous modelled (top) and resolved (bottom) turbulent kinetic energy distributions. In Figure 4.15, the bottom halves were mirrored to better compare k_{res} and k_u. The snapshot was selected in correspondence to the shedding of a vortex to investigate the ability to discard the contribution given by large coherent structures, without neglecting that of turbulence. For increasing N_S (left to right), the amount of modelled turbulent kinetic energy is reduced, especially in the vicinity of the cylinder, where $f_k \to 1$. In all cases, the resolved part is

considerably higher than the modelled counterpart, leading to the aforementioned increase in Λ. The difference is exacerbated for high N_S, where the amount of resolved turbulent kinetic energy grows significantly. In Figure 4.15 (d), the k_{res} is high even in the region of vortex shedding, meaning that the aforementioned, desired effect was not achieved. Conversely, the cases at $N_S =$ 200 and 400 show a better behaviour.

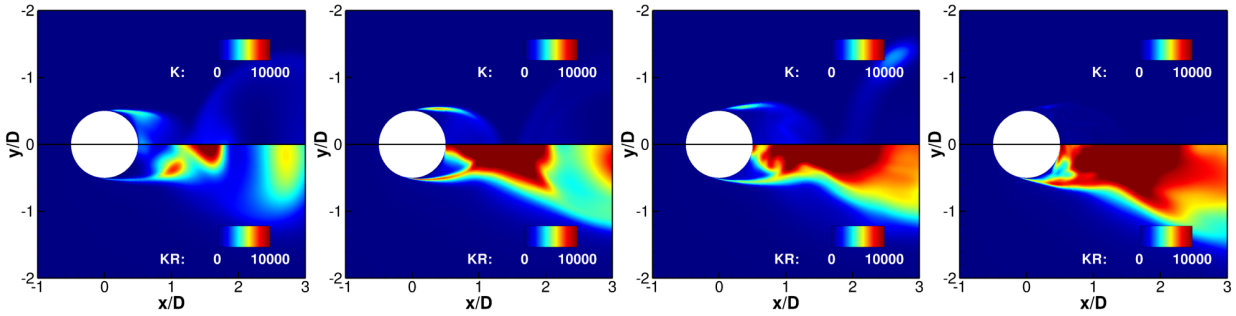

(a) $N_S = 100$ **(b)** $N_S = 200$ **(c)** $N_S = 400$ **(d)** $N_S = 800$

Figure 4.15: Instantaneous, modelled (top) and resolved (bottom) part of turbulent kinetic energy using the estimate in Section 3.4.1 for different values of N_S. Both halves of the images refer to the same semi-plane.

The results for the four cases were compared with those obtained using a constant $f_k = 0.2$, where the same value was used as $f_{k,min}$ for the dynamic estimates. Figure 4.16, left plot, shows the comparison in terms of pressure distribution. The higher N_S, the higher is $C_{p,b}$, i.e. the earlier the separation point. In the limit of $N_S = 800$, the distribution approaches that of the constant approach computation, as expected from the mean f_k distributions shown in Figure 4.14. Although this case

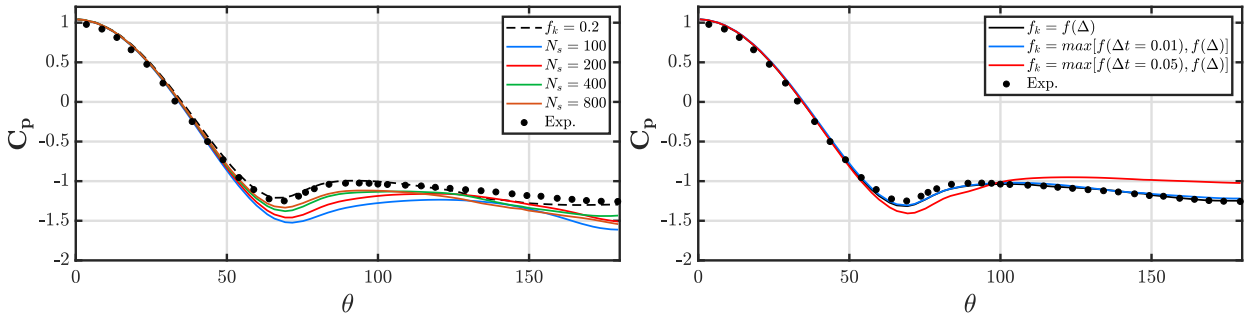

Figure 4.16: Mean C_p and longitudinal velocity in the wake for the fine grid, $\Delta t = 0.005$ and f_k as in Section 3.4.1.

provides the best agreement, it fails to select the right contribution to k. For this test case, we previously assessed that a significant reduction of eddy viscosity is beneficial for the prediction. Nevertheless, in cases with shallow separation, delaying the RANS-to-LES transition is beneficial to avoid early separation. In this view, for these latter, it might be reasonable to adopt higher N_S values. Moreover, values of $f_k \to 0$ in the incoming free stream may be beneficial when synthetic turbulence is added to simulate turbulent boundary layers.

For this case, using the estimate of Equation (3.57) with runtime statistic evaluation, led to excessively small values of f_k in the entire CFD domain.

4.2.4 Dynamic Estimates with Constraint on Δt

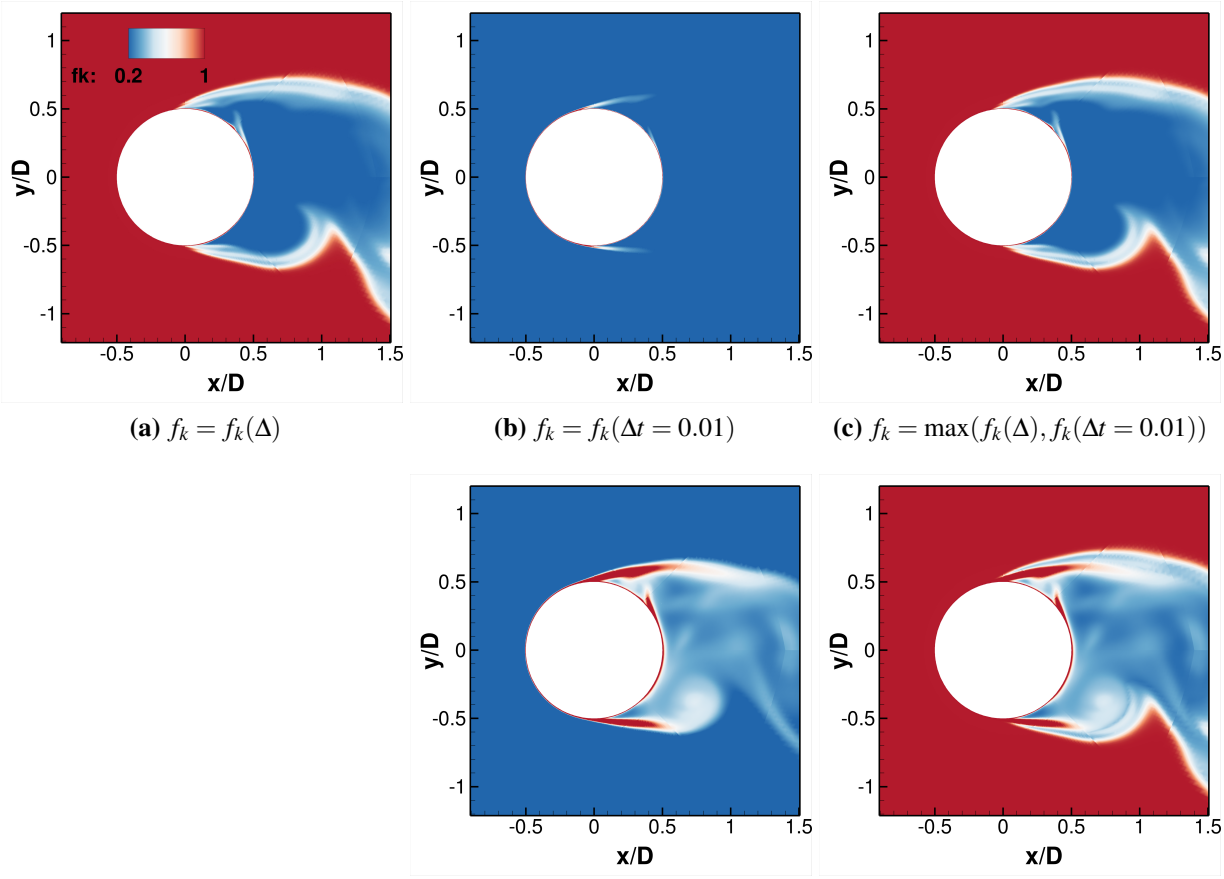

(a) $f_k = f_k(\Delta)$ **(b)** $f_k = f_k(\Delta t = 0.01)$ **(c)** $f_k = \max(f_k(\Delta), f_k(\Delta t = 0.01))$

(d) $f_k = f_k(\Delta t = 0.05)$ **(e)** $f_k = \max(f_k(\Delta), f_k(\Delta t = 0.05))$

Figure 4.17: Instantaneous f_k distributions around the circular cylinder at $\mathrm{Re}_D = 5 \times 10^4$ depending on the grid size (a), time step (b,d), and both (c,e).

In addition to the previous estimates of f_k, an application of the constraint described in Section 3.4 is given. The constraint on the time step introduced in Equation (3.70) is applied to limit the flow resolution in regions where the computational timestep is not fine enough to resolve fluctuations acting at smaller time scales. Indeed, f_k increases with the ratio $\Delta t / T_\Lambda$, i.e. for larger timesteps. The distribution given by the estimate of Equation (3.70) is shown in Figure 4.18, images (b) and (d), for different timesteps. Fig Figure 4.18 (a) shows the instantaneous estimate of Equation (3.57), while Figure 4.18, images (c) and (e), show the combined action of the estimates based on spatial and temporal discretisation. The new estimate gives $f_k \to 1$ in the boundary layer and the mixing layer, while $f_k \to 0$ in the far field where the time scales are much larger than the

computational timestep. In the wake, according to the adopted timestep, f_k assumes values between 0 and 1 for the coarser timestep, while it tends to zero for a finer timestep. In the first case, the new estimate causes an increase in f_k in selected flow regions, while in the second case, it does not modify the f_k distribution. This estimate can be used to obtain a more reasonable f_k distribution, given a selected spatio-temporal discretisation. On the other hand, the distribution given by this estimate can be used to assess the adequacy of the adopted timestep for a given grid, or vice versa.

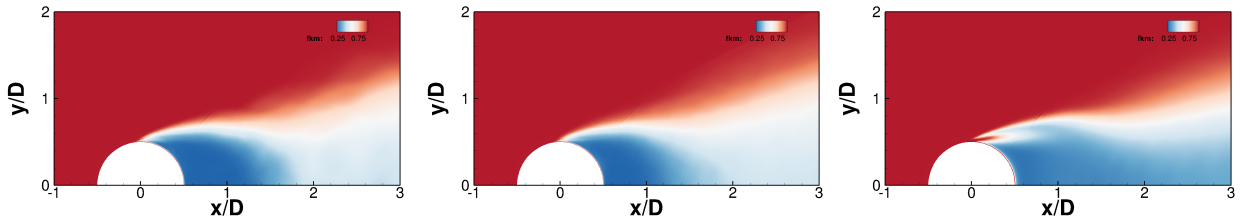

(a) $f_k = f_k(\Delta)$ **(b)** $f_k = \max(f_k(\Delta), f_k(\Delta t = 0.01))$ **(c)** $f_k = \max(f_k(\Delta), f_k(\Delta t = 0.05))$

Figure 4.18: Instantaneous f_k distributions around the circular cylinder at $\mathrm{Re}_D = 5 \times 10^4$ depending on the grid size (a), time step (b,d), and both (c,e).

From the mean f_k distributions in Figure 4.18, it is immediately noticed that differences only exist for a coarse Δt. The separation is delayed by increasing f_k at the top and the bottom of the cylinder. Moreover, the extent of the RANS region in the second part of the cylinder increased with respect to the case at fine Δt. In the wake, the region of low f_k extends further. The reason is that the modelled turbulent kinetic energy produced in the immediate vicinity of the cylinder, i.e. where $f_k(\Delta t = 0.05) > f_k(\Delta t = 0.01)$, is convected downstream. This leads to higher values of f_k in the wake.

In the mean pressure distribution (Figure 4.16, right plot), the adoption of the coarse timestep is reflected in a delay of the separation point. Moreover, the inability to resolve small temporal scales caused the pressure to be over-predicted. A similar result was shown in Figure 4.5, right plot, when a coarse timestep was adopted. Similarly to Section 4.2.3, the adoption of the new estimate led to a worsening in the prediction. Nevertheless, in this case, the method has the potential to be applied for mildly separated flows, as the estimate works in delaying the transition to scale-resolving mode close to the onset of separation.

4.3 Chapter Summary

In this chapter, several PANS calculations of the flow around a circular cylinder were carried out, and validated against the available experiments. A constant f_k approach was first considered to show **i)** the ability of PANS to accurately predict the flow for the investigated test case, and **ii)** show the strong dependence of the results on the adopted value f_k, CFD grid, and timestep. Among the dynamic approaches used in the literature, two were selected and applied to the case under analysis.

The estimate of Luo [164] given in Equation (3.56) sees the presence of an arbitrary multiplicative constant which allows for a homogeneous reduction of the eddy viscosity in the flow field. The results on a medium grid showed a desirable f_k distribution around the cylinder. The agreement with the experiments was strongly dependent on the value of the multiplicative constant, making the use of this estimate unpractical. The estimate of Elmiligui *et al.* [72] in Equation (3.57) showed good results, in agreement with the experiments, especially when adopting a fine grid and timestep.

Some new estimates were also proposed. The introduction of an arbitrary constant in Equation (3.56) comes from the difficulties in evaluating the total turbulent kinetic energy, as only the modelled part appears in the PANS equation. By computing runtime velocity first and second moments, we can estimate the value of the integral turbulent length scale required to eliminate the presence of the arbitrary constant in the estimate of Luo [164]. The statistics are computed over a limited number of samples to avoid accounting for the effect of the unsteady vortex shedding, i.e. the coherent structures, and only consider turbulence. The desired effect was achieved when sampling of $N_S/T_b \simeq 0.2 \div 0.4$. By adopting larger N_S the statistics accounted for the unsteadiness generated by the coherent structure, while small N_S led to small values of computed turbulent kinetic energy in the region of formation of vortices.

Finally, an additional constraint based on the adopted timestep was introduced to **i)** prevent f_k from assuming small vales in the viscous sub-layer and **ii)** avoid the eddy viscosity dropping in regions where the timestep is not small enough to solve turbulent developing at small time scales. For the present case, the adoption of the estimate led to a deterioration of the results. Nevertheless, the adopted timestep was not fine enough to resolve small scales in the separated region. This led to a more dissipative behaviour of the model. The behaviour of this model might be beneficial in cases with shallow separation, and further studies will be carried out to verify this eventuality.

Chapter 5

Numerical Simulation of (Quasi-)2D Transonic Buffet

The presence of shock-induced separation triggering a self-induced flow instability makes the prediction of buffet with CFD very challenging, introducing questions about the performance of different turbulence models in the RANS context, and the superiority between the available hybrid RANS-LES approaches. The frequencies associated with the nearly periodic shock motion are about two orders of magnitude lower than those associated with turbulence. Because of the large separation of scales and the need to compute several periods of oscillations, the presence of LES and DNS studies in the literature is still limited. As mentioned in Chapter 1, a number of authors investigated the ability of turbulence models to capture buffet around two- and three-dimensional configurations [16, 105, 108, 119, 258]. Appendix A presents a brief recap of buffet simulations using URANS for the configuration of interest in this work. In spite of the large number of works documented in the literature, there is no consensus on the ability of URANS to predict buffet. Therefore, many of the following works were carried out by using SRSs by means of hybrid RANS/LES approaches like those of the DES family [242, 243, 250]. These techniques showed improved results in representing the buffet physics on two- [59, 108, 117, 255] and three-dimensional [35, 170, 172] flows. On the other hand, the CPU time associated with those simulations was significantly higher because of the requirements on the temporal and spatial discretisation of the CFD domain. The scatter in the results obtained with the aforementioned techniques pushed us towards the adoption of PANS.

Among the test cases used for buffet computations, the OAT15A aerofoil has become particularly popular following the experimental campaign carried out at ONERA, results from which were partially published in the work of Jacquin *et al.* [126]. The buffet flow displayed some features of the conventional 2D buffet occurring on aerofoils. Indeed, the periodic shock-induced separation and re-attachment of the boundary layer were associated with a single frequency, corresponding to a Strouhal number of $St = 0.066$, which is in agreement with other works on 2D buffet. The

study on the influence of the wind tunnel walls from Thiery and Coustols [258] also showed little difference in terms of average quantities. Nonetheless, the flow exhibited a more complex behaviour both pre- and post-buffet onset, showing a strong impact of the wind-tunnel walls and the large wingspan. In the first case, the shock front bended under the influence of the lateral tunnel walls in a way similar to that shown in the work of Garbaruk *et al.* [89]. This caused the shock position to be over-predicted by every turbulence model (see e.g. [108]) in the unconfined configuration. Moreover, corner flow was not accounted for in 2D computations. At buffet conditions, the oil flow visualisations showed the presence of large 3D structures developing downstream of the shock, leading to an undulating shock front along the wingspan. The same phenomenon, developing even on unswept wings, was underlined in the work of Iovnovich & Raveh [122] and Plante *et al.* [210] where *buffet cells* were identified. These structures exhibit the alternation of positive and negative pressure disturbances propagating in the spanwise direction. Subsequent works on swept and unswept, untapered wings in wind tunnels from Sugioka *et al.* [252] and Sansica *et al.* [223] showed the presence of the same flow topology. In this view, we believe that the unconfined configuration with spanwise periodic boundary conditions, adopted in the majority of past CFD works, does not allow for a correct characterisation of the buffet flow dynamics.

Therefore, we retained the wind tunnel walls in the computations to investigate the effect that they have on the 3D buffet physics and provide, eventually, a fair comparison with the experiments. The large span adopted should allow for the development of large vortical structures in the boundary layer as underlined in the experiments.

So far, PANS simulations were rarely used for flows of practical relevance, as mainly canonical flow were investigated with this technique. An overview of past studies adopting PANS is given in Appendix B. In this chapter, we aim at investigating the ability of PANS to predict transonic buffet around the OAT15A aerofoil as a compromise between URANS and other more expensive approaches like those of the DES family. Attention is paid to the efficiency of the computational method over URANS, and the capability of PANS to capture the correct flow physics at a reasonable CPU cost. Recent experiments from different research groups [6, 47, 49, 142] provided new data for this configuration, pointing out differences with the previous investigation stemming from a modified experimental setup. Nevertheless, in this work, only the results of Jacquin *et al.* [126] will be used for comparison purposes. Section 5.1 presents the results for the flow around the OAT15A aerofoil, while Section 5.2 sees conclusions.

Table 5.1: Main features of the different grids used for computations.

Grid #	$N_{aerofoil}$	N_z	$\Delta z_{wall}/c$	$\Delta z_{max}/c$	N_y	$\Delta n_{aerofoil}/c$	$\Delta z_{walls}/c$	N_{wake}	$\Delta x_{TE}/c$	N_{tot}
M2	470	-	-	-	115	5×10^{-6}	-	220	5×10^{-6}	1.10×10^{5}
C3	405	76	2×10^{-6}	0.033	102	5×10^{-6}	5×10^{-3}	86	5×10^{-6}	$\simeq 5.03\times10^{6}$
M3	500	100	2×10^{-6}	0.025	114	5×10^{-6}	5×10^{-3}	120	5×10^{-6}	$\simeq 10\times10^{6}$
F3	510	164	2×10^{-6}	0.015	128	5×10^{-6}	5×10^{-3}	150	5×10^{-6}	$\simeq 16.70\times10^{6}$

5.1 Results

5.1.1 Experimental test case description

In the present study, the flow around the supercritical aerofoil OAT15A is investigated, that was studied experimentally by Jacquin *et al.* [125, 126] in the S3Ch wind tunnel of ONERA. The wing section had a chord of $c = 0.23$m and a span, coinciding with that of tunnel, of 0.78 m. The section had a thickness-to-chord ratio of $t/c = 0.123$ and a trailing edge thickness of 0.5% of the chord. The wing was mounted in a squared section wind tunnel, of nominal dimensions of $0.78\text{m}\times0.78\text{m}\times2.2\text{m}$. A wall adaptation technique based on steady flow hypothesis was used at the lower and upper walls to reproduce free-stream conditions, hence to minimise the interference of the facility on the aerofoil. Measurements were collected at free-stream Mach numbers in the range of 0.7-0.75, a chord-based Reynolds number of $\text{Re}_c = 3\times10^6$, and angle of attack in the range of 1.36 - 3.9 degrees. The adoption of static pressure measurements and Kulite sensors distributed in the vicinity of the mid-span section allowed to detect the occurrence of flow unsteadiness at an angle of attack of 3.1 degrees, culminating in a self-sustained shock-induced oscillation at an angle of 3.5 degrees. For the case at $\text{M} = 0.73$ and $\alpha = 3.5$ degrees, a LDV system was used to acquire velocity data and compute statistics. At all other flow conditions, the pressure measurements were complemented with oil-flow and schlieren visualisations.

In this work, the study is mainly focused on conditions with constant Mach number $\text{M} = 0.73$ and angles of attack of $\alpha = 2.5$, 3.5 and 3.9 degrees, representative of a statistically steady flow and two fully-established buffet flows, respectively.

5.1.2 CFD grids and numerical setup

Two configurations were analyzed. The first one, denoted 3D in Table 5.2, is a reproduction of half of the wind tunnel model used in the experimental campaign (see Figure 5.1). The grids adopted for this configuration are indicated as C3, M3, and F3 in Table 5.1.

The upper and lower walls were modelled as slip-walls, and the shape was extracted from a 2D RANS simulation, with free-stream conditions, to replicate the results of the adaptive technique

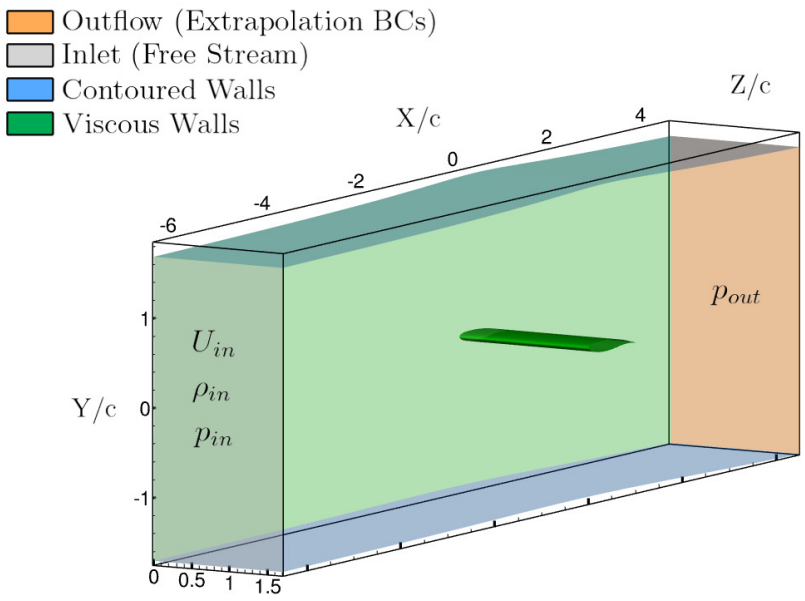

Figure 5.1: Computational domain with coloured by boundary conditions. The symmetry plane at $z/c = 1.7$ is not coloured.

used in the experimental campaign. In the study of Thiery and Coustols [258] the comparison between the confined and unconfined cases showed some differences and it is the main reason for accounting for the wind tunnel walls. As the adaptive walls in the experiments were shaped as streamlines, the adoption of slip conditions seems reasonable. This also allows for saving grid points required for the discretisation of a viscous boundary layer. Moreover, the separated flow region at the wing-wall junction triggers a three-dimensional behaviour that is not present in quasi-2D configurations with periodic boundary conditions with reduced spans [108, 117, 255].

The second configuration is called 2D in Table 5.2 and M2 in Table 5.1, and it was used for 2D preliminary computations. The aerofoil was no longer confined and free-stream values were applied at the far field, distant 80c from the aerofoil.

For both cases, at the aerofoil trailing edge, the same first cell spacing was used in both the normal and longitudinal directions to adequately describe the vortex detachment. At the solid sidewalls, the normal spacing is slightly finer than that on the aerofoil to obtain a value of Δy^+ below 1. The spacing on the slip walls is significantly coarser than that on the viscous walls. For the unsteady simulations, the convergence of the implicit scheme was based on the reduction of the flow field residual (by 3 orders of magnitude) with respect to the previous step. A maximum of 150 inner iterations were computed for each timestep.

Table 5.2: Computations performed at different angles of attack, on different grids, and using different timesteps. All computations are at $M_\infty = 0.73$ and $Re_c = 3 \times 10^6$. In the run ID, U stands for URANS, and P for PANS.

Run #	α	**2D/3D**	**Mesh**	f_k	$f_{k,\text{inf}}$	Δt	x_{tr}/c	$P_{\text{out}}/P_{\text{in}}$	Buffet
R2M25	2.5	2D	M2	-	-	steady	fully turb.	1.0	No
R3C25	2.5	3D	C3	-	-	steady	fully turb.	1.0	No
R3M25	2.5	3D	M3	-	-	steady	fully turb.	1.0	No
R3F25	2.5	3D	F3	-	-	steady	fully turb.	1.0	No
P2M25	2.5	2D	M2	$f_k = 0.7$	-	0.1	fully turb.	-	No
P3C25a	2.5	3D	C3	Eq. 3.56	0.6	0.1	fully turb.	1.0	No
P3C25b	2.5	3D	C3	Eq. 3.57	0.6	0.1	fully turb.	1.0	No
P3C25c	2.5	3D	C3	Eq. 3.57	0.6	0.025	fully turb.	1.0	No
P3C25d	2.5	3D	C3	Eq. 3.57	0.6	0.025	fully turb.	0.99	No
U3M25	2.5	3D	M3	1.0		0.025	fully turb.	1.0	No
P3M25a	2.5	3D	M3	Eq. 3.57	0.6	0.025	fully turb.	1.0	No
P3M25b	2.5	3D	M3	Eq. 3.57	0.6	0.01	fully turb.	1.0	No
P3M25c	2.5	3D	M3	Eq. 3.57	0.6	0.01	fully turb.	0.99	No
U3F25	2.5	3D	F3	1.0		0.025	fully turb.	1.0	No
P3F25a	2.5	3D	F3	Eq. 3.57	0.6	0.1	fully turb.	1.0	No
P3M25b	2.5	3D	F3	Eq. 3.57	0.6	0.01	fully turb.	1.0	No
P3M25c	2.5	3D	F3	Eq. 3.57	0.6	0.005	fully turb.	1.0	No
U3C35a	3.5	3D	C3	-	-	0.01	fully turb.	-	No
U3C35b	3.5	3D	C3	-	-	0.01	0.07	0.99	No
P2M35a	3.5	2D	M2	$f_k = 0.7$	-	0.01	fully turb.	-	Yes
P2M35b	3.5	2D	M2	$f_k = 0.7$	-	0.01	0.07	-	Yes
P3C35a	3.5	3D	C3	Eq. 3.56	0.4	0.01	fully turb.	1.0	Yes
P3C35b	3.5	3D	C3	Eq. 3.57	0.4	0.01	fully turb.	1.0	Yes
P3C35c	3.5	3D	C3	Eq. 3.57	0.4	0.01	fully turb.	0.99	Yes
P3C35d	3.5	3D	C3	Eq. 3.57	0.4	0.01	0.07	0.99	Yes
P3C35d	3.5	3D	C3	Eq. 3.57	0.4	0.01	0.25	0.99	Yes
P3C35e	3.5	3D	C3	Eq. 3.57	0.6	0.01	0.07	0.99	Yes
P3M35a	3.5	3D	M3	Eq. 3.57	0.6	0.01	0.07	0.99	Yes
P3M35b	3.5	3D	M3	Eq. 3.57	0.6	0.005	0.07	0.99	Yes
P3F35	3.5	3D	F3	Eq. 3.57	0.6	0.005	0.07	0.99	Yes
U2M39	3.9	2D	M2	-	-	0.1	fully turb.	-	No
P2M39	3.9	2D	M2	$f_k = 0.7$	-	0.1	fully turb.	-	Yes
P3C39a	3.9	3D	C3	Eq. 3.57	0.4	0.01	0.07	0.99	Yes
P3C39b	3.9	3D	C3	Eq. 3.57	0.6	0.01	0.07	0.99	Yes

5.1.3 Initial 2D study

An initial study on the 2D configuration was carried out. For this case, a constant formulation of $f_k = 0.7$ was adopted. This helped in the prediction of the shock oscillation, compensating for the inability of the SST model to predict buffet, in this case, and condition, as already documented in [207,209]. The effect of the inflow turbulence value, sustainability term, and laminar-to-turbulence transition were investigated. Figure 5.2 reveals how the addition of the transition at the 7% of the chord allowed for a better prediction of the RMS peak and trailing edge RMS. The sustainability term of Spalart and Rumsey [244], on the other hand, led to a slightly upstream shock position, and a high level of unsteadiness at the trailing edge. Because of the limited extent of the wind tunnel configuration, this correction was not applied in the following 3D study. The level of free-stream turbulence did not play a major role in the prediction of the mean shock position, and slightly influenced the peak value of the RMS. In conjunction with transition fixed at $x_{tr}/c = 0.07$, a turbulent-to-molecular eddy viscosity ratio of 10 led to the best agreement with the experiments and was used for the following 3D campaign.

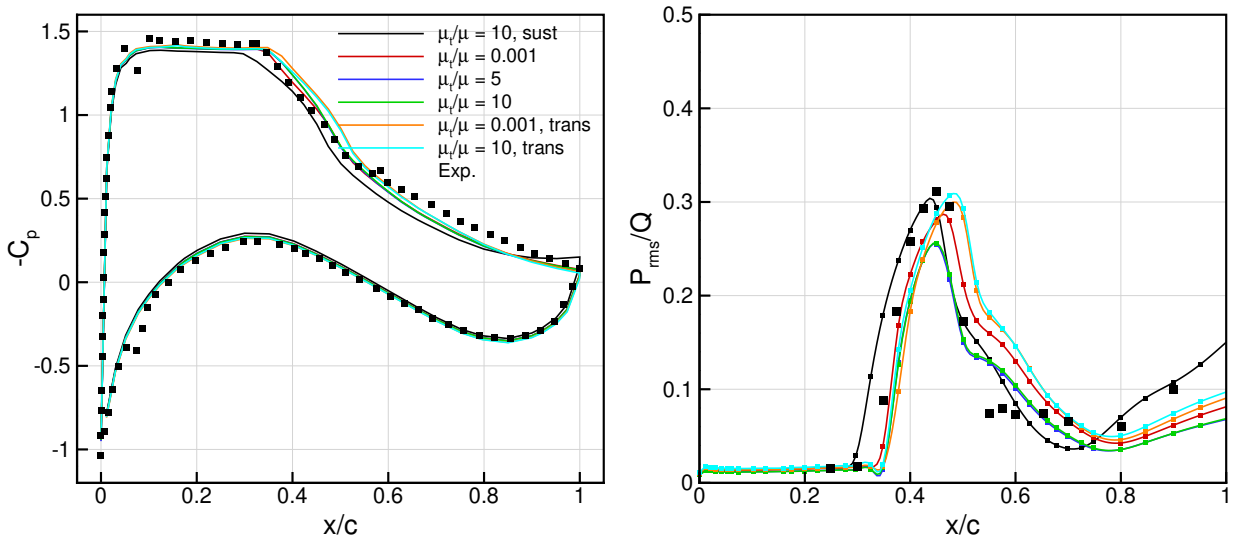

Figure 5.2: Left: time-averaged pressure coefficient at $\alpha = 3.5$ deg; right: root means square of the pressure. Experiments from [126].

5.1.4 Pre-buffet flow

In principle, SRSs should be able to reproduce the RANS solution once the mean solution is computed. In reality, because of the higher accuracy of SRSs, the results can depart from RANS, especially if the flow is highly unsteady. For the statistically steady flow at $\alpha = 2.5$ deg, the aim is to recover the RANS solution, within a certain tolerance, with the use of PANS.

Figure 5.3, right plot, was taken from the converged URANS solution and underlines one of the

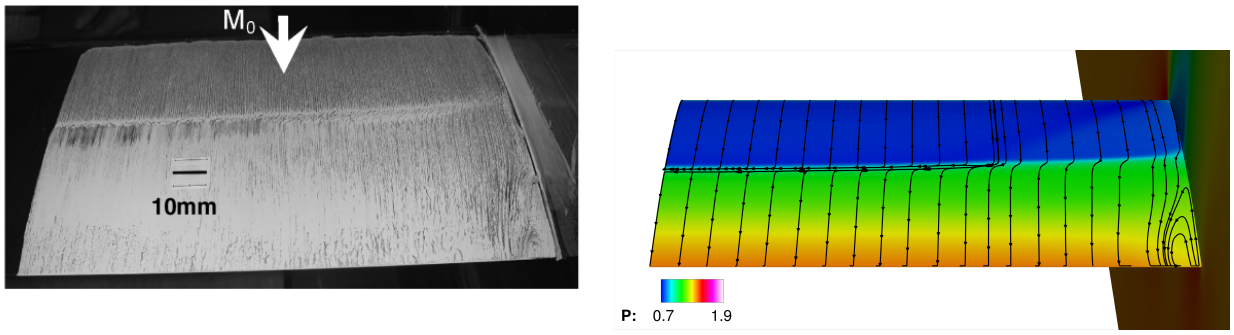

Figure 5.3: Left: oil flow visualisation around the OAT15A (picture taken from [126]) at $\alpha = 2.5$ deg; right: friction lines and surface pressure contour from CFD.

challenges of this test case by displaying the friction lines and surface pressure contour. The shock position can be detected by the negative values of the streamwise component of the stress tensor at the surface or, going toward the sidewall, from a sudden deflection of the friction lines. As the flow here exhibits a small separation at the shock foot, the pressure contour helps locate the shock. The shock bends when approaching the sidewalls because of viscous effects. Together with this, a region of separated flow is confined within 10% of the span, in agreement with the experimental results in the left image.

Moreover, because of the viscous sidewall, the turbulence level in the boundary layer grows as it approaches the aerofoil. This coincides with a growth in the turbulence length scales and a following reduction of f_k at the wall. In principle, the behaviour of the method is correct since f_k is lowered in regions of high turbulence content, but in this case, it would require a smaller timestep to resolve all flow structures developing at the wall-aerofoil junction. Therefore, we exploited

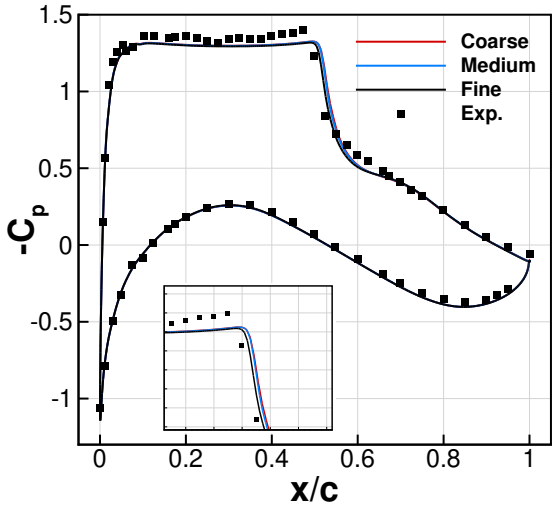

Figure 5.4: Pressure coefficient around the OAT15A at $\alpha = 2.5$ deg using URANS. Experiments of [126].

the multi-block grid to impose a RANS treatment in the very first layer of blocks on the wall.

This avoided unnecessary costs to discretise the sidewall region. This is further justified by the experiments [126], stating that the separated flow region extent was almost constant over a buffet period.

Figure 5.4 shows the comparison of the pressure coefficient C_p around the aerofoil with the experiments using URANS. The pressure was extracted at the same location of the pressure sensors used in the wind tunnel model. The left plot shows the results from URANS computations on different grids. Figure 5.5 shows the same quantities from PANS simulations, using the estimate in Equation (3.57) with $f_{k,\text{inf}} = 0.6$ and different grids. The back pressure was reduced by 1% with respect to the inlet value. This choice was motivated by the work of Thiery and Coustols [258], which shows experimental and numerical results for the case under analysis. In the current work, the shock position was slightly influenced by the grid adopted. As the adopted estimate accounts for the local grid size, f_k was lowered for finer grids. This resulted in a slight difference in the shock position, as a reduced eddy viscosity promoted boundary layer separation. A lower back pressure resulted in a pressure gap on both sides of the aerofoil. Nevertheless, a pressure difference between the inlet and outlet sections is required to counteract the viscous effect of the wind tunnel walls. By imposing such a difference, shock oscillations are also promoted.

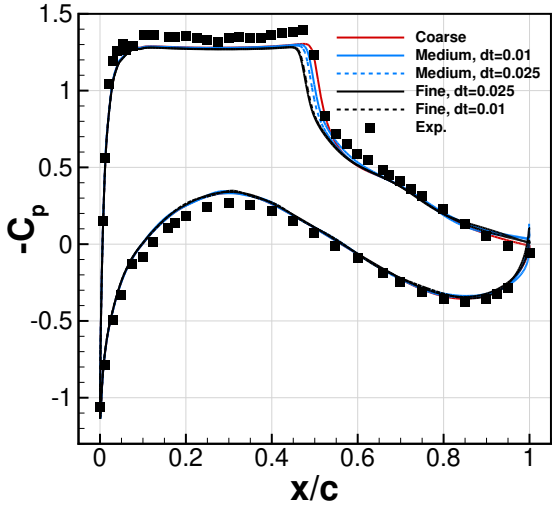

Figure 5.5: Pressure coefficient around the OAT15A at $\alpha = 2.5$ deg using PANS. Experiments of [126].

5.1.5 Fully Buffeting Flow

The buffet case is now investigated. Several simulations were performed at $\alpha = 3.5$ and 3.9 degrees, using different grids and time steps. The effect of some parameters was investigated to find the correct simulation setup. In particular, the transition location and wind tunnel back pressure were varied. Moreover, the comparison between the estimates of f_k introduced in the previous section is shown. Where not specified, the coarser grid of Table 5.1 was used as it proved able to correctly

predict the oscillatory behaviour of the solution. A comparison with finer grids is then shown.

f_k investigation

Here the different f_k distributions were compared. A previous study [207] revealed that the optimal value of C_{PANS} for the actual configuration and grid size is 0.5 when the estimate of Equation (3.56) was used. That value allowed for the desired reduction of eddy viscosity in the region around the trailing edge, and the formation of two distinct separated flow regions, one at the wing-wall junction and the other at the trailing edge. Higher values of the constant resulted in no boundary layer separation at the centreplane, and in the over-prediction of the corner separation size. Figure 5.6 shows the comparison between the f_k distributions provided by the two estimates. The similar behaviour obtained, allowed us to conclude that the model of Elmiligui *et al.* [72], at least for the case under analysis, is a better option because it does not need the calibration of any parameter. The modelled-to-total ratio of turbulent kinetic energy reacts to regions of high turbulent content and acts by lowering the level of eddy viscosity while it assumes values close to 1 in the boundary layer and the far field region, i.e. switching the formulation to RANS. The estimate of Equation (3.57) also guarantees a slightly later transition from the RANS region in the boundary layer with respect to that of Equation (3.56). As the desired value of f_k in the boundary layer is 1, this latter is a factor of merit. Moreover, the estimate of Equation (3.56) can exceed 1 in the far field, while that of Equation (3.57) is bounded between 0 and 1 by definition. The latter is seen as a minor issue as f_k can be clipped. For these reasons, the estimate in Equation (3.57) was adopted in the following

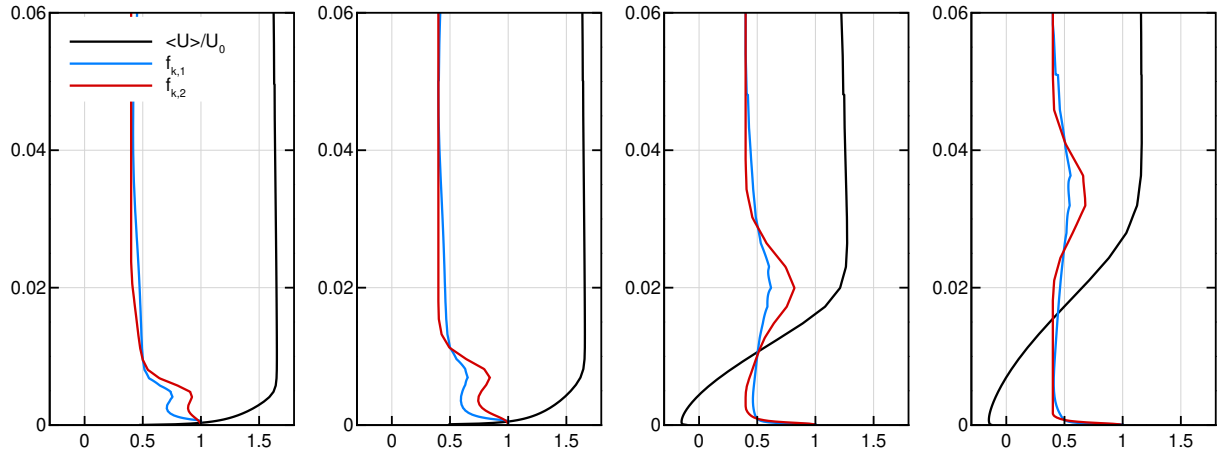

(a) $x/c = 0.28$ **(b)** $x/c = 0.45$ **(c)** $x/c = 0.60$ **(d)** $x/c = 0.75$

Figure 5.6: Instantaneous profiles of horizontal velocity, turbulent-to-molecular viscosity and f_k. Current shock position is $x/c \simeq 0.5$. In the plot legend, $f_{k,1}$ and $f_{k,2}$ refer to the estimates of Equation (3.56) and Equation (3.57), respectively.

sections.

Back pressure influence

The wind tunnel back pressure value also plays a role in the correct prediction of this phenomenon, unlike unconfined configurations where the free stream is far away from the aerofoil and the influence is negligible. Since the exact value is not available from the experiments, we had to investigate the role of this parameter. The adopted values of the back pressure were equal to and 99% of the inlet pressure, denoted $BP = 1$ and $BP = 0.99$, respectively, in Figure 5.7. The lower the back pressure, the larger the amplitude of oscillations. Moreover, because of the viscous sidewall, some losses were introduced and there was a need for lower back pressure with respect to the inflow one. In the work of Thiery and Coustols [258], the numerical and experimental wind tunnel pressure on the upper and lower wall showed a drop between inlet and outlet of around 1%. This motivated our choice of the back pressure. The application of such correction resulted in an increase in the shock oscillation amplitude and pressure RMS (see Figure 5.7) all over the wing section.

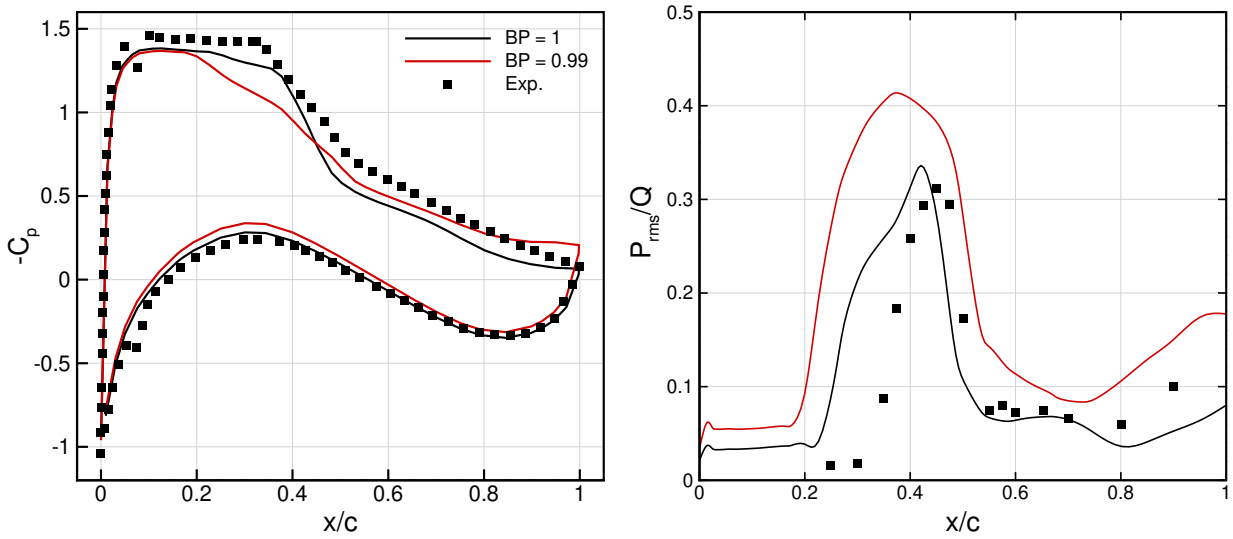

Figure 5.7: Pressure coefficient and RMS for different back pressure values.

Transition to turbulence

Here, the role of the laminar-to-turbulent transition of the boundary layer is investigated. The position of the tripping device was indicated in the experimental references, but no characterisation of the transition to turbulence was given. Therefore, there is uncertainty around the location of the actual transition point. Therefore, the scope of this study is to assess whether imposing transition at the experimental location leads to the right prediction, other than providing a comparison with the fully turbulent case. The transition was fixed by imposing $\mu_T/\mu = 0$ at different streamwise locations, i.e. $x/c = 0.07, 0.25$, and the results were compared with the fully turbulent case. The first value selected corresponds to the actual location of the tripping device in the experiments,

while the second was chosen to account for eventual delays in the boundary layer transition to turbulence. Figure 5.8 shows the streamwise velocity component on the upper surface over time for the three cases. The separation line is represented by the solid, black line. Although the average shock position moved downstream with a later transition, when the transition was set to $x/c = 0.25$, a second separated flow region took place in the laminar part of the boundary layer close to the leading edge of the aerofoil. This resulted in a higher value of the pressure RMS in the first part of the aerofoil with respect to the other cases (see Figure 5.9, right plot) and a lower value of the C_p on the suction side (see Figure 5.9, left plot).

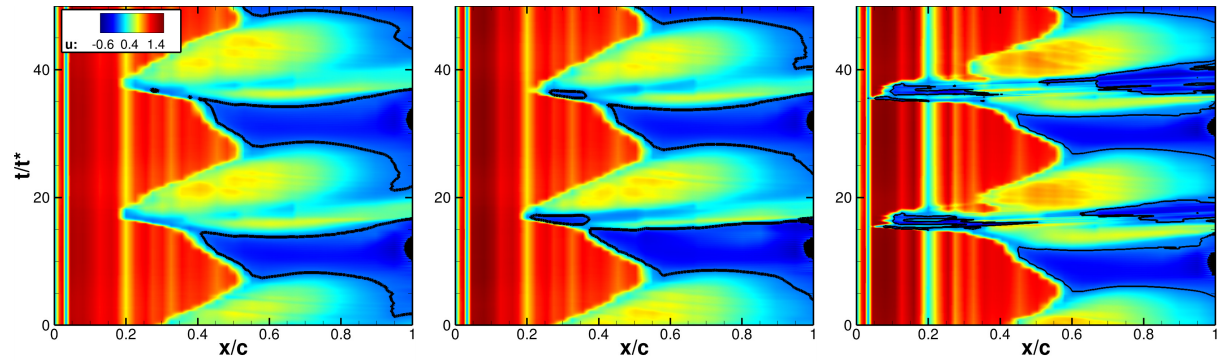

(a) Fully turbulent **(b)** $x_{tr}/c = 0.07$ **(c)** $x_{tr}/c = 0.25$

Figure 5.8: Temporal evolution of the streamwise velocity component on the upper surface of the aerofoil at $z/c = 1.6$ for different transition locations. The solid, black line represents $U = 0$ isoline.

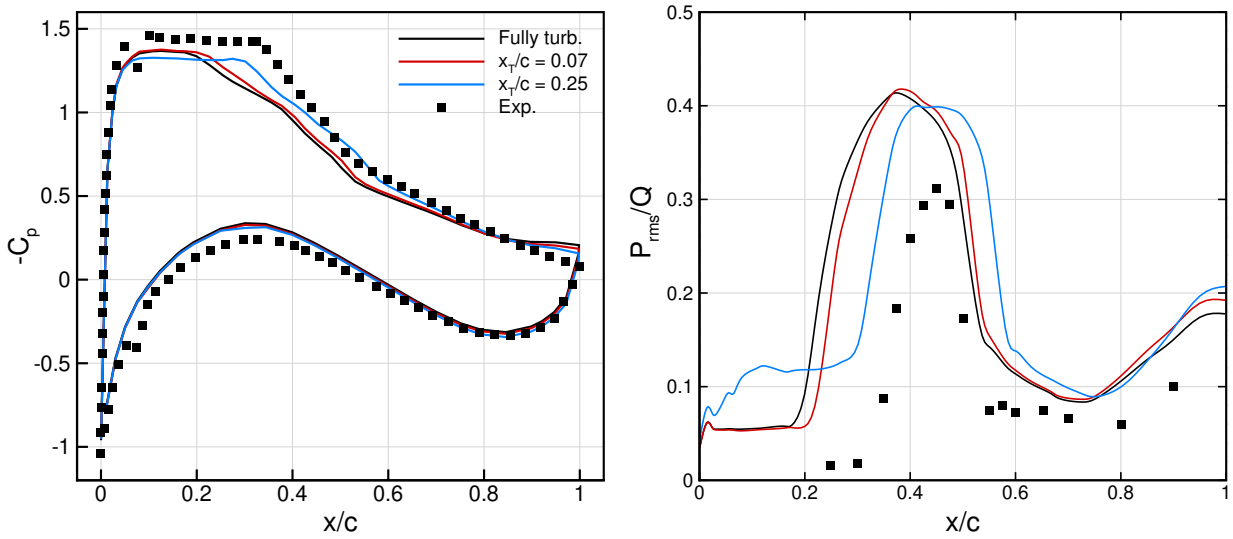

Figure 5.9: Pressure coefficient and RMS for different transition locations.

Value of f_k clip

Here, the effect of the inferior clip of the parameter f_k is studied for different angles of attack. This value is strongly related to the mesh resolution. Indeed, without clipping f_k, the risk of too-low eddy viscosity in some regions of the flow field is high, especially for coarse grids. Figure 5.10 shows the pressure coefficient and RMS for two different values of $f_{k,\text{inf}}$. Too low values of the clip, 0.4 in this case, resulted in too-upstream shock position with respect to the experiments. The low level of eddy viscosity promoted boundary layer separation and raised the level of flow unsteadiness at the trailing edge. With the current mesh resolution, this level of eddy viscosity caused a wrong prediction of the global flow features. Conversely, adopting the higher value of 0.6, the prediction was improved, at both angles of attack. The comparison is, overall, good for both angles of attack.

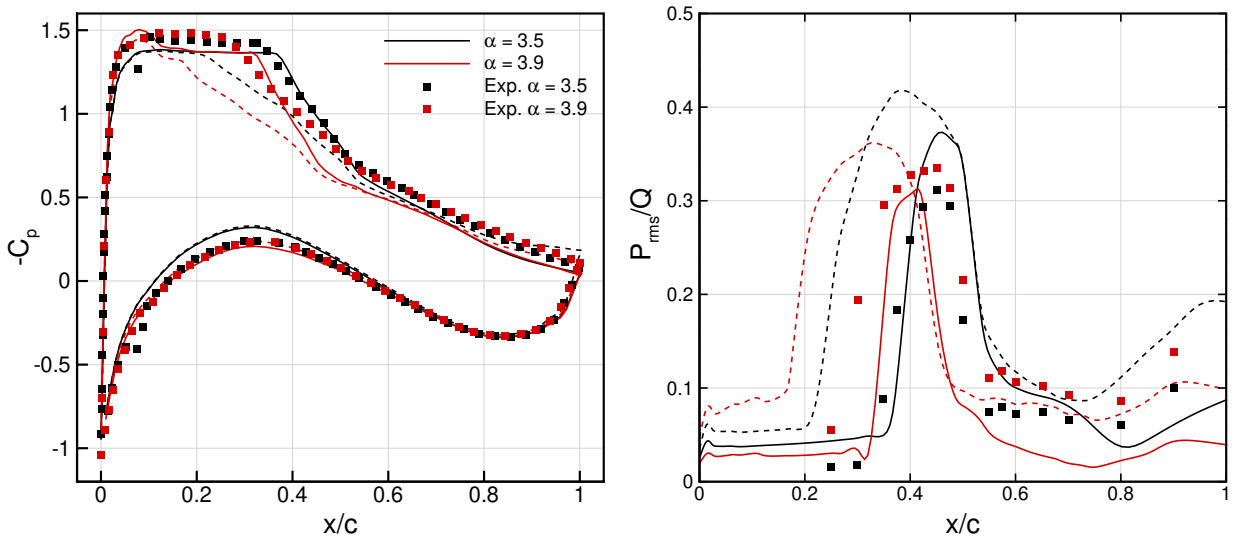

Figure 5.10: Pressure coefficient and RMS for different angles of attack and clip of f_k.

Study on different resolutions

Here the role of the mesh is investigated. The Q-Criterion isosurface in Figure 5.11 shows that the approach enabled the unsteadiness associated with buffet, and was able to describe structures with increasing resolution as the grid size increased. The finer grid was employed with a reduction of the time step to one-half of the initial one. Employing the coarse mesh, the resolution was not enough to capture the motion at smaller scales. Nevertheless, the spanwise discretisation of the C3 grid did not allow the resolution of smaller structures associated with the turbulence in the separated region and the wake. Moreover, the adoption of a coarse grid did not allow the development of any 3D structures in the separated boundary layer. Using the finer grid, it was possible to predict the same flow topology observed in the experiments. From this, we conclude that the spanwise discretisation of the coarse grid was not enough to capture all the correct flow physics. In that case,

although the boundary layer was separated from the shock foot to the leading edge, the structures generated under the influence of the sidewall could not propagate towards the center of the tunnel. The case is analogous to the computation of Thiery and Coustols [258], where the flow oscillation was predicted and just a hint of flow three-dimensionality was shown through friction lines. In that case, possibly because of the use of a RANS-like grid, mushroom-shaped cells could not be established along the span. The buffet dynamics will be discussed in further detail in the following.

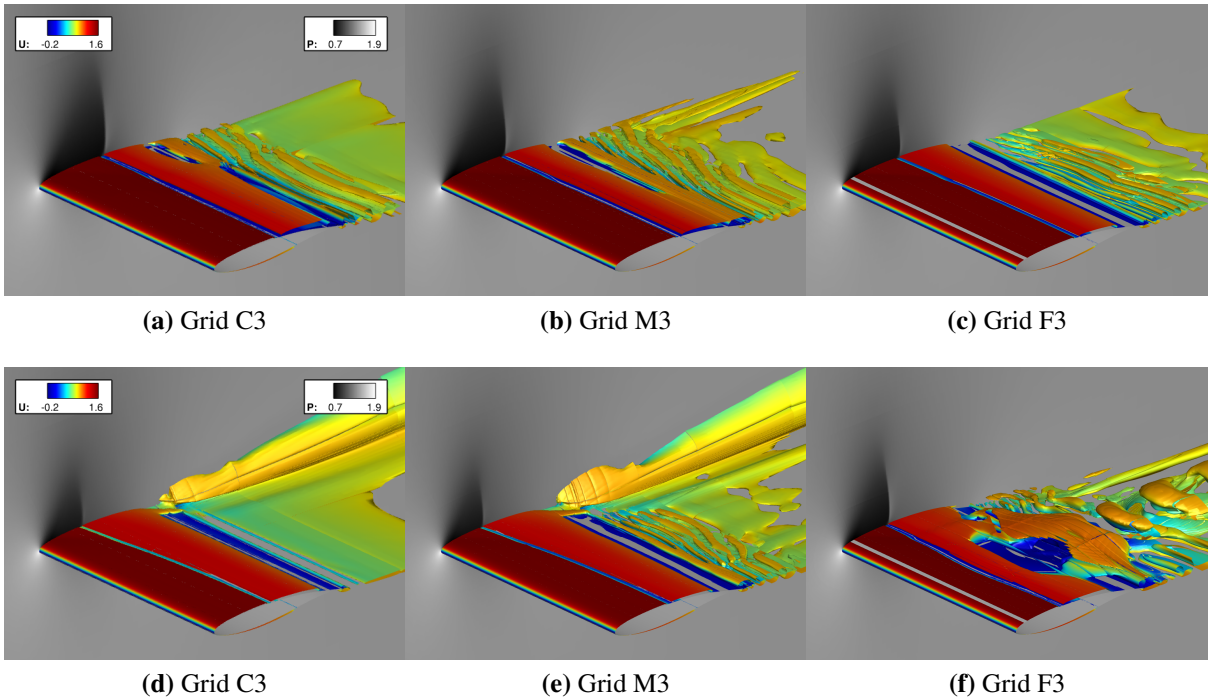

(a) Grid C3 **(b)** Grid M3 **(c)** Grid F3

(d) Grid C3 **(e)** Grid M3 **(f)** Grid F3

Figure 5.11: Iso surfaces of Q-Criterion at $Q = 0.1$ for the confined configuration at different grid sizes. Top: most downstream shock position; bottom: most upstream shock position.

In all cases, the overall agreement with the experiments of C_p and P_{RMS}, shown in Figure 5.12, was satisfactory. The mean shock position slightly moved upstream when a finer grid was used. This effect was mainly due to the non-uniform shock front and the presence of the 3D cells on the suction side of the wing. Moreover, the finer grid adopted at the trailing edge, together with the smaller timestep, allowed for the resolution of smaller scales and an increase in the level of fluctuations. This was also beneficial in terms of agreement of the mean pressure coefficient. A slight gap in terms of pressure coefficient is present on both sides. This is possibly due to the lack of knowledge of the experimental setup, and differences in the adaptive wall shape between experiments and CFD simulations.

The analysis in the following chapter was performed with data from the simulation P3F35 of Table 5.2.

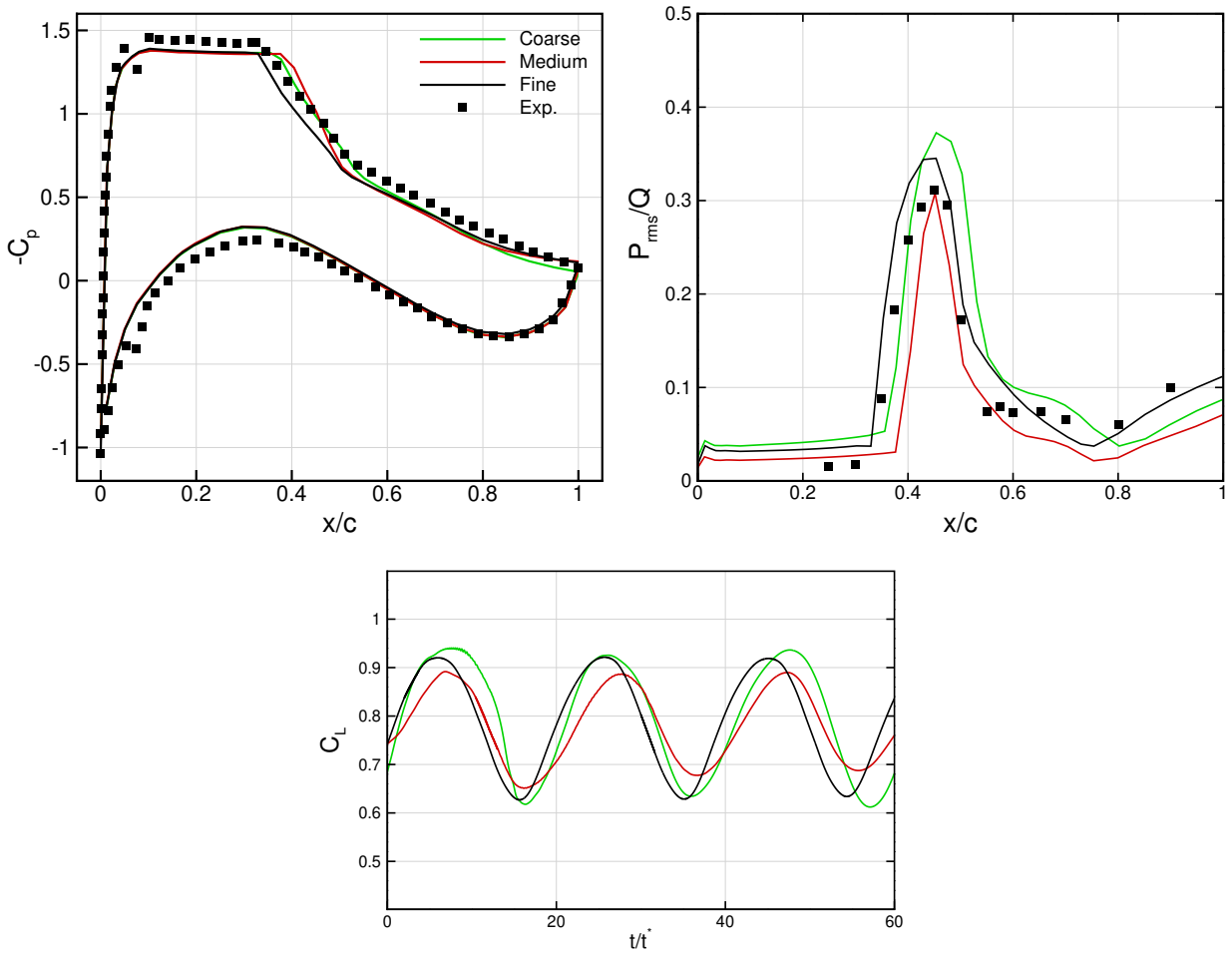

Figure 5.12: Top: pressure coefficient (left) and RMS (right) for different grid resolutions; bottom: lift coefficient history.

5.1.5.1 Mean quantities

In the previous section, the average pressure coefficient and pressure RMS were shown. The mean longitudinal component of the velocity and the RMS are shown in Figure 5.13 and Figure 5.14, respectively. The statistics were computed over several buffet periods. The probes were located at the same position as in the LDV measurements, i.e. around $z/c = 1.32$, where $z = 0$ is the sidewall and $z/c = 1.7$ is the symmetry plane. The pressure differences shown in the previous section coincide with the velocity differences outside of the boundary layer, particularly evident at $x/c = 0.45$. The slightly upstream shock position reflects in a difference in the RMS peak at $x/c = 0.45$, while the agreement is remarkable on the second part of the aerofoil. At $x/c = 0.28$, since the fluctuations in the boundary layer are not resolved, the RMS is practically zero, unlike in the experiments. Overall, very good agreement was found with the experiments.

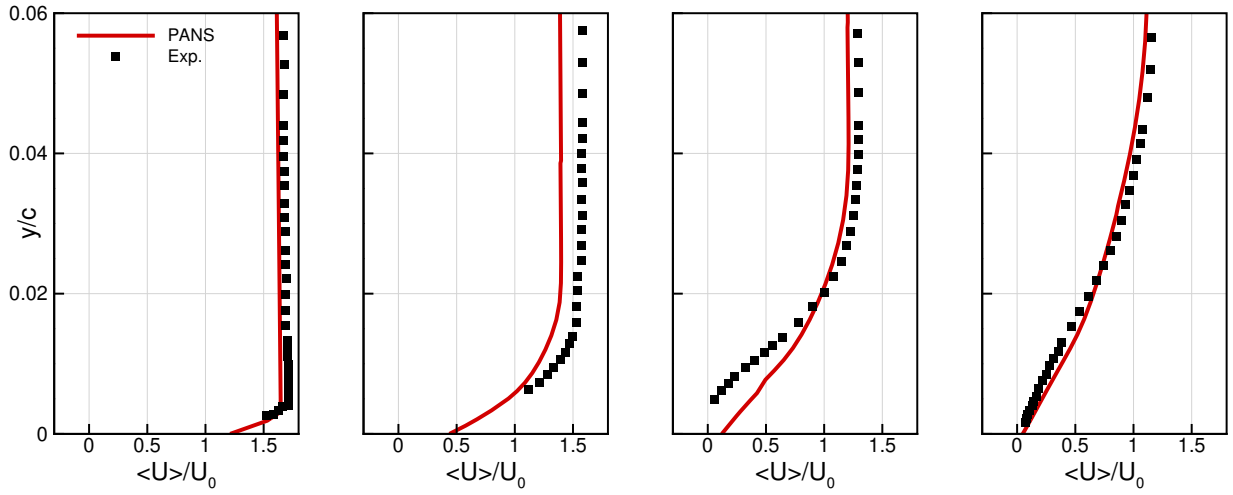

Figure 5.13: Mean value profiles of the longitudinal velocity component. From left to right: $x/c = 0.28, 0.45, 0.6, 0.75$.

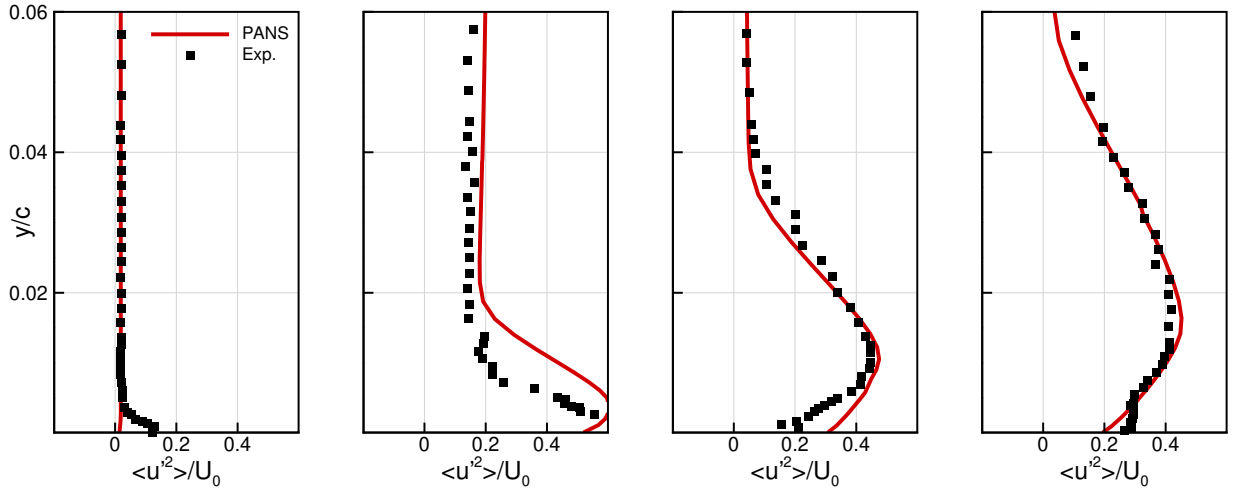

Figure 5.14: RMS profiles of the longitudinal velocity component. From left to right: $x/c = 0.28, 0.45, 0.6, 0.75$.

5.1.5.2 Buffet dynamics and flow topology

Here, further details on the 3D buffet dynamics are given. The usage of PANS introduced benefits in the prediction of transonic buffet. The URANS simulation converged to a steady state, while PANS was able to predict buffet. In the former case, the corner separation induced a spanwise flow deviation at the trailing edge that prevented the flow from separating. Even if the flow separated at the shock foot, the separation region did not merge with the one at the trailing edge and buffet was inhibited. The main reasons can be found in the excessive flow separation at the corner, together with too-high level of eddy viscosity provided from URANS, in the post-shock region. Therefore, the presence of the tunnel walls did not help the development of the self-sustained shock oscillation. Conversely, the PANS simulation predicted a buffet flow following a precise pattern. This is dis-

played in Figure 5.15 by means of CFD friction lines. Approaching the most downstream position

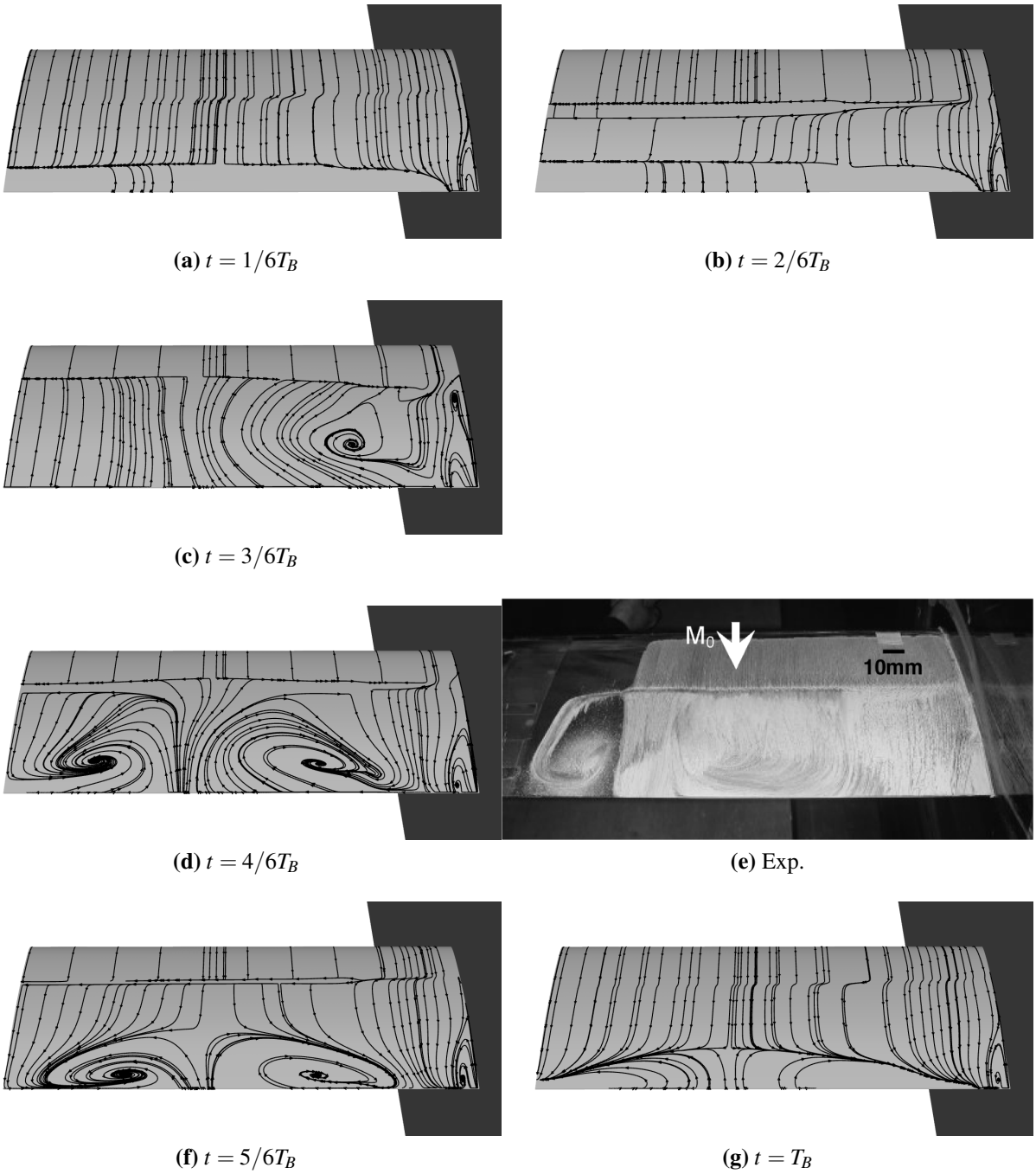

(a) $t = 1/6T_B$ **(b)** $t = 2/6T_B$

(c) $t = 3/6T_B$

(d) $t = 4/6T_B$ **(e)** Exp.

(f) $t = 5/6T_B$ **(g)** $t = T_B$

Figure 5.15: Surface friction lines at different phases of the buffet period T_B. The experimental oil flow visualisation was introduced for comparison purposes.

(a), the flow is attached and the shock strength increases until the flow separates underneath (b); at the same time, trailing edge separation occurs due to the reduced eddy viscosity. The two regions merge around the centerline inducing a flow acceleration between the corner and central separated regions (c). The effect of this is the creation of a vortical structure at the interface between the

attached and separated boundary layer. When the flow is fully separated after the shock, this is affected by the disturbances coming from the trailing edge, and the shock begins to move upstream. In parallel, the aforementioned vortical structures propagate in the separated region and extend to the entire wingspan giving rise to a separated region characterized by large 3D cells, in agreement with what was observed in the experiments (d-e). This reflects in a non-uniform shock front. Approaching the most upstream position (f), the shock strength decreases and the flow re-attaches completely so that a new period begins with the shock moving downstream (g).

The strong flow three-dimensionality is confirmed by the numerical schlieren visualisations in Figure 5.16. The visualisations were obtained by averaging the density gradient magnitude in the spanwise direction and compared with the experimental images (Figure 5.16, bottom plots). At the most downstream position (left figures), the shock front is straight for the greater part of the span and slightly deflects near the sidewall. At this condition, the boundary layer is attached. On the other hand, at the most upstream position (right figures), there is a large flow separation, and the shock front is not uniform. This is confirmed by the wide region of high density gradient (the predominant component is in the longitudinal direction) in the right plots in Figure 5.16.

5.1.5.3 Spectral analysis

Figure 5.17 shows the power spectral density (right plot) of the signal pressure at $x/c = 0.45$ and $z/c = 1.6$ (left plot), compared with experiments. The fundamental and secondary frequencies are clearly detected, although a small discrepancy with the experiments is present. This is particularly evident looking at the difference in the periods of the pressure signals in the left plot. The slight difference in the mean shock position, shown in Figure 5.12, top plots, resulted in better agreement with the pressure signal at $x/c = 0.43$. It has to be noted that the raw experimental data is not available for processing alongside the CFD, adding to the observed differences.

Figure 5.18 shows the power spectral density at different locations around the aerofoil at $z/c = 1.6$. The first three probes were located on the model at $x/c = 0.1$, 0.45 and 0.9, respectively, while the fourth probe located at $x/c = 1.2$ and $y/c = 0.03$. Three mean frequencies were detected: a fundamental buffet frequency around 50-60 Hz (the experimental buffet frequency was 69 Hz) with the secondary harmonics, a peak around 1000-2000 Hz, and another in the wake around 5000-6000 Hz. This subdivision is coherent with the analysis of Szubert *et al.* [255] that associates these three values to the buffet motion, Von Karman shedding and Kelvin-Helmholtz instabilities, respectively. While the fundamental and secondary harmonics were detected by every probe, just the last two ones were able to capture the presence of other types of instability.

The dependence of the PSD on the streamwise and spanwise coordinate was studied using SPL, defined as

$$\mathrm{SPL} = 20\,\mathrm{Log}\left(\frac{\mathrm{PSD}}{2\times 10^{-5}}\right), \tag{5.1}$$

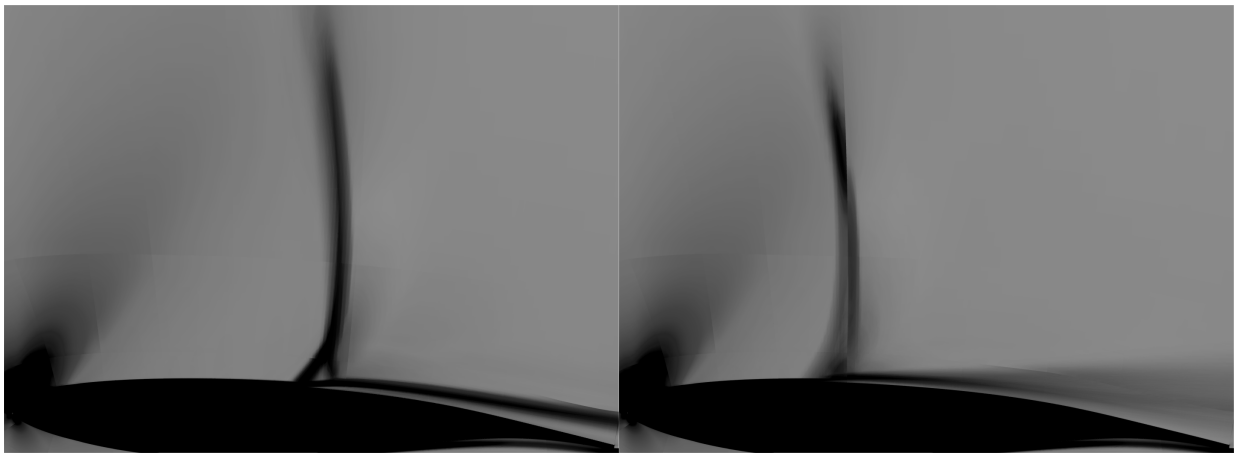

(a) Most downstream position

(b) Most upstream position

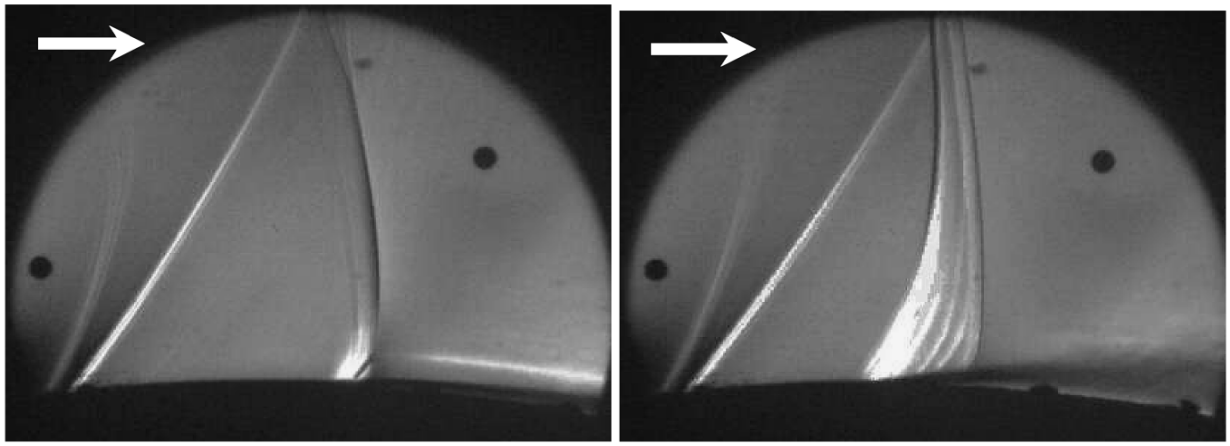

(c) Most downstream position

(d) Most upstream position

Figure 5.16: Numerical (top) and experimental (bottom) schlieren visualisations. The visualisations were obtained by averaging the density gradient magnitude in the spanwise direction. Pictures of the experiments taken from [126].

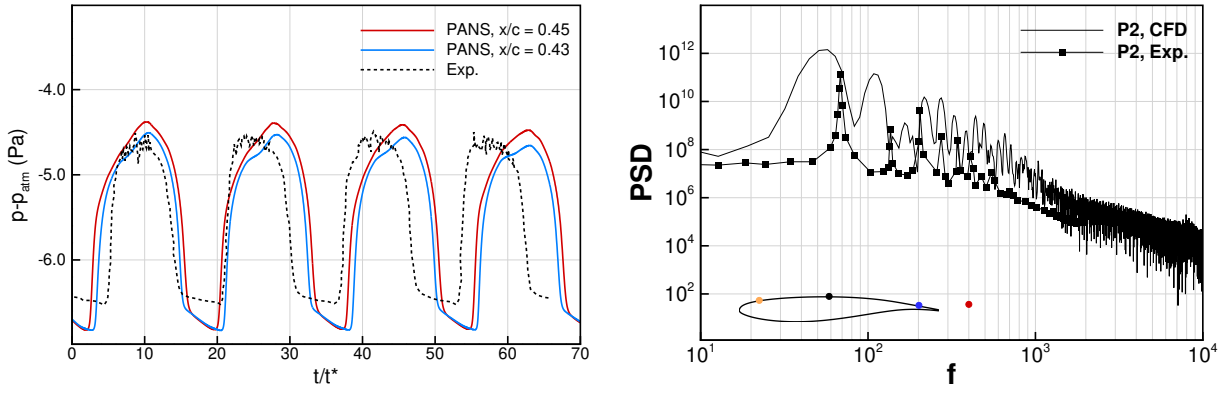

Figure 5.17: Pressure signal (left) and power spectral density (right) at $x/c = 0.45$ and $z/c = 1.6$. In the left plot, the pressure signal at $x/c = 0.43$ was also plotted.

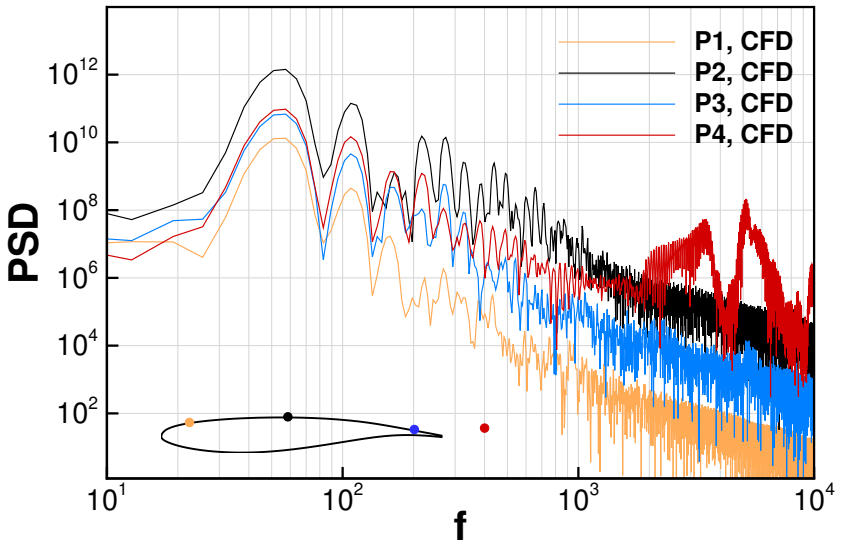

Figure 5.18: Power spectral density of the pressure at different points in the domain. The position with respect to the aerofoil is indicated in the bottom left sketch.

coherently with the paper of Jacquin *et al.* [126]. Figure 5.19 and Figure 5.20 show the distribution of SPL along the streamwise and spanwise directions, respectively. Figure 5.19 clearly shows the buffet frequency and the secondary harmonics all over the chord. The energy content associated with the pressure signals within the region of shock motion is higher than at other locations because of the higher level of fluctuations.

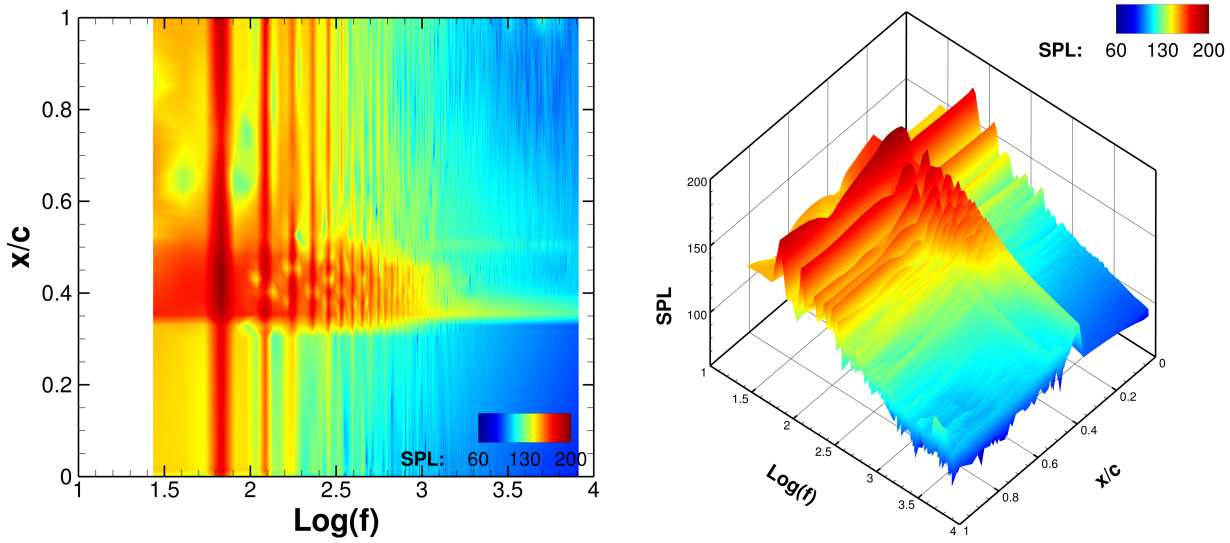

Figure 5.19: Sound pressure levels along the chord on the upper surface at $z/c = 1.6$. Left: 2D representation; right: 3D representation.

Figure 5.20 shows that the energy distribution between frequencies is invariant in the spanwise direction, in spite of the 3D flow topology developed over the buffet period. The same behaviour

was shown in the work of Jacquin *et al.* [126].

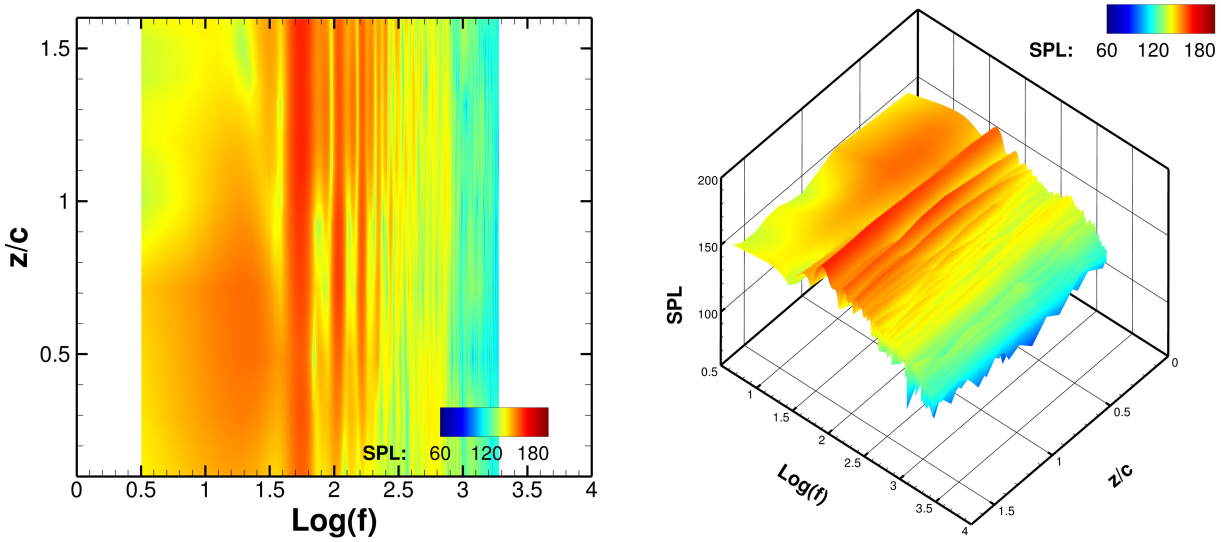

Figure 5.20: Sound pressure levels along the span on the upper surface at $x/c = 0.6$. Left: 2D representation; right: 3D representation.

5.1.6 Computational performance and cost

Table 5.3 presents the CPU cost of the PANS and URANS simulations. The comparison was done over one characteristic travel time, i.e. over 100 computational timesteps. In the analysis, the same grid, and the same number of processors were used. Since the URANS tends to a steady solution while the PANS describes an intrinsically unsteady flow, the number of inner iterations required to meet the convergence criterion on the flow residual is different; therefore, the averages were taken over the number of inner iterations of the implicit dual-time stepping scheme. This was done to identify the net additional cost of the PANS routine in the solver. From the table, it can be seen that the higher increase is that on the evaluation of the residual Jacobian, where the PANS routine is recalled to modify the source terms in the k and ω equations. Moreover, the number of iterations of the GCG algorithm for the solution of the linear scheme is slightly increased. This reflects in an increase in the total computational time of about 3% when compared to URANS.

Table 5.3: Comparison between computational times of PANS and URANS. ABAH: apply boundary and halo; IATS: initialize and time step; CHOG: calculate high order gradients; CRJ: calculate residual Jacobian; CP: calculate pre-conditioner; SLS: solve linear system.

	GCG iter.	ABAH [s]	IATS [s]	CHOG [s]	CRJ [s]	CP [s]	SLS[s]	Tot
URANS	3.86	0.31	0.055	0.00024	0.65	0.09	0.83	**1.95**
PANS	4.59	0.31 (+1%)	0.055 (-1 %)	0.00025 (+8 %)	0.70 (+7 %)	0.09 (-3 %)	0.85 (+2 %)	**2.00 (+3.1%)**

This shows the capability of PANS to work in URANS-mode, helping unlock flow unsteadiness by lowering the eddy viscosity in regions of high turbulent content, and in agreement with the grid resolution.

5.2 Chapter Summary

In this chapter, the application of PANS for the flow around the OAT15A section at high Reynolds number was presented. Computations on both confined and unconfined configurations were carried out. The wind tunnel walls were accounted and symmetry boundary conditions at the symmetry plane of the wind tunnel were imposed. The wind tunnel presence influenced the buffet dynamics by introducing a strong three-dimensionality to the flow. At pre-buffet conditions, the shock was influenced by the presence of the wind tunnel and displayed a front bending when approaching the wall. The PANS approach used in this work recovered the URANS behaviour, provided a reasonable distribution of the f_k parameter.

After the onset, although the buffet mechanism maintained its two-dimensional nature, the interaction with the separated region at the wall-wing junction was shown to be crucial in the generation of large 3D vortical structures on the wing. This was not shown in published works, where a typical 2D behaviour with an alternated separation and re-attachment of the flow on the suction side of the aerofoil was shown. For both configurations, URANS simulations were not able to predict buffet, even at an angle of attack well beyond the buffet onset, while the use of PANS unlocked the shock oscillations. The flow physics was captured correctly, as confirmed by comparison with the experiments in Figures 5.12 to 5.16, with the unsteady loads exhibiting periodic oscillations.

Because of the lack of detailed documentation for the experimental settings, some preliminary study was required to find the correct setup to obtain the correct mean shock position. The f_k parameter was clipped to a value of 0.6 to avoid an excessive reduction of the eddy viscosity, considering the spatio-temporal discretisation adopted. The PANS approach proved to be able to work at different grid resolutions. It revealed beneficial in describing the self-sustained oscillation even with a coarse, RANS-like grid and allowed for scale-resolving when a finer grid was used. In the latter, the description of the buffet dynamics was more accurate since the detection of stall cells on the upper surface of the wing was enabled. In comparison with URANS, a little, additional expense ($\simeq 3\%$) was introduced by the PANS routine.

Chapter 6

Prediction of Buffet Onset using RANS-based Criteria

*

The (lower) buffet boundary can be defined as a line in the $\alpha - M_\infty$ and $C_L - M_\infty$ planes. This coincides with the buffet onset incidence at a given Mach number (or vice versa) and represents a boundary that must not be exceeded in flight. A sketch is shown in Figure 6.1, right plot. The buffet boundary can also be related to the line separating the regions of attached or partially separated flow, and that of totally separated flow (i.e. from the shock foot to the trailing edge). The constraint on buffet must be accounted for in the aerodynamic optimisation process (see. [133]), therefore it arises the need for an accurate method for the buffet boundary estimation across a wide range of operating conditions.

To establish the buffet onset, many criteria have so far been proposed. Because of the extension of the separated region from the shock foot to the trailing edge, a common criterion, based on trailing edge measurements, is the trailing edge pressure divergence. An alternative quantity, also evaluated on pressure measurement over the aerofoil, is the unsteady normal force, whose divergence corresponds to the buffet onset. For supercritical aerofoils the first criterion is not very reliable. Alternative criteria were mentioned in the paper of Mabey [167] and consist of the wing-root strain gauges, and the breaks in the $C_L - \alpha$ and $C_D - C_L^2$ curves. These latter, compared to an actual buffet boundary, did not reveal good indicators in that work.

Chung et al. [41] assessed the validity of some of the most common criteria on the NACA0012 aerofoil, based on RANS simulations. In their work, the buffet onset was available from the experiments of McDevitt & Okuno [178], and it was possible to assess the validity of the following criteria: deviation from the linear slope of the lift coefficient, trailing edge pressure divergence,

*The content of this chapter has been published in: "A. Petrocchi, G. N. Barakos, *Buffet boundary prediction using RANS-based criteria and adjoint methods*, Aerospace Science and Technology, Vol. 126, 2022, 107664, https://doi.org/10.1016/j.ast.2022.108086".

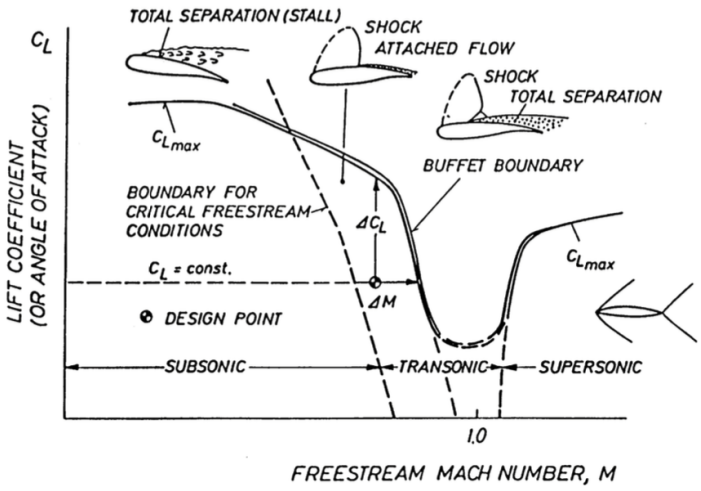

Figure 6.1: Buffet boundary sketch from Stanewsky & Basler [247].

shock motion reversal, deviation from the linear trend of the pitching moment coefficient, and kink in the center of pressure position. Together with these, the buffet onset was established by means of URANS simulations with a Baldwin-Lomax turbulence model. Overall, the URANS predictions were closer to the experiments than the empirical criteria, even though the CPU costs and memory required were higher. The results can be seen in Figure 6.2. The over-prediction of the

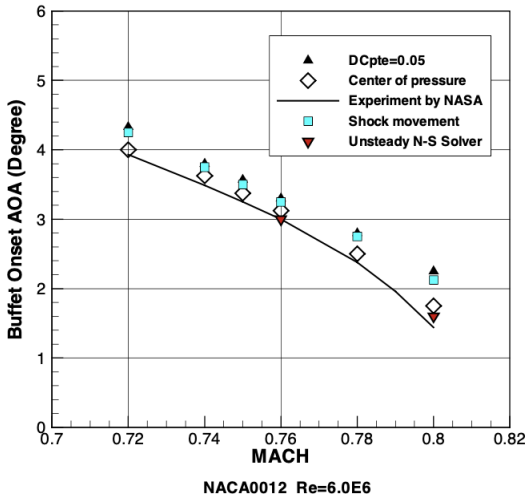

Figure 6.2: Comparison of buffet onset from empirical criteria and experimental values provided in [178]. Figure from Chung et al. [41].

onset angle of attack is not acceptable in real applications, as the design point could be selected above the buffet boundary. The paper partially assigned this over-prediction to the inadequacy of the turbulence model. The maximum difference from the experiments was always obtained using the C_p-based criteria, with the other criteria giving intermediate results. The discrepancy increased

with the Mach Number.

For swept wings, the pressure divergence criterion must be applied at a certain section of the wing, that is geometry-dependent and flight condition-dependent. In a recent work of Lawson et al. [153] the aforementioned criteria, together with two other, based on tip acceleration and pitch moment break, were compared to predict the buffet onset on the RBC12 wing. In Figure 6.3, it is shown that axial force and pitching moment criteria differed from the others and the degree of confidence increased with Mach number, meaning that some of the criteria may fail at that conditions.

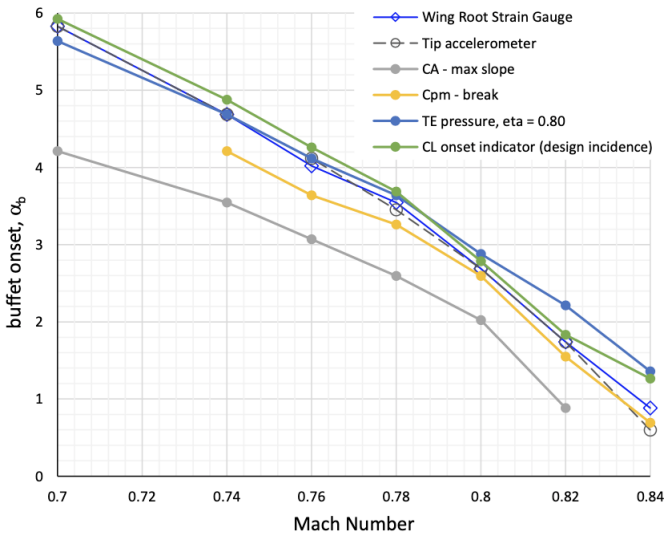

Figure 6.3: Comparison of several buffet onset indicators at different Mach numbers. Figure from Lawson et al. [153].

6.1 Numerical Method

6.1.1 RANS-based Criteria

Similar criteria to those used in this work can be found in the works of Chung et al. [41] and Lawson et al. [153]. Among them, the first indicator is the change in the lift coefficient slope, as suggested by Pearcey and Holder [204]. This relates to the effect of the flow separation at the shock foot when the shock moves downstream as the angle of attack increases. To determine the buffet onset from the lift curve, the straight line approximating the linear regime of the lift curve is shifted by $\Delta\alpha = 0.1$ deg, and the buffet onset is identified as the intersection between the line and the lift curve itself (see fig. Figure 6.4, left).

The second criterion is based on the slope of the moment coefficient. The pitching moment

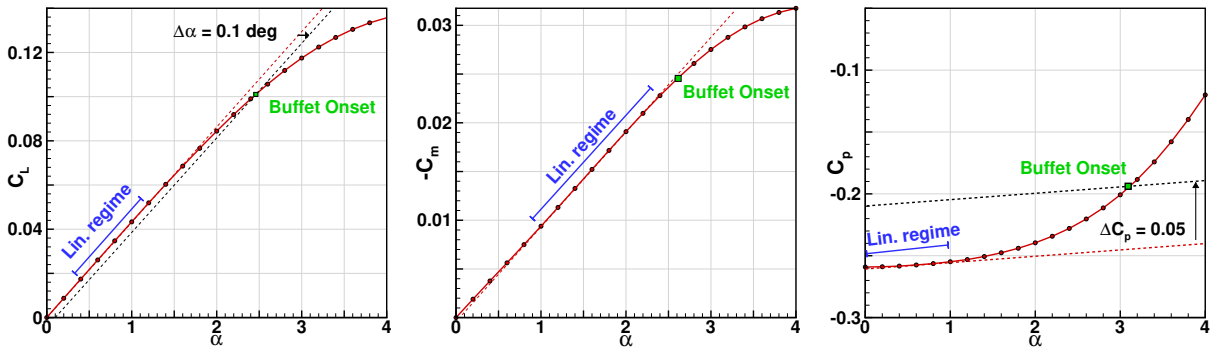

Figure 6.4: Graphical explanation of the buffet onset evaluation from the C_L (left), C_M (centre) and the trailing edge C_p (right) coefficients.

variation is sensitive to the length between the reference point and the location of the separated region. This length acts like an amplifier of the changes in the mean aerodynamic loads. Indeed, as the separated region moves aft with the movement of the shock, this effect is accentuated. The deviation point from the linear range is seen as buffet onset [41]. An example is shown in Figure 6.4 (centre).

The same procedure is used for the trailing edge pressure divergence, as shown in Figure 6.4 (right). For transonic aerofoils, the pressure coefficient changes as a result of the flow separation due to the shock on the suction side. This coincides with a lift drop and the onset of buffet. As specified by Chung et al. [41], there is no value for the exact deviation from the linear regime, but an offset of $\Delta C_p = 0.05$ was recommended in Ref. [41, 153].

The accuracy of the presented criteria is limited by the performance of RANS simulations that, in the past, showed different results according to the turbulence model, numerical scheme and spatio-temporal discretisation adopted.

6.1.2 Algorithm Formulation

The present algorithm makes use of the adjoint method implemented in the solver HMB3 to reduce the CPU cost associated with the aforementioned RANS-based criteria, and was not intended to improve the accuracy in the prediction of the buffet boundary. Indeed, the accuracy of the algorithm is strongly related to that of the criteria described in Section 6.1.1 . A flow-chart of the algorithm, implemented in MATLAB, is shown in Figure 6.5

In the current study of the buffet boundary, we will only account for Mach number and angle of attack changes (an alternative might be the lift coefficient). A third parameter like the Reynolds number can also be accounted for but it would increase the required CPU time.

The Mach number is an important parameter in defining the flight conditions, and we opted to keep it fixed and evaluate the buffet onset in terms of the angle of attack. It must be pointed out

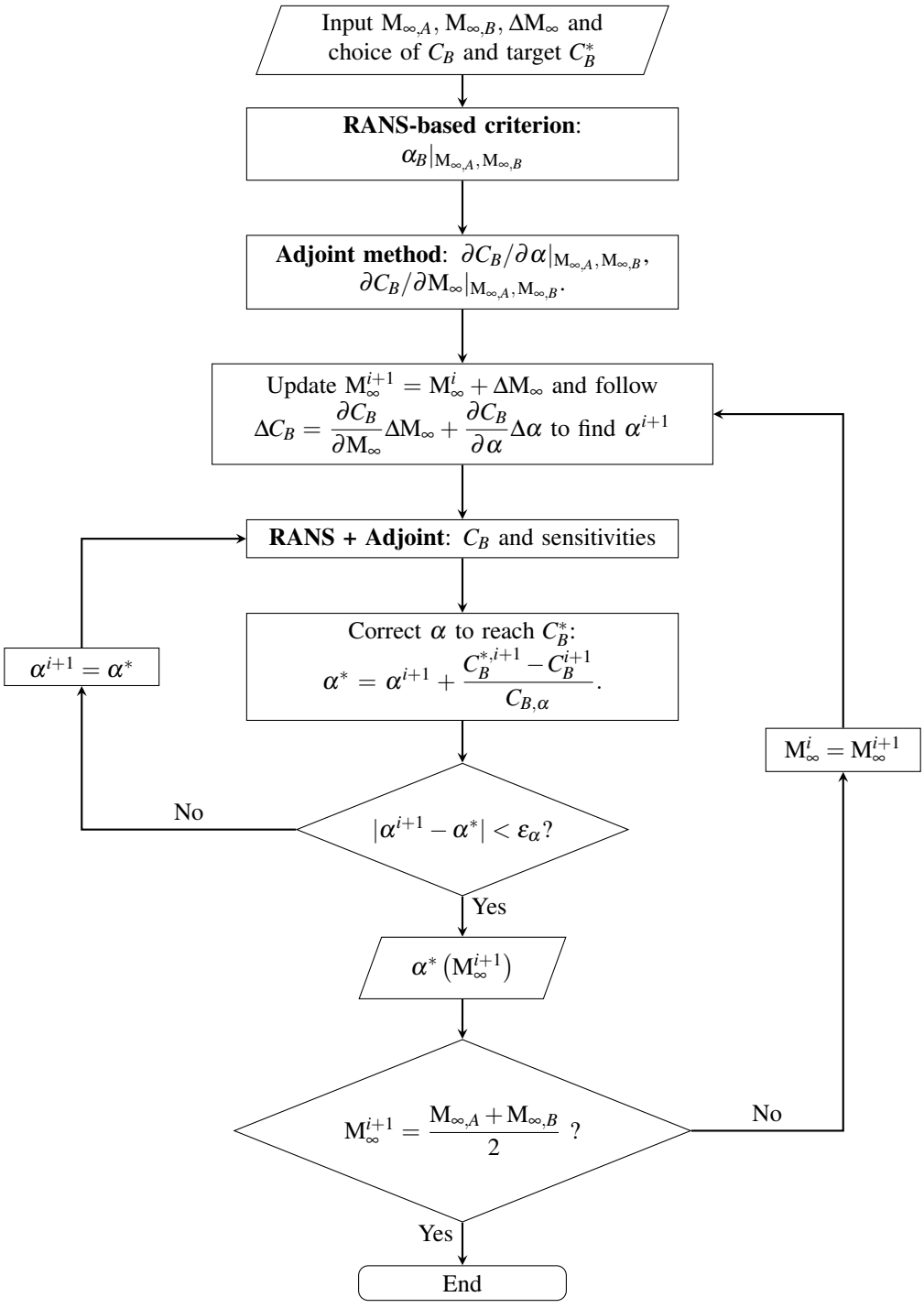

Figure 6.5: Algorithm used to trace the buffet boundary.

that the opposite is also possible. The range of flight conditions we are interested in is represented by an interval of Mach numbers $M_\infty \in (M_{\infty,A}, M_{\infty,B})$.

The selected criterion must be as accurate as possible over the entire interval of angles of attack. The efficient procedure employed here uses RANS-based criteria. A generic buffet parameter C_B

must be introduced. In the case of the aforementioned criteria, some possible candidates are the aerodynamic coefficients (C_L or C_M), the trailing edge pressure coefficient, or one of their derivatives with respect to the flight parameters. Then, a target value C_B^* for the buffet onset parameter C_B must be specified as a function of the Mach number. C_B^* is defined as the value assumed by C_B at the onset. The choice of a suitable buffet parameter is critical and will determine the outcome of the procedure. Moreover, the buffet onset parameter must be inferred from steady computations and, therefore, dynamic parameters must be avoided. The adjoint method used to move along the buffet boundary can also be used in conjunction with unsteady simulations. This is possible using parameters like the shock oscillation frequency or amplitude, and the higher order moments of the flow variables. Nevertheless, the present method is meant to be the least expensive possible, and the use of unsteady simulations increases the required CPU time. Also, a *pessimistic* method, that gives conservative estimates of the buffet boundary, is preferred.

Steady RANS computations at different angles of attack are performed at two initial points, $\mathrm{M}_{\infty,A}$ and $\mathrm{M}_{\infty,B}$, and the RANS-based criteria are applied to find the respective values of the onset angle of attack, $\alpha_B|_{\mathrm{M}_{\infty,A}}$ and $\alpha_B|_{\mathrm{M}_{\infty,B}}$. At the onset, the adjoint method is used to find the derivatives of the buffet indicator with respect to the angle of attack $\partial C_B/\partial\alpha$ and the Mach number $\partial C_B/\partial \mathrm{M}_\infty$. If the onset parameter itself is a derivative (e.g. $\partial C_L/\partial\alpha$), the adjoint calculation must be repeated at two points $\alpha_i \pm \Delta\alpha$, and the sensitivities, i.e. the second derivatives, can be obtained through finite differences.

Once an increment in the Mach number $\Delta\mathrm{M}_\infty$ is fixed, the point is propagated along the buffet boundary where C_B follows:

$$\Delta C_B = \frac{\partial C_B}{\partial \mathrm{M}_\infty}\Delta\mathrm{M}_\infty + \frac{\partial C_B}{\partial\alpha}\Delta\alpha\,. \tag{6.1}$$

The next point is evaluated increasing (or decreasing) the Mach number by the fixed increment $\Delta\mathrm{M}_\infty$ and by updating the angle of attack according to Equation (6.1):

$$\alpha^{i+1} = \alpha^i - \frac{C_{B,\mathrm{M}_\infty}}{C_{B,\alpha}}\Delta\mathrm{M}_\infty - \frac{C_B^{*,i+1} - C_B^i}{C_{B,\alpha}}\,, \quad \mathrm{M}_\infty^{i+1} = \mathrm{M}_\infty^i + \Delta\mathrm{M}_\infty\,, \tag{6.2}$$

where $C_{B,\alpha}$ and C_{B,M_∞} were now used to express the partial derivatives in Equation (6.1). The angle of attack is then corrected to reach the target value of C_B through:

$$\alpha^* = \alpha^{i+1} + \frac{C_B^{*,i+1} - C_B^{i+1}}{C_{B,\alpha}}\,. \tag{6.3}$$

To ensure that the sensitivities do not change significantly in the correction, a tolerance ε_α is introduced. If the correction exceeds the range determined by ε_α, the sensitivities are re-computed and a new correction is made; otherwise, the Mach number is updated and the next point is chased. The process is initiated at the two extremes of the Mach interval, and the buffet boundary is traced going

towards the center of the interval. If more than one corrections are needed, a higher order expansion can be used to speed up the process and increase the accuracy. In that case, when two corrections are applied, i.e. $C_B, C_{B,\alpha}$ are known at two different angles of attack, Equation (6.3) can be replaced by a quadratic expansion, where the second-order derivative is assumed constant between the two known points. The same can be done for higher order expansions. Alternatively, when the number of sample points is high, the $C_B - \alpha$ curve can be interpolated through a high-order polynomial without relying on the result of the adjoint method (since the derivatives are no longer needed). In this case, a purely RANS-based criterion is used to estimate the buffet onset. All these alternatives will be explored in Section 6.2 where results of the proposed method are presented.

6.2 Applications

6.2.1 Test cases description

OAT15A Wing Section

The first configuration is the supercritical aerofoil OAT15A, studied in an experimental campaign by Jacquin et al. [125, 126] in the S3Ch wind tunnel at ONERA. The wing section has a chord of $c = 0.23$m and a span, coinciding with that of the tunnel, of 0.78 m. The section has a thickness-to-chord ratio of $t/c = 0.123$ and a trailing edge thickness of 0.5% of the chord. The wing was mounted in a squared section wind tunnel having nominal dimensions of $0.78\text{m} \times 0.78\text{m} \times 2.2\text{m}$. An adaptation technique based on a steady flow hypothesis was used at the lower and upper walls to reproduce free-stream conditions. Measurements were collected at free-stream Mach numbers in the range of 0.7-0.75, a chord-base Reynolds number of $\text{Re}_c = 3 \times 10^6$ and angle of attack in the range of 1.36 - 3.9 deg. The adoption of static pressure measurements and Kulite sensors distributed in the vicinity of the mid-span section allowed to detect the occurrence of flow unsteadiness at an angle of attack of 3.1 deg at $\text{M}_\infty = 0.73$ and 3.5 deg at $\text{M}_\infty = 0.72$. For the case at $\text{M}_\infty = 0.73$ and $\alpha = 3.5$ deg, an LDV system was used to acquire velocity-field data and compute statistics. At all other flow conditions the pressure measurements were complemented with oil-flow and schlieren visualisations.

NACA0012 Wing Section

The experiments used for the flow around the NACA0012 section were performed in the Ames High Reynolds Number Facility [178]. The measurements of both steady and unsteady pressure measurements, allowed for the detection of the buffet onset at several conditions. The tunnel walls were adapted to follow the free air streamlines, while the sidewall interference was reduced by thinning the sidewall boundary layer by means of suction applied on porous panels. The experiments

were supported by a shadowgraph system [178].

6.2.2 RANS Computations and Comparison with Experiments

The computational grids considered are of C-H topology. The 2D grid consists of 320 or 360 cells around the aerofoil, for the sharp (NACA0012) and blunt (OAT15) trailing edges, respectively. Here, 105 cells were used in the normal direction, for a total of about 64 or 70 thousand cells over the domain extending $20c$ both ahead of the aerofoil and at the wake. The spacing distribution was set to satisfy the condition of $\Delta y^+ < 1$ at each condition, resulting in first cell size varying between $2.0 \times 10^{-6}c$ and $5.0 \times 10^{-6}c$. The grids used for computations are shown in Figure 6.6. Adiabatic wall boundary conditions were imposed at the aerofoil, and free-stream values of pressure and velocity elsewhere. The k-ω SST turbulence model of Menter [182] was used to close the RANS equations. The convergence criterion was based on the reduction of the flow field residual with

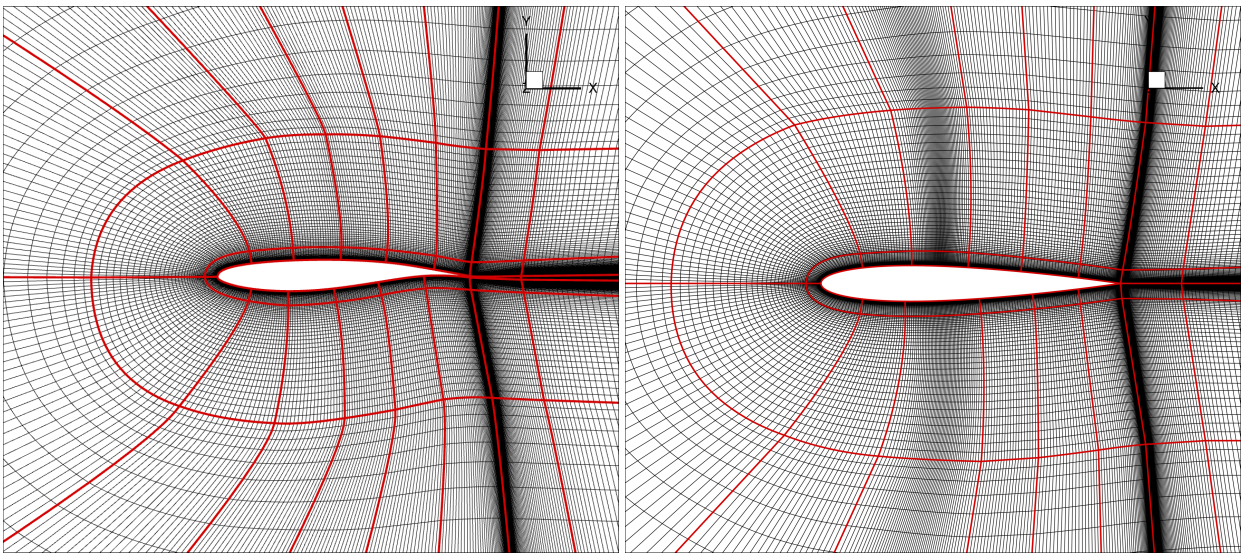

Figure 6.6: Computational grids adopted in the computations. Left: OAT15A; right: NACA0012.

respect to the initial one. For most cases, reduction of 7 orders of magnitude was reached.

Figure 6.7 shows the pressure coefficient distribution around the OAT15A aerofoil at $M_\infty = 0.73$ and $Re = 3 \times 10^6$ at two different angles of attack. Figure 6.8 displays the same results for the NACA0012 aerofoil at different settings for the angle of attack, Mach number, and Reynolds number. The agreement between computations and experiments is overall satisfying, although a slight misprediction of the shock position for the OAT15A case persists. Nevertheless, for this particular test case, 3D computations (not shown here) accounting for the wind tunnel walls were performed and predicted a more upstream position of the shock due to the presence of the sidewalls. Since the exact prediction of the shock position is beyond the scope of this work, the current agreement is seen as satisfactory.

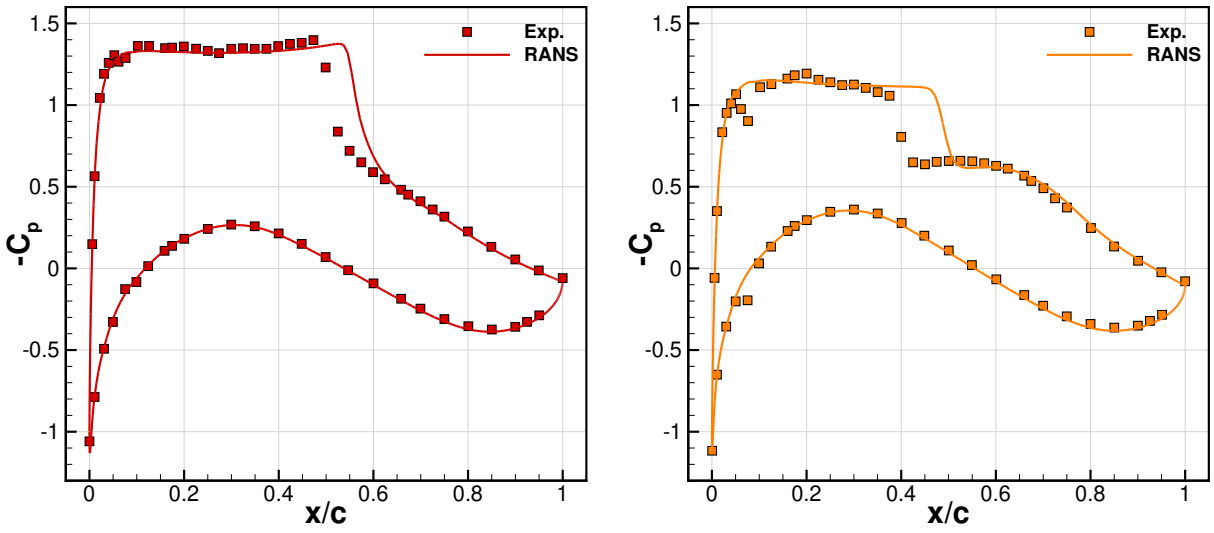

Figure 6.7: OAT15A surface pressure distribution compared with the experimental results of [126] at $\alpha =$ 2.5 deg (left) and $\alpha = 1.5$ deg (right).

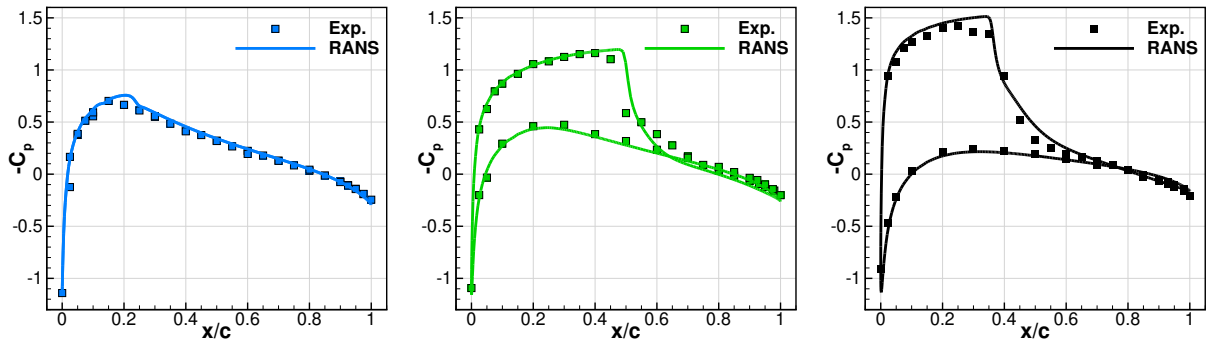

Figure 6.8: NACA0012 surface pressure distribution compared with the experimental results of [178].Left: $\alpha = -0.02$ deg, $M_\infty = 0.75$, $Re = 6.0 \times 10^6$; center: $\alpha = 2.03$ deg, $M_\infty = 0.778$, $Re = 6.0 \times 10^6$; right: $\alpha =$ 4.06 deg, $M_\infty = 0.732$, $Re = 2 \times 10^6$.

6.2.3 Adjoint method validation

The NACA0012 at $Re = 6.0 \times 10^6$ was taken as the reference case for comparing the performance of the adjoint methods in evaluating sensitivities with respect to the flight conditions. Figure 6.9 shows the comparison between the derivative $\partial C_L/\partial\alpha$ evaluated by means of the adjoint method (denoted as ADJ) and finite differences (denoted as FD). The overall agreement is good at every Mach number. Some small differences arise for angles of attack far beyond the experimental buffet onset (black vertical lines in Figure 6.9), and some oscillation are present, e.g. at $M_\infty = 0.77, 0.79$. This is due to limitations with finite differences and the employed steady flow approximation. Overall, we do not expect to cross this threshold, and the agreement is, overall, good. The same can be stated for the derivative $\partial C_L/\partial M_\infty$ in Figure 6.10. Again, the region where values differ is well beyond the buffet onset, the flow is unsteady, and cannot be used in the buffet onset estimation.

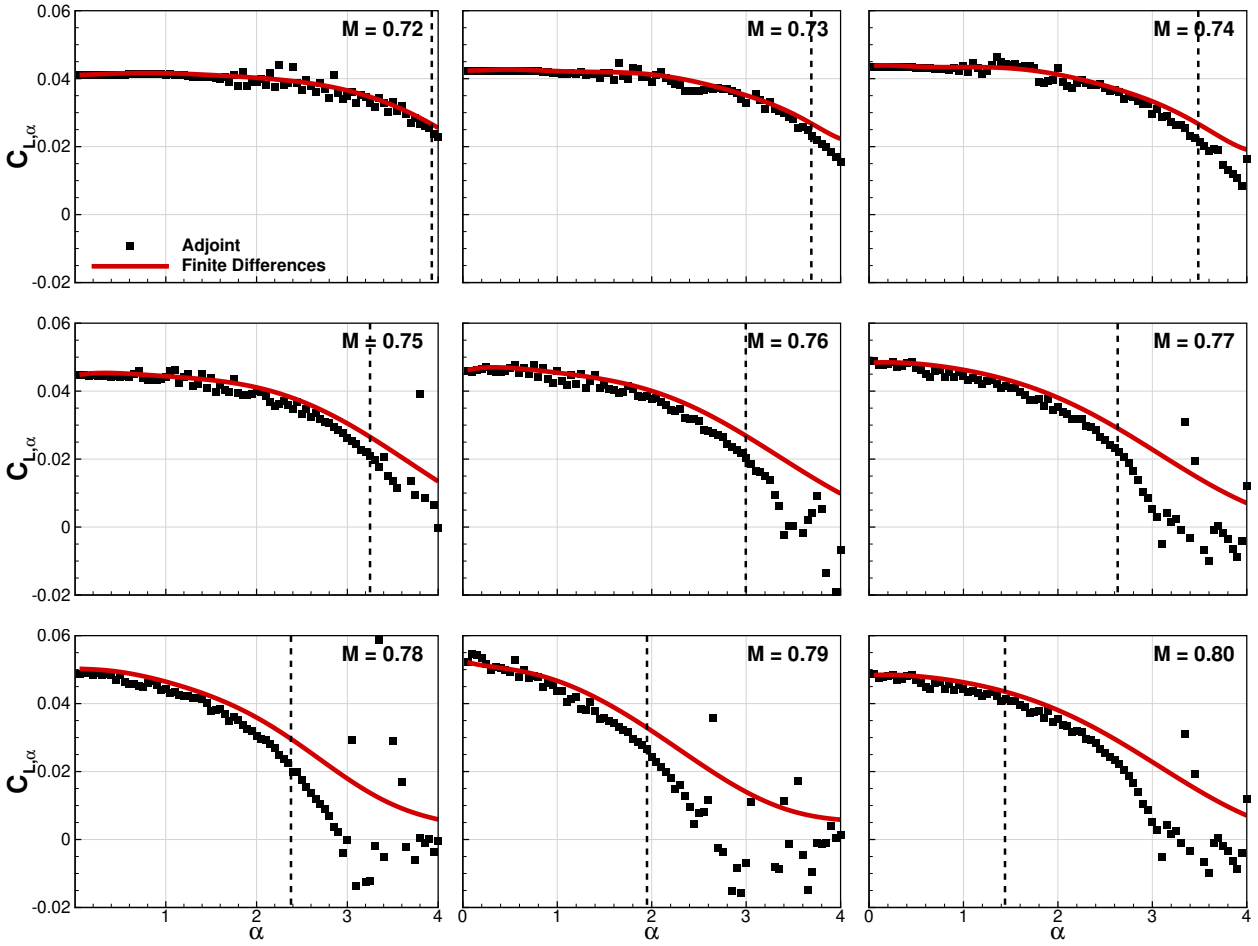

Figure 6.9: Comparison between the derivative $\partial C_L/\partial\alpha$ evaluated with finite differences and adjoint method for the NACA0012 aerofoil at $\mathrm{Re} = 6.0 \times 10^6$. The vertical, dashed lines mark the experimental onset.

6.2.4 Choice of the Onset Criterion

Among the criteria mentioned in the previous sections, the ones based on C_L and C_M were chosen to test the algorithm. The main reason is that integral aerodynamic coefficients can be efficiently used in conjunction with the adjoint method. Indeed, the criterion based on the trailing edge pressure coefficient was not used here. The adjoint variable in Equation (3.73) was introduced to avoid the evaluation of the derivatives of the flow variable with respect to the flight parameters. Building the algorithm with $\partial C_{p,TE}/\partial\alpha$ as the buffet parameter, as an example, would reintroduce the issue of evaluating such terms, and the only possible way would be to rely on finite differences. Conversely, assuming $C_B = \partial C_L/\partial\alpha$ or $C_B = \partial C_M/\partial\alpha$ allowed us to use Equation (3.72) to compute the derivatives.

Moreover, the target buffet indicator must be easy to estimate all over the interval of interest. It

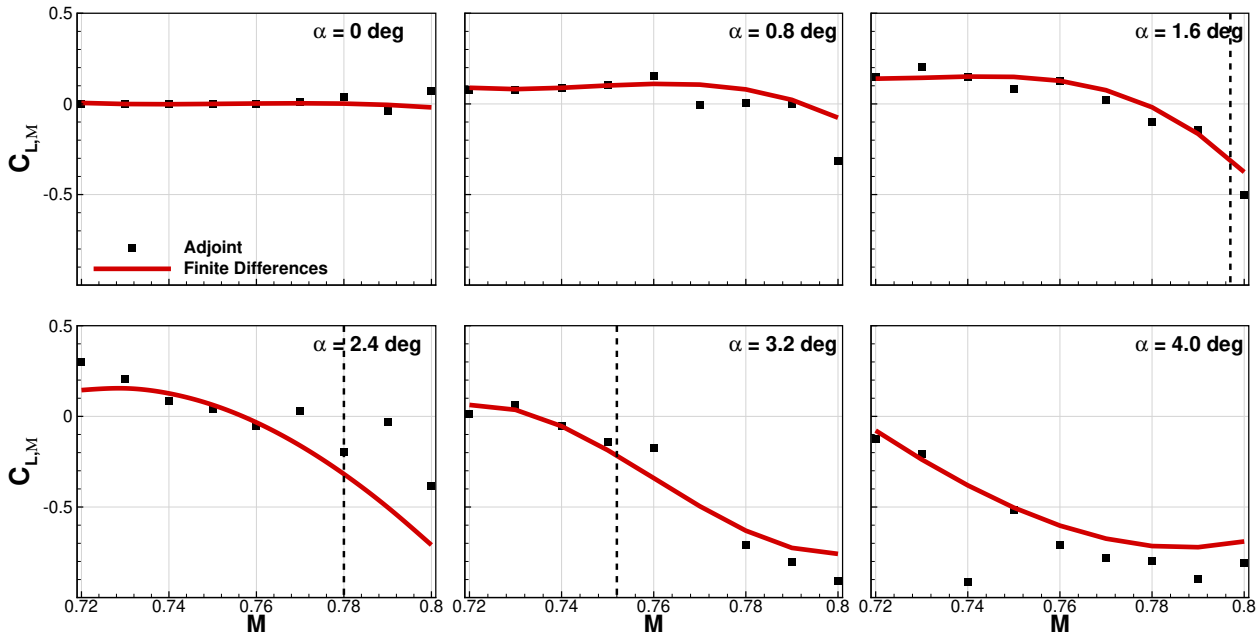

Figure 6.10: Comparison between the derivative $\partial C_L/\partial \mathrm{M}_\infty$ evaluated with finite differences and adjoint method for the NACA0012 aerofoil at $\mathrm{Re} = 6.0 \times 10^6$. The vertical, dashed lines mark the experimental onset. The experimental is not shown in some of the plots because not known from the experiments.

must also show some trend that is independent on the geometry under analysis. Figure 6.11 shows the behaviour of the two derivatives at the buffet onset predicted by the two criteria for two different geometries and Reynolds numbers. The target buffet indicator can be, in both cases, approximated with a linear function once the values at the minimum and maximum Mach number are known. We see that this approximation is more correct for $C_B = \partial C_L/\partial \alpha$ (solid lines in Figure 6.11), since the relative variations from the linear approximation are smaller with respect to the other case. On the other hand, the criterion $C_B = \partial C_M/\partial \alpha$ is more accurate in the prediction of the buffet boundary in comparison with the experiments, as shown in Figure 6.12.

6.2.5 Results and Discussion

Here the results obtained for the NACA0012 at $\mathrm{Re}_c = 6 \times 10^6$ are analysed in detail. Figure 6.13 shows the comparison between different runs corresponding to those listed in Table 6.1. The cases listed in the first column of the table correspond to different estimations of the buffet boundary by means of the algorithm proposed in Section 6.1.2. In each part of the table, the first row indicates the criterion adopted, the Mach number increment $\Delta \mathrm{M}_\infty$ used, determining the number of intermediate Mach numbers accounted for, and the number of computations required by the purely RANS-based criterion to draw the buffet boundary (194 for the NACA0012 aerofoil and 195 for the OAT15A aerofoil). The second column of the table sees the tolerance on the angle of attack used after the correction in Equation (6.3). Cases (a) and (g) employ a tolerance of 0.2 deg while the other

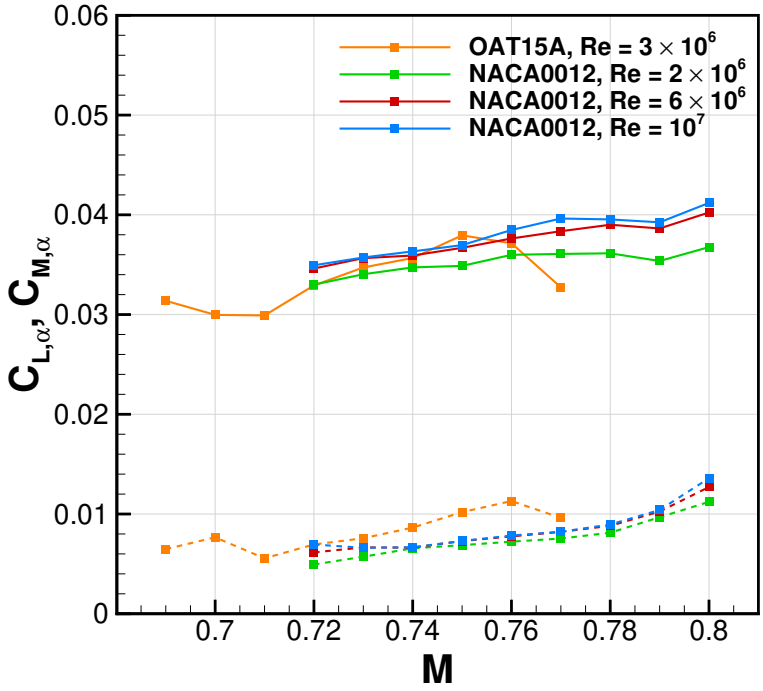

Figure 6.11: Buffet coefficients at the onset for the NACA0012 and OAT15A aerofoils. Solid lines: $\partial C_L/\partial\alpha$, dashed lines: $\partial C_M/\partial\alpha$.

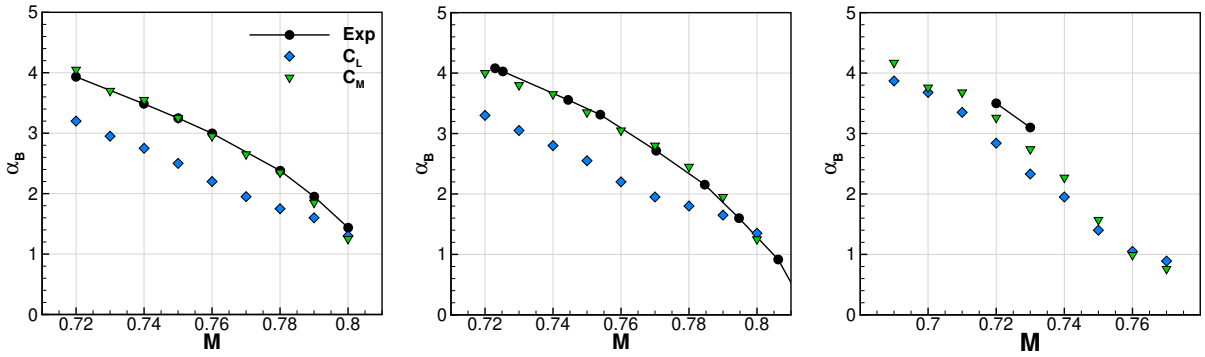

Figure 6.12: Buffet onset obtained from two purely RANS-based criteria compared with the experiments. Left: NACA0012 at Re $= 6.0 \times 10^6$; center: NACA0012 at Re $= 10.0 \times 10^6$; right: OAT15A at Re $= 3.0 \times 10^6$.

cases use a value of 0.1. The third column sees the values used for the Mach number increment introduced in Equation (6.2). For cases (a) and (b) a Mach increment ΔM_∞ of 0.005 was used, while 0.01 was used in the other cases. In the following two columns, the order of the interpolation used in Equation (6.3) and other variations to the algorithm are listed. The last three columns show the performance of the procedure in terms of number of computations required to complete the procedure, mean and maximum error in the onset estimate with respect to the purely RANS-based criteria. The procedure starts from the two extremes of the interval of interest, i.e. $M_{\infty,A} = 0.72$ and $M_{\infty,B} = 0.80$ and ends at the center of the interval. In Figure 6.13 to Figure 6.16 the reference

buffet boundary, named *RANS + FD*, is the one obtained with the purely RANS-based criterion, while *RANS + Adjoint* corresponds to the results of the algorithm of Section 6.1.2. The term *Additional runs* is used to indicate intermediate points where the angle correction of Equation (6.3) was applied before reaching the final point (*RANS + Adjoint*).

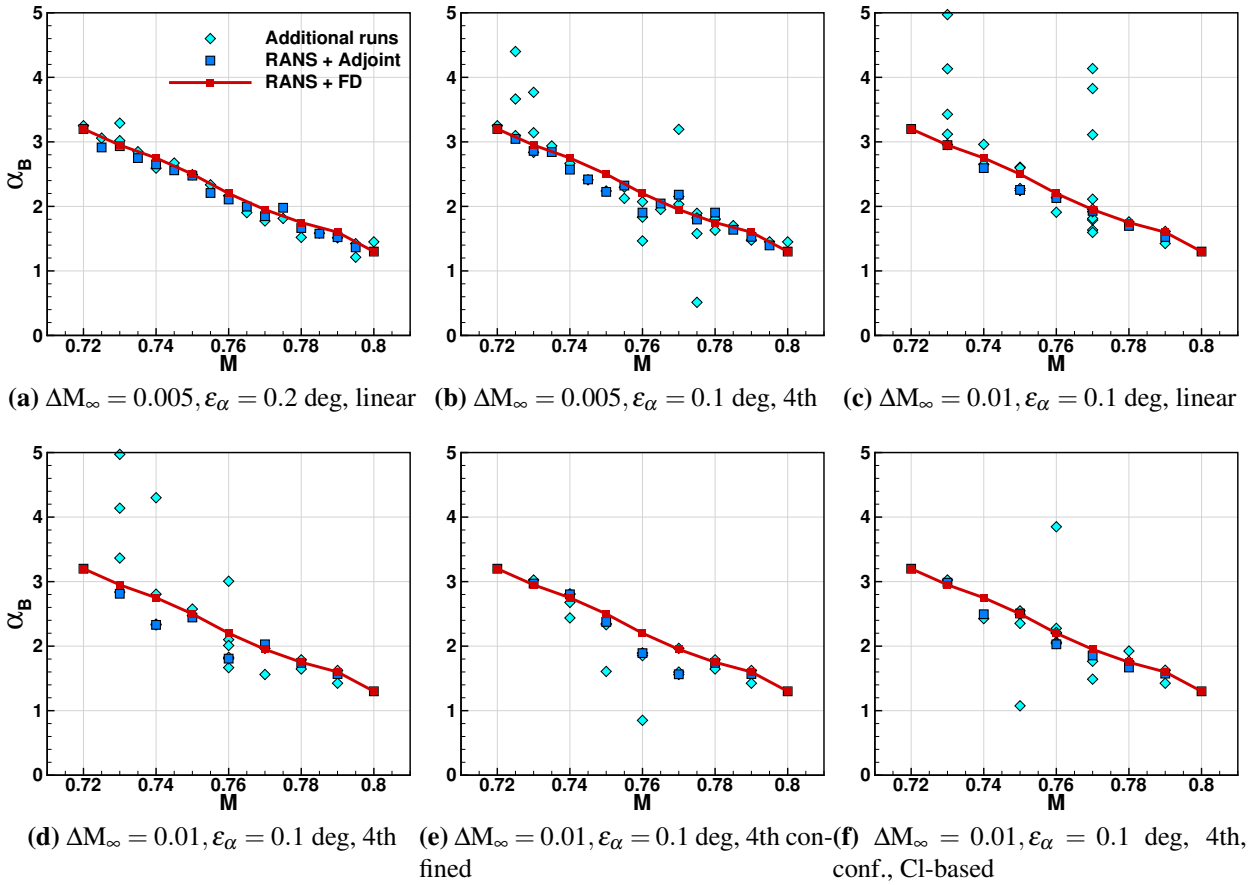

(a) $\Delta M_\infty = 0.005, \varepsilon_\alpha = 0.2$ deg, linear **(b)** $\Delta M_\infty = 0.005, \varepsilon_\alpha = 0.1$ deg, 4th **(c)** $\Delta M_\infty = 0.01, \varepsilon_\alpha = 0.1$ deg, linear

(d) $\Delta M_\infty = 0.01, \varepsilon_\alpha = 0.1$ deg, 4th **(e)** $\Delta M_\infty = 0.01, \varepsilon_\alpha = 0.1$ deg, 4th confined **(f)** $\Delta M_\infty = 0.01, \varepsilon_\alpha = 0.1$ deg, 4th, conf., Cl-based

Figure 6.13: Buffet boundary for the NACA0012 using the algorithm of Section 6.1.2, choosing $C_B = C_{L,\alpha}$.

When the tolerance ε_α is decreased, the algorithm takes more time to converge, like in the switch from case (a) to case (b). Moreover, using too fine tolerance on α, possibly emphasizes the differences between the approximated target buffet coefficient and the actual value, hence there is no guarantee that decreasing the tolerance under a certain threshold brings significant benefits in the estimate. Increasing ΔM_∞, the role of the adjoint in the evaluation of the derivatives becomes more important. If ΔM_∞ is small, an error made in the approximation is compensated by the linear correction of Equation (6.3), as long as the distance between the buffet onset and the current point α_i is relatively small. Increasing the Mach number increment, the error propagates and the first investigated point may be too far from the actual buffet onset. If this happens, the linear extrapolation may take many iterations or reach regions where the adjoint method no longer provides good estimates of the derivatives.

To overcome this drawback, some modifications were introduced. To avoid falling in regions where the derivative computed with the adjoint method has wrong value and sign, an angle restriction (*conf.* in Table 6.1) was applied. For conventional aerofoils, and in this range of Mach numbers, the buffet onset angle of attack is lower with higher Mach numbers, and it is, therefore, reasonable to estimate the buffet boundary as the straight line passing through the extreme points. From that estimate, the angle of attack is confined with a certain interval, and $1 \div 2$ degrees is a good compromise to avoid falling away from the onset without preventing non linearities of the criterion. The effect of the angle confinement can be seen comparing cases (d) and (e). In case (e), the number of additional runs required is decreased. Moreover, if the number of attempts increases, a quadratic or higher order interpolation can be used to reduce the number of points required. From two points, given the value of C_B and its derivatives, a second-order interpolation can be done, and the order increases with the number of attempts. Nevertheless, using a too high order of the interpolation may generate many different roots in the interval of interest, so in this work a maximum order of 4 was used. Using a higher-order interpolation, the number of runs required decreased. The procedure in cases (d-f) required a smaller number of runs with respect to the linear case (c). Also, when the number of attempts increases, an alternative to interpolating C_B is to reconstruct directly $C_L(\alpha)$ or $C_M(\alpha)$. While the points used to interpolate C_B are affected by the errors introduced by the adjoint evaluation, the values of the aerodynamic coefficients are in principle more accurate, coming from the same RANS computations used to evaluate the onset in the basic version of the criteria. Using this approach (C_L-based or C_M-based in Table 6.1), the number of simulations required is further reduced and the overall accuracy is increased. From now on, the results presented were obtained employing this last approach.

In case (f), the number of simulations required to draw a buffet boundary is lowered by around 60%, at the cost of a mean error of 0.074 deg and maximum error of 0.256 deg, with respect to the purely RANS-based criterion. Increasing the tolerance ε_α (case (g)), the accuracy of the algorithm is slightly reduced, as well as the CPU cost. It must be pointed out that such an estimate in the reduction of CPU costs is meaningful only if the Mach number interval and the number of intermediate Mach numbers are the same. This also puts into evidence the advantage of the proposed algorithm over the purely RANS-based criteria. While the number of computations required by the purely RANS-based criteria is proportional to the number of intermediate Mach numbers, the CPU cost of the algorithm is not so heavily affected by the number of intermediate points. Therefore, the smaller ΔM_∞, the higher is the saved CPU cost.

The same study is repeated for the OAT15A test case (Figure 6.14). The Mach number spans from 0.69 to 0.77. Once again, decreasing the Mach number increment does not necessarily result in higher costs, as long as the tolerance on the angle of attack is also increased. In terms of performance, the algorithm introduces a mean error of around 0.1 deg (that is comparable with the tolerance used) and a maximum error of 0.24-0.31 deg. The number of simulations required is

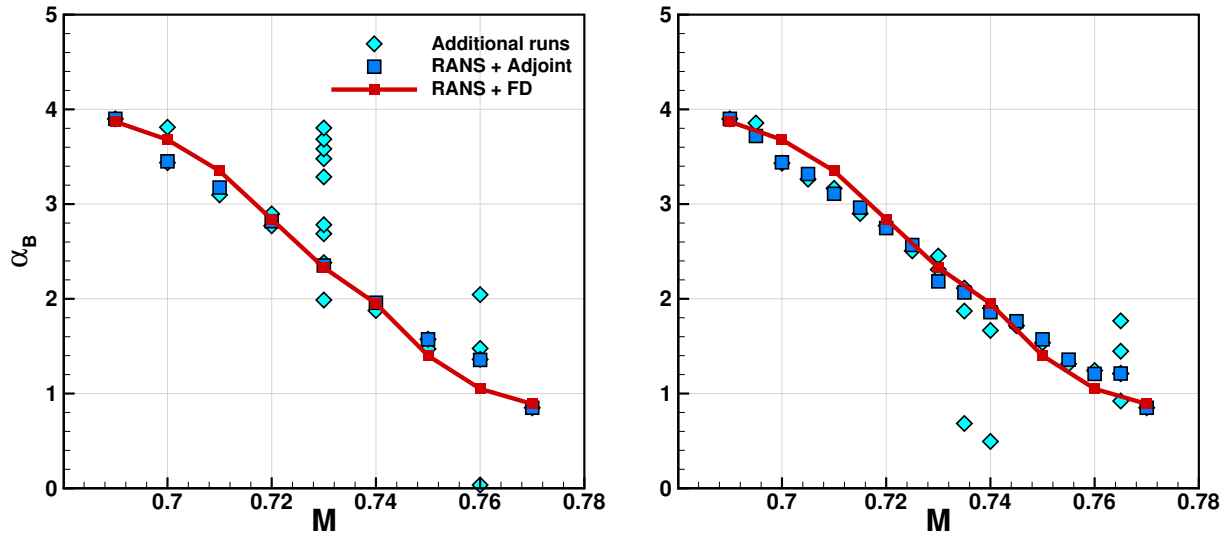

(a) $\Delta M_\infty = 0.005, \varepsilon_\alpha = 0.2$ deg **(b)** $\Delta M_\infty = 0.01, \varepsilon_\alpha = 0.1$ deg

Figure 6.14: Buffet boundary for the OAT15A using the algorithm of Section 6.1.2, choosing $C_B = C_{L,\alpha}$.

around half of those needed by the purely RANS-based criterion. Here, a slightly higher discrepancy is found with respect to the previous test case. The main reason is that the function $C_{L,\alpha}(M_\infty)$ (Figure 6.11) slightly departs from the linear behaviour assumed, making the computation less accurate.

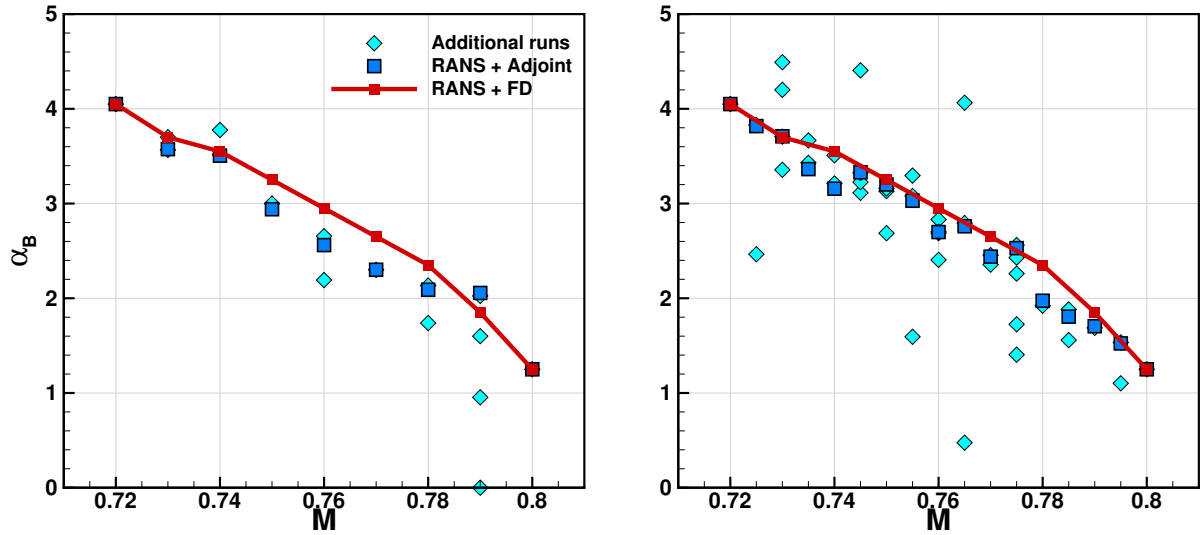

(a) $\Delta M_\infty = 0.01, \varepsilon_\alpha = 0.1$ deg **(b)** $\Delta M_\infty = 0.005, \varepsilon_\alpha = 0.1$ deg

Figure 6.15: Buffet boundary for the NACA0012 using the algorithm of Section 6.1.2, choosing $C_B = C_{M,\alpha}$.

The procedure was then applied in conjunction with the $C_{M,\alpha}$-based criterion for both configurations (Figure 6.15 and Figure 6.16). For case (b), both figures underline the drastic increase in

the number of computations required when decreasing the Mach number increment ΔM_∞, keeping a small tolerance on the angle of attack. Although the accuracy of the computation does not vary between cases (a) and (b), for cases (b) the CPU cost was higher by 70% for the NACA0012 and 27% for the OAT15A.

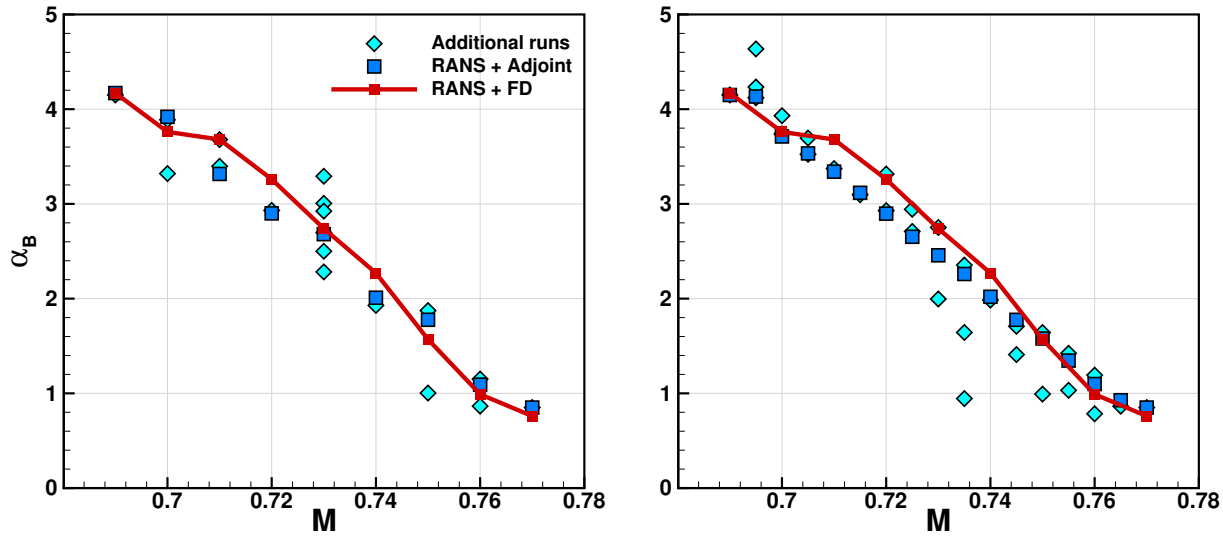

(a) $\Delta M_\infty = 0.01, \varepsilon_\alpha = 0.1$ deg **(b)** $\Delta M_\infty = 0.005, \varepsilon_\alpha = 0.1$ deg

Figure 6.16: Buffet boundary for the OAT15A using the algorithm of Section 6.1.2, choosing $C_B = C_{M,\alpha}$.

Overall, this second criterion is slightly more inaccurate, apparently due to the magnitude $|C_{M,\alpha}|$ being smaller than $|C_{L,\alpha}|$. The difference in the linear approximation of these quantities with the Mach number is hence more significant in the first case. This results in a slightly higher inaccuracy. On the other hand, this criterion was shown to be closer to the experimental results. Also in this case, the developed algorithm guarantees a reduction of 50-55% of the number of computation required by the purely RANS-based criterion.

It must be pointed out that the number of computations required included those needed to evaluate the buffet boundary at the minimum and maximum Mach numbers. This amounts to 47 computations for the NACA0012 case, and 46 for the OAT15A case. So, the actual number of computations to complete the buffet boundary with the proposed method is even smaller.

6.3 Chapter Summary

In this chapter, an algorithm for the fast prediction of the buffet boundary on aerofoils and wings was developed using steady RANS-based criteria and adjoint methods to compute flow sensitivities. The derivatives $C_{L,\alpha}$ and $C_{M,\alpha}$ were chosen as buffet indicators. Once determined, they can be approximated as linear functions of the Mach number. The algorithm fixes the Mach number and

Table 6.1: Performance of the algorithm for each case analysed.

NACA0012, Re$_c = 6\times10^6$	ε_α	ΔM_∞	**order**	**Criterion type**	**No. Runs**	$\langle\Delta\alpha\rangle$	$\Delta\alpha_{max}$
$C_{L,\alpha}$ **Criterion** (Figure 6.13)		0.01			194	0	0
(a)	0.2	0.005	1st	-	87	0.057	0.098
(b)	0.1	0.005	4th	α conf.	111	0.144	0.296
(c)	0.1	0.01	1st	-	103	0.069	0.245
(d)	0.1	0.01	4th	-	95	0.125	0.420
(e)	0.1	0.01	4th	α conf.	87	0.104	0.386
(f)	0.1	0.01	4th	α conf. C_L-based	74	0.074	0.256
(g)	0.2	0.01	4th	α conf. C_L-based	71	0.078	0.278
$C_{M,\alpha}$ **Criterion** (Figure 6.15)		0.01			194	0	0
(a)	0.1	0.01	4th	α conf. C_M-based	77	0.187	0.389
(b)	0.1	0.005	4th	α conf. C_M-based	131	0.160	0.394
OAT15A, Re$_c = 3\times10^6$	ε_α	ΔM_∞	**order**	**other**	**No. Runs**	$\langle\Delta\alpha\rangle$	$\Delta\alpha_{max}$
$C_{L,\alpha}$ **Criterion** (Figure 6.14)		0.01			195	0	0
(a)	0.1	0.01	4th	α conf. C_L-based	97	0.104	0.305
(b)	0.2	0.005	4th	α conf. C_L-based	91	0.127	0.241
$C_{M,\alpha}$ **Criterion** (Figure 6.16)		0.01			195	0	0
(a)	0.1	0.01	4th	α conf. C_M-based	83	0.168	0.364
(b)	0.1	0.005	4th	α conf. C_M-based	105	0.156	0.363

evaluates the onset angle of attack corresponding to the target value for each buffet indicator. The adjoint method was used to evaluate the derivatives with respect to the flight conditions. Other buffet onset criteria, mentioned in Section 6.1, were discarded because they involve local quantities, like the trailing edge pressure, that are not as easily available as the integrated loads.

The RANS, 2D computations and the adjoint method results were assessed separately. The RANS results were sufficiently close to experiments. Flow sensitivities calculated with the adjoint method were close to those obtained with finite differences. Some discrepancies were present for angles of attack beyond the buffet onset, due to the steady flow approximation used. For that reason, an angle confinement was introduced in the formulation.

The algorithm was tested using two configurations with available experimental results for the buffet onset. The procedure was repeated for both criteria and configurations. The use of linear extrapolation to find the angle of attack was efficient only when small Mach number increments were used. Otherwise, results could depart from the buffet boundary and the costs of the algorithm was increased. High order interpolations gave benefits both in terms of accuracy and cost reduction.

Overall, the algorithm allowed to recover the results obtained with purely RANS-based criteria. The algorithm was not formulated to improve the accuracy in the prediction of the buffet boundary with respect to the experiments, but only to improve the efficiency. Indeed, the procedure reduced the CPU costs by 50-60% with respect to the aforementioned criteria.

Chapter 7

Buffet boundary Estimation with Harmonic Balance Method

*

Because of the costly of SRSs, and of the uncertainty of URANS, few authors started to propose alternatives to the use of the aforementioned methods. Engineering criteria have been proposed for the buffet boundary prediction on wings, based on the results of experimental investigations [167, 203]. Criteria based on the trailing edge pressure coefficient or on deviations from linear trends of the lift or pitching moment coefficient are the most popular. Chung et al. [41] applied some of these using RANS computations. The CPU costs were limited, and computations of the steady solutions were repeated for several flight conditions. In the previous chapter, we proposed a method for the efficient estimation of the buffet boundary by means of the aforementioned RANS-based criteria and the adjoint method to further optimise the process of buffet boundary estimation. Nevertheless, the use of buffet criteria is limited to steady computations and their accuracy strongly depends on the employed turbulence model. When dealing with periodic flows, the use of frequency domain reduces the CPU costs needed for the several periods of oscillations, and the transient needed to reach periodic conditions. Popular methods are the time-spectral method [106], the nonlinear frequency domain method [180], and the Harmonic Balance (HB) method [109]. This latter has been widely used to study turbomachinery [71, 109] and rotor flows [281], where the frequency of the periodic flow is known *a priori*. Self-induced, unsteady flows, like vortex shedding or transonic buffet flows, introduce the problem related to the lack of knowledge of the fundamental flow frequency. So far, many attempts were made with regards to the first category [106, 192, 211], but the only application of spectral methods for transonic buffet is attributed to Plante and Laurendeau [211]. They used a time-spectral method to simulate the transonic buffet around the OAT15A

*The content of this chapter has been partially published in: "A. Petrocchi, G. N. Barakos, *Buffet boundary estimation using a harmonic balance method*, Aerospace Science and Technology, Vol. 132, 2023, 108086, https://doi.org/10.1016/j.ast.2022.108086".

aerofoil, using the GBVTP method of McMullen et al. [180] to evaluate the buffet frequency starting from a guess value.

In this chapter, we assess the ability of the harmonic balance method, implemented in HMB3, to cope with transonic buffet flows. The method is then used within a procedure for estimating the buffet boundary, of two-dimensional configurations and comparing with data available from experiments.

This chapter is structured as follows: the algorithm used to estimate the buffet boundary is presented in Section 7.1; Section 7.2 sees the results of TMS and HB computations for the test cases under analysis; Section 7.3 is devoted to discussion and conclusions.

7.1 Algorithm for buffet boundary estimation

The algorithm used to trace the buffet boundary is first presented. In the current study of the buffet boundary, only Mach number and angle of attack changes are accounted for. A third parameter like the Reynolds number can also be accounted for but it would increase the required CPU time.

The Mach number is an important parameter in defining the flight conditions, and we opted to keep it fixed and evaluate the buffet onset in terms of the angle of attack. The opposite is also possible. The range of flight conditions we are interested in is represented by an interval of Mach numbers $M_\infty \in (M_{\infty,A}, M_{\infty,B})$. The flow chart of the algorithm, implemented in MATLAB, is shown in Figure 7.1. The procedure begins with the definition of an interval of Mach numbers of interest and an initial point $(\alpha_A, M_{\infty,A})$. There, a TMS is carried out to acquire the reduced frequency associated with the buffet motion. Alternatively, a first HB computation can be carried out with an estimated reduced frequency value. This is not as safe as the first strategy because it is not possible to check the exactness of the reduced frequency found using the GBVTP method. Moreover, an incorrect initial guess for the frequency may prevent the HB equations from converging. In particular, if the value is too low, the GBVTP method may result in a solution with multiple oscillations (see. [211]). Therefore, in this study, a preliminary TMS was always performed. It is also important that the initial flow conditions correspond to buffet so that the HB computation for the next step of the procedure begins from a buffet solution. If the initial TMS fails to predict buffet, the angle of attack must be varied until buffet conditions are reached. The state of the boundary layer can be used to decide whether the angle of attack should be increased of decreased. If the boundary layer downstream of the shock is not separated from the shock foot to the trailing edge, the angle of attack must be increased to cross the lower buffet boundary, referred as *buffet onset*, for a certain Mach number. An increase in the angle of attack should favour the merging of the two distinct separated regions at the shock foot, and at the trailing edge, into a single one. If the boundary layer is fully separated and no buffet is present, the aerofoil is likely to be above the upper buffet boundary,

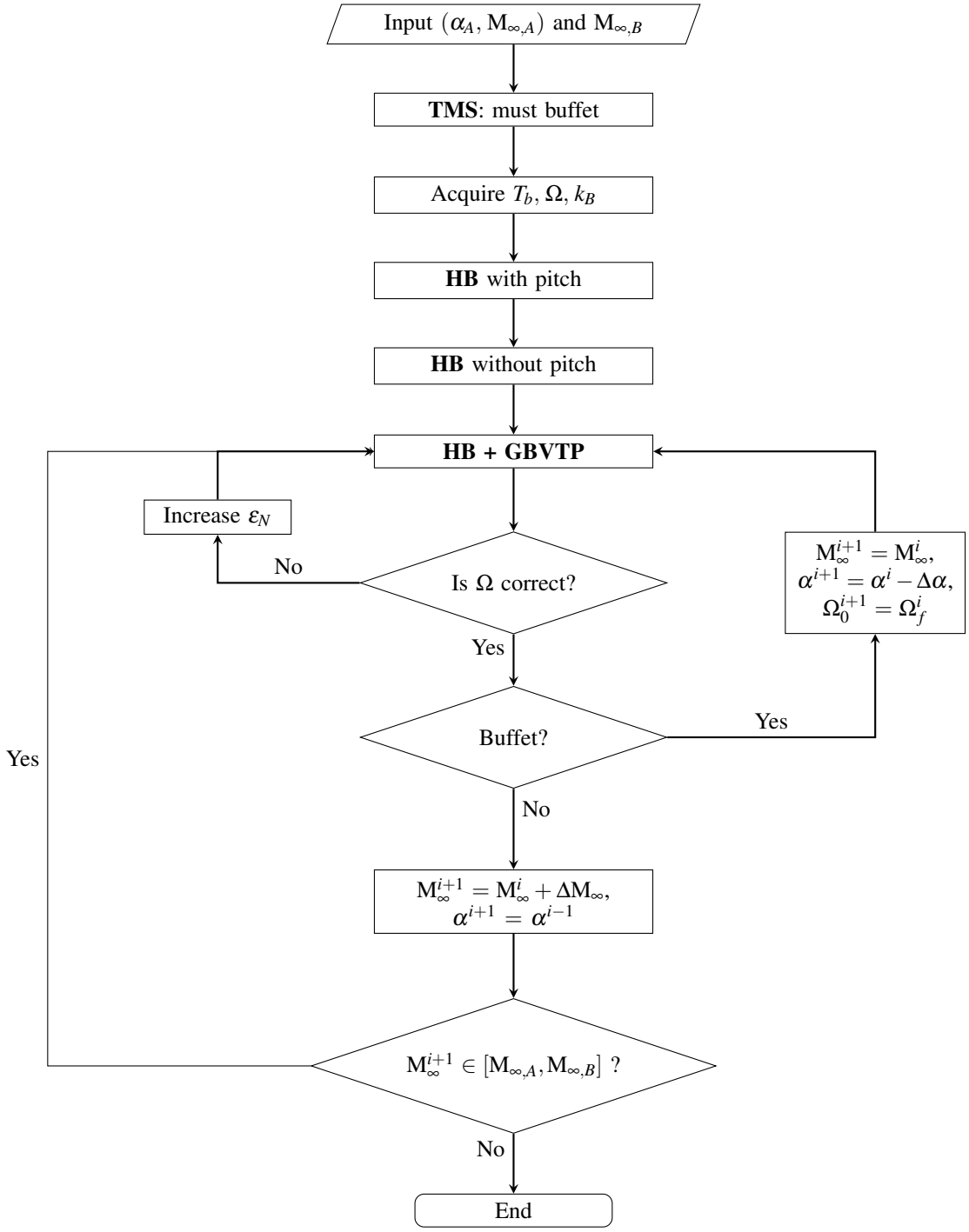

Figure 7.1: Algorithm used for tracing the buffet boundary.

buffet offset [120], and the angle of attack must be decreased.

After computing the fundamental frequency, the harmonic computation at the same conditions is initialised. As suggested by Plante and Laurendeau [211], the computations are initialised by imposing an oscillation and acquiring the initial snapshots. After that, the aerofoil is kept steady and the frequency is kept the same. After some iterations, the GBVTP method is activated. If the pitching motion is not prescribed, the HB computation starts from identical snapshots and moves towards a steady solution. This justifies the need for a buffeting flow as the initial point of the procedure. In this work, a 5 deg oscillation was imposed in all cases. This value was high enough, for the considered cases, to obtain different initial solutions.

After the first HB computation, the final frequency is acquired and used as initial guess for the next computation. At any iteration, the exactness of the frequency evaluated through the adaptive frequency method is assessed by looking at the ratio between the final and initial periods of oscillation. Indeed, if this ratio is closer to 2 (or bigger integers) than to 1, it means that the solution has two (or more) buffet periods and the computed frequency is incorrect. This is more likely to happen, according to Plante and Laurendeau [211], when starting from a low guess value with respect to the actual one. According to the study of Giannelis et al. [98], this can happen when increasing either Mach number or angle of attack. If the check detects an anomaly in the frequency estimation, the time-spectral viscosity is increased, to increase the stability of the GBVTP method.

At each iteration, the extracted loads are analysed to determine if there is buffet, corresponding to:

$$\frac{\Delta C_L}{\langle C_L \rangle} \geq B, \tag{7.1}$$

where ΔC_L is the amplitude of the oscillation in the lift coefficient, $\langle C_L \rangle$ is the mean lift coefficient, and B is some user-specified percentage. A value of 5-10% is recommended to avoid oscillations in the loads due to other factors, e.g. vortex shedding for aerofoils with blunt trailing edge, to be seen as buffet.

If the flow is buffeting, the angle of attack is reduced by a user-prescribed amount (dictated by the accuracy we need in estimating the buffet boundary) and a new HB computation is performed until a steady solution is reached. An example of how the procedure works is given in Figure 7.2, showing the loads associated with each snapshot of a single-mode HB computation around the OAT15A aerofoil, for different angles of attack. Once the loads are converged, the angle of attack was gradually decreased until steady conditions were reached. For the case in figure, an angle of attack of $\alpha = 3.0$ deg coincided with absence of buffet and, therefore, we could locate the buffet onset for $\alpha_B \in [3.0, 3.1)$. The procedure is repeated until the Mach number falls out of the interval of interest. If this is the case, the Mach number is altered, and the angle of attack and frequency are set to the ones of the last buffeting solution. We concluded that it is advisable to proceed by increasing the Mach number (by a fixed user-prescribed amount). Since for conventional configurations the

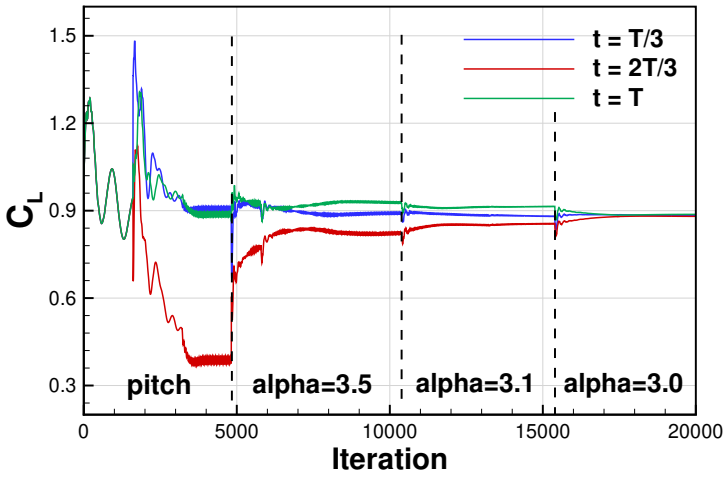

Figure 7.2: Evolution of the lift coefficient associated with each snapshot of the 1-mode harmonic balance computation at different angles of attack for the OAT15A aerofoil at $M_\infty = 0.73$ and $Re_c = 3 \times 10^6$.

buffet boundary is crossed increasing either Mach number or angle of attack, to move towards smaller Mach number, an increment of the angle of attack is also required to avoid crossing the buffet boundary. Also, increasing, at the same time both flight parameters may not be enough to avoid this inconvenience. Moreover, a change in both of them will require more time for the HB computation to converge.

7.2 Results

7.2.1 Test cases description and numerical setup

Laminar Circular Cylinder

A circular cylinder at $Re_D = 180$ and $M_\infty = 0.2$ was chosen as a test case for its simplicity. It was used for assessing the ability of the HB computation to recover the results of the TMS. In this case, several tests were carried out to evaluate the exactness of the adaptive frequency method to capture the right frequency of vortex shedding, corresponding to a Strouhal number $St \simeq 0.19$ [280].

The computations were carried out in 2D on a grid of 256×128 cells in the tangential and radial direction, respectively, and a time step $\Delta t = 0.01 D/U_\infty$, corresponding to more than one hundred steps per period of oscillation. Further refinement of the spatio-temporal grid did not lead to any significant changes in the amplitude of oscillation or the fundamental frequency.

NACA0012 Wing Section

The first aerofoil section analysed, the NACA0012 section, was studied at the Ames High Reynolds Number Facility by McDevitt and Okuno [178]. Details about the experimental setup and the

results obtained were given in Section 2.2 and Section 6.2.

The computational grids used for the aerofoils have a typical C-H topology. The 2D grid consists of 352 cells around the aerofoil, 112 cells in the normal direction, and 104 cells in the wake, for a total of about 62 thousand cells over the domain extending $80c$ both ahead of the aerofoil, and in the wake direction. The spatial distribution was chosen to satisfy the condition of $\Delta y^+ < 1$ at each condition, resulting in a first cell size of about $2.0 \times 10^{-6} c$. The grid used for computations (see Figure 7.3, left) was selected after carrying out a mesh sensitivity study (see Section 7.2.2). Adiabatic wall boundary conditions were imposed at the aerofoil, and free-stream values of pressure and velocities elsewhere. For the TMSs, a timestep of $\Delta t = 0.01 c/U_\infty$, corresponding to around 1200 steps for each buffet period at $M_\infty = 0.72$ and 6.0 deg, was employed. The convergence of the implicit scheme was based on the reduction of the summation of the conserved flow variables residual with respect to the previous step. In particular, either 3 orders of magnitude of reduction or 100 inner iterations were reached for each unsteady step.

OAT15A Wing Section

The second case is the supercritical OAT15A wing section, analysed in the S3Ch wind tunnel at ONERA [125, 126]. The test case was introduced in Section 2.2 and Section 6.2.

The numerical setup is the same as that for the NACA0012 aerofoil. The employed grid (see Figure 7.3, right) now amounts to 66 thousand cells because of the blunt trailing edge and was selected after a mesh convergence study, analogous to the previous case (see Section 7.2.2). The time step employed corresponds to at least 1500 steps for each buffet period for the flight conditions analysed.

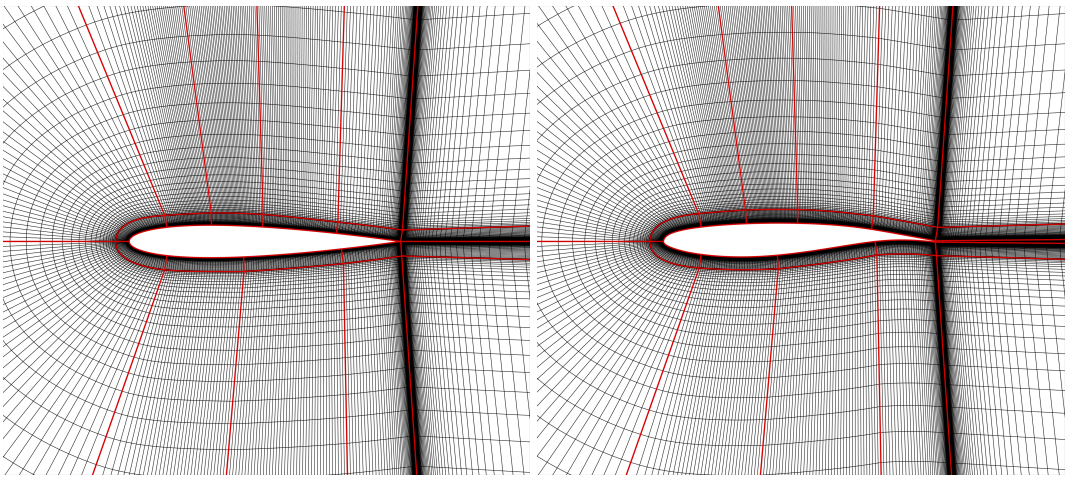

Figure 7.3: Computational grids adopted in the computations. Left: NACA0012 aerofoil; right: OAT15A aerofoil. The red lines represent the boundaries of the multi-block domain.

7.2.2 Grid Convergence Study

To guarantee grid convergence for the geometries under analysis, three different grids were tested for flow conditions before and after the buffet onset.

NACA0012

Three different grids consisting of 44, 62, and 84 thousand cells, respectively, were tested using the SST model for the steady flow at $\mathrm{Re}_c = 6 \times 10^6$, $\mathrm{M}_\infty = 0.778$ and $\alpha = 2.0$ deg around the NACA0012 aerofoil. Figure 7.4, left, shows the pressure coefficient distribution around the aerofoil. A slight difference is the pressure level at the suction side, reflecting in a difference on the third decimal digit in both the lift and drag coefficients (Table 7.1). The study was repeated at $\mathrm{Re}_c = 1 \times 10^7$, $\mathrm{M}_\infty = 0.72$ and $\alpha = 6.0$, i.e., according to the experiments, at buffet conditions. Although the difference was irrelevant for the steady case, for the buffet case, the medium and fine grids differed from the coarse in terms of the amplitude of oscillation (Figure 7.4, right). To avoid a late buffet onset, the medium grid was selected as reference in this study. Using a finer grid did not result in any significant changes in the predicted amplitude and frequency of oscillation. The buffet reduced frequency was also in agreement with the experimental value.

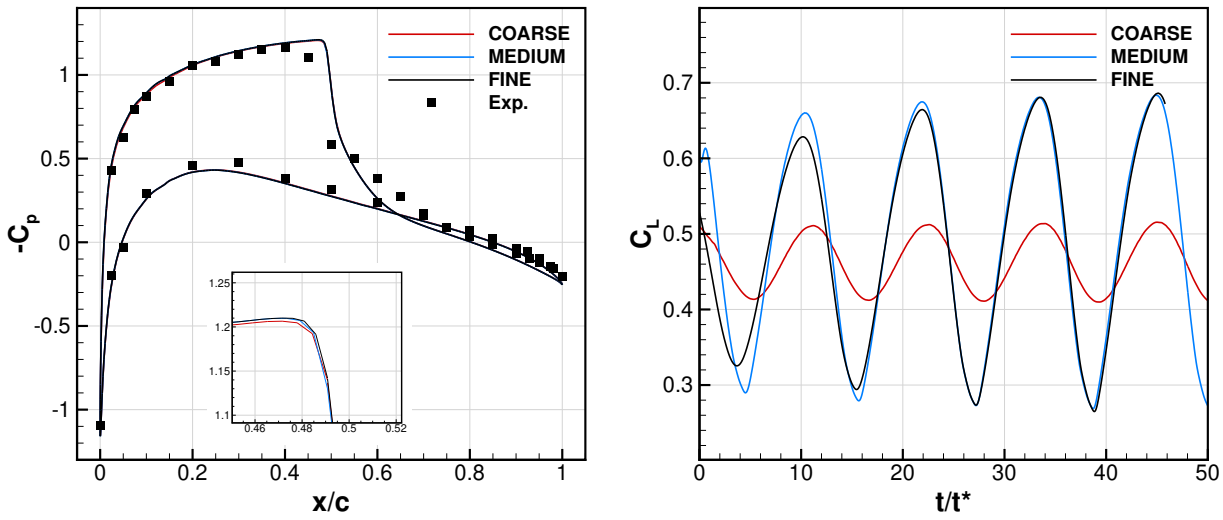

Figure 7.4: Left: pressure coefficient distribution around the NACA0012 aerofoil at $\mathrm{Re}_c = 6 \times 10^6$, $\mathrm{M}_\infty = 0.778$ and $\alpha = 2.03$ deg, with zoom on the shock region; right: Lift coefficient history for the flow at $\mathrm{Re}_c = 1 \times 10^7$, $\mathrm{M}_\infty = 0.72$ and $\alpha = 6.0$.

OAT15A

The mesh sensitivity study was carried out in a similar way to other cases. In this case, the flow conditions were $\mathrm{Re}_c = 3 \times 10^6$, $\mathrm{M}_\infty = 0.73$ and $\alpha = 2.5$, 3.5, with angles of attack corresponding to

Table 7.1: Grid convergence study for the NACA0012. C_L, C_D refers to the steady case, while $k_B, \Delta C_L$ to the buffet case.

Grid	N_x	N_y	N_{wake}	C_L	C_D	k_B	ΔC_L
Coarse	280	92	92	0.3719	0.0231	0.553	0.1115
Medium	352	112	104	0.3752	0.0224	0.546	0.4159
Fine	416	128	120	0.3757	0.0223	0.545	0.4213
Exp.				-	-	0.55	-

non-buffeting and buffeting flows, respectively. Similar considerations can be done for the steady case (Figure 7.5, left), where the SST model was used to close the equations. Indeed, the grid refinement was irrelevant. For the unsteady case (Figure 7.5, right), the grid refinement did not significantly affect the prediction of the amplitude and frequency of the shock oscillation (see Table 7.2). Therefore, the medium grid was chosen to be consistent with the previous case. Although small discrepancies with the experiments are observed, the overall agreement allows for carrying out the following studies.

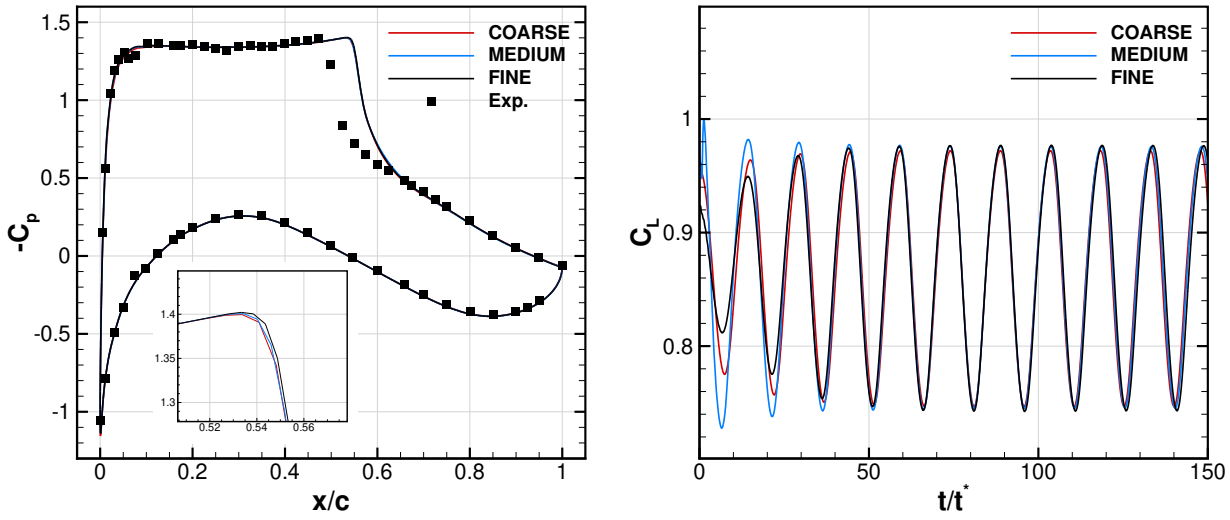

Figure 7.5: Left: pressure coefficient distribution around the OAT15A aerofoil at $\mathrm{Re}_c = 3 \times 10^6$, $\mathrm{M}_\infty = 0.73$ and $\alpha = 2.5$ deg, with zoom on the shock region; right: Lift coefficient history for the flow at $\mathrm{Re}_c = 3 \times 10^6$, $\mathrm{M}_\infty = 0.73$ and $\alpha = 3.5$.

7.2.3 TMS Results

Here the results of the TMSs for each test case are briefly discussed. The main scope is to assess the ability of the simulation strategies adopted to correctly predict unsteady flows.

The TMS for the laminar cylinder was run with no turbulence model. The vortex shedding was well captured and associated with a periodic oscillation of the aerodynamic coefficients. The fun-

Table 7.2: Grid convergence study for the OAT15A. C_L, C_D refers to the steady case, while St, ΔC_L to the buffet case.

Grid	N_x	N_y	N_{wake}	N_{TE}	C_L	C_D	St	ΔC_L
Coarse	280	92	92	41	0.9478	0.0402	0.068	0.2249
Medium	352	112	104	41	0.9519	0.0235	0.067	0.2307
Fine	416	128	120	51	0.9513	0.0235	0.067	0.2332
Exp.					-	-	0.066	-

damental frequency obtained, corresponding to a Strouhal number of 0.189, is in good agreement with the experimental results.

The computations were also carried out using a 2D PANS approach with the SST model as the parent RANS model. The PANS formulation was detailed in Section 3.4. The adoption of PANS allowed for the unlocking of the flow oscillations. We believe that adopting reasonably high values of the parameter f_k ($f_k = 0.7$ here if not differently specified), a PANS formulation can help in the prediction of this class of flows where most statistical turbulence models give too-high levels of eddy viscosity as reported, e.g., in [108, 120].

Table 7.3 shows the agreement in terms of buffet frequency for different flow conditions at $\mathrm{Re}_c = 1.0 \times 10^7$ for the NACA0012 aerofoil. At all analysed conditions, the 2D PANS computation was not able to reproduce the self-sustained shock oscillations at Mach number 0.8, a point that is difficult to predict, in the literature [45, 120]. The improvement of the ability of turbulence models or simulation strategies to predict buffet is beyond the scope of this work, and so, the current agreement is seen as satisfactory.

Table 7.3: Table of time-marching computations performed for the NACA0012 aerofoil, $\mathrm{Re}_c = 1 \times 10^7$.

M_∞	α	Buffet	k_{exp}	k_{num}
0.72	6.0	yes	0.55	0.52
0.75	4.0	yes	0.47	0.39
0.77	4.0	yes	0.44	0.45
0.80	4.0	no	0.38	-

Very good agreement, on the other hand, was found between PANS and experiments for this configuration, while URANS simulations with the SST model led to a steady-state solution even at angles of attack well beyond the buffet onset. This can be seen in Figure 7.6. The distributions of the mean pressure coefficient and the root mean square around the aerofoil were in good agreement with the experiments for several angles of attack, both at pre- and post-buffet onset. Table 7.4 shows the comparison with the experiments in terms of Strouhal number associated with the main buffet frequency at different Mach numbers and angles of attack.

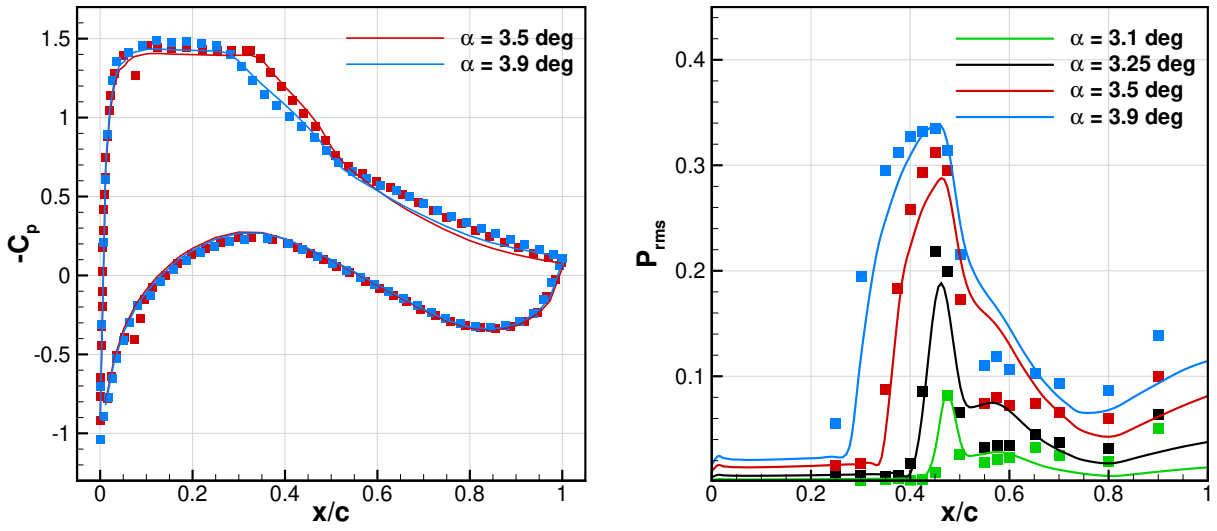

Figure 7.6: Mean pressure coefficient (left) and RMS (right) around the OAT15A coloured by angle of attack, at $M_\infty = 0.73$ and $Re_c = 3 \times 10^6$. Solid lines: CFD results; symbols: experiments of [126].

Table 7.4: Table of time-marching computations performed for the OAT15A aerofoil, $Re_c = 3 \times 10^6$.

M_∞	α	**Buffet**	St_{exp}	St_{num}
0.73	3.5	yes	0.066	0.067
0.72	3.5	yes	0.062	0.062
0.74	3.5	yes	0.074	0.071
0.73	3.1	yes	0.066	0.067
0.73	3.25	yes	0.066	0.067
0.73	3.9	yes	0.066	0.067

7.2.4 HB Results

The ability of the HB method to cope with the unsteady flows developing in the aforementioned test cases is now investigated.

7.2.4.1 Laminar Cylinder

Several simulations were run to mainly investigate the exactness of the HB computation and the GBVTP method. Figure 7.7, shows the comparison in terms of the drag and lift coefficients between the HB computations with different number of harmonics and the TMS. For this case, adopting a number of harmonics greater or equal to 3 the history of the aerodynamic coefficients over a period of oscillation is well replicated, showing almost no discrepancy with respect to the TMS.

Figure 7.8, shows the behaviour of the flow residual during the HB computation for $N_H = 7$. In this case, the GBVTP method was also used. In a similar way as for the aerofoils, the computation must be initialised by plunging the cylinder to allow the HB method to start. When the cylinder,

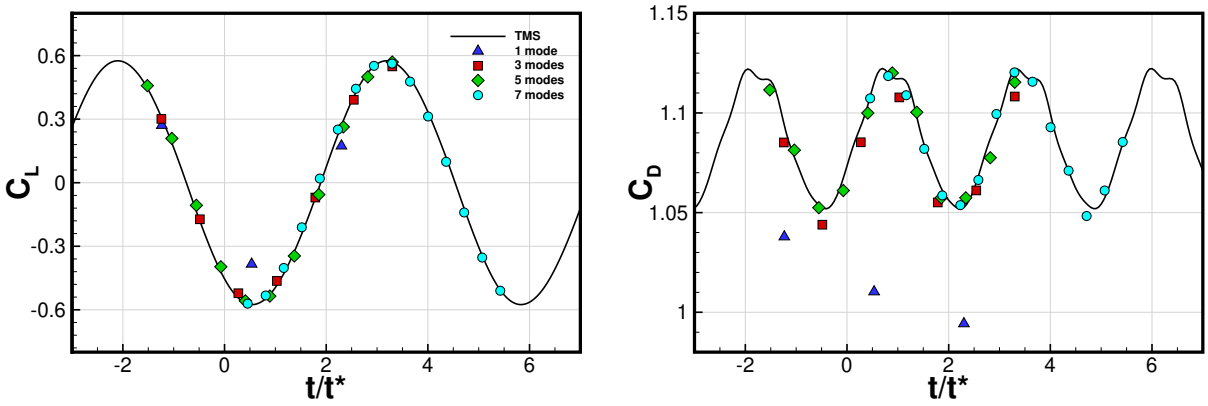

Figure 7.7: Lift (left) and drag (right) coefficients obtained with time marching simulations (TMS) and harmonic balance (HB) with different number of modes for the flow around a laminar cylinder at $\mathrm{Re}_D = 180$.

after the initial phase, is kept still, an increase in the residual is expected because of the change applied. In the following phases, the residual kept decreasing as expected.

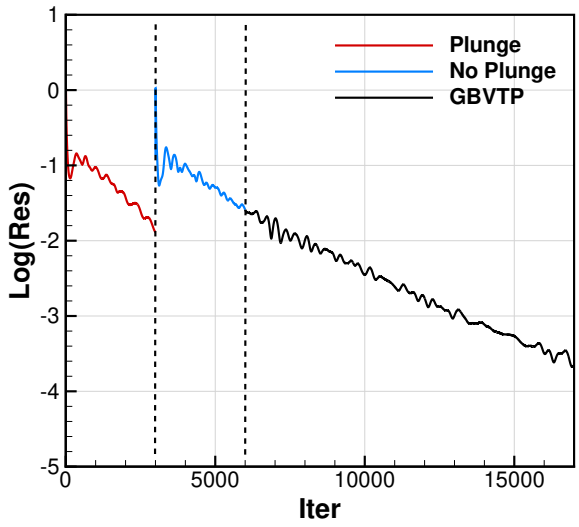

Figure 7.8: Flow residuals history for the HB computation with 7 modes for the flow around the laminar cylinder at $\mathrm{Re}_D = 180$.

The GBVTP convergence towards the right value of the reduced frequency is shown in Figure 7.9 for different values of the initial frequency (left plot) and number of harmonics (right plot). It must be noted that for a different number of harmonics the adaptive-frequency procedure points toward more accurate values of the fundamental frequency of oscillation. The underlying reason may be the decrease in the damping coefficient ε_N with the increase in the number of harmonics, limiting the effect of the temporal spectral viscosity term.

For buffet cases, the HB method worked well and predicted the self-sustained oscillations of the shock for both configurations. Figure 7.10 and Figure 7.11 show the comparison between the aerodynamic loads at the $2N_H + 1$ time snapshots for different numbers of harmonics for the

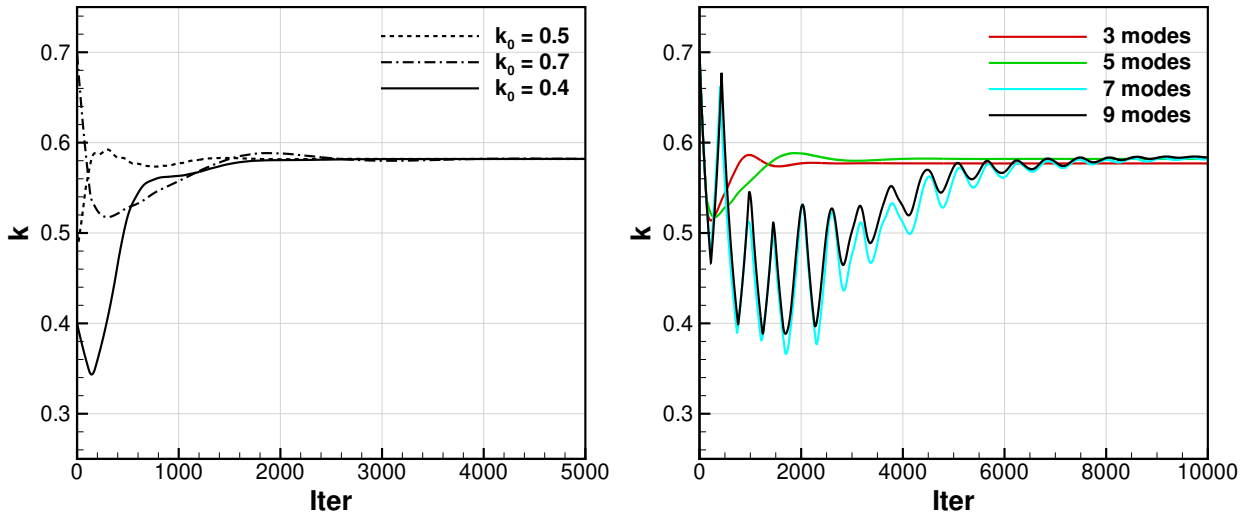

Figure 7.9: Reduced frequency history for the computation for the flow around the laminar cylinder at $\mathrm{Re}_D = 180$ with the GBVTP method. Left: different initial values for k and $N_h = 5$; right: different number of modes and $k_0 = 0.7$.

NACA0012 and the OAT15A aerofoils, respectively. In both cases, at least 3 harmonics are needed for the lift and drag oscillations to be well captured. Figure 7.12 and Figure 7.13 show how in both

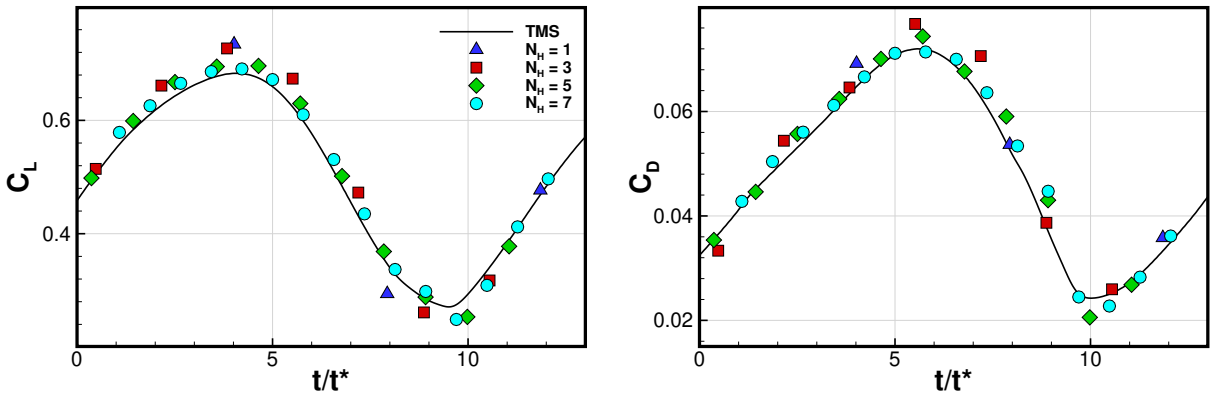

Figure 7.10: Lift (left) and drag (right) coefficients obtained with time marching simulations (TMS) and harmonic balance (HB) with different number of modes for the flow around the NACA0012 aerofoil at $\mathrm{Re}_c = 6 \times 10^6$, $\mathrm{M}_\infty = 0.72$ and $\alpha = 6.00$ deg.

cases, the 2D buffet motion is well predicted by means of Mach contours and the direct comparison with the TMS counterpart. The 7-mode computations shown here can capture the fundamental flow physics of both sections, putting into evidence the interaction between shock and boundary-layer across all the phases of buffet. One period includes the formation of the separation region at the foot of the shock, merging into a single separated flow region extending from the shock foot to the aerofoil trailing edge, the upstream shock motion with fully separated boundary layer, and the boundary layer re-attachment. The same flow characterisation, although not shown here, was

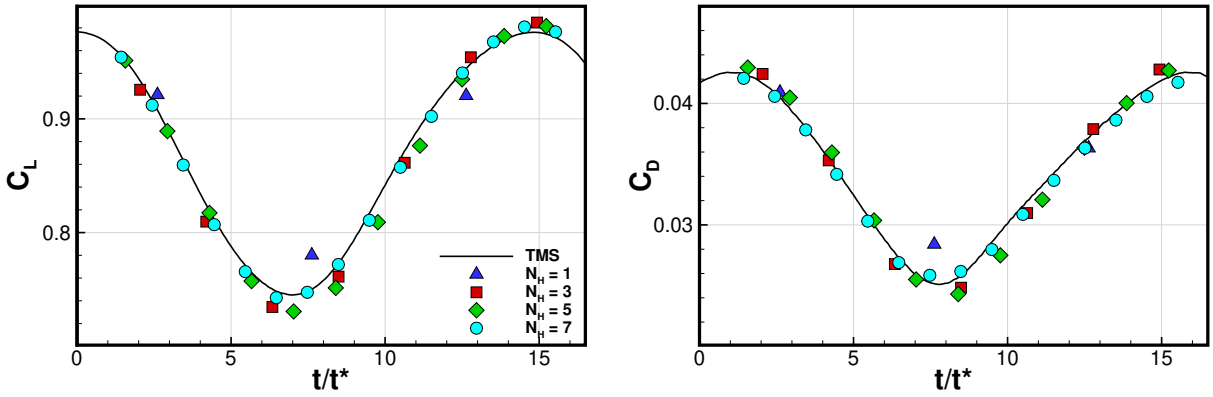

Figure 7.11: Lift (left) and drag (right) coefficients obtained with time marching simulations (TMS) and harmonic balance (HB) with different number of modes for the flow around the OAT15A aerofoil at $\mathrm{Re}_c = 3 \times 10^6$, $\mathrm{M}_\infty = 0.73$ and $\alpha = 3.5$ deg.

provided by simulations with a smaller number of harmonics ($N_H = 3, 5$).

Figure 7.14 underlines some differences between the two test cases, by showing the convergence of the lift coefficient against the number of iterations for the seven-mode computations. The displayed values represent the lift coefficient calculated from the solutions at the different time instants over a buffet period. The OAT15A case (right) displays a slightly oscillating behaviour in the lift coefficient history, while the NACA0012 (left) does not. This is possibly due to the blunt trailing edge in the OAT15A geometry, and the pseudo time-stepping method used to integrate the system of equations. Nevertheless, the peak-to-peak amplitudes of these oscillations are around two orders of magnitude smaller than the corresponding mean values and, therefore, they are not seen as a problem for the buffet boundary estimation process. To avoid a wrong detection of buffet, the B coefficient in Equation (7.1) cannot be set to zero.

The cost comparison of Table 7.5 shows the net saving in CPU time with respect to the TMSs. In all cases, simulations were run on 8 CPUs. The CPU time considered for the TMSs was that required to develop the shock oscillation and reach three almost identical buffet periods. The CPU cost grows significantly with the number of harmonics but it never exceeded the TMS time.

7.2.5 Buffet Boundary Evaluation

Here, the results of the HB computations embedded in the procedure for the buffet boundary estimation of Section 7.1 are described. Following the results of the previous section, the number of harmonics should be between 3 and 5, to avoid the undersampling of the buffet period and undesired high CPU costs.

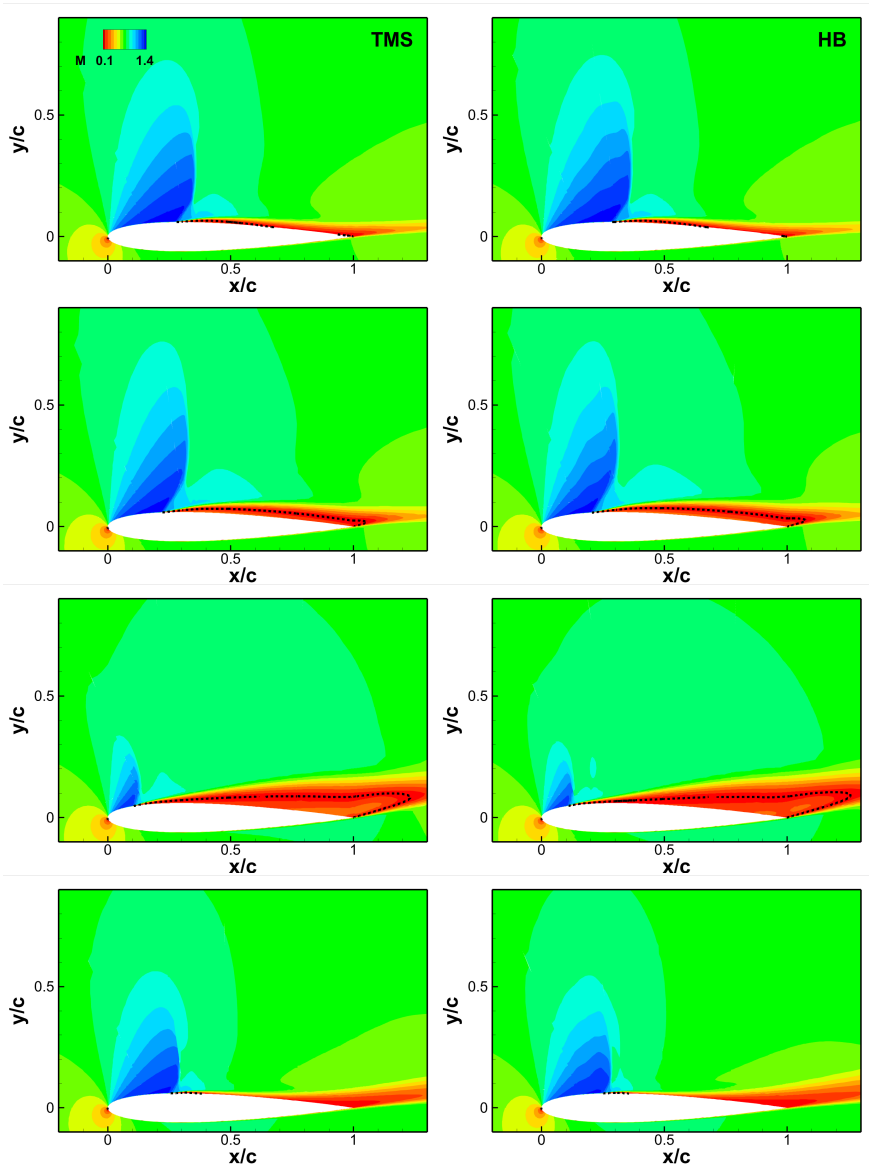

Figure 7.12: Mach number contours for the flow around the NACA0012 aerofoil computed with TMS (left) and HB (right) at different phases in a buffet period ($Re_c = 6 \times 10^6$, $M_\infty = 0.72$ and $\alpha = 6.00$ deg). From top to bottom: most downstream position, upstream moving shock, most upstream position, downstream moving shock. The dashed, black lines represent the zero-longitudinal velocity isolines.

NACA0012 computations

Figure 7.15, left plot, shows the differences in the buffet boundary, evaluated as explained in the previous section, between the three and five modes, for the flow around the NACA0012 aerofoil at Reynolds number of $Re_c = 6 \times 10^6$. The accuracy on the buffet onset was fixed to $\Delta\alpha = 0.2$ deg, while the increment on the Mach number to $\Delta M_\infty = 0.01$, and these parameters were kept constant across all simulations. Here, there is little difference between the results with different numbers of harmonics. This justifies the use the smaller number of harmonics, $N_H = 3$, since no accuracy was lost by decreasing the number of modes especially in the range of Mach numbers

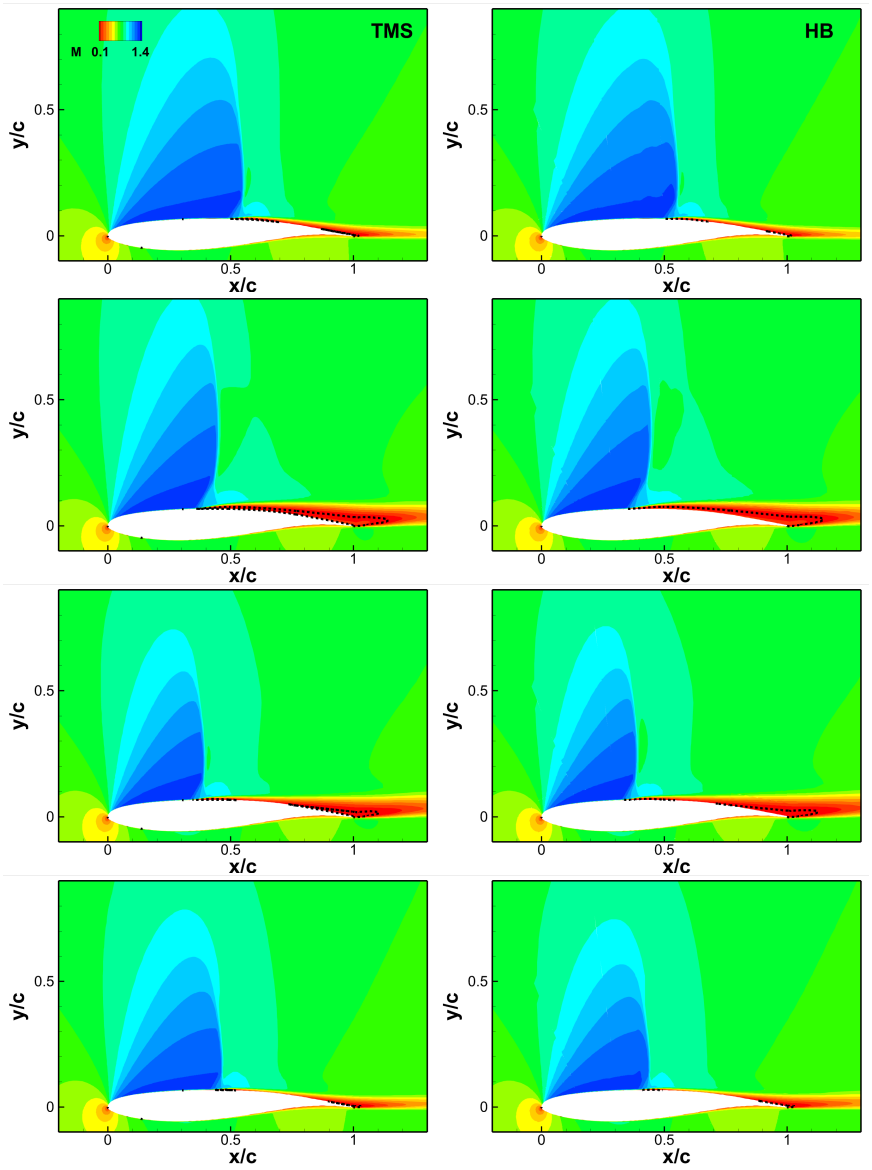

Figure 7.13: Mach number contours for the flow around the OAT15A aerofoil computed with TMS (left) and HB (right) at different phases in a buffet period ($\mathrm{Re}_c = 3 \times 10^6$, $\mathrm{M}_\infty = 0.73$ and $\alpha = 3.5$ deg). From top to bottom: most downstream position, upstream moving shock, most upstream position, downstream moving shock. The dashed, black lines represent the zero-longitudinal velocity isolines.

where the procedure agrees with the experiments. The estimation, compared to the experiments, provides good agreement for Mach numbers less than 0.78. Difficulties in the prediction of buffet at Mach number 0.8 have been reported in the literature [45, 120]. Therefore, a reduction of the eddy viscosity was adopted by reducing the PANS parameter f_k from 0.7 to 0.6. This modification reflected in an overall early prediction of the buffet boundary. Indeed, while an improved prediction is obtained at high Mach number, the reduction of the overall eddy viscosity level causes the buffet onset to be underpredicted at lower Mach number. The role of B for the unsteady buffet criterion in Equation (7.1) was also investigated. The two values tested were $B = 0.025, 0.05$. The adoption

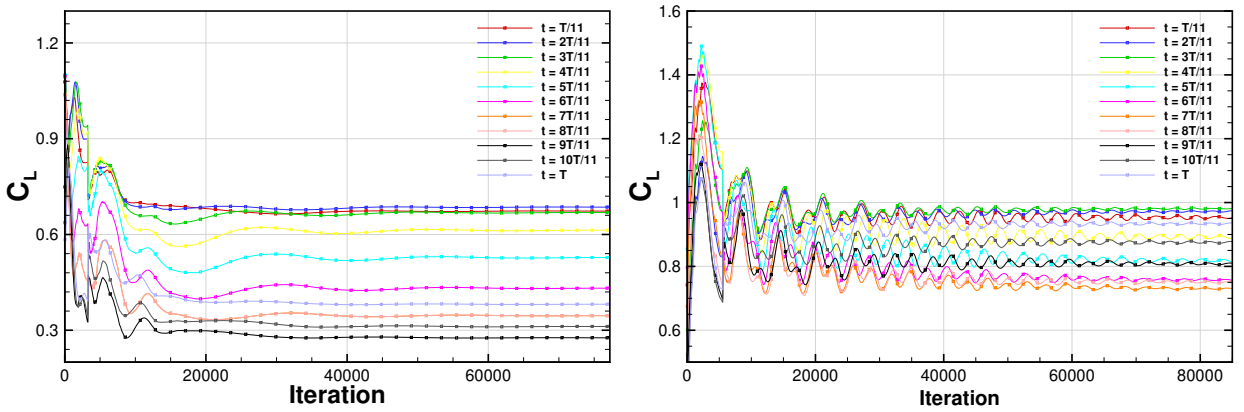

Figure 7.14: History of the lift coefficient associated with different time snapshots for the HB computations around the NACA0012 (left) and OAT15A (right) wing sections.

Table 7.5: CPU time for the time marching and harmonic balance aerofoil computations.

No. modes	CPU time [h]	Saving
NACA0012		
TMS	13.79	-
1	1.54	89%
3	4.67	66%
5	9.21	33%
7	11.77	15%
OAT15A		
TMS	16.98	-
1	1.59	91%
3	5.91	65%
5	11.56	32%
7	15.10	11%

of a lower value of this parameter allows for a slight improvement of the prediction at lower Mach numbers (Figure 7.15, right plot), giving an early prediction of the buffet onset. A lower value is also recommended to keep the estimation as conservative as possible.

Finally, the results obtained were compared with those in Chapter 6 using RANS-based criteria in Figure 7.16. The criterion based on the C_L coefficient provided an early, although conservative, prediction of the buffet boundary, under-predicting the onset of about 1 degree for the main part of the Mach number interval considered. When coupled with the adjoint method for a faster evaluation of the boundary, the criterion gave similar results. The criterion based on the pitching moment coefficient C_M provided improved results with respect to the previous one, at least for this test case. On the other side, the application of the criterion in conjunction with the adjoint method was less accurate. Therefore, to obtain higher accuracy, the estimation process would require the computation of the steady flow solution at different flight conditions, increasing the CPU cost. The performance of the procedure proposed in this work was comparable with that of the C_M-

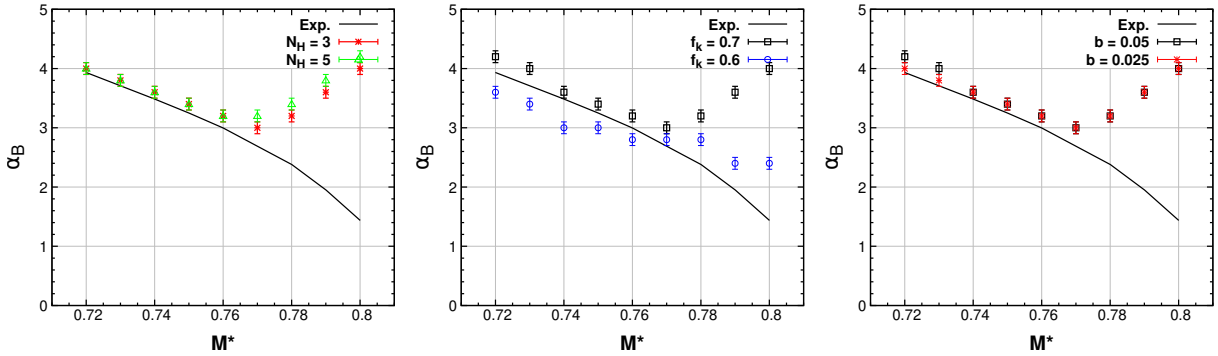

Figure 7.15: Estimated buffet boundary for the NACA0012 wing section at $\mathrm{Re}_c = 6 \times 10^6$ for different numbers of harmonics (left), value of f_k (centre), and b (right). Experiments of [178]. RANS-based criteria results from [208].

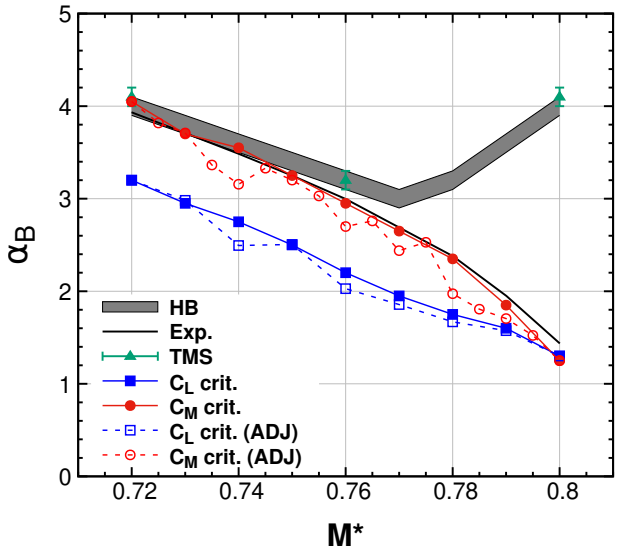

Figure 7.16: Estimated buffet boundary for the NACA0012 wing section at $\mathrm{Re}_c = 6 \times 10^6$. Experiments of [178]. RANS-based criteria results from [208].

based criterion for the first part of the Mach number interval of interest. In the second part, the inability of the adopted turbulence model to predict buffet reflected in a late buffet onset. This test case demonstrates the advantages and disadvantages of this procedure over a RANS-based one. While it improves too-conservative methods based on steady computations, by accounting for the unsteadiness of buffet by means of HB computations, its performance is strongly influenced, in this case limited, by the underlying turbulence model. This latter affects, in the same way, the HB and TMSs, as shown in Figure 7.16, where the TMS onset was pointed at selected points over the buffet boundary.

OAT15A computations

Similar computations were repeated for the OAT15A wing section. In this case, the experimental buffet onset was only known at $M_\infty = 0.72$ and 0.73, making difficult to draw definitive conclusions for the entire interval of interest. For this test case, the HB brings some improvements in the prediction of buffet, which was underpredicted by both criteria employed in Ref. [208]. To extend the validity of the provided results to a broader interval of Mach numbers, a comparison with the work of Giannelis et al. [98] was provided. In their work, a reduction of the a_1 coefficient of the SST model was adopted, and several computations, with an increment in the flight parameters of $\Delta\alpha = 0.5$ and $\Delta M_\infty = 0.01$, were carried out. The two numerical predictions are in good agreement. In the same plot, the comparison with the onset from TMS using the PANS model is also provided, showing, once again, the ability of the HB method to reproduce the results of the TMS.

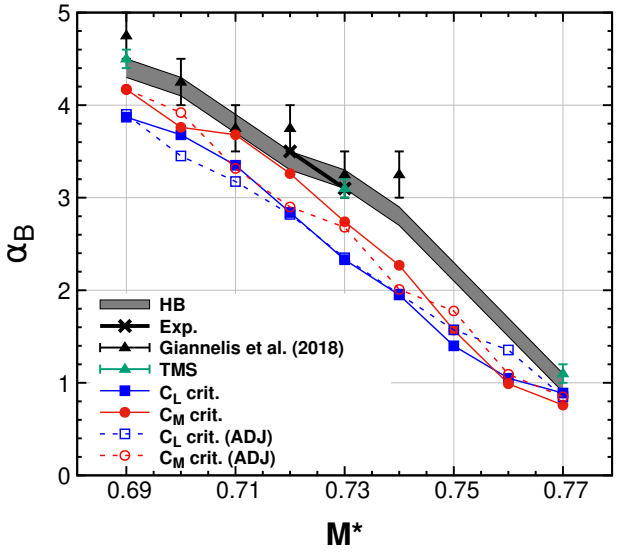

Figure 7.17: Estimated buffet boundary for the OAT15A wing section at $Re_c = 3 \times 10^6$. Experiments of [126]. RANS-based criteria results from [208].

7.3 Chapter Summary

In this chapter, the ability of the harmonic balance method to deal with transonic buffet flows has been evaluated. The method aims at approximating the results of time-marching simulations through a small number of instantaneous solutions over a period of oscillation. A 2D PANS formulation was used for the time-marching computations and was accurate in predicting the main quantities associated with the oscillating motion, like fundamental frequency of oscillation and mean pressure coefficient and RMS (where available). The harmonic balance equation was run together with an adaptive frequency technique, given the lack of knowledge of the fundamental flow

frequency of oscillation, which is, in turn, required to carry out harmonic balance computations. The method was tested for the vortex shedding flow around a circular cylinder at laminar conditions and provided accurate results, regardless of the initial guess of the reduced frequency and the number of harmonics adopted. The same results were obtained for flows around the NACA0012 and OAT15A aerofoil, starting from a number of harmonics equal to three. A slightly higher number of harmonics should be used if one wants to avoid the risk of undersampling the period of oscillation. In any case, when compared to time-marching simulations, the CPU cost is reduced. For the cases under consideration, a number of harmonic higher than 7 would result in CPU costs equal or higher to those of time-marching simulations. Using 3-5 harmonics, the flow physics of 2D buffet was correctly predicted in all its phases over a period of oscillation.

The harmonic balance computations were then embodied in a simple procedure for the buffet boundary estimation for the two 2D configurations. The results confirmed the noticeable decrease in the CPU cost associated with the buffet boundary characterisation with respect to time-marching simulations. As hinted by the preliminary computations performed, the algorithm is insensitive to the number of harmonics used, as long as it is sufficient to adequately sample one period of oscillation. Compared to the previous chapter, where RANS-based criteria were adopted, the prediction of the buffet boundary was improved for flight conditions where the turbulence model adequately predicted the buffet onset. Unfortunately, the harmonic balance computations inherited the ability to predict flow unsteadiness from the underlying turbulence model, and failed in predicting buffet at high Mach numbers for the NACA0012 section, as happened in other works on the topic [45, 120]. This clearly puts into evidence how the harmonic balance accuracy is limited by the performance of the underlying turbulence model. For the OAT15A configuration, the procedure gave a good prediction of the buffet onset compared to the limited data available.

Chapter 8

Flow Control of Transonic Buffet

*

As discussed in Chapter 1, flow control techniques mainly distinguish into vortex generators (VGs) [55,169,190], shock-control bumps (SCB) [25,48,176,177], and trailing edge devices (TED) [38, 39, 87, 261]. All methods proved to be more or less able to eliminate the shock oscillations at design conditions. Unfortunately, all of them introduce some penalties (installation drag, reduced off-design performance, etc.), as discussed in Section 2.3.

This chapter presents some alternatives to the aforementioned methods by taking advantage of existing control surfaces available in most airplanes. Recently, attention has been paid to three-dimensional buffets, and both experimental [53,251,253] and numerical [122,199,215,264] studies have been conducted. The numerical study of Iovnovich and Raveh [122] first identified the presence of spanwise-propagating waves called *buffet cells*. These structures exhibit the alternation of positive and negative pressure disturbances mostly propagating towards the wing tip. The presence of buffet cells represents one of the main differences with respect to 2D cases and was experimentally verified by subsequent studies [53, 251, 253]. The literature on conventional 3D transonic wings locates buffet cells around 45-60% of the wingspan [172, 199, 253, 264]. Therefore, spoilers can possibly be used for buffet alleviation. UTEFs and Gurney flaps represent a valid alternative to spoilers as they can be easily implemented and deployed only when required.

UTEFs act at the trailing edge by enforcing separation. The local angle of attack reduction results in a more upstream shock position. The weaker shock no longer separates the boundary layer. Under this condition, the separated flow regions at the shock foot and at the trailing edge cannot merge, and buffet is suppressed. The work of Tian *et al.* [261] showed the ability of UTEFs to cancel buffet on the RAE2822 aerofoil by altering the aerofoil chamber and curvature. The addition of the UTEF allows for a delay in the the onset of buffet but induces a reduction of lift

*The content of this paper has been partially published in "A. Petrocchi, M. Mauriello, G. N. Barakos, *Transonic Buffet Alleviation via Virtual Surfaces*, Aerospace Science and Technology, Vol. 140, 2023, 108478, https://doi.org/10.1016/j.ast.2023.108478".

at both pre- and post- onset by shifting the shock upstream, and reducing the flow acceleration at the leading edge and the suction peak. Therefore, in our view, the use of such devices must be limited to buffet conditions. The results of Tian *et al.* [261] were partially confirmed by the experimental investigation of D'Aguanno *et al.* [51] on the OAT15A. The use of a 1-2%*c* UTEF showed increasing efficiency in alleviating buffet, without suppressing it completely.

On the other hand, the use of spoilers alters the state of the boundary layer, and the buffet phenomenon can be interrupted according to the established buffet mechanisms. The acoustic feedback mechanism of Lee [159] sees the downstream propagation of disturbances generated at the shock foot in the boundary layer. Upon reaching the trailing edge, other upstream propagating waves are generated. These latter travel in the subsonic flow above the boundary layer and feed the shock motion, completing a feedback loop that allows for the self-sustained shock motion. This mechanism was further investigated by several authors [75, 111] who confirmed the central role of upstream-travelling acoustic waves in feeding the shock motion. Instead, the works from Crouch et al. [44,45] and subsequent works ([46,264] among others) studied transonic buffet as a global flow instability. In these works, buffet was seen as the result of a first unstable mode, involving the entire flow field. In both cases, the propagation of disturbances in the boundary layer is crucial. Whether one or the other explanation is preferred, the use of spoilers in hampering the mechanism seems reasonable. A sketch of the working principle compared to the mechanism of Lee [159] is given in Figure 8.1. The spoiler deployment (see Figure 8.1, right) generates fixed point separation at the

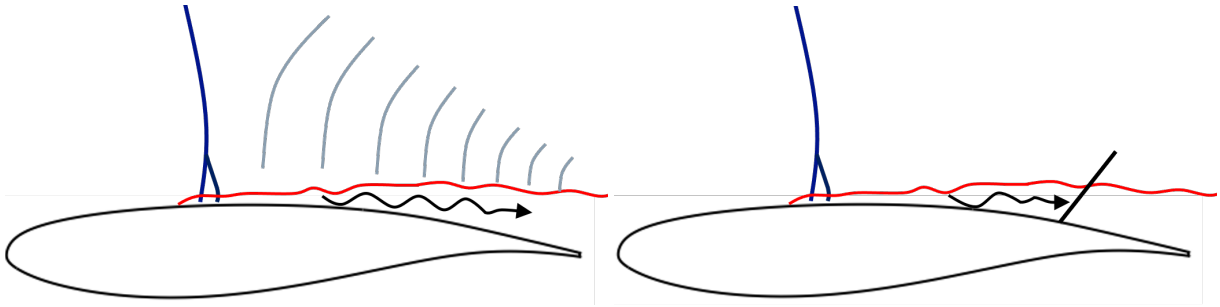

Figure 8.1: Left: sketch of the acoustic feedback mechanism of Lee [159]; right: effect of the spoiler in stopping the downstream propagation of disturbances in the boundary-layer

device tip, resulting in an increase in the wing camber and a local reduction of the angle of attack. The shock is pushed upstream where it loses its intensity and can no longer separate the boundary layer. If the boundary layer separates, the spoiler blocks the merging of the trailing edge and shock foot separation regions, alleviating or suppressing the SIO. Retracted in the wing, spoilers do not introduce installation drag or off-design penalties like VGs or SCBs [13]. When buffet is detected, spoilers are deployed to reduce and/or suppress the SIO. An overview of adaptive concepts for shock control is given in the review paper of Künnecke *et al.* [149].

Tian et al. [259] performed numerical simulations by modelling spoilers with a thickening of

the aerofoil/wing sections between 80% of the chord and the trailing edge. The results were encouraging on both 2D and 3D configurations, since the buffet onset was delayed. The thicker trailing edge resulted in an upstream position of the shock. This helped delay buffet at higher angles of attack or Mach numbers. In their work, the hypothesis of separated flow behind the spoiler allowed for the aforementioned approach, consisting of a simple thickening of the aerofoil. This approach does not account for changes in the size of the separated region behind the spoiler, nor for flow re-attachment in case of small spoiler deployments. Moreover, a change in the spoiler angle would require a modification of the mesh. At pre-buffet conditions, the presence of the spoiler caused an increase in the aerofoil chamber and caused the shock to move upstream, resulting in lift loss. Therefore, to avoid undesired effects associated with the presence of control devices at non-buffet conditions, they must be deployed only under buffet conditions.

In the CFD framework, the position of all control devices within the wing and their movement result in difficulties in modelling both trailing edge flaps and spoilers. The aforementioned CFD works only accounted for the presence of fixed controlled devices. In this work, the technique of Pastrikakis and Barakos [202] is adopted to simulate virtual control surfaces. The technique works on cell faces to simulate the presence of no-slip walls. Without using a moving grid, this method allows for studying the flow response to different spoiler deployments and UTEF lengths and reproducing a dynamical deployment of the control surfaces. The ability to vary the position and extent of deployable control devices over time opens the door to closed-loop control on wings by means of the aforementioned strategies. Nonetheless, in this work, only a demonstration of automatic deployment and retraction is given.

The method is first tested for 2D configurations with upper trailing edge, Gurney flaps, and spoilers. The influence of the test section is presented by comparing the results of 2D computations for the flow around different aerofoils with activated control surfaces. The sensitivity to the spoiler deflection angle and the UTEF length is studied. For a selected case, the spoiler deployment was complemented with a decrease in Mach number to simulate the pilot action in a flight scenario. Among the pool of spoiler angles considered, the optimal value and a different, higher, one were tested on a 3D configuration with a finite wingspan to underline differences between the 2D and 3D cases.

8.1 Test Case Description and Numerical Setup

OAT15A Wing Section

The first configuration of interest is the supercritical OAT15A wing section, experimentally investigated in the S3Ch wind tunnel at ONERA [125, 126], and described in Section 2.2 and Section 6.2. In this work, simulations at $\mathrm{Re}_c = 3 \times 10^6$, $\mathrm{M}_\infty = 0.73$ and $\alpha = 3.5$ deg were carried out.

NACA0012 Wing Section

The second test section analysed is the NACA0012 section. More detail was given in Section 2.2 and Section 6.2. In this work, simulations at $\mathrm{Re}_c = 10 \times 10^6$, $\mathrm{M}_\infty = 0.72$ and $\alpha = 6.0$ deg ($\simeq 2.0$ deg above the onset) were carried out.

V2C Wing Section

The last configuration is the V2C aerofoil of Dassault Aviation, studied during the European project TFAST [24]. It is a laminar, supercritical aerofoil, designed to operate between Mach numbers of 0.7 and 0.75 and was studied in the Trisonic wind tunnel of the Polish Institute of Aviation. The wind tunnel facility has 0.6 × 0.6 m test section, and it was equipped with 1.58 m long solid walls deflected 0.5 deg from each other. The model chord was 0.2 m, the span was 0.6 m, and the relative thickness was 15%. A transition strip - of varying height - was added on the upper side and tested at several streamwise positions and fixed along the wingspan. The mean value of static pressure on the V2C profile was measured by means of a 64 pressure tab system connected to tubes mounted inside the model, grouped in two rows. An aerodynamic rake was used to estimate the drag. Kulite pressure transducers were used to measure unsteady pressure in the vicinity of the shock, while SENFLEX sensors on the suction side were used to locate transition. A strain gauge bridge was used to measure the root-mean-square of the bending tension to detect the buffet onset. The angle of attack was varied in the range of 0 to 8 degrees. In this work, simulations at $\mathrm{Re}_c = 3 \times 10^6$, $\mathrm{M}_\infty = 0.70$ and $\alpha = 7.0$ deg ($\simeq 3.0$ deg above the onset) were carried out.

8.1.1 Grid and Numerical Setup

The unsteady computations were carried out using a PANS approach with the SST model as a RANS parent. The PANS formulation was detailed in Section 3.4. The adoption of PANS allowed for capturing the shock oscillations. We believe that adopting reasonably high values of the parameter f_k ($f_k = 0.7$ here), the PANS formulation can help in the prediction of this class of flows where most statistical turbulence models give too high levels of eddy viscosity [108, 120], even working in RANS mode and for 2D simulations. Very good agreement was found between PANS and experiments for two of the aforementioned configurations [209]. On the other hand, URANS simulations with the SST model led to a steady-state solution even at angles of attack well beyond the buffet onset. The failure of the SST model to accurately predict buffet was also documented in earlier works [108, 120, 207].

The computational grids used for the Gurney/UTEF configurations have a typical C-H topology. A grid-sensitivity study was carried out for the uncontrolled cases [209] (see Chapter 7). For this work, a local refinement was applied to increase the resolution of the regions around the trail-

ing edge and in the boundary layer, resulting in no modifications on the predicted frequency and amplitude of shock oscillation. The grid consists of $N_{aerofoil} = 456$, $N_{TE} = 50$ for blunt trailing edges, $N_y = 180$ in the normal direction and $N_w = 110$ in the wake.

For the spoiler configurations, the multi-block topology was slightly modified because of the hinge presence, as shown in Figure 3.5. To guarantee an adequate resolution around the virtual spoiler, more grid points around the hinge and in the boundary layer were used. The numbers of cells around the aerofoil and in the normal direction now amount to $N_{aerofoil} = 756$ and $N_y = 170$, respectively. In this case, neither the presence of the hinge nor the local grid refinement led to significant changes in the quantities associated with the shock oscillation. The spacing distribution was selected to satisfy the condition of $\Delta y^+ < 1$ at each condition, resulting in a first cell size of about $2.0 - 5.0 \times 10^{-6} c$ for the aforementioned flow conditions. Adiabatic wall boundary conditions were imposed at the aerofoil, and free-stream boundary conditions elsewhere. A timestep of $\Delta t = 0.01 c/U_\infty$ was employed, and corresponds to approximately 1200, 1500 and 1300 unsteady steps for the NACA0012, OAT15A and V2C sections, respectively. The convergence of the implicit scheme was based on the reduction of the flow field residual with respect to the previous step. More precisely, either a reduction of 3 orders of magnitude or 100 inner iterations of the dual-time stepping scheme must be reached for each unsteady step.

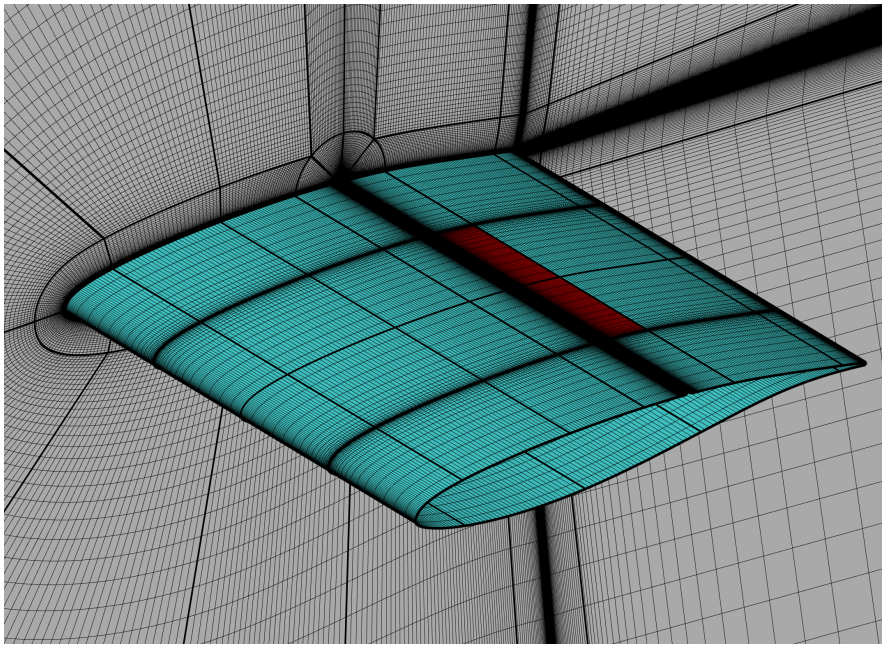

Figure 8.2: CFD grid around the 3D OAT15A aerofoil with spoiler (red).

The CFD domain for the 3D computations has an extension of $L_z = c$ in the span and it is discretised using $N_z = 100$ cells in the spanwise direction. A refinement around the two spoiler ends was applied allowing for an adequate resolution of the tip vortices expected in that region. The final grid consists of about 14 million points. In this case, periodic boundary conditions were

applied at the sidewalls. Figure 8.2 shows the grid employed for the 3D computation, where the 2D grid, displayed on the grey plane, is the same adopted for the 2D calculations. The hinge covers the whole span and it is placed at $0.6c$ from the aerofoil leading edge. Its radius is $r_h = 0.00625c$. The spoiler is $0.08c$ long and extends over half the wing span.

8.2 Results

In this section, the effect of infinite and finite virtual control surfaces is investigated. In Chapter 7, the accuracy of the PANS approach to predict buffet was established. The PANS model based on a $k-\omega$ SST model gave good results for the 2D cases and is employed in this work. First, results are shown for the three aerofoil configurations in the uncontrolled case. Then, results for infinite UTEF and spoilers, i.e. for 2D computations, are presented using both static and automatic control by means of flow reversal detection. Some aspects related to the influence of aerofoil section, angle, and length of the devices on the aerodynamic performance are also discussed. Since spoilers, unlike UTEF and Gurney flaps, are mounted on every commercial airplane, these are studied in more detail. Moreover, a combination of spoiler deployment and grid motion to simulate an aerofoil deceleration is presented to provide a simple strategy to prevent buffet from taking place when the device is retracted. Finally, a 3D computation with finite spoiler extent is presented and the results are compared with the 2D case.

An overview of the computations carried out for this work is given in Table 8.1. In the table, only the simulations used for testing control strategies are mentioned. Other flow conditions investigated for the uncontrolled cases for validation purposes are listed in the following section. Because of the proximity to the buffet onset for the OAT15A aerofoil, smaller UTEF lengths have been adopted.

8.2.1 Uncontrolled Buffet Cases

The uncontrolled cases were first run to guarantee an accurate prediction of buffet for the test cases under analysis. For the NACA0012, four combinations of Mach number and angle of attack were investigated. They correspond to the ones investigated by McDevitt and Okuno [178] for which the reduced frequency $k_{exp} = 2\pi f_B c/U_\infty$ is available. The results are in overall good agreement with the experiments (see Table 8.2), although the current simulations were unable to predict buffet for the highest Mach number. This difficulty was already pointed out in the literature [45, 120].

The OAT15A was investigated at $\mathrm{Re}_c = 3 \times 10^6$. Very good agreement was found between PANS and the experiments for this aerofoil for different Mach numbers and angles of attack. The distributions of the mean pressure coefficient and the root mean square around the aerofoil were in good agreement with the experiments for several angles of attack, both at pre- and post-buffet onset

Table 8.1: Table of time-marching computations performed in this work.

M_∞	α	Control	L_G/c[%]	δ_S[deg]
NACA0012 ($Re_c = 1 \times 10^7$)				
0.72	6.0	-	-	-
0.72	6.0	Spoiler	-	5, 10, 20
V2C ($Re_c = 3 \times 10^6$)				
0.70	7.0	-	-	-
0.70	7.0	UTEF	0.625, 2.5, 5, -5	-
OAT15A ($Re_c = 3 \times 10^6$)				
0.73	3.5	-	-	-
0.73	3.5	UTEF	0.15, 0.3, 0.6, -0.6	-
0.73	3.5	Spoiler	-	1, 2, 3, 5, 10, 15, 20
0.73	3.5	Spoiler 3D	-	5, 15

Table 8.2: Table of time-marching computations performed for the NACA0012 aerofoil, $Re_c = 1 \times 10^7$. Experimental results from [178].

M_∞	α	Buffet	k_{exp}	k_{num}
0.72	6.0	yes	0.55	0.52
0.75	4.0	yes	0.47	0.39
0.77	4.0	yes	0.44	0.45
0.80	4.0	no	0.38	-

(see Figure 8.3, left and centre). Table 8.3 shows the comparison with the experiments in terms of Strouhal number associated with the main buffet frequency at different Mach numbers and angles of attack. Below $\alpha = 3.1$ deg, no SIO was detected, according to the experimental reference, while for $\alpha \geq 3.1$ deg, the amplitude of shock motion and aerodynamic coefficients (see Figure 8.3, right) increases with the angle of attack. This leads to a greater smearing of the mean pressure coefficient and a higher peak in the pressure root-mean-square.

The V2C was tested at $Re_c = 3 \times 10^6$, $M_\infty = 0.70$ and $\alpha = 7.0$ deg. This combination of angle of attack and Mach number was widely investigated during the TFAST European Project [24], where both tripped and laminar interaction were investigated. In the TFAST CFD campaign, the use of different methods led to discrepancies with the experiments. Even among experiments, large differences were found depending on the adopted test facility, transition location, and surface roughness. Nonetheless, at the selected flow conditions, large SIOs were displayed, as shown in Figure 8.4, and allowed us to clearly describe transonic buffet in all its phases. In general, as the angle of attack increases, the shock on a transonic aerofoil moves downstream. The shock gains intensity, and leads to boundary layer separation. Two regions of flow reversal were generated at the shock

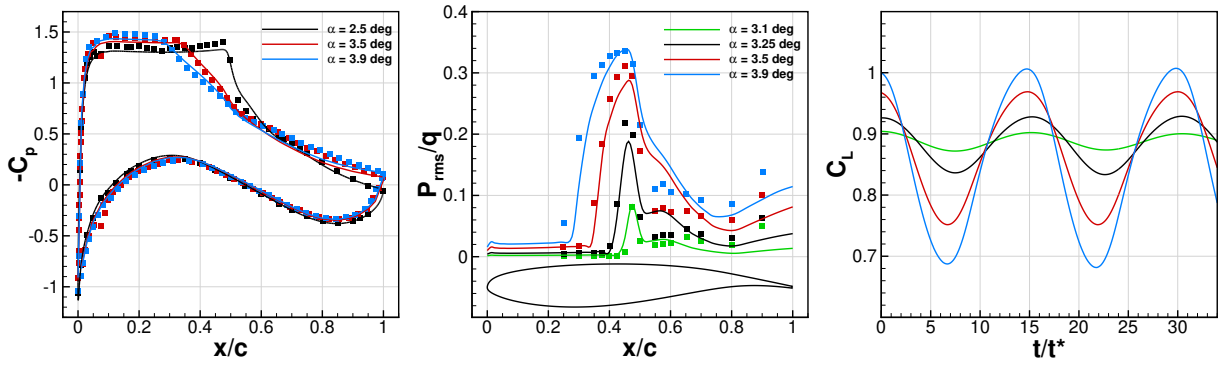

Figure 8.3: Comparison between CFD and experiments [126] for the OAT15A aerofoil, $\mathrm{Re}_c = 3 \times 10^6$. Left: mean pressure coefficient; centre: pressure RMS; right: lift coefficient history. Lines and symbols are coloured by angle of attack.

Table 8.3: Table of time-marching computations performed for the OAT15A aerofoil, $\mathrm{Re}_c = 3 \times 10^6$. Experimental results from [126].

M_∞	α	Buffet	St_{exp}	St_{num}
0.73	3.5	yes	0.066	0.067
0.72	3.5	yes	0.062	0.062
0.74	3.5	yes	0.074	0.071
0.73	3.1	yes	0.066	0.067
0.73	3.25	yes	0.066	0.067
0.73	3.9	yes	0.066	0.067

foot, and at the aerofoil trailing edge. For a further increase of the angle of attack, the two separated flow regions merge onto a unique one, and SIO takes place. Figure 8.4 shows the Mach number contours at four different instants over a period of buffet, complemented by instantaneous velocity streamlines which help visualise the local boundary layer separation. At the most downstream shock position (a), boundary layer separation takes place at the shock foot and trailing edge. Their merging onto a single, large, reversed flow region causes the local angle of attack to decrease and the shock to move upstream (b). At the most upstream position (c), the shock reaches a region of negative (favourable) pressure gradient and its intensity is reduced. Therefore, the boundary layer re-attaches, and the shock starts its downstream motion (d) where both trailing edge and shock-foot separation are limited, if not absent. As the shock oscillates over a portion of the suction side, the aerodynamic coefficients undergo large oscillations, as shown in Figure 8.4 (d). Most upstream and downstream shock positions coincide with minimum and maximum lift coefficient, respectively. The drag and pitching moment coefficients exhibit an analogous behaviour.

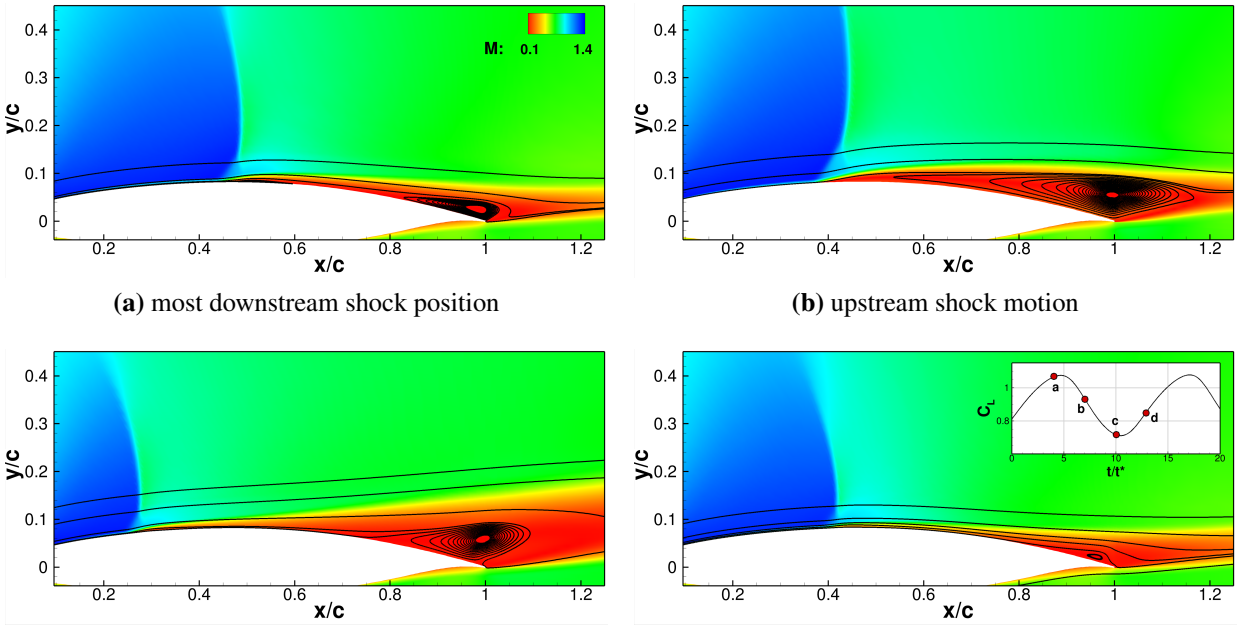

(a) most downstream shock position

(b) upstream shock motion

(c) most upstream shock position

(d) downstream shock motion

Figure 8.4: Mach number contours and streamlines around the V2C aerofoil at $\mathrm{Re}_c = 3 \times 10^6$, $\mathrm{M}_\infty = 0.70$ and $\alpha = 7.0$ deg at selected instants over a buffet period.

8.2.2 2D UTEF/Gurney Flaps

Results for the UTEF/Gurney configurations are presented here. For this device, the V2C and OAT15A configurations are analysed. In the first case ($\mathrm{Re}_c = 3 \times 10^6$, $\mathrm{M}_\infty = 0.70$ and $\alpha = 7.0$ deg), the results show very developed buffet that exhibits a larger separation region, while in the second case ($\mathrm{Re}_c = 3 \times 10^6$, $\mathrm{M}_\infty = 0.73$ and $\alpha = 3.5$ deg), the separation is less prominent. Indeed, the two configurations were analysed at angles of attack 3 and 0.5 deg higher than the respective buffet onset angles. For the following simulations, an actuation time of $\Delta t_{act} = 0.001$, corresponding to 10 characteristic travel times, was used.

V2C Section

Trailing edge flaps were tested both as Gurney flaps and UTEF (Gurney extended on the suction side). As expected, the use of the former ones resulted in an amplification of the shock oscillation. In principle, Gurney flaps were used to enhance the performance of aerofoils at incompressible flow conditions. Here, the deployment of Gurney flaps causes flow separation on the pressure side near the trailing edge. This results in a local increase in the angle of attack. Therefore, all the aerodynamic coefficients grow in both their mean value and amplitude of oscillation (see Figure 8.5, dashed lines). The only way to stop buffet would be to deploy the flap in such a way that crosses the lower buffet boundary (also known as *buffet offset* [120]) and induce stall. Nevertheless, since

cruise flight conditions are below the upper buffet boundary (*buffet onset*), it is advisable to suppress the SIO by a reduction of either angle of attack or Mach number. Therefore, the aforementioned strategy is discouraged.

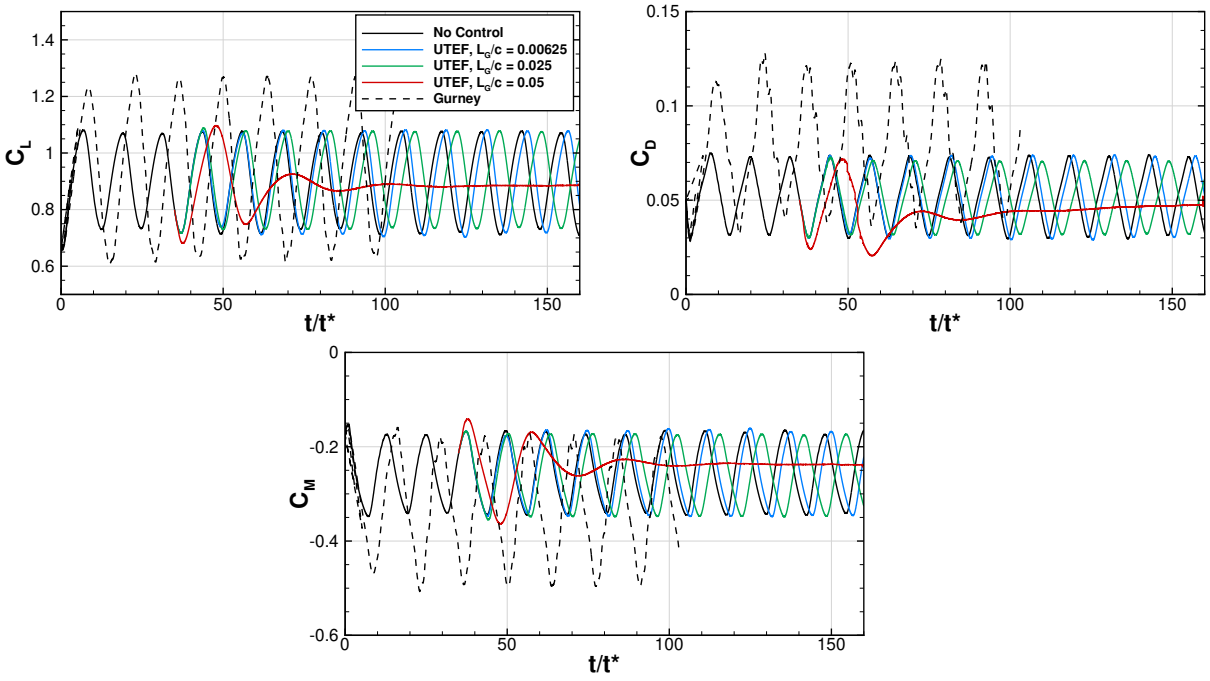

Figure 8.5: Aerodynamic coefficients for the V2C aerofoil at $\mathrm{Re}_c = 3 \times 10^6$, $\mathrm{M}_\infty = 0.70$ and $\alpha = 7.0$ deg, for different lengths of the Gurney/UTEF.

Given the inadequacy of Gurney flaps for this problem, the UTEF configuration was studied. Three UTEF lengths were tested: $L_{\mathrm{UTEF}}/c = 0.00625$, 0.025, and 0.05. Figure 8.5 shows a progressive decrease in the amplitude of oscillation of the aerodynamic coefficient as the UTEF length increases for $L_{\mathrm{UTEF}}/c > 0.00625$. While a short device ($L_{\mathrm{UTEF}}/c = 0.025c$) only contributes by alleviating buffet, a longer one ($L_{\mathrm{UTEF}}/c = 0.05c$) is able to suppress the oscillation. Figure 8.6 shows the longitudinal velocity contour around the aerofoil with longest UTEF at steady state. Contrarily to the UTEF case, the separation region generated near the trailing edge on the suction side results in a local angle of attack decrease. As a consequence, the shock is pushed upstream, and the separation region is split into two, one at the shock foot and another at the trailing edge. The aerofoil curvature and angle of attack are such that result in a strong flow acceleration ($U_{\mathrm{max}}/U_\infty \simeq 1.7$). The resulting shock, even if weakened by the effect of the UTEF, is strong enough to separate the boundary layer underneath. Since the shock is now in the first half of the aerofoil, i.e. in a region of favourable pressure gradient, the boundary layer re-attaches almost immediately, and the separated region does not merge with the one at the trailing edge. The detailed view of the aerofoil trailing edge (Figure 8.6, right image) shows the streamlines around the UTEF. The flow stagnates and recirculation takes place in front of the UTEF. This figure shows the ability of the method of im-

posing no slip conditions on the infinitely thin device and capturing the vortices detaching behind the flap.

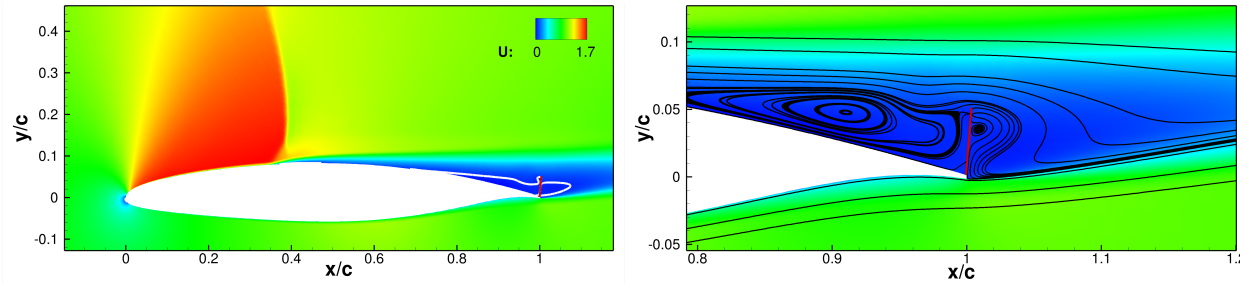

Figure 8.6: Longitudinal velocity contour around the V2C aerofoil at $\mathrm{Re}_c = 3 \times 10^6$, $\mathrm{M}_\infty = 0.70$ and $\alpha = 7.0$ deg, with UTEF. The solid, white line indicates the $U/U_\infty = -0.001$ isoline.

The steady-state values of the aerodynamic coefficients are approximately equal to the mean at buffet conditions. This device did not introduce penalties in terms of drag nor a lift/moment increase.

OAT15A Section

The same study was repeated for the OAT15A aerofoil. As the angle of attack is only 0.4 deg above the predicted buffet onset, shorter UTEF heights were used compared to the previous case. Similar considerations hold for the Gurney and UTEF configurations. The main difference are the values of the aerodynamic coefficients with respect to the mean values at buffet conditions. Indeed, an increase in the amplitude of the aerodynamic coefficients is visible in Figure 8.7. The main reason is that the upstream shock position no longer induces boundary layer separation at the shock foot (see Figure 8.8), while in the previous case, prominent separation was still present.

For the UTEF configuration, even a 0.15% c long device was able to suppress the SIO. Given the proximity to the buffet onset ($\alpha - \alpha_{\text{onset}} = 0.4$ deg), a smaller effort was required to alleviate buffet.

8.2.3 2D Spoilers

8.2.3.1 Open Loop Control

This section presents the results for an open loop control by means of spoilers. The NACA0012 and OAT15A were analysed at buffet conditions. The first configuration was studied under buffet conditions with prominent separation on the aerofoil suction side. The OAT15A was investigated at the same flow conditions of Section 8.2.2. Moreover, for the latter case, a sensitivity study to the spoiler angle was carried out. Differences between the configurations are then discussed.

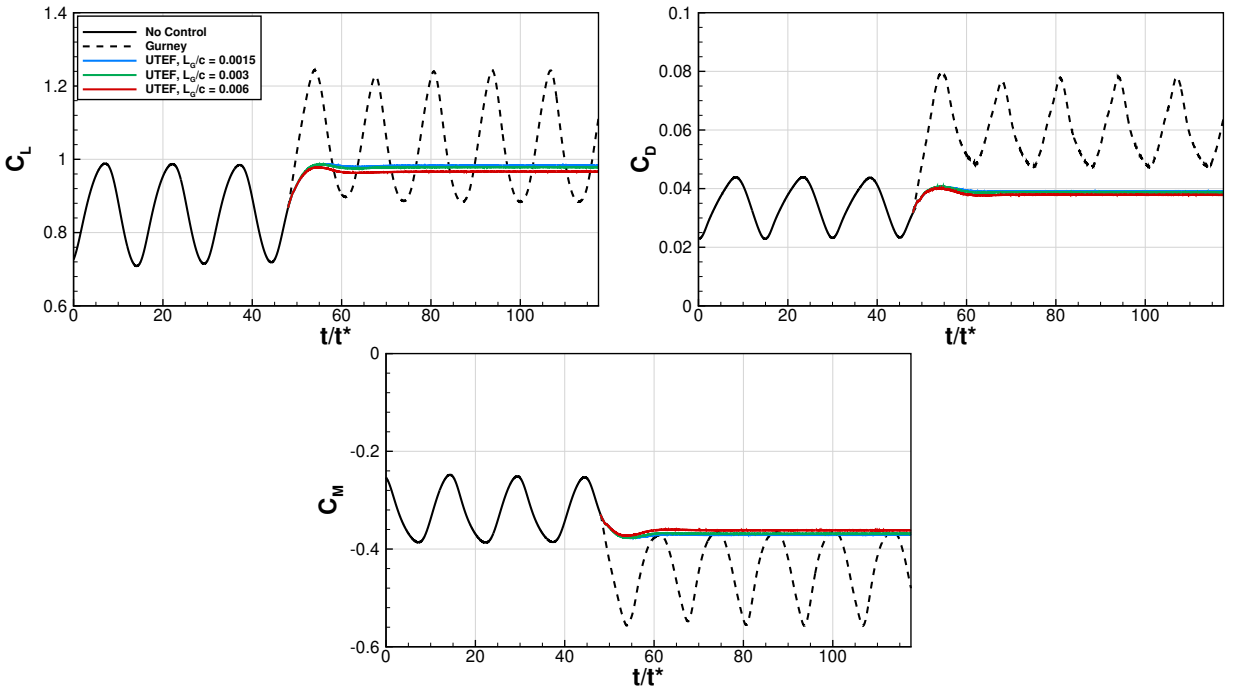

Figure 8.7: Aerodynamic coefficients for the OAT15A aerofoil at $\mathrm{Re}_c = 3 \times 10^6$, $\mathrm{M}_\infty = 0.73$ and $\alpha = 3.5$ deg, for different lengths of the Gurney/UTEF.

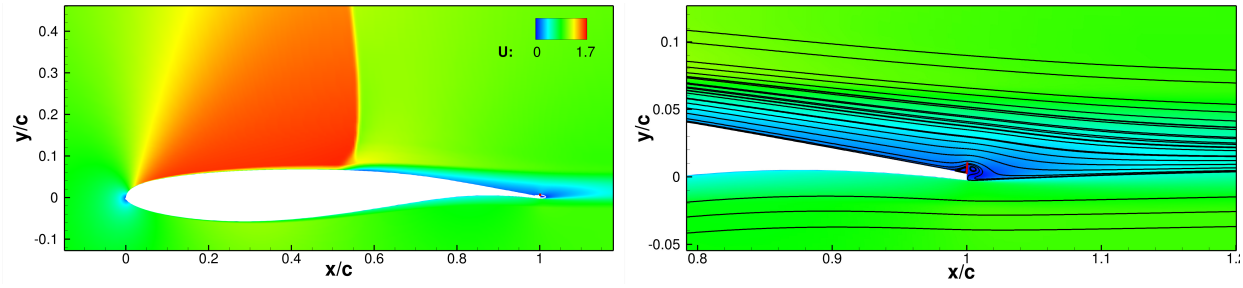

Figure 8.8: Longitudinal velocity contour around the OAT15A aerofoil at $\mathrm{Re}_c = 3 \times 10^6$, $\mathrm{M}_\infty = 0.73$ and $\alpha = 3.5$, with UTEF. The solid, white line indicates the $U/U_\infty = -0.001$ isoline.

NACA0012 Section

At buffet conditions around the NACA0012 aerofoil, the spoiler deployment angles amount to 10 and 20 deg. When the spoiler is not deployed, "$\delta_s = 0$" deg in Figure 8.9, the effect of the hinge slightly dampens the oscillations as can be seen from the aerodynamic coefficients histories in Figure 8.9. When the spoiler is deployed, the oscillations are suppressed, with a transient time that shortens with the amplitude of δ_s. Figure 8.10 shows the effect of the spoiler on the separated region by means of longitudinal velocity contours and streamlines. The separation region is perturbed in the low angle-case while it is broken into two parts in the high angle-case, resulting in a stabilisation of the shock position. This situation is particular because the separation is prominent even for the baseline flow. Therefore, the size of the separated region does not vary significantly when the

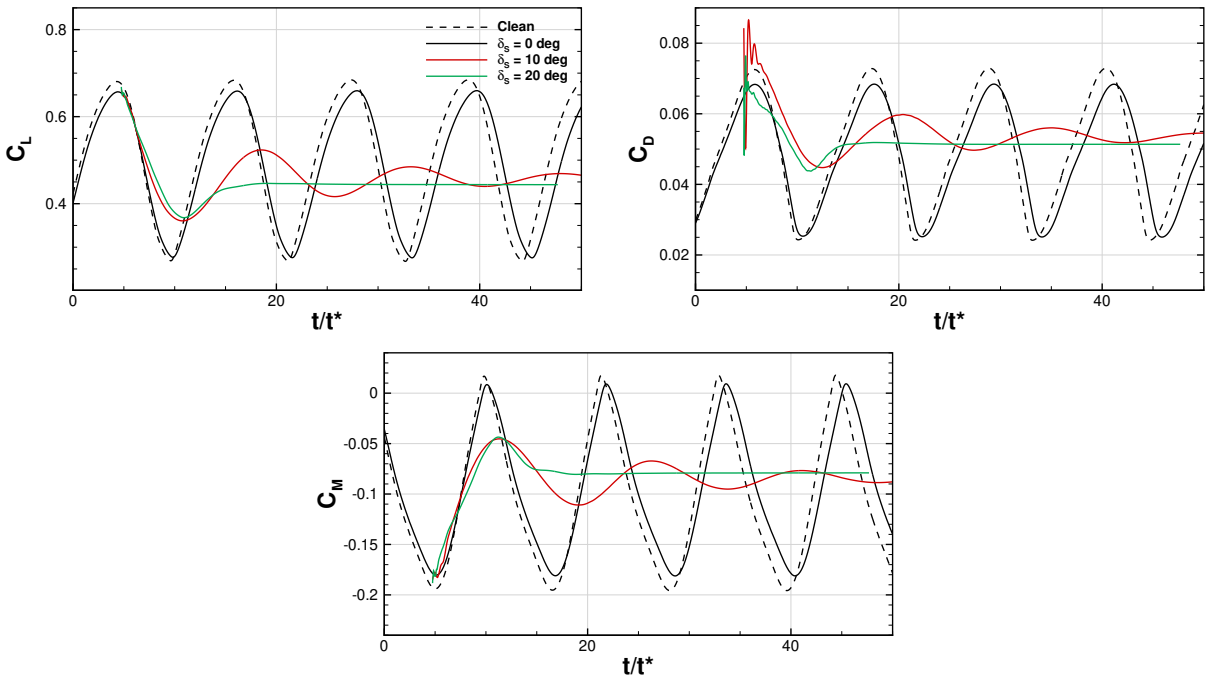

Figure 8.9: Aerodynamic coefficients history for different angles of spoiler deployment δ on the NACA0012 at $\mathrm{Re}_c = 10 \times 10^6$, $\mathrm{M}_\infty = 0.72$ and $\alpha = 6.0$.

spoiler is added, and the spoiler only contributes by avoiding the propagation of disturbances in the boundary layer. For smaller δ_s, the separated flow region is not completely broken and the transient is longer. For this case, the values of the aerodynamic coefficients at steady state do not differ

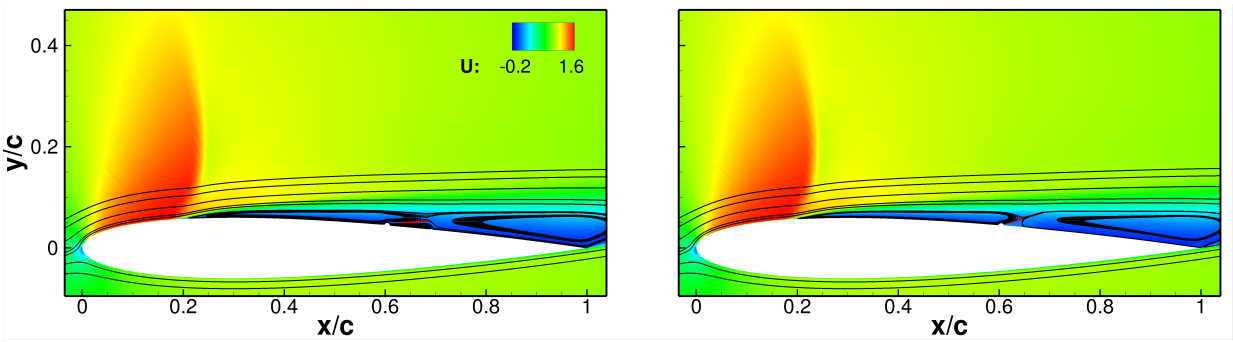

(a) $\delta_S = 10$ deg **(b)** $\delta_S = 20$ deg

Figure 8.10: Streamwise velocity component contours for different angles of spoiler deployment δ on the NACA0012 at $\mathrm{Re}_c = 10 \times 10^6$, $\mathrm{M}_\infty = 0.72$ and $\alpha = 6.0$.

significantly from the average one in baseline case, as for the V2C in Section 8.2.2.

OAT15A Section

For the OAT15A case, the history of the aerodynamic coefficients in response to an instantaneous deployment of the spoiler at different angles δ_s is shown in Figure 8.11. In Table 8.4, the contribution of the spoiler is distinguished from the part of the loads that does not account for the additional surface. Also, the viscous and pressure contributions to the drag are given in Table 8.4. The steady-state values of the four coefficients are collected in Table 8.4 and Figure 8.14. The lift coefficient

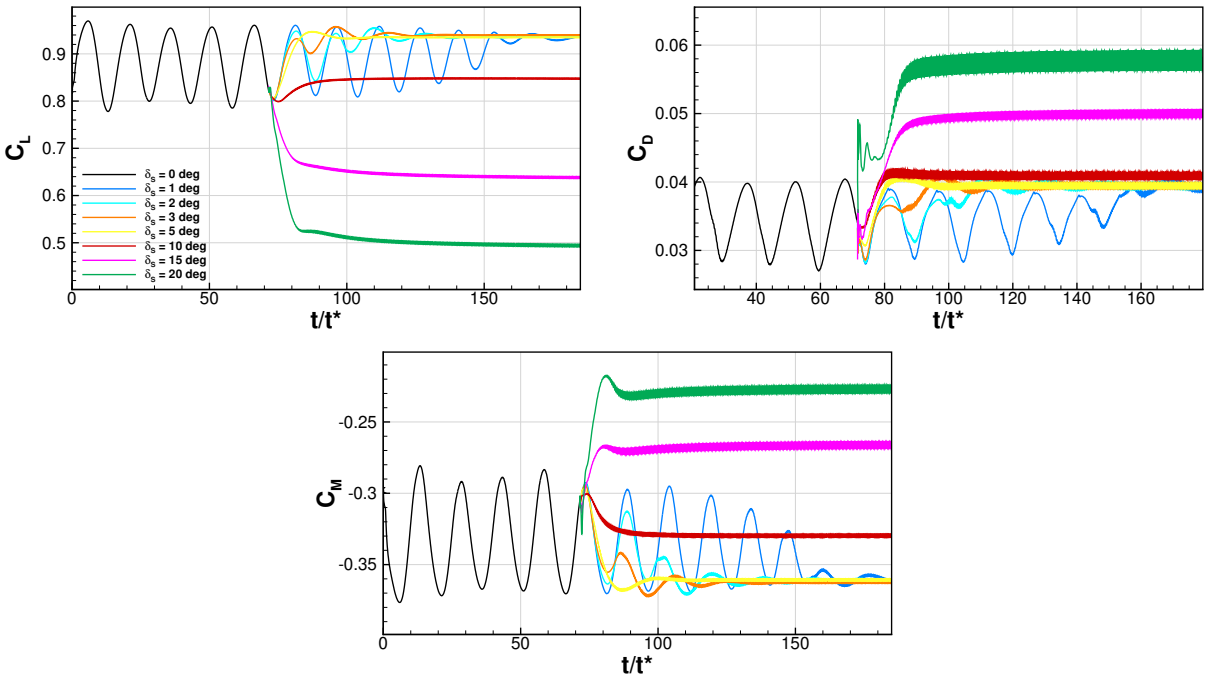

Figure 8.11: Histories of aerodynamic coefficients for different angles of spoiler deployment δ on the OAT15A aerofoil at $\mathrm{Re}_c = 3 \times 10^6$, $\mathrm{M}_\infty = 0.73$ and $\alpha = 3.5$ deg.

C_L tends towards a steady-state value even for a small deflection of the spoiler (see Figure 8.11 (a)). Unlike for the NACA0012 case, a small deflection of the spoiler allowed for the buffet to be canceled. The lift increase was not due to the presence of the spoiler itself, but to the ability of the device to stabilize the shock at a position that is downstream of the mean position during the buffet motion. The main drawback with respect to the previous geometry is the increase in the drag coefficient C_D (see Figure 8.11 (b)). In the previous case, of prominent separation, the spoiler was immersed in the separated flow region, and no significant pressure difference was present between the two faces. In this case, a net pressure jump is visible across the spoiler hinge, as shown in Figure 8.12, left plot. The pressure jump has a local minimum for $\delta_s = 5$ deg, and increases significantly at higher angles. In this situation, the spoiler no longer represents a shock control device, and behaves as an air-brake. Under such conditions, the drag significantly increases with respect to the uncontrolled case value.

The right panel of Figure 8.12 shows the pressure distribution comparison between the con-

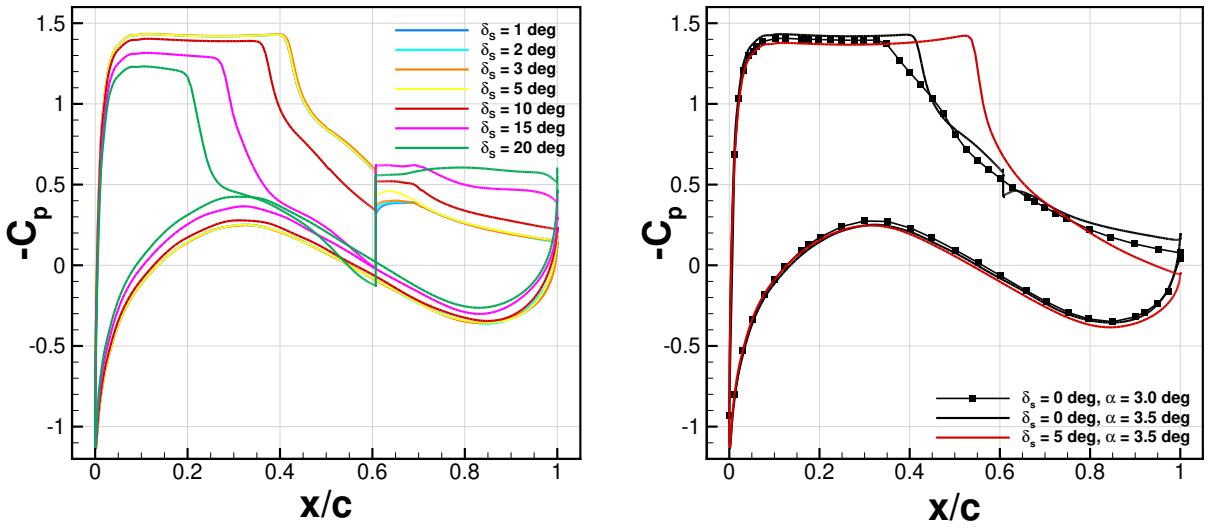

Figure 8.12: Pressure coefficient distribution for different angles of spoiler deployment δ_S around the OAT15A aerofoil, $\mathrm{Re}_c = 3 \times 10^6$, $\mathrm{M}_\infty = 0.73$ and $\alpha = 3.5$.

trolled case at $\alpha = 3.5$ deg and the uncontrolled case, at pre- and post-buffet onset. For the uncontrolled buffet case, the mean pressure coefficient distribution is smeared because of the shock oscillation on the suction side. In the other two cases, the pressure jump corresponding to the shock can be easily detected. The presence of the spoiler creates a separated flow region where the pressure is lowered. As a result, the shock intensity required to obtain a smaller pressure jump leads to a more upstream position of the shock itself. As a consequence of the modified load distribution, the pitching moment C_m increases (see Figure 8.11 (c)). At small δ_S, the shock position is fixed at a downstream position, with respect to the mean shock position for the uncontrolled case. Therefore, the lift distribution is higher in the first half of the aerofoil, while it is almost unchanged in the second part. This results in a mild nose-up effect. On the other hand, higher spoiler deflection angles correspond to an upstream shock position, and reduced pressure after the hinge on the suction side. In these cases ($\delta_S > 10$ deg), the lift distribution along the chord compared to the uncontrolled case is visibly smaller before the hinge, and higher after the hinge. As a consequence, the aerofoil undergoes a nose-down effect.

To better understand the spoiler effect at different angles, velocity contours complemented with streamlines are shown in Figure 8.13, top panels, for a spoiler deflection angle of $\delta_s = 5,\ 10,$ and 20. The separated flow region behind the spoiler acts by reducing the angle of attack and pushing the shock close to the leading edge where it loses strength. This effect is more evident as δ_s increases. For $\delta_s = 5$ deg and $\delta_s = 10$ deg, the shock is strong enough to separate the boundary layer and the spoiler breaks the communication between the two recirculation regions. In the other case, the shock is pushed further upstream and the boundary layer is attached upstream of the spoiler. This is particularly interesting because not only the spoiler stabilises the shock in response to a

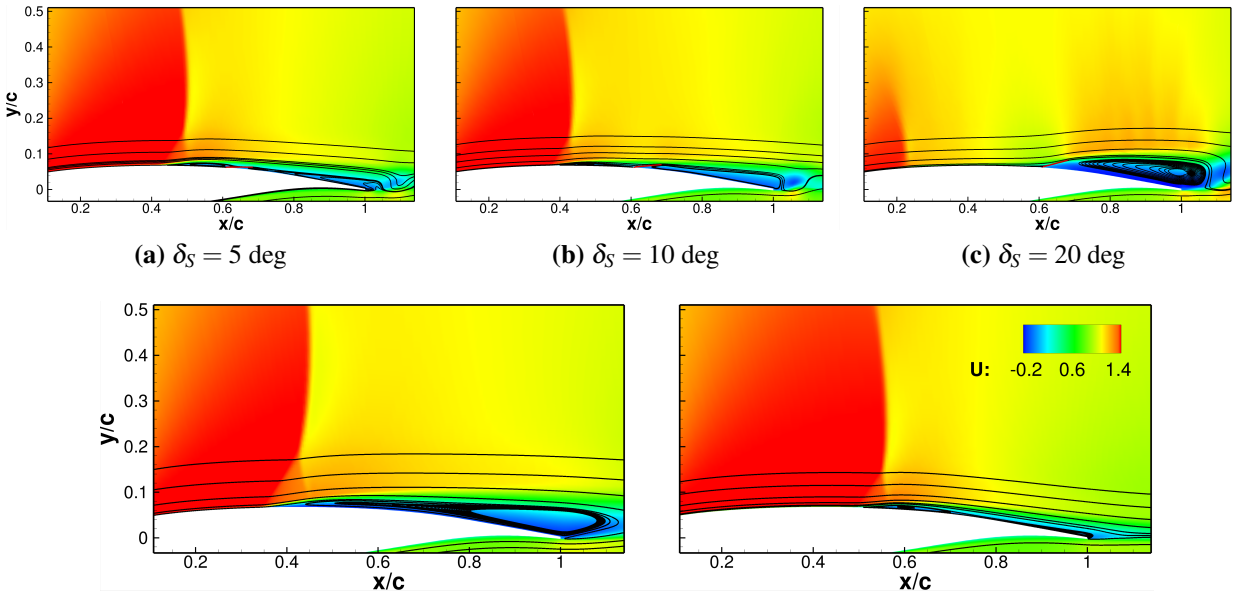

(a) $\delta_S = 5$ deg **(b)** $\delta_S = 10$ deg **(c)** $\delta_S = 20$ deg

(d) $\delta_S = 0$ deg, upstream shock motion **(e)** $\delta_S = 0$ deg, downstream shock motion

Figure 8.13: Top: streamwise velocity component contours for different angles of spoiler deployment δ_S on the OAT15A aerofoil at $\mathrm{Re}_c = 3 \times 10^6$, $\mathrm{M}_\infty = 0.73$ and $\alpha = 3.5$; bottom: same visualisation during upstream and downstream shock motion.

trailing edge action, like in the UTEF case, but it proves useful in blocking the communication in the separated region with its presence. The presence of the spoiler for $\delta_s \leq 10$ prevents the merging of the two separated flow regions into a fully separated boundary layer (see Figure 8.13, bottom panels), which is a necessary condition for buffet.

Table 8.4 and Figure 8.14 summarise the effect of δ_s on the aerofoil aerodynamic performance. Even a small deflection of the spoiler ($\delta_s = 1$ deg was the smallest value) resulted in buffet suppression. For a small spoiler deflection $\delta_s = 1 - 5$ deg, the lift increased with respect to the mean one at buffet conditions, and the smallest drag penalty was introduced together with an additional nose-up contribution. At higher δ_s, the lift decreased and the drag penalty was even higher. Due to the modified pressure distribution in "air-brake mode", the aerofoil undergoes a nose-down effect. Figure 8.14 (d) shows the activation-to-steady state time t_{ss}. Due to the reduced t_{ss} with respect to the other angles, $\delta_s = 5$ deg was chosen to be the optimal angle. Although a short response time is not optimal for applications, it is convenient because it reduces the CFD cost associated with an higher response times (as in the case of $\delta_s = 1$).

It is worth noting that the aerodynamic coefficients exhibit increasingly wider oscillations as δ_s increases. The reason is that the vortex shedding occurs behind the aerofoil as the size of the separated flow region changes. Regardless of the spoiler angle, the flow separates behind the spoiler up to the trailing edge, and the thickness of the separated region increases with δ_s (see Figure 8.15). The separated flow region acts as a thickened trailing edge, and vortex shedding with increasing

Table 8.4: Steady-state aerodynamic coefficient for different spoiler deflection angles for the OAT15A aerofoil, $\mathrm{Re}_c = 3 \times 10^6$, $\mathrm{M}_\infty = 0.73$ and $\alpha = 3.5$ deg. C_L: lift coefficient; C_D: drag coefficient; C_m: pitching moment coefficient; t_{ss} activation-to-steady state time; v-subscript: viscous component; p-subscript: pressure component; s-subscript: spoiler contribution. The $\overline{(\cdot)}$ indicates that these are averages takes over several periods of the residual oscillations in the flow.

δ_s [deg]	$\overline{C_L}$	$\overline{C_{L_s}}$	$\overline{C_{D,p}}$	$\overline{C_{D,p_s}}$	$\overline{C_{D,v}}$	$\overline{C_{D,v_s}}$	$\overline{C_m}$	$\overline{C_{m_s}}$	t_{ss}/t^*
0	0.867		0.0346		0.00375		-0.327		
1	0.927	0.0085	0.0398	0.0011	0.00411	0.00035	-0.359	-0.00061	$\simeq 150$
2	0.929	0.0079	0.0392	0.0009	0.00399	0.00022	-0.361	-0.00058	$\simeq 90$
3	0.933	0.0072	0.0396	0.0007	0.00392	0.00015	-0.363	-0.00053	$\simeq 85$
5	0.927	0.0019	0.0396	0.0001	0.00379	0.00005	-0.362	-0.00036	$\simeq 50$
10	0.838	-0.0146	0.0404	0.0004	0.00346	-0.00006	-0.331	0.00016	$\simeq 45$
15	0.625	-0.0374	0.0494	0.0045	0.00353	-0.00009	-0.265	0.00094	$\simeq 110$
20	0.485	-0.0416	0.0570	0.0082	0.00368	-0.00006	-0.224	0.00134	$\simeq 110$

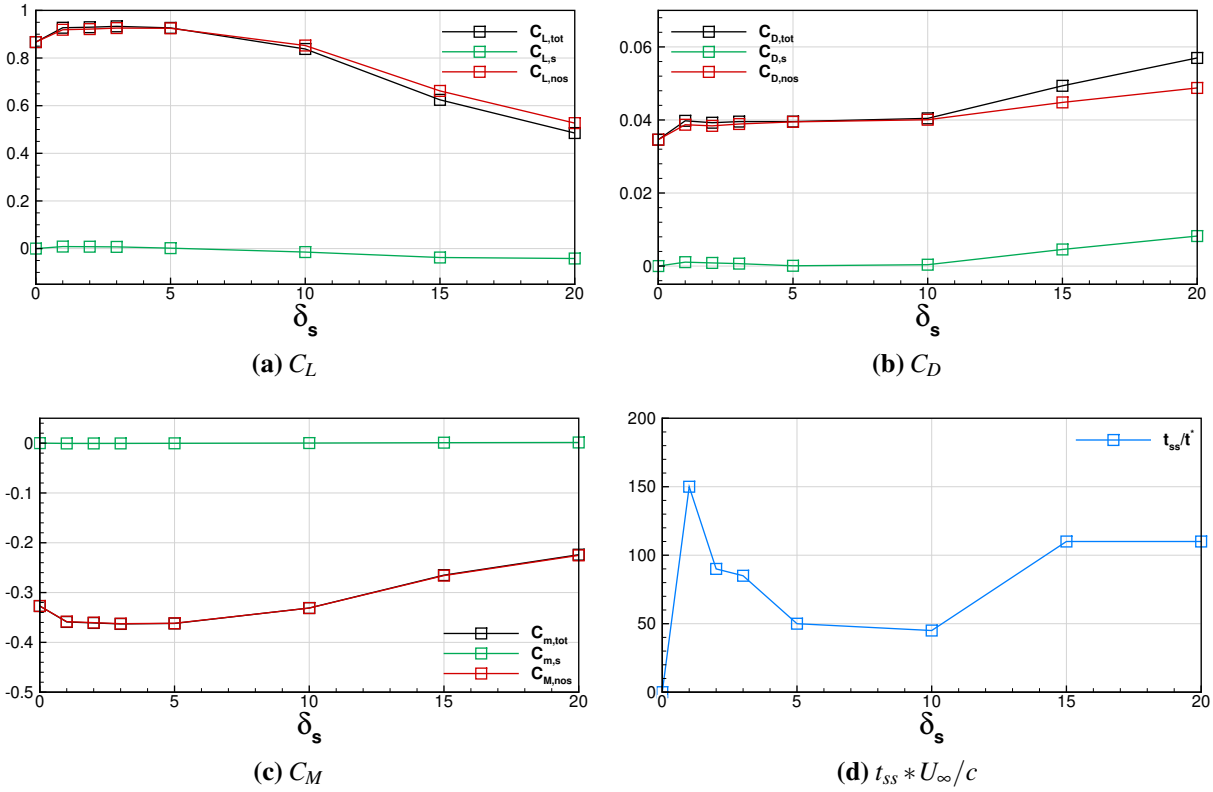

(a) C_L **(b)** C_D

(c) C_M **(d)** $t_{ss} * U_\infty / c$

Figure 8.14: Steady-state values of the aerodynamic coefficients for different angles of spoiler deployment δ_s around the OAT15A aerofoil, $\mathrm{Re}_c = 3 \times 10^6$, $\mathrm{M}_\infty = 0.73$ and $\alpha = 3.5$. The spoiler (s subscript) is distinguished from the one with no spoiler (*nos* subscript).

vortex size takes place. Larger vortices result in wider fluctuations in the aerodynamic coefficients, as shown by the correlation between Figure 8.15 and Figure 8.11.

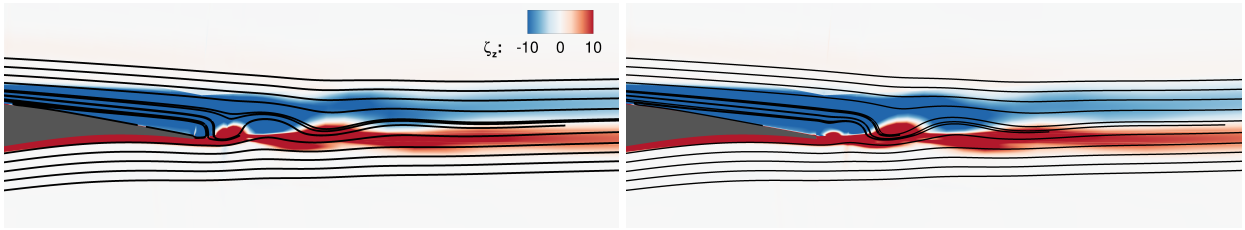

(a) $\delta_S = 1$ deg

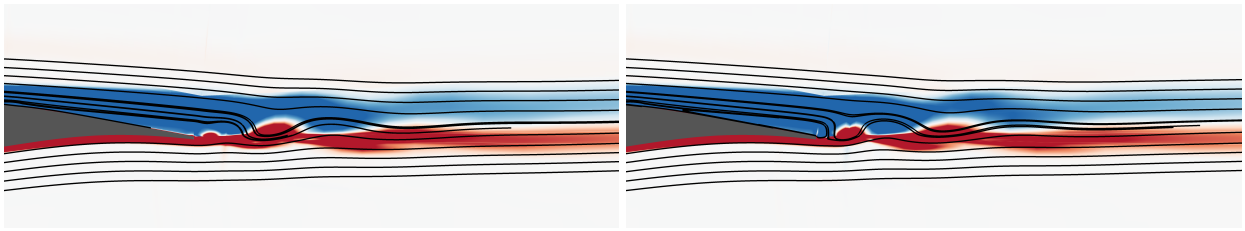

(b) $\delta_S = 5$ deg

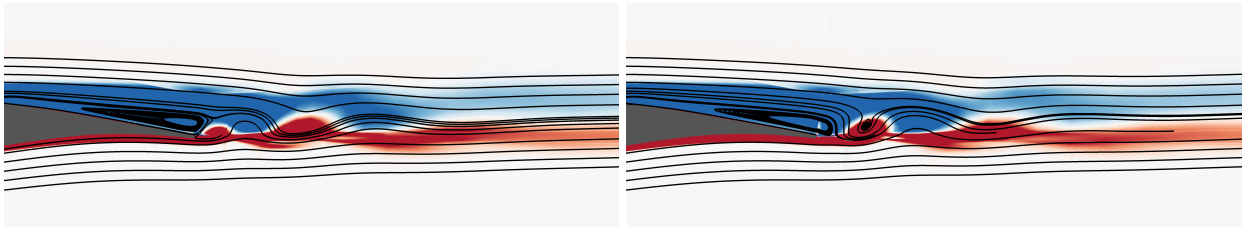

(c) $\delta_S = 10$ deg

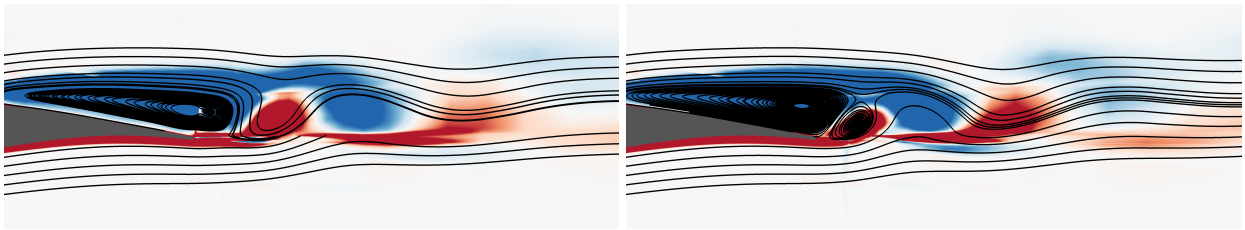

(d) $\delta_S = 20$ deg

Figure 8.15: Z-vorticity contour and streamlines around the TE of OAT15A aerofoil at $\mathrm{Re}_c = 3 \times 10^6$, $\mathrm{M}_\infty = 0.73$ and $\alpha = 3.5$ deg. From top to bottom: $\delta_S = 1, 5, 10, 20$ deg. Left and right snapshots are taken at different instants over a period of the oscillations highlighted in Figure 8.11.

8.2.3.2 Automatic Spoiler Deployment

Here it is shown how the spoiler is activated when flow separation is detected by a probe placed on the aerofoil surface at $x/c = 0.7$. The effect of the deployment duration T_{on} on the aerodynamic loads was previously studied. T_{on} is evaluated as $T_{\mathrm{on}} = dt\,\Delta t_{\mathrm{act}}$. Longer T_{on} resulted in a slower suppression of buffet. For practical applications, considered the short buffet period (the buffet frequency for the OAT15A case is $f_B = 69$ Hz), a relatively long actuation time is recommended. It avoids too-sudden changes in the aerodynamic loads that could create passenger discomfort. From the CFD point of view, a slower deployment of the control surface is advisable as drastic changes in

the flow field can be avoided. In the case considered here, the full deployment over 1000 unsteady steps was considered a compromise between accuracy and efficiency.

Figure 8.16 shows the drag coefficient (top) and local longitudinal velocity (bottom) for the simulation around the NACA0012 aerofoil for a $\delta_{\max}$ of 5 deg. Because of its rapid increase, C_D

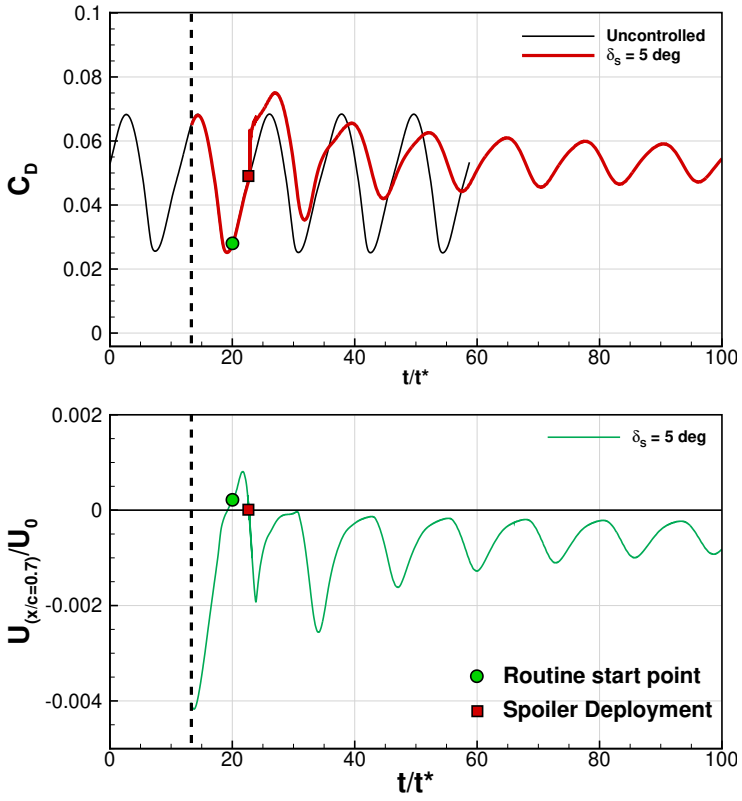

Figure 8.16: Aerodynamic coefficients history in response to an automatic spoiler deployment on the NACA0012 aerofoil at $\mathrm{Re}_c = 10 \times 10^6$, $\mathrm{M}_\infty = 0.72$ and $\alpha = 6.0$.

clearly shows the control activation. In this case, the control started at $t/t^* = 20$, and flow reversal was detected at $t/t^* \simeq 23$. After the drastic increase in drag, the oscillations are alleviated. As shown in Figure 8.10, after the spoiler deflection, the region behind the spoiler is fully separated and this is confirmed by the negative velocity in Figure 8.16, bottom plot.

8.2.3.3 Spoiler Retraction and Aerofoil Deceleration

As mentioned in Section 3.7.1.2, the spoiler must be retracted after the oscillations are suppressed. As underlined in the previous sections, the deployment of the spoiler results in a variation of the aerodynamic coefficients. For instance, a sudden increase in the drag coefficient should result in the aerofoil deceleration and the addition of a local velocity component (positive if the free stream is aligned with the positive x-axis). In turn, the load distribution changes. If not by moving the CFD grid, this effect should be taken into account by modifying Mach number and angle of attack

(if the aerofoil undergoes changes in the moment coefficient).

Changes in the aerodynamic loads are usually not accounted for in CFD simulations. As a result, once the spoiler is retracted, the oscillation occurs again and cancels the effect of the flow control. An example is given in Figure 8.17. It shows the history of the aerodynamic loads during and after the spoiler deployment. When the spoiler is retracted within the aerofoil (blue and red lines in figure), the coefficients come back to the pre-actuation oscillating behaviour.

Here, the aerofoil deceleration is simulated by moving the CFD grid in the direction of the free stream, as explained in Section 3.7.1.2. The motion was prescribed along the free-stream direction to only represent the drag variation, deemed as preponderant over lift and moment in the previous section. The CFD grid acceleration, velocity and position follow Equation (3.98), where the initial

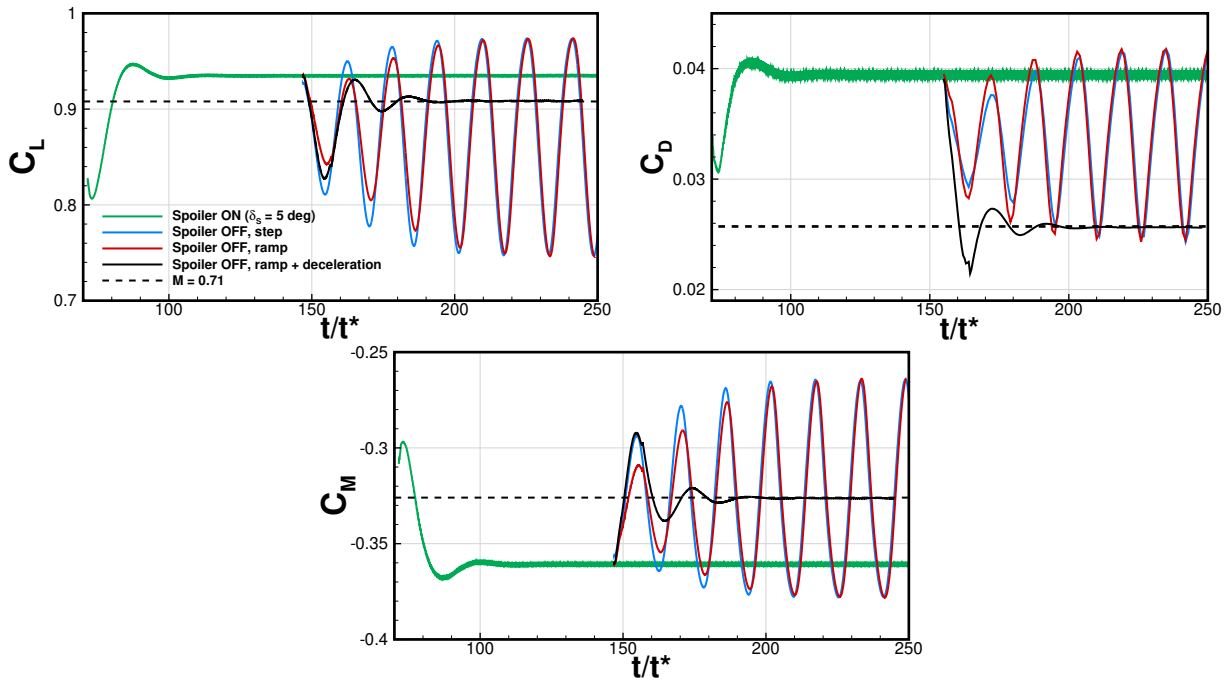

Figure 8.17: Aerodynamic coefficients history for 2D simulations on the OAT15A wing section at $\mathrm{Re}_c = 3 \times 10^6$, $\mathrm{M}_\infty = 0.73$ and $\alpha = 3.5$ deg in response to the spoiler retraction. The dashed lines represent the steady-state values of the aerodynamic coefficients at $\mathrm{Re}_c = 3 \times 10^6$, $\mathrm{M}_\infty = 0.71$ and $\alpha = 3.5$ deg.

and final Mach number are 0.73 and 0.71, respectively. The method is effective in preventing buffet from taking place again, as indicated by the black line in Figure 8.17. For the sake of clarity, the steady-state values of the aerodynamic coefficients at $\mathrm{M}_\infty = 0.71$ were added. These latter were rescaled by a factor $(0.71/0.73)^2$ to account for the difference in reference Mach number with respect to the other simulations (solid lines).

However, some aspects must be discussed. The one degree-of-freedom assumption made for this case is only a crude approximation to describe a possible deceleration due to a pilot action or an increase in drag caused by the spoiler deployment. In reality, the dynamic response to the spoiler deployment would generate an imbalance of lift, drag, and pitching moment (see, e.g., Fig-

ure 8.11), significantly complicating the treatment of this problem. Therefore, the use of a spoiler alone cannot be defined as successful unless the dynamic response of the aerofoil is studied. This consideration holds for any other dynamic control strategy. In principle, buffeting flows see strong oscillations in the aerodynamic coefficients and their study should account for the dynamic response of the structure. So far, this practice has not been adopted, with the exception of works presented in Section 2.2.3. Here, the applied deceleration can be seen as a first step towards this kind of approach to simulate a response to the spoiler deployment. On the other hand, the imposed deceleration can be interpreted as an action of the pilot to escape the buffet boundary. In particular, the spoiler deployment temporarily suppresses buffet, and the deceleration allows moving towards conditions where SIO is not present. The shock stabilisation is desirable to avoid a possible momentaneous increase in the oscillation amplitude due to the aerofoil deceleration. Therefore, spoilers (and UTEF) thought as a temporary solution for buffet alleviation, do not extend the buffet boundary. When needed, they can be deployed to suppress the shock-induced oscillations, allowing the pilot to return to conditions below the buffet boundary. If the effect of these devices is considered as a simple shape modification, it can be said that spoilers and UTEF delay the onset of buffet (see the works of Tian et al. [259, 261]).

8.2.4 3D Control

This section presents results for the finite spoiler case applied on the OAT15A wing. The investigated angles of attack are $\delta_s = 5$ and 15 deg. The first is optimum for the 2D case when it comes to lift increase and time of actuation, while the second corresponds to an off-design actuation.

Figure 8.18 shows the influence of flow control on the aerodynamic coefficients. In every case, the SIO is suppressed within some buffet periods. With respect to the 2D counterpart, the 3D case at $\delta_s = 5$ deg is affected by the limited spanwise extent of the flow control device and the response time is increased. The same holds for the effect the spoiler has on the steady-state value of the aerodynamic coefficient. This is extremely positive when one looks at the drag coefficient, as it drops significantly with respect to the 2D case. For the case $\delta_s = 5$, the steady-state values of moment and lift coefficients now roughly coincide with their mean values at buffet conditions. The delay in the time response is not significant: given the frequency of buffet, a response time of 3 to 5 buffet periods corresponds to less then 0.1 s, which is more than satisfactory for every practical application. The $\delta_s = 15$ case presents a different behaviour, in agreement with the 2D results of Section 8.2.3.1. Lift and moment coefficients have similar values to the 2D computation, while the drag is drastically reduced. In both cases, small oscillations in the aerodynamic coefficients remain (see the zoomed view in Figure 8.18, top-right). The causes were explored in Section 8.2.3.1 and the same considerations hold for the 3D cases. As the vortex shedding shown in Figure 8.15 now only occurs on roughly half of the spanwise extent of the domain, the influence on the aerodynamic

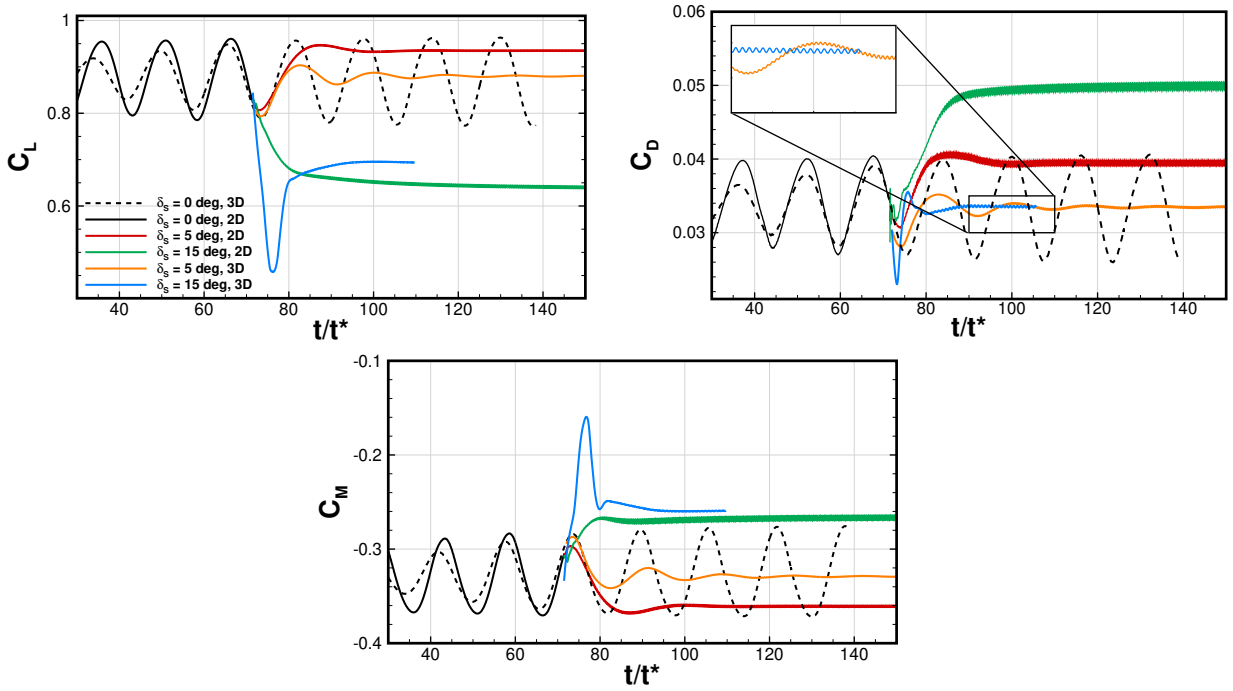

Figure 8.18: Aerodynamic coefficients history for 2D and 3D simulations on the OAT15A wing section at $\mathrm{Re}_c = 3 \times 10^6$, $\mathrm{M}_\infty = 0.73$ and $\alpha = 3.5$ deg.

coefficients is milder with respect to the 2D cases.

The steady-state pressure distribution in Figure 8.19, top figures, shows a curved shock front at both angles. In agreement with the 2D cases, the shock is pushed upstream with respect to its pre-onset position. This effect is more significant at the spanwise positions seeing the presence of the spoiler, while the shock position is more downstream elsewhere. In the $\delta_s = 15$ deg case, the flow is compressed between the shock and the spoiler, accentuating the pressure jump across the hinge. The high δ_s case sees a stronger 3D effect, since the pressure distribution differs significantly according to the spanwise section considered. The lower pressure jump across the hinge with respect to the 2D case justifies the drop in drag observed in Figure 8.18.

Friction lines in Figure 8.20 complement the results of Figure 8.19 and corroborate those of the 2D computations. In the same plot, $\mathrm{M}_\infty = 1$ Mach surfaces show the shock position, $U/U_0 = -0.001$ iso-surfaces indicate the extent of the separated regions, and friction lines help visualize the spanwise flow organisation. In the $\delta_s = 5$ case, the rear shock position results in a separated flow region spanning from the shock foot to the spoiler, while for a higher spoiler angle, an aft shock position allows the boundary layer to re-attach. In the latter, the flow decelerates before turning around the spoiler resulting in a higher pressure jump across the control surface and drag penalty. The results are in line with the 2D cases. The main difference consists of the flow structure out of the portion covered by the spoiler, where the flow re-attaches. Therefore, the effect of the finite control surface is mitigated.

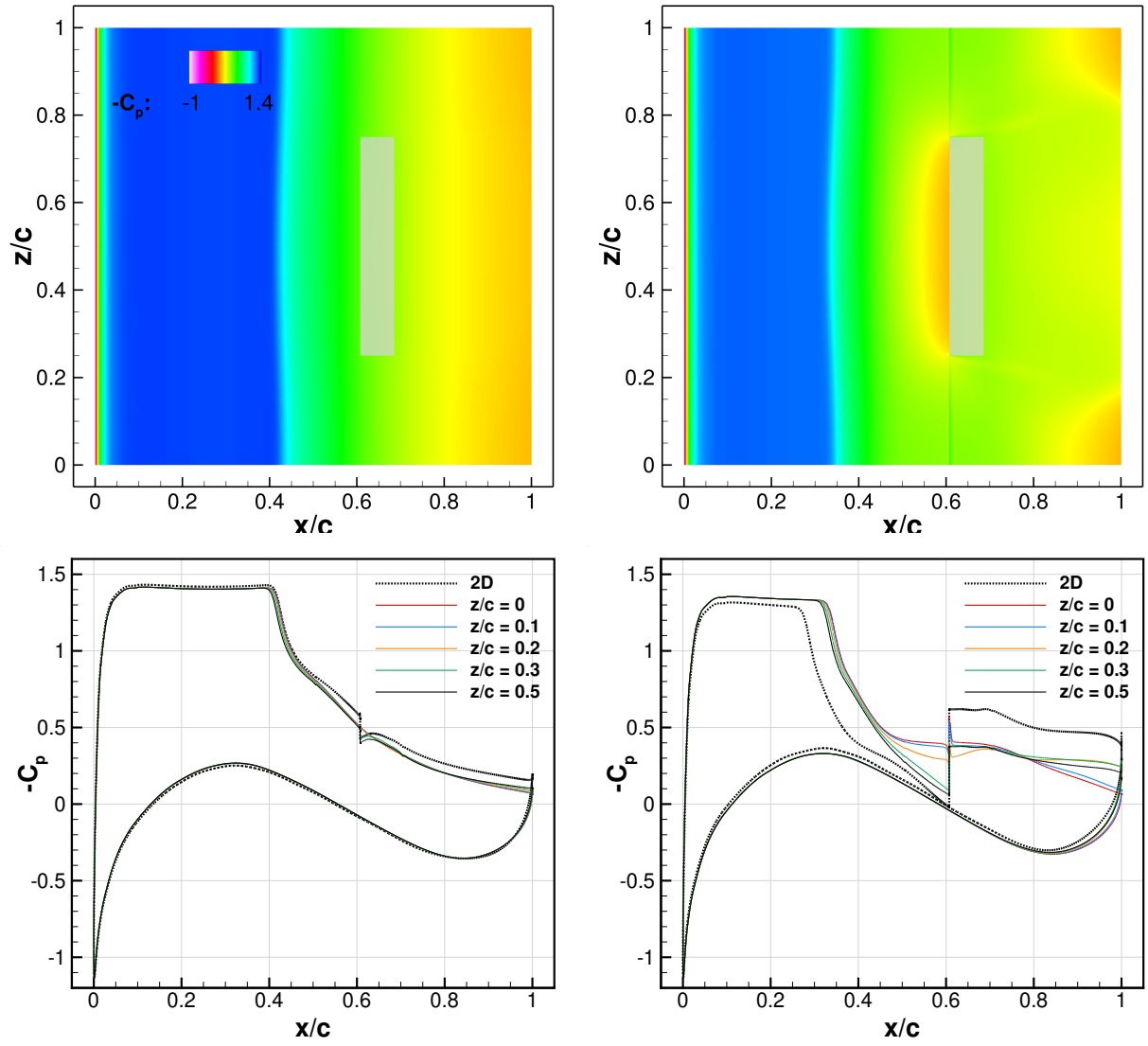

(a) $\delta_S = 5$ deg

(b) $\delta_S = 15$ deg

Figure 8.19: Contours (top) and line plots at different spanwise locations (bottom) of the pressure coefficient around the OAT15A wing at $\mathrm{Re}_c = 3 \times 10^6$, $\mathrm{M}_\infty = 0.73$ and $\alpha = 3.5$ deg. $z/c = 0$ corresponds to the domain sidewall while $z/c = 0.5$ corresponds to the symmetry plane. Dashed, black lines indicate the results of the 2D computations at the same angles.

The pressure difference between the upper and lower surface of the spoiler results in two counter-rotating tip vortices which are well captured in the computations. The higher the δ_s, the more intense the vortices, as shown in Figure 8.21. Overall, the spanwise finite spoiler gives rise to two systems of vortices: the spanwise vortices detaching as a result of the trailing edge thickening, typical of the 2D case, and the longitudinal tip vortices. The deployment of the spoiler leads to the suppression of buffet by fixing flow separation on a portion of the wing.

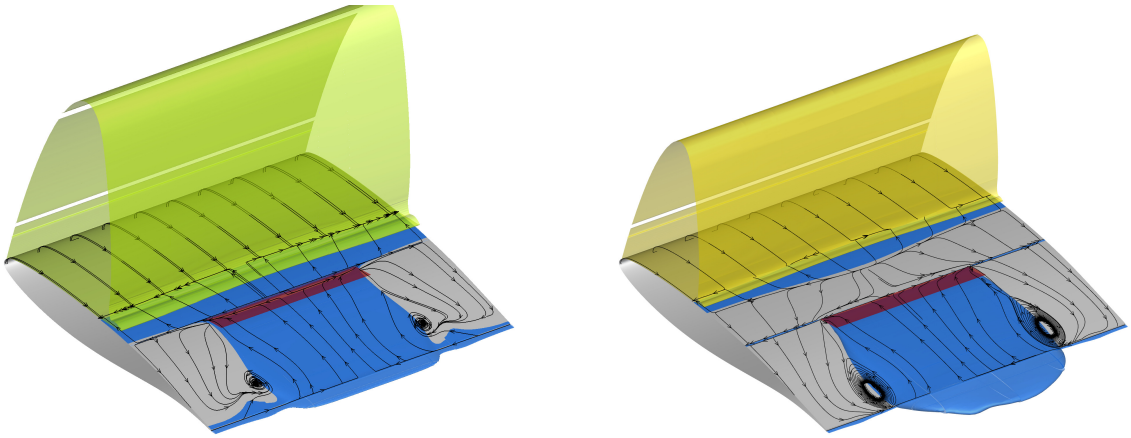

(a) $\delta_S = 5$ deg **(b)** $\delta_S = 15$ deg

Figure 8.20: $M_\infty = 1$ (yellow) and $U/U_0 = -0.001$ (blue) iso-surfaces for the flow around the OAT15A wing at $Re_c = 3 \times 10^6$, $M_\infty = 0.73$ and $\alpha = 3.5$ deg. The spoiler is indicated by the red surface.

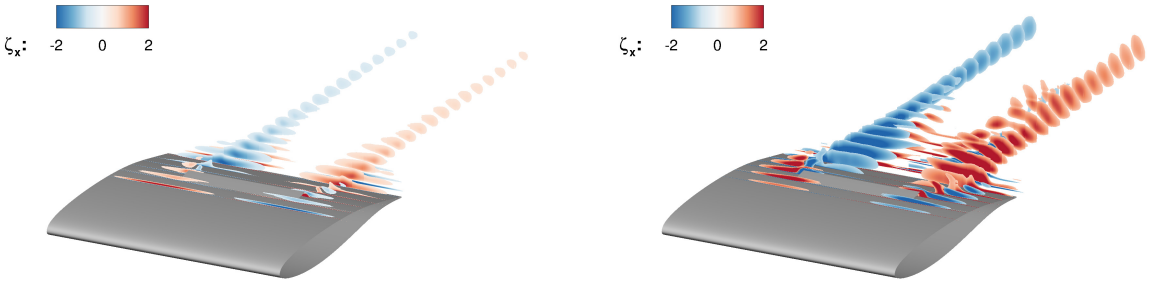

(a) $\delta_S = 5$ deg **(b)** $\delta_S = 15$ deg

Figure 8.21: Longitudinal component of the vorticity vector around the OAT15A wing at $Re_c = 3 \times 10^6$, $M_\infty = 0.73$ and $\alpha = 3.5$.

8.3 Chapter Overview

In this chapter, numerical simulations of virtual spoilers, upper trailing edge flaps, and Gurney flaps were carried out in the context of transonic buffet control. A PANS model based on a k-ω SST model was used to simulate the flow around two- and three-dimensional configurations, providing accurate results for the prediction of the SIO. Control devices were approximated by means of no-slip, infinitely thin surfaces. The adoption of the method used in this work allowed for an easy study of the same flow with different geometric properties of spoilers and flaps, such as angle of deployment, length of the devices, deployment schedule, etc. Even with the adoption of virtual surfaces, the simulations captured well flow separation and vortices in 2D and 3D computations.

Gurney flaps and UTEFs were tested for two 2D configurations, namely the V2C and OAT15A aerofoils. The separation region generated on the pressure side by the Gurney flaps resulted in an

increase of the local angle of attack. Therefore, Gurney flaps did not alleviate buffet. Conversely, they caused an increase in the shock oscillation amplitude, as well as in the fluctuations of the aerodynamic coefficients.

The deployment of the Gurney on the suction side was able to alleviate, if not fully suppress, the shock oscillations around the aerofoils. The separated flow region at the trailing edge generated by these devices resulted in an upstream shock position. The shock weakened and the separation could be avoided. For both configurations, the SIO was suppressed only when the shock was pushed upstream enough to prevent merging of the two separated flow regions at the shock foot and at the trailing edge. For the V2C aerofoil, studied at well-developed buffet conditions, a small device did not produce the desired effect, and a longer one was needed.

On the other hand, spoilers proved able to stop the buffet by hampering the communication between the shock-foot and the trailing edge separation regions. Two aerofoils were investigated in the 2D campaign: the NACA0012 and the OAT15A. In the first case, because of the flow conditions and the aerofoil geometry, the separated flow region in the buffet case was much larger. Therefore, a greater spoiler deployment was necessary to suppress buffet. Nevertheless, even a small spoiler angle alleviated the shock oscillations. For the OAT15A aerofoil, even a small deployment of the spoiler revealed effective in reducing the SIO. If the spoiler was deployed enough, the shock position was such to avoid boundary layer separation, otherwise two distinct regions remained and the spoiler prevented their interaction. Unlike the UTEF, spoilers proved able to suppress the oscillations even when the boundary layer was fully separated after the shock since the separated flow region is broken by the presence of the device. For small spoiler deployment angles, the control surface functioned as an obstacle, blocking disturbances traveling in the boundary layer.

On the OAT15A, 3D simulations were repeated adopting a finite spoiler at two deployment angles. The limited span of the control surface resulted in a mitigation of its effect compared to the 2D case. While the differences in the lift and pitching moment were negligible between the 2D and 3D cases, the drag penalty was significantly reduced in the 3D configurations. At a higher deployment angle, the separation behind the spoiler was more severe, and the device acted as an air-brake.

The use of flow control was also complemented with an aerofoil deceleration to simulate the effect of the pilot action to evade the buffet regime. While the spoiler was able to suppress the oscillations, the deceleration applied by means of CFD grid motion resulted in a local Mach number decrease and a successful prevention of buffet. The test performed here did not account for the dynamic response of the aerofoil to the spoiler deployment.

Chapter 9

Conclusions and Future Work

This thesis studied transonic buffet by means of CFD. The focus was on buffet predictions using time-marching simulations, engineeristic criteria, and, in a second phase, buffet control. For the former purpose, a compromise between the accuracy of the description and the efficiency of the computation was sought; for the latter, the use of existing control surfaces to alleviate buffet was studied.

Time marching simulations were carried out using PANS, having reduced CPU cost compared with other hybrid RANS/LES methods. The method was tested on a circular cylinder and was extended to transonic buffet Q-2D computations. Engineeristic criteria from the literature, based on integrated loads, were used to predict the buffet onset for 2D aerofoils. An algorithm adopting the aforementioned criteria, and the adjoint method, was formulated for fast onset prediction, and tested on the same configurations. To improve the prediction by accounting for the results of TMSs, a similar algorithm using the harmonic balance method was proposed.

Flow control was applied to 2D and 3D configurations using UTEFs and spoilers. To circumvent the problem of meshing slotted control surface devices, these were modelled by means of *ad hoc* boundary conditions.

9.1 Summary and Conclusions

The PANS model implemented in HMB3 was validated for a circular cylinder at $\mathrm{Re}_D = 5 \times 10^4$ with the aim to assess the ability of the method to cope with flows presenting self-induced unsteadiness and separation. Several computations were carried out to investigate the sensitivity of the model to grid size, time step, and the estimate of the parameter f_k of the PANS equations. The constant-f_k approach was sensitive to the spatio-temporal discretisation adopted. On the other hand, a dynamic-f_k approach was able to adapt to the local grid size and turbulent content. By using estimates based on the turbulent length scale, the method switched from RANS in the attached boundary layer, to

SRS mode in the separated flow regions and the wake, reverting back to RANS in the far field. In this work, two modifications of pre-existing dynamic estimates have been proposed and tested for the case under analysis. The results were encouraging and deserve further investigations.

A dynamic-f_k approach was used to predict buffet around an OAT15A unswept wing at several angles of attack. The CFD domain also included the wind tunnel walls to **(i)** account for the effects of the wing-wall junction, and **(ii)** provide a fair comparison with the experiments. 2D, unconfined computations showed minor, if not negligible, influence of the incoming turbulence level. For the full configuration, the wind tunnel back pressure, and the transition location of the airfoil played an important role. These parameters were selected to match the experimental flow conditions. The PANS method showed good performance in the prediction of buffet, and in the description of the flow topology at pre-buffet conditions. After the onset, the method provided improved results over RANS on CFD grids of different sizes. Although the mean flow quantities, i.e. pressure coefficient distribution, peak RMS, and extent of shock excursion were correctly predicted on all grid levels, a finer grid was necessary to improve the prediction of the buffet dynamics. In fact, using a refined grid in the spanwise direction, it was possible to observe the development of 3D vortical structures in the separated boundary layer. These were formed at the interface between the attached boundary layer and the separated corner flow and propagated toward the tunnel centreplane. The result was a non-uniform shock front over the span. Nevertheless, the frequency content was independent of the spanwise location, as observed in the experiments [126]. The obtained results are in agreement with recent experimental and numerical studies on similar configurations [223, 252]. In particular, the propagation pattern of pressure disturbance matches the results of the global stability analysis of [223]. The time-marching nature of the computation allowed for a detailed characterisation of the buffet dynamics. Compared to the parent RANS, the PANS routine led to a negligible increase in CPU power required when used with the same spatio-temporal CFD resolution. In view of the research carried out in this work, dynamic-f_k estimates are necessary to consolidate the use of PANS for flows of practical interest.

In parallel, two criteria from the literature were tested in 2D. The criteria were based on results for the lift and pitching moment coefficients. Their value was extracted from steady RANS simulations, and proved efficient compared to TMS. Nevertheless, the estimation of the buffet onset for several flight conditions needs a high number of simulations. To avoid this, an algorithm using the adjoint method in HMB3 was formulated. It was found that the derivatives $\partial C_L/\partial\alpha$ and $\partial C_M/\partial\alpha$ at the onset, representing the *buffet indicator*, follow an almost linear trend in the range of Mach numbers typical of cruise conditions. Therefore, it was possible to estimate their value for intermediate Mach numbers, once the extremes were known. The adjoint method allowed for the efficient computations of the sensitivities of the buffet indicator with respect to the flight parameters. Therefore, the buffet boundary could be traced by moving towards the points having the expected values of the buffet indicator. Among the ones tested, the indicator on $\partial C_M/\partial\alpha$ provided better agreement

with experimental data. Nevertheless, the behaviour of this indicator deviated from a purely linear function of the Mach number, introducing bigger errors in the adjoint method. The $\partial C_L/\partial\alpha$ was, with good approximation, a linear function of the Mach number, and worked well in the optimised algorithm. On the other end, the criterion based on ∂C_L led to a slight under-prediction of the onset angle of attack. Overall, the adjoint-based algorithm led to savings in the order of 50% in CPU time, for a bi-parametric study. Should one or more parameters be accounted for in the analysis (e.g. the Reynolds number), the expected savings would be significantly higher.

Partially better agreement was shown by estimating the buffet boundary using the harmonic balance method implemented in HMB3. Due to the dependency of the fundamental buffet frequency on the flight conditions, a frequency-adaptive method was implemented. This allowed for the reduced frequency evaluation for each combination of Mach number and angle of attack. The harmonic balance computations successfully reproduced the unsteady behaviour of vortex shedding around a circular cylinder and transonic buffet flows around 2D aerofoils. By using a number of harmonics equal to or smaller than 7, the CPU was reduced compared to TMS. The computations were also able to reproduce the correct physics of 2D transonic buffet. When embodied in an algorithm for buffet onset prediction, the results were improved, compared to the aforementioned RANS-based criteria. In this case, a PANS approach with constant $f_k = 0.7$ was adopted as a less dissipative version of URANS. With the current value of f_k, no scale-resolving was unlocked. However, the improvement was limited to certain flight conditions. For the NACA0012, the underlying turbulence model could not predict buffet for $M_\infty \geq 0.78$, and this resulted in a failure of the algorithm in that range of Mach numbers. For those flow conditions, the RANS-based criteria worked significantly better, as they were not related to the performance of TMS, and the prediction of the pre-buffet loads was accurate. Therefore, the dependency on the underlying turbulence model for flows like buffet is a disadvantage. On the other hand, the adoption of the harmonic balance method with adaptive frequency computation provided knowledge of the frequency and amplitude of oscillation, which can be useful in the design phase of wings.

Lastly, flow control was simulated using spoilers and UTEFs. Both devices were helpful to alleviate or suppress buffet around 2D configurations. The employed virtual surface method allowed for changes in some geometrical parameters, such length of the devices, and deployment angle. Moreover, it allowed for dynamic deployment and changes in the orientation of the surfaces. Spoilers, located on the second part of the airfoil, split the separated flow region in two zones, and blocked the communication between them. This way, the propagation of disturbances in the boundary layer was prevented. Because of the chamber increase, the shock was pushed upstream, where it lost its intensity and the ability to separate the downstream boundary layer. UTEFs worked in a similar manner, as the chambering effect was obtained by enforcing boundary layer separation at the suction side trailing edge of the airfoil. Therefore, the length of the device must be enough to obtain a sufficient foreshift in the shock position. Conversely, small deployments of spoilers were

sufficient to alleviate, if not suppress, the SIO. Moreover, spoilers are already installed on every commercial airplane, while UTEFs have not been used so far. For these latter, the aerodynamic loads could compromise the structural integrity of the device, given their orientation with respect to the free-stream flow direction. Therefore, spoilers were the most promising option.

Spoilers simulations on a 3D configuration with a finite device span were also carried out. Finite spoilers resulted in a reduced influence on the aerodynamic coefficients, in particular on the drag coefficient. The presence of finite devices strongly modified the flow topology around the wing, introducing cross flow, i.e. strong flow three-dimensionality. Spoilers were also adopted in conjunction with grid motion to simulate an action from the pilot. The velocity reduction together with the spoiler retraction prevented SIOs from taking place after the control was removed.

9.2 Future Work

The main aspects not covered in this research are those related to 3D effects. Therefore, the computational apparatus built in a 2D/Q-2D framework could be extended to 3D configurations in future studies.

The PANS model used in Chapter 4 and Chapter 5 can be adopted for different unsteady flows with SBLI. In this view, the estimate of f_k should be improved to allow for a more automatic clipping according to grid size and local turbulence content to avoid any preliminary calibration. Dynamic estimates looked promising and more adequate for statistically unsteady flows like those of interest in the present work. Nevertheless, further work is required to find an estimate that works well for a broad variety of flows. In particular, research in non-linear correction of the Reynolds stress, and a 3-equation model could improve the performance when dealing with corner and transitional flows, respectively.

The buffet mechanism must be studied further. In particular the link between 2D and 3D buffet remains unclear. In this study, the buffet dynamics could be described as a mixture of both. To understand how the transition from 2D to 3D buffet happens, a large experimental or numerical campaign on realistic geometries is necessary. The link between the influence of the sweep angle, the wing aspect ratio, and tip effects must be studied in more detail. In a CFD framework, a compromise between accuracy and cost must be found, and that is where the adoption of PANS can help future studies.

Future work will be devoted to exploring the ability of the algorithms proposed in Chapter 6 and Chapter 7 to work on more complex geometries e.g., transonic wings. Moreover, the focus will be on modifying the method to use unsteady simulations. Unsteady parameters may provide improved predictions of the buffet boundary. Finally, the present study may be enriched with the introduction of a third parameter like the Reynolds number, to widen the range of flight conditions considered.

The lack of reliability and consistency of statistical turbulence models in predicting buffet demands for the use of scale-resolving simulations, e.g. DES or even LES. Therefore, it would be worth investigating the performance of the harmonic balance method proposed here in conjunction with one of the aforementioned approaches. Nevertheless, it is reasonable to believe that the number of modes required to obtain a degree of accuracy comparable with time-marching simulations would be too high to justify the employment of a harmonic balance technique. The application of this method with formulations like SAS or PANS can be seen as a compromise in terms of costs and accuracy between URANS and DES/LES and seems a viable option for future studies.

Another task would be to assess if a harmonic balance method is still worth using for 3D flows when more accurate and resolved solutions are sought. As 3D buffet is broadband, a fundamental flow frequency cannot be determined. Mathematically speaking, buffet cells arise when several eigenvalues (i.e. at different frequencies) cross the imaginary axis. The superposition of several modes would lead to the spanwise propagation proper of 3D cases. Using a guess value among the most energetic frequencies, the risk is to confine buffet to a 2D behaviour. Perhaps a multi-frequency harmonic balance could help here.

With regard to flow control, future efforts will be devoted to account for the effect of the non-equilibrium of forces and pitching moments as a result of surface motion, perhaps as part of active flow control.

Moreover, 3D wing configurations should be tested to assess the efficiency of the aforementioned methods. The position of spoilers in relation to the development of buffet along 3D wings gives hope for a successful outcome. In Chapter 8, the ability of spoilers to block 2D buffet was verified, but the potential propagation along the span should be looked at.

Appendix A

Past OAT15A Simulation using URANS

This appendix provides an overview of CFD computations using URANS for the OAT15A aerofoil at $Re_c = 3 \times 10^6$, $M_\infty = 0.73$ and $\alpha = 3.5$ deg. This test case at the reported flow conditions was widely investigate because of the availability of experimental data. Therefore, it was used to validate the ability of different turbulence models and CFD solvers to predict buffet.

Table A.1: Overview of computations for the OAT15A 2D configuration with different closure models. SA: Spalart-Allmaras; BSL: baseline k-ω ; SST: Menter's Shear Stress Model; KKL: $k-kL$ model; SALSA: Spalart–Allmaras with strain-adaptive formulation; LEA: Linearized Explicit Algebraic k-ω ; EHRSM: ε^h-Reynolds stress model; EDW: Edwards-Chandra modification of SA; KWW: Wilcox's k-ω ; CC: compressibility correction; RC: rotation correction; SORSM: stress-Omega RSM; EARSM: Explicit Algebraic Reynolds Stress Model.

Authors	**Year**	**Solver**	**Model**	Buffet	f_B [Hz]	ΔC_L
Deck [59]	2005	FLU3M	SA	no SIO		
Thiery & Coustols [258]	2006	elsA	SA	no SIO		
			BSL	no SIO		
			KKL	SIO	$71 \div 78$	$\simeq 0.22$
			SST	SIO	$71 \div 78$	$\simeq 0.14$
Huang [117]	2012	UNITs	SST	no SIO		
Illi *et al.* [119]	2012	TAU	SA	no SIO		
			SALSA	SIO	$74 \div 76$	$0.10 \div 0.16$
			SST	no SIO		
			LEA	no SIO		
			EHRSM	SIO	$\simeq 0.69$	$\simeq 0.30$
Grossi *et al.* [108]	2014	NSMB	SA	no SIO		
			SA+CC	no SIO		
			SST	no SIO		
			EDW	SIO		
			EDW+CC	SIO	73.2	$\simeq 0.30$
			SALSA	SIO		
			KWW	SIO		
Sartor *et al.* [226]	2015	elsA	SA	SIO	77	$\simeq 0.06$
Tian [259]	2017	-	SA	SIO		

Continued on next page

Table A.1 – *Continued from previous page*

Authors	**Year**	**Solver**	**Model**	Buffet	f_B [Hz]	ΔC_L
Giannelis *et al.* [98]	2018	ANSYS Fluent	SA-RC	no SIO		
			SST	no SIO		
			SST-mod*	SIO	72.2	0.16
			SORSM	SIO	74.7	0.33
Zimmernann [293]	2018	FLOWer	SALSA	SIO	$69.56 \div 72.63$	
		TAU	SALSA	SIO	$69.94 \div 73.0$	
Plante & Laurendeau [211]	2019	NSCODE	SA	no SIO		
			SA+CC	SIO	73.9	$\simeq 0.27$
			EDW	no SIO		
			EDW+C	SIO	73.9	$\simeq 0.30$
Zhao *et al.* [290]	2020	-	SA	SIO	75	
			SST	SIO †		
			EARSM	no SIO		
Petrocchi & Barakos [209]	2023	HMB3	SST	no SIO		

Tab. A.1 is a collection of CFD works using a wide variety of solvers (column 3) and turbulence models (column 4). In the last column, the ability to predict shock-induced oscillations (SIO: yes; no SIO: no) is reported. The results shows a big scatter in the prediction of the main quantities of interest, i.e. buffet frequency, amplitude of oscillations, mean and RMS pressure distribution. As the results for the aforementioned works were not consistently reported in the cited works, they were not included in the table. Also, works providing results with the same setup (CFD solver, turbulence model, grid, timestep) of one of those in the table were not mentioned to avoid redundancy.

*a reduction of the a_1 coefficient of the SST model was applied.

†Very mild oscillations were detected.

Appendix B

Literature on PANS Works

The PANS approach was used with increasing frequency over the years. Appendix B is a collection of works solving PANS equations to show the increased popularity of the approach over the years. While, in principle, the method was only tested on canonical flow cases, mostly using a *constant* approach for f_k estimate, more sophisticated estimates were developed, extending the use of PANS to other applications.

Table B.1: List of PANS computations found in literature. RSM: Reynolds-stress model; NL: non-linear; SST: shear stress model; LR: low-Reynolds; RSM-GLVY: Reynolds stress model of Gerolymos-Lo-Valley-Younis [95].

Authors	Year	Test case	Re	M_∞	Model
Constant					
Girimaji *et al.* [101–103]	2005-2006	Turb. Square Jet	1.84×10^5	-	k-ε
Lakshimpathyi & Girimaji [151, 152]	2006	Circular Cylynder	1.4×10^4	-	k-ε
	2010	Circular Cylynder	1.4×10^4	-	k-ε
Frendi *et al.* [78]	2007	Backward-facing step	3.75×10^4	-	k-ε
Gerolymos & Vallet [96]	2007	Rod/Airfoil	4.7×10^4	0.21	RSM
Jeong & Girimaji [129]	2010	Square Cylynder	2.2×10^4	-	k-ε
Huang & Wang [115]	2011	Hydrofoil with cavitation	7×10^5	-	k-ε
Ma *et al.* [165, 166]	2011	Hill flow	3.7×10^4	-	k-ε /LR-k-ε
		Channel flow	9.5×10^2	-	
		Curved Duct	9.5×10^2	-	
Srinivasan & Girimaji [245]	2014	Jet in cross stream	5.3×10^6	-	k-ω SST
Roy *et al.* [9]	2015	Lid-driven Cavity	1×10^4	-	k-ω
Pereira *et al.* [205, 206]	2015, 2018	Circular Cylynder	3.9×10^3	-	k-ω SST
Bonnifet *et al.* [28]	2017	OAT15A	3×10^6	0.73	RSM-GLVY
Klapwijk *et al.* [134–136]	2019, 2020	Channel flow	$180 \div 395$	-	k-ω SST
Saroha *et al.* [224, 225]	2020	Heated Sphere	1×10^4	-	NL k-ε
	2020	Heated Cylinder	2.14×10^4	-	
Dzanic *et al.* [67]	2022	Periodic hill	1.0595×10^4	-	k-ω SST
		Circular cylinder	3.9×10^3	-	
Static					
Elmiligui *et al.* [72]	2004	Circular Cylinder	5×10^4	0.3	k-ε
Abdol-Hamid & Girimaji [1]	2004	Circular Cylinder	5×10^4	0.3	k-ε

Continued on next page

Table B.1 – *Continued from previous page*

Authors	**Year**	**Test case**	**Re**	**M_∞**	**Model**
Song & Park [238]	2009	Square Cylynder	2.14×10^4	-	k-ω
Foroutan & Yavuzkurt [77]	2014	Swirling jet	3×10^4	-	LR-k-ε
Dynamic					
Basu *et al.* [20]	2007	Cavity	0.6×10^6/ft	1.19	k-ε
Basara *et al.* [17–19]	2011	Turbulent Channel	6.5×10^2	-	k-ε -ξ-f
	2015	Wall-mounted Cube	1.3×10^4	-	
	2018	Square Cylinder	2.14×10^4	-	
Krajnovic *et al.* [146–148]	2012	Landing Gear	1×10^6	-	k-ε -ξ-f
	2015	Bluff body	4.0×10^4	-	
	2016	Simplified Vehicle	9.0×10^5	-	
Han *et al.* [110]	2013	Bluff body	3.0×10^4	-	k-ε -ξ-f
Luo *et al.* [164]	2015	Circular Cylinder	4.5×10^7	2.46	k-ω SST
		Ramped Cavity	4.5×10^7	2.92	
Mirzaei *et al.* [187]	2015	Bluff body	3.0×10^4	-	k-ε -ξ-f
Minelli *et al.* [185, 186]	2017	Simplified Track Cabin	5.0×10^5	-	k-ε -ξ-f
	2018	Oscillating Track Cabin	5.0×10^5	-	
Zhang *et al.* [287]	2018	Ship	8.0×10^4	-	k-ε -ξ-f
Luo [163]	2019	Backward-facing Step	5.1×10^3	-	k-ω SST
Davidson & Friess [58, 79]	2019, 2020	Channel flow	5.2×10^3	-	LR-k-ε
		Hump flow	9.36×10^5	-	
		Hill flow	1.06×10^4	-	
Liu *et al.* [161]	2022	Rotating Channel Flow	7000	-	k-ω SST
		Centrifugal pump	5.5×10^4	-	
Moosavifard *et al.* [191]	2022	Circular Cylinder	4.8×10^4	0.21	k-ε -ξ-f
Nastac & Frendi [194]	2022	Supersonic retropropulsion	5.0×10^6	4.61	k-ω SST
Wang *et al.* [278]	2023	Square-back Van	2.5×10^5	-	k-ε -ξ-f

Bibliography

[1] K.S. Abdol-Hamid and S.S. Girimaji. A Two-Stage Procedure Toward the Efficient Implementation of PANS and Other Hybrid Turbulence Models. Technical report, National Aeronautics and Space Administration, 2004. NASA/TM-2004-213260.

[2] K. Abramova, K. Khairullin, A. Ryzhov, and V. Soudakov. Numerical simulation of transonic buffet and its control using tangential jet blowing. In *ECCOMAS 2016*, Crete Islang, Greece, 2016.

[3] K. Abramova, A. V. Petrov, A. V. Potapchick, and V. G. Soudakov. Control of buffet onset by plasma-based actuators. *AIP Conference Proceedings*, 1770:020017, 2016. https://doi.org/10.1063/1.4963940.

[4] K. Abramova, A. V. Petrov, A. V. Potapchik, and V. G. Soudakov. Experimental investigation of transonic buffet control on a Wing Airfoil using tanjential jet blowing. *Fluid Dynamics*, 55:545–553, 2020. https://doi.org/10.1134/S0015462817020168.

[5] K. Abramova, A. A. RyzhovA., and V. G. Soudakov. Numerical Modeling of Transonic Buffeting and its Control by Means of Tangential Jet Blowing. *Fluid Dynamics*, 52:329–335, 2017. https://doi.org/10.1134/S0015462817020168.

[6] A. Accorinti, T. Baur, S. Scharnowski, and C.J. Kahler. Experimental Investigation of Transonic Shock Buffet on an OAT15A Profile. *AIAA Journal*, 2022. https://doi.org/10.2514/1.J061135.

[7] A. Accorinti, T. Korthauer, S. Scharnowski, and C.J. Kahler. Characterization of transonic shock oscillations over the span of an OAT15A profile. *Experiments in Fluids*, 64:61, 2023. https://doi.org/10.1007/s00348-023-03604-z.

[8] A. Accorinti, T. Korthauer, S. Scharnowski, and C.J. Kahler. Flow Development toward Shock Buffet on OAT15A Airfoil. In *2023 AIAA SciTech Forum*, Washington, DC, USA, 2023. https://doi.org/10.2514/6.2023-0244.

[9] B. Akula, P. Roy, P. Razi, S. Anderson, and S. Girimaji. Partially-averaged navier-stokes (pans) simulations of lid-driven cavity flow—part 1: Comparison with urans and les, 2015. http://doi.org/10.1007/978-3-319-15141-0_29.

[10] R.M. Apetrei. *Numerical prediction and characterization of shock-buffet in transport aircraft*. PhD thesis, University of Sheffield, 2019.

[11] O Axelsson. *Iterative Solution Methods*. Cambridge University Press, 1994.

[12] H. Babinsky and H. Ogawa. Three-Dimensional SBLI Control for Transonic Airfoils. In *3rd AIAA Flow Control Conference*, San Francisco, CA, USA, 2006.

[13] H. Babinsky and H. Ogawa. SBLI control for wings and inlets. *Shock Waves*, 18:89–96, 2008. http://doi.org/10.1007/s00193-008-0149-7.

[14] B. Baldwin and H. Lomax. Thin-layer approximation and algebraic model for separated turbulent flows. In *16th Aerospace Sciences Meeting*, 1978. https://doi.org/10.2514/6.1978-257.

[15] G. Barakos and D. Drikakis. Investigation of Nonlinear Eddy-Viscosity Turbulence Models in Shock/Boundary-Layer Interaction. *AIAA Journal*, 38:461–469, 2000. http://doi.org/10.2514/2.983.

[16] G. Barakos and D. Drikakis. Numerical simulation of transonic buffet fow using various turbulence closures. *International Journal of Heat and Fluid Flow*, 21:620–626, 2000. http://doi.org/10.1016/S0142-727X(00)00053-9.

[17] B Basara. Fluid flow and conjugate heat transfer in a matrix of surface-mounted cubes: A PANS study. *International Journal of Heat and Fluid Flow*, 51:166–174, 2015. http://doi.org/10.1016/j.ijheatfluidflow.2014.10.012.

[18] B Basara, S. Krajnovic, S. Girimaji, and Z. Pavlovic. Near-Wall Formulation of the Partially Averaged Navier–Stokes Turbulence Model-Layer Interaction. *AIAA Journal*, 49:2627–2636, 2011. http://doi.org/10.2514/1.J050967.

[19] B Basara, Z. Pavlovic, and S. Girimaji. A new approach for the calculation of the cut-off resolution parameter in bridging methods for turbulent flow simulation. *International Journal of Heat and Fluid Flow*, 74:76–88, 2018. http://doi.org/10.1016/j.ijheatfluidflow.2018.09.011.

[20] D. Basu, A. Hamed, and K. Dias. Assessment of partially averaged Navier/Stokes (PANS) multiscale model in transonic turbulent separated flows. In *ASME/AJME 2007 5th Joint Fluids Engineering Conference*, San Diego, CA, USA, 2007.

[21] B. Benoit and I. Legrain. Buffeting prediction for transport aircraft applications based on unsteady pressure measurements. In *5th Applied Aerodynamics Conference*, Monterey, CA, USA, 1987.

[22] M. Biava and G. N. Barakos. Optimisation of ducted propellers for hybrid air vehicles using high-fidelity CFD. *The Aeronautical Journal*, 120:1632–1657, 2016. http://doi.org/10.1017/aer.2016.78.

[23] M. Biava, M. Woodgate, and G. N. Barakos. Fully implicit discrete-adjoint methods for rotorcraft applications. *AIAA Journal*, 54:735–749, 2016. http://doi.org/10.2514/1.J054006.

[24] Flavien Billard, Todd Davidson, Holger Babinsky, Robert Placek, Marek Miller, Paweł Ruchała, Wit Stryczniewicz, Tomasz Kwiatkowski, Wieńczysław Stalewski, Janusz Sznajder, Sara Kuprianowicz, Matteo Bernardini, Sergio Pirozzoli, George Barakos, George

Zografakis, Benoit Tartinville, Charles Hirsch, Damien Szubert, Marianna Braza, Ioannis Asproulias, Nikos Simiriotis, Jean-Baptiste Tô, and Yannick Hoarau. *WP-5 External Flows—Wing*, pages 347–512. Springer International Publishing, Cham, 2021. https://doi.org/10.1007/978-3-030-47461-4_6.

[25] J. Birkenmeyer, H. Rosemann, and E. Stanewsky. Shock control on a swept wing. *Aerospace Science and Technology*, 4:147–156, 2000. https://doi.org/10.1016/S1270-9638(00)00128-0.

[26] S. Bogdanski, P. Gansel, T. Lutz, and E. Krämer. Impact of 3d shock control bumps on transonic buffet. In Wolfgang E. Nagel, Dietmar H. Kröner, and Michael M. Resch, editors, *High Performance Computing in Science and Engineering '14*, pages 447–461. Springer International Publishing, 2015.

[27] Steffen Bogdanski, Klemens Nübler, Thorsten Lutz, and Ewald Krämer. Numerical investigation of the influence of shock control bumps on the buffet characteristics of a transonic airfoil. In Andreas Dillmann, Gerd Heller, Ewald Krämer, Hans-Peter Kreplin, Wolfgang Nitsche, and Ulrich Rist, editors, *New Results in Numerical and Experimental Fluid Mechanics IX: Contributions to the 18th STAB/DGLR Symposium, Stuttgart, Germany, 2012*, pages 23–32. Springer International Publishing, 2014.

[28] V. Bonnifet, G.A. Gerolymos, and I. Vallet. Transonic Buffet Prediction using Partially Averaged Navier-Stokes. In *23rd AIAA Computational Fluid Dynamics Conference*, Denver, Colorado, USA, 2017.

[29] J.P. Boris, F.F. Grinstein, E.S. Oran, and R.L. Kolbe. New insights into large eddy simulations. *Fluid Dynamics Research*, 10:199–228, 1992.

[30] R. Bourguet, M. Braza, G. Harran, and R. El Akoury. Anisotropic Organised Eddy Simulation for the prediction of the non-equilibrium turbulent flow around bodies. *Journal of Fluid and Structures*, 24:1240–1251, 2008. http://doi.org/10.1016/j.jfluidstructs.2008.07.004.

[31] V. Brion, J. Dandois, J.-C. Abart, and P. Paillart. An experimental and numerical study of an oscillating transonic shock wave in a duct. In *Experimental Analysis of the Shock Dynamics on a Transonic Laminar Airfoil*, 2017.

[32] V. Brion, J. Dandois, R. Mayer, P. Reijasse, T. Lutz, and L. Jacquin. Laminar buffet and flow control. *Proceedings of the Institution of Mechanical Engineers, Part G: Journal of Aerospace Engineering*, 234:124–139, 2020. https://doi.org/10.1177/0954410018824516.

[33] P.J.K. Bruce, D.M.F. Burton, N.A. Titchener, and H. Babinsky. Corner effect and separation in transonic channel flows. *Journal of Fluid Mechanics*, 679:247–262, 2011. http://doi.org/10.1017/jfm.2011.135.

[34] P.J.K. Bruce and S.P. Collins. Review of research into shock control bumps . *Shock Waves*, 25:451–471, 2015. http://doi.org/10.1007/s00193-014-0533-4.

[35] V. Brunet and S. Deck. Zonal-Detached Eddy Simulation of Transonic Buffet on a Civil Aircraft Type Configuration. In *38th Fluid Dynamics Conference and Exhibit*, Seattle, WA, USA, 2008.

[36] M. A. Bruytan, A. V. Volkov, and A. V. Potapchik. An Experimental Study of a Passive Method of Attenuating a Transonic Buffet Phenomenon. *Technical Physics Letters*, 45:1082–1084, 2019.

[37] B. Cantwell and D. Coles. An experimental study of entrainment and transport in the turbulent near wake of a circular cylinder. *Journal of Fluid Mechanics*, 136:321–374, 1983. https://doi.org/10.1017/S0022112083002189.

[38] D. Caruana, A. Mignosi, M. Corrège, A. Le Pourhiet, and A.M. Rodde. Buffet and buffeting control in transonic flow. *Aerospace Science and Technology*, 9:605–616, 2005. http://doi.org/10.1016/j.ast.2004.12.005.

[39] D. Caruana, A. Mignosi, C. Robitaillié, and M. Corrège. Separated Flow and Buffeting Control. *Flow, Turbulence and Combustion*, 71:221–245, 2003. http://doi.org/10.2514/1.40932.

[40] B. Chaouat. The State of the Art of Hybrid RANS/LES Modeling for the Simulation of Turbulent Flows. *Flow, Turbulence and Combustion*, 99:279–327, 2017. http://doi.org/10.1007/s10494-017-9828-8.

[41] I. Chung, D. Lee, and T. Reu. Prediction of transonic buffet onset for an airfoil with shock induced separation bubble using steady Navier-Stokes solver. In *20th AIAA Applied Aerodynamic Conference*, St. Louis, MO, USA, 2002.

[42] I. Chung, D. Lee, T. Reu, and D. Ko. Prediction of Transonic Buffet Onset for Airfoils with Separation Bubble Using Steady Approaches. *Journal of Aircraft*, 40:795–797, 2003. http://doi.org/10.2514/2.3160.

[43] T. Clemens and V. Narayanaswamy. Low-Frequency Unsteadiness of Shock Wave/Turbulent Boundary Layer Interactions. *Annual Review of Fluid Mechanics*, 46:469–492, 2014. http://doi.org/10.1146/annurev-fluid-010313-141346.

[44] J.D. Crouch, A. Gargaruk, and D. Magidov. Predicting the onset of flow unsteadiness based on global instability. *Journal of Computational Physics*, 224:924–940, 2007. http://doi.org/10.1016/j.jcp.2006.10.035.

[45] J.D. Crouch, A. Gargaruk, D. Magidov, and A. Travin. Origin of transonic buffet on aerofoils. *Journal of Fluid Mechanics*, 628:357–369, 2009. http://doi.org/10.1017/S0022112009006673.

[46] J.D. Crouch, A. Gargaruk, and M. Strelets. Global instability in the onset of transonic-wing buffet. *Journal of Fluid Mechanics*, 881:3–22, 2019. http://doi.org/10.1017/jfm.2019.748.

[47] A. D'Aguanno, F.F.J. Schrijer, and B.W. van Oudheusden. Experimental investigation of the transonic buffet cycle on a supercritical airfoil. *Experiments in Fluids*, 621:214, 2021. http://doi.org/10.1007/s00348-021-03319-z.

[48] A. D'Aguanno, F.F.J. Schrijer, and B.W. van Oudheusden. Investigation of 3D Shock Control Bumps for Transonic Buffet Alleviation. In *AIAA Aviation 2021 Forum*, Virtual Event, 2021.

[49] A. D'Aguanno, F.F.J. Schrijer, and B.W. van Oudheusden. Spanwise organization of upstream traveling waves in transonic buffet. *Physics of Fluids*, 33:106105, 2021. https://doi.org/10.1063/5.0062729.

[50] A. D'Aguanno, F.F.J. Schrijer, and B.W. van Oudheusden. Finite-Wing and Sweep Effects on Transonic Buffet Behavior. *AIAA Journal*, 60:6715–6725, 2022. http://doi.org/10.2514/1.J061974.

[51] A. D'Aguanno, F.F.J. Schrijer, and B.W. van Oudheusden. Experimental Characterization of Upper Trailing Edge Flaps for Transonic Buffet Control. *Flow, Turbulence and Combustion*, 110:325–320, 2023. http://doi.org/10.1007/s10494-022-00381-3.

[52] A. D'Aguanno, F.F.J. Schrijer, and B.W. van Oudheusden. Investigation of Three-Dimensional Shock Control Bumps for Transonic Buffet Alleviation. *AIAA Journal*, 2023. http://doi.org/10.2514/1.J062633.

[53] J. Dandois. Experimental study of transonic buffet phenomenon on a 3D swept wing. *Physics of Fluids*, 28:1–23, 2016. http://doi.org/10.1063/1.4937426.

[54] J. Dandois, V. Brunet, P. Molton, and J.-C. Abart. Buffet Control by Means of Mechanical and Fluidic Vortex Generators. In *5th Flow Control Conference*, Chicago, IL, USA, 2010.

[55] J. Dandois, A. Lepage, J.-B. Dor, P. Molton, F. Ternoy, A. Geeraert, V. Brunet, and É. Coustols. Experimental study of transonic buffet phenomenon on a 3D swept wing. *Comptes Rendus Mécanique*, 342:425–436, 2014. http://doi.org/10.1016/j.crme.2014.01.015.

[56] J. Dandois, I. Mary, and V. Brion. Large-eddy simulation of laminar transonic buffet. *Journal of Fluid Mechanics*, 850:156–178, 2018. http://doi.org/10.1063/1.4937426.

[57] H. Dang, J. Zhao, Z. Yand, and H. Dang. Postponing the Onset and Alleviating the Load of Transonic Buffet by Using Steady and Periodic Tangential Slot Blowing. *Applied Sciences*, 9:4132, 2019. http://doi.org/10.3390/app9194132.

[58] L. Davidson and C. Friess. A new formulation of f_k for the PANS model. *Journal of Turbulence*, 20:5:322–336, 2019. http://doi.org/10.1080/14685248.2019.1641605.

[59] S. Deck. Numerical Simulation of Transonic Buffet over a Supercritical Airfoil. *AIAA Journal*, 43:1556–1566, 2005. http://doi.org/10.2514/1.9885.

[60] E. Degregori and J. W. Kim. Mitigation of transonic shock buffet on a supercritical airfoil through wavy leading edges. *Physics of Fluids*, 33:026104, 2021. http://doi.org/10.1063/5.0036821.

[61] J. Délery and R. S. Bur. The Physics of Shock Wave / Boundary Layer Interaction Control: Last LessonsLearned. In *European Congress of Computational Methods in Applied Science and Engineering, ECOMAS 2000*, Barcelona, Spain, 2000.

[62] J. Délery and J.P. Dussauge. Some physical aspects of shock wave/boundary layer interaction. *Shock Waves*, 19:453–468, 2009. http://doi.org/10.1007/s00193-009-0220-z.

[63] J. M. Delery. Shock wave/turbulent boundary layer interaction and its control. *Progress in Aerospace Sciences*, 22:209–280, 1985. http://doi.org/10.1016/0376-0421(85)90001-6.

[64] P. Doerffer and O. Szulc. Shock Wave Strength Reduction by Passive Control Using Perforated Plates. *Journal of Thermal Science*, 16:97–104, 2007. http://doi.org/10.1007/s11630-007-0097-z.

[65] D. S. Dolling. Fifty Years of Shock-Wave/Boundary-Layer Interaction Research: What Next? *AIAA Journal*, 39:1517–1531, 2001. http://doi.org/1.02514/2.1476.

[66] J.P. Dussauge, P. Dupont, and J.F. Debiève. Unsteadiness in shock wave boundary layer interactions with separation. *Aerospace Science and Technology*, 10:85–91, 2006. http://doi.org/10.1016/j.ast.2005.09.006.

[67] T. Dzanic, S.S. Girimaji, and F.D. Witherden. Partially-averaged Navier–Stokes simulations of turbulence within a high-order flux reconstruction framework. *Journal of Computational Physics*, 456:110992, 2022. http://doi.org/10.1016/j.jcp.2022.110992.

[68] J. P. Eastwood and J. P. Jarrett. Toward Designing with Three-Dimensional Bumps for Lift/Drag Improvement and Buffet Alleviation. *AIAA Journal*, 50:2882–2898, 2012. http://doi.org/10.2514/1.J051740.

[69] J.R. Edwards and S. Chandra. Comparison of Eddy Viscosity-Transport Turbulence Models for Three-Dimensional, Shock-Separated Flowfields. *AIAA Journal*, 34:756–763, 1996. http://doi.org/10.2514/3.13137.

[70] M. Ehrle, A. Waldmann, T. Lutz, and E. Kramer. Simulation of transonic buffet with an automated zonal DES approach. *CEAS Aeronautical Journal*, 11:1025–1036, 2020. http://doi.org/10.1007/s13272-020-00466-7.

[71] K. Ekici and K.C. Hall. Nonlinear Analysis of Unsteady Flows in Multistage Turbomachines Using Harmonic Balance. *AIAA Journal*, 45:1047–1061, 2007. http://doi.org/10.2514/1.22888.

[72] A. Elmiligui, K.S. Abdol-Hamid, S.J. Massey, and S. Paul Pao. Numerical Study of Flow Past a Circular Cylinder Using RANS, Hybrid RANS/LES and PANS Formulations. In *22nd Applied Aerodynamics Conference and Exhibit*, Providence, Rhode Island, 2004.

[73] A. Elmiligui, K.S. Abdol-Hamid, S.J. Massey, and S. Paul Pao. Numerical Study of Flow Past Circular Cylinder Using Hybrid Turbulence Formulations. *Journal of Aircraft*, 47:434–440, 2010. https://doi.org/10.2514/1.18765.

[74] A. Feldhusen-Hoffmann, C. Lagermann ans S. Loosen, P. Meysonnat, M. Klaas, and W. Schroder. Analysis of transonic buffet using dynamic mode decomposition. *Experiments in Fluids*, 62:66, 2021. http://doi.org/10.1007/s00348-020-03111-5.

[75] A. Feldhusen-Hoffmann, V. Statnikov, M. Klaas, and W. Schroder. Investigation of shock–acoustic-wave interaction in transonic flow. *Experiments in Fluids*, 59:1–20, 2018. http://doi.org/10.1007/s00348-017-2466-z.

[76] A. A. Firsov, I. Moralve, Y. Isaenkov, S.B. Leonov, and V. Soudakov. Suppression of transonic buffet phenomenon by spark plasma actuator. In *2018 AIAA Aerospace Sciences Meeting*, Kissimmee, FL, USA, 2018. http://doi.org/10.2514/6.2018-2050.

[77] H. Foroutan and S. Yavuzkurt. A partially-averaged Navier–Stokes model for the simulation of turbulent swirling flow with vortex breakdown. *International Journal of Heat and Fluid Flow*, 50:402–416, 2014. http://doi.org/10.1016/j.ijheatfluidflow.2014.10.005.

[78] A. Frendi, A. Tosh, and S.S. Girimaji. Flow Past a Backward-Facing Step: Comparison of PANS, DES and URANS Results with Experiments. *International Journal for Computational Methods in Engineering Science and Mechanics*, 8:23–38, 2007. http://doi.org/10.1080/15502280601006207.

[79] C. Friess and L. Davidson. A formulation of PANS capable of mimicking IDDES. *International Journal of Heat and Fluid Flow*, 86:1–25, 2020. http://doi.org/10.1016/j.ijheatfluidflow.2020.108666.

[80] Y. Fukushima and S. Kawai. Wall-Modeled Large-Eddy Simulation of Transonic Airfoil Buffet at High Reynolds Number. *AIAA Journal*, 56:2372–2388, 2018.

[81] C. Fureby and F.F. Grinstein. Monotonically Integrated Large Eddy Simulation of Free Shear Flows. *AIAA Journal*, 37:544–556, 1999. http://doi.org/10.2514/2.772.

[82] A. M. Gaifullin and K. G. Khairullin. Buffet control by a moving surface. *Journal of Applied Mechanics and Technical Physics*, 61:986–993, 2020. http://doi.org/10.1134/S0021894420060127.

[83] D. V. Gaitonde. Progress in shock wave/boundary layer interactions. *Progress in Aerospace Sciences*, 72:80–99, 2015. http://doi.org/10.1016/j.paerosci.2014.09.002.

[84] C. Gao, W. Zhang, J. Kou, Y. Liu, and Z. Ye. Active control of transonic buffet flow. *Journal of Fluid Mechanics*, 824:312–351, 2017. http://doi.org/10.1017/jfm.2017.344.

[85] C. Gao, W. Zhang, and X. Li. Passive feedback control of transonic buffet flow. *Physics of Fluids*, 31:046103, 2019. http://doi.org/10.1063/1.5087014.

[86] C. Gao, W. Zhang, X. Li, Y. Liu, J. Quan, Z. Ye, and Y. Jiang. Mechanism of frequency lock-in in transonic buffeting flow. *Journal of Fluid Mechanics*, 818:528–561, 2017. http://doi.org/10.1017/jfm.2017.120.

[87] C. Gao, W. Zhang, and Z. Ye. Numerical study on closed-loop control of transonic buffet suppression by trailing edge flap. *Computers and Fluids*, 132:32–45, 2016. http://doi.org/10.2514/2.2071.

[88] C. Gao, W. Zhang, and Z. Ye. Reduction of transonic buffet onset for a wing with activated elasticity. *Aerospace Science and Technology*, 77:670–676, 2018. http://doi.org/10.1016/j.ast.2018.03.047.

[89] A. Garbaruk, M. Shur, M. Strelets, and P. R. Spalart. Numerical Study of Wind-Tunnel Walls Effects on Transonic Airfoil Flow. *AIAA Journal*, 44:1046–1054, 2003. http://doi.org/10.1016/j.compfluid.2016.03.03.

[90] D.J. Garmann, M.R. Visbal, and P.D. Orkwis. Comparative study of implicit and subgrid-scale model large-eddy simulation techniques for low-Reynolds number airfoil applications. *International Journal for Numerical Methods in Fluids*, 71:1546–1565, 2013. http://doi.org/10.1002/fld.3725.

[91] E. Garnier and S. Deck. Large-eddy simulation of transonic buffet over a supercritical airfoil. *in: Direct and Large-Eddy Simulation VII, ERCOFTAC Series*, 13:549–554, 2010.

[92] J.A. Geoghegan, N.F. Giannelis, and G.A. Vio. A numerical study on transonic shock buffet alleviation through oscillating shock control bumps. In *2018 AIAA SciTech Forum*, Kissimmee, FL, USA, 2018.

[93] J.A. Geoghegan, N.F. Giannelis, and G.A. Vio. A Numerical Investigation of the Geometric Parametrisation of Shock Control Bumps for Transonic Shock Oscillation Control. *Fluids*, 12:1–29, 2020. http://doi.org/10.3390/fluids12083421.

[94] J.A. Geoghegan, N.F. Giannelis, and G.A. Vio. Parametric study of active shock control bumps for transonic shock buffet alleviation. In *AIAA SciTech Forum 2020*, Orlando, FL, USA, 2020.

[95] G.A. Gerolymos, C. Lo, I. Vallet, and B.A. Younis. Term-by-Term Analysis of Near-Wall Second-Moment Closures. *AIAA Journal*, 50:2848–2864, 2012. http://doi.org/10.2514/1.J051654.

[96] G.A. Gerolymos and I. Vallet. Influence of temporal integration and spatial discretization on hybrid rsm–vles computationss and iles. In *18th AIAA Computational Fluid Dynamics Conference*, Miami, FL, USA, 2007.

[97] N. F. Giannelis, A. J. Murray, and G. A. Vio. Influence of control surface deflections on a thin aerofoil at transonic buffet conditions . In *AIAA Scitech 2019 Forum*, San Diego, CA, USA, 2019.

[98] N.F. Giannelis, O. Levinski, and G.A. Vio. Influence of Mach number and angle of attack on the two-dimensional transonic buffet phenomenon. *Aerospace Science and Technology*, 78:89–101, 2018. http://doi.org/10.1016/j.ast.2018.03.045.

[99] N.F. Giannelis, O. Levinski, and G.A. Vio. Origins of atypical shock buffet motions on a supercritical aerofoil. *Aerospace Science and Technology*, 107:106304, 2020. http://doi.org/10.1016/j.ast.2020.106304.

[100] N.F. Giannelis, G.A. Vio, and O. Levinski. A review of recent developments in the understanding of transonic shock buffet. *Progress in Aerospace Sciences*, 92:39–84, 2017. http://doi.org/10.1016/j.paerosci.2017.05.004.

[101] S.S. Girimaji. Partially-averaged navier-stokes model for turbulence: A reynolds-averaged navier-stokes to direct numerical simulation bridging method. *Journal of Applied Mechanics, Transactions ASME*, 73:413–421, 2006. http://doi.org/10.11151.2151207.

[102] S.S. Girimaji. Partially-averaged Navier-Stokes model for turbulence: Fixed Point Analysis and Comparison With Unsteady Partially Averaged Navier Stokes. *Journal of Applied Mechanics, Transactions ASME*, 73:422–429, 2006. http://doi.org/10.1115/1.2173677.

[103] S.S. Girimaji and K.S. Abdol-Hamid. Partially-averaged Navier Stokes Model for Turbulence: Implementation and Validation. In *AIAA Aerospace Sciences Meeting and Exhibit*, Reno, NE, USA, 2005.

[104] S.S. Girimaji and S. Wallin. Closure modeling in bridging regions of variable-resolution (VR) turbulence computations. *Journal of Turbulence*, 14:72–98, 2013. http://doi.org/10.1080/14685248.2012.754893.

[105] E. Goncalves and R. Houdeville. Turbulence model and numerical scheme assessment for buffet computations. *International Journal for Numerical Methods in FLuids*, 46:1127–1152, 2004. http://doi.org/10.1002/d.777.

[106] A.K. Gopinath and A. Jameson. Application of the Time Spectral Method to Periodic Unsteady Vortex Shedding. In *44th AIAA Aerospace Sciences Meeting and Exhibit*, Reno, NE, USA, 2006.

[107] F. Grossi, M. Braza, and Y. Hoarau. Delayed Detached-Eddy Simulation of the Transonic Flow around a Supercritical Airfoil in the Buffet Regime. *Notes on Numerical Fluid Mechanics and Multidisciplinary Design*, 117:369–378, 2012. http://doi.org/10.1007/978-3-642-31818-4-32.

[108] F. Grossi, M. Braza, and Y. Hoarau. Prediction of Transonic Buffet by Delayed Detached-Eddy Simulation. *AIAA Journal*, 52:2300–2312, 2014. http://doi.org/10.2514/1.J052873.

[109] K.C. Hall, J.P. Thomas, and W.S. Clark. Computation of Unsteady Nonlinear Flows in Cascades Using a Harmonic Balance Technique. *AIAA Journal*, 40:879–886, 2002. http://doi.org/10.2514/2.1754.

[110] X. Han, S. Krajnovic, and B. Basara. Study of active flow control for a simplified vehicle model using the PANS method. *International Journal of Heat and Fluid Flow*, 42:139–150, 2013. http://doi.org/110.1016/j.ijheatfluidflow.2013.02.001.

[111] A. Hartmann, A. Feldhusen, and W. Schröder. On the interaction of shock waves and sound waves in transonic buffet. *Physics of Fluids*, 25:026101, 2013. https://doi.org/10.1063/1.4791603.

[112] A. Hartmann, M. Klaas, and W. Schröder. Time-resolved stereo PIV measurements of shock–boundary layer interaction on a supercritical airfoil. *Experiments in Fluids*, 52:591–604, 2011. http://doi.org/10.1007/s00348-011-1074-6.

[113] A. Hartmann, M. Klaas, and W. Schröder. Coupled Airfoil Heave/Pitch Oscillations at Buffet Flow. *AIAA Journal*, 51:1542–1552, 2013. https://doi.org/10.2514/1.J051512.

[114] W. He and S. Timme. Triglobal Shock Buffet Instability Study on Infinite Wings. In *AIAA SciTech Forum 2020*, Orlando, FL, USA, 2020.

[115] B. Huang and G.-Y. Wang. Partially Averaged Navier-Stokes method for time-dependent turbulent cavitating flows. *Journal of Hydrodynamics*, 23:26–33, 2011. http://doi.org/10.1016/S1001-6058(10)60084-4.

[116] H. Huang and K. Ekici. Stabilization of High-Dimensional Harmonic Balance Solvers Using Time Spectral Viscosity. *AIAA Journal*, 52:1784–1794, 2014. http://doi.org/10.2514/1.J052698.

[117] J.B. Huang, Z.X. Xiao, J. Liu, and S. Fu. Simulation of shock wave buffet and its suppression on an OAT15A supercritical airfoil by IDDES. *Science China: Physics, Mechanics and Astronomy*, 55:260–271, 2012. http://doi.org/10.1007/s11433-011-4601-9.

[118] W. Huang, H. Wu, Y. Yang, L. Yan, and S. Li. Recent advances in the shock wave/boundary layer interaction and its control in internal and external flows. *Acta Astronautica*, 174:103–122, 2020. http://doi.org/10.1016/j.actaastro.2020.05.001.

[119] S. Illi, T. Lutz, and E. Kramer. On the capability of unsteady RANS to predict transonic buffet. In *Proceeding of the Third Symposium Simulation of Wing and Nacelle Stall*, Braunschweig, Germany, 2012.

[120] M. Iovnovich and D. E. Raveh. Reynolds-Averaged Navier–Stokes Study of the Shock-Buffet Instability Mechanism. *AIAA Journal*, 50:880–890, 2012. http://doi.org/10.2514/1.J051329.

[121] M. Iovnovich and D. E. Raveh. TTransonic unsteady aerodynamics in the vicinity of shock-buffet instability. *Journal of Fluid and Structures*, 29:131–142, 2012. http://doi.org/10.1016/j.jfluidstructs.2011.12.015.

[122] M. Iovnovich and D. E. Raveh. Numerical study of shock buffet on three-dimensional wings. *AIAA Journal*, 53:449–463, 2015. http://doi.org/10.2514/1.J053201.

[123] T. Ishida, A. Hashimoto, Y. Ohimichi, T. Aoyama, T. Yamamoto, and K. Takekawa. Transonic buffet simulation over nasa-crm by unsteady-fastar codelf wing-body configuration. In *55th AIAA Aerospace Sciences Meeting*, Grapevine, TX, USA, 2017.

[124] T. Ishida, K. Ishiko, A. Hashimoto, T. Aoyama, and K. Takekawa. Transonic buffet simulation over supercritical airfoil by unsteady-fastar code. In *54th AIAA Aerospace Sciences Meeting*, San Diego, CA, USA, 2016.

[125] L. Jacquin, P. Molton, S. Deck, B. Maury, and D. Soulevant. An experimental study of shock oscillation over a transonic supercritical profile. In *AIAA Aerospace Sciences Meeting and Exhibit*, Toronto, Ontario Canada, 2005.

[126] L. Jacquin, P. Molton, S. Deck, B. Maury, and D. Soulevant. Experimental study of shock oscillation over a transonic supercritical profile. *AIAA Journal*, 47:1985–1994, 2009. http://doi.org/10.2514/1.30190.

[127] A. Jameson. Time-Dependent Calculations Using Multigrid, with Applications to Unsteady Flows past Airfoils and Wings. In *AIAA 10th Computational Fluid Dynamics Conference*, 1991.

[128] T. Jana and M. Kaushik. Survey of control techniques to alleviate repercussions of shock-wave and boundary-layer interactions. *Advances in Aerodynamics*, 4:27, 2022. http://doi.org/10.1186/s42774-022-00119-9.

[129] E. Jeong and S.S. Girimaji. Partially averaged Navier-Stokes (PANS) method for turbulence simulations-flow past a square cylinder. *Journal of Fluids Engineering, Transactions of the ASME*, 132:1–11, 2010. http://doi.org/10.1115/1.4003153.

[130] R. Jiang, Y. Tian, P. Liu, S. Gao, and Q. Qu. Transonic Buffet Control Research on Supercritical Wing Using Rear-Mounted Bump. *Journal of Aerospace Engineering*, 31:04018053, 2018. http://doi.org/10.1061/(ASCE)AS.1943-5525.0000875.

[131] W.P. Jones and B.E. Laundert. Experimental Study of Shock Oscillation over a Transonic Supercritical Profile. *International Journal of Heat and Mass Transfer*, 15:301–314, 1972. http://doi.org/10.1016/0017-9310(72)90076-2.

[132] L.L. Levy Jr. Experimental and Computational Steady and Unsteady Transonic Flows about a Thick Airfoil. *AIAA Journal*, 16:564–572, 1978. https://doi.org/10.2514/3.60935.

[133] G. K. W. Kenway and J. R. R. A. Martins. Buffet-Onset Constraint Formulation for Aerodynamic Shape Optimization. *AIAA Journal*, 55:1930–1947, 2017. http://doi.org/10.2514/1.J055172.

[134] M. Klapwijk, T. Lloyd, and G. Vaz. On the accuracy of partially averaged Navier–Stokes resolution estimates. *International Journal of Heat and Fluid Flow*, 80:1–10, 2019. http://doi.org/10.1016/j.ijheatfluidflow.2019.108484.

[135] M. Klapwijk, T. Lloyd, G. Vaz, and O. Van Terwisga. PANS Simulations: Low Versus High Reynolds Number Approach. In *VIII International Conference on Computational Methods in Marine Engineering*, Goteborg, Sweden, 2019.

[136] M. Klapwijk, T. Lloyd, G. Vaz, and T. van Terwisga. Evaluation of scale-resolving simulations for a turbulent channel flow. *Computers and Fluids*, 209:104636, 2020. http://doi.org/10.1016/j.compfluid.2020.104636.

[137] S. Koike, K. Nakakita, T. Nakajima, S. Koga, M. Sato, H. Kanda, K. Kusunose, M. Murayama, Y. Ito, and K. Yamamoto. Experimental investigation of vortex generator effect on two- and three-dimensional NASA Common Research Models. In *53rd AIAA Aerospace Sciences Meeting*, Kissimmee, FL, USA, 2016.

[138] S. Koike, M. Ueno, K. Nakakita, and A. Hashimoto. Unsteady pressure measurement of transonic buffet on NASA Common Research Model. In *34th AIAA Applied Aerodynamics Conference*, Washington, D.C., USA, 2016.

[139] Y. Kojima and A. Hashimoto. Embedded Large Eddy simulation of transonic flow over an OAT15A airfoil. In *AIAA SciTech Forum 2022*, San Diego, CA, USA and Online, 2022.

[140] Y. Kojima and A. Hashimoto. An Application of Embedded Large Eddy Simulation for Transonic Buffet Prediction. In *AIAA SciTech Forum 2023*, National Harbor, MD, USA and Online, 2023.

[141] I.W. Kokkinakis and D. Drikakis. Near-Wall Behaviour of Implicit Large Eddy Simulations. In *VII European Congress on Computational Methods in Applied Sciences and Engineering*, Crete Island, Greece, 2016.

[142] K. Kokmanian, S. Scharnowski, C. Schafer, A. Accorinti, T. Baur, and C.J. Kahler. Investigating the flow field dynamics of transonic shock buffet using particle image velocimetry. *Experiments in Fluids*, 63:149, 2022. https://doi.org/10.1007/s00348-022-03499-2.

[143] T. Korthauer, A. Accorinti, S. Scharnowski, T. Baur, and C.J. Kahler. Effect of Mach Number and Pitching Eigenfrequency on Transonic Buffet Onset. *AIAA Journal*, 61:112–124, 2023. https://doi.org/10.2514/1.J061915.

[144] T. Kouchi, S. Yamaguchi, S. Koiked, T. Nakajima, M. Sato, H. Kanda, and S. Yanase. Wavelet analysis of transonic buffet on a two-dimensional airfoil with vortex generators. *Experiments in Fluids*, 57:166, 2016. http://doi.org/10.1007/s00348-016-2261-2.

[145] T. Kouchi, S. Yamaguchi, S. Yanase, S. Koike, T. Nakajima, M. Sato, and H. Kanda. Wavelet Analysis of Unsteady Shock-wave Motion on Two-dimensional Airfoil with Vortex Generators. In *54th AIAA Aerospace Sciences Meeting*, San Diego, CA, USA, 2016.

[146] S. Krajnovic, R. Larusson, and B. Basara. Superiority of PANS compared to LES in predicting a rudimentary landing gear flow with affordable meshes. *International Journal of Heat and Fluid Flow*, 37:109–122, 2012. http://doi.org/10.1016/j.ijheatfluidflow.2012.04.013.

[147] S. Krajnovic, G. Minelli, and B. Basara. Partially-averaged Navier–Stokes simulations of two bluff body flowsn. *Applied Mathematics and Computation*, 2015. http://doi.org/10.1016/j.amc.2015.03.136.

[148] S. Krajnovic, G. Minelli, and B. Basara. Partially-averaged navier-stokes simulations of flows around generic vehicle at yaw. In *SAE 2016 World Congress and Exhibition*, Detroit, MI, USA, 2016.

[149] S.C. Künnecke, S. Vasista, J. Riemenschneider, and R. Keimer. Review of Adaptive Shock Control Systems. *Applied Sciences*, 11:817, 2021. https://doi.org/10.3390/app11020817.

[150] Y. Kuya, K. Boda, and K. Sawada. Numerical Study of Transonic Shock Buffet Control over a Supercritical Airfoil. *Journal of Aircraft*, 57:1242–1251, 2020. http://doi.org/10.2514/1.C035902.

[151] S. Lakshimpathy and S.S. Girimaji. Partially Averaged Navier–Stokes (PANS) Method for Turbulence Simulations: Flow Past a Circular Cylinder. *Journal of Fluids Engineering*, 132:121202, 2010. http://doi.org/10.1115/1.4003154.

[152] S. Lakshimpathy, S.S. Girimaji, and K.S. Partially-averaged Navier Stokes method for turbulent flows: $k-\omega$ model implementation. In *AIAA Aerospace Sciences Meeting and Exhibit*, Reno, NE, USA, 2006.

[153] S.G. Lawson, D. Greenwell, and M. Quinn. Characterisation of buffet on a civil aircraft wing. In *54th AIAA Aerospace Sciences Meeting*, San Diego, CA, USA, 2016.

[154] B.H.K. Lee. Investigation of flow separation on a supercritical airfoil. *Journal of Aircraft*, 26:1032–1037, 1989. http://doi.org/10.2514/3.25144.

[155] B.H.K. Lee. Transonic buffet of a supercritical airfoil with trailing-edge flap. *Journal of Aircraft*, 26:459–464, 1989. http://doi.org/10.2514/3.45785.

[156] B.H.K. Lee. Effects of trailing-edge flap on buffet characteristics of a supercritical airfoil. *Journal of Aircraft*, 29:93–100, 1992. http://doi.org/10.2514/3.46130.

[157] B.H.K. Lee. Self-sustained shock oscillations on airfoils at transonic speeds. *Progress in Aerospace Sciences*, 37:147–196, 2001. http://doi.org/10.1016/S0376-0421(01)00003-3.

[158] B.H.K. Lee and L.H. Ohman. Unsteady pressure and forces during transonic buffeting on a supercritical airfoil. *Journal of Aircraft*, 21:439–441, 1986. http://doi.org/10.2514/3.45876.

[159] B.H.K. Lee and F. C. Tang. Oscillatory shock motion caused by transonic shock boundary-layer interaction. *AIAA Journal*, 28:942–944, 1990. http://doi.org/10.2514/3.25144.

[160] P.M. Ligrani, E.S. McNabb, H. Collopy, M. Anderson, and S.M. Marko. Recent investigations of shock wave effects and interactions. *Advances in Aerodynamics*, 2:4, 2020. http://doi.org/10.1186/s42774-020-0028-1.

[161] B. Liu, W. Yang, and Z. Liu. A PANS Method Based on Rotation-Corrected Energy Spectrum for Efficient Simulation of Rotating Flow. *Frontiers in Energy Research*, 10:894258, 2022. http://doi.org/10.3389/fenrg.2022.894258.

[162] J. Liu and Z. Yang. Numerical study on transonic shock oscillation suppression and buffet load alleviation for a supercritical airfoil using a microtab. *Engineering Applications of Computational Fluid Mechanics*, 10:529–544, 2016. http://doi.org/10.1080/19942060.2016.1210029.

[163] D. Luo. RNumerical simulation of turbulent flow over a backward facing step using partially averaged Navier-Stokes method. *Journal of Mechanical Science and Technology*, 33:2137,2148, 2019. http://doi.org/10.1007/s12206-019-0416-9.

[164] D. Luo, C. Yan, and X. Wang. Computational study of supersonic turbulent-separated flows using partially averaged Navier-stokes method. *Acta Astronautica*, 107:234–246, 2015. http://doi.org/10.1016/j.actaastro.2014.11.029.

[165] J.-M. Ma, S.-H. Peng, L. Davidson, and F.J. Wang. A low Reynolds number variant of partially-averaged Navier–Stokes model for turbulence. *International Journal of Heat anf Fluid Flow*, 32:652–669, 2011. http://doi.org/10.1016/j.ijheatfluidflow.2011.02.001.

[166] J.-M. Ma, F.-J. Wang, X. Yu, and Z.-Q. Liu. A Partially-Averaged Navier-Stokes model for hill and curved duct flow. *Journal of Hydrodynamics*, 23:466–475, 2011. http://doi.org/10.1016/S1001-6058(10)60137-0.

[167] D. G. Mabey. Beyond the buffet boundary. *The Aeronautical Journal*, 77:201 – 215, 1973. http://doi.org/10.1017/S0001924000040811.

[168] L. G. Margolin and W. J. Rider. The design and construction of implicit LES model. *International Journal fon Numerical Methods in Fluids*, 47:1173–1179, 2005. http://doi.org/10.1002/fld.862.

[169] L. Masini, A. Peace, and S. Timme. Influence of Vane Vortex Generators on Transonic Wing Buffet: Further Analysis of the BUCOLIC Experimental Dataset. In *52nd 3AF International Conference on Applied Aerodynamics*, Lyon, France, 2017.

[170] L. Masini, A. Peace, and S. Timme. Scale-Resolving Simulation of Shock Buffet Onset Physics on a Civil Aircraft Wing. In *Royal Aeronautical Society 2018 Applied Aerodynamics Conference*, Bristol, United Kingdom, 2018.

[171] L. Masini, A. Peace, and S. Timme. Reynolds Number Effects on Wing Shock Buffet Unsteadiness. In *AIAA Aviation 2019 Forum*, Dallas, Texas, USA, 2019.

[172] L. Masini, S. Timme, and A. J. Pace. Scale-Resolving Simulations of a Civil Aircraft Wing Transonic Shock-Buffet Experiment. *AIAA Journal*, 58:4322–4338, 2020. http://doi.org/10.2514/1.J059219.

[173] L. Masini, S. Timme, and A.J. Peace. Analysis of a civil aircraft wing transonic shock buffet experiment. *Journal of Fluid Mechanics*, 884:1–42, 2019. http://doi.org/10.1017/jfm.2019.906.

[174] J. Matheis and S. HIckel. On the transition between regular and irregular shock patterns of shock-wave/boundary-layer interactions. *Journal of Fluid Mechanics*, 776:200–234, 2015. http://doi.org/10.1017/jfm.2015.319.

[175] R. Mayer, T. Lutz, and E. Kramer. A Numerical Study on the Ability of Shock Control Bumps for Buffet Alleviation. In *AIAA SciTech 2017 Forum*, Grapevine, Texas, USA, 2017.

[176] R. Mayer, T. Lutz, and E. Kramer. Numerical Study on the Ability of Shock Control Bumps for Buffet Control . *AIAA Journal*, 56:1978–1987, 2018. http://doi.org/10.2514/1.J056737.

[177] R. Mayer, T. Lutz, and E. Kramer. Control of Transonic Buffet by Shock Control Bumps on Wing-Body Configuration. *AIAA Journal*, 56:556–568, 2019. http://doi.org/10.2514/1.C034969.

[178] J.B. McDevitt and A.F.Okuno. Static and dynamic pressure measurements on a NACA 0012 airfoil in the Ames high Reynolds number facility. Technical report, National Aeronautics and Space Administration, 1985. NASA-TP-2485.

[179] J.B. McDevitt, L.L. Levy Jr., and G.S. Deiwert. Transonic Flow about a Thick Circular-Arc Airfoil. *AIAA Journal*, 14:606–613, 1975. Rhttps://doi.org/10.2514/3.61402.

[180] M. McMullen, A. Jameson, and J. Alonso. Demonstration of Nonlinear Frequency Domain Methods. *AIAA Journal*, 44:1428–1435, 2006. http://doi.org/10.2514/1.151275.

[181] A. Memmolo, M. Bernardini, and S. Pirozzoli. Scrutiny of buffet mechanisms in transonic flow. *International Journal of Numerical Methods for Heat & Fluid Flow*, 28:1031–1046, 2018. http://doi.org/10.1108/HFF-08-2016-0300.

[182] F.R. Menter. Two-equation eddy-viscosity turbulence models for engineering applications. *AIAA Journal*, 32:1598–1605, 1994. http://doi.org/10.2514/3.121495.

[183] F.R. Menter and Y. Egorov. The Scale-Adaptive Simulation Method for Unsteady Turbulent Flow Predictions. Part 1: Theory and Model Description. *Flow, Turbulence and Comsbustion*, 85:113–138, 2010. http://doi.org/10.1007/s10494-010-9264-5.

[184] F.R. Menter, R.B. Langtry, S.R. Likki, Y.B. Suzen, P.G. Huang, and S. Volker. Two-Equation Eddy-Viscosity Turbulence Models for Engineering Applications. *Journal of Turbomachinery*, 128:413–422, 2006. http://doi.org/10.1115/1.2184352.

[185] G. Minelli, E.A. Hartono, V. Chernoray, L. Hjelm, B. Basara, and S. Krajnovic. Validation of PANS and active flow control for a generic truck cabin. *Journal of Wind Engineering & Industrial Aerodynamics*, 171:148–160, 2017. http://doi.org/10.1016/j.jweia.2017.10.001.

[186] G. Minelli, S. Krajnovic, and B. Basara. A Flow Control Study of a Simplified, Oscillating Truck Cabin Using PANS. *Journal of Fluids Engineering*, 140:121101–1, 2018. http://doi.org/10.1115/1.4040225.

[187] M. Mirzaei, S. Krajnovic, and B. Basara. Partially-averaged Navier–Stokes simulations of flows around two different Ahmed bodies. *Computers and Fluids*, 117:273–286, 2015. http://doi.org/10.1016/j.compfluid.2015.05.010.

[188] P. Moise, M. Zauner, and N.D. Sandham. Large-eddy simulations and modal reconstruction of laminar transonic buffet. *Journal of Fluid Dynamics*, 944:A16, 2022. http://doi.org/10.1017/jfm.2022.471.

[189] P. Moise, M. Zauner, N.D. Sandham, S. Timme, and W. He. Transonic Buffet Characteristics Under Conditions of Free and Forced Transition. *AIAA Journal*, 61:1061–1076, 2023. http://doi.org/10.1017/jfm.2022.471.

[190] P. Molton, J. Dandois, A. Lepage, V. Brunet, and R. Bur. Control of buffet phenomenon on a transonic swept wing. *AIAA Journal*, 51:761–772, 2013. http://doi.org/10.2514/1.J051000.

[191] A. Moosavifard, E. Kolb, M. Schafer, and S. Jakirlic. Investigation of the PANS Method for the Prediction of Aerodynamic Noise Around a Circular Cylinder. In *ECCOMAS 2022*, Oslo, Norway, 2022.

[192] A. Mosahebi and S. Nadarajah. An implicit and adaptive nonlinear frequency domain approach for periodic viscous flows. *Journal of Computational Physics*, 278:92–116, 2014. http://doi.org/10.1016/j.jcp.2014.08.022.

[193] A. R. G. Mundell and D. G. Mabey. Pressure fluctuations caused by transonic shock/boundary-layer interaction. *The Aeronautical Journal*, 90(897):274–282, 1986. http://doi.org/10.1017/S0001924000015864.

[194] G. Nastac and A. Frendi. An Investigation of Scale-Resolving Turbulence Models for Supersonic Retropropulsion Flows. *Fluids*, 7:362, 2022. http://doi.org/10.3390/fluids7120362.

[195] C. Norberg. Pressure forces on a circular cylinder in cross flow. In Helmut Eckelmann, J. Michael R. Graham, Patrick Huerre, and Peter A. Monkewitz, editors, *Bluff-Body Wakes, Dynamics and Instabilities*, pages 275–278. Springer Berlin Heidelberg, 1993.

[196] C. Norberg. An experimental investigation of the flow around a circular cylinder: Influence of aspect ratio. *Journal of Fluid Mechanics*, 258:287–316, 1994. http://doi.org/10.1017/S0022112094003332.

[197] H. Ogawa, H. Babinsky, M. Patzold, and T. Lutz. Shock-Wave/Boundary-Layer Interaction Control Using Three-Dimensional Bumps for Transonic Wing. *AIAA Journal*, 46:1442–1452, 2008. http://doi.org/10.2514/1.32049.

[198] Y. Ohmichi, T. Ishida, and A. Hashimoto. Numerical Investigation of Transonic Buffet on a Three-Dimensional Wing using Incremental Mode Decomposition. In *AIAA SciTech Forum 2017*, Grapevine, TX, USA, 2017.

[199] Y. Ohmichi, T. Ishida, and A. Hashimoto. Modal Decomposition Analysis of Three-Dimensional Transonic Buffet Phenomenon on a Swept Wing. *AIAA Journal*, 56:3938–3950, 2018. http://doi.org/10.2514/1.J056855.

[200] S. Osher and S. Chakravarthy. Upwind schemes and boundary conditions with applications to Euler equations in general geometries. *Journal of Computational Physics*, 50:447–481, 1983. http://doi.org/10.1016/0021-9991(83)90106-7.

[201] E. Paladini, J. Dandois, D. Sipp, and J.-Ch. Robinet. Analysis and Comparison of Transonic Buffet Phenomenon over Several Three-Dimensional Wings. *AIAA Journal*, 57:379–396, 2019. http://doi.org/10.2514/1.J056473.

[202] V.A. Pastrikakis and G.N. Barakos. Effect of active Gurney flaps on overall helicopter flight envelope. *The Aeronautical Journal*, 120:1230–1261, 2016. http://doi.org/10.1017/aer.2016.57.

[203] H. H. Pearcey. A method for the prediction of the onset of buffeting and other separation effects from wind-tunnel tests on rigid models. Technical report, 1958. AGARD Report 223.

[204] H. H. Pearcey and D. W. Holder. Simple method for the prediction of wing buffeting resulting from bubble type separation. Technical report, NPL, 1962. Aero Report 1024.

[205] F.S. Pereira, G. Vaz, and L. Eca. An assessment of Scale-Resolving Simulation models for the flow around a circular cylinder. *Turbulence, Heat and Mass Transfer*, 8, 2015.

[206] F.S. Pereira, G. Vaz, L. Eca, and S.S. Girimaji. Simulation of the flow around a circular cylinder at Re=3900 with Partially-Averaged Navier-Stokes equations. *International Journal of Heat and Fluid Flow*, 69:234–246, 2018.

[207] A. Petrocchi and G. N. Barakos. Transonic Buffet Simulation using a Partially-averaged Navier-Stokes Approach. In *ECCOMAS 2022*, Oslo, Norway, 2022.

[208] A. Petrocchi and G.N. Barakos. Buffet boundary prediction using RANS-based criteria and adjoint methods. *Aerospace Science and Technology*, 126:107664, 2022. http://doi.org/10.1016/j.ast.2022.107664.

[209] A. Petrocchi and G.N. Barakos. Buffet boundary estimation using a harmonic balance method. *Aerospace Science and Technology*, 132:108086, 2023. http://doi.org/10.1016/j.ast.2022.108086.

[210] F. Plante, J. Dandois, and E. Laurendeau. Similarities Between Cellular Patterns Occurring in Transonic Buffet and Subsonic Stall. *AIAA Journal*, 58:71–84, 2020. http://doi.org/10.2514/1.J058555.

[211] F. Plante and E. Laurendeau. Simulation of Transonic Buffet Using a Time-Spectral Method. *AIAA Journal*, 57:1275–1277, 2019. http://doi.org/10.2514/1.J057224.

[212] P.A. Polivanov and A.A. Sidorenko. Active flow control of transonic buffet at low Reynolds number by electric discharge. *AIP Conference Proceedings*, 2288:030039, 2020. https://doi.org/10.1063/5.0028697.

[213] P.A. Polivanov, A.A. Sidorenko, and A.A. Maslov. Effective plasma buffet and drag control for laminar transonic aerofoil. *Proceedings of the Institution of Mechanical Engineers, Part G: Journal of Aerospace Engineering*, 234:58–67, 2018. http://doi.org/10.1177/0954410018795542.

[214] S.B. Pope. *Turbulent Flows*. Cambridge University Press, 1st edition, 2006.

[215] L. Poplingher and D. Raveh. Comparative Modal Study of the Two-Dimensional and Three-Dimensional Transonic Shock Buffet. *AIAA Journal*, 61:125–144, 2023. https://doi.org/10.2514/1.J061797.

[216] L. Poplingher, D. Raveh, and E. H. Dowell. Modal Analysis of Transonic Shock Buffet on 2D Airfoil. *AIAA Journal*, 57:2851–2867, 2019. http://doi.org/10.2514/1.J057893.

[217] D.E. Raveh. Numerical Study of an Oscillating Airfoil in Transonic Buffeting Flows. *AIAA Journal*, 47:505–515, 2009. http://doi.org/10.2514/1.35237.

[218] K. Ren, Y. Cheng, C. Gao, and W. Zhang. Adaptive control of transonic buffet flows over an airfoil. *Physics of Fluids*, 32:096106, 2020. http://doi.org/10.1063/5.0020496.

[219] K. Ren, C. Gao, F. Zhou, and W. Zhang. Transonic Buffet Active Control with Local Smart Skin. *Actuators*, 11:155, 2022. http://doi.org/10.3390/act11060155.

[220] F.W. Roos. Some Features of the Unsteady Pressure Field in Transonic Airfoil Buffetinge Formulation. *AIAA Journal*, 17:781–788, 1980. https://doi.org/10.2514/6.1979-351.

[221] J. Runpei, T. Yun, and L. Peiqing. Transonic buffet control by rearward Buffet Breather on supercritical airfoil and wing. *Aerospace Science and Technology*, 89:204–219, 2019. https://doi.org/10.1016/j.ast.2019.03.043.

[222] T. Yun S. Gao, P. Liu, and Q. Qu. Flap upward deflection and rearward bump combination to alleviate transonic buffet of supercritical wing. In *AIAA SciTech Forum 2018*, Kissimmee, FL, USA, 2018.

[223] A. Sansica, A. Hashimoto, S. Koike, and T. Kouchi. Side-wall effects on the global stability of swept and unswept supercritical wings at buffet conditions. In *AIAA SciTech 2022 Forum*, San Diego, CA, USA & Online, 2022.

[224] S. Saroha, K. Chakraborty, S.S. Sinha, and S. Lakshimpathy. An OpenFOAM-Based Evaluation of PANS Methodology in Conjunction with Non-Linear Eddy Viscosity: Flow Past a Heated Cylinder. *Journal of Applied Fluid Mechanics*, 13:1453–1469, 2020. http://doi.org/10.36884/jafm.13.05.30894.

[225] S. Saroha, K. Chakraborty, S.S. Sinha, and S. Lakshimpathy. Evaluation of PANS Methodology With Nonlinear Eddy Viscosity Closure: Flow Past a Heated Sphere. *Journal of Fluids Engineering*, 142:091502–1, 2020. http://doi.org/10.1115/1.4047233.

[226] F. Sartor, C. Mettot, and D. Sipp. Stability, Receptivity, and Sensitivity Analyses of Buffeting Transonic Flow over a Profile. *AIAA Journal*, 53:1980–1993, 2015. http://doi.org/10.2514/1.J053588.

[227] F. Sartor, < Minervino, J. Wild, S. Wallin, H. Maseland, J. Dandois, V. Soudakov, and P. Vrchota. A CFD benchmark of active flow control for buffet prevention. *CAES Aeronautical Journal*, 11:837–847, 2020. http://doi.org/10.1007/s13272-019-00415-z.

[228] F. Sartor and S. Timme. Reynolds-averaged navier-stokes simulations of shock buffet on half wing-body configuration. In *53rd AIAA Aerospace Sciences Meeting*, Kissimmee, FL, USA, 2015.

[229] F. Sartor and S. Timme. Mach number effects on buffeting flow on a half wing-body configuration. *International Journal of Numerical Methods for Heat & Fluid Flow*, 26:2066–2080, 2016. http://doi.org/10.1108/HFF-07-2015-0283.

[230] F. Sartor and S. Timme. Delayed Detached–Eddy Simulation of Shock Buffet on Half Wing–Body Configuration. *AIAA Journal*, 55:1230–1240, 2017. http://doi.org/10.2514/1.J055186.

[231] S. Scharnowski, K. Kokmanian, C. Schafer, T. Baur, A. Accorinti, and C.J.Kahler. Shock-buffet analysis on a supercritical airfoil with a pitching degree of freedom. *Experiments in Fluids*, 63:93, 2022. http://doi.org/10.1007/s00348-022-03427-4.

[232] M.L. Shur, P.R. Spalart, M.K. Strelets, and A.K. Travin. A hybrid RANS-LES approach with delayed-DES and wall-modeled LES capabilities. *International Journal of Heat and Fluid Flow*, 29:1638,1649, 2008. http://doi.org/10.1007/s00162-006-0015-0.

[233] M.L. Shur, P.R. Spalart, M.K. Strelets, and A.K. Travin. An Enhanced Version of DES with Rapid Transition from RANS to LES in Separated Flows. *Flow, Turbulence and Combustion*, 95:709,737, 2015. http://doi.org/10.1007/s10494-015-9618-0.

[234] A.A. Sidorenko, A.D. Budovsky, P.A. Polivanov, O.I. Vishnyakov, V.G. Sudankov, and V.N. Ishchennko. Suppression of transonic buffet with plasma vortex generators. *Thermophysics and Aeromechanics*, 26:465–480, 2019. http://doi.org/10.1134/S0869864319040012.

[235] J. Smagorinsky. General Circulation Experiments with the Primitive Equations. *Monthly Weather Revies*, 91:99–164, 1963. http://doi.org/10.1175/1520-0493(1963)091<0099:GCEWTP>2.3.CO;2.

[236] A. N. Smith, H. Babinsky, J. L. Fulker, and P. R. Ashill. Shock-Wave/Boundary-Layer Interaction Control Using Streamwise Slots in Transonic Flows. *JOURNAL OF AIRCRAFT*, 41:540–546, 2004. http://doi.org/10.2514/1.11479.

[237] A.M.O. Smith and T. Cebeci. Numerical solution of the turbulent boundary layer equations. Technical report, Douglas aircraft division report, 1967. DAC 33735.

[238] C-S. Song and S.-O Park. Numerical simulation of flow past a square cylinder using Partially-Averaged Navier–Stokes model. *Journal of Wind Engineering and Industrial Aerodynamics*, 97:37–47, 2009. http://doi.org/10.1016/j.jweia.2008.11.004.

[239] L.J. Souverein and J.F. Debièvet. Effect of air jet vortex generators on a shock wave boundary layer interaction. *Experiments in Fluids*, 49:1053–1064, 2010. http://doi.org/10.1007/s00348-010-0854-8.

[240] P. Spalart and C.L. Streett. Young-Person's Guide to Detached-Eddy Simulation Grids. Technical report, National Aeronautics and Space Administration, 2001. NASA/CR-2001-211032.

[241] P.R. Spalart and S. R. Allmaras. A one-equation turbulence model for aerodynamic flows. In *30th Aerospace Sciences Meeting and Exhibit*, 1992.

[242] P.R. Spalart, S. Deck, M.L. Shur, K.D. Squires, M.K. Strelets, and A. Travin. A new version of detached-eddy simulation, resistant to ambiguous grid densities. *Theoretical and Computational Fluid Dynamics*, 20:181–195, 2006. http://doi.org/10.1016/j.ijheatfluidflow.2008.07.001.

[243] P.R. Spalart, W.H. Jou, M. Strelets, and S.R. Allmaras. Comments on the feasibility of les for wings, and on a hybrid rans/les approach. In *Advances in DNS/LES: Direct numerical simulation and large eddy simulation*, Reno, NV, USA, 1997.

[244] P.R. Spalart and C.L. Rumsey. Effective Inflow Conditions for Turbulence Models in Aerodynamic Calculations. *AIAA Journal*, 45:2544–2553, 2007. http://doi.org/10.1025/1.29737.

[245] R. Srinivasan and S.S. Girimaji. Partially-Averaged Navier–Stokes Simulations of High-Speed Mixing Environmentediction. *Journal of Fluids Engineering*, 136:060903–1, 2011. http://doi.org/10.1115/1.4026234.

[246] W. Stalewski and J. Snazdjer. Load control of natural-laminar-flow wing via boundary layer control. In *ECCOMAS Congress 2016*, Crete Island, Greece, 2016.

[247] E. Stanewsky and D. Basler. Experimental investigation of buffet onset and penetration on a supercritical airfoil at transonic speeds. In *AGARD Specialists Meeting on 'Aircraft Dynamic Loads due to Flow Sepa ration', 1-6 April 1990, Sorrento, Italy.*, 1990.

[248] R. Steijl and G. Barakos. Sliding mesh algorithm for CFD analysis of helicopter rotor–fuselage aerodynamics. *International Journal for Numerical Methods in Fluids*, 58:527–549, 2008. http://doi.org/10.1002/fld.1757.

[249] R. Steijl, G. Barakos, and K. Badcock. A framework for CFD anal-ysis of helicopter rotors in hover and forward flight. *International Journal for Numerical Methods in Fluids*, 51:819–847, 2006. http://doi.org/10.1002/fld.1086.

[250] M. Strelets. Detached eddy simulation of massively separated flows. In *39th Aerospace Sciences Meeting and Exhibit*, Reno, NV, USA, 2001.

[251] Y. Sugioka, S. Koike, K. Nakakita, D. Numata, T. Nonomura, and K. Asai. Experimental analysis of transonic buffet on a 3D swept wing using fast-response pressure-sensitive paint. *Experiments in Fluids*, 59:1–20, 2018. http://doi.org/10.1007/s00348-018-2565-5.

[252] Y. Sugioka, T. Kouchi, and S. Koike. Experimental comparison of shock buffet on unswept and 10-deg swept wings. *Experiments in Fluids*, 632:132, 2022. http://doi.org/10.1007/s00348-022-03482-x.

[253] Y. Sugioka, K. Nakakita, S. Koike, T. Nakajima, T. Nonomura, and K. Asai. Characteristic unsteady pressure field on a civil aircraft wing related to the onset of transonic buffet. *Experiments in Fluids*, 62:20, 2021. http://doi.org/10.1007/s00348-020-03118-y.

[254] Y. Sugioka, D. Numata, K. Asai, S. Koike, K. Nakakita, and S. Koga. Unsteady psp measurement of transonic buffet on a wing. In *53rd AIAA Aerospace Sciences Meeting*, Kissimmee, FL, USA, 2015.

[255] D. Szubert, F. Grossi, A.J. Garcia, Y. Hoarau, J.C.R. Hunt, and M. Braza. Shock-vortex shear-layer interaction in the transonic flow around a supercritical airfoil at high Reynols number in buffet conditions. *Journals of Fluids and Structures*, 55:276–302, 2020. http://doi.org/10.1016/j.jfluidstructs.2015.03.005.

[256] O. Szulc, P. Doerffer, P. Flaszynski, and T. Suresh. Numerical modelling of shock wave-boundary layer interaction control by passive wall ventilation. *Computers and Fluids*, 200:1–21, 2020. http://doi.org/10.1016/j.compfluid.2020.104435.

[257] M. Thiery and E. Coustols. URANS Computations of Shock-Induced Oscillations Over 2D Rigid Airfoils: Influence of Test Section Geometry. *Flow, Turbulence and Combustion*, 74:331–354, 2005. http://doi.org/10.1007/s10494-005-0557-z.

[258] M. Thiery and E. Coustols. Numerical prediction of shock induced oscillations over a 2D airfoil: Influence of turbulence modelling and test section walls. *International Journal of Heat and Fluid Flow*, 27:661–670, 2006. http://doi.org/10.1016/j.ijheatfluidflow.2006.02.013.

[259] Y. Tian, P. Feng, P. Liu, T. Hu, and Q. Qu. Spoiler Upward Deflection on Transonic Buffet Control of Supercritical Airfoil and Wing. *Journal of Aircraft*, 54:1227–1231, 2017. http://doi.org/10.2514/1.C033574.

[260] Y. Tian, S. Gao, P. Liu, and J. Wang. Transonic buffet control research with two types of shock control bump based on RAE2822 airfoil. *Chinese Journal of Aeronautics*, 30:1681–1696, 2017. http://doi.org/10.1016/j.cja.2017.07.011.

[261] Y. Tian, Z. Li, and P.Q. Liu. Upper Trailing-Edge Flap for Transonic Buffet Control. *Journal of Aircraft*, 55:382–389, 2018. http://doi.org/10.2514/1.C033134.

[262] H. Tijdeman. Investigation of the transonic flow around oscillating airfoils. Technical report, National Aerospace Laborator, The Netherlands, 1977. RNLR TR 77090 U.

[263] S. Timme. Global shock buffet instability on nasa common research model. In *AIAA SciTech 2019 Forum*, San Diego, CA, USA, 2019.

[264] S. Timme. Global instability of wing shock-buffet onset. *Journal of Fluid Mechanics*, 885:A37, 2020. http://doi.org/10.1017/jfm.2019.1001.

[265] S. Timme and F. Sartor. Passive control of transonic buffet onset on a half wing-body configuration. In *International Forum on Aeroelasticity and Structural Dynamics*.

[266] S. Timme and R. Thormann. Towards three-dimensional global stability analysis of transonic shock buffet. In *AIAA Atmospheric Flight Mechanics Conference*, Washington D.C., USA, 2016.

[267] N. Titchener and H. Babinsky. Numerical modelling of shock wave-boundary layer interaction control by passive wall ventilation. *AIAA Journal*, 51:1221–1233, 2013. http://doi.org/10.2514/1.J052079.

[268] N. Titchener and H. Babinsky. A review of the use of vortex generators for mitigating shock-induced separation. *Shock Waves*, 25:473–494, 2015. http://doi.org/10.1007/s00193-015-0551-x.

[269] A. Travin, M. Shur, M. Strelets, and P. Spalart. Detached-Eddy Simulations Past a Circular Cylinder. *Flow. Turbulence and Combustion*, 63:293–313, 2000. http://doi.org/10.1023/A:1009901401183.

[270] K. Uchida, Y. Sugioka, M. Kasai, Y. Saito, T. Nonomura, K. Asai, K. Nakakita, Y. Nishizaki, Y. Shibata, and S. Sonoda. Analysis of transonic buffet on ONERA-M4 model with unsteady pressure-sensitive paint. *Experiments in Fluids*, 62:133–151, 2021. http://doi.org/10.1007/s00348-021-03228-1.

[271] A. Uzun and M.R. Malik. Wall-resolved large-eddy simulations of transonic shock-induced flow separation. *AIAA Journal*, 57:1955–1972, 2020. http://doi.org/10.2514/1.J057850.

[272] G. van Aldaba, B. van Leer, and W. Roberts. A comparativestudy of computational methods in cosmic gas dynamics. *Astronomics and Astrophysics*, 108:76–84, 1982.

[273] B. van Leer. Towards the ultimate conservative difference scheme. V. A second-order sequel to Godunov's method. *Journal of Computational Physics*, 32:101–136, 1979. http://doi.org/10.1016/0021-9991(79)90145-1.

[274] V.N. Vatsa and B.A. Singer. Evaluation of a second-order accurate navier-stokes code for detached eddy simulation past a circular cylinder. In *21st AIAA Computational Fluid Dynamics Conference*, Orlando, FL, USA, 2003.

[275] M.R. Visbal, P.E. Morgan, and D.P. Rizzetta. An implicit iles approach based on high-order compact differencing and filtering schemes. In *16th AIAA Computational Fluid Dynamics Conference*, Orlando, FL, USA, 2003.

[276] O.I. Vishnyakov, P.A. Polivanov, A.D. Budovskiy, A.A. Sidorenko, and A.A. Maslov. Control of buffet onset by plasma-based actuators. *AIP Conference Proceedings*, 1770:030024, 2016. https://doi.org/10.1063/1.4963966.

[277] A. V. Voevodin, A. A. Kornyakov, A. S. Petrov, D. A. Petrov, and G. G. Soudakov. Wing buffet control by using an ejector-type device. *Journal of Applied Mechanics and Technical Physics*, 62:308–316, 2021. https://doi.org/10.1134/S0021894421020152.

[278] J. Wang, G. Minelli, G. Cafiero, G. Iuso, K. He, B. Basara, G. Gao, and S. Krajnovic. Validation of PANS and effects of ground and wheel motion on the aerodynamic behaviours of a square-back vani. *Journal of Fluid Mechanics*, 958:A47, 2023. http://doi.org/10.1017/jfm.2023.47.

[279] D. C. Wilcox. Formulation of the $k-\omega$ Turbulence Model Revisited. *AIAA Journal*, 46:2823–2838, 2008. http://doi.org/10.2514/1.36541.

[280] C.H.K. Williamson. Defining a Universal and Continuous Strouhal– Reynolds Number Relationship for the Laminar Vortex Shedding of a Circular Cylinder. *Physics of Fluids*, 31:2741, 1988. http://doi.org/10.1063/1.866978.

[281] M. A. Woodgate and G. N. Barakos. Implicit Computational Fluid Dynamics Methods for Fast Analysis of Rotor Flows. *AIAA Journal*, 50:1217 – 1244, 2012. http://doi.org/10.2514/1.J051155.

[282] M. A. Woodgate, V. A. Pastrikakis, and G. N. Barakos. Rotor computations with active gurney flaps. In Marianna Braza, Alessandro Bottaro, and Mark Thompson, editors, *Advances in Fluid-Structure Interaction*, pages 133–166. Springer International Publishing, 2016.

[283] Q. Xiao, H. M. Tsai, and F.Liu. Numerical Study of Transonic Buffet on a Supercritical Airfoil. *AIAA Journal*, 44:620 – 628, 2006. http://doi.org/10.2514/1.16658.

[284] Z. Yang and H. Ogawa. Numerical analysis of transonic buffet control using a two-dimensional bump for a supercritical aerofoil. In X. Zhang, editor, *The Proceedings of the 2018 Asia-Pacific International Symposium on Aerospace Technology (APISAT 2018)*, pages 854–869. Springer Singapore, 2018.

[285] M. Zauner, P. Moise, and N.D. Sandham. On the co-existence of transonic buffet and separation-bubble modes for the OALT25 laminar-flow wing section. *Flow, Turbulence and Combustion*, 110:1023–1057, 2023. http://doi.org/10.1007/s10494-023-00415-4.

[286] M. Zauner and N.D. Sandham. Wide domain simulations of flow over an unswept laminar wing section undergoing transonic buffet. *Physical Review Fluids*, 5:083903, 2020. http://doi.org/10.1103/PhysRevFluids.5.083903.

[287] J. Zhang, G. Minelli, A.N. Rao, B. Basara, R. Bensow, and S. Krajnovic. Comparison of PANS and LES of the flow past a generic ship. *Ocean Engineering*, 165:221–236, 2018. http://doi.org/10.1016/j.oceaneng.2018.07.02333.

[288] S. Zhang, F. Deng, and N. Qin. Cooperation of Trailing-Edge Flap and Shock Control Bump for Robust Buffet Control and Drag Reduction. *Aerospace*, 9:657, 2022. http://doi.org/10.3390/aerospace9110657.

[289] Y. Zhang, P. Yang, R. Li, and H. Chen. Unsteady Simulation of Transonic Buffet of a Supercritical Airfoil with Shock Control Bump . *Aerospace*, 8:203, 2021. http://doi.org/10.3390/aerospace8080203.

[290] Y. Zhao, Z. Dai, Y. Tian, and Y. Xiong. Flow characteristics around airfoils near transonic buffet onset conditions. *Chinese Journal of Aeronautics*, 33:1405–1420, 2020. http://doi.org/10.1016/j.cja.2019.12.022.

[291] W. Zhou, Z. Zhang, K. Qu, and H. S. Tang. Numerical investigation of shock oscillation over airfoils at transonic speeds influenced by trailing edge jet. In *21st AIAA Computational Fluid Dynamics Conference*, San Diego, CA, USA, 2013.

[292] W. Zhou, Z. Zhang, K. Qu, and H. S. Tang. Numerical investigation of transonic airfoil buffet suppression. In *AIAA SciTech Forum 2015*, Kissimmee, FL, USA, 2015.

[293] D.-M. Zimmermann, R. Mayer, T. Luiz, and E. Kramer. Impact of Model Parameters of SALSA Turbulence Model on Transonic Buffet Prediction. *AIAA Journal*, 56:874–877, 2018. http://doi.org/10.2514/1.J056193.